

Pertanika Journal of
**SCIENCE &
TECHNOLOGY**

JST

VOL. 25 (S) MAR. 2017

A special issue devoted to
Advances in Science & Technology Research

Guest Editors
Aidah Jumahat, Chen Ai Hong & Ismail Musirin



PERTANIKA
JOURNALS

A scientific journal published by Universiti Putra Malaysia Press

Journal of Science & Technology

About the Journal

Overview

Pertanika Journal of Science & Technology (JST) is the official journal of Universiti Putra Malaysia published by UPM Press. It is an open-access online scientific journal which is free of charge. It publishes the scientific outputs. It neither accepts nor commissions third party content.

Recognized internationally as the leading peer-reviewed interdisciplinary journal devoted to the publication of original papers, it serves as a forum for practical approaches to improving quality in issues pertaining to science and engineering and its related fields.

JST is a **quarterly** (January, April, July and October) periodical that considers for publication original articles as per its scope. The journal publishes in **English** and it is open to authors around the world regardless of the nationality.

The Journal is available world-wide.

Aims and scope

Pertanika Journal of Science and Technology aims to provide a forum for high quality research related to science and engineering research. Areas relevant to the scope of the journal include: bioinformatics, bioscience, biotechnology and bio-molecular sciences, chemistry, computer science, ecology, engineering, engineering design, environmental control and management, mathematics and statistics, medicine and health sciences, nanotechnology, physics, safety and emergency management, and related fields of study.

History

Pertanika was founded in 1978. A decision was made in 1992 to streamline Pertanika into three journals as Journal of Tropical Agricultural Science, Journal of Science & Technology, and Journal of Social Sciences & Humanities to meet the need for specialised journals in areas of study aligned with the interdisciplinary strengths of the university.

After almost 25 years, as an interdisciplinary Journal of Science & Technology, the revamped journal now focuses on research in science and engineering and its related fields.

Goal of *Pertanika*

Our goal is to bring the highest quality research to the widest possible audience.

Quality

We aim for excellence, sustained by a responsible and professional approach to journal publishing. Submissions are guaranteed to receive a decision within 14 weeks. The elapsed time from submission to publication for the articles averages 5-6 months.

Abstracting and indexing of *Pertanika*

Pertanika is almost 40 years old; this accumulated knowledge has resulted in Pertanika JST being abstracted and indexed in SCOPUS (Elsevier), Thomson (ISI) Web of Knowledge [BIOSIS & CAB Abstracts], EBSCO & EBSCOhost, DOAJ, ERA, Cabell's Directories, Google Scholar, MyAIS, ISC & Rubriq (Journal Guide).

Future vision

We are continuously improving access to our journal archives, content, and research services. We have the drive to realise exciting new horizons that will benefit not only the academic community, but society itself.

Citing journal articles

The abbreviation for Pertanika Journal of Science & Technology is *Pertanika J. Sci. Technol.*

Publication policy

Pertanika policy prohibits an author from submitting the same manuscript for concurrent consideration by two or more publications. It prohibits as well publication of any manuscript that has already been published either in whole or substantial part elsewhere. It also does not permit publication of manuscript that has been published in full in Proceedings.

Code of Ethics

The Pertanika Journals and Universiti Putra Malaysia takes seriously the responsibility of all of its journal publications to reflect the highest in publication ethics. Thus all journals and journal editors are expected to abide by the Journal's codes of ethics. Refer to Pertanika's **Code of Ethics** for full details, or visit the Journal's web link at http://www.pertanika.upm.edu.my/code_of_ethics.php

International Standard Serial Number (ISSN)

An ISSN is an 8-digit code used to identify periodicals such as journals of all kinds and on all media—print and electronic. All Pertanika journals have ISSN as well as an e-ISSN.

Journal of Science & Technology: ISSN 0128-7680 (*Print*); ISSN 2231-8526 (*Online*).

Lag time

A decision on acceptance or rejection of a manuscript is reached in 3 to 4 months (average 14 weeks). The elapsed time from submission to publication for the articles averages 5-6 months.

Authorship

Authors are not permitted to add or remove any names from the authorship provided at the time of initial submission without the consent of the Journal's Chief Executive Editor.

Manuscript preparation

Refer to Pertanika's **INSTRUCTIONS TO AUTHORS** at the back of this journal.

Most scientific papers are prepared according to a format called IMRAD. The term represents the first letters of the words **I**ntroduction, **M**aterials and **M**ethods, **R**esults, **A**nd, **D**iscussion. IMRAD is simply a more 'defined' version of the "IBC" [Introduction, Body, Conclusion] format used for all academic writing. IMRAD indicates a pattern or format rather than a complete list of headings or components of research papers; the missing parts of a paper are: *Title, Authors, Keywords, Abstract, Conclusions, and References*. Additionally, some papers include Acknowledgments and Appendices.

The *Introduction* explains the scope and objective of the study in the light of current knowledge on the subject; the *Materials and Methods* describes how the study was conducted; the *Results* section reports what was found in the study; and the *Discussion* section explains meaning and significance of the results and provides suggestions for future directions of research. The manuscript must be prepared according to the Journal's **INSTRUCTIONS TO AUTHORS**.

Editorial process

Authors are notified with an acknowledgement containing a *Manuscript ID* on receipt of a manuscript, and upon the editorial decision regarding publication.

Pertanika follows a **double-blind peer-review** process. Manuscripts deemed suitable for publication are usually sent to reviewers. Authors are encouraged to suggest names of at least three potential reviewers at the time of submission of their manuscript to Pertanika, but the editors will make the final choice. The editors are not, however, bound by these suggestions.

Notification of the editorial decision is usually provided within ten to fourteen weeks from the receipt of manuscript. Publication of solicited manuscripts is not guaranteed. In most cases, manuscripts are accepted conditionally, pending an author's revision of the material.

As articles are double-blind reviewed, material that might identify authorship of the paper should be placed only on page 2 as described in the first-4 page format in Pertanika's **INSTRUCTIONS TO AUTHORS** given at the back of this journal.

The Journal's peer-review

In the peer-review process, three referees independently evaluate the scientific quality of the submitted manuscripts.

Peer reviewers are experts chosen by journal editors to provide written assessment of the **strengths** and **weaknesses** of written research, with the aim of improving the reporting of research and identifying the most appropriate and highest quality material for the journal.

Operating and review process

What happens to a manuscript once it is submitted to *Pertanika*? Typically, there are seven steps to the editorial review process:

1. The Journal's chief executive editor and the editorial board examine the paper to determine whether it is appropriate for the journal and should be reviewed. If not appropriate, the manuscript is rejected outright and the author is informed.
2. The chief executive editor sends the article-identifying information having been removed, to three reviewers. Typically, one of these is from the Journal's editorial board. Others are specialists in the subject matter represented by the article. The chief executive editor asks them to complete the review in three weeks.

Comments to authors are about the appropriateness and adequacy of the theoretical or conceptual framework, literature review, method, results and discussion, and conclusions. Reviewers often include suggestions for strengthening of the manuscript. Comments to the editor are in the nature of the significance of the work and its potential contribution to the literature.

3. The chief executive editor, in consultation with the editor-in-chief, examines the reviews and decides whether to reject the manuscript, invite the author(s) to revise and resubmit the manuscript, or seek additional reviews. Final acceptance or rejection rests with the Editor-in-Chief, who reserves the right to refuse any material for publication. In rare instances, the manuscript is accepted with almost no revision. Almost without exception, reviewers' comments (to the author) are forwarded to the author. If a revision is indicated, the editor provides guidelines for attending to the reviewers' suggestions and perhaps additional advice about revising the manuscript.
4. The authors decide whether and how to address the reviewers' comments and criticisms and the editor's concerns. The authors return a revised version of the paper to the chief executive editor along with specific information describing how they have answered the concerns of the reviewers and the editor, usually in a tabular form. The author(s) may also submit a rebuttal if there is a need especially when the author disagrees with certain comments provided by reviewer(s).

5. The chief executive editor sends the revised paper out for re-review. Typically, at least one of the original reviewers will be asked to examine the article.
6. When the reviewers have completed their work, the chief executive editor in consultation with the editorial board and the editor-in-chief examine their comments and decide whether the paper is ready to be published, needs another round of revisions, or should be rejected.
7. If the decision is to accept, an acceptance letter is sent to all the author(s), the paper is sent to the Press. The article should appear in print in approximately three months.

The Publisher ensures that the paper adheres to the correct style (in-text citations, the reference list, and tables are typical areas of concern, clarity, and grammar). The authors are asked to respond to any minor queries by the Publisher. Following these corrections, page proofs are mailed to the corresponding authors for their final approval. At this point, **only essential changes are accepted**. Finally, the article appears in the pages of the Journal and is posted on-line.



Pertanika Journal of
**SCIENCE &
TECHNOLOGY**

A special issue devoted to
Advances in Science & Technology Research

Vol. 25 (S) Mar. 2017
(Special Edition)

Guest Editors
Aidah Jumahat, Chen Ai Hong & Ismail Musirin

A scientific journal published by Universiti Putra Malaysia Press



EDITOR-IN-CHIEF

Mohd Adzir Mahdi

Physics, Optical Communications

CHIEF EXECUTIVE EDITOR

Nayan Deep S. Kanwal

Environmental Issues – Landscape Plant Modelling Applications

UNIVERSITY PUBLICATIONS COMMITTEE

Husaini Omar, Chair

EDITORIAL STAFF

Journal Officers:

Kanagamalar Silvarajoo, *ScholarOne*

Tee Syin-Ying, *ScholarOne*

Editorial Assistants:

Zulinaardawati Kamarudin

Florence Jiyom

Ummi Fairuz Hanapi

Rahimah Razali

COPY EDITORS

Doreen Dillah

Crescentia Morais

Pooja Terasha Stanslas

PRODUCTION STAFF

Pre-press Officers:

Nur Farrah Dila Ismail

Layout & Typeset:

Loh Kian Lin

WEBMASTER

Mohd Nazri Othman

PUBLICITY & PRESS RELEASE

Magdalene Pokar (*ResearchSEA*)

Florence Jiyom

EDITORIAL OFFICE

JOURNAL DIVISION

Office of the Deputy Vice Chancellor (R&I)

1st Floor, IDEA Tower II

UPM-MTDC Technology Centre

Universiti Putra Malaysia

43400 Serdang, Selangor Malaysia.

Gen Enq.: +603 8946 1622 | 1616

E-mail: executive_editor.pertanika@upm.my

URL: www.journals-ijd.upm.edu.my

PUBLISHER

Kamariah Mohd Saidin

UPM Press

Universiti Putra Malaysia

43400 UPM, Serdang, Selangor, Malaysia.

Tel: +603 8946 8855, 8946 8854

Fax: +603 8941 6172

E-mail: penerbit@putra.upm.edu.my

URL: <http://penerbit.upm.edu.my>

EDITORIAL BOARD

2015-2017

Abdul Halim Shaari

Superconductivity and Magnetism, Universiti Putra Malaysia, Malaysia.

Adem Kilicman

Mathematical Sciences, Universiti Putra Malaysia, Malaysia.

Ahmad Makmom Abdullah

Ecophysiology and Air Pollution Modelling, Universiti Putra Malaysia, Malaysia.

Ali A. Moosavi-Movahedi

Biophysical Chemistry, University of Tehran, Tehran, Iran.

Amu Therwath

Oncology, Molecular Biology, Université Paris, France.

Angelina Chin

Mathematics, Group Theory and Generalisations, Ring Theory, University of Malaya, Malaysia.

Bassim H. Hameed

Chemical Engineering: Reaction Engineering, Environmental Catalysis & Adsorption, Universiti Sains Malaysia, Malaysia.

Biswa Mohan Biswal

Medical, Clinical Oncology, Radiotherapy, Universiti Sains Malaysia, Malaysia.

Christopher G. Jesudason

Mathematical Chemistry, Molecular Dynamics Simulations, Thermodynamics and General Physical Theory, University of Malaya, Malaysia.

Hari M. Srivastava

Mathematics and Statistics, University of Victoria, Canada.

Ivan D. Rukhlenko

Nonlinear Optics, Silicon Photonics, Plasmonics and Nanotechnology, Monash University, Australia.

Kaniraj R. Shenbaga

Geotechnical Engineering, Universiti Malaysia Sarawak, Malaysia.

Kanury Rao

Senior Scientist & Head, Immunology Group, International Center for Genetic Engineering and Biotechnology, Immunology, Infectious Disease Biology and System Biology, International Centre for Genetic Engineering & Biotechnology, New Delhi, India.

Karen Ann Crouse

Chemistry, Material Chemistry, Metal Complexes – Synthesis, Reactivity, Bioactivity, Universiti Putra Malaysia, Malaysia.

Ki-Hyung Kim

Computer and Wireless Sensor Networks, AIOU University, Korea.

Kunnawee Kanitpong

Transportation Engineering-Road Traffic Safety, Highway Materials and Construction, Asian Institute of Technology, Thailand.

Megat Mohd Hamdan

Megat Ahmad Mechanical and Manufacturing Engineering, Universiti Pertahanan Nasional Malaysia, Malaysia.

Miralini Kandiah

Public Health Nutrition, Nutritional Epidemiology, UCSI University, Malaysia.

Mohamed Othman

Communication Technology and Network, Scientific Computing, Universiti Putra Malaysia, Malaysia.

Mohd. Ali Hassan

Bioprocess Engineering, Environmental Biotechnology, Universiti Putra Malaysia, Malaysia.

Mohd Sapuan Salit

Concurrent Engineering and Composite Materials, Universiti Putra Malaysia, Malaysia.

Narongrit Sombatsompop

Engineering & Technology: Materials and Polymer Research, King Mongkut's University of Technology Thonburi (KMUTT), Thailand.

Prakash C. Sinha

Physical Oceanography, Mathematical Modelling, Fluid Mechanics, Numerical Techniques, Universiti Malaysia Terengganu, Malaysia.

Rajinder Singh

Biotechnology, Biomolecular Sciences, Molecular Markers/ Genetic Mapping, Malaysia Palm Oil Board, Kajang, Malaysia.

Renuganth Varatharajoo

Engineering, Space System, Universiti Putra Malaysia, Malaysia.

Riyanto T. Bambang

Electrical Engineering, Control, Intelligent Systems & Robotics, Bandung Institute of Technology, Indonesia.

Sabira Khatun

Engineering, Computer Systems & Software Engineering, Applied Mathematics, Universiti Malaysia Pahang, Malaysia.

Shiv Dutt Gupta

Director, IHMR, Health Management, Public Health, Epidemiology, Chronic and Non-communicable Diseases, Indian Institute of Health Management Research, India.

Suan-Choo Cheah

Biotechnology, Plant Molecular Biology, Asiatic Centre for Genome Technology (ACGT), Kuala Lumpur, Malaysia.

Wagar Asrar

Engineering, Computational Fluid Dynamics, Experimental Aerodynamics, International Islamic University, Malaysia.

Wing Keong Ng

Aquaculture, Aquatic Animal Nutrition, Aqua Feed Technology, Universiti Sains Malaysia, Malaysia.

Yudi Samyudia

Chemical Engineering, Advanced Process Engineering, Curtin University of Technology, Malaysia.

INTERNATIONAL ADVISORY BOARD

2017-2019

Adarsh Sandhu

Editorial Consultant for Nature Nanotechnology and Contributing Writer for Nature Photonics, Physics, Magneto-resistive Semiconducting Magnetic Field Sensors, Nano-Bio-Magnetism, Magnetic Particle Colloids, Point of Care Diagnostics, Medical Physics, Scanning Hall Probe Microscopy, Synthesis and Application of Graphene, Electronics-inspired Interdisciplinary Research Institute (EIIRIS), Toyohashi University of Technology, Japan.

Graham Megson

Computer Science, The University of Westminster, U.K.

Kuan-Chong Ting

Agricultural and Biological Engineering, University of Illinois at Urbana-Champaign, USA.

Malin Premaratne

Advanced Computing and Simulation, Monash University, Australia.

Mohammed Ismail Elnaggar

Electrical Engineering, Ohio State University, USA.

Peter G. Alderson

Bioscience, The University of Nottingham, Malaysia Campus.

Peter J. Heggs

Chemical Engineering, University of Leeds, U.K.

Ravi Prakash

Vice Chancellor, JUIT, Mechanical Engineering, Machine Design, Biomedical and Materials Science, Jaypee University of Information Technology, India.

Said S.E.H. Elnashaie

Environmental and Sustainable Engineering, Penn. State University at Harrisburg, USA.

Suhash Chandra Dutta Roy

Electrical Engineering, Indian Institute of Technology (IIT) Delhi, India.

Vijay Arora

Quantum and Nano-Engineering Processes, Wilkes University, USA.

Yi Li

Chemistry, Photochemical Studies, Organic Compounds, Chemical Engineering, Chinese Academy of Sciences, Beijing, China.

ABSTRACTING/INDEXING

Pertanika is now over 40 years old; this accumulated knowledge has resulted the journals being indexed in abstracted in SCOPUS (Elsevier), Thomson (ISI) Web of Knowledge [ESCI, BIOSIS & CAB Abstracts], EBSCO & EBSCOhost, ERA, DOAJ, AGRICOLA (National Agric. Library, USA), Cabell's Directories, Google Scholar, MyAIS, Islamic World Science Citation Center (ISC), ASEAN Citation Index (ACI) & Rubriq (Journal Guide).



The publisher of *Pertanika* will not be responsible for the statements made by the authors in any articles published in the journal. Under no circumstances will the publisher of this publication be liable for any loss or damage caused by your reliance on the advice, opinion or information obtained either explicitly or implied through the contents of this publication.

All rights of reproduction are reserved in respect of all papers, articles, illustrations, etc., published in *Pertanika*. *Pertanika* provides free access to the full text of research articles for anyone, web-wide. It does not charge either its authors or author-institution for refereeing/publishing outgoing articles or user-institution for accessing incoming articles.

No material published in *Pertanika* may be reproduced or stored on microfilm or in electronic, optical or magnetic form without the written authorization of the Publisher.

Copyright © 2017 Universiti Putra Malaysia Press. All Rights Reserved.



Preface

We are very pleased to present this special issue of the *Pertanika Journal of Science and Technology (JST)*, a compilation of selected papers that were presented at the 3rd International Conference on Science and Social Research (CSSR2016). The CSSR2016 was held from 6th – 7th December 2016 in Putrajaya. Themed “Waves of Interdisciplinary Research” the conference track was divided into: Track 1: Engineering, Science & Technology; Track 2: Clinical & Health sciences; and Track 3: Arts, Humanities & Social sciences. The papers were subjected to rigorous peer reviewing process to ensure quality. A total of 188 papers in Track 1 and Track 2 were presented during the conference, 38 of which were accepted for publication in this special issue.

The theme of the issue is “Advances in Science and Technology Research” and In line with this, the areas covered included biotechnology, aerospace engineering, infrastructural engineering, medical biochemistry, pharmacology, biomass energy, environmental sciences, clinical sciences, materials processing, composite materials, wastewater treatment, hydrology, optometry, analytical chemistry, electronic materials, nanotechnology, tribology, metals and alloys, plastics, polymers, artificial Intelligence, food industry, information system, electrical engineering, image processing, electrochemical materials, chemistry, applied statistics and power engineering.

We would like to thank the contributors and reviewers for their commitment and patience which made JST-CSSR2016 a success. It is hoped that this publication would encourage academicians from around the world to be more active in publishing their research output. Special thanks to the Chief Executive Editor, UPM Journals, Dr. Nayan Kanwal, and his staff for their guidance and support.

Guest Editors:

Aidah Jumahat (*Assoc. Prof. Dr.*)

Chen Ai Hong (*Prof. Dr.*)

Ismail Musirin (*Prof. Dr.*)

March 2017



Pertanika Journal of Science & Technology
Vol. 25 (S) Mar. 2017

Contents

Advances in Science and Technology Research

- Ganoderma boninense* Efficacy in Delignifying Oil Palm Empty Fruit Bunches 1
Siti Sarah Jumali and Shaleha Ismail
- Numerical Study of Aerodynamic Characteristics on Blended Wing Body Aircraft with Small Canard 9
Zurriati Mohd Ali, Wahyu Kuntjoro, Wirachman Wisnoe, Rizal Effendy Mohd Nasir and Noor Iswadi Ismail
- Investigation on Moisture Susceptibility and Rutting Resistance of Asphalt Mixtures incorporating Nanosilica Modified Binder 19
Ahmad Kamil Arshad, Khairil Azman Masri, Juraidah Ahmad and Mohamad Saifullah Samsudin
- Mechanism of Aloe Emodin-Induced Apoptosis in ER+-Breast Cancer Cells, MCF-7 31
Indah Mohd Amin, Siti Hamimah Sheikh Abdul Kadir, Mohamad Rodi Isa, Nik Mohd Mazuan Nik Mohd Rosdy and Narimah Abdul Hamid Hasani
- Anti- Oral Ulcer Activity of *Ficus deltoidea* Leaves Extract on Animal Model 41
Vivi Noryati Ahmad and Indah Mohd Amin
- Comparison of Energy and Performance from Biodegradation of Freeze Dried and Spray Dried Algae Biomass 53
Muhamad Haikal Zainal, Khairul Baqir Alkhair Khairul Amin, Oskar Hasdinor Hassan, Sharifah Aminah Syed Mohamad, Abd Malik Marwan Ali, Fathiah Abdullah and Muhd Zu Azhan Yahya
- The Effects of Automotive Windscreen Glass Waste Powder (WGWP) On Strength Performance of Cement Mortar 63
Nik Anisah Nik Ngah, Mohamad Awang and Kartini Kamaruddin
- Preliminary Study of Cosmetic Coloured Contact Lenses Chemical Elements Analysis using Energy Dispersive X-Ray Spectroscopy 73
Syazwan Hafiz Mohd, Wan Elhami Wan Omar and Ai-Hong Chen
- Microstructure, Microhardness and Density of Shot Blasting and Paste Boronizing on 316L Stainless Steel 83
Muhamad Hafizuddin Mohamad Basir, Mohd Faizul Idham, Bulan Abdullah and Muhammad Hussain Ismail

Correlation of Case Depth with Mechanical Properties of Low Carbon Steel Using Paste Carburizing Method <i>Bulan Abdullah, Muhammad Hafizuddin Jumadin, Muhammad Hussain Ismail, Siti Khadijah Alias and Samsiah Ahmad</i>	91
Effects of Two Cycle Heat Treatment on the Microstructure and Hardness of Ductile Iron <i>Mohd Faizul Idham, Bulan Abdullah and Khalissah Muhammad Yusof</i>	99
Ferroelectric Stability of Annealed PVDF-TrFE Thin Film Incorporated with MgO Nanofillers <i>Mohamad Hafiz Mohd Wahid, Rozana Mohd Dahan, Adillah Nurashikin Arshad, Habibah Zulkefle, Siti Zaleha Sa'ad, Mohamad Rusop Mahmood, W. C. Gan and Wan Haliza Abd. Majid</i>	107
Occurrence, Source Apportionment and Environmental Risk Assessment of Pharmaceuticals in Klang River, Malaysia <i>Siti Norbayu Mohd. Subari, Rozita Osman and Norashikin Saim</i>	119
Adsorption of Acid Dyes onto Zinc Chloride-Modified Cocoa (<i>Theobroma cacao</i>) Pod Husk-Based Carbon <i>Nur Aqilah Zainal, Shariff Ibrahim and Borhannuddin Arifin</i>	129
New Method of Curve Number Derivation with Inferential Statistics <i>Lloyd Ling, Zulkifli Yusop and Yuk Feng Huang</i>	139
Discrepancy in the Accuracy of Vision Screening Program Performed by Allied Health Personnel in a Preschool <i>Nurul Farhana Abu Bakar and Ai-Hong Chen</i>	151
Effect of Blood Cockle Shell and Palm Kernel Shell Weight Ratio on the Acid Neutralizing Capacity of Calcined Products <i>Noor Mohamad Amin Salleh, Dayangku Kamilah Pengiran Ismail and Yong Soon Kong</i>	159
Optimization of Headspace Solid Phase Microextraction (HS-SPME) for the Extraction of Volatile Organic Compounds (VOCs) in Mangoes (<i>Harumanis</i> cv.) Using 2 Stages Multivariate Analysis <i>Siti Raihan Zakaria, Ruziyati Tajuddin, Rozita Osman, Norashikin Saim and Mardiana Saaid</i>	167
Optimisation of Pressurised Liquid Extraction of Bioactive Compounds from <i>Ananas comosus</i> (Pineapple) Fruit <i>Almie Amira Munaras Khan, Norashikin Saim and Rossuriati Dol Hamid</i>	174

Physical and Conductivity Studies of Plasticised Methyl Cellulose-Lithium Triflate based Polymer Electrolyte <i>Nursyahida Sahli, Nordiana Nabilla Ramly, Muhd Zu Azhan Yahya and Ab Malik Marwan Ali</i>	183
The Effect of Saccharin Concentration on the Electrochemical Behaviour of Electrodeposited Nanocrystalline Cobalt-Iron Coating <i>Nik Rozlin Nik Masdek, Wan Muhammad Aniq Aiman, Mardziah Che Murad, Zuraidah Salleh and Koay Mei Hyie</i>	191
Wear Properties of Carbon Nanotubes Filled Epoxy Polymers and Woven Glass Fiber Reinforced Polymer Composites <i>Anis Adilah Abu Talib, Aidah Jumahat, Napisah Sapiai and Ahmad Shahrul Mohd Roslan</i>	201
Effect of Acid and Silane Treated Carbon Nanotubes on Wear Properties of Epoxy Polymer Composite <i>Aidah Jumahat, Napisah Sapiai and Eliya Farah Hana Mohd Kamal</i>	213
Mechanical Behaviour and Microstructure Aluminium Foam Tube Produce (AFTP) Using Infiltration Method with Vacuum- Gas <i>Ismail Lias, Muhammad Hussain Ismail, Iskandar Dzulkernain Md Raffee and Mohd Aman Ihsan Mamat</i>	223
Analysis of Fill Time and Injection Pressure of Multiple 20 gram Parisons during Injection Moulding Process <i>Najiy Rizal Suriani Rizal, Azuddin Mamat and Aidah Jumahat</i>	233
Fuzzy Lambda-Max Criteria Weight Determination for Feature Selection in Clustering <i>Nurul Adzlyana Mohd Saadon, Rosma Mohd Dom and Nurazzah Abd Rahman</i>	241
Green Lean TQM Islamic Management Practices in Malaysian Food Companies <i>Nur Asiah Kuzaiman, Argustina Zainuddin, Nor Azlina Mohd Salleh and Salmiah Kasolang</i>	255
GPU Implementation of Sub-Iris Technique in Iris Recognition System <i>Shahrizan Jamaludin, Nasharuddin Zainal and W. Mimi Diyana W. Zaki</i>	263
Adaptive Particle Swarm Optimisation for Solving Non-Convex Economic Dispatch Problems <i>Nurhafzah Jamain, Ismail Musirin, Mohd Helmi Mansor, Muhammad Murtadha Othman and Siti Aliyah Mohd Salleh</i>	275

SURF Based 3D Object Recognition for Robot Hand Grasping <i>Nurul Hanani Remeli, Ruhizan Liza Ahmad Shauri, Faieza Hanum Yahaya, Norshariza Mohd Salleh, Khairunnisa Nasir and Ahmad Ihsan Mohd Yassin</i>	287
EIS and DFT Investigations on Corrosion Inhibition of Imines containing Mono- and Diisatin Moieties <i>Aliyin Abdul Ghani, Hadariah Bahron, Mohamad Kamal Harun, Karimah Kassim and El Hassane Anouar</i>	297
Synthesis and characterisation of Mononuclear and Tetranuclear Zinc(II) Complexes of Schiff Bases Derived from Phenylenediamine <i>Hadariah Bahron, Siti Solihah Khaidir, Amalina Mohd Tajuddin and Syed Abdul Illah Alyahya Syed Abd Kadir</i>	309
Corrosion Inhibition of Azomethines Containing Hydroxyl Group at <i>Ortho</i> and <i>Para</i> Positions on Mild Steel <i>Syaidah Athirah Dzolin, Yusairie Mohd, Hadariah Bahron and Nurul Huda Abdul Halim</i>	317
Assessment of the Genetic Variability and Fibre Composition of Gamma Ray induced Mutant Lines of Ginger (<i>Zingiber officinale</i> Roscoe) <i>Nor Yuliza Kamaruddin and Shamsiah Abdullah</i>	325
Development of Palm Oil Extraction Performance Index (EPI) Based on Oil Extraction Rate (OER) and Oil Loss (OL) <i>Julia Andrew, Alawi Sulaiman, Mohd Noriznan Mokhtar, Azhari Samsu Baharuddin and Norzaidi Mohd Daud</i>	335
Chromatographic Fingerprint and Chemometric Approach for Quality Control of Tongkat Ali (<i>Eurycoma longifolia</i>) <i>Nor Nasriah Zaini, Mardiana Saaid, Hafizan Juahir and Rozita Osman</i>	345
Optimisation of Distributed Generation Unit Using Particle Swarm Optimisation Method and Voltage Stability Indicator <i>Aimi Iznina Ahameed Tarmizi, Roslina Mohamad, Saiful Izwan Suliman and Murizah Kassim</i>	355
Electrical Properties of Plasticised Proton Conducting MG49 Polymer Electrolyte <i>Zaidatul Salwa Mahmud, Siti Nor Hafiza Mohd Yusoff, Nur Hamizah Mohd Zaki, Mohamad Fariz Mohamad Taib, Mohamad Kamil Yaakob, Oskar Hasdinor Hassan and Ab Malik Marwan Ali</i>	363



***Ganoderma boninense* Efficacy in Delignifying Oil Palm Empty Fruit Bunches**

Siti Sarah Jumali* and Shaleha Ismail

Faculty of Plantation and Agrotechnology, Universiti Teknologi MARA (UiTM) Jasin, 77300 Merlimau, Melaka, Malaysia

ABSTRACT

Oil palm empty fruit bunches (EFB) were subjected to microbial pre-treatment of lignocellulosic biomass bioconversion to fermentable sugar. Microbial pre-treatment was carried out by inoculating *Ganoderma boninense* spores through solid state fermentation. The samples were initially treated with Sulphuric acid method prior to reading with UV-Visible Spectrometer. The readings were taken before and after inoculation of EFB with *G. boninense*. Bioconversion of 20 g EFB via solid state fermentation was done in five different amounts of *G. boninense* spore namely 0.0 g (control), 0.5 g (T2), 0.7 g (T3), 0.9 g (T4) and 1.1 g (T5) in 7 days. The result shows the highest delignification in sample inoculated with 1.1g of *G. boninense* spores, in which the spores are successfully reduced by 61.97% of lignin from total EFB biomass in 7 days compared to 60.08% (T4), 58.65% (T3) and 54.85% (T2). Meanwhile, for control the lignin content was reduced by 5.07% in 7 days. The study shows that *G. boninense* has the ability to remove lignin from EFB whereby longer incubation period and higher number of spores contribute to higher delignification percentage.

Keywords: Delignification, *G. boninense*, ligninolytic enzymes, oil palm empty fruit bunch (EFB)

INTRODUCTION

The palm oil industry has contributed significantly to the economic growth of Malaysia for more than four decades with 3.5 million in 2001 or 60% of the total agricultural land in the country (Ming & Chandramohan, 2002). Malaysia is also the largest country planting oil palm in Southeast Asia after Indonesia. Globally, the increase in crude oil palm production was 48.99 million metric tonnes per year in 2011 (Geng, 2013), where Indonesia together with Malaysia contribute 85% of the palm oil production in the world. This constitutes 23%

ARTICLE INFO

Article history:

Received: 28 September 2016

Accepted: 03 February 2017

E-mail addresses:

sarahjumali@melaka.uitm.edu.my (Siti Sarah Jumali),

gempax1992@yahoo.com (Shaleha Ismail)

*Corresponding Author

of world's oils and fats production (Abdullah & Wahid, 2010). In 2011, oil palm is the second most produced fats and oils after soya bean oil in the world in which oil palm produce is 23.6 million tonnes from 20% of the production (Ming & Chandramohan, 2002).

The processing of oil palm renders oil palm wastes demanding waste management strategies. Current practices include the use of oil palm empty fruit bunches (EFB) as mulching as well as biofertilizers after inoculation with certain types of fungi and bacteria. EFB is considered to be a special biomass of the palm oil industry (Ferrer, Vega, Ligeró, & Rodríguez, 2011). The lignocellulosic content of EFB indicates cellulose at 57.8%, Hemicellulose 21.2% and Lignin 22.8% (Nurhayati & Fauziah, 2013). EFB delignification allows the introduction of other valuable products such as biogas, bioethanol, butanol, biodiesel, hydrogen and compost as delignification allows the stripping off the cell wall and exposing the cellulosic material underneath. The cellulosic material may then be converted through thermo-chemical transformation, hydrolysis of cellulose and hemicellulose to sugars through fermentation.

The structural lignin is among the most abundant structures in the plant as it is responsible for plant organelle protection. It builds up the cell wall along with cellulose and hemicellulose resulting in lignin-carbohydrate network, a recalcitrant structure in the plant. The complexity of lignin causes its isolation and identification to be challenging making *G. boninense* element for a more efficient and environmentally sound deconstruction of plant cell wall (Martinez, Ruiz-Duen, Martinez, del Rio, & Gutierrez, 2009).

This research is focused on discovering the efficiency of *G. boninense* in degrading EFB through solid state fermentation (SSF) using spores of differing amounts to investigate the efficiency of the basidiomycete *G. boninense*.

METHOD

Substrate

The shredded oil palm empty fruit bunch (OPEFB) was obtained from a local palm oil mill in Sime Darby Kempas Melaka, Malaysia. The EFB was soaked in detergent for 24 hours to remove dust and any oil residues. The EFB was washed with distilled water and oven-dried at 80°C for 24 hours. EFB was ground with a grinder and kept in a dry place.

Cultivation of fungus

The locally isolated fungus *G. boninense* was obtained from the Malaysian Palm Oil Board (MPOB) Bangi, Malaysia. The culture was maintained on potato dextrose agar (PDA) and incubated at room temperature (26°C – 28°C) for 7 days.

Experimental Design

Experimental design for the treatment is as shown in Table 1. Each of the flasks was filled with 20 g Oil Palm Empty Fruit Bunch (EFB), 5 ml sterilized distilled water and their respective amount of *G. boninense* spores.

Table 1

Experimental design to determine the effects of G. boninense spore towards EFB

Experimental designation	Number of spores (g)
T1 (Control)	0
T2	0.5
T3	0.7
T4	0.9
T5	1.1

Solid State Fermentation (SSF)

Solid State Fermentation (SSF) was conducted in sterile 250 mL Erlenmeyer flasks containing 20 g of oil palm empty fruit bunch (EFB). EFB was poured with 5 mL sterilized distilled water and spore was added according to designated treatment T1 (0.0 g of spore), T2 (0.5 g of spore), T3 (0.7 g of spore), T4 (0.9 g of spore) and T5 (1.1 g of spore). Number of spores were weighed using balance. Fermentation was done at 39°C.

Lignin Content Analysis

1 g of EFB sample was treated with 70% sulphuric acid in a water bath at 80°C for 2 hours. The sample was neutralized with 2% (w/v) NaOH. It was then filtered through Whatman 12 mm filter paper. The lignin content was read using UV-Visible spectrometer of 340 nm wavelength. Lignin content reading was repeated every day for 7 days to investigate on its decomposition.

RESULTS AND DISCUSSION

Basal stem rot in oil palm plantation is a very serious disease for the oil palm industry. It is spread by *G. boninense* and can cause severe economic loss of about 43% within 6 months (Assis, Chong, Idris, & Ho, 2016). This study showed after 7 days of inoculation the lignin content of the empty fruit bunches were reduced to up to 61% arising from the production of Lignin peroxidase (LiP), Manganese peroxidase (MnP) and laccase by *G. boninense* (Goh, Ganeson, & Supramaniam, 2014). Table 2 indicates that the ligninolytic enzymes produced by fungus were effective in reducing the lignin content in the EFB. The evaluation of lignin amount through UV-Visible spectrometer estimation revealed dramatic lignin decomposition in the sample inoculated with *G. boninense* compared to the uninoculated sample. The significant decrease is related to the damage incurred to the lignin-carbohydrate network in the EFB whereby lignocelluloses are the substrates required for the growth of the white-rot fungus *G. boninense* (Sánchez, Sierra, Carlos, & Díaz, 2011). Comparatively, the lignin content of empty fruit bunches that are not inoculated with *G. boninense* shows a slow and steady decrease of 5.07% in 7 days.

Table 2
Percentage of lignin after day(s) of inoculation

Day(s) after inoculation	Lignin percentage (%)				
	T1	T2	T3	T4	T5
1	1.740	1.707	1.519	1.308	1.173
2	1.701	1.604	1.427	0.958	0.971
3	1.647	1.478	1.219	0.910	0.876
4	1.620	1.307	1.041	0.829	0.769
5	1.633	0.960	0.839	0.754	0.630
6	1.645	0.880	0.760	0.665	0.515
7	1.652	0.771	0.628	0.552	0.446

Table 3
Total reduction percentage of lignin from initial inoculation

Designation	Amount of spores (g)	Percentage of lignin reduction (%)	Rate of reduction (%/day)	Rate of reduction (%/hour)
T1 (Control)	0.0	5.07	0.724	0.030
T2	0.5	54.85	7.835	0.326
T3	0.7	58.65	8.379	0.349
T4	0.9	60.08	8.582	0.357
T5	1.1	61.97	8.853	0.369

Following Solid State Fermentation (SSF), sugar and carbohydrate concentration will rise due to the action of ligninolytic enzymes which catalyses the removal of lignin. SSF technique pose better delignification rate as considerable amount of ligninolytic enzymes are produced quickly with minimum downstream processing due to the smaller amount of impurities (Robinson, McMullan, Marchant, & Nigam, 2001). Research conducted in treating lignin through enzymatic delignification via indirect usage of fungi such as delignification of *Bambusa bambos* resulted in 84% delignification after 8 hours using laccase and cellulose (Kuila, Mukhopadhyay, Tuli, & Banerjee, 2011). Meanwhile in *Saccharum spontaneum*, maximum delignification was 84.67% at 6.21 hour of incubation with laccase (Rajak & Banerjee, 2015) which implies a total reduction of 13.63% per hour. A research conducted on oil palm EFB through an attempt of ionic liquid utilization to delignify EFB showed an overall reduction of 15.5% from the total biomass recorded (Financie, Moniruzzaman, & Uemura, 2016). The study employs the use of ionic liquid 1-ethyl-3-methylimidazolium-diethyl phosphate and commercial laccase attained from *Trametes* sp. as delignification agent. Compared to which the production of ligninolytic enzymes produced by *G. boninense* is found to be far more efficient than *Trametes* sp..

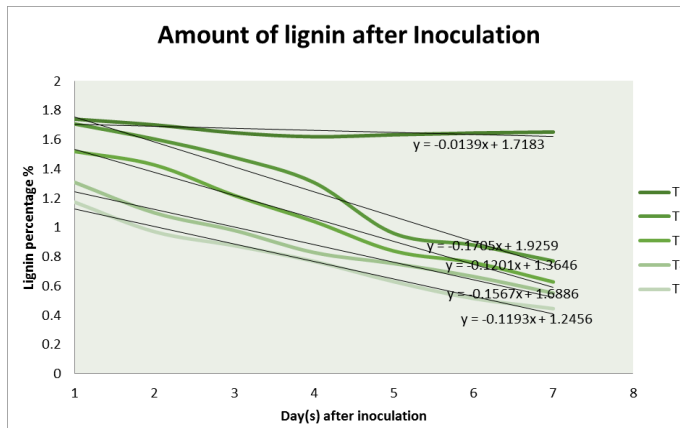


Figure 1. Changes in residual lignin level after inoculation with of *G. boninense* strains

From Figure 1, the highest rate for lignin degradation is shown by the slope T2 where the slope is the steepest at $m=-0.1705$ followed by T4, T3, T5 and T1. Meanwhile, Table 3 exhibits the total reduction percentage of each lignin from initial inoculation where T5 which is 1.1 g of spores contributed to the highest delignification percentage of 61.97% followed by T4 (60.08%), T3 (58.65%), T2 (54.85%) and T1 5.07%. As expected, the higher the contact with surface areas, the higher the delignified EFB. It strongly suggests the production of ligninolytic enzymes during the course of decomposition. The higher number of spores contribute to

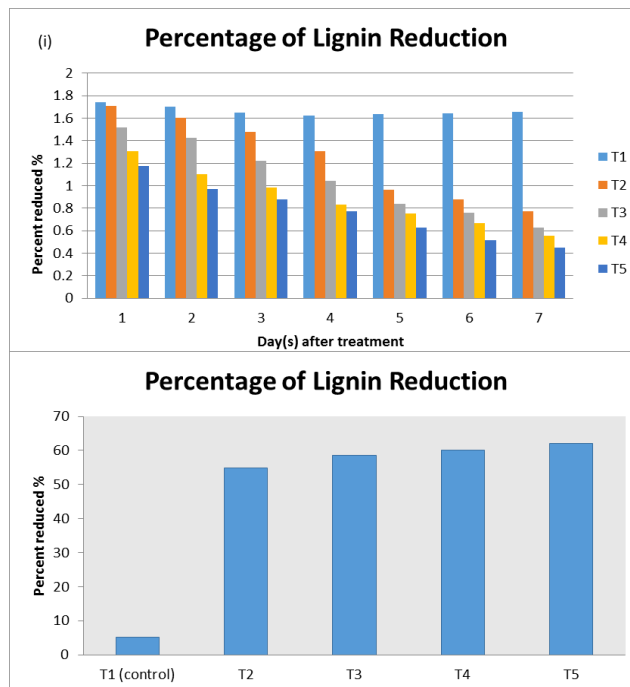


Figure 2. Percentage of lignin reduction

more enzyme production thus more substrates are hydrolysed. Table 3 shows that 1.1 g of *G. boninense* spores is able to reduce as much as 8.853% of EFB per day which is equal to 0.369% per hour. Although the production is slower than that of *S. spontaneum* which degrades 13.63% lignin per hour (Rajak & Banerjee, 2015); the figure represented is still significant due to the locally abundant *G. boninense* and the high disparity of lignin content before and after application. Other research has found out that laccase can be produced to up to 43.07 UI-1 while Manganese Peroxide 16.21 UI-1 (Goh et al., 2014).

Microbial biocatalysis for decomposition is relatively inexpensive therefore enzymatic action of microbes is now the predominant feature for biological substitutes to speed up reaction (Grommen & Verstraete, 2002). The fast reaction of its containing enzymes (Robinson et al., 2001) may be further exploited through enzyme extraction for waste management and transforming biomasses into biofuel and energy generation. Researches have demonstrated the outstanding performance of ligninolytic enzymes of basidiomycetes in assisting oxygen delignification of craft pulp, and acting as a substitute to conventional chemical bleaching (Bourbonnais, Paice, Freiermuth, Bodie, & Borneman, 1997). Similar to the other white-rot fungi, *G. boninense* is also a potent bioremediation agent in degrading various xenobiotic compounds, dyes and polymeric products, thus protecting the environment from chemical pollution (Maciel, Silva, & Ribeiro, 2010). The lignonolytic enzymes that is produced may also contribute in pulp and paper industry (Kaur & Nigam, 2014; Górska et al., 2014) as well as benefit agriculture, forestry, sawmill, woodworking, furniture, milling and papermaking industry when produced in a large enough scale (Górska et al., 2014).

CONCLUSION

The white-rot fungi *G. boninense*, although a potent destroyer of oil palm, is also a potential basidiomycete that can promote numerous enzymatic degradation and decomposition of wastes and by-products. The lignocellulases that is produced reduces the need for chemicals and thereby improve environmental hygiene and sustainability.

ACKNOWLEDGEMENTS

The author would like to acknowledge Malaysian Palm Oil Berhad (MPOB), Bangi, Malaysia for the supply of *G. boninense* culture and also Sime Darby Kempas Malacca, Malaysia, and Universiti Teknologi MARA (UiTM).

REFERENCES

- Abdullah, R. & Wahid, M. B. (2010). *World Palm Oil Supply, Demand, Price and Prospects: Focus on Malaysian and Indonesian Palm Oil Industry*. Malaysian Palm Oil Board Press: Malaysia.
- Assis, K., Chong, K. P., Idris, A.S., & Ho, C. M. (2016). Economic Loss due to Ganoderma Disease in Oil Palm. *International Journal of Social, Behavioral, Educational, Economic, Business and Industrial Engineering*, 10(2), 631-635.

- Bourbonnais, R., Paice, M. G., Freiermuth, B., Bodie E., & Borneman, S. (1997). Reactivities of Various Mediators and Laccases with Kraft Pulp and Lignin Model Compounds. *Applied Environmental Microbiology*, 63(12), 4627–4632.
- Ferrer, A., Vega, A., Ligeró, P., & Rodríguez, A. (2011). Biorefinery of empty fruit. *BioResources*, 6(4), 4282-4301.
- Financie, R., Moniruzzaman, M., & Uemura, Y. (2016) Enhanced enzymatic delignification of oil palm biomass with ionic liquid pretreatment. *Biochemical Engineering Journal*. 110, 1–7.
- Geng, A. (2013). Conversion of Oil Palm Empty Fruit Bunch to Biofuels, Liquid, Gaseous and Solid Biofuels - Conversion Techniques, *InTech*, 16, 479-490.
- Gellerstedt, G. & Henriksson, G. (2008) Lignins: major sources, structure and properties. *Monomers, Polymers and Composites from Renewable Resources*. (pp. 201-224) Amsterdam: Elsevier.
- Goh, K. M., Ganeson, M. & Supramaniam, C. V. (2014). Infection potential of vegetative incompatible *Ganoderma boninense* isolates with known ligninolytic enzyme production. *African Journal of Biotechnology*, 13(9), 1056-1066.
- Górska, E. B., Jankiewicz, U., Dobrzynski, J., Gałazka, A., Sitarek, M., Gozdowski, D., Russel, S., & Kowalczyk, P. (2014). Production of Ligninolytic Enzymes by Cultures of White Rot Fungi. *Polish Journal of Microbiology*, 63(4), 461–465.
- Grommen, R. & Verstraete, W. (2002). Environmental biotechnology: the ongoing quest. *Journal of Biotechnology*, 98(1), 113–123.
- Kaur, S. & Nigam, V. (2014). Production and Application of Laccase Enzyme in Pulp and Paper Industry. *International Journal of Research in Applied, Natural and Social Sciences*, 2(4), 153-158.
- Kuila, A., Mukhopadhyay, M., Tuli, D. K., & Banerjee, R. (2011). Accessibility of Enzymatically Delignified *Bambusa bambos* for Efficient Hydrolysis at Minimum Cellulase Loading: An Optimization Study. *SAGE-Hindawi Access to Research Enzyme Research*.
- Maciel, M. J. M., Silva, A. C., & Ribeiro, H. C. T. (2010). Industrial and biotechnological applications of ligninolytic enzymes of the basidiomycota: A review. *Electronic Journal of Biotechnology*. 13(6).
- Martinez, A. T., Ruiz-Duen, F. J., Martinez, M. J., del Rio, J. C., & Gutierrez, A. (2009). Enzymatic delignification of plant cell wall: from nature to mill. *Current Opinion in Biotechnology*, 20, 348–357.
- Ming, K. K. & Chandramohan, D. (2002). Malaysian Palm Oil Industry at Crossroads and its Future Direction. *Oil Palm Industry Economic Journal*, 2(2), 10-15.
- Nurhayati, A. & Fauziah, S. (2013). The Properties of the Washed Empty Fruit Bunches of Oil Palm. *Journal of Physical Science*, 24(2), 117–137.
- Sánchez, O., Sierra, R., Carlos, J., & Díaz, A. (2011). Delignification Process of Agro-Industrial Wastes an Alternative to Obtain Fermentable Carbohydrates for Producing Fuel, Alternative Fuel, *InTech*.
- Pilotti, C. A. (2005). Stem rots of oil palm caused by *Ganoderma boninense*: pathogen biology and epidemiology. *Mycopathologia*, 159(1), 129-37.
- Rajak, R. C. & Banerjee, R. (2015). Enzymatic delignification: an attempt for lignin degradation from lignocellulosic feedstock. *Royal Society of Chemistry Advances*, 5, 75281-75291.

- Robinson, T., McMullan, G., Marchant, R., & Nigam, P. (2001). Remediation of dyes in textile effluent: a critical review on current treatment technologies with a proposed alternative. *Bioresource Technology*, 77, 247-255.
- Yusof, B. (2007). Palm oil Production through Sustainable Plantations. *European Journal of Lipid Science and Technology*, 109, 289–295.

Numerical Study of Aerodynamic Characteristics on Blended Wing Body Aircraft with Small Canard

Zurriati Mohd Ali^{1*}, Wahyu Kuntjoro², Wirachman Wisnoe²,
Rizal Effendy Mohd Nasir² and Noor Iswadi Ismail³

¹Faculty of Mechanical Engineering, Universiti Teknologi MARA (UiTM), 81750 Pasir Gudang, Johor, Malaysia

²Faculty of Mechanical Engineering, Universiti Teknologi MARA (UiTM), 40450 Shah Alam, Selangor, Malaysia

³Faculty of Mechanical Engineering, Universiti Teknologi MARA (UiTM), 13500 Permatang Pauh, Pulau Pinang, Malaysia

ABSTRACT

The blended wing body (BWB) aircraft has a unique design. The main body and wing of BWB are merged to increase the lift force on the aircraft. However, BWB has poor stability arising from the absence of the tail. Hence, a small horizontal stabilizer called as canard has been incorporated in front of the main wing to improve BWB's stability. Computational Fluid Dynamics (CFD) simulations conducted to obtain the aerodynamics parameters of the BWB i.e. lift, drag and moment coefficients, showed that overall, the canard is beneficial to the BWB aerodynamics performance.

Keywords: Aerodynamics, blended wing body (BWB), canard, Computational Fluid Dynamics (CFD)

INTRODUCTION

The blended wing body (BWB) is specifically designed to meet the objectives of greater internal volume, aerodynamics and structural efficiency, noise reduction and significant improvement on cost-per-seat-mile (Ordoukhanian & Madni, 2014). The numerical study on the canard is difficult due to the need to identify, re-design and model the viscous flow area. The fluid flow over a BWB aircraft complicated by the rounded trailing edge and canard surfaces.

Many researches in numerical study examine the possibility of using Navier-Stokes equations to predict the aerodynamics characteristics of BWB or an aircraft with

ARTICLE INFO

Article history:

Received: 28 September 2016

Accepted: 03 February 2017

E-mail addresses:

zurriatimohdali@johor.uitm.edu.my (Zurriati Mohd Ali),
wkuntjoro@salam.uitm.edu.my (Wahyu Kuntjoro),
wira_wisnoe@salam.uitm.edu.my (Wirachman Wisnoe),
rizal524@salam.uitm.edu.my (Rizal Effendy Mohd Nasir),
iswadi558@ppinang.uitm.edu.my (Noor Iswadi Ismail)

*Corresponding Author

canard at best developed an unsteady three-dimensional Navier-Stokes analysis for circulation control wing (CCW) configurations. The solver can be used in a 2-D and a 3-D mode, and thus model air foils as well as finite wings. The Spalart Almaras, one-equation turbulence model was used by Mamat et al. (2011) to calculate the flow around the BWB aircraft model. The data obtained from the study confirmed the experimental result. Nangia et al. (2006) investigates the design of conventional and unconventional wings with winglet. The BWB research team from Universiti Teknologi MARA (UiTM) had studied BWB incorporated with canard since 2005.

The canard is a small wing located in front of the main wing and used as a longitudinal stabilizer and increase lift (Nasir et al., 2010). A CFD simulations and wind tunnel experiment on the BWB aircraft by Wisnoe et al. (2010), Reduan et al. (2010) and Mohamad et al. (2010) found that higher stall angle and maximum lift to drag (L/D) ratio is observed on BWB-Baseline II. However, in computational fluid dynamic CFD study by Nasir et al. (2011) show small differences of aerodynamic parameters between CFD and wind tunnel experiment at the linear lift region. To simulate flight conditions beyond the linear lift region, different turbulence model is proposed by Nasir et al. (2011).

The study of BWB with a small rectangular canard using CFD at Mach number 0.1 was studied by Ali (2012). The differences from the maximum lift coefficient, C_{Lmax} between CFD and wind tunnel is small (9%). Adding the canard surface at certain setting angle will increase the moment at zero lift, C_{M0} . This paper will extend the findings of previous studies by investigating the canard-setting angle to the aerodynamics of BWB subjected to variation canard setting angles.

METHOD

Numerical Methods

The geometry in this study (Figure 1) is based on the wind tunnel model (one-sixth scaled from the real BWB configuration). Two lifting bodies (wings and body) are blended together to form the BWB geometry. As BWB is symmetrical where only half body is generated, thereby saving computer memory space as well as time spent on modelling and simulation.

The rectangular canard is attached to the wing-body and acts as a horizontal stabilizer. The canard's aspect ratio, ($AR = \text{span wise}/\text{chord}$) was designed, and incorporated to the wing body. The ratio of canard size area, S_c to wing-body area, S is 13.6 % (0.005 m^2), following the same canard size used in Nasir et.al (2010). Theoretically, the higher aspect ratio, the slimmer and thinner the body will be. The canard is a control canard, so it is free to rotate. The deflected canard rotates about the span wise axis at the 1/4 of the canard's chord. Canard deflection angles δ are calculated relative to the wing-body axis, with positive δ indicates a canard is pitching upwards and negative δ is pitching downward as shown in Figure 2.

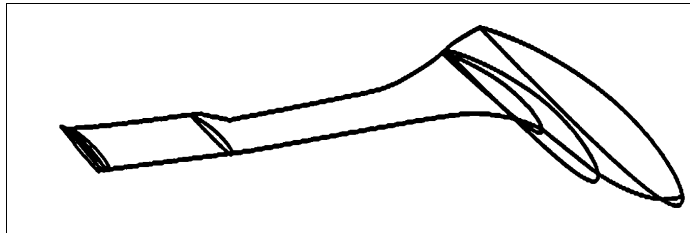


Figure 1. BWB-Baseline layout

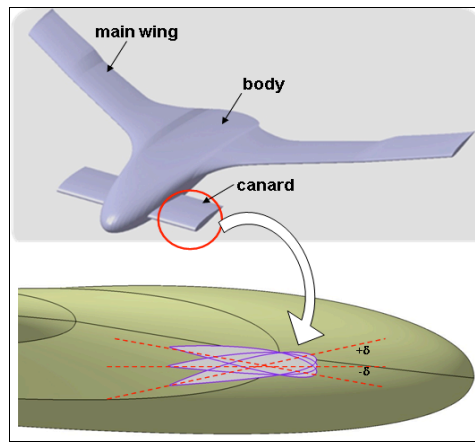


Figure 2. Sign convention for canard deflection

The centreline plane was modelled as a symmetry plane and the BWB surface as a solid wall with no slip condition. The symmetrical plane for flow domain and BWB half body is coincide. The distribution of all flow variables needs to be specified at inlet boundaries. The incoming and outgoing flow was set as an inlet and outlet. The BWB described as a wall are located at 0.468 m from inlet boundary, respectively.

The domain bounded by BWB is covered using mesh or grid. Mesh was used to convert the partial differential equations into algebraic equation. The advantage of unstructured mesh is its flexibility in handling complex geometries. In this grid generator, three-dimensional (3D) unstructured hexahedral meshes was used to compute flow around the aircraft configuration. The finer mesh was created near the aircraft model, to ensure the accuracy of the results.

In a mathematical model, turbulence-Navier Stokes flow model was selected as a flow model, which means the turbulence was taken into account through a turbulence models such as; Spalart Allmaras, extended wall function $k-\epsilon$, $k-\omega$ and many more. Turbulence is generated above a critical Reynolds number that may range in values from 400 to 2000 depending on the specific case. In the current work, the Spalart-Allmaras (SA), one equation model was selected due to the low Reynolds number, 3×10^5 . The advantage of this model is its robustness and the lower CPU and memory usage. Besides, the SA turbulent model has also been successfully

implemented in previous BWB aircraft analysis. The reference length was 0.114 m, taken from mean aerodynamic chord (MAC). The turbulent eddy viscosity μ_t is equal to $\rho\nu_t$, and ν_t state by Liu (2003) is given by:

$$\nu_t = \tilde{\nu} f_{v1}, f_{v1} = \frac{1-\chi^3}{\chi^3 + c_{v1}^3}, \chi = \frac{\tilde{\nu}}{\nu} \quad [1]$$

Where ν is the molecular viscosity. The working variable, $\tilde{\nu}$, is governed by the transport equation.

$$\frac{D\tilde{\nu}}{Dt} = c_{D1}(1 - f_{t2})\tilde{S}\tilde{\nu} + \frac{1}{\sigma}[\nabla \cdot ((\nu + \tilde{\nu})\nabla\tilde{\nu} + c_{b2}(\nabla\tilde{\nu})^2)] + [c_{w1}f_w - \frac{c_{b1}}{K^2} f_{t2}][\frac{\tilde{\nu}}{d}]^2 + f_{t1}\Delta U^2 \quad [2]$$

Here, $\tilde{S} = S + \frac{\tilde{\nu}}{K^2 d^2} f_{v2}$, $f_{v2} = 1 - \frac{\chi}{1-\chi f_{v1}}$

S is a magnitude of the vortices and d is distance to the closest wall.

At the inlet the incoming velocity to the domain is specified at 35 m/s and static temperature of 273 K. The BWB model is set as a solid wall for forces and torque calculation (the lift, drag and moment).

RESULTS AND DISCUSSION

Parameter Validation

Parameter validation is an approach to estimating the reliability of the software in predicting the aerodynamics loads of this study, and set as a benchmark for the CFD results. The lift coefficient of the airfoil profile, NACA 2415 was derived using CFD software NUMECA. Figure 3 illustrates the comparison between CFD and our experiment.

Data is based on the same Reynolds number. As the angles of attack increase, the lift too increases. The trend is all the same. The only noted difference is at higher angles of attack, the differences between the CFD and wind tunnel result was large. However, this can be neglected due to the fact that the case of the study are only limited between -10 to 10 degrees angles of attack.

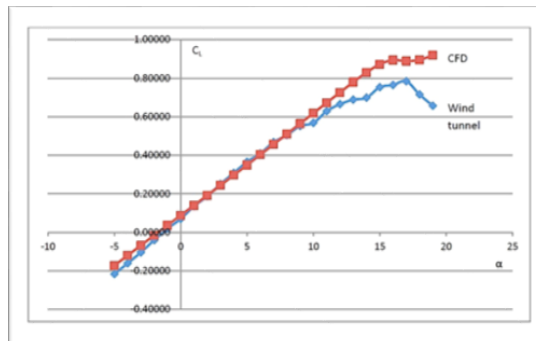


Figure 3. Lift coefficient versus angles of attack (CFD and experimental)

Lift Coefficient

The BWB lift coefficient with respect to angles of attack for various canards' aspect ratio, the AR predicted by CFD is shown in Figure 4. By adding the canard surface on the BWB the lift gradient specifically at low angles of attack is observed. The increase of lift is proportional to higher canard aspect ratio. However, in Figure 5, the result is contrary where all the canards were stall at higher angles of attack. Due to the fact that the canard surface stalled at angles of attack lower than that for wing-body stall, these results, however, do not come as a surprise. This study shows that the main lift contributor comes from the body and wing and that the canard's contribution of lift enhancement to the BWB is not significant due to its size.

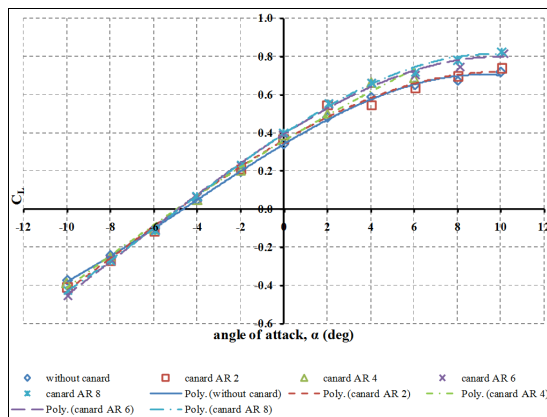


Figure 4. Lift curves of BWB at setting angles, $\delta = 5^\circ$

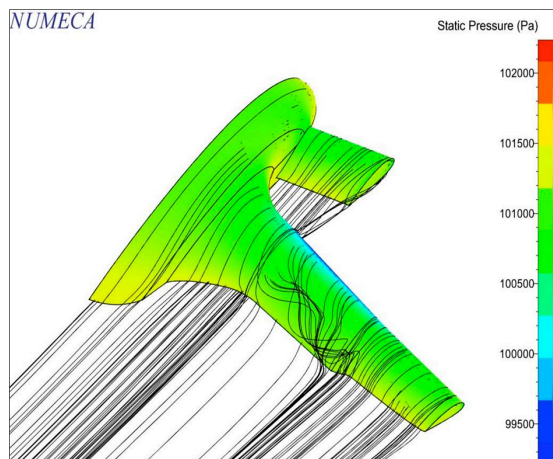


Figure 5. BWB with canard AR 2 at $\alpha = 4^\circ$, $\delta = 0^\circ$

Lift to Drag Coefficient

The lift-to-drag ratio i.e. L/D versus angles of attack α , is shown in Figure 6. A higher L/D means better flight performance, where the drag of aircraft decreases as L/D is increased. In an airplane, T_R is generated to overcome drag and maintain the flight condition. The L/D curves show that as angles of attack increase L/D increases. The point where α reaches the maximum L/D is denoted as $\alpha_{(L/D) \max}$. With L/D a function of α , lift and drag coefficient is also a function of α . The BWB without canard has the maximum lift-to-drag ratio while with canard the maximum L/D of the BWB decreases. The BWB with canard AR 2 and 4 have maximum L/D compared to situations when the canard-setting angle is not deflected. Depending on the canard aspect ratio, the L/D reduces when the setting angle of the canard is increased.

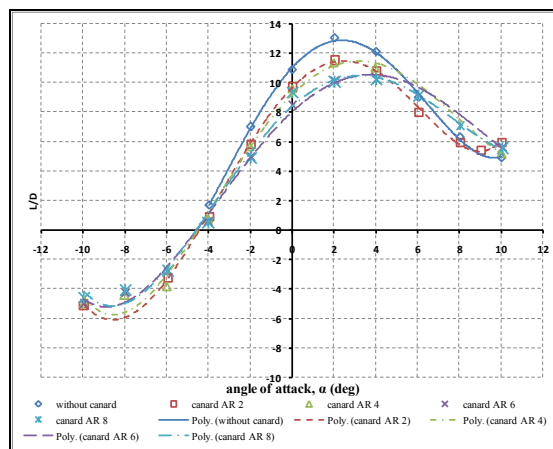


Figure 6. Lift- to-Drag curves of BWB with different canard aspect ratio at setting angles, $\delta = 5^\circ$

Moment Coefficient

The essential criteria that qualifies an aircraft to be statically stable during flight is the pitching moment curve must have a negative slope. By convention, negative moment refers to moment that causes the aircraft nose down, while positive moment gives opposite effect. The pitching moment at zero lift, C_{M0} must be positive. Figure 7, Figure 8 and Figure 9 show the pitching moments C_{Mref} versus angles of attack, α and C_{Mref} versus coefficient of lift, C_L measured from 19.8 % from mean aerodynamic chord, MAC. The overall trend is similar, where the pitching moment is reduced when the angles of attack and lift increases. Although there are many advantages of BWB configurations for examples lighter, high lift-to-drag ratio, and lower fuel burn, this kind of aircraft is technically unstable. The absence of horizontal tail causes the BWB aircraft to have no longitudinal control, and therefore always tends to diverge from the equilibrium position when disturbed. To correct this behaviour the BWB is usually incorporated with elevons or canard. In the present study, the canard is used to produce positive lift, hence, creating a clockwise moment about the centre gravity. If this moment is strong enough, C_{M0}

for the BWB configuration is positive and balance maintained. The graph below shows by adding canard can lead $C_{M\alpha}$ to change dramatically and moment at zero angle of attack, $C_{M,\alpha=0}$ to increase.

Canard shows a significant effect with the moment coefficient of the BWB. Increasing the canard setting angles increases the trimmed angles of attack and moment at zero lift. The result shows that the BWB with the canard fulfils the static stability criteria, and that the BWB with canard AR 6 and 8 are the most effective ones.

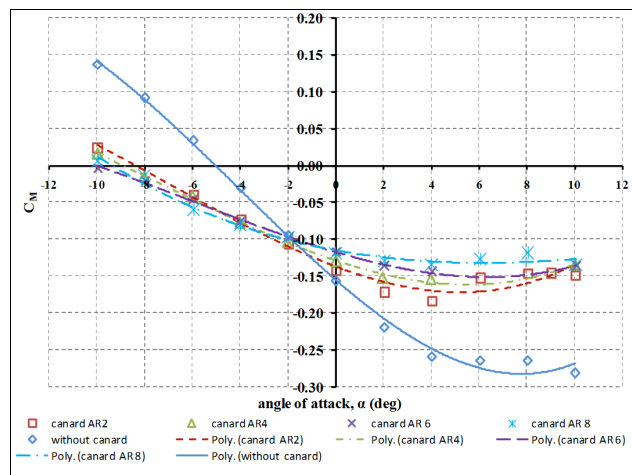


Figure 7. Moment coefficient, $\delta = 0^\circ$

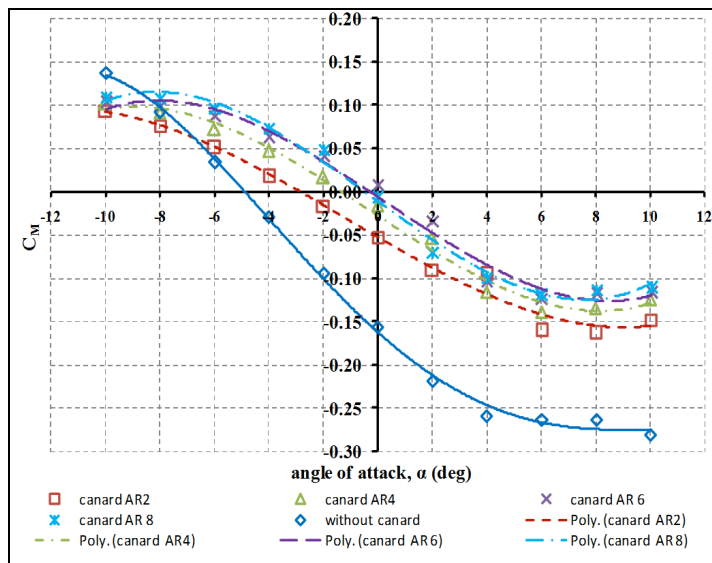


Figure 8. Moment coefficient $\delta = 5^\circ$

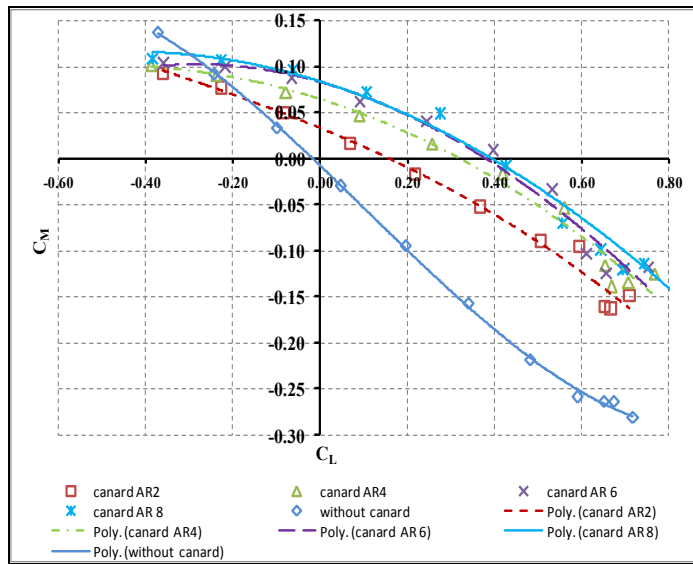


Figure 9. Moment coefficient, $\delta = 10^\circ$

CONCLUSION

A new control surface consisting of a canard located at the front of the major wing of the BWB was studied. It involves the determination of aerodynamics characteristic (C_L , L/D and C_M) of BWB incorporated with the canard. A summary of major findings of this research are:

- i. It is found that BWB has an optimum lift, drag and moment coefficient at lower angles of attack and canard setting angles. The differences of the aerodynamics coefficients between canards aspect ratio are small;
- ii. The canard with aspect ratio 6 and 8 have a significant effect towards the moment coefficient of the aircraft configuration where it improves the trim angle and moment at zero lift. The trim angle is shifted toward the positive angles of attack and moment at zero lift is increases;
- iii. The pitching moment is improved when the canard is deflected to a higher canard setting angles ($\delta = 10^\circ$).

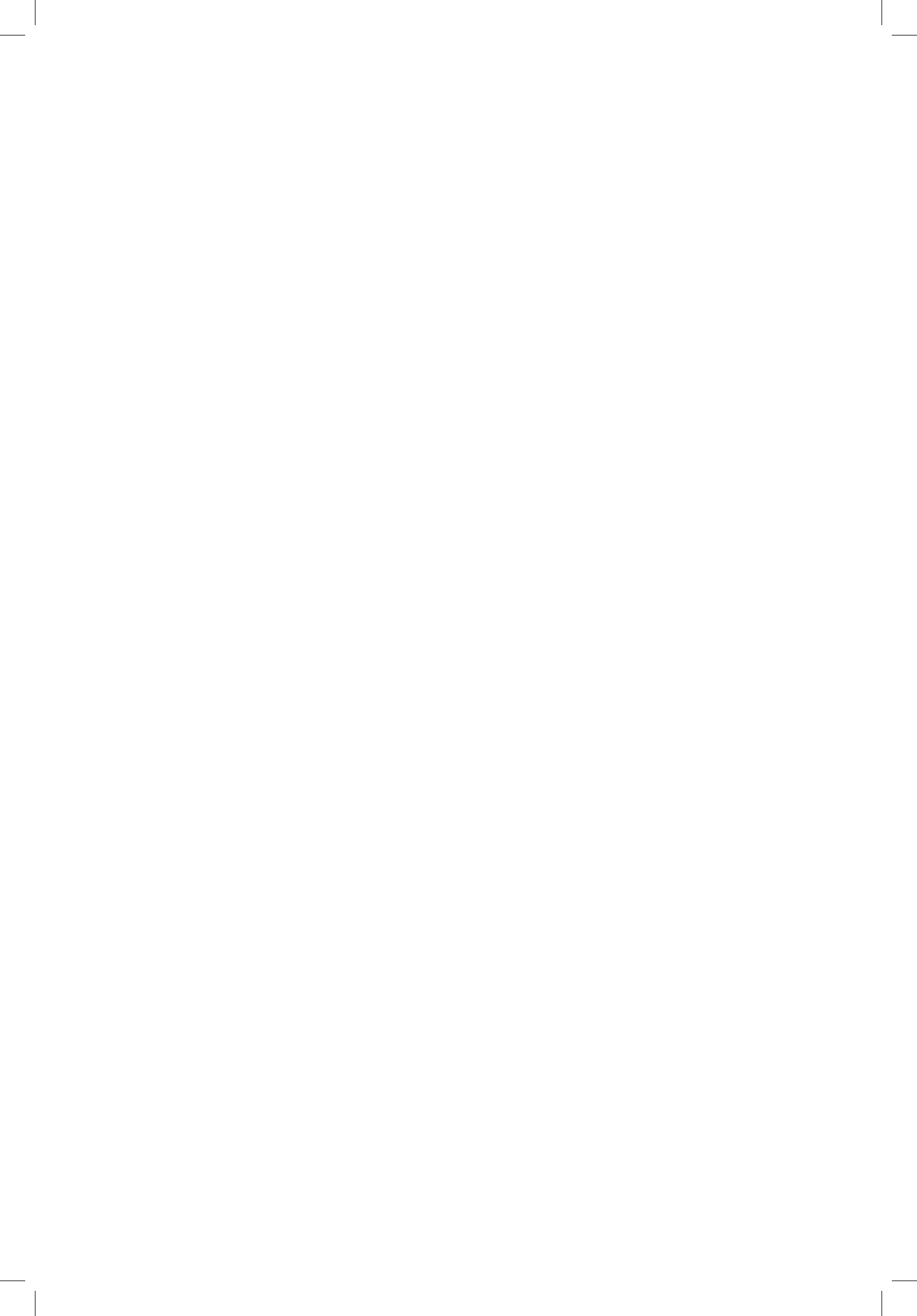
The result shows that these configurations can improve pitching moment of BWB.

ACKNOWLEDGMENTS

This research benefitted from the financial support of the Kementerian Pengajian Tinggi (KPT) and Universiti Teknologi MARA (UiTM).

REFERENCES

- Liu, Y. (2003). *Numerical Simulations Of The Aerodynamic Characteristics of Circulation Control Wing Sections*. (Doctoral dissertation). Georgia Institute of Technology.
- Mamat, A. M. I., Nasir, R. M., Ngah, Z., Kuntjoro, W., Wisnoe, W., & Ramly, R. (2008). Aerodynamics Of Blended Wing Body (BWB) Unmanned Aerial Vehicle (UAV) Using Computational Fluid Dynamics (CFD). *Journal of Mechanical Engineering*, 5(2), 15-25.
- Mohamad, F., Wisnoe, W., Kuntjoro, W., Nasir R. E. M., Ali, Z. M. & Reduan. N. F. (2010). Experiment Results of UiTM's Blended Wing Body (BWB) Baseline-II UAV using Low Speed Wind Tunnel. In *International Conference on Advances in Mechanical Engineering (ICAME 2010)*. Selangor, Malaysia.
- Nangia, D. R., Palmer, D. M., & Doe, M. R. (2006). Aerodynamic Design Studies of Conventional & Unconventional Wings with Winglets. In *25th Applied Aerodynamics Conference*. San Francisco, CA, USA.
- Nasir, R. E. M., Kuntjoro, W., Wisnoe, W., Ali, Z., Reduan, N., Mohamad, F. & Suboh, S. (2010). Baseline-II" Blended Wing- Body (BWB) Unmanned Aerial Vehicle (UAV): Achieving Higher Aerodynamic Efficiency Through Planform Redesign and Low-Fidelity Inverse Twist Method. In *3rd Engineering Conference on Advancement in Mechanical and Manufacturing For Sustainable Environment (EnCon 2010)*. Sarawak, Malaysia.
- Nasir, R. E. M., Ali, Z., Kuntjoro, W. & Wisnoe, W. (2011). Investigation on Aerodynamic Characteristics of Baseline-II E-2 Blended Wing-Body Aircraft with Canard via Computational Simulation. In *The International Meeting on. Advances in Thermofluids (4th IMAT 2011)*.
- Ordoukhanian, E., & Madni, A. M. (2014). Blended Wing Body Architecting and Design : Current Status and Future Prospects. *Procedia - Procedia Computer Science*, 28(Cser), pp. 619–625. <http://doi.org/10.1016/j.procs.2014.03.075>
- Reduan, N., Wisnoe, W., Kuntjoro, W., Nasir, R. E., Mohamad, F., & Ali, Z.M. (2010). Study of Aerodynamics Characteristic of BWB Baseline-II. In *International Conference on Advances in Mechanical Engineering (ICAME 2010)*. Selangor, Malaysia.
- Wisnoe, W., Kuntjoro, W., Mohamad, F., Nasir, R. E. ., Reduan, N. F. & Ali, Z. (2010). Experimental results analysis for UiTM BWB Experimental Results Analysis for UiTM BWB Baseline-I and Baseline-II UAV Running at 0 . 1 Mach number, (September 2015).
- Zurriati, M. A., Wahyu, K., Wisnoe, W., & Rizal, E. M. (2012). The effect of canard on aerodynamics of blended wing body. In *Applied Mechanics and Materials*, Vol. 110, pp. 4156-4160). Switzerland: Trans Tech Publications. <http://doi.org/10.4028/www.scientific.net/AMM.110-116.4156>



Investigation on Moisture Susceptibility and Rutting Resistance of Asphalt Mixtures incorporating Nanosilica Modified Binder

Ahmad Kamil Arshad^{1,2}, Khairil Azman Masri^{2*}, Juraidah Ahmad^{1,2} and Mohamad Saifullah Samsudin²

¹*Institute for Infrastructure Engineering and Sustainable Management, IIESM, Faculty of Civil Engineering, Universiti Teknologi MARA (UiTM), 40200 Shah Alam, Selangor, Malaysia*

²*Faculty of Civil Engineering, Universiti Teknologi MARA (UiTM), 40450 Shah Alam, Selangor, Malaysia*

ABSTRACT

This paper presents the outcome of a laboratory investigation on mix design, resilient modulus, moisture susceptibility and rutting resistance of Stone Mastic Asphalt (SMA) and Dense Graded Asphalt (AC) that is incorporated with Nanosilica (NS) modified binder. Penetration Grade 60-70 (PEN60-70) types of binder were mixed with nanoparticles (NS) using concentration of 0wt%, 2wt%, 4wt% and 6wt% by weight of asphalt binder. The mixtures were tested for resilient modulus, indirect tensile strength and rutting, in order to evaluate the performance of NS-SMA and NS-AC. The results show that the existence of NS is capable of enhancing the performance of both asphalt mixtures, and the addition of NS decreases the susceptibility of moisture damage and provides better resistance against permanent deformation. Furthermore, the addition of 4wt% NS appears to be the most effective amount for the performance enhancement in AC and SMA mixtures.

Keywords: Dense grade asphalt, moisture susceptibility, nanosilica, resilient modulus, rutting, Stone Mastic Asphalt

ARTICLE INFO

Article history:

Received: 28 September 2016

Accepted: 03 February 2017

E-mail addresses:

khairilazmanmasri@yahoo.com (Khairil Azman Masri),
drahmadkamil@salam.uitm.edu.my (Ahmad Kamil Arshad),
juraidah@salam.uitm.edu.my (Juraidah Ahmad),
spark_black90@yahoo.com (Mohamad Saifullah Samsudin)

*Corresponding Author

INTRODUCTION

Asphalt mixture especially hot mix asphalt (HMA) is usually regarded as having stripping and permanent deformation problems. Temperatures of around 30-35o together with frequent rain exposes asphalt pavement to moisture susceptibility and rutting. Both issues are usually inter-related and the existence of moisture leads to stripping and severe rutting, leading to low ride-ability,

comfort-ability, general performance and motorist safety. There are several advantages of using Stone Mastic Asphalt. First, it provides more resistance towards permanent deformation or rutting (30% - 40% less than dense graded asphalt). Second, SMA relies on stone to stone contact in terms of mechanical properties, so they are less sensitive to binder variations than the conventional mixes (Brown et al., 1996). But, the costs related to producing SMA is higher due to its higher binder content and fibres additive. It is also high in filler content, thus resulting to productivity reduction, Furthermore, there is a possible delay in opening the road to traffic as SMA mixtures must be cooled to below 40°C in order to prevent flushing of the binder surface (Nejad et al., 2012). However, this may be overcome by suitable modifications. Figure 1 shows rutting phenomena that usually occurred on the asphalt pavement.



Figure 1. Rutting phenomena

Resilient modulus can be used to determine the mechanical characteristics and provides empirical approached in designing the pavement structure and predicting the rutting roughness. Asphalt mixture behaves elastically and plastically when a load is applied (El-Shafie et al., 2012). Resilient modulus is important for evaluating the performance of asphalt mixtures subjected to repeated loads. This parameter is used as an input parameter to evaluate the response of pavement under traffic loading. Venudharan and Biligiri (2015) also defined resilient modulus as the ratio of deviator stress to the recoverable strain at any particular temperature and frequency. Resilient modulus values are determined via laboratory tests which subjecting the cylindrical specimen to loads using Universal Testing Machine (UTM). This test helps to measure the elasticity of the asphaltic specimens, evaluate the quality of the materials, and provide input for pavement design. According to Shafabakhsh and Tanakizadeh (2015), the asphaltic layers can be considered elastic if the load applied is small compared to the strength of material. It involves subjecting the specimen to a large number of load applications and the deformation under each load recorded. The factors that can influence resilient modulus are water, dry density and stress level. The value of resilient modulus can decrease when the water content increases and increase with increases in dry density, confining and deviator stress.

Besides rutting, another primary cause of distress in asphalt mixture is moisture susceptibility. If the internal bonds between aggregates and asphalt are weakened in the presence of water, the asphalt mixtures may be considered susceptible to moisture. Moisture susceptibility

is a major reason for the premature failure of asphalt mixtures. Moisture susceptibility is also known as moisture damage, or the degradation of the material's mechanical properties that attribute to the presence of moisture in its microstructure (Kumar & Anand, 2012). The factors that can affect moisture susceptibility in asphaltic mixtures are the type of aggregates, type of source of crude oil and refining process in asphalt cement manufacturing, asphalt mixtures properties which are influenced by the degree of compaction, asphalt film thickness and environmental condition and traffic (Ebrahim & Behiry, 2013). The chief means by which moisture enters the pavement structure are infiltration of surface water, the capillary rise of subsurface water, and the diffusion of water vapor.

Studies done to enhance the performance of asphalt mix suggest the use of binder modification. One type of binder modification is the use of nanotechnology, nanosilica (NS), which shows a promising result in improving binder properties. This study utilizes colloidal NS to enhance the properties of asphalt binder. SMA and AC asphalt containing different amounts of NS are studied by subjecting them to resilient modulus, rutting resistance and moisture susceptibility tests.

METHOD

Materials

The binder used in this study was PEN 60/70 grade. Asphalt binder was blended with 2wt%, 4wt% and 6wt% of nanosilica. The quantity of each additive was selected based on the weight of the asphalt binder and mixed in a binder mixer. To conduct the mixing process, an aluminium can was filled with 250 – 260 g of binder and placed in a mixer. After reaching a temperature of 160°C, a specified amount of nanosilica was added to the asphalt binder and mixing process was continued for one hour at 1800 rpm. Nanosilica should be fully added into the binder in the first 30 minutes of the mixing process (Arshad et al., 2016).

Marshall Mix Design

The Optimum Binder Content (OBC) for SMA20 and AC14 were determined based on Marshall Mix Design Method. This process was carried out in accordance with the Malaysian Public Works Department *JKR/SPJ/2008, 2008*.

Three specimens were prepared for each binder content within the range of 5-7% for SMA20 and 4%-6% for AC14 with the increment of 0.5%. The bulk specific gravity of each test specimen was determined in accordance to ASTM D 2726, as soon as the freshly compacted specimens cooled to the room temperature. The stability and flow values of each test specimen was obtained in accordance with ASTM D 1559. Specific gravity and void analysis was carried out for each test specimen after the completion of the stability and flow test in order to determine the percentage air voids in mineral aggregate (VMA) and the percentage air voids in the compacted mix (VIM). The average values of bulk specific gravity, stability, flow, VFB and VMA obtained above was plotted separately against the binder content and a smooth curve was drawn through the plotted values. Table 1 lists the properties of NS while Table 2 shows the aggregate gradation for SMA20 and AC14.

Table 1
Properties of nanosilica

Properties	Value
Appearance	Slight milky transparent
SiO ₂ (%)	30%
Na ₂ O (%)	0.5%
pH	8.5-10.5
Density	1.19-1.22 g/cm ³
Particle Size	10-15 nm

Table 2
SMA20 & AC14 aggregate gradation

Sieve Size (mm)	Passing (%)	Targeted Passing (%)	Retained (%)	Sample Weight (g)	Sieve Size (mm)	Passing (%)	Targeted Passing (%)	Retained (%)	Sample Weight (g)	
SMA20					AC14					
19.0	100	100	0	0	20	100	100	0	0	
12.5	100	90	10	120	14	90-100	95	5	60	
9.5	72-83	70	20	240	10	76-86	81	14	168	
4.75	25-38	24	46	552	5	50-62	56	25	300	
2.36	16-24	20	4	48	3.35	40-54	47	9	108	
0.600	12-16	14	6	72	1.18	18-34	26	21	252	
0.300	12-15	13.5	0.5	6	0.425	12-24	18	8	96	
0.075	8-10	9	4.5	54	0.15	6-14	10	8	96	
Filler	0	0	7	84	0.075	4-8	6	4	48	
Lime	0	0	2	24	Filler	0	0	4	48	
Total			100	1200	Lime	0	0	2	24	
								Total	100	1200

Resilient Modulus

The Indirect Tension was used to determine resilient modulus of bituminous mixtures by applying compressive loads with a haversine waveform. The resilient modulus value was obtained by the elastic modulus based on the recoverable strain under repeated loads. The results were shown in the total resilient axial deformation response of a specimen using Universal Testing Machine (Figure 2). Three Marshall Specimens for each mixture (SMA and AC) and NS content (0wt%, 2wt%, 4wt%, and 6wt%) were tested. This test was conducted in accordance to ASTM D4123-82. All the samples were tested at fixed temperature (25°C), two positions and three different pulse repetitions (1000ms, 2000ms and 3000ms).



Figure 2. (a) UTM machine; and (b) sample position

Rutting Resistance

This test was carried out in accordance to AASHTO TP-63 using Asphalt Pavement Analyzer (APA) Equipment. The APA machine was used to measure the rutting resistance of a modified and unmodified AC and SMA mixtures. Rutting resistance was evaluated by running a steel wheel over the pressurized tubing which rests on top of the specimens (Apeageyi, 2011). According AASHTO specification, asphalt mixes specimens that were used are 75 mm in height and 150 mm in diameter. The specimens had to be conditioned in the mould at the required temperature for 6 hours, when a concave wheel was used to run over pressurized rubber hosing that was set on top of three gyratory specimens in the temperature-controlled chamber. The rubber air lines on the load rack was pressurized to 0.69 ± 0.03 MPa and the wheel load was set up to 0.45 ± 0.02 KN. The asphalt mixture specimens were subjected to 8000 cycles of wheel loading in the chamber. The raw data was recorded on rut depth for each cycle, and the test repeated and to allow the mean of rut depth to be calculated. Figure 3 illustrates rut samples before and after testing.

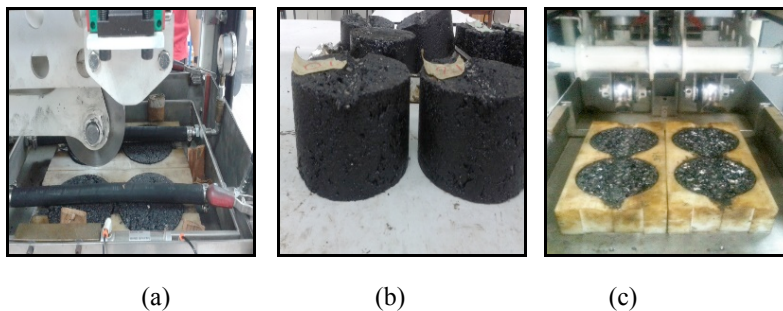


Figure 3. (a) Sample position; (b) sample after test; and (c) sample before test

Moisture Susceptibility

Moisture susceptibility also known as moisture damage is the most common concern for asphalt pavements. In this research, moisture damage was evaluated in accordance with AASHTO T283. Stripping samples for both SMA and AC were compacted to obtained 7 ± 1 % air voids according to AASHTO T283 standard requirement. The indirect tensile strength test to determine the tensile properties of cylindrical samples was performed by applying a compression load along a diametrical plane of two opposite loading heads. For indirect tensile strength test, the samples were placed between the steel loading strips using an indirect tensile strength machine.

Two sets of samples were prepared for each mixture, dry samples were tested without moisture conditioning while the second was conditioned by saturating with water at 70 – 80% degree of saturation. The conditioned samples were immersed in water for 24 hours at 60°C in a water bath and conditioned at 25°C. The samples were then subjected to indirect tensile strength test (Figure 4).

A constant rate of 50 mm per minute at 25°C was applied on the diameter of the specimens. The specimen usually fails by splitting along with the loaded plane when the loading acts perpendicularly to the applied load plane. The maximum load carried by a specimen at the point of failure can be calculated by equation 1;

$$ITS = (2000P)/\pi hD \quad [1]$$

Where;

ITS = Indirect tensile strength

P = Maximum load

h = Thickness of specimen

D = Diameter of specimen

The ratio of the average tensile strength of the dry conditioned and wet conditioned specimens or also known as Tensile Strength Ratio (TSR) is obtained using the following equation 2;

$$TSR = \left(\frac{S_2}{S_1}\right) \times 100 \quad [2]$$

Where;

TSR = Tensile strength ratio

S₁ = Average tensile strength of the dry subset

S₂ = Average tensile strength of the conditioned subset

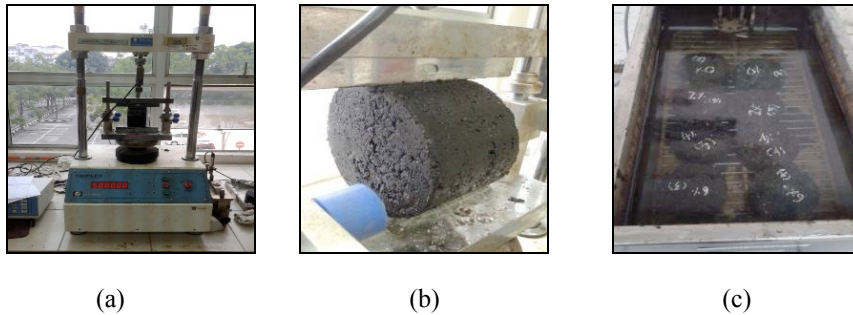


Figure 4. ITS Test: (a) ITS machine; (b) sample position; and (c) wet conditioned samples

RESULTS AND DISCUSSION

Volumetric Properties

The value of Optimum Binder Content (OBC) is based on the volumetric properties values. Table 3 below shows the Marshall result for SMA20 and AC14. Results indicate all values were in the specified range.

Table 3
Marshall result for SMA20 and AC14

Properties	Specification JKR/SPJ/2008	SMA20	Status	Properties	Specification JKR/SPJ/2008	AC14	Status
OBC, %	5-7	6.16	PASS	OBC, %	4-6	4.85	PASS
VTM, %	3-5	4.55	PASS	VTM, %	3-5	3.9	PASS
VFB, %	Min 17	69	PASS	VFB, %	70-80	74	PASS
VMA, %	-	26.8	PASS	VMA, %	-	15.8	PASS
Stability, N	Min 6200	22563	PASS	Stability, N	Min 8000	18150	PASS
Flow, mm	2-4	3.10	PASS	Flow, mm	2-4	3.85	PASS
Draindown	0.3	0.25	PASS	Stiffness, N/mm	Min 2000	5000	PASS

SMA20 & AC14 volumetric properties

Resilient Modulus

For SMA20, the increment in the amount of NS will result in a higher value of resilient modulus. At 1000ms pulse period, the resilient modulus for 0wt% NS-SMA20 was 3138 MPa. The highest M_r value obtained at 4wt% NS-SMA20 was 4076 MPa. However, the results for resilient modulus values at different pulse period did not show any trend in uniformity. For AC14, the highest resilient modulus value was obtained at 4wt% NS-AC14 which was 8217 MPa at 1000ms pulse repetition. The lowest average value of resilient modulus obtained was

3849 MPa for 6wt% NS-AC14 at 2000ms pulse repetition. In general, higher pulse repetitive period loads the lower was the resilient modulus value. For instant, at 4wt% NS-AC14, the average resilient modulus was 8217 MPa at 1000ms, 6060 MPa at 2000ms and 5644 MPa at 3000ms. Table 4 shows the results of resilient modulus for both mixtures and how 4wt% NS can be considered the optimum amount for enhancing PA performance.

Table 4
NS-SMA20 & NS-AC14 resilient modulus

Sample	Point	Mean Pulse Repetitive Period (ms) SMA20			Mean Pulse Repetitive Period (ms) AC14		
		1000	2000	3000	1000	2000	3000
0% NS	A	3493.00	2712.50	3143.50	4568.00	4402.50	4534.50
	B	2784.00	2831.50	2749.00	6387.00	6787.00	5843.00
	Mr _{mean}	3138.50	2772.00	2946.30	5477.50	5594.75	5188.75
2% NS	A	3623.00	3038.50	3347.50	4224.50	4160.00	4403.00
	B	3127.50	2864.50	2791.00	3705.50	3694.00	3721.00
	Mr _{mean}	3375.30	2951.50	3069.30	3965.00	3927.00	4062.00
4% NS	A	3941.50	4536.00	4804.50	6086.50	6210.50	5446.50
	B	4211.50	4101.00	4577.00	10348.50	5910.00	5841.50
	Mr _{mean}	4076.50	4318.50	4690.75	8217.50	6060.25	5644.00
6% NS	A	3656.00	3194.00	3486.00	2366.50	2766.00	2864.00
	B	3259.00	3339.00	3288.00	6320.50	4933.50	5053.50
	Mr _{mean}	3457.50	3266.50	3387.00	4343.50	3849.75	3958.75

Rutting Resistance

The objective of this test is to determine the rut depth of asphalt mixtures with the Asphalt Pavement Analyzer (APA). The Asphalt Pavement Analyzer counter was set to run at 8000 cycles. For this test, all the specimens were tested at 60°C. This test was conducted in accordance with AASHTO TP 63. The most effective amount of NS in enhancing the performance of asphalt mixtures i.e. 4wt% NS was used in both mixtures.

From Figure 5, for SMA20, it can be seen the rut depth increased rapidly at the beginning of the test which is between 0 to 6000 cycles and the critical part happened at the range between 0 to 1000 cycles and subsequently maintained at a range of 7000 to 8000 cycles. The result was still in the range of depth measurement (4 mm) complied with the AASHTO TP 63 specifications. Meanwhile, it can be stated that the sample for 4wt% NS-SMA20 is better because the rut depth recorded was lower than the control sample of 0wt% NS-SMA20. The percent changes were highest at 4000 cycles with 87.47% to decrease to 24.92% at 8000 cycles. On the other hand, for 4wt% NS-SMA20, the highest percentage change of 89.68% was also at 4000 cycles and the value decreased to 28.12% at the 8000 cycles.

For AC14, the modified asphalt mix specimen selected for this test was also 4wt% NS-AC14. From Figure 6, it can be seen that the percentage changes for the control specimen was higher than that of the modified specimen (4wt% NS-AC14). After 8000 cycles, rut depth

for the control specimen was 5.002 mm and for the modified specimen was 4.473 mm. The percentage change of rut depth of the control specimen changed to a high of 52.68% compared with the modified specimen which changed to 55.26%. This shows that, the presence of NS in AC14 can decrease the rut depth. Lower rut depth indicates that NS-AC14 provides better rutting resistance.

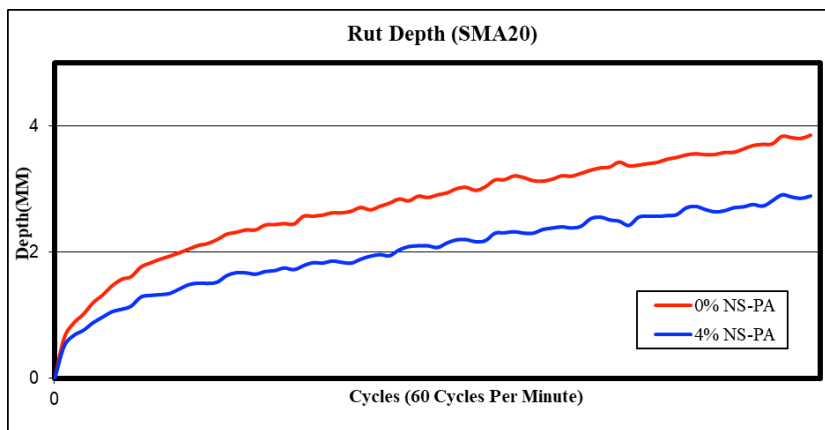


Figure 5. NS-SMA20 rut depth

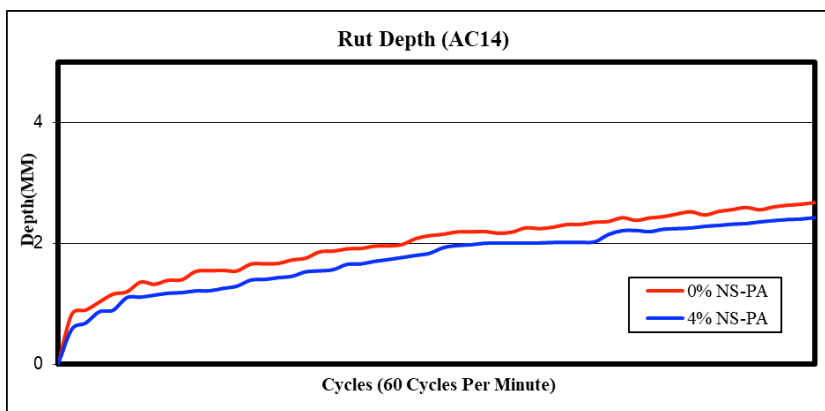


Figure 6. NS-AC14 rut depth

Moisture Susceptibility

The objective of this test was to determine moisture susceptibility values for SMA20 and AC14 using the indirect tensile strength test. Samples were tested under dry and wet conditions in accordance to AASHTO T283.

For SMA20, the value of moisture susceptibility for dry condition was higher compared to the wet condition. The value of TSR increased roughly 10% for modified specimens. In addition, the TSR value for control sample which was 0wt% NS-SMA20 was 84% while 94%

for modified specimens. Both achieved the minimum requirement based on AASTHO T283 specification. If the TSR value is more than 80%, resistance towards moisture is higher and if the TSR value is below 80%, it is sensitive to moisture damage.

For AC14, dry ITS value for 0wt% NS-AC14 mixtures was only 499 Kpa while 537 Kpa for modified specimens. For wet conditions, the value of ITS for control specimen and modified specimen were 420 Kpa and 505 Kpa respectively. TSR value for both control sample and modified sample passed the minimum requirement which were 86% and 91% respectively. The result indicated the indirect tensile strength values of wet conditioned values were lower than that for dry conditioned, and the presence of NS in the bituminous mixes increased the mixtures strength to resist damage created by moisture. Figure 7 illustrates the result of ITS and TSR value for both asphalt mixtures.

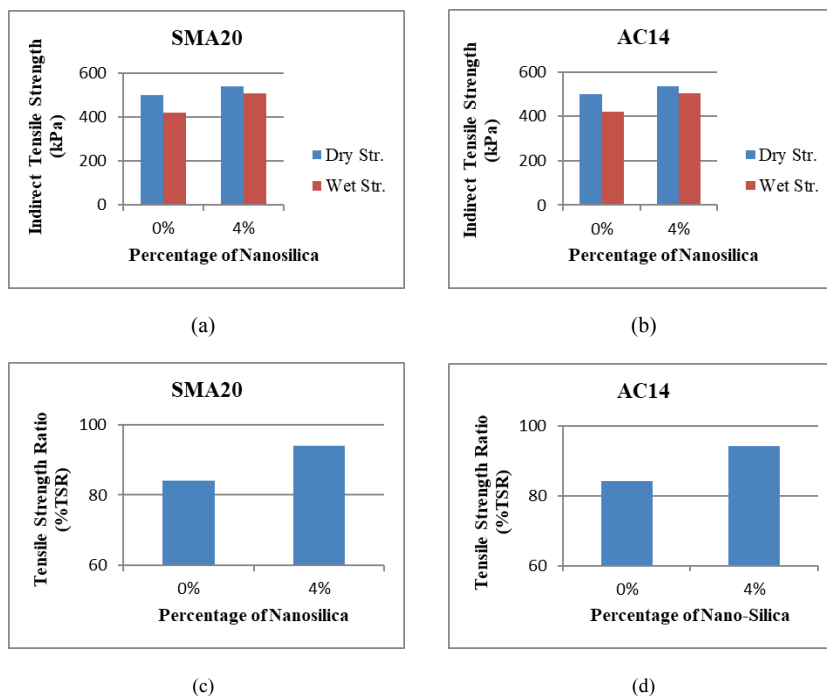


Figure 7. (a) ITS SMA20; (b) ITS AC14; (c) TSR SMA20; and (d) TSR AC14

CONCLUSION

The findings of this study indicate that the existence of nanoparticle in particular 4wt% NS can enhance the performance of SMA20 and AC14 in terms of mix design, resilient modulus, rutting resistance and moisture susceptibility.

ACKNOWLEDGEMENTS

The authors would like to acknowledge FRGS Research Grant: FRGS/1/2015/TK08/UITM/02/3 and UiTM Shah Alam Malaysia for funding this study and to the IIESM UiTM Shah Alam Malaysia to allow this article to be written.

REFERENCES

- Amelian, S., Mahdi, S., & Mahdi, S. (2014). Moisture susceptibility evaluation of asphalt mixes based on image analysis. *Construction and Building Materials*, 63, 294–302.
- Apeageyi, A. K. (2011). Rutting as a Function of Dynamic Modulus and Gradation. *Journal of Materials in Civil Engineering*, 23(9), 275-284.
- Arshad, A. K., Masri, K. A., Samsudin, S., & Ahmad, J. (2016). Mechanical Properties of Porous Asphalt with Nanosilica modified Binder. *Jurnal Teknologi*, 78(7-2), 139–146.
- Brown, B. E. R., Kandbal, P. S. K., Lee, D. Y., & Lee, K. W. (1996, February). Significance Of Tests For Highway Materials, *ASCE* 8(pp. 26–40).
- Ebrahim, A., & Behiry, A. E. (2013). Laboratory evaluation of resistance to moisture damage in asphalt mixtures. *Ain Shams Engineering Journal*, 4(3), 351–363.
- El-Shafie, M., Ibrahim, I. M., & Abd El Rahman, a. M. M. (2012). The addition effects of macro and nano clay on the performance of asphalt binder. *Egyptian Journal of Petroleum*, 21(2), 149–154.
- JKR/SPJ/2008*. (2008). *Standard Specification for Road Works*. Kuala Lumpur, 1-161.
- Kumar, P., & Anand, P. (2012). Laboratory Study on Moisture Susceptibility of Dense Graded Mixes. *Journal of Transportation Engineering*, 138(1), 105–113.
- Moghadas Nejad, F., Azarhoosh, a. R., Hamed, G. H., & Azarhoosh, M. J. (2012). Influence of using nonmaterial to reduce the moisture susceptibility of hot mix asphalt. *Construction and Building Materials*, 31, 384–388.
- Shafabakhsh, G., & Tanakizadeh, A. (2015). Investigation of loading features effects on resilient modulus of asphalt mixtures using Adaptive Neuro-Fuzzy Inference System. *Construction and Building Materials*, 76, 256–263.
- Venudharan, V., & Biligiri, K. P. (2015). Estimation of phase angles of asphalt mixtures using resilient modulus test. *Construction and Building Materials*, 82, 274–286.





Mechanism of Aloe Emodin-Induced Apoptosis in ER⁺-Breast Cancer Cells, MCF-7

Indah Mohd Amin^{1,4*}, Siti Hamimah Sheikh Abdul Kadir^{1,2}, Mohamad Rodi Isa³,
Nik Mohd Mazuan Nik Mohd Rosdy⁵ and Narimah Abdul Hamid Hasani²

¹Institute for Medical Molecular Biotechnology (IMMB), Faculty of Medicine, Universiti Teknologi MARA (UiTM), 40450 Shah Alam, Selangor, Malaysia

²Department of Biochemistry and Molecular Medicine, Faculty of Medicine, Universiti Teknologi MARA (UiTM), 40450 Shah Alam, Selangor, Malaysia

³Department of Population Health and Preventive Medicine, Faculty of Medicine, Universiti Teknologi MARA (UiTM), 40450 Shah Alam, Selangor, Malaysia

⁴Centre of Preclinical Sciences Studies, Faculty of Dentistry, Universiti Teknologi MARA (UiTM), 47000 Sungai Buloh, Selangor, Malaysia

⁵Centre of Oral and Maxillofacial Diagnostic and Medicine Studies, Faculty of Dentistry, Universiti Teknologi MARA (UiTM), 47000 Sungai Buloh, Selangor, Malaysia

ABSTRACT

The objective of this research is to investigate the regulation of apoptotic associated-genes and proteins expression of aloe emodin on oestrogen receptor (ER)-positive (MCF-7). Oestrogen receptor (ER)-positive (MCF-7) cells were cultured in complete RPMI media. Cells were treated with aloe emodin at its IC₅₀ of 80uM. Maximum treatment time was set for 72 hours in all assays. Both genes and proteins involved in the regulation of apoptosis (Fas, FADD, Caspase-3, Caspase-8, Caspase-9, Bax, Bcl-2, and Cytochrome c) in aloe emodin-treated MCF-7 were determined using Quantigene 2.0 Plex and protein ELISA assays respectively. Aloe emodin, previously reported as anti-cancer agent, was found to act as an apoptotic inducer on MCF-7 cells. In intrinsic apoptosis signalling, Bax, Cytochrome c and Caspase-9 proteins were upregulated (54.11% ± 4.51, 25.17% ± 4.13 and 36.05% ± 11.75); while no change was observed in Bcl-2 protein. Except for Caspase-9, these results are in accordance with gene expression. In extrinsic apoptosis, Fas and Caspase-8 were upregulated (133.82% ± 2.85 and 26.44% ± 2.48), contrary to gene expression. These findings indicate that aloe emodin activates both extrinsic and intrinsic apoptosis pathways. The data suggests (i) aloe emodin has the potential to be a selective apoptotic inducer in ER⁺-breast cancer management; and (ii) the present study could be used as a basis for in vivo experiment..

ARTICLE INFO

Article history:

Received: 28 September 2016

Accepted: 03 February 2017

E-mail addresses:

indahma@salam.uitm.edu.my (Indah Mohd Amin),

sitih587@salam.uitm.edu.my (Siti Hamimah Sheikh Abdul Kadir),

rodi@salam.uitm.edu.my (Mohamad Rodi Isa),

nikmohd@salam.uitm.edu.my (Nik Mohd Mazuan Nik Mohd Rosdy),

drnarimah@salam.uitm.edu.my (Narimah Abdul Hamid Hasani)

*Corresponding Author

Keywords: Aloe emodin, MCF-7, intrinsic and extrinsic apoptosis, Quantigene 2.0 Plex

INTRODUCTION

Breast cancer which accounts for 18.1% of all cancers has a 32.1% rate among Malaysian women compared with other types of cancers (Omar & Tamin, 2011). Approximately two-thirds of breast cancer patients expressed oestrogen receptor (ER), and received endocrine treatment with anti-oestrogens such as tamoxifen, toremifene, raloxifene, and fulvestrant (Clarke et al., 2003; Baumgarten & Frasor, 2012). Despite these therapeutic treatments, the overall incidence rate remains high. (Baumgarten & Frasor, 2012).

Although it is well accepted that cancer refers to uncontrolled cell growth, anti-cancer drugs affect not only cancer cells but also normal active proliferating cells such as bone marrow, gastrointestinal epithelial and dermal papilla of hair follicle. Thus treatment unfortunately worsens the patients' situation as increasing evidences of toxicity have been observed (Thavendiranathan et al., 2013). Besides being non-selective, most of the drugs lead to resistance in cancer patients and have adverse effects when exposed to prolonged periods (Fisher et al., 2001).

Natural sources have been used in traditional remedies to cure many types of diseases such as diabetes, wound healing, osteoarthritis, malaria, skin diseases, cancer and other critical diseases for many years. In fact, phytochemicals and their significant healing properties have been well recognised in the scientific research (Singh, 2007).

Aloe emodin has been recommended as a potential natural chemotherapeutic agent. Aloe is a genus of the widely known species Aloe Vera or also known as Aloe barbadensis Miller. Aloe emodin is the well-known anthraquinone active compound that can be found in some species of Aloe (ElSohly et al., 2004). Accumulative evidences of aloe emodin as anti-cancer agent from in vitro as well in vivo studies were well documented. Unlike tamoxifen, it selectively inhibits proliferation of cancer cells including prostate, neuroectodermal tumour and cervical, without affecting normal cells (Guo et al., 2007; Liu et al., 2012; Pecere et al., 2000).

Apoptosis, or programmed cell death, is a normal process. The apoptotic signal is a response to defective cells to commit suicide in a natural way without harming neighbouring and surrounding cells (Johnstone et al., 2002; Elmore, 2007). Thus, deregulation in apoptosis has been implicated in a variety of diseases such as cancer (Brown & Attardi, 2005). Molecular mechanism studies suggest that its anti-cancer property was through the promotion of cell cycle arrest and apoptosis (Chen et al., 2004; Kuo et al., 2002). Although, there is a significant relationship between apoptosis and aloe emodin, its induction on breast cancer cells has not been studied sufficiently. Current studies suggest that aloe emodin reduces the expression of ER α in both time- and dose-dependent manners, thus reducing oestrogen proliferative effect on MCF-7 cells (Huang et al., 2013). In addition, there was evidence that aloe emodin inhibited the activation of ER α even at lower dosage compared to its isomer, emodin (Huang et al., 2013).

In our previous investigation (Amin et al., 2013), aloe emodin inhibited the proliferation of MCF-7 with IC₅₀ of 80 μ M using WST-1 proliferation. No IC₅₀ value was obtained on MDA-MB-231 and MCF-10A, even up to 150 μ M. In contrast, tamoxifen was non-selective to all cells tested. By using the cellular apoptotic assay, our previous findings suggested that the anti-proliferation effect was through activation of apoptosis signalling. The activation of apoptosis was observed through the morphological changes and the increasing percentage of

apoptotic population at 48 and 72 hours treatment using flow-cytometry analyses (Amin et al, 2015, 2016). In the present study we further investigate the underlying molecular mechanism by looking at the regulation of apoptosis associated-genes and protein expressions.

METHOD

Materials

An oestrogen receptor-positive breast cancer cell, MCF-7 was purchased from American Type Cell Collection (Virginia, USA) Complete culture media RPMI, foetal bovine was from GIBCO Invitrogen (GIBCO Invitrogen, California, USA), phosphate buffer saline (PBS), accutase and dimethyl sulfoxide (DMSO; Sigma Chemical Co., St. Louis, USA), QuantiGene 2.0 Multiplex Assay was purchased from Affymetrix California, USA. MCF-7. Aloe emodin and tamoxifen from Sigma Chemical Co. (St Louis, USA).

Cell and Treatments

Cells were cultured in complete RPMI media supplemented with 10% foetal bovine serum and 1% of penicillin and streptomycin. The cells were maintained as monolayer up to 70% to 90% confluence in humidified atmosphere of 5% CO₂, at 37°C in T25 and T75 flasks. Aloe emodin is synonym as 1,8-Dihydroxy-3-(hydroxymethyl) anthraquinone, 3-Hydroxymethylchryszazine is in purity of ≥95% as assayed by high performance liquid chromatography (HPLC). Tamoxifen or (Z)-1-(p-Dimethylaminoethoxyphenyl)-1,2-diphenyl-1-butene, trans-2-[4-(1,2-Diphenyl-1-butenyl)phenoxy]-N,N- dimethylethylamine is ≥99% in purity and used as positive control. Aloe emodin was measured and dissolved separately in DMSO to prepare primary stocks of 50 mM. Both primary stock (aloe emodin and tamoxifen) solutions were filtered with a 0.2 µm sterile filter and stored in aliquots at -20°C protected from light. The final working solutions of aloe emodin and tamoxifen were diluted with culture media so that the final concentration of DMSO in cell culture was <0.1%. Tamoxifen, a non-steroidal oestrogen antagonist was used as positive control. All the preparations were performed under sterile conditions.

QuantiGene 2.0 Multiplex Assay

QuantiGene 2.0 Multiplex Assay is based on a series of hybridization method that capture target RNA in samples. Initially, target RNAs were captured by fluorescent microspheres (Capture Beads). Following from this, the target-specific RNA was measured by mixing it with high stringent of cocktails which include Capture Extenders (CEs), Label Extenders (LEs) and Blocker (BLs). They bound to RNA region and selectively capture the target RNA by a series of complex hybridization. The hybridization step was performed overnight at a temperature of 55°C. These resulted in sandwich multifaceted form which includes probe and the target sequence. The final step was the signal amplification and detection of target mRNA. The target mRNA was sequentially hybridized with specific Pre-amplifier, Amplifier and Label probes. The luminescent signal detected is proportionate to the amount of target mRNA present in the sample. Prior to the experiment, cells were seeded at 1 x 10⁶ into six different T25 flasks in 5% CO₂, at 37°C. Each group was treated separately with aloe emodin (IC₅₀), and non- treated

cells were used as control. After 72 hours of treatment, cells were washed with PBS, detached with accutase and centrifuged at 15,000 rpm for 5 minutes. Cell pellets were re-suspended in complete media, adjusted to 1×10^6 cells/ml and kept in 15 ml tubes at -20°C before used. This assay was conducted following the protocol outlined in QuantiGene 2.0 Plex User Manual (Affymetrix., California, USA). Hypoxanthine-guanine phosphoribosyltransferase (HPRT) was used as housekeeping gene.

ELISA Assay

Concentrations of 1×10^6 cells were cultured in 1 ml complete media in 6-well plate with 5% CO_2 , at 37°C for 24 hours. Cells in each well were treated separately with aloe emodin. Non-treated cells were used as control. After washing the cells twice with cold PBS, 380 μl of cold RIPA buffer containing Pierce protease inhibitors. The plate was incubated on ice for 5 minutes, swirled gently to ensure uniform spreading of lysis buffer on each well. Each cell lysate was collected using cell scraper and transferred to a 10-ml tube. Each lysate was sonicated at 50% pulse for 1 minute and centrifuged at $14,000 \times g$ for 15 minutes. Standard solution was reconstituted with 1.0 ml of sample diluents and allowed to stand for 15 minutes. A series of standard solutions ranging from S0 to S6 was prepared by two-fold serial dilution of standard stock with its diluents. Using the standard curve, all the samples from different treatment groups were standardized at 3 mg/ml. Concentration of 100 μl of treatment samples and standard were loaded into a pre-coated 96-well microplate.

Statistical Analysis

The Statistical Package for Social Sciences (SPSS) version 16.0 was used to analyse the data. Each experiment was carried out in triplicates and repeated three times. The differences between the groups were evaluated using the one-way ANOVA test.

RESULTS AND DISCUSSION

Effects of Aloe Emodin on Apoptosis Associated-Gene Expressions in MCF-7 cells

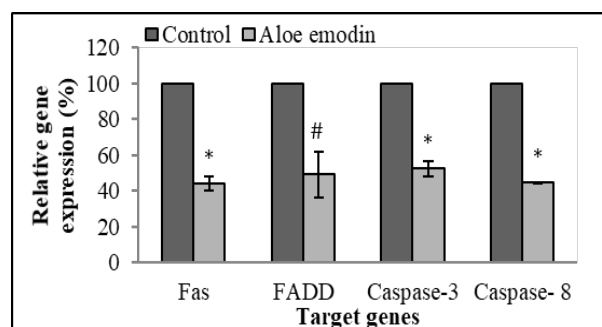


Figure 1. Fas, FADD, Caspase-3 and Caspase-8 gene expressions of ER⁺-breast cancer, MCF-7 cells after treatment with aloe emodin against control (untreated) cells and normalization with HPRT.

Note: *Significant as compared to control (untreated) cells at $p < 0.01$; # Significant as compared to control (untreated) cells at $p < 0.05$

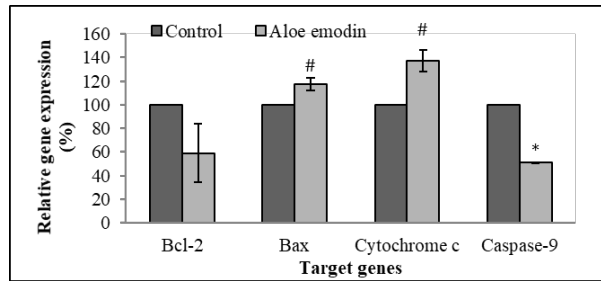


Figure 2. Bcl-2, Bax, Cytochrome c and Caspase-9 gene expressions of ER⁺-breast cancer, MCF-7 cells after treatment with aloe emodin against control (untreated) cells and normalization with HPRT

Note: *Significant as compared to control (untreated) cells at $p < 0.01$; # Significant as compared to control (untreated) cells at $p < 0.05$

Fas, FADD, Caspase-3 and Caspase-8 gene expressions were down regulated by $65.91\% \pm 0.93$, $50.83\% \pm 12.77$, $47.42\% \pm 4.31$ and $55.23\% \pm 0.01$ ($p < 0.05$, $n=3$), respectively after being normalized with HPRT (Fig. 1). Based on these findings, it appears that the apoptosis effect of aloe emodin on MCF-7 cells is independent of the extrinsic pathway. In addition, Bax, Cytochrome c gene expressions were upregulated by $17.47\% \pm 5.29$ and $37.29\% \pm 9.37$ ($p < 0.05$, $n=3$), respectively after being normalised with HPRT gene. On the contrary, Caspase-9 was downregulated by $48.79\% \pm 0.17$ ($p < 0.05$, $n=3$) while Bcl-2 shown changes when compared with the control however was not significant. This data suggests that the apoptosis effect of aloe emodin on MCF-7 cells is mitochondrial-dependent. However, more studies on the effect of aloe emodin on the expression associated apoptosis proteins that mediated both intrinsic and extrinsic apoptosis signalling needs to be done to validate gene expression results.

Effects of Aloe Emodin on Apoptosis Associated-Protein Expressions in MCF-7 cells

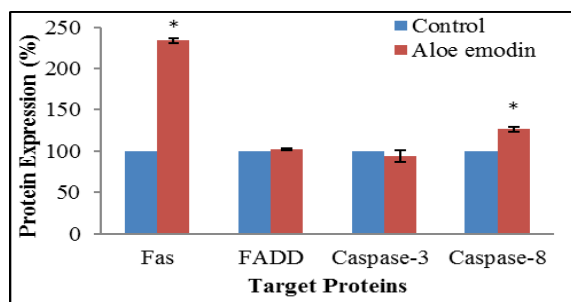


Figure 3. Fas, FADD, Caspase-3 and Caspase-8 protein expressions of MCF-7 cells after treatment with aloe emodin

Note: *Significant as compared to control (untreated) cells at $p < 0.01$

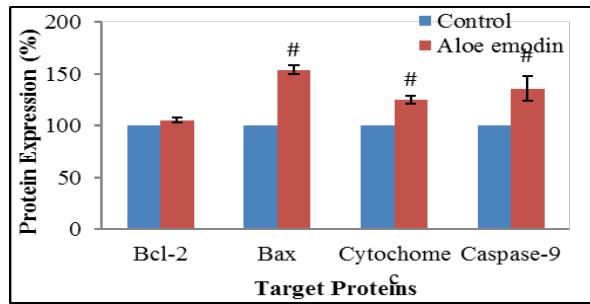


Figure 4. Bcl-2, Bax, Cytochrome c and Caspase-9 protein expressions of MCF-7 cells after treatment with aloe emodin

Note: #Significant as compared to control (untreated) cells at $p < 0.05$

Contrary to gene expression, Fas and Caspase-8 proteins were upregulated by $133.82\% \pm 2.85$ and $26.44\% \pm 2.48$ respectively (Figure 3). This indicates the apoptosis effect of aloe emodin on MCF-7 cells is via the extrinsic pathway. However, FADD and Caspase-3 gene expression results did not agree with their protein expressions. No changes were observed in the expression of FADD and Caspase-3 proteins. Aloe emodin upregulated the expression of Bax, Cytochrome c and Caspase-9 proteins by $54.11\% \pm 4.51$, $25.17\% \pm 4.13$ and $36.05\% \pm 11.75$, respectively. No change was seen in Bcl-2 protein (Figure 4). Except for Caspase-9, these results are in accordance with gene expression profiles. This indicates the apoptosis effect of aloe emodin on MCF-7 cells is through the intrinsic pathway targeting the mitochondrial function.

The present findings show the significant downregulation of associated-extrinsic apoptotic genes such as Fas, FADD, Caspase-3 and Caspase-8 after being normalised with both HPRT. Contrary to the above results, Fas and Caspase-8 proteins were unregulated but no changes were observed in FADD and Caspase-3. Based on Fas and Caspase-8 protein expressions, aloe emodin apoptosis effect on MCF-7 cells is suggested to act through the activation of the extrinsic pathway. Chemotherapy drug such as doxorubicin induces Fas/FasL interaction on the surface of tumour cells to activate apoptosis (Mitsiades et al., 2001). Similarly, in vivo and in vitro studies 5-fluorouracil showed to mediate the apoptosis signal through Fas/FasL interaction (Eichhorst et al., 2001). The lack of death receptors and their ligand expressions in leukemic cells after chemotherapy is suggested to be due to the failure of apoptosis and which in turn contributed to poor treatment outcome (Tourneur et al., 2004). In breast cancer treatment, the Fas system was used as a biomarker to evaluate the chemo responsiveness of anthracycline-based adjuvant therapy for type I and II breast cancer patients. It was suggested that the prognostic value of Fas receptor and FasL is strongly associated with the aggressive tumour phenotype that can be correlated with the progression of the disease (Botti et al., 2004). Activation of Fas system by aloe emodin in MCF-7 cells support the suggestion that this agent could be as competitive as other available drugs such doxorubicin and tamoxifen. Similar findings were also observed in different type of human cancer cells such as lung squamous CH27 (Lee et al., 2001), bladder T24 (Lin et al., 2006) and tongue squamous SCC-4 (Chiu et al., 2009) cells.

It also appears that the apoptosis action of aloe emodin on MCF-7 cells is mitochondrial-dependent. Interestingly, the expressions of Bax, Cytochrome c and Caspase-9 proteins were upregulated while no changes were observed for Bcl-2. Thus, it is suggested that aloe emodin apoptosis effect on MCF-7 cells does involve the activation of the intrinsic pathway. Deregulation of Bcl-2 family members is constantly associated with attribution of human malignant diseases. Understanding how they become involved in the regulation of death signal can be useful in designing targeted therapeutic regimen. One of the spectacular achievements of anti-cancer therapies is the direct targeting of Bcl-2 family proteins in mitochondria (Frenzel et al., 2009). Clinical trials using drugs targeting these Bcl-2 family members such as ABT-263, oblimersen sodium GX15-070 and AT-101 are ongoing (Kang & Reynolds, 2009). Figure 5 shows the suggested pathways that illustrate the effect of aloe emodin in inducing the intrinsic and extrinsic apoptosis pathways.

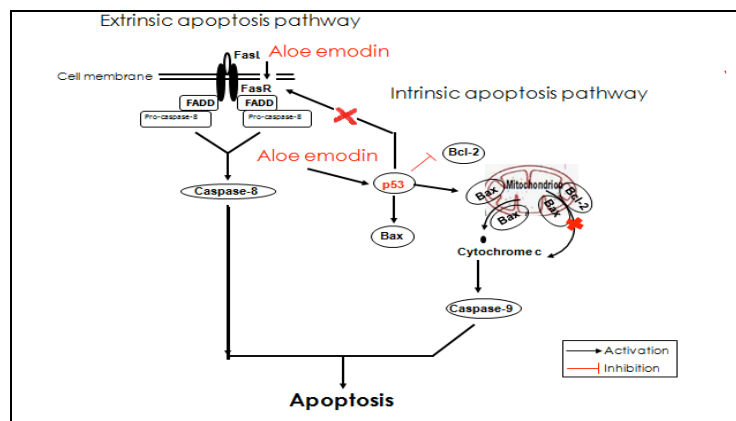


Figure 5. Schematic diagram of the suggested pathways of aloe emodin in inducing the intrinsic and extrinsic apoptosis

It is noted that the gene expression study reported in this work is not in accordance with the protein study. There are three main possible explanations for the poor correlation between mRNA and protein levels in experimental designs (Greenbaum et al., 2003): (i) post-transcriptional mechanisms might affect the regulation at gene and protein levels; (ii) different protein half-lives limited the capacity to directly measure their precise concentrations; and (iii) error and noise involved throughout the mRNA and protein experiment setting. Even with where the latest technology is used, discrepancies were observed between mRNA and protein measurements (Pradet-Balade, 2001; Vasconcelos et al., 2002; Pascal et al., 2008).

CONCLUSION

Our findings suggest aloe emodin to be used in combination with anti-oestrogen therapy in the treatment of cancer. The findings could provide a foundation for in vivo study and widen the possibility for future clinical experiment setting.

ACKNOWLEDGEMENTS

This research was funded by Universiti Teknologi MARA, Malaysia (600-RMI/ST/DANA 5/3/Dst (304/2009)) and Ministry of Higher Education (MOHE), Malaysia (600-RMI/RAGS 5/3 (86/2013)).

REFERENCES

- Amin, I. M., Isa, M. R., NMMNM, R., & Hasani, N. A. H. (2016). Aloe emodin enhances tamoxifen cytotoxicity effect on *erα*-positive breast cancer cells, MCF-7, through downregulation of MEK1 and MEK2. *JUMMEC*, 19(1), 1-10.
- Amin, I. M., Kadir, S. A., Siti, H., Rosdy, N. M. M. N. M., Siran, R., & Hasani, N. (2013, August). Anti-cancer effect of aloe emodin on breast cancer cells, MCF-7. In *Systems Biology (ISB), 2013 7th International Conference on* (pp. 103-108). IEEE.
- Amin, I. M., Kamaludin, R., Yeap, S. K., Isa, M. R., Rosdy, N., Siran, R. & Hasani, N. A. H. (2015). Aloe Emodin Induces Apoptosis in ER+-breast Cancer Cells; MCF-7 through IGF-1R Signalling Pathway. *Sains Malaysiana*, 44(8), 1137-1143.
- Baumgarten, S. C., & Frasar, J. (2012). Minireview: inflammation: an instigator of more aggressive oestrogen receptor (ER) positive breast cancers.
- Botti, C., Buglioni, S., Benevolo, M., Giannarelli, D., Papaldo, P., Cognetti, F., et al. (2004). Altered expression of FAS system is related to adverse clinical outcome in stage I-II breast cancer patients treated with adjuvant anthracycline-based chemotherapy. *Clinical Cancer Research*, 10(4), 1360-1365.
- Brown, J. M., & Attardi, L. D. (2005). The role of apoptosis in cancer development and treatment response. *Nature Reviews Cancer*, 5(3), 231-237.
- Chen, H. C., Hsieh, W. T., Chang, W. C., & Chung, J. G. (2004). Aloe-emodin induced in vitro G2/M arrest of cell cycle in human promyelocytic leukemia HL-60 cells. *Food and Chemical Toxicology*, 42(8), 1251-1257.
- Chiu, T. H., Lai, W. W., Hsia, T. C., Yang, J. S., Lai, T. Y., Wu, P. P., et al. (2009). Aloe-emodin induces cell death through S-phase arrest and caspase-dependent pathways in human tongue squamous cancer SCC-4 cells.
- Clarke, R., Liu, M. C., Bouker, K. B., Gu, Z., Lee, R. Y., Zhu, Y., et al. (2003). Antiestrogen resistance in breast cancer and the role of oestrogen receptor signalling. *Oncogene*, 22(47), 7316-7339.
- Eichhorst, S. T., Mürköster, S., Weigand, M. A., & Krammer, P. H. (2001). The chemotherapeutic drug 5-fluorouracil induces apoptosis in mouse thymocytes in vivo via activation of the CD95 (APO-1/Fas) system. *Cancer Research*, 61(1), 243-248.
- Elmore, S. (2007). Apoptosis: a review of programmed cell death. *Toxicologic Pathology*, 35(4), 495-516.
- ElSohly, M. A., Gul, W., & Murphy, T. P. (2004). Analysis of the anthraquinones aloe-emodin and aloin by gas chromatography/mass spectrometry. *International Immunopharmacology*, 4(14), 1739-1744.
- Fisher, B., Dignam, J., Bryant, J., & Wolmark, N. (2001). Five versus more than five years of tamoxifen for lymph node-negative breast cancer: updated findings from the National Surgical Adjuvant Breast and Bowel Project B-14 randomized trial. *Journal of the National Cancer Institute*, 93(9), 684-690.

- Frenzel, A., Grespi, F., Chmielewski, W., & Villunger, A. (2009). Bcl2 family proteins in carcinogenesis and the treatment of cancer. *Apoptosis*, 14(4), 584-596.
- Greenbaum, D., Colangelo, C., Williams, K., & Gerstein, M. (2003). Comparing protein abundance and mRNA expression levels on a genomic scale. *Genome Biology*, 4(9), 117, 1-8.
- Guo, J., M., Xiao, B. X., Liu, Q., Zhang, S., Liu, D. H., & Gong, Z. H. (2007). Anticancer effect of aloe-emodin on cervical cancer cells involves G2/M arrest and induction of differentiation. *Acta Pharmacologica Sinica*, 28(12), 1991-1995.
- Huang, P. H., Huang, C. Y., Chen, M. C., Lee, Y. T., Yue, C. H., Wang, H. Y., & Lin, H. (2013). Emodin and Aloe-Emodin Suppress Breast Cancer Cell Proliferation through ER α Inhibition. *Evidence-Based Complementary and Alternative Medicine*, 2013, 1-12.
- Johnstone, R. W., Ruefli, A. A., & Lowe, S. W. (2002). Apoptosis: a link between cancer genetics and chemotherapy. *Cell*, 108(2), 153-164.
- Kang, M. H., & Reynolds, C. P. (2009). Bcl-2 inhibitors: targeting mitochondrial apoptotic pathways in cancer therapy. *Clinical Cancer Research*, 15(4), 1126-1132.
- Kuo, P. L., Lin, T. C., & Lin, C. C. (2002). The antiproliferative activity of aloe-emodin is through p53-dependent and p21-dependent apoptotic pathway in human hepatoma cell lines. *Life Sciences*, 71(16), 1879-1892.
- Lee, H. Z., Hsu, S. L., Liu, M. C., & Wu, C. H. (2001). Effects and mechanisms of aloe-emodin on cell death in human lung squamous cell carcinoma. *European Journal of Pharmacology*, 431(3), 287-295.
- Lin, J. G., Chen, G. W., Li, T. M., Chouh, S. T., Tan, T. W., & Chung, J. G. (2006). Aloe-emodin induces apoptosis in T24 human bladder cancer cells through the p53 dependent apoptotic pathway. *The Journal of Urology*, 175(1), 343-347.
- Liu, K., Park, C., Li, S., Lee, K. W., Liu, H., He, L., et al. (2012). Aloe-emodin suppresses prostate cancer by targeting the mTOR complex 2. *Carcinogenesis*, bgs156, 1-6.
- Mitsiades, N., Yu, W. H., Poulaki, V., Tsokos, M., & Stamenkovic, I. (2001). Matrix metalloproteinase-7-mediated cleavage of Fas ligand protects tumour cells from chemotherapeutic drug cytotoxicity. *Cancer Research*, 61(2), 577-581.
- Omar, Z. A., & Tamin, N.S.I. (Feb. 2011). National Cancer Registry (NCR) report, Malaysian cancer statistics - data and figure 2007. Ministry of Health, Malaysia, ISBN 978-983-3433-87-2, 1-82.
- Pascal, L. E., True, L. D., Campbell, D. S., Deutsch, E. W., Risk, M., Coleman, I. M., et al. (2008). Correlation of mRNA and protein levels: cell type-specific gene expression of cluster designation antigens in the prostate. *BMC genomics*, 9(1), 246,1-13.
- Pecere, T., Gazzola, M. V., Mucignat, C., Parolin, C., Dalla Vecchia, F., Cavaggioni, et al. (2000). Aloe-emodin is a new type of anticancer agent with selective activity against neuroectodermal tumors. *Cancer Research*, 60(11), 2800-2804.
- Pradet-Balade, B., Boulmé, F., Beug, H., Müllner, E. W., & Garcia-Sanz, J. A. (2001). Translation control: bridging the gap between genomics and proteomics? *Trends in Biochemical Sciences*, 26(4), 225-229.
- Singh, S. (2007). From exotic spice to modern drug. *Cell*, 130(5), 765-768.

Indah Mohd Amin, Siti Hamimah Sheikh Abdul Kadir, Mohamad Rodi Isa, Nik Mohd Mazuan Nik Mohd Rosdy and Narimah Abdul Hamid Hasani

- Thavendiranathan, P., Wintersperger, B. J., Flamm, S. D., & Marwick, T. H. (2013). Cardiac MRI in the assessment of cardiac injury and toxicity from cancer chemotherapy a systematic review. *Circulation: Cardiovascular Imaging*, 6(6), 1080-1091.
- Tourneur, L., Delluc, S., Lévy, V., Valensi, F., Radford-Weiss, I., Legrand, O., et al. (2004). Absence or low expression of fas-associated protein with death domain in acute myeloid leukemia cells predicts resistance to chemotherapy and poor outcome. *Cancer Research*, 64(21), 8101-8108.
- Vasconcelos, M. H., Tam, S. C., Hesketh, J. E., Reid, M., & Beattie, J. H. (2002). Metal-and tissue-dependent relationship between metallothionein mRNA and protein. *Toxicology and Applied Pharmacology*, 182(2), 91-97.



Anti- Oral Ulcer Activity of *Ficus deltoidea* Leaves Extract on Animal Model

Vivi Noryati Ahmad* and Indah Mohd Amin

Centre of Preclinical Science Studies, Faculty of Dentistry, Universiti Teknologi MARA (UiTM),
47000 Sg. Buloh, Selangor, Malaysia

ABSTRACT

The purpose of this study is to investigate the effectiveness of *Ficus deltoidea* (*F. deltoidea*) as an anti-oral ulcer on animal models. Adult male Sprague Dawley rats were sedated with Nembutal through intraperitoneal route; oral ulcer models were made by applying 99.5% of glacial acetic acid moistened paper disc on rat buccal mucosa. Four groups of these rats were treated respectively with: no treatment (group 1: negative control); Triamcinolone acetonide (group 2: positive control); 250 mg kg⁻¹ *F. deltoidea* extract (group 3: experimental); 500 mg kg⁻¹ *F. deltoidea* extract (group 4: experimental) for 10 consecutive days, respectively. On days 2, 4, 6, 8 and 10, the ulcers size was assessed. Data was analysed statistically by using SPSS. The negative control rats exhibited buccal mucosa injury whereas treatment with *F. deltoidea* and Triamcinolone acetonide resulted in significantly reduced size of oral ulcer. The percentage of inhibitory area of oral ulcer was more prominent in 500 mg kg⁻¹ *F. deltoidea* extract than 250 mg kg⁻¹. Meanwhile, in vivo study showed that *F. deltoidea* extract not toxic up to 1000 mg kg⁻¹. The present findings suggest that *F. deltoidea* extract effectively accelerates oral ulcer healing process, and could therefore be developed as a therapeutic agent for healing oral ulcer.

Keywords: *Ficus deltoidea*, Mas Cotek, oral health, oral hygiene, oral ulcer

ARTICLE INFO

Article history:

Received: 28 September 2016

Accepted: 03 February 2017

E-mail addresses:

vivi_noryati@salam.uitm.edu.my (Vivi Noryati Ahmad),

indahma@salam.uitm.edu.my (Indah Mohd Amin)

*Corresponding Author

INTRODUCTION

Oral health is essential to general health and the quality of life. It is a state of being free from mouth pain, diseases and disorders. In current clinical practice, oral ulcer has become one of the most common oral pathological conditions found in oral cavity. Oral ulcer occurs on the mucous membrane of the oral cavity and it is a sore lesion in the mouth (Sukhitashvili et al., 2012). There are several

types of oral ulcerations which are recurrent aphthous stomatitis (RAS), primary herpetic gingivo-stomatitis traumatic ulcer and vesiculobullous disorders. RAS is one of the most common painful oral mucosal conditions observed in patients. It is a common condition, restricted to the mouth, that typically starts in childhood or adolescence as multiple, small, round, or ovoid ulcers, with circumscribed margins, yellow or grey floors surrounded by erythematous haloes (Halim et al., 2014).

Treatment of oral ulcers depend on the aetiology and aimed primarily at symptom management, that is, suppressing inflammatory responses and reducing frequency of recurrences or avoiding occurrence altogether (Preeti et al., 2011; Srinivas-Rao, 2010). Treatment can be non-therapeutic and therapeutic management. Non-therapeutic treatment includes supportive measures with attention to immaculate oral hygiene, prevention of trauma and avoiding certain foods (Novianty et al., 2011). Therapeutic treatment options are including anti-inflammatory agents, immuno-modulatory agents and antibiotics (Srinivas-Rao, 2010). Herbal medicine is considered as a therapeutic agents (Osemene et al., 2011).

According to the World Health Organization (WHO), approximately 80% of people in developing countries depend on herbal medicines for primary health care, of which major portion involves the use of plants extracts or active principles originating from parts of plants. In most parts of the world, plant extracts are still used in their crude forms. These extracts are generally administered orally (Salleh & Ahmad, 2013). Today there is a worldwide resurgence in herbal medicine for medicinal purpose (Salleh & Ahmad, 2013) as can be seen in the fact that more than 40% of commonly prescribed medicine originate directly or indirectly in plants (Schulz & Tyler, 2001; Farnsworth & Soejarto, 1991). In Malaysia, herbal medicines have gained popularity as an alternative to modern medicine particularly with the establishment of Traditional and Complementary Medicine Division under the Ministry of Health, Malaysia, and also the presence of NKEA EPP#1 Research Grant Scheme (NRGS) under Ministry of Agriculture, Malaysia.

Ficus deltoidea (*F. deltoidea*) is a herbal plant popular with Malay people. It is traditionally used in treating ulcer and other diseases. *F. deltoidea* is a small perennial herb which rarely exceeds 2 meters in height and is domestically cultivated. It is known by various names such as Mas Cotek in Malaysia, Tabat Barito in Indonesia, Agoluran in the Philippines and Kangkalibang in Africa (Salleh & Ahmad, 2013). In Malaysia, most of *F. deltoidea* species are mostly y found in the eastern states of Terengganu and Kelantan. *F. deltoidea* is known as Mas Cotek in Malay language, with the word 'Mas' means gold and 'Cotek' means spot. Thus, the Malays called this plant *Mas Cotek* to refer to the golden spots found on the surface of the leaf (Ahmad et al., 2016).

Each part of the plant is known to have medicinal properties. The fruits are chewed to relieve headache, toothache and cold; powdered root and leaves of the plant has been applied externally to wounds and sores and around the joints for relief of rheumatism (Abkhan, 2009). It is also traditionally consumed as herbal drink for women after childbirth to help in strengthening the uterus (Salleh & Ahmad, 2013) and acts as a libido booster for both men and women (Bodeker, 2009).

Some studies have demonstrated the antioxidant role of *F. deltoidea* extracts (Hakiman & Maziah, 2009; Aris et al., 2009), antinociceptive, photocytotoxic (Hasham et al., 2013),

antidiabetic activities (Adam et al., 2012), antihypertensive activity (Razali et al., 2013), wound healing on neck skin of rats (Abdulla et al., 2010), and uterine contraction activities via multiple binding receptor (Salleh & Ahmad, 2013). Zahra et al. (2009) meanwhile reported that *F. deltoidea* water extract can significantly reduce peptic ulcer- induced by ethanol. In addition, preliminary acute toxicity studies reveal that *F. deltoidea* is not toxic based on brine shrimp toxicity test (Aminudin et al., 2007). In spite of these evidences the effect of *F. deltoidea* on oral ulceration has not been no scientifically documented.

METHOD

Preparation of *F. deltoidea* aqueous extract

Aqueous extract preparation was made based on Salleh and Ahmad (2013). The leaves of *F. deltoidea* from female sub-species used in this study were purchased from Herbal Plantation, Kuala Selangor, Malaysia. The leaves were air-dried, cut into small pieces and grounded into powder form. Each of the pulverized parts was weighed (100 g) and boiled twice in 1 L distilled water for 4 hours. The aqueous extract was then concentrated by heating at 60°C and was later subjected to freeze- drying (yield 7.36% and 11.61% w/w, dry weight basis for leaf) and was stored in a container until further use. Stock solution was obtained by dissolving small aliquots of this extract in distilled water based on desired concentration (Salleh & Ahmad, 2013).

Preparation of Triamcinolone acetonide dental, 0.1%

Triamcinolone acetonide dental is known as a medium-strength corticosteroid. In this study, Triamcinolone was used as a positive control and it was obtained from the Green Pharmacy, Puncak Alam. The drug was administered orally to the experimental models (Halim et al., 2014).

Animals preparation and experimental procedures

Adult male Sprague Dawley (SD) rats weighing 180 – 200 g were purchased from the animal house, Faculty of Pharmacy, Universiti Teknologi MARA. The rats were housed under controlled environment with temperature kept at 27°C, relative humidity between 30 - 70%, 12 hours' dark and 12 hours' light cycle and had free access to rodent food pellet and water ad libitum. The cleanliness of housing environment was maintained daily. Each group of rats to be studied consists of six animals (n = 6). All experimental procedures were approved by the Universiti Teknologi MARA Animal Ethics Committee.

An oral ulcer model was made by modification based on Slomiany et al. (1999) and Fujisawa et al. (2003). The rats were sedated with dose of 50 mg kg⁻¹ of Nembutal through intraperitoneal route. The anaesthetic effect was confirmed by monitoring the reduced respiratory rate and no response to gentle pinching of foot pad. The rats were placed under heat pad to maintain its core body temperature, while rectal temperature is continuously observed (Salleh et al., 2011). 4 mm filter paper disc (Whatman No. 1) soaked in glacial acetic acid (99.5%) was applied to the left buccal mucosa of the rats for 30 seconds. This technique generated an immediate tissue necrosis, which then produced a single crateriform ulcer in each of the

experimental rats 2 days later. The ulcer normally remains for 14 days (Novianty et al., 2011; Fujisawa et al., 2003), normally.

On the day of the experiment, the rats were randomly divided into 4 groups of 6 rats each as shown in Table 1. The groups were numbered 1- 4. In this study, the extract powder was dissolved in distilled water based on the concentration before being administered on the animal models. The animals were treated with application of medicament for 2 - 3 minutes, twice a day for 10 consecutive days. On day 2, 4, 6, 8 and 10, the ulcer size was assessed.

Table 1
The groups of sample based on type of treatments

Group 1:	rats were negative controls
Group 2:	treated with Triamcinolone acetonide, 0.1% as positive control (referred study done by Daddy et al. 2014 on oral ulcer)
Group 3:	treated with 250 mg kg ⁻¹ <i>F. deltoidea</i> leaves aqueous extract
Group 4:	treated with 500 mg kg ⁻¹ <i>F. deltoidea</i> leaves aqueous extract

Gross lesion and oral ulcer size evaluation

The evaluation procedure was made by modification based on Zahra et al. (2009). Each oral ulcer at buccal mucosa was examined. The length (mm) and width (mm) of the ulcer was measured by a sliding calliper and ruler. Ulcer size was taken on day 2, day 4, day 6, day 8 and day 10. The inhibition percentage (I%) was calculated by the following formula (based on Kauffman & Grossman, 1987 with modification):

$$I\% = \frac{UA_{\text{control}} - UA_{\text{treated}}}{UA_{\text{control}}} \times 100\% \quad (1)$$

UA: The sum of the areas of all lesions for each buccal mucosa

In vivo acute toxicity study

LD₅₀ is defined as the dose required to kill half the members of a tested population in the specified duration. LD₅₀ figures are frequently used as a general indicator of a substance's acute toxicity. In this part of the study, six rats were used for each dose. They were weighed and marked with a coloured marker pen. *F. deltoidea* leaves aqueous extract at doses 50, 150, 250, 500 and 1000 mg kg⁻¹ were administered orally. The time of administration was noted. The numbers of death in each dose within 48 hours were recorded. The probit units were obtained from the percentage of death occurring by referring to the simplified statistical table (Finney, 1971). The probit units were plotted against log-dose-concentration. The LD₅₀ was obtained using the following formula, with n= the total number of rats in each group:

$$SD = \frac{\text{dose of probit 6} - \text{dose of probit 4}}{2 \times 2n} \quad (2)$$

For gross behaviour study, each rat was observed for any abnormal signs and behaviours within 30 minutes after oral administration of varying concentrations of *F. deltoidea* aqueous extract. Animal surviving the observation period of 45 minutes were examined at interval of 2 hours for another 8 hours. Each rat was graded according to whether there were any changes in behaviour (spontaneous or induced) from the control rats:

- 0 = no change
- + = increased activity; subdivided into +1 (moderate) and +2 (significant)
- - = decreased activity; subdivided into -1 (moderate) and -2 (significant).

Statistical analysis

The collected data were analysed by SPSS version 21.0 for Windows. The data were analysed statistically by Independent t-test with significant p values of <0.05.

RESULTS AND DISCUSSION

Table 2 shows the comparison of oral ulcer size and inhibition percentage area between group 1 (negative control) and group 2 (positive control, treated with Triamcinolone acetonide dental, 0.1%). From day 2 until day 10, the oral ulcer size for group 1 (negative control) was = 15.90 ± 1.1 mm², with no occurrence of inhibition percentage. Thus, no healing process occurred for the oral ulcer. Meanwhile, for group 2 the effect of Triamcinolone on oral ulcer significantly reduced its size starting on day 6 with percentage of inhibition of 66.48% (*P<0.05) and full healing on day 10.

Triamcinolone acetonide dental is commonly used for the temporary relief of symptoms of mouth sores resulting from injury (Halim et al., 2014). This drug comes in the form of a dental paste which is applied to affected area on the inside of the mouth. It works by reducing the swelling and pain that can occur with mouth sores. However, there are side effects which include burning, irritation, dryness, or redness of the treated area (Fani et al., 2012; Khandwala et al., 1997).

Table 2

Comparison of oral ulcer size difference and inhibition percentage between group 1 (negative control) and group 2 (positive control/ treated with Triamcinolone acetonide)

Variable	Observed oral ulcer size and inhibition % in rats					
	Group 1 (negative control)	Group 2: treated with Triamcinolone acetonide, 0.1% (positive control)				
		Day 2	Day 4	Day 6	Day 8	Day 10
Mean \pm SEM (ulcer size, mm ²)	15.90 \pm 1.1	15.90 \pm 1.1	10.90 \pm 1.30	5.33 \pm 0.50	2.22 \pm 0.30	0.00
Inhibition (%)	0.00	0.00	31.45	66.48	86.04	100
p- values	-	-	-	*	**	***

All values are expressed as mean \pm standard error mean. Value with different superscripts are significantly different, *p<0.05; **p<0.01; ***p<0.001

Arguably, this study is the first to display the anti-oral ulcer effect of *F. deltoidea*, and role in healing oral cavity caused by oral ulcer. Table 3 shows the presence of 250 mg kg⁻¹ *F. deltoidea* aqueous extract can significantly reduce the size of oral ulcer and increase the percentage of inhibition area of oral ulcer. The size of oral ulcer started to reduce on day 6 with percentage inhibition area of 52.64% (*P<0.05). On day 8, the effect of *F. deltoidea* with the dose of 250 mg kg⁻¹ vigorously reduced the size of ulcer with percentage inhibition area of 92% (P<0.001). By day 10, the percentage inhibition area was 100% showing full recovery.

Table 3
Comparison of oral ulcer size difference and inhibition percentage between group 1 (negative control) and group 3 (treated with 250 mg kg⁻¹ of *F. deltoidea* extract)

Variable	Observed oral ulcer size and inhibition % in rats					
	Group 1 (negative control)	Group 3: treated with 250 mg kg ⁻¹ of <i>F. deltoidea</i> extract				
		Day 2	Day 4	Day 6	Day 8	Day 10
Mean ± SEM (ulcer size, mm ²)	15.90±1.1	15.60±0.8	12.20±0.40	7.53±0.50	1.22±0.90	0.6±0.30
Inhibition (%)	0.00	1.89	23.27	52.64	92.33	96.22
p- values	-	-	-	*	***	***

All values are expressed as mean ± standard error mean. Value with different superscripts are significantly different, *p<0.05; **p<0.01; ***p<0.001

Similarly, 500 mg kg⁻¹ of *F. deltoidea* aqueous extract also significantly reduced the size of the ulcer and increased the percentage of inhibitory area (Table 4). The size of oral ulcer significantly started to reduce from day 4 with percentage of inhibition area of 59.69%. By day 6, the percentage area increased to 92.33%, with full recovery on day 10.

Table 4
Comparison of oral ulcer size difference and inhibition percentage between group 1 (negative control) and group 4 (treated with 500 mg kg⁻¹ of *F. deltoidea* extract)

Variable	Observed oral ulcer size and inhibition % in rats					
	Group 1 (negative control)	Group 4: treated with 500 mg kg ⁻¹ of <i>F. deltoidea</i> extract				
		Day 2	Day 4	Day 6	Day 8	Day 10
Mean ± SEM (ulcer size, mm ²)	15.90±1.1	14.60±0.5	6.41±0.40	1.33±0.20	0.22±0.10	0.00
Inhibition (%)	0.00	8.18	59.69	91.64.64	98.62	100
p- values	-	-	*	**	***	***

All values are expressed as mean ± standard error mean. Value with different superscripts are significantly different, *p<0.05; **p<0.01; ***p<0.001

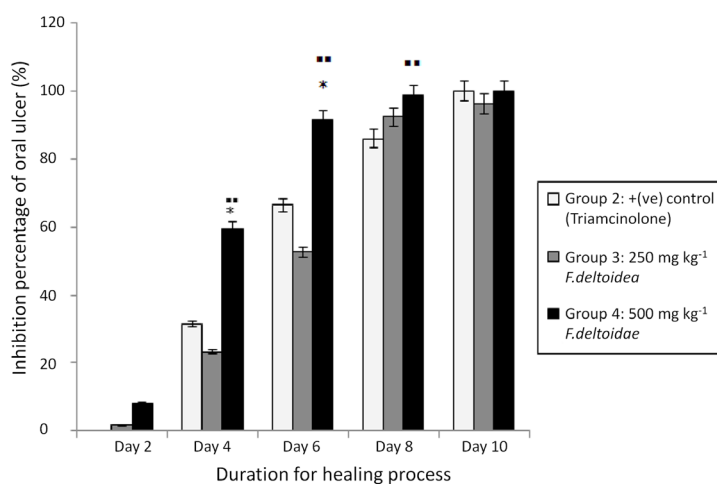


Figure 1. Inhibition percentage area of oral ulcer with different treatments. *Group 4 was significant as compared to positive control $p < 0.05$ (triamcinolone); ** Group 4 was significant as compared to group 3, $p < 0.01$

Figure 1 shows the percentage inhibitory area of oral ulcer increased rapidly in group 4 (treated with 500 mg kg^{-1} of *F. deltoidea* extract), and starting as early as day 4 compared with group 2 (treated with Triamcinolone) and group 3 (250 mg kg^{-1} *F. deltoidea*). Moreover, in day 6 the treatment with 500 mg kg^{-1} of *F. deltoidea* has vigorously increased the inhibition percentage area of oral ulcer to achieve full recovery on day 10. Thus, our findings suggest that 500 mg kg^{-1} of *F. deltoidea* leaves aqueous extract is more effective for the treatment of oral ulcer than 250 mg kg^{-1} and o Triamcinolone acetamide.

Apart from its effect on oral ulcer, *F. deltoidea* whole plant aqueous extract is also reported to reduce the size of peptic ulcer in rats (Zahra et al., 2009). In another study, Novianty et al. (2011) found that allicin from garlic extract significantly reduced the size of oral ulcer resembling the effect of Triamcinolone acetamide and that of *F. deltoidea* leaves aqueous extract. It is speculated that the effect of *F. deltoidea* leaves aqueous extract must work the same way as reported by Novianty et al. (2011) and Zahra et al. (2009).

F. deltoidea extract contain flavonoids with a high anti-oxidant (Hakiman & Maziah, 2009) content. Flavonoids are thought to provide health benefits through cell signalling pathways and antioxidant effects. They have been reported to possess anti- inflammatory and high antioxidant activities (Chua et al., 2015; Omar et al., 2011). Other phytochemical components in *F. deltoidea* such as tannins too possess significant anti-inflammatory activity (Sulaiman et al., 2008; Abdullah et al., 2009). Therefore, we predict that the effect of *F. deltoidea* aqueous extract on oral ulcer may increase cellular antioxidant enzyme and restore the impaired antioxidant defence system in patients with aphthous ulcer and their recurrences. Based on anti- inflammatory action of *F. deltoidea*, we also suggest that it may accelerate the healing process via re-epithelization at buccal mucosa.

In toxicological studies, five dose: 50, 150, 250, 500, 1000 mg kg^{-1} of *F. deltoidea* extract were administered orally to rats. Results indicated absence of lethal effects on rats as in the case

of each tested dose there were no acute toxicity symptoms and spontaneous activities and other physiological behaviours were unchanged (Table 5). According to the study done by Fazliana et al. (2008), *F. deltoidea* had no toxic effects to the bone marrow, liver and renal functions. Based on the haematological and biochemical results, their study also suggested that when *F. deltoidea* aqueous extract is administered to rats daily for 90 days no toxic effect were noted thereby suggesting it might be safe for humans too. According to the study done by Aminudin et al. (2007), non-toxicity of *F. deltoidea* leaves aqueous extract was also established by brine shrimp toxicity test. Farsi et al. (2013) too, showed no significant increase in urea and creatinine levels were observed, suggesting that this extract does not have an effect on renal functions. Thus, our study shows that *F. deltoidea* leaves aqueous extract is safe for consumption.

Table 5
Gross behavioural effects of the *F. deltoidea* leaves aqueous extract on rats ($n = 6$)

Activity	Doses (mg kg ⁻¹)				
	50	150	250	500	1000
Spontaneous activity	50	150	250	500	1000
Aggressiveness	0	0	0	0	0
Convulsion	0	0	0	0	0
Corneal reflex	0	0	0	0	0
Cyanosis	0	0	0	0	0
Exophthalmos	0	0	0	0	0
Gaspings	0	0	0	0	0
Hind limb placing	0	0	0	0	0
Piloerection	0	0	0	0	0
Positional	0	0	0	0	0
Straub tail	0	0	0	0	0
Stretching	0	0	0	0	0
Tail pinch	0	0	0	0	0
Tremors	0	0	0	0	0
Visual placing	0	0	0	0	0

Keys:

- 2 Significantly decrease in activity/ response
- 1 Moderate decrease in activity/ response
- 0 No change compared to the control
- +1 Moderate increase in activity/ response
- +2 Significant increase in activity/ response

CONCLUSION

F. deltoidea had significantly reduced the size of the oral ulcer and increased the percentage of inhibition area. *F. deltoidea* can be an alternative for the treatment of oral ulcer. The present study provides preliminary scientific evidences on the anti- oral ulcer potential of *F. deltoidea* leaves extract which has been found to have no significant toxic effect on rats. The findings thus justify the traditional use of *F. deltoidea* to heal oral ulcer.

ACKNOWLEDGEMENTS

This study was supported by the Faculty of Dentistry, Universiti Teknologi MARA. Authors would like to thank Prof. Dr. Mohamed Ibrahim Abu Hassan, the founder dean of Faculty of Dentistry, UiTM for his continuous support.

REFERENCES

- Abdulla, M. A., Ahmed, K. A. A., Abu-Luhoom, F. M., & Muhanid, M. (2010). Role of *Ficus deltoidea* extract in the enhancement of wound healing in experimental rats. *Biomedical Research*, 21(3), 241-245.
- Abdullah, Z., Hussain, K., Ismail, Z., & Ali, R. M. (2009). Anti-inflammatory activity of standardised extracts of leaves of three varieties of *Ficus deltoidea*. *International Journal of Pharmaceutical and Clinical Research*, 1(3), 100-105.
- Abkhan, J. K. (2009). Traditional healing of Ficus Family in Human Health. *eCAM*, 5(9), 91- 94.
- Adam, Z., Khamis, S., Ismail, A., & Hamid, M. (2012). *Ficus deltoidea*: A potential alternative medicine for diabetes mellitus. *Evidence-Based Complementary and Alternative Medicine*, 2012.
- Ahmad, V. N., Salleh, N., Indah, M. A., Sarmin, N. I. M., & Khan, N. L. A. (2016). Growing creative and innovative solutions. Series1, Chapter 24: The miracle of *Ficus deltoidea* on uterus. MNNF Publisher, ISBN 978-967-13637-2-0; Perpustakaan Negara Malaysia.
- Aminudin, N., Sin, C. Y., Chee, E. S., Nee, K. I., & Renxin, L. (2007). Blood glucose lowering effect of *Ficus deltoidea* aqueous extract. *Malaysian Journal of Science*, 26(1).
- Aris, S. R. S., Mustafa, S., Ahmat, N., Jaafar, F. M., & Ahmad, R. (2009). Phenolic content and antioxidant activity of fruits of *Ficus deltoidea* var *angustifolia* sp. *Malays. J. Anal. Sci*, 13(2), 146-150.
- Bodeker, G., Salleh, H., & Shekar, S. C. (2009). *Health and beauty from the rainforest: Malaysian traditions of ramuan*. Biotropics Ramuan.
- Fani, M. M., Ebrahimi, H., Pourshahidi, S., & Aflaki, E. (2012). Comparing the effect of phenytoin syrup and triamcinolone acetonide ointment on aphthous ulcers in patients with Behçet's syndrome. *Iranian Red Crescent Medical Journal*, 2012(2, Feb), 75-78.
- Farnsworth, N. R., & Soejarto, D. D. (1991). Global importance of medicinal plants. *The Conservation of Medicinal Plants*, 25-51
- Farsi, E., Shafaei, A., Hor, S. Y., Ahamed, M. B. K., Yam, M. F., & Asmawi, M. Z., & Ismail, Z. (2013). Genotoxicity and acute and subchronic toxicity studies of a standardized methanolic extract of *Ficus deltoidea* leaves. *Clinics*, 68(6), 865-875.
- Fazliana, M. S., Muhajir, H., Hazilawati, H., Shafii, K., & Mazleha, M. (2008). Effects of *Ficus deltoidea* aqueous extract on hematological and biochemical parameters in rats. *The Medical Journal of Malaysia*, 63, 103-104.
- Finney, D. J. (1971). A statistical treatment of the sigmoid response curve. *Probit analysis*, 3rd edn. Cambridge University Press, London, 333.

- Fujisawa, K., Miyamoto, Y., & Nagayama, M. (2003). Basic fibroblast growth factor and epidermal growth factor reverse impaired ulcer healing of the rabbit oral mucosa. *J Oral Pathol Med*, 32, 358-66.
- Hakiman, M., & Maziah, M. (2009). Non enzymatic and enzymatic antioxidant activities in aqueous extract of different *Ficus deltoidea* accessions. *Journal of Medicinal Plants Research*, 3(3), 120-131.
- Halim, D. S., Abdullah, N. A., Alam, M. K., Samsee, S. N. B., & May, T. S. (2014). Comparison of the effectiveness between virgin coconut oil (VCO) and triamcinolone for treatment of minor recurrent aphthous stomatitis (RAS). *Int Med J*, 21(3), 319-20.
- Hasham, R., Choi, H. K., Sarmidi, M. R., & Park, C. S. (2013). Protective effects of a *Ficus deltoidea* (Mas cotek) extract against UVB-induced photoageing in skin cells. *Biotechnology and Bioprocess Engineering*, 18(1), 185-193.
- Johnston, L. D., O'Malley, P. M., & Bachman, J. G. (1999). *National Survey Results on Drug Use from the Monitoring the Future Study, 1975-1998. Volume I: Secondary School Students*. US Government Printing Office, Superintendent of Documents, Mail Stop: SSOP, Washington, DC 20402-9328.
- Khandwala, A., Van Inwegen, R. G., & Alfano, M. C. (1997). 5% amlexanox oral paste, a new treatment for recurrent minor aphthous ulcers: I. Clinical demonstration of acceleration of healing and resolution of pain. *Oral Surgery, Oral Medicine, Oral Pathology, Oral Radiology, and Endodontology*, 83(2), 222-230.
- Novianty, R. A., Chrismawaty, B. E., & Subagyo, G. (2011). Effect of allicin for re-epithelialization during healing in oral ulcer model. *The Indonesian J Dent Res*, 1(2), 87- 93.
- Omar, M. H., Mullen, W., & Crozier, A. (2011). Identification of proanthocyanidin dimers and trimers, flavone C-Glycosides, and antioxidants in *Ficus deltoidea*, a Malaysian herbal tea. *Journal of Agricultural and Food Chemistry*, 59(4), 1363-1369.
- Osemene, K. P., Elujoba, A. A., & Ilori, M. O. (2011). A comparative assessment of herbal and orthodox medicines in Nigeria. *Res J Med Sci*, 5(5), 280-285.
- Preeti, L., Magesh, K. T., Rajkumar, K., & Karthik, R. (2011). Recurrent aphthous stomatitis. *Journal of Oral and Maxillofacial Pathology*, 15(3), 252.
- Razali, N., Dewa, A., Asmawi, M. Z., Ismail, Z., Manshor, N. M., & Hassan, Z. (2013). Vascular reactivity on aortic rings of spontaneously hypertensive rats treated with methanolic and water extracts of *Ficus deltoidea*. *Journal of Experimental and Integrative Medicine*, 3(2), 93-102.
- Salleh, N., & Ahmad, V. N. (2013). In-Vitro effect of *Ficus deltoidea* on the contraction of isolated rat's uteri is mediated via multiple receptors binding and is dependent on extracellular calcium. *BMC Complementary and Alternative Medicine*, 13(1), 1.
- Salleh, N., Ahmad, V. N., Kasim, N., Amri, S. M., & Onn, Y. S. (2011). The effect of progesterone on uterine fluid ph and endometrial nhe-1 protein expression in rats. *Health*, 3(01), 66.
- Schulz, V., Hänsel, R., & Tyler, V. E. (2001). *Rational phytotherapy: a physician's guide to herbal medicine*. Psychology Press.
- Slomiany, B. L., Piotrowski, J., Slomiany, A. (1999). Suppression of caspace-3 and nitric-oxide synthase-2 during buccal mucosal ulcer healing: effect of chronic alcohol ingestion. *Biochem Mol Biol Int*, 48, 121-5.

- Srinivas-Rao, P. (2010). Recurrent Aphthous Stomatitis. *A Review. J Orofac Sci*, 2(3), 60- 65.
- Sukhitashvili, N., Imnadze, I., Tabaghua, G., Gogilashvili, Q., & Amiranashvili, I. (2012). Characterization of oral ulcer and pathological scar in nude mice model. *Georgian Medical News*, (205), 82-87.
- Sulaiman, M. R., Hussain, M. K., Zakaria, Z. A., Somchit, M. N., Moin, S., Mohamad, A. S., & Israf, D. A. (2008). Evaluation of the antinociceptive activity of *Ficus deltoidea* aqueous extract. *Fitoterapia*, 79(7), 557-561.
- Zahra, S. F., Mahmood, A. A., Hapipah, M. A., Suzita, M. N., & Salmah, I. (2009). Anti-ulcerogenic activity of aqueous extract of *Ficus deltoidea* against ethanol-induced gastric mucosal injury in rats. *Res J Med Sci*, 3(2), 42-6.



Comparison of Energy and Performance from Biodegradation of Freeze Dried and Spray Dried Algae Biomass

Muhamad Haikal Zainal^{1*}, Khairul Baqir Alkhair Khairul Amin¹,
Oskar Hasdinor Hassan², Sharifah Aminah Syed Mohamad¹,
Abd Malik Marwan Ali^{1,3}, Fathiah Abdullah⁴ and Muhd Zu Azhan Yahya⁵

¹Faculty of Applied Sciences, Universiti Teknologi MARA (UiTM), 40450 Shah Alam, Selangor, Malaysia

²Faculty of Art and Design, Universiti Teknologi MARA (UiTM), 40450 Shah Alam, Selangor, Malaysia

³Institute of Science, Universiti Teknologi MARA (UiTM), 40450 Shah Alam, Selangor, Malaysia

⁴Faculty of Applied Sciences, Universiti Teknologi MARA (UiTM) Perak, 35400 Tapah, Perak, Malaysia

⁵Faculty of Science and Defence Technology, Universiti Pertahanan Nasional Malaysia (UPNM),
Kem Sungai Besi, 57000 Kuala Lumpur, Malaysia

ABSTRACT

Many kinds of substrates have been used to investigate bioelectricity production with Microbial Fuel Cell (MFC). Dry algae biomass has the highest maximum power density compared to other substrates due to high carbon sources from its lipid. However, the bacterial digestion of algae biomass is not simple because of the complexity and strength of the algal cell wall structure. An algae biomass extraction is needed to break the cell wall structure and facilitate digestion. Spray drying method is commonly used in high-value products but may degrade some algal components which are crucial for microbial degradation in MFC, while the freeze-drying method is able to preserve algal cell constituents. The MFC was fed with freeze dried and spray dried algae biomass to produce energy and determine the degradation efficiency. Results showed the average voltage generated was 739 mV and 740 mV from freeze dried and spray

dried algae biomass, respectively. The maximum power density of freeze dried algae biomass is 159.9 mW/m² and spray dried algae biomass is 152.3 mW/m². Freeze dried algae biomass has 54.2% of COD removal and 28.4% of Coulombic Efficiency while spray dried algae biomass has 50.1% of COD removal and 24.9% of Coulombic Efficiency.

ARTICLE INFO

Article history:

Received: 28 September 2016

Accepted: 03 February 2017

E-mail addresses:

muhammadhaikalzainal@gmail.com (Muhamad Haikal Zainal),

khairulbaqiralkhair@gmail.com

(Khairul Baqir Alkhair Khairul Amin),

oskar@salam.uitm.edu.my (Oskar Hasdinor Hassan),

sharifah459@salam.uitm.edu.my

(Sharifah Aminah Syed Mohamad),

ammali@salam.uitm.edu.my (Abd Malik Marwan Ali),

fathiah@perak.uitm.edu.my (Fathiah Abdullah),

mzay@upnm.edu.my (Muhd Zu Azhan Yahya)

*Corresponding Author

Keywords: Algae biomass, energy storage and conversion, freeze dry, Microbial Fuel Cell, spray dry

INTRODUCTION

A review by Zhao et al. (2009) states that generally Microbial Fuel Cell (MFC) produces low power (less than 6 W m^{-2} or same and less than 500 Wm^{-3}) because of some factors such as anode, cathode, chemical species in electrolyte, proton exchange membrane (PEM), application of microbe species, the configurations of fuel cell and the condition of the operation. These 'acceptable loss' in lab scale, are still far from reaching the level of commercial scale. In this study (Zainal et al., 2016), the maximum power density is found to be lower than that recorded by previous studies on algae biomass (Kondaveeti et al., 2013; Rashid et al., 2013; Velasquez-Orta et al., 2009). The large differences of maximum power density is because of the same reason given by Kondaveeti et al. (2013), which is probably due to several factors such as size of the anode electrode, type of algae species, substrate concentration and internal resistances. Although MFC has the potential to generate electricity, the materials and substances used and applied for its configuration have limited MFC from reaching their real potential to generate power.

Dry algae biomass as a substrate can produce high maximum power density compared to other substrates in generating bioelectricity via MFC. It has high carbon sources from its lipid. Rashid et al. (2013) did apply sonication, thermal and unpre-treated to break down cell wall and facilitate algae degradation by microbes, and found unpre-treated algae biomass has the highest cell voltage profile. A premature conclusion is made that lipid extracted algae cannot be used for substrate degradation to generate electricity. Also, un-pre-treated algae biomass mixture has produced a maximum voltage of 0.604 V and pre-treated mixture has produced a maximum voltage of 0.290 V. The reason of the negative effect of sonication is still unknown (Rashid et al., 2013). More investigations are needed to be carried out pertaining to pre-treatment method algae species biomass.

Microalgae lipids are required for biofuel and bioelectricity. To obtain lipids, a multi-steps process is required, such as photoautotrophic cultivation, harvesting, biomass dewatering, and lipid extraction. Light, carbon dioxide, inorganic nutrients, and water are also needed for the purpose of microalgae growth. In commercializing the production of microalgae, harvesting and dewatering are important steps. Harvesting methods involves flocculation, filtration, floatation, centrifugation and any combination of these methods. Upon harvesting, the wet biomass need to be freeze dried, drum dried, oven-dried, spray-dried and fluidized bed-dried in order to increase the viability of biomass for lipid extraction. Spray drying method causes deterioration of some algal components such as pigments. Furthermore, high temperature pre-treatment can cause further degradation and denaturation of desired products (Hammed et al., 2013; Sander & Murthy, 2009). Freeze drying is commonly used for dewatering microalgal biomass while preserving cell constituents and cell wall (Brennan & Owende, 2010; Chen et al., 2009; Guldhe et al., 2014; Halim et al., 2012), allowing for better power generation by MFC. In this paper, freeze dried and spray dried pre-treated algae biomass are compared to ascertain their energy production and performance.

METHOD

MFC Construction and Operation. A 1500 ml glass chamber with a net liquid volume of 1200 ml was used as an MFC reactor (Figure 1). A manganese based catalysed carbon electrode (E-4, Electric Fuel Ltd.) was applied as an air cathode (thickness is 0.5 mm in diameter of 6 cm). The catalysed part was positioned towards the anodic solution and carbon side in the direction of air. For the anode, a projected surface area of 100 cm² of activated carbon fibre fabric (Carbon Technology Co., Ltd. Taiwan) was used, without any pre-treatment. The distance between anode and air cathode is about 17 cm. The single chamber was filled and inoculated with anaerobic sludge (collected from wastewater treatment plant Universiti Teknologi MARA (UiTM), Shah Alam, Malaysia). A medium of 50 mM phosphate buffer medium (PBS) consists of 4.576 g Na₂HPO₄, 2.452 g Na₂HPO₄, 0.31 g NH₄Cl and 0.13 g KCl, 12.5 ml of minerals and 5 ml of vitamins solution was made to feed the MFC. After 14 days of inoculation, 2.5 g/L freeze dried *Chlorella vulgaris* biomass powder (Algaetech International Sdn. Bhd. Malaysia) was mixed with 50 mM PBS and fed into the MFC. Microalgal biomass was extracted using the bead-milling method and dewatering by the freeze dry method. The same MFC operation was conducted for 2.5 g/L spray dried *Chlorella vulgaris* biomass. Spray dried *Chlorella vulgaris* biomass were purchased (Jarrow Formulas).

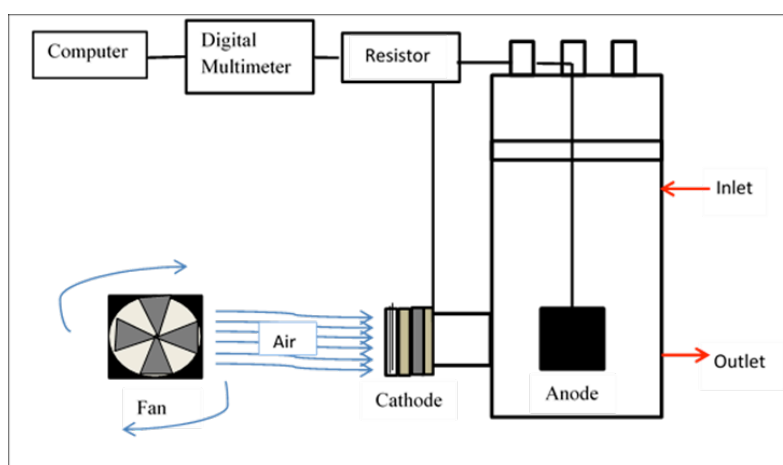


Figure 1. A schematic diagram of glass MFC device with fabricated anode and air-cathode

Data Collection and Analysis

A digital multimeter (UT803, Uni-Trend Technology Ltd. China) and a computer with data logger software was installed to measure voltage for 21 days, simultaneously which a variable resistor was connected to the system (from 10 M Ω to 2 Ω) to determine power density and current density during voltage stabilization. Starting from Open Circuit Voltage (OCV), each voltage was recorded (delayed about 10 seconds). The current was calculated using Ohm's Law,

$I = E_{\text{cell}} / R_{\text{ext}}$ where E_{cell} is cell voltage generated for each resistance, I is the current for each resistance, and R_{ext} is the external load resistor. A formula, $P = I \times E_{\text{cell}}$ was used to calculate power, where P is power generated for each resistance, I is the current for each resistance and E_{cell} is the cell voltage for each resistance. The total surface area of electrode (100 cm^2) was used to determine the current and power, as current density and power density. 2 ml sample was taken to determine its chemical oxygen demand (COD) during the initial and final of MFC operation, in mg/L, by using the reactor digestion method (High Range, 20-1500 mg/L, HACH Co., USA). COD removal efficiency (ΔCOD) was calculated according to where COD_{int} is the initial COD concentration of substrate (mg/L) and COD_{end} is the final COD concentration of the batch test.

$$\Delta\text{COD} = \frac{(\text{COD}_{\text{int}} - \text{COD}_{\text{end}})}{\text{COD}_{\text{int}}} \times 100\% \quad [1]$$

As fed batch system, a formula [2] was used to analyse Coulombic efficiency where ΔCOD is change of COD concentration (mg/L), I is current (A), t is change in time (s), V_{An} is working volume (volume liquid in anode compartment, L), F is Faraday's constant ($96,500 \text{ C mol}^{-1} \text{ e}^-$), and 8 is a constant, according to $M_{\text{O}_2} = 32$ for the molecular weight of oxygen and $b = 4$ for the number of electrons transferred per mole of oxygen.

$$\text{CE} (\%) = \frac{8 \int_0^t I dt}{F V_{\text{An}} \Delta\text{COD}} \quad [2]$$

Environmental Scanning Electron Microscope (ESEM) Image

Environmental Scanning Electron Microscopy (Quanta 450 FEG ESEM, USA) was performed at Imaging Centre, Faculty of Pharmacy, Universiti Teknologi MARA (UiTM) Puncak Alam campus. A 2 mm x 2 mm section of carbon cloth was cut (taken out of the fuel cell) using a sterile scalpel. The carbon cloth was placed in a sterile falcon tube filled with 4% phosphate buffered glutaraldehyde in distilled water. The sample was immersed for 4 hours after which it was rinsed gently with 50 ml distil water for 1-2 minutes. The rinsed sample was placed in the Peltier cooling chamber device inside the ESEM chamber. The temperature inside the ESEM chamber was maintained at about 4°C , and water vapour pressure was between 4.5 and 5.5 Torr, to ensure the sample was maintained in a moist condition.

RESULTS AND DISCUSSION

Voltage Generation from Freeze Dried and Spray Dried Pre-Treated Algae Biomass

The anode compartment of MFC was inoculated with wastewater for 14 days. Then, the wastewater was replaced with PBS medium and 2.5 g/L of substrate (freeze dried and spray dried algae biomass). The voltage generation from both substrates is shown in Figure 2.

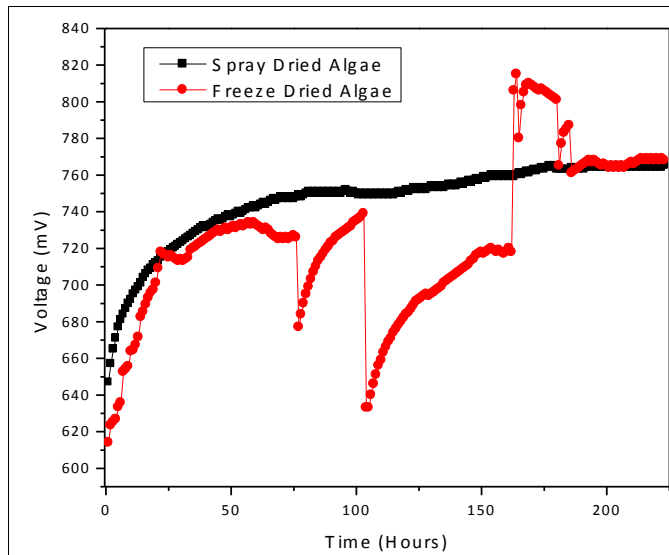


Figure 2. Voltage generation over time (hours) as result of degradation of both 2.5 g/L of freeze dried and spray dried algae biomass

From Figure 2, spray dried algae biomass was generated a stable voltage averagely about 740 mV while that of freeze dried algae biomass was unstable, averagely about 739 mV for 200 hours. The highest voltage recorded was 820 mV by freeze dried algae biomass, until its voltage was stable as the voltage generated from spray dried algae biomass, from 175 hours onwards. The voltage generation by MFC is related to the growth curve of microbial consortia in its anode compartment. Firstly, voltage increase is the product of exponential growth of microbes to form biofilm on top of the surface of the electrode (carbon cloth) in the anode compartment. Secondly, maintained biofilm formation causes voltage stabilisation. Lastly, the voltage decreases when microbes are in the death phase (Nair et al., 2013; Venkata Mohan et al., 2008). The unstable voltage generated by freeze dried algae biomass is probably due to the large size of the organic matter which makes the process of degradation more difficult (Kondaveeti et al., 2013).

Maximum Power Density from Freeze Dried and Spray Dried *Chlorella Vulgaris* Biomass

Two different pre-treatment algae biomass (freeze dried and spray dried) was used to compare power density generation (Figure 3). Both have similar concentrations of 2.5 g/L of algae biomass, and the MFC was connected to a variable external load resistor (range of 0.5 Ω to 10 $M\Omega$), to determine power density by starting at Open Circuit Voltage (OCV). The OCV of freeze dried algae biomass is about 795 mV while the OCV of spray dried algae biomass is 765 mV. During an open circuit condition, no current is generated, therefore no power is produced. When the current is increased, power is also increases until reached the maximum power point. Beyond the point, the MFC is in a state of short circuit condition where ohmic

loss and the electrode overpotential is increased, until no power is produced. In Figure 3, the maximum power density of freeze dried algae biomass is 159.9 mW/m^2 and spray dried algae biomass is 152.3 mW/m^2 . Therefore, freeze dried algae biomass produces higher power than spray dried algae biomass. However, there was no significant difference in power generation between freeze dried and spray dried algae biomass in this study probably due to the capability of exoelectrogens growing inside of MFC. Therefore, the application of different pre-treated algae biomass in the MFC is not very effective in increasing power generation (Lee et al., 2015).

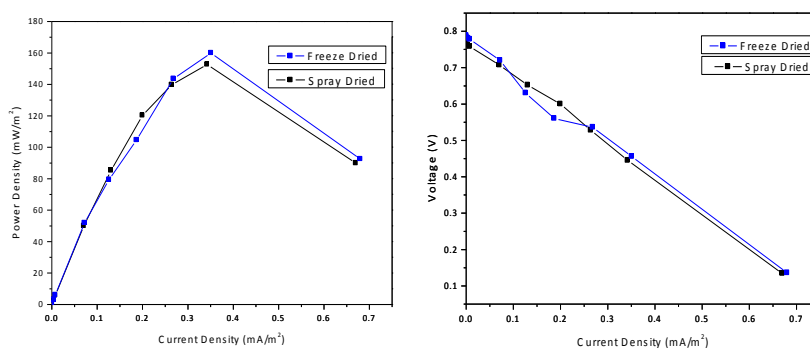


Figure 3. Power density and voltage generation against current density as a result of external load resistance control to determine maximum power density from freeze dried and spray dried algae biomass

Chemical Oxygen Demand (COD) removal percentage and Coulombic efficiency

To determine the degradation of algae biomass the anodic solution of MFC was tested for wastewater treatment efficiency, which is known as Chemical Oxygen Demand (COD) removal percentage. COD removal is a measurement of organic matter degradation efficiency. COD removal was recorded is 79.8% in MFC compared to 59% in the control experiment, proving that COD removal from MFC is better than COD removal without power generation (Kondaveeti et al., 2013). COD removal is also required to calculate Coulombic efficiency. Coulombic efficiency is a measure of maximum total coulombs transferred from substrate towards the anode to generate power (Logan et al., 2006). Table 1 shows that freeze-dried algae biomass has 54.2% of COD removal and 28.4% of Coulombic Efficiency while spray dried algae biomass has 50.1% of COD removal and 24.9% of Coulombic Efficiency. Therefore, freeze dried has higher COD removal percentage and total coulombs transferred to the anode compared to spray dried algae biomass. However, the differences of pre-treated algae biomass were not significant. The coulombs may be limited by a requirement growth of exoelectrogens and only some coulombs were transferred to the anode surface for power generation, although substrate used are not the same (Lee et al., 2015). In the anode biofilm community, fermenting microbes have sufficient retention time to dominate the anode-respiring bacteria, and consuming electrons for reduced products. Thus, the electron cost reduced coulombic efficiency (Logan et al., 2006).

Table 1
Chemical Oxygen Demand (COD) removal percentage and Coulombic Efficiency determination from both freeze dried and spray dried algae biomass degradation in the MFC

Substrate concentration	2.5 g/L Freeze Dried Algae Biomass	2.5g/L Spray Dried Algae Biomass
Chemical Oxygen Demand (COD) removal	54.2%	50.1%
Coulombic Efficiency	28.4%	24.9%

Environmental Scanning Electron Microscope (ESEM) image on the surface of the anode

Figure 4(a) shows Environmental Scanning Electron Microscope (ESEM) image of the surface of carbon cloth fibre (as the anode) before MFC operation. Figure 4(b) shows a formation of biofilm on top of the surface of the anode. The biofilm covers the anode with a kind of monolayer to multilayer structure with variable thickness on the surface of carbon fibre. Sufficient organic matter (algae biomass) and nutrients from PBS medium favours growth of biofilm. Biofilm formation consists of three basic components: (1) surface for biofilm growth attachment; (2) microbes acting as the unit for biofilm; and (3) glycocalyx, which is a secreted protecting polymer matrix by microbes to form biofilm (Dunne, 2002). The biofilms play an important role in transferring electrons directly to the anode surface, as a result of biochemical reaction between biofilm and the substrate.

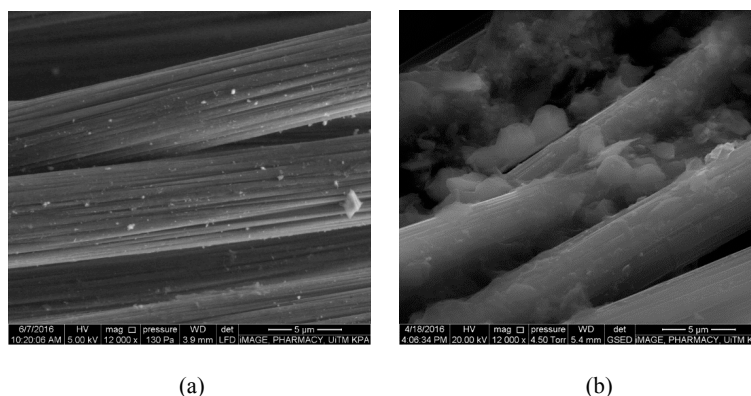


Figure 4. Environmental Scanning Electron Microscope (ESEM) image of the anode surface. The anode surface of carbon fibre (a) before; and (b) after MFC operation

CONCLUSION

The energy and performance of freeze dried and spray dried *Chlorella vulgaris* biomass was compared using single chamber air-cathode Microbial Fuel Cell (MFC). Freeze dry pre-treatment was able to conserve algae biomass constituents and help in increasing power generation compared to spray dried algae biomass. As a result, maximum power density of freeze dried algae biomass is 159.9 mW/m² and spray dried algae biomass is 152.3 mW/m². The average

voltage generated is 739 mV and 740 mV from freeze dried and spray dried algae biomass, respectively. The COD removal percentage of freeze dried algae biomass is 54.2% and spray dried algae biomass is 50.1%. The Coulombic Efficiency for freeze dried algae biomass is 28.4% and spray dried algae biomass is 24.9%. Therefore, freeze dried algae biomass has potential as pre-treated substrate to improve energy production in MFC.

ACKNOWLEDGEMENTS

The authors would like to express gratitude to Ministry of Education (MOE) for supporting this research under the RAGS grant (600-RMI/RAGS 5/3 (32/2014)), and Universiti Teknologi MARA (UiTM) for making the study possible.

REFERENCES

- Brennan, L., & Owende, P. (2010). Biofuels from microalgae—A review of technologies for production, processing, and extractions of biofuels and co-products. *Renewable and Sustainable Energy Reviews*, 14(2), 557–577. <http://doi.org/10.1016/j.rser.2009.10.009>
- Chen, P., Min, M., Chen, Y., Wang, L., Li, Y., Chen, Q., ... Ruan, R. (2009). Review of the biological and engineering aspects of algae to fuels approach. *International Journal of Agricultural and Biological Engineering*, 2(4), 1–30. <http://doi.org/10.3965/j.issn.1934-6344.2009.04.001-030>
- Dunne, W. M. (2002). Bacterial adhesion: seen any good biofilms lately? *Clinical Microbiology Reviews*, 15(2), 155–66. Retrieved from <http://www.ncbi.nlm.nih.gov/pubmed/11932228>
- Guldhe, A., Singh, B., Rawat, I., Ramluckan, K., & Bux, F. (2014). Efficacy of drying and cell disruption techniques on lipid recovery from microalgae for biodiesel production. *Fuel*, 128, 46–52. <http://doi.org/10.1016/j.fuel.2014.02.059>
- Halim, R., Danquah, M. K., & Webley, P. A. (2012). Extraction of oil from microalgae for biodiesel production: A review. *Biotechnology Advances*, 30(3), 709–732. <http://doi.org/10.1016/j.biotechadv.2012.01.001>
- Hammed, A. M., Jaswir, I., Amid, A., Alam, Z., Asiyani-H, T. T., & Ramli, N. (2013). Enzymatic Hydrolysis of Plants and Algae for Extraction of Bioactive Compounds. *Food Reviews International*, 29(4), 352–370. <http://doi.org/10.1080/87559129.2013.818012>
- Kondaveeti, S., Choi, K. S., Kakarla, R., & Min, B. (2013). Microalgae *Scenedesmus obliquus* as renewable biomass feedstock for electricity generation in microbial fuel cells (MFCs). *Frontiers of Environmental Science and Engineering*. <http://doi.org/10.1007/s11783-013-0590-4>
- Lee, D. J., Chang, J. S., & Lai, J. Y. (2015). Microalgae-microbial fuel cell: A mini review. *Bioresource Technology*, 198, 891–895. <http://doi.org/10.1016/j.biortech.2015.09.061>
- Logan, B. E., Regan, J. M., Potter, M. C., Kim, B. H., al., et, Kim, B. H., ... Lovley, D. R. (2006). Electricity-producing bacterial communities in microbial fuel cells. *Trends in Microbiology*, 14(12), 512–8. <http://doi.org/10.1016/j.tim.2006.10.003>
- Logan, B. E., Verstraete, W., & Rabaey, K. (2006). Critical Review Microbial Fuel Cells: Methodology and Technology †, 40(17), 5181–5192.

- Nair, R., Renganathan, K., Barathi, S., & Venkatraman, K. (2013). Performance of salt-bridge microbial fuel cell at various agarose concentrations using hostel sewage waste as substrate, *2*(5), 326–330.
- Rashid, N., Cui, Y.-F., Saif Ur Rehman, M., & Han, J.-I. (2013). Enhanced electricity generation by using algae biomass and activated sludge in microbial fuel cell. *The Science of the Total Environment*, *456-457*, 91–4. <http://doi.org/10.1016/j.scitotenv.2013.03.067>
- Sander, K., & Murthy, G. (2009). Enzymatic degradation of microalgal cell walls. *ASABE Annual International Meeting, Reno*, 0300(09). Retrieved from http://www.researchgate.net/publication/228865662_Enzymatic_degradation_of_microalgal_cell_walls/file/d912f508732a29f4a6.pdf
- Velasquez-Orta, S. B., Curtis, T. P., & Logan, B. E. (2009). Energy from algae using microbial fuel cells. *Biotechnology and Bioengineering*, *103*(6), 1068–76. <http://doi.org/10.1002/bit.22346>
- Venkata Mohan, S., Mohanakrishna, G., Srikanth, S., & Sarma, P. N. (2008). Harnessing of bioelectricity in microbial fuel cell (MFC) employing aerated cathode through anaerobic treatment of chemical wastewater using selectively enriched hydrogen producing mixed consortia. *Fuel*, *87*, 2667–2676. <http://doi.org/10.1016/j.fuel.2008.03.002>
- Zainal, M. H., Hassan, O. H., Ab Samad, L. S., Ali, A. M. M., & Yahya, M. Z. A. (2016). Energy conversion from biodegradation of non-thermal pre-treated algae biomass for microbial fuel cell. *Journal of Mechanical Engineering*, *13*(1), 26-31.
- Zhao, F., Slade, R. C., & Varcoe, J. R. (2009). Techniques for the Study and Development of Microbial Fuel Cells: An Electrochemical Perspective, (0), 1–54. Retrieved from <http://epubs.surrey.ac.uk/chemistry/61>





The Effects of Automotive Windscreen Glass Waste Powder (WGWP) On Strength Performance of Cement Mortar

Nik Anisah Nik Ngah¹, Mohamad Awang^{1*} and Kartini Kamaruddin²

¹*School of Ocean Engineering, Universiti Malaysia Terengganu (UMT), 21030 Kuala Terengganu, Terengganu, Malaysia*

²*Faculty of Civil Engineering, Universiti Teknologi MARA (UiTM), 40450 Shah Alam, Selangor, Malaysia*

ABSTRACT

This aim of this study is to study the effects of various contents of Automotive Windscreen Glass Waste Powder (WGWP) as a cement replacement. Mortar incorporating several compositions of WGWP (0%, 5%, 10%, 15% and 20%) by weight of cement was prepared. Three batching systems of cement to sand (C:S) ratios of 1:2.5 superplasticizers (SP), 1:3.0 SP and 1:3.5 SP was also employed. Fixed water to cement (w/c) ratio of 0.5 was used. The samples were water cured and the assessment of the strength performance of mortar cubes carried out at 7 and 28 days. Studies conducted have shown that WGWP has good pozzolanic properties. In term of compressive strength, it was observed that employing C:S ratio of 1:3.5 SP is better than 1:2.5 SP and 1:3.0 SP.

Keywords: Cement replacement, compressive strength, pozzolanic, superplasticizers, windscreen glass waste powder

INTRODUCTION

The cement industry is the second largest that producer of CO₂ (Environmental Impact Assessment (EIA), 2006). The increased demand for cement in Malaysia raises challenges for environment protection.

Schwarz et al. (2008) reported that the durability of concrete can be improved when the fine glass powder passing 45 µm is used. According to Shao et al. (2000), the crushed glass particle size is finer than 38 µm exhibited a pozzolanic behaviour with high reactivity through lime and higher compressive strength in concrete.

Since glass is amorphous silica, it contains analogies of traditional pozzolanic material,

ARTICLE INFO

Article history:

Received: 28 September 2016

Accepted: 03 February 2017

E-mail addresses:

aniesaa1977@gmail.com (Nik Anisah Nik Ngah),

mohamada@umt.edu.my (Mohamad Awang),

kartini@salam.uitm.edu.my (Kartini Kamaruddin)

*Corresponding Author

and in its finer form can be used as supplementary cementitious materials (Pereira-de-Oliveira et al., 2012; Khmiri et al., 2013; Kim et al., 2015). Nassar and Soroushian (2012), reported that particles finer than 100 μm may even clash with to expansion of coarser glass particles. Conversely, finely ground glass may contribute to the strength of mortar or concrete due to the pozzolanic reaction with lime produced by the hydration of Portland cement clinker (Shayan & Xu, 2004, 2006; Federico & Chidiac, 2009).

Concrete technologists aim to make concrete at the lowest possible water/cement ratio while at the same time ensuring high workability. Therefore, the arrival of superplasticizers has completed their aim. Neville (1995) in his study mentioned that the superplasticizers (SP) are referred to as high range water reducing admixture by American Society for Testing and Materials, ASTM-C494 (2013) which mainly disperses the water in concrete matrix. SP has been used for important projects such as high rise buildings, prestressed concrete, lean components with congested densely packed reinforcement, beams and slab pre-cast elements and long slender columns. High workability can be achieved with water/cement ratio and compressive strength of concrete with SP are usually higher than the corresponding strength of the control mixes without SP (Saeed et al., 2005).

This study aims to identify the effect of automotive windscreen waste glass powder as a pozzolanic admixture in mortar, and the physical, chemical and compressive strength of cement mortar with SP on different cement to sand (C:S) ratios.

METHOD

The test of fineness of OPC and WGWP was performed using the nitrogen absorption method and Brunauer, Emmatt and Teller (BET) equipment. The density was identified by Gas Pycnometry- Micromeritics 1340 and the particle size distribution determined using Mastersizer 2000 Laser Particle Size Analyzer. Scanning Electron Microscope (SEM) model JM6100 was used to ascertain particle morphology of the sample of OPC and WGWP. The Energy Dispersing X-ray Spectroscopy (EDAX) and X-ray Diffraction (XRD) analyser was used to determine the content element of WGWP.

The automotive windscreen glass was obtained from nearby workshops in Terengganu, Malaysia. The process involved the removal of the gluing polymer from the glass using Organo Cycler machine at Mariwealth Engineering & Consultancy Sdn. Bhd, Selangor. The Los Angeles machine was used to grind windscreen glass up to 10,000 revolutions to produce the automotive windscreen glass waste powder (WGWP). Figure 1 shows the flow of the preparation of WGWP. Supplementary materials used in the mortar were Ordinary Portland Cement (OPC) and fine aggregate of 5 mm maximum size. Superplasticizer Rheobuild 1100 was used in the preparation of mortar.

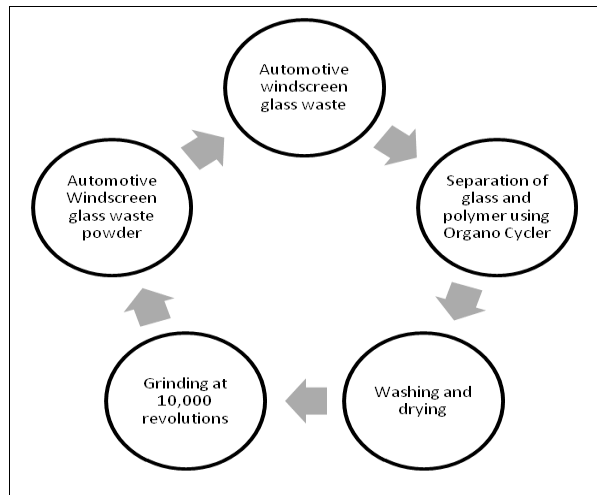


Figure 1. Preparation of automotive windscreen glass waste powder (WGWP)

This study was done on 90 mortar cube specimens with dimensions of 50 mm x 50 mm x 50 mm. Five mix proportions were adopted comprising various percentages of WGWP (0%, 5%, 10%, 15% and 20%) by weight of cement, whilst employing three batches of cement to sand (C:S) ratio of 1:2.5 SP, 1:3.0 SP and 1:3.5 SP. The water to cement (w/c) ratio was fixed at 0.5. The mortar cube specimens were cured in the water to the compressive testing at 7 and 28 days. For mix compositions of 1:2.5 SP, 1:3.0 SP and 1:3.5 SP, the cement contents were 2.27 kg, 2.07 kg and 1.89 kg respectively. The sand contents were 6.39 kg, 6.93 kg and 7.37 kg respectively. The SP for mix compositions of 1:2.5 SP and 1:3.0 SP were 25 g, while the mix compositions of 1:3.5 SP was 20 g.

The compressive strength was conducted in compliance to ASTM C:109:2013 (American Society for Testing And Materials). Three replicates were used for each batch. The strength activity index calculation based on ASTM C 618- 12a:2012 was adopted (American Society for Testing and Materials ASTM –C618 -12a).

RESULTS AND DISCUSSION

Table 1 shows the result of BET surface area and total area in pores for both OPC and WGWP. It shows that WGWP has smaller surface area compared to OPC. Practically, surface area is inversely proportional to particle size. The specific surface area increases as the particle size decreases. In this research, WGWP also has higher total area in pores compared to OPC indicating its density too is lower. Surface area is important in determining workability, water absorption and the durability of concrete. Surface area affects cement hydrates, adsorption capacity of air and water purifiers, and the processing of most powders and porous materials. Whenever solid matter becomes smaller particles new surfaces are created thereby increasing the surface area.

Table 1
Surface area and total area in pores of OPC and WGWP

Parameter/Material	OPC	WGWP
BET Surface Area (m ² /g)	1.0242	0.6462
Total area in pores (m ² /g)	0.1250	0.2100
Density (g/cm ³)	2.9885	2.5318

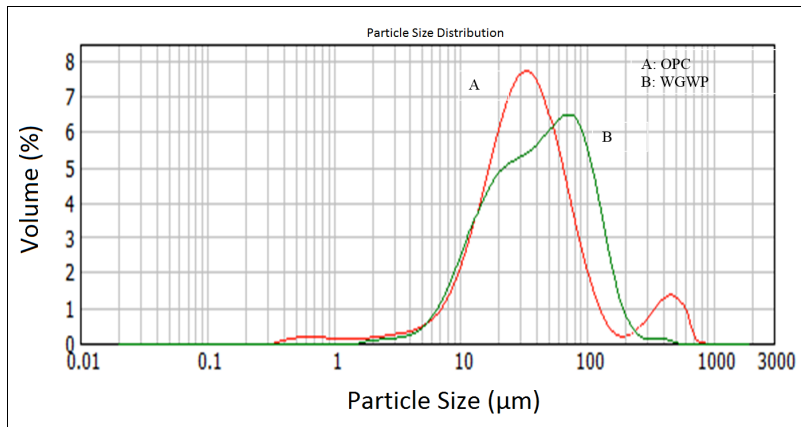


Figure 2. Particles size distributions of OPC and WGWP

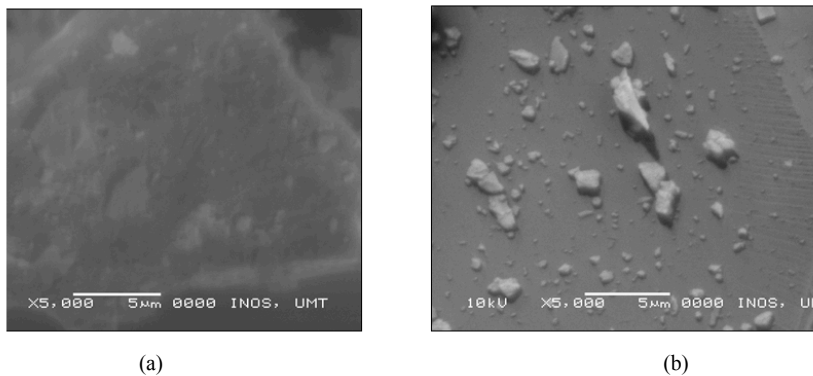


Figure 3. SEM of OPC and WGWP particles; (a) OPC particles – 5000× magnification; and (b) WGWP particles – 5000× magnification

Figure 2 shows the particle size distribution of OPC and WGWP. The WGWP was expected to serve as a filler and a supplementary cementitious material with pozzolanic activity (Nassar & Soroushian, 2012). Figure 3 (a) and (b), shows the particle morphology of OPC and WGWP

obtained using Scanning Electron Microscopy (SEM). The particles of WGWP had angular and crushed shapes.

From Table 2, shows the chemical composition of OPC and WGWP with the calcium oxide (CaO) content for OPC was about 69.06%, while the silicon dioxide (SiO₂) of WGWP was about 76.11%. The chemical compositions of raw materials were determined using Energy Dispersing X-ray Spectroscopy (EDAX). This finding is in agreement with ASTM C618-02 (American Society for Testing and Materials ASTM –C618 -12a, 2012), which requires a sum of SiO₂ + Al₂O₃ + Fe₂O₃ that is greater than 70% for good pozzolan. As shown in this study a total of 79.94% is obtained for WGWP. In order to predict the pozzolanic activity, the chemical compositions should not be used as the only criterion. It is because the amorphous state is also required and it has been confirmed for WGWP using XRD analyser as shown in Figure 4. Indeed, no peaks attributed to any crystallized compound can be identified except a broad diffraction halo, which is attributed to the glassy phase while Figure 5 and Figure 6 showed the EDAX of OPC and WGWP. Figure 4 shows the XRD of WGWP particles. The XRD of WGWP shown in Figure 4 indicates that the structure of silica in WGWP is amorphous with a diffused peak of 120 counts at about $\theta = 20^\circ$.

Table 2
Chemical compositions of raw materials

Material	Chemical compositions (%)						
	SiO ₂	CaO	Al ₂ O ₃	Fe ₂ O ₃	Na ₂ O	MgO	K ₂ O
OPC	16.03	69.06	4.14	5.09	0.02	0.67	1.3
WGWP	76.11	5.01	3.45	0.38	10.10	4.00	0.33

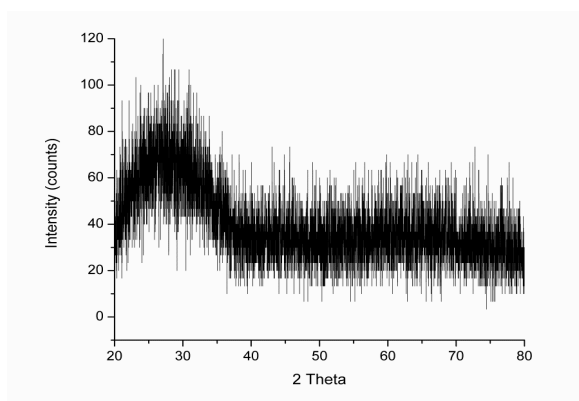


Figure 4. X-ray diffraction of WGWP

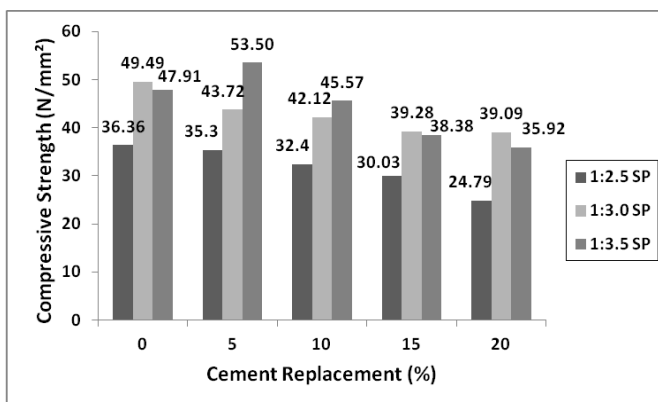


Figure 8. Compressive strength of cement-WGWP mortar at 28 days for different C:S ratios

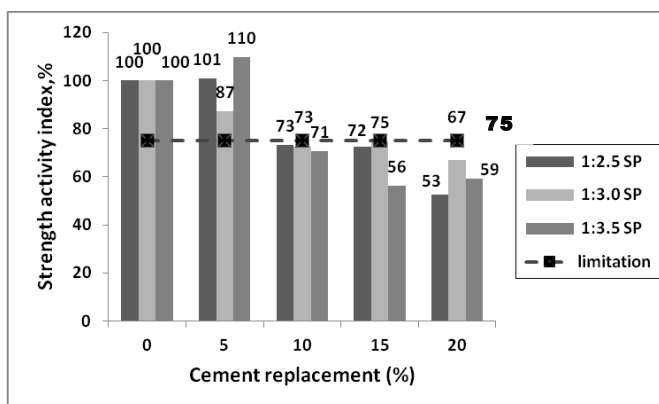


Figure 9. Dashed line indicates the limit of strength activity index at 7 days confirm to standard ASTM C 618

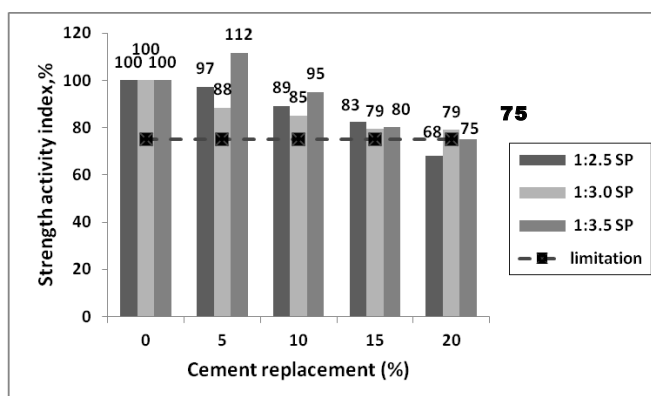


Figure 10. Dashed line indicates the limit of strength activity index at 28 days confirm to standard ASTM C 618

The SAI of the cement-WGWP mortar curing at 7 and 28 days is shown in Figure 9 and 10. The minimum requirement for SAI as prescribed by ASTM C 618 value is 75%. Figure 9, for all (C:S) ratio containing 5% cement replacement at 7 days shows mortar achieved the SAI of 101%, 87% and 110% respectively. At 28 days curing the highest SAI is shown in Figure 10. For 5%, 10%, 15% and 20% cement replacement the SAI were 112%, 95%, 80% and 75% respectively. The SAI of cement-WGWP mortar increased with time, and consistent with Patel et al. (2012) and Khmiri et al. (2013) that glass can significantly improve the strength of the mortar. It can be concluded that SAI achieved (C:S) of ratio through 1:3.5 SP at 20% by mass.

CONCLUSIONS

The surface area of WGWP was coarser and its density lower than of OPC. The surface area increased as the particle size was reduced - a small particle will react faster than a larger one. The XRD pattern indicates that WGWP is an amorphous material and can be classified as Class N natural Pozzolan. Replacing 5% cement with WGWP produces the highest compressive strength at both 7 and 28 days. The ratio of 1:3.5 SP was chosen as the best ratio which gave an improved compressive strength as compared to that of other C:S ratios and cement replacement of the WGWP in the mortar achieved the SAI ratio through 1:3.5 SP at 20% by mass.

ACKNOWLEDGEMENTS

The authors would like to express their appreciation to Universiti Malaysia Terengganu (UMT) and Universiti Teknologi MARA for their assistance, cooperation and support.

REFERENCES

- American Society for Testing And Materials ASTM-C618 -12a (2012). Standard Specification for Coal Fly Ash and Raw or Calcined Natural Pozzolan for Use in Concrete.
- American Society for Testing And Materials, ASTM-C109 (2013). Test Method for Compressive Strength of Hydraulic Cement Mortars (50mm) Cube Specimens.
- American Society for Testing And Materials, ASTM 494-92 (2013). Specification for chemical admixtures for concrete.
- Environmental Impact Assessment (EIA) (2006). Emission of Greenhouse Gases in the U.S Carbon Dioxide Emission, Emission of Greenhouse Gases Report, <http://www.eia.doe.gov/oiaf/1605/ggrpt/carbon.html>.
- Federico, L.M., & Chidiac S.E. (2009). Waste glass as a supplementary cementitious material in concrete – Critical review of treatment methods. *Cement and Concrete Composites*, 31, 06-10.
- Khmiri, A., Chaabouni, M., & Samet, B. (2013). Chemical behaviour of ground waste glass when used as partial cement replacement in mortar. *Construction and Building Materials*, 44, 74-80.
- Kim J., Yi C., & Zi G. (2015). Waste glass sludge as a partial cement replacement in mortar. *Construction and Building Materials*, 75, 242-246.

- Nassar, R., & Soroushian, P. (2012). Strength and durability of recycled aggregate concrete containing milled glass as partial replacement for cement. *Construction Building Material*, 29, 368-377.
- Neville, A. M. (1995). Properties of concrete, Fourth and Final Edition, *Sir Isaac Pitman and sons LTD*. London.
- Patel, D., Yadav, R. K., & Chandak, R. (2012). Strength characteristic of cement mortar paste containing coarse and fine waste glass powder. *International Journal of Engineering Sciences Research*, 03, 683-686
- Pereira-de-Oliveira, L. A., Castro-Gomes, J. P., & Santos, M. S. (2012). The potential pozzolanic activity of glass and red-clay ceramic waste as cement mortars components. *Construction and Building Materials*, 31, 197-203.
- Ruth M, & Dell'Anno P. (1997). An industrial ecology of the US glass industry. *Resources Policy* 23, 109-124.
- Schwarz, N., Cam, H. & Neithalath, N. (2008). Influence of a fine glass powder on the durability characteristics of concrete and its comparison to fly ash. *Cement and Concrete Composites* 30, 486-496.
- Saeed, A., Muhammad, N., & Ayub, E. (2005). *Effect of superplasticizers on workability and strength of concrete*. Paper presented at 30th Conference on Our World in Concrete and Structures.
- Shayan, A. (2002). *Value-added utilization of waste glass in concrete*. Paper presented at IABSE Symposium, Melbourne.
- Shayan, A., & Xu, A. (2004). Value-added utilization of waste glass in concrete. *Cement and Concrete Research*, 34, 1-9.
- Shayan, A., & Xu, A. (2006). Performance of glass powder as a pozzolanic material in concrete: A field trial on concrete slabs. *Cement and Concrete Research*, 36, 457-468.
- Shao, Y., Lefort, T., Mora, S., & Rodriguez, D. (2000). Studies on concrete containing ground waste glass. *Cement and Concrete Composites*, 30, 91-100.
- Taha, B., & Nounu, G. (2008). Properties of concrete contains mixed color waste recycled glass as sand and cement replacement. *Construction and Building Materials* 22, 713-720.





Preliminary Study of Cosmetic Coloured Contact Lenses Chemical Elements Analysis using Energy Dispersive X-Ray Spectroscopy

Syazwan Hafiz Mohd, Wan Elhami Wan Omar and Ai-Hong Chen*

Faculty of Health Sciences, Universiti Teknologi MARA (UiTM), 42300 Puncak Alam, Selangor, Malaysia

ABSTRACT

This paper examines the chemical elements used as colour additives in cosmetic coloured contact lenses (Cos-CCL) using Field Emission Scanning Electron Microscope equipped with Energy Dispersive X-ray Spectroscopy (FESEM-EDX) analysis. The samples comprised two different Cos-CCL brands and colours (sample A1-black iris colour & B1-gray iris colour) with their respective clear contact lens counterparts as controls (sample A2 & B2). The parameters of Cos-CCL were observed carefully so that they resembled their respective controls. All the samples were analysed for chemical element characterisation by using EDX spectroscopy surface mapping analysis on both front and back surfaces. EDX spectroscopy point analysis was done on cross-section surface of Cos-CCL when colour additive pattern could not be detected by FESEM on either surface. FESEM-EDX spectroscopy analysis has revealed iron element in the colour additives of the A1 sample and aluminium elements in the B2 sample. These two elements were not present in the respective control samples. It can be concluded that iron and aluminium elements are exclusively attributed to the colour additive in Cos-CCL samples. It is important for manufacturers of Cos-CCL to disclose information of their products and create greater awareness on the risks facing users.

Keywords: Colour additives, cosmetic coloured contact lens, elemental analysis, energy dispersive x-ray analysis

ARTICLE INFO

Article history:

Received: 28 September 2016

Accepted: 03 February 2017

E-mail addresses:

chenaihong@salam.uitm.edu.my (Ai-Hong Chen),

syaz.hafiz@yahoo.com.my (Syazwan Hafiz Mohd),

elhami@salam.uitm.edu.my (Wan Elhami Wan Omar)

*Corresponding Author

INTRODUCTION

Cosmetic colour contact lenses (Cos-CCLs) is used to change the physical colour appearance of the eyes. They are commonly used as a fashion accessory rather than for refractive correction purpose. Cos-CCL is usually worn by teenagers and adolescents especially in Asian countries (Morgan et al., 2012; Morgan

et al., 2013). As their popularity increases, many reported cases of complications caused by Cos-CCLs wear have become a public concern. In general, these adverse clinical reports are linked with poor user compliance (Schanzer et al., 1989; Bucci et al., 1997) and acquisition of the Cos-CCL without prescriptions from authorised optical shops (Singh et al., 2012; Steinemann et al., 2003). Thus, it is believed that any adverse contact lens-related ocular occurrence is solely the result of external factors. In fact, none of the studies was found to concisely demonstrate the potential threat from the Cos-CCL materials per se.

A study by Sauer and Bourcier (2011) has reported poor prognosis following microbial keratitis (MK) treatment by Cos-CCL users compared to the control group using clear corrective contact lenses. This discrepancy is probably due to the existence of exclusive Cos-CCL elements used in colour additives despite the presence of a long-standing list of approved colour additives used for Cos-CCL provided by Food & Drug Administration (FDA) of the United States (US).

A recent study on colour additives in Cos-CCL reported the presence of various elements such as iron, chlorine and titanium in Cos-CCL samples (Hotta et al., 2015). However, the study is inconclusive because the researchers were unable to confirm whether the elements belong to the colour additives of Cos-CCL. This study aims to examine the characterisation of chemical elements used as colour additives in different coloured range of Cos-CCL in the presence of their respective clear contact lens counterparts using Field Emission Electron Scanning Microscope equipped with Energy Dispersive X-ray (FESEM-EDX) spectroscopy analysis.

METHOD

The characterisation of chemical elements in contact lens samples was set up in an experimental laboratory study design. Direct comparison of the chemical elements between Cos-CCL samples and their respective clear contact lens control samples was made. The chemical elements found exclusively on Cos-CCL samples by EDX spectroscopy analysis showed their presence as components of colour additives. The findings were also confirmed by observing the similarities between colour additives patterns of the EDX elemental mappings with the respective FESEM images. To examine the chemical elements in different colour types, the EDX spectroscopy findings were compared between two Cos-CCLs of different colours. The instrument used was Field Emission Electron Microscope (FESEM) JSM-6701F equipped with energy dispersive X-ray (EDX) spectroscopy (JEOL).

Materials and Instrumentation

Contact lenses. Two brands of contact lenses (brand A and B) were studied. These two brands were selected because each brand manufactures both Cos-CCLs and clear corrective contact lenses. The chosen colours were black iris from brand A and grey iris from brand B. The parameters of each Cos-CCL were studied so that they resembled parameters of the respective clear contact lens used as control samples. Brand A contact lens samples (Cos-CCL in black iris colour and its clear contact lens counterpart), are made from etafilcon A. The water content in

each sample is 58%. The diameter and base curve on the other hand is 14.2 mm and 8.5 mm, respectively. Brand B contact lens samples (Cos-CCL in grey iris colour and its clear contact lens counterpart), are made from lotrafilcon B with 33% water content in each sample. The diameter of each is 14.2 mm with 8.6 mm base curve. The parameters are listed in Table 1.

Table 1
The respective parameters of the contact lens samples

Brand	Sample	Product name	Colour	Contact lens material	Water content (%)	Diameter (mm)	Base curve (mm)	Colour additive information
A	A1	FAE	Mystical black	Etafilcon A	58	14.2	8.5	NIL
	A2 (control)	58F	Clear	Etafilcon A	58	14.2	8.5	N/A
B	B1	AOC	Grey	Lotrafilcon B	33	14.2	8.6	NIL
	B2 (control)	AO	Clear	Lotrafilcon B	33	14.2	8.6	N/A

Note: NIL – no information listed; N/A – not applicable

Field Emission Electron Microscope with energy dispersive X-ray attachment (FESEM-EDX). The instrument used to characterise the chemical elements in contact lens samples is the Field Emission Electron Microscope (FESEM) JSM-6701F with energy dispersive X-ray (EDX) spectroscopy attachment (JEOL). This instrument works by analysing the X-ray spectrum emitted by the samples bombarded with a focused beam of electrons. Thus, FESEM was used in this study as it has electron probe capabilities. The FESEM was equipped with the EDX spectroscopy to scan the X-ray beam for characterisation of chemical element analysis.

Protocol

Preparation of the contact lens samples. The contact lenses were cut into sizes to fit the scanning electron microscope's stubs. They were cut specifically into approximate quarters by applying single pressure on them using a clean razor blade. Each individual piece was then manually torn and held with a clean tweezer and pat dry, prior to being placed on the FESEM's stub. For each contact lens, two different surface orientations (front surface and back surface) were prepared for analysis.

Characterisation of chemical element of the contact lens samples. The stubs containing the samples were placed carefully into the FESEM chamber and examined closely to locate the position of colour additives. Where localisation of colour additives on the sample surfaces were not visible by FESEM, a scanning process was performed on the cross-section surface.

The characterisation of chemical components of the colour additives was performed by EDX surface mapping analysis. The surface of every sample was analysed by EDX surface mapping analysis or EDX point analysis. Summary on the protocol involving FESEM-EDX spectroscopy analysis is shown in Figure 1.

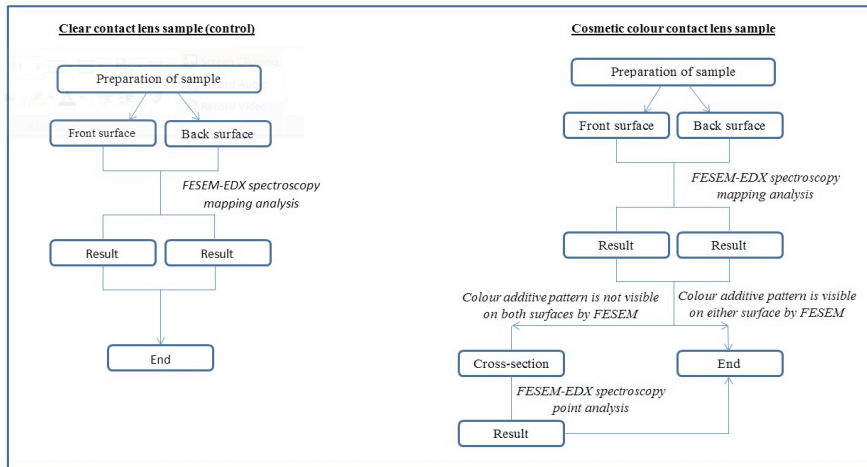


Figure 1. Schematic workflow of the FESEM-EDX spectroscopy analysis

RESULTS

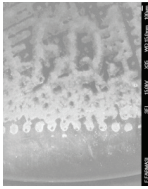
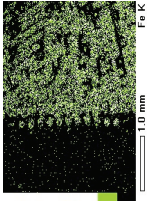
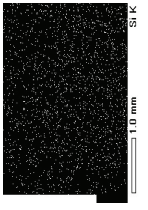
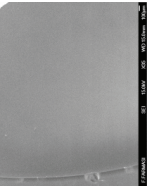
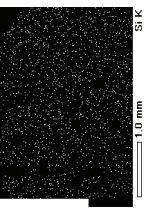
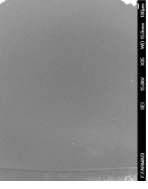
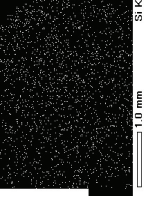
The existence of chemical elements attributable to colour additives of the Cos-CCL samples were established through comparison with the chemical elements found in the respective control samples. Comparison of the chemical elements between two Cos-CCL samples was also done to acquire variation of chemical elements in different colour types. The data in Table 2 and Table 3 feature the manufacture related Cos-CCL samples with their respective control samples.

Chemical Element Analysis of the Cos-CCL Samples Featuring the Control Samples

As presented in Table 2, chemical elements found by EDX spectroscopy analysis on brand A Cos-CCL sample (A1) were iron, on the front surface and silicon, on its back surface. In contrast, EDX spectroscopy analysis has shown only silicon element on the front and back surface of the control sample (A2). The findings suggested that the element iron is exclusively attributed to the colour additives of the sample. Furthermore, the mapping pattern of iron was concentrated in the area of colour additive portion imaged by FESEM. For the back surface EDX spectroscopy analysis of the same sample found silicon to be diffusely distributed without any specific pattern. These findings were similar to the A2 sample surfaces. Hence, it is suggested that iron is used as a colour additive in A1 sample.

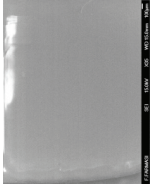
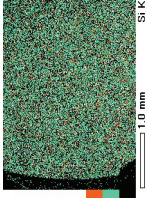
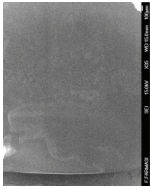
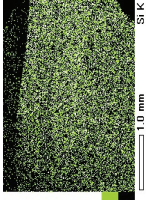
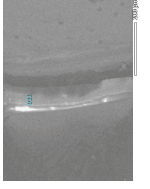
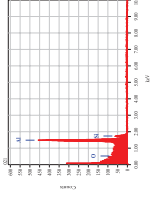
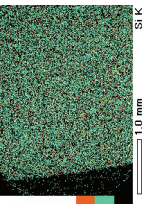
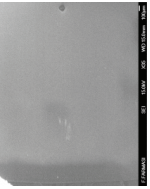
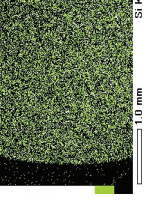
For brand B samples as shown in Table 3, the element of silicon has been analysed on the front and back surface of both Cos-CCL sample (B1) and its control sample (B2). These findings conceded with FESEM image analysis in which the colour additives pattern of the B1 sample was undetected in either surface despite of its visibility by the naked eyes. However, upon performing cross-section FESEM image analysis, the portion of colour additive was found embedded in the matrix of the B1 sample. Hence, the EDX spectroscopy analysis was done by point analysis and revealed the colour additives for B1 sample which is grey in colour contained aluminium.

Table 2
 FESEM-EDX spectroscopy findings of the brand A: Comparison of chemical elements between Cos-CCL samples with control samples

Colour / Sample	Surface analysis					
	Front		Back		Cross-section	
	FESEM image	EDX spectroscopy mapping	FESEM image	FESEM image	EDX spectroscopy mapping	EDX spectroscopy mapping
Black iris / A1					N/A	N/A
Clear / A2					N/A	N/A

Chemical elements descriptions: Fe – iron element, Si – silicon element; N/A – not applicable

Table 3
 FESEM-EDX spectroscopy findings of the brand B: Comparison of chemical elements between Cos-CCL samples with control samples

Colour / Sample	Surface analysis					
	Front		Back		Cross-section	
	FESEM image	EDX spectroscopy mapping	FESEM image	EDX spectroscopy mapping	FESEM image	EDX spectroscopy mapping
Gray iris / B1						
	(i)	(j)	(k)	(l)	(m)	(n)
Clear / B2					N/A	N/A
	(o)	(p)	(q)	(r)		

^aEDX spectroscopy point analysis result – Aluminium element was found in higher count (shown in the highest peak) relative to silicon and oxygen element; Chemical elements descriptions: Al – aluminium element, Si – silicon element; N/A – not applicable

Chemical elements analysis between Cos-CCL samples of different colours

Table 2 and Table 3 shows the chemical elements of two different colours represented by A1 and B1 samples. Sample A1 contained an iron element as a colour additive and sample B1 contained aluminium element, indicating that chemical elements vary with colours.

DISCUSSION

In this present study, iron has been found in black iris coloured contact lens whilst grey iris coloured contact lens contained aluminium. We developed an improved protocol by comparing the EDX spectroscopy findings between Cos-CCL samples with their respective clear contact lens control samples and found iron and aluminium elements were only detectable by EDX spectroscopy in the area where the colour additives patterns were visible through FESEM images. For example, the iron element was found on the front surface of the A1 sample in which the colour additives pattern were also imaged by FESEM. In the same sample, silicon was found at the back surface where the colour additive pattern could not be detected by FESEM. Similarly, in the EDX spectroscopy mapping analysis that was performed on B1 sample's front and back surfaces (Cos-CCL sample) the results showed the presence of silicon which was not different from the respective control samples. It was only during the EDX spectroscopy analysis on the separated middle layer of the sample B1 through cross-section image, the aluminium element was detected. Hence, we can conclude that EDX spectroscopy is able to characterise materials on the surface area focused by FESEM.

The characterisation of the chemical elements used as colour additives in Cos-CCL by EDX spectroscopy can be regarded as superior and reasonable compared to the other techniques. In a review article Brennan and Coles (2001) organised the techniques or methods for evaluating contact lens surface into three broad classifications: clinical assessment methods, microscopy and imaging methods and assays method. According to their classification, FESEM-EDX method is classified under the microscopy and imaging category. In order to characterise more complex unknown elements the clinical assessment methods seems unsuitable because it seeks to assess the condition based on Rudko grading system (Rudko & Proby, 1974; Guillon et al., 1992; Hurst et al., 1994) rather than identifying the elements. The assays methods, despite the fact that it can provide promising information on the characterisation of elements, is complicated because it involves a cumbersome sample preparation based on the material being investigated (Wedler, 1977). To date, there is no study conducted to investigate the implication of the chemical elements used as colour additives in Cos-CCL on the human cornea. Thus despite having identifies the presence of iron and aluminium elements in colour additives, their implications on the wearers' eyes cannot be conclusively asserted.

Although this study may provide insights on the biomaterial of Cos-CCL, it has two limitations. First, only one sample for each contact lens was analysed. Second, only a small number of samples, i.e. two different colours of Cos-CCLs were analysed. It can therefore be conclude that users of Cos-CCL should be aware of the chemicals used as colour additives. Even though some chemical elements maybe safe determining whether those 'safe' chemicals

have been used is the challenge. Hence, it is preferable to urge manufacturers of cosmetic coloured contact lenses to disclose information regarding the colour additives used in their products.

ACKNOWLEDGEMENTS

This study was supported by 600-RMI/RAGS 5/3 (71/2014). The authors thank the Imaging Centre, Faculty of Pharmacy UiTM Puncak Alam Campus for providing technical support during our work with the Field Emission Electron Microscope (FESEM) JSM-6701F with the energy dispersive X-ray (EDX) spectroscopy attachment (JEOL).

REFERENCES

- Brennan N. A. & Coles M. L. C. (2000). Deposits and symptomology with soft contact lens wear. *JCLC*, 27, 75-100.
- Bucci, F., Evans, R., Moody, K., Tanner, J., Capozza, R., & Klyce, S. (1997). The annular tinted contact lens syndrome: corneal topographic analysis of ring-shaped irregular astigmatism caused by annular tinted contact lenses. *CLAO J.*, 23, 161-167.
- Eaton, J. W., & Qian, M. (2002). Molecular bases of cellular iron toxicity. *Free Radical Biology and Medicine*, 32(9), 833-840.
- Guillon, M., Allary, J. C., Guillon, J. P., & Orsborn, G. (1992). Clinical management of regular replacement: Part 1. Selection of replacement frequency. *Int Contact Lens Clin.*, 19, 104-120.
- Hotta, F., Eguchi, H., Imai, S., Miyamoto, T., Mitamura-Aizawa, S., & Mitamura, Y. (2015). Scanning electron microscopy findings with energy-dispersive x-ray investigations of cosmetically tinted contact lenses. *Eye and Contact Lens* 0:1-6.
- Hurst, M. A., Mitchell, S. E., & Douthwaite, W. A. (1994). Contact lens opacity grading system (CLOGS). *J Brit Contact Lens Assoc*, 17, 19-24.
- Jang, H. J., Kim, J. M., & Choi, C. Y. (2014). Elemental analysis of sunflower cataract in Wilson's disease: A study using scanning transmission electron microscopy and energy dispersive spectroscopy. *Experimental Eye Research*, 121, 58-65.
- Morgan, P. B., Woods, C. A. G., Helland, T. I., Efron, M., Orihuela, N., & Grupcheva, N. C. N. (2013). International contact lens prescribing in 2012. *Cont. Lens Spectr.*, 28(2), 31-38.
- Morgan, P. B., Woods, C. A. G., Helland, T. I., Efron, M., Grupcheva, N. C. N. & Tan, D. J. (2012). International contact lens prescribing in 2011. *Cont. Lens Spectr.*, 27(1), 26-31.
- Rudko, P., & Proby, J. (1974). A method for classifying and describing protein deposition on the hydrophilic contact lens. *Allergan Report Series No.94*.
- Sauer, A., & Bourcier, T. (2011). Microbial keratitis as a foreseeable complication of cosmetic contact lenses: a prospective study. *ActaOphthalmol.*89, e439-e442.
- Schanzer, M. C., Mehta, R. S., Arnold, T. P., Zuckerbrod, S. L., & Koch, D. (1989). Irregular astigmatism induced by annular tinted contact lenses. *CLAO J.*, 15, 207-211.

- Singh, S., Satani, D., Patel, A., & Vhankade, R. (2012). Colored cosmetic contact lenses: an unsafe trend in the younger generation. *Cornea*, *31*(7), 777-779.
- Steinemann, T. L., Pinninti, U., Szczotka, L. B., Eiferman, R. A., & Price, F. W. Jr. (2003). Ocular complications associated with the use of cosmetic contact lenses from unlicensed vendors. *Eye and Contact Lens* *29*(4), 196-200.
- Wedler, F. C. (1977). Analysis of biomaterials deposited on soft contact lenses. *J Biomed Mater Res*. *11*, 525-569.





Microstructure, Microhardness and Density of Shot Blasting and Paste Boronizing on 316L Stainless Steel

Muhamad Hafizuddin Mohamad Basir¹, Mohd Faizul Idham², Bulan Abdullah^{1*} and Muhammad Hussain Ismail¹

¹Faculty of Mechanical Engineering, Universiti Teknologi MARA (UiTM), 40450 Shah Alam, Selangor, Malaysia

²Faculty of Mechanical Engineering, Universiti Teknologi MARA (UiTM), 23200 Bukit Besi, Dungun, Terengganu, Malaysia

ABSTRACT

The aim of this study is to examine the effect of surface treatments involving shot blasting and paste boronizing on the microstructure, microhardness and density of 316L stainless steel. Shot blasting using glass beads was carried out prior to paste boronizing at fix boronizing temperature and soaking time of 850°C and 8 hours respectively. The results show paste boronizing produces boride layers that consist of FeB and Fe₂B on the surface of 316L stainless steel with high hardness. Shot blasting on the other hand creates grain refinement on the metal's surface which increases boron diffusion into the surface and improves the case depth of boride layers formed and also its hardness. Higher shot diameter used in shot blasting also influence in improving the case depth of boride layers produced and hardness of 316L stainless steel. The effect of shot blasting using a higher shot diameter and paste boronizing reduces the density of 316L stainless steel very slightly.

Keywords: Boride layers, microhardness, paste boronizing, shot blasting, stainless steel

ARTICLE INFO

Article history:

Received: 28 September 2016

Accepted: 03 February 2017

E-mail addresses:

firedon89@gmail.com (Muhamad Hafizuddin Mohamad Basir),
mohdfaizulidham@gmail.com (Mohd Faizul Idham Mohd Zulkipli),
bulanabdullah@gmail.com (Bulan Abdullah),
hussain305@salam.uitm.edu.my (Muhammad Hussain Ismail)

*Corresponding Author

INTRODUCTION

Stainless steel is a high corrosion resistant and hence, widely used in the food, petrochemical, automotive and marine industries (Ceschini et al., 2012; Wood et al., 2013). 316 stainless steel is an austenitic stainless steel and has low carbon composition, and hence beneficial for welding purposes (AKSteel, 2013; Kianersi et al., 2014). Although it has excellent corrosion resistance, it nevertheless has low mechanical and tribological characteristics (Karimzadeh et al., 2013).

Boronizing is a case hardening process that involves diffusing boron into the surface of a metal (Gunes et al., 2011; Yang et al., 2014; Yoon et al., 1999). Paste boronizing is a recent method which can reduce the boronizing temperature and time, compared to the powder pack method. Shot blasting is a plastic deformation technique used for improving the case depth of boride layers produced by paste boronizing. This study examines the microstructure, microhardness and density of 316L stainless steel before and after applying surface treatments.

METHODS

The raw material for the study consisted of rod 316L stainless steel that was cut into samples 10 mm length for microstructure observation, microhardness test and density test using an Abrasive Cutter. The Hot mounting process was conducted on the samples with microstructure observation and microhardness test undertaken with a Hot Mounting Machine. Samples were ground using a grinding machine with various grades of Silicon Carbide, SiC sand paper, and polished with DIAMAT Polycrystalline Diamond.

Shot blasting was conducted on samples using glass beads with various shot diameter of 100 micron and 250 microns at fix blasting pressure of 6 bar. Paste boronizing was performed on the samples using fix boronizing temperature and soaking time of 850°C and 8 hours respectively. Table 1 shows the surface treatments and parameters involved.

Table 1
Sample labelling according to the surface treatment and parameter applied

Sample	Surface Treatment and Parameter
UN	Untreated 316L Stainless Steel
S10(6)	Shot Blasted 316L Stainless Steel Using 100 Micron Glass Beads at 6 Bar of Blasting Pressure
S25(6)	Shot Blasted 316L Stainless Steel Using 250 Micron Glass Beads at 6 Bar of Blasting Pressure
S10(6)P85(8)	Shot Blasted 316L Stainless Steel Using 100 Micron Glass Beads at 6 Bar of Blasting Pressure and Paste Boronized Subsequently at 850°C for 8 Hours
S25(6)P85(8)	Shot Blasted 316L Stainless Steel Using 250 Micron Glass Beads at 6 Bar of Blasting Pressure and Paste Boronized Subsequently at 850°C for 8 Hours

Microstructure of samples was observed under Olympus BX60 Optical Microscope (Figure 1(a)) at 200x magnification after they were etched. Samples' hardness was determined using MITUTOYO MVK-H1 Vickers Micro Hardness Tester (Figure 1(b)) using 50 gf of indentation load. Density of the samples was obtained using Analytical Balance Machine (Figure 1(c)) by applying the Archimedes concept.

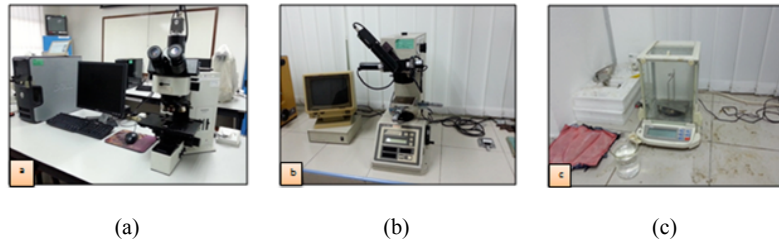


Figure 1. (a) Optical Microscope; (b) Vickers Micro Hardness Tester; and (c) Analytical Balance Machine

RESULTS AND DISCUSSION

Microstructure Observation

Figure 2(a) illustrates the austenitic structure of 316L stainless steel. Following shot blasting grain refinement with high dislocation density can be observed on the surface of 316L stainless steel as displayed in Figure 2(b) and Figure 2(c). Balusamy et al. (2013) also reported on the observation of grain refinement after performing SMAT. As presented in Figure 3, increasing the shot diameter of glass beads from 100 microns to 250 microns used in shot blasting increases the thickness of grain refinement produced on the metal's surface which the S10(6) sample produces the thickness value of 40.1 micron while S25(6) sample produces the value of 78.7 micron.

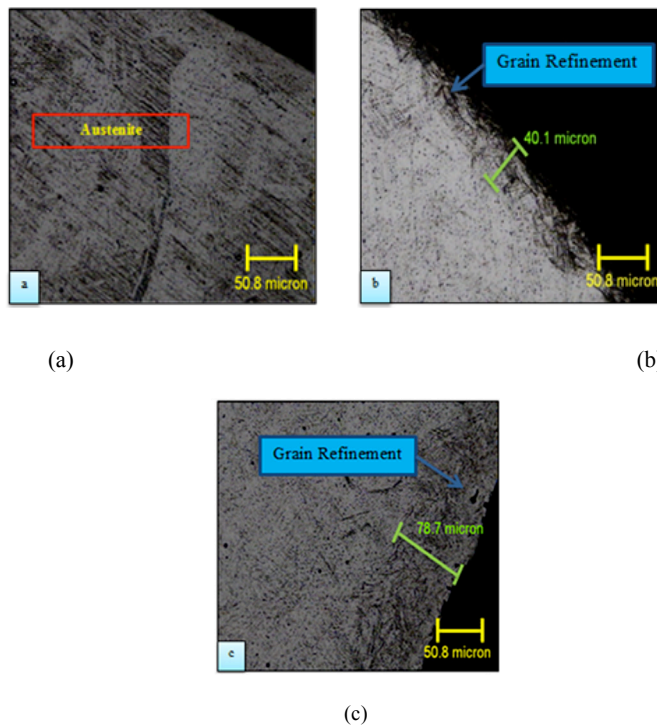


Figure 2. Microstructure of (a) UN; (b) S10(6); and (c) S25(6) sample

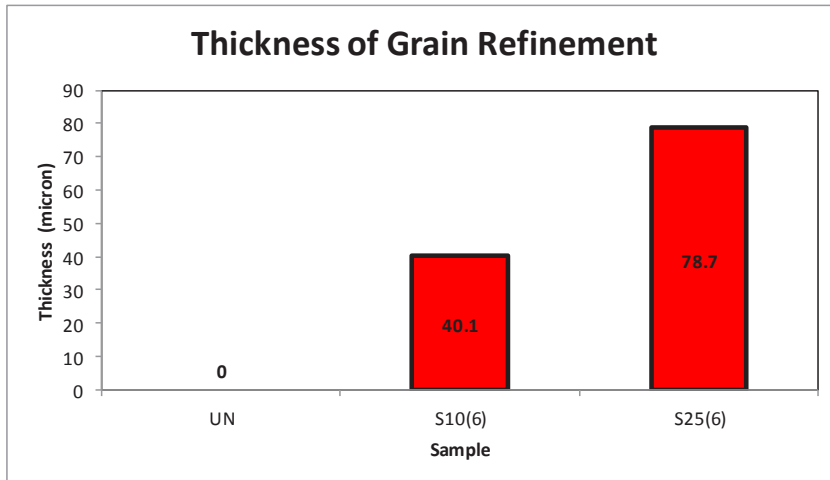


Figure 3. Thickness of grain refinement on shot blasted 316L stainless steel samples

Subsequent to performing paste boronizing, boride layers which consist of FeB and Fe₂B form on the surface of 316L stainless steel. It is also reported on the presence of both phases on impact of boronizing elsewhere (Balusamy et al., 2013; Basir et al., 2014; Basir et al., 2015; Gunes et al., 2011; Yang et al., 2014; Yoon et al., 1999). However, single Fe₂B phase can be observed on the S10(6)P85(8) sample while the growth of FeB phase can be seen on S25(6)P85(8) sample as shown in Figure 4. Applying different shot diameter of glass beads in shot blasting produces different case depths of boride layers that form on the surface of 316L stainless steel following paste boronizing.

The graph in Figure 5 shows greater shot diameter of glass beads used in shot blasting increases the case depth of boride layers. The case depth of Fe₂B layer on S10(6)P85(8) sample is 13.5 micron while the case depth of Fe₂B layer on S25(6)P85(8) sample is 14.0 micron with total case depth of boride layers of 20.3 micron. This improvement is the result of enhanced boron diffusion into the surface of 316L stainless steel.

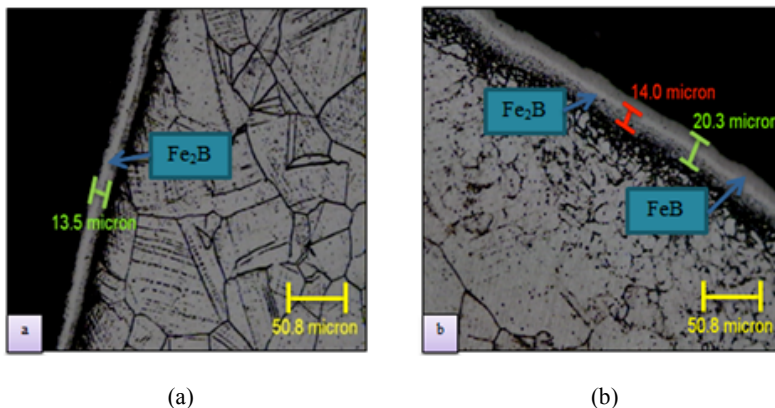


Figure 4. Microstructure of (a) S10(6)P85(8); and (b) S25(6)P85(8) Sample

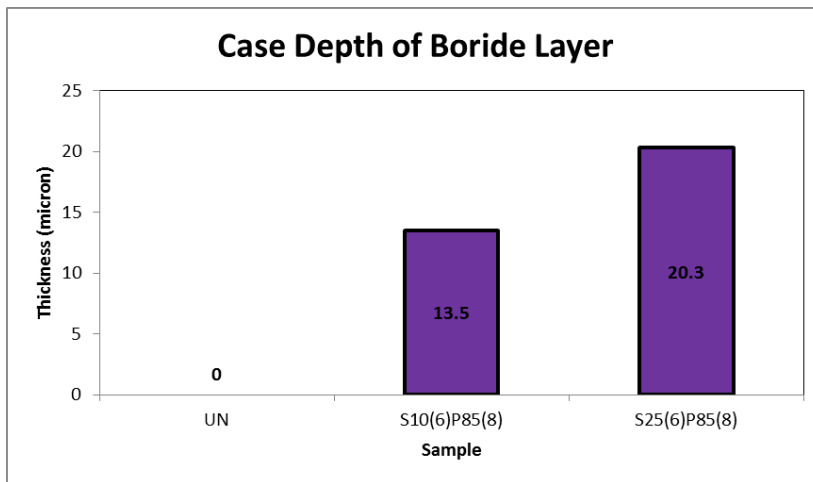


Figure 5. Case depth of boride layers of shot blasted-paste boronized 316L stainless steel samples

Microhardness Measurement

Figure 6 shows the microhardness of the untreated, shot blasted and shot blasted-paste boronized 316L stainless steel. It can be seen that the effect of shot blasting increases the microhardness of 316L stainless steel, as the process creates grain refinement with atom dislocation on the surface of the metal, inducing strain hardening as a result of high dislocation density (Callister, 2003). Raising the shot diameter from 100 micron to 250 micron improves the microhardness of 316L stainless steel. Arifvianto et al. (2011) reported that higher ball size used in SMAT produced greater sample's hardness.

It also can be seen that the combination of shot blasting together with paste boronizing can increase the microhardness of 316L stainless steel so too employing higher shot diameter of glass beads resulting from the enhancement of boron diffusion and its effect on the depth of the boride layers produced.

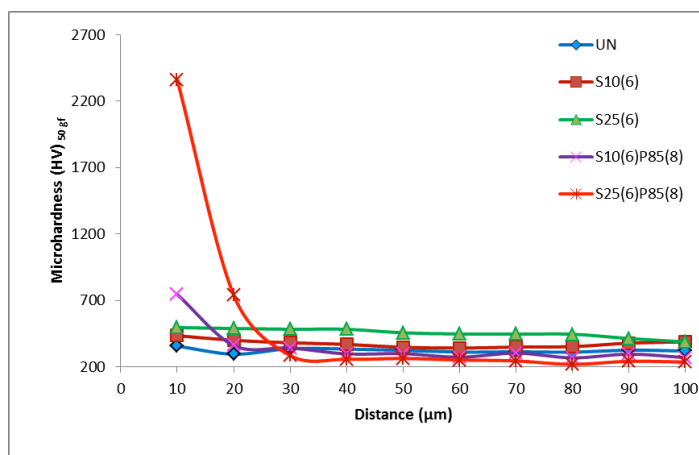


Figure 6. Microhardness of untreated, shot blasted and shot blasted-paste boronized samples

Density Measurement

Figure 7 shows the density of untreated, shot blasted and shot blasted-paste boronized 316L stainless steel. The average density of UN, S10(6), S25(6), S10(6)P85(8) and S25(6)P85(8) samples are 7.95772 g/cm³, 7.90234 g/cm³, 7.90025 g/cm³, 7.90004 g/cm³ and 7.85886 g/cm³ respectively. Shot blasting and paste boronizing appears to reduce the density of 316L stainless steel. Higher shot diameter used in shot blasting with the application of paste boronizing reduces the density of 316L stainless steel further. Although applying both of the surface treatments reduces the density of 316L stainless steel, the reduction is negligible.

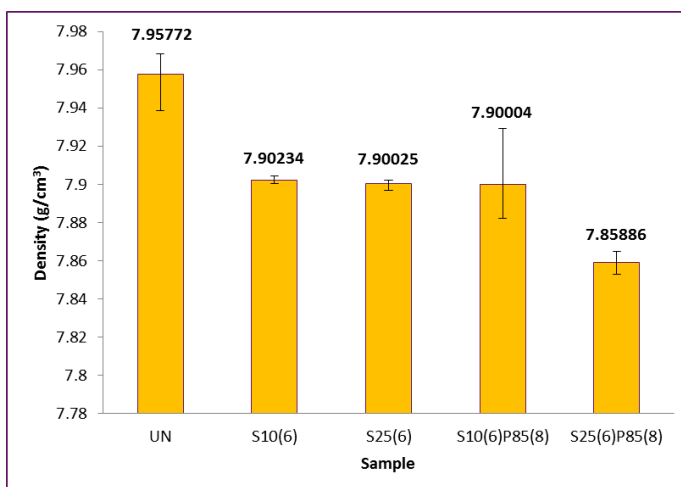


Figure 7. Density of untreated, shot blasted and shot blasted-paste boronized 316L stainless steel

CONCLUSION

Microstructure of shot blasted 316L stainless steel shows grain refinement on the surface which improves when the shot diameter is increased. Paste boronizing produces the boride layers of FeB and Fe₂B and applying shot blasting prior to paste boronizing with higher shot diameter increases the case depth of boride layers. The effect of shot blasting and paste boronizing also raises the microhardness of 316L stainless steel. Increasing the shot diameter of glass beads used in shot blasting also improves the microhardness of 316L stainless steel. The effect of shot blasting and paste boronizing reduces the density of 316L stainless steel slightly and raising the shot diameter in shot blasting decreases the metal's density.

ACKNOWLEDGEMENTS

The authors would like to express their gratitude to Ministry of Higher Education Malaysia and RMC UiTM for RAGS grant (600-RMI/RAGS 5/3 (206/2014)) and RAGS grant (600-RMI/RAGS 5/3 (160/2014)) for making this study possible.

REFERENCES

- AKSteel. (2013). Stainless Steel 316/316L Product Data Bulletin, 2–4. Retrieved from http://www.aksteel.com/pdf/markets_products/stainless/austenitic/316_316l_data_bulletin.pdf
- Arifvianto, B., Suyitno, Mahardika, M., Dewo, P., Iswanto, P. T., & Salim, U. A. (2011). Effect of Surface Mechanical Attrition Treatment (SMAT) on Microhardness, Surface Roughness and Wettability of AISI 316L. *Materials Chemistry and Physics*, *125*(3), 418–426.
- Balusamy, T., Sankara Narayanan, T. S. N., Ravichandran, K., Song Park, I., & Lee, M. H. (2013). Pack Boronizing of AISI H11 Tool Steel: Role of Surface Mechanical Attrition Treatment. *Vacuum*, *97*, 36–43.
- Basir, M. H. M., Abdullah, B., & Alias, S. K. (2014). Wear Properties of Paste Boronized 316 Stainless Steel Before and After Shot Blasting Process. *Scientific Research Journal*, *11*(2).
- Basir, M. H. M., Abdullah, B., Alias, S. K., Jumadin, M. H. M., & Ismail, M. H. (2015). Analysis on Microstructure, Hardness and Surface Roughness of Shot Blasted-Paste Boronized 316 Austenitic Stainless Steel. *Jurnal Teknologi*.
- Callister, W. D. (2003). *Materials Science and Engineering: An Introduction* (Sixth Edit). John Wiley & Sons, Inc.
- Ceschini, L., Chiavari, C., Lanzoni, E., & Martini, C. (2012). Low-Temperature Carburised AISI 316L Austenitic Stainless Steel: Wear and Corrosion Behaviour. *Materials and Design*, *38*, 154–160.
- Gunes, I., Ulker, S., & Taktak, S. (2011). Plasma Paste Boronizing of AISI 8620, 52100 and 440C Steels. *Materials and Design*, *32*, 2380–2386.
- Karimzadeh, N., Moghaddam, E. G., Mirjani, M., & Raeissi, K. (2013). The Effect of Gas Mixture of Post-Oxidation on Structure and Corrosion Behavior of Plasma Nitrided AISI 316 Stainless Steel. *Applied Surface Science*, *283*, 584–589.
- Kianersi, D., Mostafaei, A., & Ali, A. (2014). Resistance Spot Welding Joints of AISI 316L Austenitic Stainless Steel Sheets : Phase Transformations, Mechanical Properties and Microstructure Characterizations. *Materials and Design*, *61*, 251–263.
- Lopes, N., & Vila Real, P. M. M. (2014). Class 4 Stainless Steel I Beams Subjected to Fire. *Thin-Walled Structures*, *83*(November), 137–146.
- Wood, R. J. K., Walker, J. C., Harvey, T. J., Wang, S., & Rajahram, S. S. (2013). Influence of Microstructure on the Erosion and Erosion-Corrosion Characteristics of 316 Stainless Steel. *Wear*, *306*(1-2), 254–262.
- Yang, H., Wu, X., Yang, Z., Pu, S., & Wang, H. (2014). Enhanced Boronizing Kinetics of Alloy Steel Assisted by Surface Mechanical Attrition Treatment. *Journal of Alloys and Compounds*, *590*, 388–395.
- Yoon, J. H., Jee, Y. K., & Lee, S. Y. (1999). Plasma Paste Boronizing Treatment of the Stainless Steel AISI 304. *Surface and Coatings Technology*, *112*(1-3), 71–75.





Correlation of Case Depth with Mechanical Properties of Low Carbon Steel Using Paste Carburizing Method

Bulan Abdullah*, Muhammad Hafizuddin Jumadin, Muhammad Hussain Ismail, Siti Khadijah Alias and Samsiah Ahmad

Faculty of Mechanical Engineering, Universiti Teknologi MARA (UiTM), 4050 Shah Alam, Selangor Malaysia

ABSTRACT

Powder carburising compound used for pack carburizing has limited potential in producing thicker case depth. Paste carburizing has proved to be an option to replace powder in conventional pack carburizing as it requires less time and temperature to diffuse carbon atoms, and thereby produce greater case depth. The correlation between case depth and mechanical properties using paste carburising is the objective of this paper where the relationship between case depth with mechanical and tribological properties using powder, paste 1:1 and paste 3:1 compounds at 1000°C for 9 hours are studied. Samples were subjected to microhardness tests, tensile tests and wear tests. Results showed paste 1:1 compound produced the highest case depth (>0.5 mm), allowing us to greater tensile strength, 6.61% and high wear resistance, 49%.

Keywords: Carburising compound, case depth, low carbon steel, pack carburizing, paste carburizing, wear

INTRODUCTION

Carburizing is a case hardening process to maintain substrate's ductility of steel by increasing the carbon content of its interior. It is a process usually applied to components that require greater wear resistance such as gears and shafts. The component that need to be carburised

is heated to austenite phase temperature (800°C-1000°C) and soaked for 3 to 10 hours for carbon to diffuse on the steel's surface before proceeding to the next process i.e. quenching, normalizing or annealing (Kalpajian & Schmid, 2010). Carburizing compound is a source medium for supplying carbon atoms (carbon monoxides) during the carburizing process. Compounds come in various forms and properties, such as solid, fluid and gases (Lou, 2009). The most

ARTICLE INFO

Article history:

Received: 28 September 2016

Accepted: 03 February 2017

E-mail addresses:

bulanabdullah@gmail.com (Bulan Abdullah),
muh.hafizuddin@yahoo.com (Muhammad Hafizuddin Jumadin),
hussain305@salam.uitm.edu.my (Muhammad Hussain Ismail),
khadijah_alias@yahoo.com (Siti Khadijah Alias),
samsiah.ahmad@johor.uitm.edu.my (Samsiah Ahmad),
*Corresponding Author

effective carburizing compound was by using gases as it already in the form of carbon monoxide gases. For pack carburizing, solid or powder compound requires additional temperature and time before they compose into carbon monoxides gases.

Paste compound made of e.g. nitrogen, silicon, boron, carbon, can be used to replace powder for pack case hardening process. For pack carburizing, paste compound consists of a mixture of a carbon resource powder, an inert powder, one or more catalyst and a binder solution (Campos et al., 2005). Paste compound has better diffusion rate than powder compound because of the formability of medium structure, allowing the medium to release more carbon monoxide (CO) and produce thicker carbon-rich layer up to 10-25% on carburized steels (Chen, 2000). Carbon atom diffusion also depends on the level of carbon concentration in the carburizing compound. The ratio of the solute and soluble, the size of the powder and the surface of the sample influences the concentration of the compound and effect the dispersion of carbon during carburizing process. Lou et al. (2009) stated that paste compound was contributory as a self-protective diffusion paste. By using paste carburizing compound, the case depth was thicker compared to conventional pack carburizing. The application of paste has resulted in less distortion since it requires non-intensive temperature. The activation energy of paste compound was less than that of conventional thermal diffusion and the concentration-mixing ratio of paste was ranged from 30% to 70%. The existence of water (H₂O) in the paste mixture has astounding effect in the diffusion of carbon during the case hardening process. The production of hydrogen (H₂) from water-powder mix of the paste relatively speeds up the carburizing rate of the charcoal gas to steel. The production of N₂+CO+H₂ was faster than N₂+CO (Jumadin et al., 2015). However, there are limits to the maximum amount of H₂O that can be present since higher water content in the mixture may reduce the compound's ability to produce the carbonaceous gas from the charcoal because of reduction of carbon concentration (Chen, 1992).

Aswani (2001) and Panda (2014) observed carburizing improves the hardness of low carbon steel. The precipitation of carbon particles to iron, has formed a carbon-based Fe element that allows carbon to be bonded without breaking. Mechanically, the formation of cementite, Fe₃C is very hard and brittle. Another factor contributing to increasing hardness of steel is the formation of martensite achieved by controlling the cooling rate and process parameters. Jumadin et al. (2015) found carburised steel has its highest hardness level at 950°C-1000°C.

Elzanaty (2014) found that the tensile strength of low carbon steel is improved using pack carburizing to 441 MPa-1960 MPa. The higher carbon content has indirectly increased the tensile strength of carburised steel.

Abrasive wear occurs when two different materials come into contact. This study investigates the series of grooves in between carbon steels and stainless steel and observe the wear particles and weight loss. The high hardness value influences the wear rate of a coating subjected to a steady state of wear. Wear resistance on carburised steel has shown great potential due to the formation of cementite towards the surface of the steel, thereby making it harder. Elzanaty (2014) found that weight loss was higher for uncarburised low carbon steel because of its low carbon content. Panda et al. (2014) found that carburised steel at 950°C has better wear properties compared to untreated low carbon steel, reducing wear by up to 45%. Georgieva et al. (2004) thus indicate carburizing when used in sintered gear wheels subjected to contact stresses of 250 MPa no wear was detected.

In this research, the case depth production on low carbon steel using powder carburizing and paste carburizing is studied to better understand the potential of paste carburizing process.

METHOD

In this research, low carbon steel, ASTM 850 Grade 70 steels was used. Experiments were conducted for microhardness, tensile and wear using dog-bone type, pin-type and cube-type samples.

For the microhardness test, a load of 1 kg and 15-second indentation time was set at Hardness Vicker Tester Machine model Mitutoyo MCK-H1. Ten microhardness indentions were taken from the steel's surface towards the core, and the distance between each indentation was 0.05 mm. Average microhardness values were calculated. The procedure for finding the hardness value of carburised samples were based on standard ASTM E2834 – 11e1 and referred to the method used by Lou et al. (2009). In tensile test, sample of dog-bone type was prepared according to the standard ASTM A283-A283M-12. The sample was pulled until the sample failed with a speed rate of 2 mm/min. Three samples were tested for each carburizing parameter and average data recorded. The procedures for this test follow ASTM A283-A283M-12a. Pin-on-disc tribometer was used to define the friction coefficient and wear properties. A pin-type sample was prepared and a load of 2 kg was applied on a sample which was in contact with a rotating stainless steel counterpart. Initial speed of 200 rpm and test duration of 3600 seconds was set for this experiment. Standard ASTM G190-06 and ASTM G118-02 was used as a reference for the test.

As for carburizing heat treatment process, three different carburizing compounds were prepared; (1) powder compound; (2) paste 1:1 compound; and (3) paste 3:1 compound. These compounds were selected based on the carbon concentration for each sample. Paste 1:1 has 52.8 M and Paste 3:1 has 17.6 M. Powder compound was the combination of charcoal powder with sodium carbonate (Na_2CO_3) and barium chloride (BaCO_3). Paste compound refers to the mixture of powder compound with distilled water. The paste compounds were prepared according to the weight ratio of distilled water to powder. Samples were placed inside a steel box and covered with the carburizing compound, heated with temperature of 1000°C for 9 hours inside furnace. At temperature 1000°C, steel is in the austenite phase where solubility is at an optimum, and carbon diffused up to 2.03% C (Kalpajian & Schmid, 2010) deep inside the steel surface at 9 hours. The sample was cooled at room temperature. Table 1 shows the label for different carburizing compound used in this research.

Table 1
Carburizing parameter with different type of compound

Sample	Carburizing Compound
A	Untreated
B	Powder
C	Paste 1:1
D	Paste 3:1

RESULTS AND DISCUSSION

In order to choose the optimum compound, carburizing soaking time and temperature had to be fixed. Microhardness profile was plotted to determine the case depth of carburised low carbon steel. Figure 1 presents the microhardness profile based on the compound used. Sample A shows the microhardness values along 0.5 mm from the surface does not exceed 150 HV. The addition of carbon particles to iron has formed a carbon based Fe element, cementite, Fe_3C that is hard and brittle, resulting from more α -ferrite being transformed to cementite. (Alias et al., 2013).

Paste compound shows a stimulating trend where it has greater case depth and microhardness value compared to powder compound. Sample C and sample D indicate the formation of case depth of up to 0.5 mm while sample B only produces a depth of 0.25 mm. Paste compound has lower activation energy on carbon medium reaction to produce carbon monoxide compares to powder compound (Jumadin et al., 2015). From Figure 1, it can be seen the pattern of sample B and sample D indicates that both microhardness has increased at 0.1 mm and decreased at 0.15 mm, showing the collection of cementite and carbon atoms is at a maximum at 0.1 mm hardness value. However, carbon diffusion was limited and the transformation of cementite started to fade at 0.15 mm due to the low carbon concentration on both paste compound, thus causing the hardness value to decrease from this point onwards. Paste compound has better diffusion rate than powder compound because of the formability of medium structure, allowing the medium to release more CO and produce thicker carbon-rich layer up to 10-25% on carburised steels (Chen, 1992). The ratio of the solute and soluble, 1 parts of waters and 1 part of powder is the optimum composition for paste carburising process. The carbon atom diffusion was also determined by the level of carbon concentration of the carburizing compound (Kulka et al., 2011).

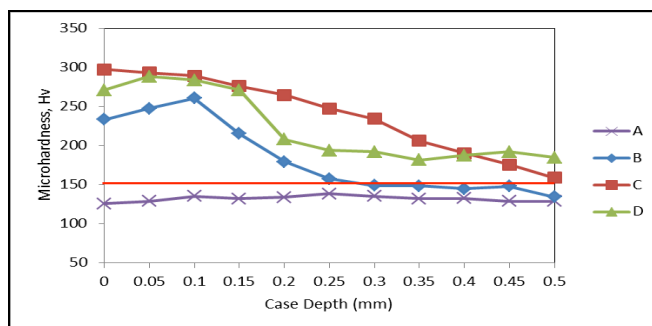


Figure 1. Microhardness and case depth profile

Tensile test was conducted in order to determine the maximum load, tensile stress and strain of the carburised samples. The stress-strain curve shown in Figure 2 shows that untreated sample (sample A) has the typical structural steel stress-strain for low carbon steel (Oyetunji & Adeosun, 2012), demonstrating that sample A was more ductile and has elastic deformation. The ultimate tensile strength sample A was 458 MPa. Sample A has the highest strain, which was 21.91 %.

Correlation of Case Depth with Mechanical Properties

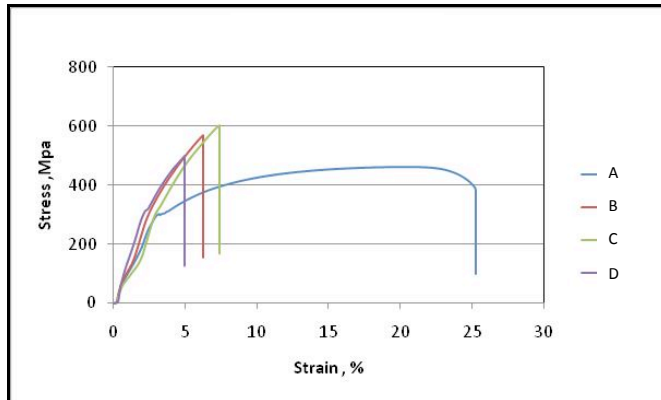


Figure 2. Stress-strain curve

Table 2 and Figure 3 shows the values and the correlation between elongation and tensile strength for carburised samples. Figure 3 shows that elongation was reduced linearly as the case depth increased. Carburising process increased the hardness of the surface material and its brittleness (Aramide et al., 2009). Nevertheless, powder carburising has higher tensile strength compared to untreated low carbon steel. Sample C has the highest tensile strength of 6.61% due to the practice of paste 1:1 compound. Carburising helped to increase the hardness and tensile strength of steel proportionally. The relationship between hardness and strength were also determined by the microstructure of the material. Thus an increase in the microstructure transformation from ferrite to cementite influences tensile strength as ferrite is more ductile compared to cementite which has a more brittle microstructure.

Table 2
Elongation and tensile strength of carburised low carbon steels

Sample	A	B	C	D
Elongation (mm)	21.91	6.28	7.22	5.98
Tensile Strength (MPa)	458.15	558.91	596.02	507.33

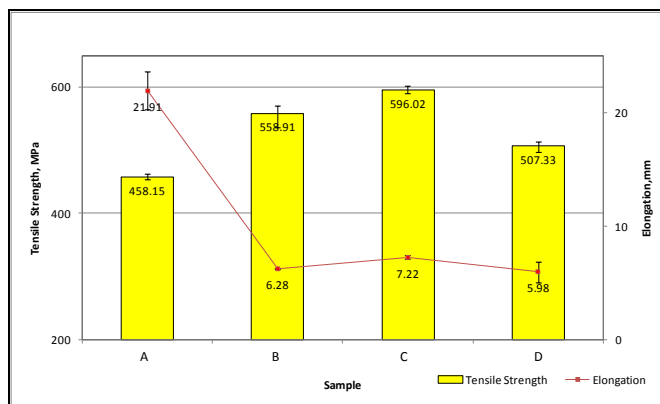


Figure 3. Correlation between tensile strength and elongation

Pin-on-disc test was conducted to investigate the wear properties and the results are tabulated in Table 3. Untreated sample shows the highest weight loss up to 1.7 g after the carburizing process since no case hardening to protect the sample during the friction process between pin and disk.

Table 3
Pin-on-disc weight loss, wear rate and wear resistance

Samples	Weight Loss (g)	Wear Rate (mm ³ /Nm)	Wear resistance (Nm/mm ³)
A	1.70	3.62E-06	2.77E+05
B	0.16	3.62E-07	2.77E+06
C	0.08	1.81E-07	5.53E+06
D	0.12	2.65E-07	3.77E+06

Figure 4 shows the wear rate and wear resistance for sample A, B, C and D. Sample A has highest wear rate value of $36.2 \times 10^{-7} \text{ mm}^3/\text{Nm}$. Carburizing process has reduced the wear rate of low carbon steel. As expected, paste carburizing has better wear resistance compared to powder carburizing because the deeper case depth prevents the surface material from detaching during contact with another surface. Sample C shows the highest wear resistance, $53.3 \times 10^7 \text{ Nm/mm}^3$. The relationship between the wear rate and wear resistance indicates that where the wear rate of the material is high, wear resistance is low.

Carburizing process based on paste 1:1 compound provides better wear resistance because of high carbon content, greater case depth and microhardness, influencing the properties of low carbon steels by constructing cementite (Georgieva et al., 2004).

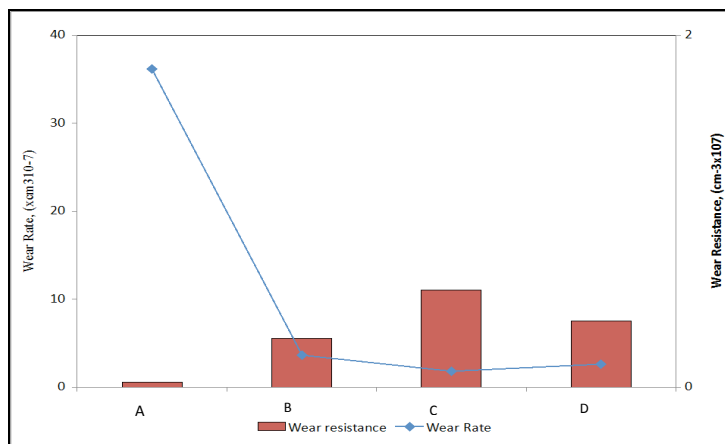


Figure 4. Wear rate and wear resistance of carburised samples

Figure 5 indicates the coefficient of friction versus time of each sample. From the pin-on-disc test result, sample A shows high coefficient of friction compared to the other samples. Higher weight loss indicated low resistance to friction. The figure also shows that the carburizing process increases the wear resistance of low carbon steel. From the test, it can be perceived that paste carburizing improves better wear resistance up to 49%. Wear resistance of carburised steel increases due to greater carbon dispersion on the surface thus providing better coverage from erosion.

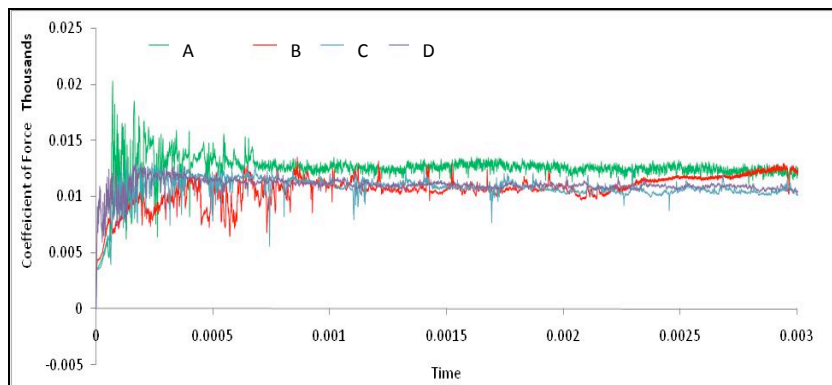


Figure 5. Coefficient of friction versus time for wear analysing wear behaviour

CONCLUSION

In this paper, the correlation between case depth with mechanical and tribological properties using paste carburizing method shows that paste 1:1 has the highest performance compound, generating a case depth of carburised steel up to 0.5 mm. By diffusing more carbon, greater case depth was produced and the microhardness values of steel increased up to 300 HV. The higher case depth from paste 1:1 compound led to increased tensile strength of up to 6.61%. Paste 1:1 carburizing has higher hardness value and wear resistance of up to 49%.

ACKNOWLEDGEMENTS

This research was funded by the Ministry of Education (MOE), Malaysia and Faculty of Mechanical Engineering, Universiti Teknologi MARA, Malaysia, via grant no. 600-RMI/RAGS 5/3 (160/2014) and part supported by grant no. 600-RMI/RAGS 5/3 (50/2013).

REFERENCES

- Alias, S. K., Abdullah, B., Jaffar, A., Latip, S. A., Kasolang, S., Izham, M. F., & Ghani, M. A. A. (2013). Mechanical properties of paste carburized ASTM A516 steel. *Procedia Engineering*, 68, 525-530.
- Alias, S. K., Abdullah, B., Abdullah, A. H., Latip, S. A., Wahab, N. A., & Ghani, M. A. A. (2013). The Effect of Carburizing Medium on Carbon Dispersion Layer of ASTM A516 Steel. In *Applied Mechanics and Materials* (Vol. 393, pp. 212-216). Trans Tech Publications.

Bulan Abdullah, Muhammad Hafizuddin Jumadin, Muhammad Hussain Ismail, Siti Khadijah Alias and Samsiah Ahmad

- Aramide, F. O., Ibitoye, S. A., Oladele, I. O. & Borode, J. O. (2009). Effects of Carburization Time and Temperature on Mechanical Properties of Carburized Mild Steel, Using Activated Carbon as Carburizer. *Material Research*, 12(4), 483-87.
- Aswani, K. G. (2001). *A Textbook of Material Science (For B.Sc., B.E. and AMIE Students)*. New Delhi: S. Chand & Company Ltd.
- Campos, I., Bautista, O., Ramírez, G., Islas, M., De La Parra, J., & Zúñiga, L. (2005). Effect of boron paste thickness on the growth kinetics of Fe₂B boride layers during the boriding process. *Applied Surface Science*, 243(1), 429-436.
- Chen, F. -S., & Wang, K. -L. (2000). Super-Carburization of Low Alloy Steel and Low Carbon Steel By. *Surface and Coatings Technology*, 132, 36-44.
- Elzanaty, H. (2014). Effect of Carburization on the Mechanical Properties of the Mild Steel. *Innovative Space of Scientific Research Journals*, 6(4), 987-994.
- Elzanaty, H. (2014). The Effect of Carburization on Hardness and Wear Properties of the Mild. *International Journal of Innovation and Applied Studies*, 6(4), 995-1001.
- Georgieva, J., Pieczonkab, T., Stoytcheva, M., & Teodosievc, D. (2004). Wear Resistance Improvement of Sintered Structural Parts by C7H7 Surface Carburizing. *Surface and Coatings Technology*, 180-181, 90-96.
- Jumadin, M. H., Abdullah, B., Ismail, M. H., Alias, S. K., & Ahmad, S. (2015). Investigation on temperature effect of carburized steel using powder and paste compound. *Jurnal Teknologi, UTM*, 76(3), 56-61.
- Kalpajian, S., & Schmid, S. (2010). *Manufacturing Engineering and Technology, Sixth Edition In SI Units*.
- Lou, D. C., Solberg, J. K., Akselsen, O. M., & Dahl, N. (2009). Microstructure and property investigation of paste boronized pure nickel and Nimonic 90 superalloy. *Materials Chemistry and Physics*, 115, 239-44.
- Lou, D. C., Solberg, J. K., & T. Børvik. (2009). Surface Strengthening Using A Self-Protective Diffusion Paste And Its Application For Ballistic Protection Of Steel Plates.
- Panda, R. R., Mohanty, D. A. M., & Mohanta, D. K. (2014). Mechanical and Wear Properties of Carburized Low Carbon Steel Samples. *International Journal of Multidisciplinary and Current Research*, 2(Jan/Feb 2014), 118-12.
- Straffelini, G., & Versari, L. (2008). Brittle Intergranular Fracture of a Thread: The Role of a Carburizing Treatment. *Engineering Failure Analysis*, 16, 1448-1453.



Effects of Two Cycle Heat Treatment on the Microstructure and Hardness of Ductile Iron

Mohd Faizul Idham¹, Bulan Abdullah^{2*} and Khalissah Muhammad Yusof²

¹Fakulti Kejuruteraan Mekanikal, Universiti Teknologi MARA (UiTM) Terengganu, 23200 Bukit Besi, Terengganu, Malaysia

²Fakulti Kejuruteraan Mekanikal, Universiti Teknologi MARA (UiTM), 40450 Shah Alam, Selangor, Malaysia

ABSTRACT

Austempering is one of the trendiest heat treatment processes to promote the strength and toughness of ductile iron. However, such practice is complex because it involves using aqueous solutions as quenchant (salt bath solution). This study was conducted to analyse the heat treatment of the combination processes of annealing-austenitising and evaluate the correlation between microstructure constituent and hardness of the ductile iron. Ductile iron samples in form of double cylinder was produced by conventional CO₂ sand casting method. The new heat treatment process was started by annealed at 873 K for 1.8 ks before being oil quenched. Subsequently, the samples were austenitised at austenitising temperatures 1123 K, 1173 K and 1223 K for 3.6 ks respectively before being immediately oil quenched to room temperature. A series of microstructure analysis tests, including optical microscopy and X-ray diffraction (XRD) was applied. Vickers microhardness tester was used to measure the hardness for each microstructure constituent. The results showed that ductile iron matrix transforms to martensitic during heat treatment of annealing-austenitising combination processes, which in turn contributes to increasing microhardness of martensite and the bulk hardness of ductile iron

Keywords: Ductile iron, hardness, heat treatment, microhardness

ARTICLE INFO

Article history:

Received: 28 September 2016

Accepted: 03 February 2017

E-mail addresses:

mohdfaizulidham@gmail.com (Mohd Faizul Idham),

bulanabdullah@gmail.com (Bulan Abdullah),

ykhalissah@yahoo.com.my (Khalissah Muhammad Yusof)

*Corresponding Author

INTRODUCTION

Ductile iron is an engineering material with good mechanical properties due to its microstructural control (Fatahalla, AbuEIEzz, & Semeida, 2009; Nabuo et al., 2003). There has been many attempts to quantitatively and qualitatively diversify the microstructure appearance either by adding alloying elements or heat treatment (Susil et al., 2006; Yusuf et

al., 2010; Salman et al., 2007; Kiani-Rashid & Edmonds, 2008). According to Yusuf et al. (2010), surface and hardness of ductile iron will be improved by combining conventional boronizing and tempering processes. Previous researcher, have added a new sub-cycle called preheat process into conventional austempering cycle (Hsu et al., 2009). Abdullah (2011) also used the similar manner where it was combined with conventional tempering process to improve the mechanical properties of niobium alloyed ductile iron (Abdullah., 2011). Konecná et al. (2013) combined oil quenching and austempering methods in a cycle as new heat treatment practice to heat treat ductile iron (Konecná et al., 2013). Sahin et al. (2010) and Ayman et al., (2009) introduced the new two-steps austempering process where it consists of two stages of austempering process instead of one stage in conventional practice (Sahin et al., 2010; Ayman et al., 2009). The latter is preferred because of the cost and complexity of adding the alloying elements (Chang et al., 2008).

The awareness that heat treatment can improve the physical and mechanical properties of ductile iron this study considers the combination of modified annealing, austenitising processes. It will examine the matrix compositions and transformations in order to evaluate the correlation between microstructure constituent and material hardness on each subsequent cycle in the heat treatment process.

METHOD

Experimental Procedure

The metals used in the present study were made in the laboratory induction furnace with high purity raw materials such as pig iron, carburizer and steel scraps. At 1450°C the molten metal was poured into a 60 kg capacity preheated ladle. The Special alloy recognized as Ferrosilicon Magnesium was used as nucleating agent to nucleate graphite in spherical form. 1.6 wt % of this alloy was placed in treated ladle. The sample was allowed to cool at room temperature before the moulds were broken to get the sample form the double cylinder with dimension of 300 mm long and 25± 2 mm by diameter. The chemical compositions of ductile iron samples were studied with a spectrometer test and results shown in Table 1. Samples were cut into small pieces and initially annealed at 773 K and 873 K in a tubular furnace before being oil quenched. All the samples were continuously austenitised at three different austenitising temperatures which were 1123 K, 1173 K and 1223 K for 3.6 kilo seconds respectively. The samples were then immediately oil quenched to room temperature.

Characterization of microstructure constituents nucleated in the as-cast and heat-treated condition were carried out by optical microscopy. 2% Nital etchant was applied before microstructure was observed and characterized under Olympus BX 41M optical microscope. IMAPs 4.0 edition software was used to capture the presented microstructure. The quantification of the volume of retained FCC austenite, BCC ferrite and BCT martensite were undertaken by X-ray diffraction (XRD) in an Ultima IV diffractometer using Cu- α radiation in a range

between of 20–120° (Sahin et al., 2010). Vickers Microhardness tester is used in this study to measure hardness of each microstructure constituent. Indentation was employed by applying 25 g load on each microstructure constituent.

Table 1
Chemical composition of ductile iron sample

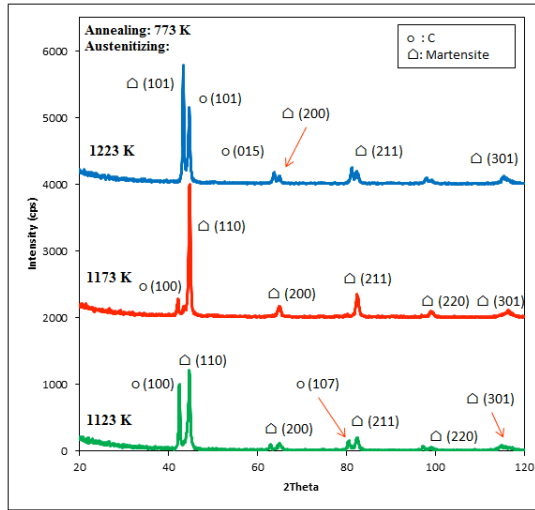
C	Si	Mn	P	S	Cu	Mg	Fe
3.49	2.62	0.55	0.069	0.0074	0.0072	0.014	Balance

RESULTS AND DISCUSSION

XRD

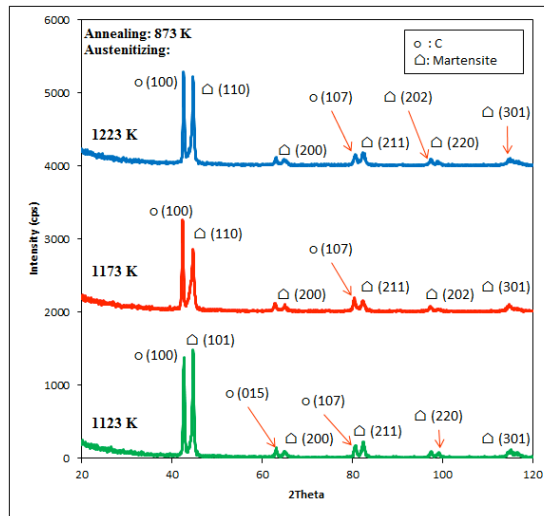
The planes indicated in the XRD pattern of as-austenitised samples annealed at 773 K, as shown in Figure 1. The peaks of martensite are also identified at 2θ angle 44° with the planes (101) and (110) in the XRD patterns of as-austenitised samples annealed at 873 K, as indicated in Figure 2. The presence of both planes also suggests that BCT martensite is the main constituent for the as-austenitised samples annealed at 773 K and 873 K. Annealing process does not influence the phase in the as-austenitised samples even the samples were annealed to the elevated temperature which below than critical eutectoid temperature. Despite annealing process was initially changed in quantitative the phase constituents such as pearlite and ferrite in the first stage of heat treatment, but it shows no effect yet when the sample was further austenitised to critical eutectoid temperature. Aside of the martensite, a graphite peak is likewise presented in the planes (100) and (101) between 2θ angles of 42° and 44° , in all cluster of samples which was austenitised at different temperatures. Graphite peaks are present in the XRD patterns for all samples because carbon is one of the main alloying elements in producing ductile iron (Chang et al., 2008).

Based on the XRD patterns shown in all clusters of as-austenitised sample, martensite transforms at austenitising temperature of 1123 K (Chang et al., 2008). Austenite generally nucleates when the temperature rises beyond the critical eutectoid temperature, so too were samples austenitised at 1173 K and 1223 K (Sahin et al., 2010). Rao and Putatunda (2003) stated that volume fraction and carbon content of austenite increases when austenitising temperature rises beyond the critical eutectoid temperature (Rao & Putatunda, 2003) as carbon atoms trapped in the crystal structure when austenite are diffused during heating.



Graphite, C – (ICDD: 261079); Martensite, α' -Fe – (ICDD: 441289)

Figure 1. XRD pattern of as-austenitised ductile iron (annealed: 773 K) at different austenitising temperatures



Graphite, C – (ICDD: 261079); Martensite, α' -Fe – (ICDD: 441289)

Figure 2. XRD pattern of as-austenitised ductile iron (annealed: 873 K) at different austenitising temperatures

Microstructure

The annealing process did not influence the appearance of as-austenitised microstructure as shown in Figure 3 and Figure 4 where the samples were initially annealed at 773 K and 873 K respectively before austenitised at 1123 K, 1173 K and 1223 K. Figure 3(a) and Figure 4(a) depict the microstructures of as-annealed ductile iron at temperatures of 773 K and 873 K respectively. The microstructures of as-annealed sample consist of typical microstructure constituents which contains graphite nodules, the sea of ferrite (white region) and the island of pearlite (dark region). The microstructures are almost similar qualitatively with as-cast microstructure where graphite nodules are surrounded by ferrite and pearlite.

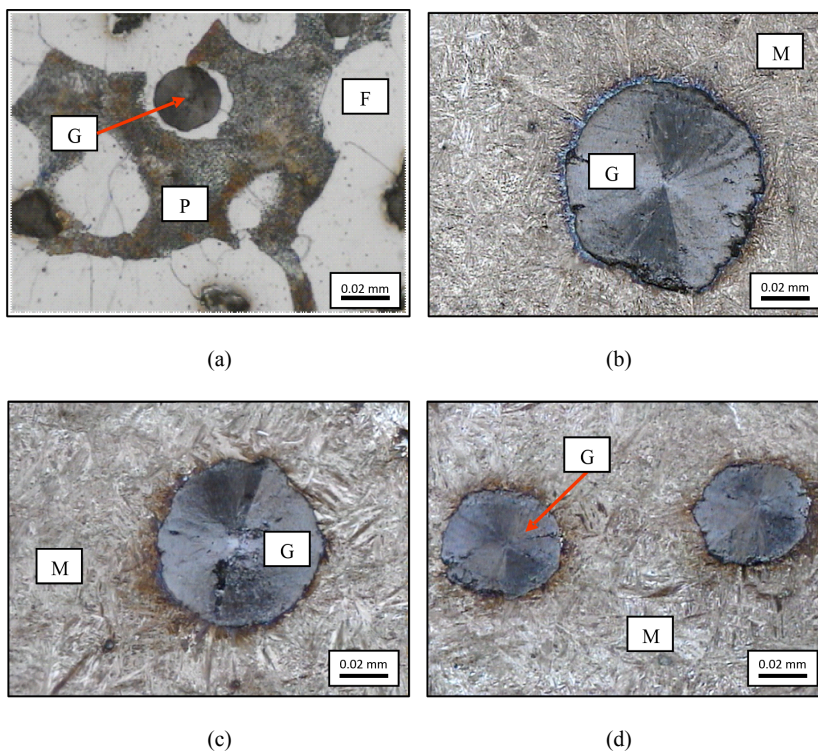


Figure 3. Microstructure of As-Austenitised Ductile Iron (Annealed: 773 K) at Different Temperatures: (a) As-Annealed; (b) 1123 K; (c) 1173 K; and (d) 1223 K. Note: G is Graphite; F is Ferrite; P is Pearlite; M is Martensite

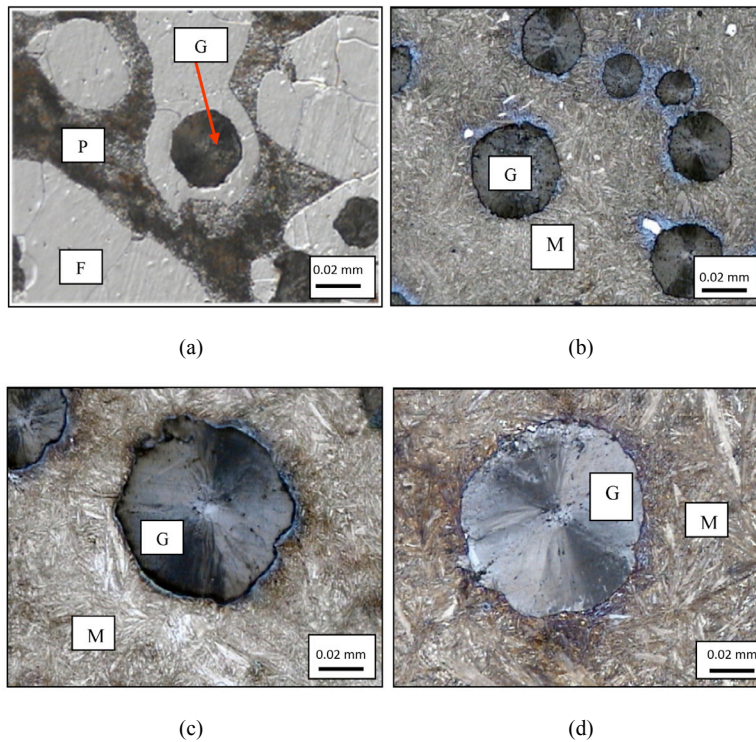


Figure 4. Microstructure of As-Austenitised Ductile Iron (Annealed: 873 K) at Different Temperatures: (a) As-Annealed; (b) 1123 K; (c) 1173 K; and (d) 1223 K. Note: G is Graphite; F is Ferrite; P is Pearlite; M is Martensite

Martensite is remarkably transformed because austenite nucleated during the austenitising process was rapidly cooled to room temperature via oil quenching. Austenite with low residual carbon content trapped in the crystal structure did not have time to stabilize and diffuse out of the crystal structure (Kiani-Rashid & Edmonds, 2009), leading to its transformation into martensite at room temperature. The lath-shaped crystal grains of martensite became coarser when austenitising temperature increased till 1223 K (Rao & Putatunda, 2003) resulting from the volume fraction and carbon content of austenite which increased when austenitising temperature rises beyond the critical eutectoid temperature (Rao & Putatunda, 2003).

Hardness

Figure 5 shows the average values of Vickers microhardness of martensite and graphite structures of as-austenitised ductile iron annealed at 773 K and 873 K. Hardness of martensite increased gradually when austenitising temperature increased till 1223 K. on the other hand, the average graphite hardness values remained constant at range of 38 HV to 39 HV. The microhardness trends of martensite and graphite show no changes though annealing

temperature increases up to 873 K. Nevertheless, the average martensite hardness values of the samples slightly increased as a result of greater carbon diffusion in the matrix when annealing temperature is raised.

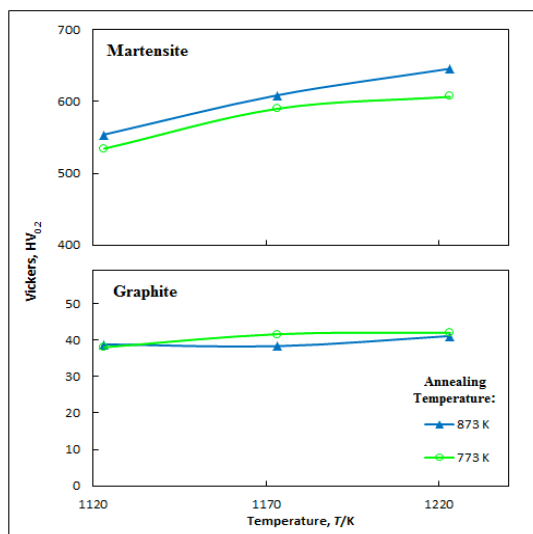


Figure 5. Vickers Microhardness (Load: 0.2 N) of Martensite and Graphite at different austenitising temperatures (Annealed: 773 K and 873K)

Graphite is less hard compared to Martensite. Graphite nodules presented in the matrix do not contribute to the precipitation hardening though all clusters of sample have been austenitised beyond critical eutectoid temperature. Furthermore, the increase in Martensite hardness as function of austenitising temperature is caused by carbon precipitation and enrichment of the matrix constituents (Kiani-Rashid & Edmonds, 2009; Rao & Putatunda, 2003).

CONCLUSION

The new heat treatment process, combination of annealing and austenitising process, found that ductile iron matrix transforms to martensitic instead of ferritic-pearlitic matrix shown. Austenitising temperature does slightly influence the martensite morphology, and increasing it results in the increasing of microhardness of martensite and the bulk hardness of ductile iron.

In conclusion, microstructure constituents have good correlation with hardness of ductile iron. The type of microstructure and hardness of each constituent require consideration to effectively improve the hardness of ductile iron. Proven that, this hardness could be estimated using mixture law of hardness for each microstructure constituent.

ACKNOWLEDGEMENTS

The authors would like to express their gratitude to RMI UiTM Shah Alam for RAGS grant 600-RMI/RAGS 5/3 (206/2014) and Faculty of Mechanical Engineering UiTM Shah Alam for their contribution to this research.

REFERENCES

- Ayman, H. E., Megahed., Sadek., & K. M. Abouelela. (2009). Fracture toughness characterization of austempered ductile iron produced using both conventional and two-step austempering processes. *Materials and Design*, 30, 1866–1877.
- Bulan, A. (2011). An Improvement of Mechanical Properties of Ductile Iron and Niobium Alloyed Ductile Iron through New Heat Treatment Cycles. *Universiti Teknologi Mara, Shah Alam, PhD Thesis*.
- Chang, L. C., Hsui, I. C., Chen, L. H., & Lui, S. T. (2008). Influence of austenization temperature on the erosion behavior of austempered ductile irons. *Journal of University of Science and Technology Beijing, Mineral, Metallurgy, Material*, 15(1), 29-33.
- Fatahalla, N., AbuElEzz, A., & Semeida, M. (2009). C, Si and Ni as alloying elements to vary carbon equivalent of austenitic ductile cast iron: microstructure and mechanical properties. *Materials Science and Engineering: A*, 504(1), 81-89.
- Hsu, C. H., Chen, K. L., Lee, C. Y., & Lu, K. C. (2009). Effects of low-temperature duplex coatings on corrosion behavior of austempered ductile iron. *Surface and Coatings Technology*, 204(6), 997-1001.
- Kiani-Rashid, A. R., & Edmonds, D. V. (2008). Phase transformation study of aluminium-containing ductile cast irons by dilatometry. *Materials Science and Engineering: A*, 481, 752-756.
- Konečná, R., Nicoletto, G., Bubenko, L., & Fintová, S. (2013). A comparative study of the fatigue behavior of two heat-treated nodular cast irons. *Engineering Fracture Mechanics*, 108, 251-262.
- Nabuo N., Toru Y., Junaidi S., Toshihiro T., & Setsuo T. (2003). Effect of Cu Addition on Formation of Reversed Austenite and Hardness in 9% Ni steels. *Tetsu-to-hagané*, 89(10).
- Prasad, R., & Susil, K. (2003). Investigations on the fracture toughness of austempered ductile irons austenitized at different temperatures. *Materials Science and Engineering*, 349, 136-149.
- Salman, S., Findik, F., & Topuz, P. (2007). Effects of various austempering temperatures on fatigue properties in ductile iron. *Materials and Design*, 28(7), 2210-2214.
- Susil, K., Putatunda., Sharath, K., Ronald, T., & Gavin, L. (2006). Development of austenite free ADI (austempered ductile cast iron). *Materials Science and Engineering*, 435-436, 112-122.
- Yusuf, K., Sukru, T., Sinan, U., & Yilmaz, Y. (2010). Investigation of mechanical properties of boron-tempered ductile iron. *Materials and Design*, 31, 1799-1803.
- Yusuf, S., Volkan, K., Melika, O., & Mehmet, E. (2010). Comparison of abrasive wear behavior of ductile iron with different dual matrix structures. *Wear*, 268, 153–165.



Ferroelectric Stability of Annealed PVDF-TrFE Thin Film Incorporated with MgO Nanofillers

Mohamad Hafiz Mohd Wahid¹, Rozana Mohd Dahan^{1*},
Adillah Nurashikin Arshad¹, Habibah Zulkefle², Siti Zaleha Sa'ad¹,
Mohamad Rusop Mahmood², W. C. Gan³ and Wan Haliza Abd. Majid³

¹Faculty of Applied Sciences, Universiti Teknologi MARA (UiTM), 40450 Shah Alam, Selangor, Malaysia

²NANO-ElecTronic Center (NET), Faculty of Electrical Engineering, Universiti Teknologi MARA (UiTM), 40450 Shah Alam, Selangor, Malaysia

³Low Dimension Material Research, Department Of Physics, Faculty of Science, University Malaya (UM), 50605 Kuala Lumpur, Malaysia

ABSTRACT

Spin coated polyvinylidene fluoride-trifluoroethylene (PVDF-TrFE 70/30mol%) copolymer thin film were initially produced and annealed at varying temperatures (100°C to 160°C). The morphology, dielectric and ferroelectric analysis showed that PVDF-TrFE film annealed at 120°C produced the highest remnant polarization, P_r of 92 mC/m², with orderly and grain-like shaped crystallites. The filled PVDF-TrFE, loaded with various volume percentages (1 – 7%) of Magnesium Oxide (MgO) nanofillers and then, annealed at 120°C, produced homogenous filler distribution with low agglomerates, especially for 3% PVDF-TrFE filled films. Moreover, the annealed PVDF-TrFE/MgO(3%) generated the highest value of P_r in comparison to the other filled nanocomposite thin films. Most importantly, the saturation of hysteresis loop, P_s for annealed PVDF-TrFE/MgO(3%) film was relatively improved by 20% as compared to the unfilled annealed thin film. This study established that, 3% MgO loaded in PVDF-TrFE thin film and annealed at 120 °C demonstrated a stable ferroelectric thin film, closed to an ideal ferroelectric film, in which the ratio P_r/P_s for the film established a value approaching unity (value of 1).

Keywords: Annealing, dielectric, ferroelectric, MgO, PVDF-TrFE, spin coating

ARTICLE INFO

Article history:

Received: 28 September 2016

Accepted: 03 February 2017

E-mail addresses:

hafizwahid87@gmail.com (Mohamad Hafiz Mohd Wahid),

rozanadahan@gmail.com (Rozana Mohd Dahan),

adillaharshad@gmail.com (Adillah Nurashikin Arshad),

habibahzulkefle@yahoo.com (Habibah Zulkefle),

siti_leha@hotmail.com (Siti Zaleha Sa'ad),

nanouitm@gmail.com (Mohamad Rusop Mahmood),

wegan@gmail.com (W. C. Gan),

q3haliza@gmail.com (Wan Haliza Abd Majid)

*Corresponding Author

INTRODUCTION

The development of polymeric film with high dielectric properties has sparked interest in the application of small electronic devices such as organic capacitors and organic field effect transistors. The utilisation of these

polymeric materials is the simplest route in fabricating thin film, owing to their flexibility, high strength and ease of processing. Polyvinylidene fluoride (PVDF) copolymerised with trifluoroethylene (TrFE) is a favourable polymer for organic devices due to its high permittivity and ferroelectricity (Bae et al., 2010; Furukawa et al., 2010, Müller et al., 2007; Ismail et al., 2012). The ferroelectricity in PVDF-TrFE originates from the H⁺ (hydrogen) atoms and F- (fluorine) atoms. The arrangement of these atoms in the PVDF-TrFE chains induced the parallel packing of the all-trans conformation of PVDF-TrFE chains resulting in large spontaneous polarisation (Furukawa, 1989).

In volatile memory devices, data may not be retained when the system is turned off in contrast with non-volatile memory devices, which have the ability to store charges even after the electric field is removed (Ling et al., 2008). The latter is true for PVDF-TrFE. The performance of PVDF-TrFE as memory device relies mainly on the remnant polarisation (P_r), which is largely affected by the crystallinity of β phase crystals and the degree of dipole orientation in PVDF-TrFE (Furukawa et al., 2006; Ling et al., 2008). In order to achieve high P_r , additional treatments such as annealing, mechanical stretching and poling are widely employed. However, for thin film, annealing process is the most appropriate and practical as it poses minimal damage to the thin film compared with the mechanical stretching or poling at high electric field, which is more suitable for bulk film. Moreover, the distinctive crystal phase transitions during annealing treatment led to an interest in exploring the ferroelectric behaviour of polymeric material (Lee et al., 2010; Prabu et al., 2006; Wahid et al., 2013). In 1980, Furukawa et al. discovered the Curie transition in PVDF-TrFE, which indicated the ability of polymeric material to polarise spontaneously (Furukawa et al., 1980). Beyond Curie temperature, the ferroelectric constants of PVDF-TrFE dropped to zero due to the thermal heating, which demote dipole rotational motion and hence, destroy all-trans chain configuration. In addition, this phase transition of PVDF-TrFE was very much affected by the VDF content. Furukawa discovered that 50% to 80% of VDF content in PVDF-TrFE produced high dielectric and ferroelectric properties (Furukawa, 1997). Previous study reported that, annealing at temperature slightly above the Curie temperature, (T_c), but below the melting temperature (T_m) resulted in an improved crystallinity of the PVDF-TrFE film. This condition is favourable due to aligning and packing of C-F dipoles of PVDF-TrFE. This will lead to an increase in the amount of aligned dipoles, hence, increasing the polarisation and dielectric properties of PVDF-TrFE film (Nguyen et al., 2008).

In this research, a batch of spin coated PVDF-TrFE thin films of approximately 250 nm thick were annealed at varying temperatures, in accordance with the thermal transition temperatures attained by differential scanning calorimetry (DSC) analysis. The optimised annealing temperature was predetermined by observing the surface morphology, and subsequent attainment of the dielectric and ferroelectric properties of PVDF-TrFE thin film. The optimised PVDF-TrFE was loaded with MgO nanofillers at various volume percentages. Similar characterisations were noted on the PVDF-TrFE/MgO nanocomposite thin films.

METHOD

PVDF-TrFE Thin Film Preparation

Prior to producing the PVDF-TrFE thin films, aluminum (Al) coated glass substrates were prepared, which represented the bottom electrode for electrical measurements. These glass substrates were cut and cleaned with acetone, methanol and de-ionised water for 10 minutes in an ultrasonic bath, before they were dried with inert nitrogen gas flow. A layer of 30 nm in thick was evaporated on the glass substrates, using Edward AUTO306 high vacuum evaporation system. The PVDF-TrFE (70:30mol %, PiezoTech, France) pallets were dissolved in the solvent (methyl ethyl ketone) with the concentration of 30g/L and stirred for 24 hours. The solution was then spin coated at 1500 rpm for 90 seconds. Finally, PVDF-TrFE film was spin coated as thin film on the Al coated glass substrate with an average film thickness of 250 nm to 300 nm.

Annealing Process

Prior to annealing, the thermogravimetric analysis was carried out on PVDF-TrFE pallets in order to determine the Curie's transition temperature (T_C) and the melting temperature (T_m). The two endothermic peaks (during heating) were 113°C (T_C) and 154°C (T_m) (Figure 1). These temperatures were set as benchmarks for annealing the PVDF-TrFE thin films.

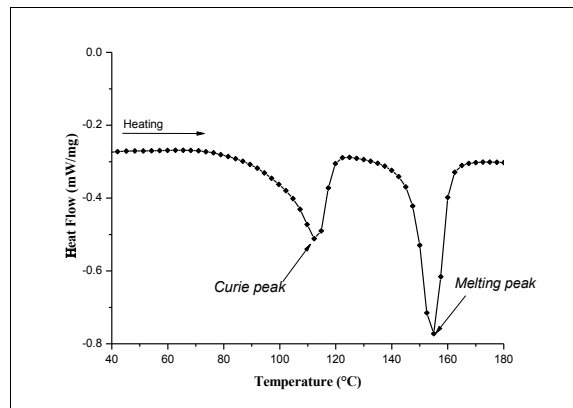


Figure 1. Thermogravimetric spectrum of PVDF-TrFE (70:30mol%)

The annealing was conducted for 2 hours in an oven at temperatures shown in Table 1. All annealed films were allowed to cool at ambient temperature before they were removed from the oven. The unannealed thin film (UN) was utilised as a control film sample in this study.

Table 1
Annealing temperatures of PVDF-TrFE thin films

Acronym	Annealing Temperature (°C)
AN100	100
AN120	120
AN140	140
AN160	160

PVDF-TrFE Loaded with MgO Nanofillers (PVDF-TrFE/MgO Thin Film)

Magnesium oxides (MgO) of particle sizes ≤ 50 nm were supplied by Sigma-Aldrich. Predetermined MgO volume percentages (1, 3, 5 and 7 vol %) were incorporated in PVDF-TrFE solution individually at concentration of 30 g/L and stirred at room temperature for 24 hours. The PVDF-TrFE/MgO solution was agitated and sonicated in an ultrasonic processor (SONICS Vibracell VCX500, 400 watt) at 60 % amplitude for 12 minutes. A tapered ultrasonic horn was utilised with an end tip of 3 mm in diameter. The sonicated solution was spin coated on the Al-coated glass at 1500 rpm for 90 seconds to produce 250 nm thick nanocomposite films. These nanocomposite thin films were then annealed in the oven at 120°C for 2 hours.

Characterisation

The morphological study of the thin film was carried out using field emission scanning electron microscope (FESEM, JEOL JSM-7800F). All thin films were coated with 10 nm of platinum prior to FESEM imaging in order to reduce electro charging, as well as increasing the image quality. The top electrical contact was produced by evaporating 3 mm² of Al above the thin film (Figure 2). Dielectric properties were measured at frequencies of 100 Hz to 10 MHz using high frequency range impedance analyser (Agilent, Impedance Analyzer 4294A), while the ferroelectric measurements were done using the Precision LC system (Radiant Tech. Inc.) at 100 Hz frequency, at an operating voltage of 100 V.

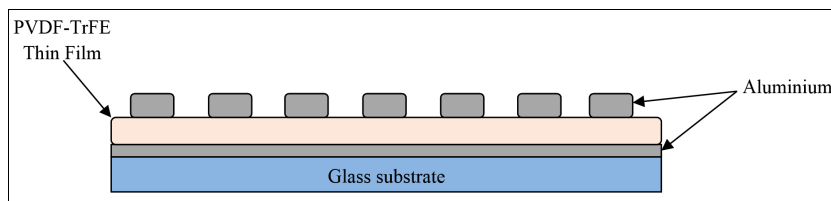


Figure 2. Schematic diagram of PVDF-TrFE thin film with aluminum top and bottom electrodes

RESULTS AND DISCUSSION

Optimisation of the annealing temperature for PVDF-TrFE thin films

First, the morphology of unannealed and annealed PVDF-TrFE thin films was observed at 100k magnification using FESEM (Figure 3). Significant growth of defined crystallite structures was observed in PVDF-TrFE films annealed at 100°C (AN100) (Figure 3(b)). As the annealing temperature was increased to 120°C, the crystallite sizes in the AN120 films were extended in length and width (Figure 3(c)). Previous studies suggested that elongated structure of PVDF-TrFE crystallites signified typical characteristics of ferroelectric crystallites (Lee et al., 2007; Li et al., 2008). In this study, the elongated grain-like crystallites were found to increase in size as the annealing temperature was further increased to 140°C for AN140 film (Figure 3(d)). On the contrary, the PVDF-TrFE thin film annealed at 160°C, temperature above T_m , the crystallites lost its grain-like structure. Instead, most of these crystallites in AN160 film

were observed to merge with the neighbouring crystallites forming fibrous crystallites (Figure 3(e)). This may be due to the recrystallisation process, in which these films were cooled directly from melt. During melting, the increase in thermal energy encouraged mobility of the polymer molecules. This caused high thermal heating, which disorientate most of the PVDF-TrFE crystallites. Upon cooling, these crystallites were unable to re-orientate to form the grain-like crystallites structures, which were formed through annealing, at temperatures below melting temperature. The fibrous-like shaped structures formed in all of the recrystallised films suggested a changed in the crystal phases during recrystallization. The splitting of the fibrous surfaces was quite apparent, which may be commonly caused by differential cooling of the film surfaces. The presence of these defects, typically reduced the performance of the AN160 films (Gan & Majid, 2014).

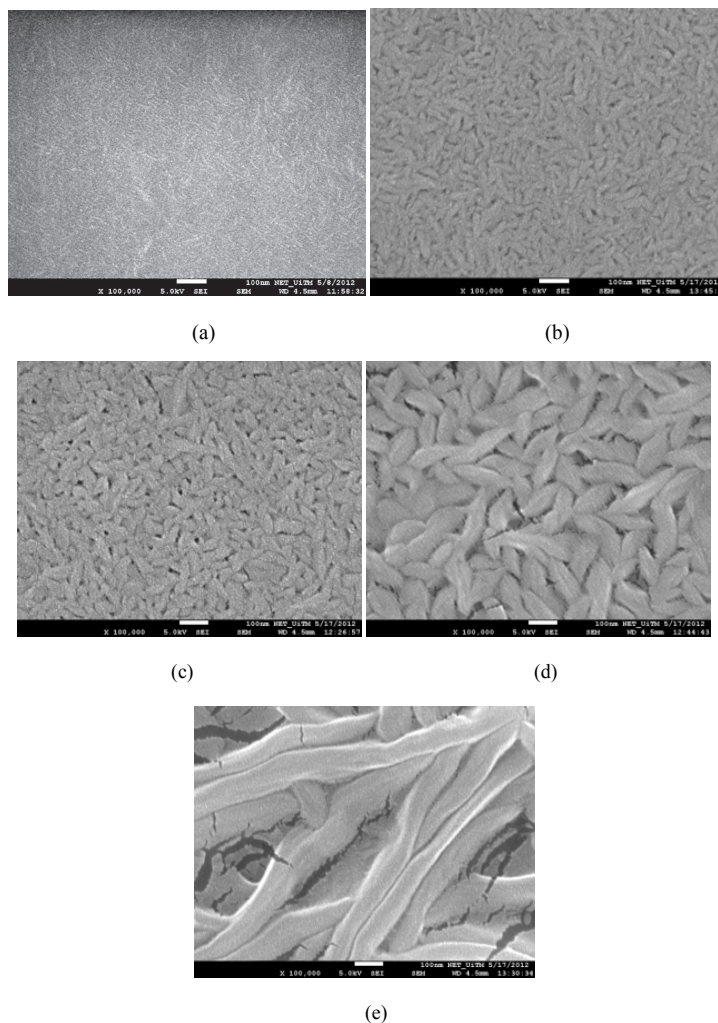


Figure 3. FESEM micrograph at 100K magnification for PVDF-TrFE thin film of (a) UN; (b) AN100; (c) AN120; (d) AN140; and (e) AN160

Figure 4 shows plots of the (a) dielectric constant as a function of frequency; and (b) the ferroelectric hysteresis loops of UN and annealed PVDF-TrFE thin films. The dielectric constant for all annealed PVDF-TrFE thin film increased upon annealing temperatures, at frequency range of between 10^3 to 10^5 Hz. On the contrary, the unannealed thin films showed the lowest dielectric constant of 9.7 at 10^3 Hz frequency. Annealing at 100°C , the dielectric constant increased to 12 measured at the same frequency. However, a insignificant reduction in the value of the dielectric constant to 11.6 for AN120 was observed when the film was annealed at 120°C . When the annealing temperatures were further increased to 140°C and 160°C , the dielectric constant value further increased to 12.7 and 13.8 for AN140 and AN160 films respectively. The increase in dielectric constant with annealing temperatures was consistent with FESEM micrographs, in which the growth and packing of the crystallite structures were significantly improved (Figure 3). This is consistent with previous studies, which reported crystallite growth contributed to an improvement in the electrical properties of PVDF-TrFE (Lee et al., 2010; Li et al., 2008).

However, in ferroelectric analysis, thin film annealed at 120°C (AN120) showed relatively high P_r of 93 mC/m^2 . Increasing the annealing temperature to 140°C , caused a reduction in the P_r value to 78 mC/m^2 for AN140 thin film. The P_r continued to decrease as the temperature in the AN160 film was annealed to 160°C . The drop in P_r was consistent with the presence of splits (Figure 3(e)). The splitting may have caused diffusion of Al from the electrodes in the film surface, and hence led to the formation of conductive tracks in the film during electrical measurements (Ismail et al., 2012).

The tightly packed elongated crystallite exhibited by AN120 thin film, coupled with its high P_r value, established that the film demonstrated superior ferroelectric properties (Lee et al, 2010). The AN120 thin film was the preferred film to be utilised for inclusion of MgO. The morphology and ferroelectricity stability of PVDF-TrFE film incorporated with various percentage loading of MgO nanofillers were investigated.

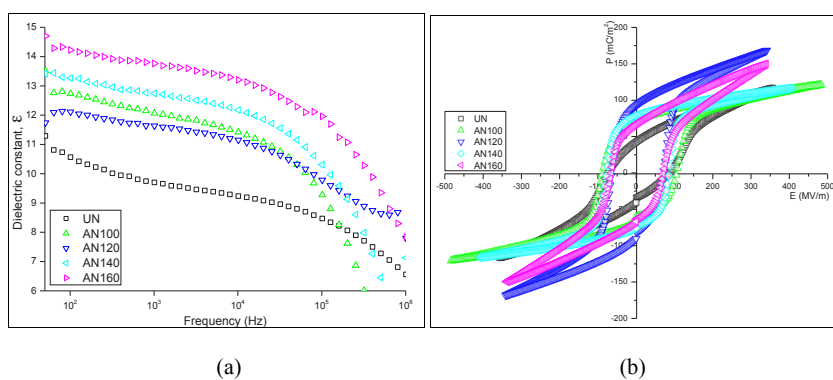


Figure 4. (a) Dielectric constant, ϵ' ; and (b) ferroelectric hysteresis loops of unannealed and annealed PVDF-TrFE thin films

PVDF-TrFE Incorporated with MgO nanofiller

PVDF-TrFE nanocomposite films (with various MgO nanofiller loadings) produced by spin coating method were then annealed at the optimised temperature of 120°C for 2 hours, and allowed to cool at ambient temperature before they were removed from the oven. The FESEM surface morphology of film for 1%, 3%, 5% and 7% of MgO nanofiller loadings at 30K magnification are shown in Figure 5. These images were observed to be consistent with the MgO imaged by previous authors (Habibah et al., 2013). Due to the low percentage of MgO nanofiller loading, 1%, minimal dispersion of the MgO nanofillers was observed, along with the PVDF-TrFE crystals observed as fine fibrils in the AN120/1%MgO film (Figure 5(a)). At 3% MgO loading, the distribution of the nanofillers in the AN120/3%MgO was apparent throughout the nanocomposite film, with insignificant agglomerations (Figure 5(b)). Specifically, the PVDF-TrFE crystals observed in the AN120/3%MgO were defined and elongated in shaped. This is due to the growth of the crystallites slightly hindered by the presence of nanofillers. These MgO nanofillers acted as nucleation sites that enhanced the formation of elongated packed PVDF-TrFE crystallites. The film formed was smooth, with relatively low porosity in the thin film. These observations are consistent with those of previous reports by other researchers, which suggested smooth non porosity film surfaces correlated to a high dielectric properties in the film (Furukawa et al., 2006; Thomas et al., 2010). However, with increase in nanofillers loading to 5%, agglomerations of MgO were significant on the AN120/5%MgO

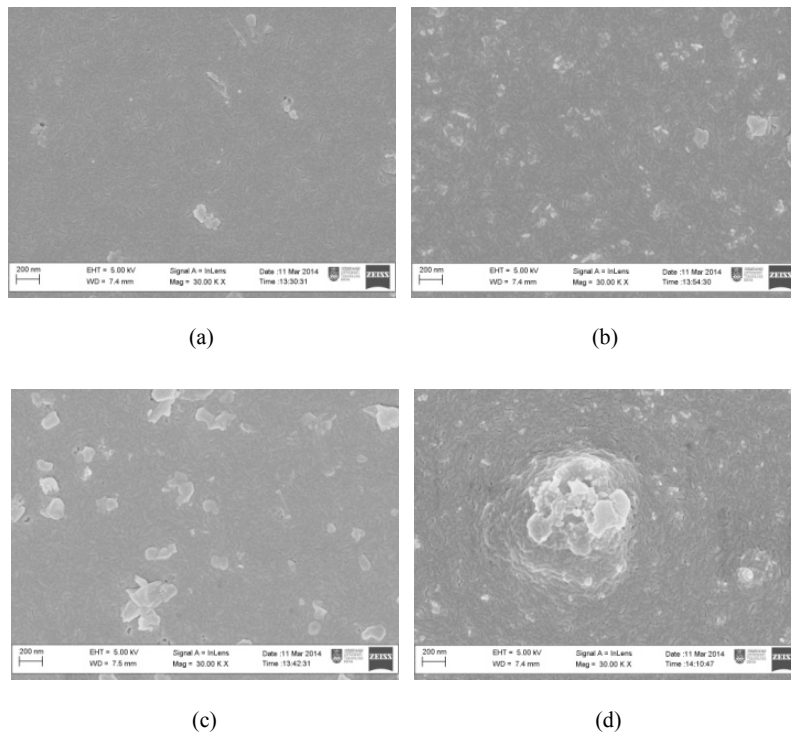


Figure 5. FE-SEM micrograph at 30K magnification for sample of (a) 1% (b) 3%, (c) 5%, and (d) 7% MgO nanofiller incorporated into AN120 thin film

film surfaces (Figure 5(c)), and presence of black areas may indicate porosity in the film surface. With further addition of MgO nanofillers to 7%, these agglomerations were observed to develop into massive clusters of MgO, followed by ripples-like structures of PVDF-TrFE in the AN120/7%MgO film (Figure 5(d)). However, it is interesting to note that the presence of these clusters had deterred the formation of PVDF-TrFE crystallites in the film, which were not apparent in the AN120/7%MgO film.

Figure 6 presents the (a) ferroelectric hysteresis loop and dielectric constant, ϵ' ; (b) for AN120 thin films incorporated with 1%, 3%, 5% and 7% of MgO nanofiller. The ferroelectric hysteresis loops were observed in all filled nanocomposite thin films. This confirmed that though MgO nanofiller were present in the PVDF-TrFE film, the AN120/1%MgO, AN120/3%MgO, AN120/5%MgO and AN120/7%MgO nanocomposite thin films sustained their ferroelectric properties. For AN120/1%MgO, the P_r obtained was 79 mC/m², which was lower than the unfilled AN120 ($P_r = 92$ mC/m²). Nevertheless, the highest P_r value (88 mC/m²) was obtained from AN120/3%MgO film filled with 3% MgO. As the nanofiller loadings increased between 5% and 7%, significant reduction in P_r values was observed, which were 69 mC/m² and 57 mC/m² for AN120/5%MgO and AN120/7%MgO films respectively. This was a drop of 22 % and 35% for AN120/5%MgO and AN120/7%MgO films, respectively. This is consistent with the observation by FESEM (Figure 5), in which more than 3% MgO loaded film, agglomerates in the film were obvious. These agglomerations were more significant for 7% MgO loaded thin films. The inconsistency of surface morphology produced from the agglomerations led to the reduction of contact area between electrodes. This may have resulted in restrained ferroelectric performance for the AN120/7%MgO thin film, consistent with previous study (Thomas et al., 2010). This phenomenon was consistent with the trend observed for dielectric measurements shown in Figure 4(b). The 3% MgO loaded film showed the highest dielectric constant of 13.6 at the frequency of 10³ Hz. An abrupt reduction of dielectric constant was observed as the MgO loadings were increased to 5% and 7%. From the dielectric and ferroelectric results, 3% loading of the MgO nanocomposite thin films (annealed at 120°C) was the optimised percentage nanofillers loading required for a PVDF-TrFE dielectric film suitable to be utilised for storage organic memory device.

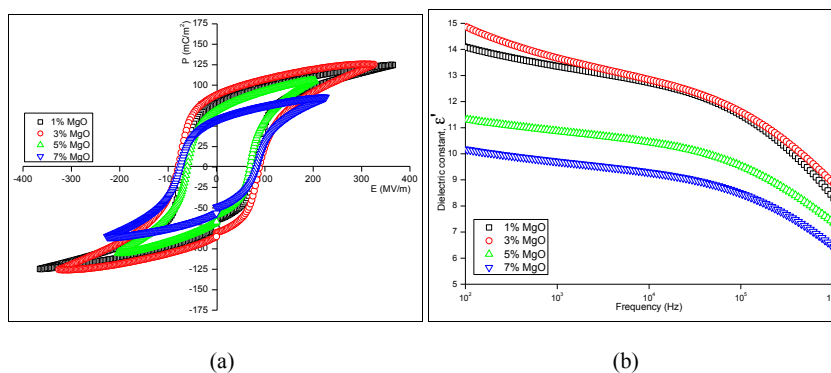


Figure 6. (a) Ferroelectric hysteresis loops; and (b) dielectric constant, ϵ' of AN120/1%MgO, AN120/3%MgO, AN120/5% and AN120/7%MgO thin films

Figure 7(a) represents the ferroelectric hysteresis loops for unannealed (UN), PVDF-TrFE annealed at 120°C and annealed PVDF-TrFE thin film incorporated with 3% MgO nanofillers. The loops showed a significant improvement in the remnant polarisation (P_r) and saturation polarisation (P_s) upon inclusion of MgO nanofillers. However, the coercive fields (E_c) were insignificant in these films. Interestingly enough, the shaped of the hysteresis loops were rectangular-like for both annealed PVDF-TrFE (AN120) and annealed filled PVDF-TrFE (AN120/3%MgO) films. This was associated with an increased in polarisation for both annealed films (unfilled and filled), which improved the crystallinity of these films, hence, producing stability during ferroelectric switching (Furukawa, 1989). This finding was further established by observing the ratio of P_r/P_s as shown by the plot in Figure 7(b). The unannealed (UN) thin film obtained the lowest P_r/P_s ratio of 0.36. Annealed thin film without MgO (AN120), produced well saturated hysteresis loop with improved P_r/P_s ratio of 0.55, which is 53% higher in value compared with unannealed thin film (UN). Meanwhile, the P_r/P_s ratio continued to increase to 0.7 for AN120/3%MgO, which is 94% higher than annealed thin film without MgO nanofillers. This suggests that, annealed MgO nanofiller thin film produced enhanced saturation polarisation, which was evident by the improved ferroelectric stability of AN120/3%MgO. An ideal ferroelectric film should be able to produce P_r/P_s value close to unity ($P_r/P_s = 1$), thus suggesting AN120/3% MgO thin film as the favorable film developed in this study.

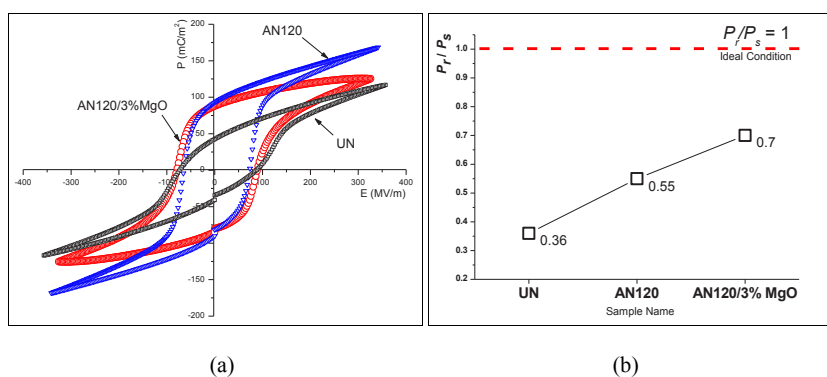


Figure 7. a) Comparison of ferroelectric loop; and (b) P_r/P_s ratio of the UN, AN120 and AN120/3%MgO films

CONCLUSION

The study has successfully produced a stable ferroelectric thin film of P_r/P_s close to unity (value of 1). The PVDF-TrFE thin film was loaded with 3% MgO nanofiller and annealed at 120°C (AN120/3%MgO). The morphology of the 3% MgO loaded in PVDF-TrFE thin film was found to produce favourable dispersion of nanofiller in comparison to the other loading percentage films. Hence, annealing the films at temperature of 120°C was found to produce elongated crystallites of defined structures, which contributed to outstanding ferroelectric properties of the AN120/3%MgO nanocomposite film.

ACKNOWLEDGEMENTS

This research was fully supported by Fundamental Research Grant Scheme (FRGS) from Ministry of Education, Faculty of Applied Sciences, Centre of Nanoscience and Nanotechnology (NANO-SciTech), Institute of Science and Nano-Electronic Centre (NET), Faculty of Electrical Engineering, Universiti Teknologi MARA, Malaysia. Our highest appreciation goes to Microwave Technology Centre (MTC), Faculty of Electrical Engineering, Universiti Teknologi MARA for their assistance in sample preparations. Our special thanks to Fellowship Scheme, Universiti Teknologi MARA Malaysia for funding this study.

REFERENCES

- Bae, I., Kang, S. J., Park, Y. J., Furukawa, T., & Park, C. (2010). Organic ferroelectric field-effect transistor with P(VDF-TrFE)/PMMA blend thin films for non-volatile memory applications. *Current Applied Physics*, 10(1, Supplement 1), e54-e57.
- Furukawa, T. (1989). Ferroelectric properties of vinylidene fluoride copolymers. *Phase Transitions*, 18(3-4), 143-211.
- Furukawa, T. (1997). Structure and functional properties of ferroelectric polymers. *Advances in Colloid and Interface Science*, 71-72, 183-208.
- Furukawa, T., Date M., Fukada E., Tajitsu Y. & Chiba A. (1980). Ferroelectric Behavior in the Copolymer of Vinylidene fluoride and Trifluoroethylene. *Japanese Journal of Applied Physics*, 19(2), L109-L112.
- Furukawa, T., Nakajima, T., & Takahashi, Y. (2006). Factors Governing Ferroelectric Switching Characteristics of Thin VDF/trFE Copolymer Films. *IEEE Transactions on Dielectrics and Electrical Insulation*, 13(5), 1120-1131.
- Furukawa, T., Takahashi, Y., & Nakajima, T. (2010). Recent advances in ferroelectric polymer thin films for memory applications. *Current Applied Physics*, 10(1, Supplement 1), e62-e67.
- Gan, W. C., & Majid, W. H. A. (2014). Effect of TiO₂ on enhanced pyroelectric activity of PVDF composite. *Smart Materials and Structures*, 23(4), 045026.
- Gan, W. C., & Majid, W. H. A. (2014). Effect of TiO₂ on enhanced pyroelectric activity of PVDF composite. *Smart Materials and Structures*, 23(4), 045026.
- Habibah, Z., Yusof, K. A., Ismail, L. N., Bakar, R. A., & Rusop, M. (2013). Sol-Gel Derived Nano-Magnesium Oxide: Influence of Drying Temperature to the Dielectric Layer Properties. *IOP Conference Series: Materials Science and Engineering*, 46(1), 012006.
- Ismail, L. N., Mohamad, N. N. H. N., Shamsudin, M. S., Zulkefle, H., Abdullah, M. H., Herman, S. H., & Rusop, M. (2012). Effect of solvent on the dielectric properties of nanocomposite poly (methyl methacrylate)-doped titanium dioxide dielectric films. *Japanese Journal of Applied Physics*, 51(6S), 06FG09.
- Lee, J. S., Prabu, A. A. & Kim, K. J. (2010). Annealing effect upon chain orientation, crystalline morphology, and polarizability of ultra-thin P(VDF-TrFE) film for nonvolatile polymer memory device. *Polymer*, 51(26), 6319-6333.

- Lee, J. S., Prabu, A. A., & Kim, K. J. (2007). Ferroelectric P(VDF/TrFE) Ultrathin Film for SPM-based Data Storage Devices *Solid State Phenomena*, 124-126, 303-306.
- Li, W., Zhu, Y., Hua, D., Wang, P., Chen, X., & Shen, J. (2008). Crystalline morphologies of P (VDF-TrFE)(70/30) copolymer films above melting point. *Applied Surface Science*, 254(22), 7321-7325.
- Ling, Q. D., Liaw, D. J., Zhu, C., Chan, D. S. H, Kang, E. T., & Neoh, K. G. (2008). Polymer electronic memories: Materials, devices and mechanisms. *Progress in Polymer Science*, 33(10), 917-978.
- Müller, K., Henkel, K., Paloumpa, I. & Schmeier, D. (2007). Organic field effect transistors with ferroelectric hysteresis. *Thin Solid Films*, 515(19), 7683-7687.
- Nguyen, C. A., Mhaisalkar, S. G., Ma, J. & Lee, P. S. (2008). Enhanced organic ferroelectric field effect transistor characteristics with strained poly(vinylidene fluoride-trifluoroethylene) dielectric. *Organic Electronics*, 9(6), 1087-1092.
- Prabu, A. A., Lee, J. S., Kim, K. J., & Lee, H. S. (2006). Infrared spectroscopic studies on crystallization and Curie transition behavior of ultrathin films of P(VDF/TrFE) (72/28). *Vibrational Spectroscopy*, 41(1), 1-13.
- Thomas, P., Varughese, K. T., Dwarakanath, K. & Varma, K. B. R. (2010). Dielectric properties of Poly(vinylidene fluoride)/CaCu₃Ti₄O₁₂ composites. *Composites Science and Technology*, 70(3), 539-545.
- Wahid, M. H. M., Dahan, R. M., Sa'ad, S. Z., Arshad, A. N., Sarip, M. N., Mahmood, M. R. & Majid, W. H. A. (2013). Optimization of annealing temperature for PVDF-TrFE (70:30 mol %) thin film. *Advanced Materials Research*, 626, 721-726.





Occurrence, Source Apportionment and Environmental Risk Assessment of Pharmaceuticals in Klang River, Malaysia

Siti Norbayu Mohd. Subari, Rozita Osman and Norashikin Saim*

Faculty of Applied Science, Universiti Teknologi MARA (UiTM), 40450 Shah Alam, Selangor, Malaysia

ABSTRACT

This study examined the presence and sources of 10 pharmaceuticals in Klang River were studied. The most common pharmaceuticals were caffeine and acetaminophen, 0.57-20.62 ng/mL and “not detected”-1.45 ng/mL. Water samples were clustered based on pharmaceutical concentrations. Source apportionment analysis showed that treated wastewater discharged from treatment plants contributed 18.43% of pharmaceuticals in Klang River. An environmental risk assessment by means of the risk quotient (RQ) was done whereby the latter was more than one for salicylic acid and diclofenac in surface water posing threats to the aquatic environment. Salicylic acid showed high risk for acute toxicity, while diclofenac showed high risk for chronic toxicity. The results indicated a need for regular monitoring on pharmaceutical levels in Klang River and increasing the efficiency of wastewater treatment here.

Keywords: Environmental risk assessment, Klang River, Malaysia, occurrence, pharmaceuticals, source apportionment

INTRODUCTION

Many studies have examined the presence of pharmaceuticals in water samples (Al-Odaini et al., 2013; Lindberg et al., 2014; Silva et al., 2014). Findings showed high frequency of pharmaceuticals detected in water samples, mainly from point sources, such as influent wastewater, treated wastewater, and receiving water (Al-Odaini et al., 2013; Carmona et al., 2014; Oppenheimer et al., 2011; Schaidler et al., 2014). The presence of pharmaceuticals in aquatic ecosystems is due to its high consumption. Pharmaceuticals enter the water compartment through municipal wastewater, hospitals waste and pharmaceutical industries effluent (Cardoso et al., 2014; Collado et al.,

ARTICLE INFO

Article history:

Received: 28 September 2016

Accepted: 03 February 2017

E-mail addresses:

noras691@salam.uitm.edu.my (Siti Norbayu Mohd. Subari),

rozit471@salam.uitm.edu.my (Rozita Osman),

noras691@salam.uitm.edu.my (Norashikin Saim)

*Corresponding Author

2014; Golovko et al., 2014). The discharge of treated wastewater effluent into receiving water is responsible for the contamination.

Klang River basin is a densely populated and developed area in Malaysia and flows through major urban areas: Kuala Lumpur - Petaling Jaya - Shah Alam - Klang. The objectives of this study were to study the occurrence and distribution of pharmaceuticals in Klang River and its tributaries, to interpret the contribution of sources of pharmaceuticals loadings into Klang River through source apportionment analysis utilising principal component analysis (PCA) with multiple linear regression (MLR) method and to assess the potential environmental risk of surface water by evaluating the ratio between the measured environmental concentration (MEC) and the predicted no-effect concentration (PNEC) for these surface waters.

METHOD

Chemicals and Materials

The selected pharmaceuticals include caffeine (CAF), acetaminophen (ACT), salicylic acid (SAL), diclofenac (DIC), ibuprofen (IBU), mefenamic acid (MEF), gemfibrozil (GEM), carbamazepine (CBZ), estrone (EST) and methanesulfonic acid (MSA) purchased from Sigma-Aldrich (purity assay in range of 98-101%). Acetonitrile (ACN) (HPLC grade) was purchased from Merck (Darmstadt, Germany). Ultrapure water was produced by Barnstead Nanopure (Thermo Scientific).

Sampling

The Klang River (Figure 1) originates from the Ulu Gombak Forest Reserve and flows through Kuala Lumpur and Selangor before finally entering the Straits of Malacca. Klang River and its 13 tributaries run through a densely populated area and is the receiving water body for discharges from sewage treatment, hospitals, industries and urban through its tributaries and sewerage system. Therefore, the river is subjected to pharmaceuticals from point and non-point source. A sampling of surface water was conducted from August 2014 to October 2014. Water samples were collected at 6 sites on the main stem of Klang River and 7 sites on 5 tributaries (Figure 1). One litre of each sample was collected in polypropylene bottles, acidified using

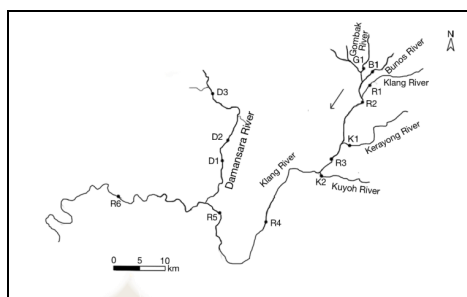


Figure 1. Sampling sites in the Klang River and its tributaries.

Note: The arrow indicates flow direction

hydrochloric acid (3 M) and vacuum-filtered using Whatman 45 μm GF/A filters (Whatman International Ltd Maidstone, England). The filtered wastewater samples were stored in the dark at 4°C prior to online SPE-HPLC analysis.

Instrumentation

The online solid phase extraction high performance liquid chromatography (SPE-HPLC) was performed using Dionex Ultimate 3000 (Sunnyvale, CA, USA) system. The system consists of a large volume loop (10.2 mL) autosampler (WPS-3000SL Analyt.), dual gradient pump, left and right (Pump DGP-3600A), a thermostated column (TCC-3200 2x2P-6P) and a diode array detector (DAD) (PDA-3000 Photodiodearray). The system was equipped with a programmable 6 port/2 position switching valve for several modes (loading, clean-up, elution and separation). Data were processed by the Chromeleon Software v.6.8 (Dionex, USA). SPE clean-up was performed using Dionex IonPac AG14A RFIC (4.0×50 mm) (Thermo Scientific, USA), and analytical separation was performed with Acclaim Polar Advantage II (5 μm , 120 Å, 4.6×150 mm) (Thermo Scientific, USA). The temperature was set at 40°C. A gradient elution with a flow rate of 1 mL/min was used throughout the analysis. The DAD was set at wavelength of 220 nm (diclofenac, salicylic acid, mefenamic acid, estrone), 250 nm (acetaminophen) and 280 nm (caffeine, ibuprofen, carbamazepine, gemfibrozil). The gradient elution consisted of acetonitrile, 10 mM methanesulfonic acid (MSA) and ultrapure water.

Sample Extraction and Analysis

An online SPE-HPLC-DAD method was used to preconcentrate and separate the samples. The method had three steps. At equilibration mode, 10 mL of water sample was loaded onto sample loop using autosampler (fitted with a 100 μL syringe and 10 mL loop). Then, SPE column was positioned in loading mode using the switching valve. In the first step (loading), the left pump was used to load sample from sample loop onto SPE column at 1 mL/min and simultaneously the analytical column was equilibrated with the right pump. Co-retained sample matrix was then flushed out using a washing composition of 10 mM MSA and ACN (95:5). In the second step (elution), the switching valve was switched to elution position to couple the SPE column with the analytical column and analytes were transferred using gradient elution mobile phase composition. In the third step (separation), the switching valve was switched back into equilibration mode, disconnected the SPE column with the analytical column and analytes were separated in an analytical column using the right pump. All analytes were simultaneously analysed using DAD. Recoveries of 10 target pharmaceuticals were determined by spiking surface water samples at 5 ng/mL. The recoveries ranged between 86.6% and 108.6% and the reproducibility in relative standard deviation was between 0.8% and 10.2%. Limit of detections (LOD) were determined using regression method that ranged between 0.01 and 0.26 ng/mL.

Source Apportionment Method

Source apportionment analysis was conducted using Principal Component Analysis-Multi Linear Regression (PCA-MLR) method with XLSTAT 2014 (USA) software. The PCA was

used to analyse the most significant variables by excluding the less significant variables with minimum loss of original information (Kannel et al., 2007). Principal components (PCs) with Eigenvalue more than one were selected for factor analysis (FA). Then, PCA with varimax rotation was performed containing four pharmaceuticals detected in columns and sampling sites in rows to obtain varimax functions (VFs). The relationship between the principal component and the pharmaceutical is indicated by the factor loadings. Stepwise MLR was then performed on the significant factor scores to determine the source apportionment of each source based on total concentrations. The source apportionment from each factor was estimated using MLR utilising factor score values as independent variables and measured total pharmaceuticals as dependent variables. The basic equation of this model is:

$$Y = \beta_0 + \beta_1x_1 + \beta_2x_2 + \dots + \beta_{p-1}x_{p-1} + e \quad \text{Eq. (1) (Juahir et al, 2011)}$$

where Y is the response variable, x as explanatory variables x_1, x_2, \dots, x_{p-1} , β as p parameters (regression coefficients) $\beta_0, \beta_1, \beta_2, \dots, \beta_{p-1}$ and e as the random error.

Ecotoxicological Risk Assessment

The risk of quotient (RQ) is a useful tool to characterise the potential ecological risk of contaminants in three trophic levels (fish, invertebrates and algae) of the aquatic environment (Gros et al., 2010). Based on EMEA guideline, RQ was calculated as the ratio between Measured Environmental Concentration (MEC) and Predicted No-Effect Concentration (PNEC) (Eq. (2)). The MEC is the maximum concentration of target compounds found in the effluent sample. The PNEC was estimated using the lowest values of acute EC_{50} or LC_{50} or the chronic No-Observed Effect Concentration (NOEC) (Kosma et al., 2014), divided by a default assessment factor (AF). For acute toxicity test results, PNEC was estimated using Eq. (3) and for chronic toxicity test results, the PNEC was estimated using Eq. (4) (Kosma et al., 2014).

$$RQ = \text{exposure/toxicity}$$

$$RQ = \text{highest concentration (MEC)/ PNEC}, \quad \text{Eq. (2)}$$

where,

$$PNEC_{\text{acute}} = EC_{50} \text{ or } LC_{50} / 1000 \quad \text{Eq. (3)}$$

$$PNEC_{\text{chronic}} = NOEC / AF \quad \text{Eq. (4)}$$

The ratio between the exposure concentration and predicted no effect concentration determines the potential environmental risk. A “high risk” is suspected when $RQ \geq 1$, “medium risk” is suspected when $1 > RQ > 0.1$ and “low risk” is suspected when $0.1 > RQ > 0.01$.

RESULTS AND DISCUSSION

Presence of Pharmaceuticals

The concentrations of selected pharmaceuticals in surface water samples are shown in Table 1. Surface water of Klang River showed presence of caffeine, acetaminophen, salicylic acid and diclofenac. Caffeine showed the highest mean concentration and ranged from 0.57-20.62 ng/mL. The variation in concentration could be due to the effect of dilution of compounds after discharge into surface water, and physical phenomena such as adsorption to sediments or suspended solids, biodegradation or photo degradation (Lopez-Serna, 2010) and concentrations of compounds in the surface water. A lower concentration of caffeine was reported in rivers in Korea (0.26 ng/mL) (Sim et al., 2010), and rivers in the United States (0.013-0.3 ng/mL) (Oppenheimer et al., 2011). Caffeine was reported as a promising marker for urban faecal contamination due to its persistence, solubility and high occurrences (Fenech et al., 2013).

Acetaminophen was detected in most of the sampling sites, while diclofenac and salicylic acid were detected in most of the tributaries of Klang River. The concentration of acetaminophen, diclofenac and salicylic acid in surface water ranged from 0.12-1.45 ng/mL, 0.05-3.21 ng/mL and 0.19-13.0 ng/mL, respectively. High concentration of these pharmaceuticals can be explained by high consumption of these pharmaceuticals in Malaysia and are available as over-the-counter medications. In addition, it was reported that acetaminophen is discharged as conjugates, and these conjugates might be broken down to its parent compound during wastewater treatment, resulting in the high amount of acetaminophen released into surface water (Al-Odaini, 2013). A comparable concentration for acetaminophen was reported in Malaysian rivers (maximum 0.35 ng/mL) (Al-Odaini, 2013) and Ebro River, Spain (n.d-0.71 ng/mL) (Lopez-Serna, 2012). The observed pharmaceuticals concentration range indicated that the studied water bodies were exposed to various sources including surface runoff from the urban zone, treated wastewater discharged from treatment plants and untreated wastewater.

A cluster analysis was performed to classify the river according to their pharmaceutical concentrations. As shown in Figure 2, sampling sites D2 and K1 were grouped in Cluster 1. High concentration of pharmaceuticals detected in these sampling sites may be due to the direct input of treated wastewater discharged from treatment plant that received wastewater from developed housing areas (Taman Tun Dr Ismail (TTDI) Jaya) and Kerayong River (K1). D1 and D3 from Damansara River (Cluster 2) showed moderate pharmaceutical concentration with discharges from Section 13, Shah Alam and Kampung Melayu Subang. Low concentrations of pharmaceuticals from six sites along Klang River were grouped in Cluster 3.

Table 1
Concentrations of pharmaceuticals in surface water samples (ng/mL)

River	Sampling site	Caffeine	Acetaminophen	Salicylic acid	Diclofenac
Klang	R6	1.46	0.46	n.d	n.d
Klang	R5	1.7	1.42	n.d	n.d
Klang	R4	2.65	1.39	n.d	n.d
Klang	R3	4.08	1.15	n.d	n.d
Klang	R2	0.62	0.12	n.d	0.04
Klang	R1	0.57	n.d	n.d	n.d
Damansara	D1	7.9	1.44	1.36	2.11
Damansara	D2	20.62	1.45	4.13	n.d
Damansara	D3	8.26	0.66	3.15	n.d
Kuyoh	K2	2.36	0.72	n.d	3.21
Kerayong	K1	4.92	1.11	13.0	1.87
Gombak	G1	0.74	n.d	n.d	0.05
Bunos	B1	2.59	1.40	0.19	0.23

*n.d = not detected

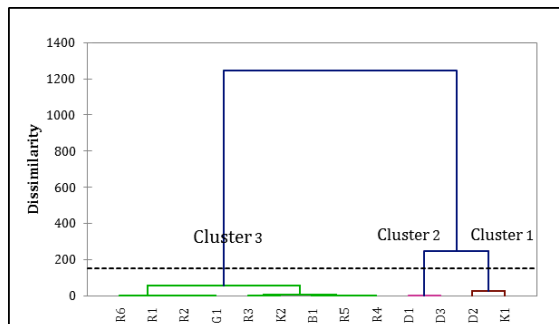


Figure 2. Dendrogram showing cluster of sampling sites

Pharmaceutical Profile and Source Apportionment

In order to study the sources pharmaceutical in surface water samples, their presence in influent and effluent wastewater samples from six extended aeration wastewater treatment plants (WWTPs) located on Klang River were studied (Table 2). The WWTPs mainly treat wastewater from domestic sewage. Table 2 shows the frequency of pharmaceuticals detected in influent and effluent. Caffeine and acetaminophen were detected in all samples with the frequency of 87% to 100%. High removal rate of caffeine (96.2%), acetaminophen (97.2%) and salicylic acid (97.5%), while lower removal rate of diclofenac (38.7%) were observed. Similar results were also reported by Gros et al. (2010), Papageorgiou et al. (2016) and Dutta et al., (2014).

The PCA with Varimax rotation was applied using data set samples versus pharmaceuticals, to study the influence of pharmaceutical contamination in Klang River. The PCA results showed that 71.6% of the variance of the original data might be explained by the two main components. Table 3 shows factor loadings for the pharmaceuticals variables. The PC1 represents 40.23% of the data variability, and the highest loading variables in this PC were caffeine and acetaminophen (>0.75). The high removal rate of these two compounds indicated no significant contribution of these pharmaceuticals from treated wastewater into the river and hence, the sources of caffeine and acetaminophen were mainly from untreated wastewater. Diclofenac is the most influential variable in PC2, which explains 31.18% of the variance. The low removal rates of diclofenac resulted in high contribution of this compound from treated wastewater into the river. MLR analysis was performed on PCA scores to determine source apportionment of the compounds in all surface water samples. In this study, the factor scores from PCA for PC1 and PC2 as independent variables were regressed against total sum of four pharmaceuticals, as dependent variables. The resulting equation was:

$$\text{SumPharma} = 7.63 + 6.67 * \text{PC1} + 3.18 * \text{PC2} \quad (\text{Eq. 5})$$

The standardised coefficients (β) of the model presented in Table 3 indicate the relative influence of the PCs. Pharmaceuticals from untreated wastewater greatly influenced the total pharmaceutical loading into receiving water ($\beta = 0.8525$), followed by treated wastewater discharged from treatment plant ($\beta = 0.4063$). The β values describe the relative relationship between pharmaceuticals and each VF. Thus, the source apportionment of pharmaceutical sources in Klang River came from untreated wastewater (81.57%) and treated wastewater discharged from treatment plant (18.43%), and these findings are consistent with a study conducted on Beijing River (Dai et al., 2015).

Table 2
Concentrations of pharmaceuticals in influent and effluent wastewater samples

Sample		Caffeine	Acetaminophen	Salicylic acid	Diclofenac
Influent	Frequency of detection (%)	100	100	50	83
	Range (ng/mL)	6.59-68.8	6.93-191.9	n.d-13.47	n.d-88.95
Effluent	Frequency of detection (%)	67	100	16	83
	Range (ng/mL)	n.d-1.81	0.14-0.76	n.d-0.48	n.d-0.35
	Removal rate (%)	96.2	97.2	97.5	38.7

Table 3
Factor loadings of the PCA analysis of pharmaceuticals in surface water samples

	PC1	PC2
Caffeine	0.8879	-0.0094
Acetaminophen	0.7857	0.1158
Salicylic acid	0.4575	0.6270
Diclofenac	-0.0451	0.9169
Eigenvalue	1.8088	1.0555
Variability (%)	40.4233	31.1839
Cumulative %	40.4233	71.6073
Standardise coefficient (β)	0.8525	0.4063

Note: Strong loading >0.75

Risk assessment

An assessment of the risk quotient (RQs) in the surface waters of the Klang River was done. Results for the RQ value were calculated from acute and chronic toxicity data for the three trophic levels (fish, invertebrates and algae) as shown in Figure 3 and Figure 4. Salicylic acid showed high risk for acute toxicity in fish, while diclofenac displayed high risk for chronic toxicity in fish ($RQ > 1$). However, the levels of these pharmaceuticals were not toxic for invertebrates and algae. Similar findings were reported by Tewari et al. (2013). The findings indicated the significance of assessing and classifying the potential environmental impact of these pharmaceuticals (Gros et al., 2010; Kosma et al., 2014; Papageorgiou et al., 2016). As diclofenac showed high risk in chronic toxicity, this compound should be monitored in surface water.

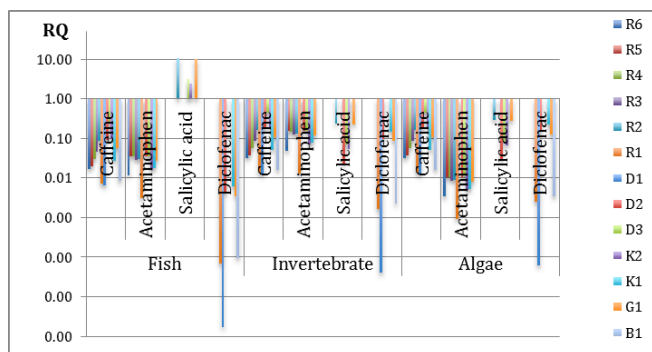


Figure 3. Risk quotients for pharmaceuticals in surface waters estimated for fish, invertebrates and algae for acute toxicity

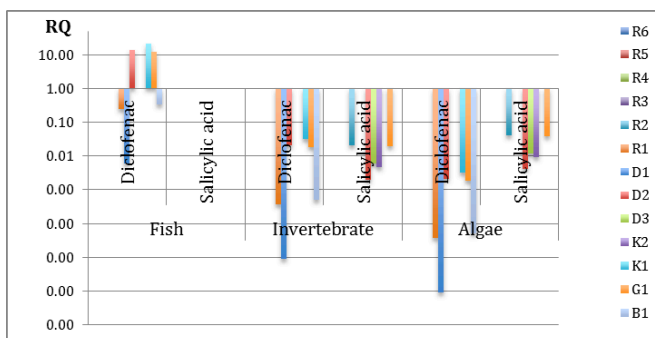


Figure 4. Risk quotients for pharmaceuticals in surface waters estimated for fish, invertebrates and algae for chronic toxicity

CONCLUSION

The occurrence and sources of 10 pharmaceuticals in the surface water of the Klang River were studied. The concentrations of pharmaceuticals varied in the range of “not detected” to 20.62 ng/mL. The significant contribution of pharmaceuticals from treated wastewater discharged from treatment plants (18.43%) indicated a need to increase efficiency of wastewater systems in eliminating pharmaceuticals. Results from environmental risk assessment showed salicylic acid and diclofenac exhibited $RQ > 1$, which can threaten the aquatic ecosystem. Therefore, active monitoring is important to detect the presence of pharmaceuticals in order to protect the river quality.

ACKNOWLEDGEMENTS

The authors would like to acknowledge the financial support from Organisation for the Prohibition of Chemical Weapons (OCPW) (L/ICA/ICB/170997/11) and Research Management Centre (RMC) Universiti Teknologi MARA.

REFERENCES

- Al-Odaini, N. A., Zakaria, M. P., Yaziz, M. I., Surif, S., & Abdulghani, M. (2013). The occurrence of human pharmaceuticals in wastewater effluents and surface water of Langat River and its tributaries, Malaysia. *International Journal of Environmental Analytical Chemistry*, 93(3), 245-264.
- Cardoso, O., Porcher, J. M., & Sanchez, W. (2014). Factory-discharged pharmaceuticals could be a relevant source of aquatic environment contamination: Review of evidence and need for knowledge. *Chemosphere*, 115, 20-30.
- Carmona, E., Andreu, V., & Pico, Y. (2014). Occurrence of acidic pharmaceuticals and personal care products in Turia River Basin: from waste to drinking water. *Science of Total Environment*, 484, 53-63.
- Collado, N., Rodriguez-Mozaz, S., Gros, M., Rubirola, A., Barcelo, D., Comas, J., & Buttiglieri, G. (2014). Pharmaceuticals occurrence in a WWTP with significant industrial contribution and its input into the river system. *Environmental Pollution*, 185, 202-212.

- Dutta, K., Lee, M. Y., Lai, W. W., Lee, C. H., Lin, A. Y., Lin, C. F., & Lin, J. G. (2014). Removal of pharmaceuticals and organic matter from municipal wastewater using two-stage anaerobic fluidized membrane bioreactor. *Bioresourcer Technology*, *165*, 42-49.
- Fenech, C., Nolan, K., & Rock, L. Morrissey, A. (2013). An SPE LC-MS/MS method for the analysis of human and veterinary chemical markers within surface waters: an environmental forensics application. *Environmental Pollution*, *181*, 250-256.
- Golovko, O., Kumar, V., Fedorova, G., Randak, T., & Grabic, R. (2014). Seasonal changes in antibiotics, antidepressants/psychiatric drugs, antihistamines and lipid regulators in a wastewater treatment plant. *Chemosphere*, *111*, 418-426.
- Gros, M., Petrovic, M., Ginebreda, A., & Barcelo, D. (2010). Removal of pharmaceuticals during wastewater treatment and environmental risk assessment using hazard indexes. *Environment International*, *36*(1), 15-26.
- Juahir, H., Retnam, A., Zali, M.A., & Hashim, M.F. (2011). A comparison between multiple linear regression (MLR) and artificial neural network (ANN) for river class prediction at Klang River, Malaysia. In: Zakaria, M. P., Mohamed, M. I., Kasmin, S., Hashim, N. R., Samah, M. A. A., Zainuddin, M. F., Zaid, S. S. M. (Eds.), *Contemporary Environmental Quality Management in Malaysia and Selected Countries*. Universiti Putra Malaysia Press, Serdang.
- Kannel, P. R., Lee, S., Kanel, S. R., & Khan, S. P. (2007). Chemometric application in classification and assessment of monitoring locations of an urban river system. *Analytica Chimica Acta*, *582*, 390-399.
- Kosma, C. I., Lambropoulou, D. A., & Albanis, T. A. (2014). Investigation of PPCPs in wastewater treatment plants in Greece: occurrence, removal and environmental risk assessment. *Science of the Total Environment*, *466-467*, 421-438.
- Lindberg, R. H., Ostman, M., Olofsson, U., Grabic, R., & Fick, J. (2014). Occurrence and behaviour of 105 active pharmaceutical ingredients in sewage waters of a municipal sewer collection system. *Water Research*, *58C*, 221-229.
- Oppenheimer, J., Eaton, A., Badruzzaman, M., Haghani, A. W., & Jacangelo, J. G. (2011). Occurrence and suitability of sucralose as an indicator compound of wastewater loading to surface waters in urbanized regions. *Water Research*, *45*(13), 4019-4027.
- Papageorgiou, M., Kosma, C., & Lambropoulou, D. (2016). Seasonal occurrence, removal, mass loading and environmental risk assessment of 55 pharmaceuticals and personal care products in a municipal wastewater treatment plant in Central Greece. *Science of the Total Environment*, *543*(Pt A), 547-569.
- Schaider, L. A., Rudel, R. A., Ackerman, J. M., Dunagan, S. C., Brody, J. G. (2014). Pharmaceuticals, perfluorosurfactants, and other organic wastewater compounds in public drinking water wells in a shallow sand and gravel aquifer. *Science of the Total Environment*, *468-469*, 384-393.
- Sim, W. J., Lee, J. W., & Oh, J. E. (2010). Occurrence and fate of pharmaceuticals in wastewater treatment plants and rivers in Korea. *Environmental Pollution*, *158*(5), 1938-1947.
- Tewari, S., Jindal, R., Kho, Y. L., Eo, S., & Choi, K. (2013). Major pharmaceutical residues in wastewater treatment plants and receiving waters in Bangkok, Thailand and associated ecological risks. *Chemosphere*, *91*, 697-704.



Adsorption of Acid Dyes onto Zinc Chloride-Modified Cocoa (*Theobroma cacao*) Pod Husk-Based Carbon

Nur Aqilah Zainal*, Shariff Ibrahim and Borhannuddin Arifin

Faculty of Applied Sciences, Universiti Teknologi MARA (UiTM), 40450, Shah Alam, Selangor, Malaysia

ABSTRACT

An agricultural waste, the cocoa pod husk was chemically modified using a dehydrating agent, zinc chloride ($ZnCl_2$), carbonised and used for the remediation of acid dyes in an aqueous solution. The targeted acid dyes are: (i) Acid Violet 17 (AV17); (ii) Acid Yellow 36 (AY36); and (iii) Acid Blue 29 (AB29). The physicochemical properties of the zinc chloride-modified cocoa pod husk-based carbon (ZCPHC) were characterised by ash content, bulk density, pH slurry, pH_{pzc} and Field Emission Scanning Electron Microscopy (FESEM) and Energy Dispersive X-Ray (EDX) analysis. The bulk density and ash content of the prepared carbon is 0.55 g cm^{-1} and 7.0% respectively. The photograph of SEM shows distinct changes at the ZCPHC carbon surface as it has large pores formed due to $ZnCl_2$ modification. The adsorption tests were performed in a batch adsorption system using an aqueous solution of the understudy acid dyes. The influence of pH and dose of an adsorbent on the acid dye uptake was investigated and discussed. The adsorption was in favour at acidic condition with maximum removal observed at pH 2. The removal efficiency of the aqueous acid dye solution increased with the increase in adsorbent dosage. The kinetic experiment showed equilibrium time is less than 40 minutes and the kinetic data for all three understudy acid dyes fitted well with the pseudo-second-order model with a correlation coefficient (R^2) values above 0.98.

Keywords: Acid dyes, adsorption, carbon, chemical activation, cocoa pod husks, zinc chloride

ARTICLE INFO

Article history:

Received: 28 September 2016

Accepted: 03 February 2017

E-mail addresses:

keyla.zainal@yahoo.com (Nur Aqilah Zainal),

sha88@salam.uitm.edu.my (Shariff Ibrahim),

barifin112@gmail.com (Borhannuddin Arifin)

*Corresponding Author

INTRODUCTION

The large volume of wastewater as a result of water consumption in the dyeing process manufacturing is very alarming (Babu et al., 2007). The discharge of dyes is considered critical for both toxicological and aesthetical reasons. Furthermore, Métivier-Pignon et al. (2003) highlighted the serious adverse effects of dye water discharge on many forms of life.

Various industries for all sorts of products utilised acid dyes in their production (Yagub et al., 2014).

Adsorption is one of the most promising methods because its versatility and ability in removing various types of colours as well as its insensitivity to toxic pollutants (Elizalde-Gonzalez & Hernandez-Montoya, 2007; Yagub et al., 2014). Crini (2006) reported that adsorption on activated carbon is the most effective for dye removal and to produce high quality treated dye effluent. Agricultural wastes with no practical uses are discarded irresponsibly and this will eventually lead to odour and environmentally aesthetical problem. Suitable alternative carbon raw material from agricultural wastes are rice hull, orange peels, coir pith, guava seed and almond shells (Salleh et al., 2011) that are cheap, readily available and environmentally friendly.

Cocoa is one of the largest and most important commodity in Malaysia (Tuah, 2013). Cocoa pod husks (CPH) constitute about 70% of the cocoa fruit, so for each tonne of dry beans produced, 10 tonnes of CPH wastes are generated (Ofori-Boateng & Lee, 2013). This proves that agricultural waste by-product is abundantly available. Therefore, cocoa pod husks have great potential for low cost carbon. Zinc chloride, $ZnCl_2$ is one of the most common dehydrating agents used in the activation process in activated carbon production (Ozdemir et al., 2014). Hesas et al., (2013) reported with the use of $ZnCl_2$ as activating agents, the carbon produced has a high surface area and high yield.

In this study, the zinc chloride-modified cocoa pod husk-based carbon (ZCPHC) is used as adsorbent for the removal of acid dyes from aqueous solution. The effect of the operating parameters, such as solution pH and adsorbent dosage, was studied. The batch contact time method was used to measure the adsorption rate and the kinetics parameter were then evaluated. The pseudo-first-order and pseudo-second-order equation were used to fit the dynamics adsorption kinetics.

METHOD

Preparation of the Adsorbent

The CPH was collected at the local cocoa farm in Pahang. They were washed in deionised water to remove impurities and later air dried. The CPH was further dried in the oven overnight at 80°C to remove any residual moisture left. The production of modified carbon using simple technology was accomplished through chemical activation method as suggested by Cobb et al. (2012) with the carbon produced by heating the dried CPH at temperature of 600°C in the furnace for six hours to form carbonised cocoa pod husks (CPHC).

In the chemical activation process, 0.5M Zinc Chloride, $ZnCl_2$ (10 g CPHC and 100 ml $ZnCl_2$ solution ratio) was used. The CPHC was immersed in the $ZnCl_2$ solution and was mixed by using an orbital shaker at 200 rpm and left overnight. The strainer was used to separate the prepared adsorbent and rinsed with deionised water until the pH value of rinsed water becomes neutral. The $ZnCl_2$ -modified cocoa pod husk-based carbon produced is then dried in the oven at 80°C overnight, sieved to 500 μm sizes and stored in the air tight container and labelled as ZCPHC.

Characterisation of the Adsorbent

The ZCPHC was examined for its ash content and bulk density based on Kwaghger and Adejoh (2012). Zero point of charge (pH_{pzc}) for ZCPHC was determined as per Hameed et al's recommendation (2008). As for morphological measurement, the prepared adsorbent (CPHC & ZCPHC) samples were sputter coated with gold for 2 minutes and examined using a field emission scanning electron microscopy (FESEM, Zeiss Supra 40VP, Germany) at a 5-kV accelerating voltage and EDX analysis was carried out using same instrument.

Adsorption Batch Studies

Adsorption studies were performed by shaking ZCPHC with 100 ml acid dye (AV17, AY36 and AB29 respectively) solution at three different concentrations of 50, 75, 100 mg/L respectively at room temperature. The pH was fixed at 2 and the mixture was shaken at 200 rpm using orbital shaker. The samples were withdrawn at selected time and the dye solution was separated from the adsorbent via filtration using filter paper of 15 mm size. Dye concentration was measured based on its absorbance value at a maximum wavelength (545, 414 and 602 nm for AV17, AY36 and AB29 respectively). Adsorption kinetics were estimated by interpreting the uptake of the acid dyes from aqueous solution at various time intervals. The effect of pH on dye uptake was investigated over a pH range from 2 – 12 and the effect of adsorbent dosage on dye removal was studied over an adsorbent dosage range from 0.25 g to 4.0 g. The removal percentage and adsorption capacity were calculated using the following mathematical equation:

$$\text{Percentage removal (\%)} = \frac{C_o - C_e}{C_o} \times 100\% \quad [1]$$

$$\text{Adsorption capacity } (q_e) = \frac{C_o - C_e (V)}{W} \quad [2]$$

Where C_o and C_e are the initial and the equilibrium concentrations of dye (mg/L) respectively, W is the mass of adsorbent (g) and V is the volume of dye solution (ml). The experiments were duplicated in batch mode and the average result was reported.

Best Fitting Model Estimation

The fit of experimental data with the mathematical model was decided by two considerations; (i) regression coefficient, R^2 by assuming the value closest to one is the best fit; and (ii) error estimation, where the best fit is indicated by the lower value. The error function of the Sum of Square Error (SSE) (Tan et al., 2007, 2008) was employed and expressed as:

$$\text{SSE} = \sqrt{\frac{\sum [q_{e\text{exp}} - q_{e\text{cal}}]^2}{N}} \quad [3]$$

Where N is the number of data points, $q_{e\text{exp}}$ and $q_{e\text{cal}}$ (mg/g) refer to experimental and calculated adsorption capacity from kinetic model data.

RESULTS AND DISCUSSION

Characterisation of Adsorbent

The bulk density of ZCPHC is 0.55 g cm^{-1} in which the values are consistent with Adeyi and Oladayo (2010) using the same raw material that is cocoa pod husks. The ash content value of ZCPHC was observed as low at 7.0%. Yang and Lua (2003) suggested that the value of ash content should be in the range between 2% and 10% and Soleimani and Kaghazchi (2007) reported that high ash content is inadmissible for activated carbon and it can reduce its mechanical strength and adsorptive capacity. The pH slurry of the prepared ZCPHC is 8.03 while the pH_{pzc} is 8.

The comparison of morphology structure between CPHC and ZCPHC is exhibited in the SEM photographs. In Figure 1(a), the surface texture of CPHC was observed as very packed, compact with no large and well develop pores formed on the carbon surface whereas in Figure 1(b) the surface texture clearly displays large pores with crevices and cracks on the carbon surface; thus, large well pronounced porosity was formed around the ZCPHC surface due to ZnCl_2 modification. The ZnCl_2 effect towards the carbon surface is also reported by Mahamad et al., (2015). From EDX analysis represented in Table 1, the existence of Zn^{2+} and Cl^- ions shows the effect of modification using ZnCl_2 . Hu and Vansant (1995) proposed that the formation of pore structures was due to charring and aromatisation of carbon skeleton upon introduction of ZnCl_2 .

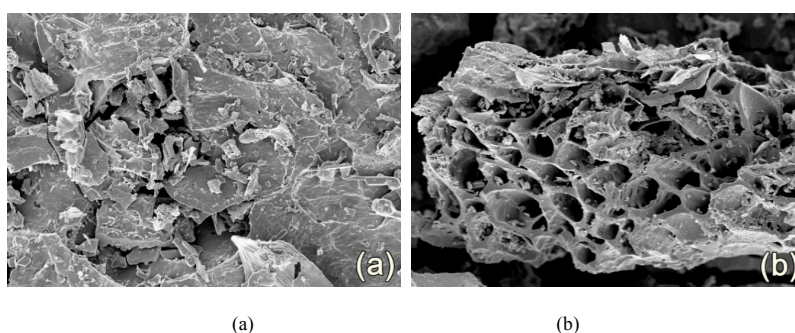


Figure 1. (a) SEM images of raw unmodified carbon (CPHC); and (b) SEM images of ZnCl_2 modified carbon (ZCPHC)

Table 1
EDX analysis of prepared adsorbents

Element	Weight (%)	
	CPHC	ZCPHC
C	58.06	79.08
O	16.03	13.28
S	0.84	0.60
Zn	0.00	5.85
Cl	0.00	1.20

Effect of Initial pH on Acid Dye Adsorption

The solution pH is among the crucial parameter that affects dye adsorption. Predominantly, for anionic dye adsorption which includes acid dyes, the removal percentage of the dye is in favour at lower pH rather than a high pH solution (Salleh et al., 2011). Figure 2 shows the removal percentage of under study acid dyes decreases as the initial pH of the solution increases. It was observed that the percentage removal of under study acid dyes decreased from 74.0% to 27.08% for AV17, 60.27% to 27.83% for AY36 and 71.05% to 25.76% for AB29 with an increase in initial pH from 2 – 12. At pH 2, the surface of ZCPHC becomes positively charged by absorbing H^+ ions and the H^+ ion concentration in the system increased. Thus, at lower pH, it will promote the electrostatic attraction between the positively charged surface of ZCPHC and an anionic dye molecule of under study acid dyes, AV17, AY36 and AB29 respectively, leading to highest uptake capacity, adoption of respective acid dyes which is consistent with the effect of pH of anionic dyes in the works of Amin (2009).

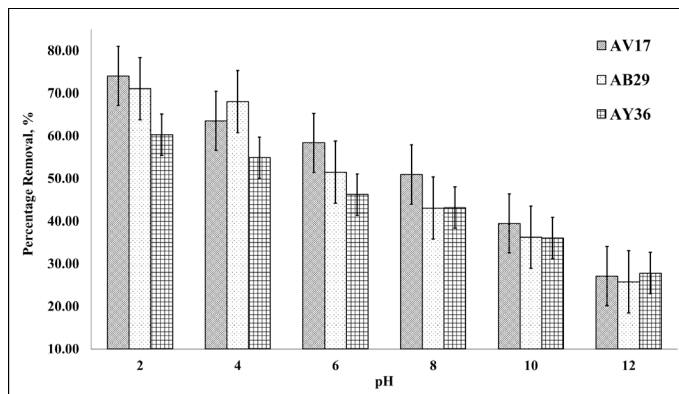


Figure 2. Effect of initial pH on adsorption of various acid dyes onto ZCPHC

Effect of Adsorbent Dosage on Acid Dye Adsorption

Adsorbent dosage is crucial as it provides the foresight of adsorbent capacity for a given amount of the adsorbent at the operating conditions (Yagub et al., 2014). In most cases, the dye's percentage removal increases with increasing adsorbent dosage and in contrast, the adsorption capacity decreases with increasing adsorbent dosage. Figure 3 shows the removal percentage of under study acid dyes increases as the adsorbent dosage increases up to 1.0 g. However, the trend remains almost constant for an adsorbent dosage of 2.0 g and 4.0 g. As proposed by Shukla et al. (2002), at a high adsorbent dosage, unsaturation of the adsorption site might happen and also the aggregation of adsorbent particle that leads to decrease in total surface area of the adsorbent which resulted in an increase in the diffusion path length. It was observed that the percentage removal of various acid dyes increased from 74.82% to 96.89% for Acid Violet 17, 60.42% to 94.08% for Acid Yellow 36 and 71.66% to 92.79% for Acid Blue

29 with an increase in adsorbent dosage from 0.25 g to 4.0 g respectively. The high percentage removal at the high adsorbent dosage is due to the large adsorbent surface area and availability of more adsorption sites (Wang et al., 2010).

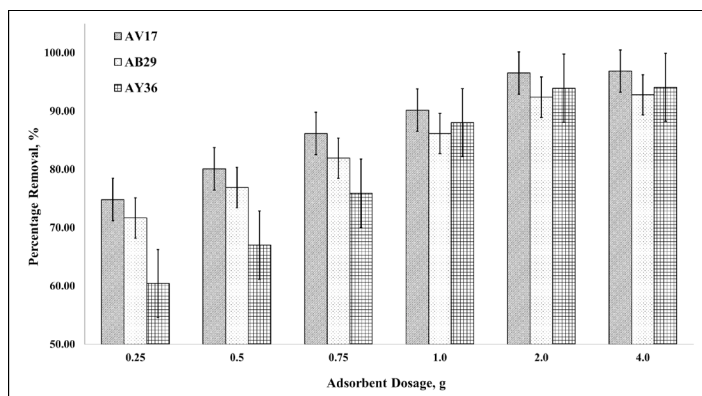


Figure 3. Effect of adsorbent mass on adsorption of various acid dyes onto ZCPHC

Dynamic Adsorption Studies

The kinetic rate constants order is related to the adsorption dynamics. The kinetic adsorption study usually applies the pseudo-first-order models and pseudo-second-order models (Salleh et al., 2011). The non-linear equation of the pseudo-first-order model of Lagergren and pseudo-second-order model is defined by the following relationship (Ho & McKay, 1998):

$$q_t = q_e (1 - e^{-k_1 t}) \quad [4]$$

$$q_t = \frac{q_e^2 k_2 t}{(1 + q_e k_2 t)} \quad [5]$$

In Equations [4] and Eq. [5], the rate constants of the pseudo-first-order and pseudo-second-order models are represented by k_1 and k_2 , meanwhile, the amount of dye adsorbed at equilibrium and time t , are tagged as q_e and q_t , respectively (Ho & McKay, 1998). The nonlinear equation [4] and [5] were constructed using Polymath software and presented in Figure 4, Figure 5 and Figure 6. It can be seen from the kinetics plots based on the adsorption non-linear kinetics expression as shown in Figure 4, Figure 5 and Figure 6 that both pseudo-first-order kinetics and pseudo-second-order kinetics are in agreement with the experimental data. Table 2 shown that, for both models $q_{e\text{ cal}}$ and $q_{e\text{ exp}}$, there was not much difference; however, pseudo second-order model was observed to give higher unity correlation coefficient, R^2 (>0.98) and lower SSE error value which ranged between 0.05% and 1.00%. Data in Table 3 show the mechanism of pseudo second-order adsorption is pre-dominant, and the rate of the all three acid dye adsorption process seems to be guarded by the chemical adsorption process (Hameed et al., 2007).

Adsorption of Acid Dyes onto Zinc Chloride-Modified Cocoa

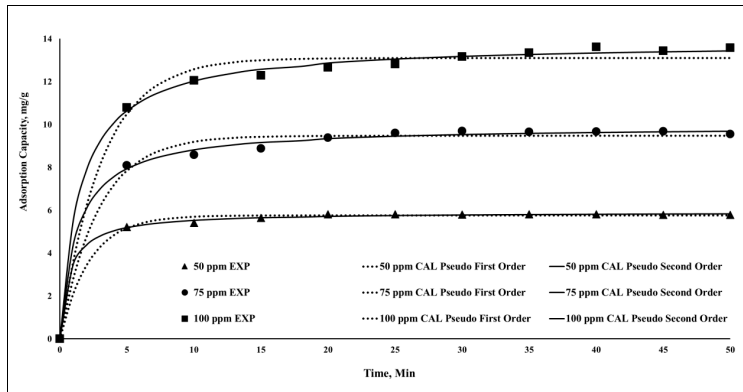


Figure 4. Adsorption kinetic model by a non-linear method for adsorption of AV17 onto ZCPHC

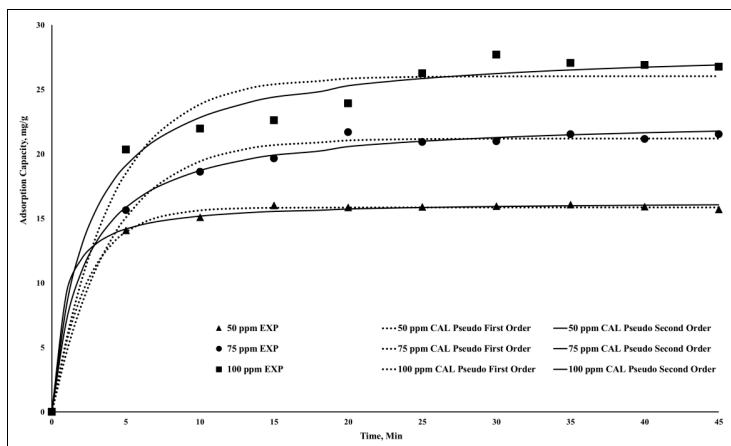


Figure 5. Adsorption kinetic model by a non-linear method for adsorption of AY36 onto ZCPHC

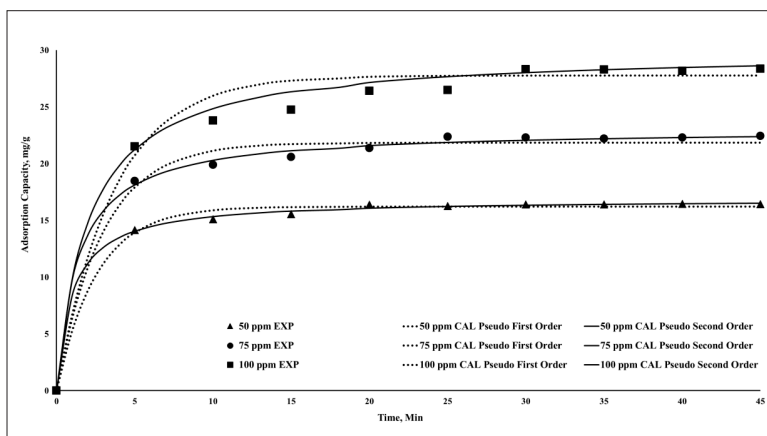


Figure 6. Adsorption kinetic model by a non-linear method for adsorption of AB29 onto ZCPHC

Table 2

Comparison between the first pseudo-order and second pseudo-order rate constant with the calculated and experimental q_e values for adsorption of various initial dye concentrations of understudy acid dyes onto ZCPHAC

Various Anionic Dyes	Initial Concentration (mg L ⁻¹)	$q_{e \text{ Exp}}$ (mg g ⁻¹)	Pseudo first-order kinetic model			Pseudo second-order kinetic model		
			$q_e \text{ Cal}$ (mg g ⁻¹)	R^2	SSE (%)	$q_e \text{ Cal}$ (mg g ⁻¹)	R^2	SSE (%)
AV17	50	5.81	5.75	0.99	0.10	5.71	0.99	0.05
	75	9.69	9.47	0.98	0.29	9.53	0.99	0.15
	100	13.62	13.10	0.98	0.40	13.34	0.99	0.17
AY36	50	16.01	15.83	0.99	0.20	15.56	0.99	0.19
	75	21.69	20.99	0.99	0.52	20.52	0.99	0.41
	100	27.70	25.96	0.96	1.54	26.19	0.98	1.00
AB29	50	16.39	16.20	0.99	0.36	16.07	0.99	0.16
	75	22.37	21.86	0.98	0.67	21.87	0.99	0.31
	100	28.31	27.27	0.97	1.18	27.51	0.99	0.60

CONCLUSION

Data indicated that zinc chloride-modified carbon prepared from agricultural waste that is cocoa pod husk carbons have suitable adsorption capacity with regards to the removal of Acid Violet 17, Acid Yellow 36 and Acid Blue 29 from its aqueous solution. The adsorption is highly dependent on pH and adsorbent dosage. The optimal pH for favourable adsorption of various acid dyes tested in this study is 2. The removal percentage is highly dependent on the adsorbent dosage, where high adsorbent dosage eventually leads to higher removal percentage of understudy acid dyes from aqueous solution. The adsorption kinetics of all the three acid dyes tested follows the pseudo-second-order kinetic model which shows the high value of correlation coefficient, R^2 (>0.98) and a lower percentage of SSE value (<1.00) as compared against pseudo-first-order kinetic model.

ACKNOWLEDGEMENTS

The authors gratefully acknowledge the scholarship provided by Ministry of Higher Education through MyBrain15 MyMaster programme and financial support by the Research Management Centre, Universiti Teknologi MARA under the ZAMALAH grant (600-RMI/DANA 5/3/PSF (13/2014)). We also gratefully acknowledge the support provided by Centre of Graduate Studies, Faculty of Applied Sciences, Universiti Teknologi MARA.

REFERENCES

- Adeyi, O. (2010). Proximate composition of some agricultural wastes in Nigeria and their potential use in activated carbon production. *Journal of Applied Science and Environmental Management*, 14(1), 55–58.

- Amin, N. K. (2009). Removal of direct blue-106 dye from aqueous solution using new activated carbons developed from pomegranate peel: Adsorption equilibrium and kinetics. *Journal of Hazardous Materials*, 165(1-3), 52–62.
- Babu, B. R., Parande, a K., Raghu, S., & Kumar, T. P. (2007). Cotton Textile Processing: Waste Generation and Effluent Treatment. *The Journal of Cotton Science*, 153(11:141), 141–153.
- Cobb, A., Warms, M., Maurer, E. P., & Chiesa, S. (2012). Low-Tech Coconut Shell Activated Charcoal Production. *International Journal for Service Learning in Engineering*, 7(1), 93–104.
- Crini, G. (2006). Non-conventional low-cost adsorbents for dye removal: A review. *Bioresource Technology*, 97(9), 1061–1085.
- Elizalde-Gonzalez, M. P., & Hernandez-Montoya, V. (2007). Characterization of mango pit as raw material in the preparation of activated carbon for wastewater treatment. *Biochemical Engineering Journal*, 36(3), 230–238.
- Hameed, B. H., Ahmad, A. L., & Latiff, K. N. A. (2007). Adsorption of basic dye (methylene blue) onto activated carbon prepared from rattan sawdust. *Dyes and Pigments*, 75(1), 143–149.
- Hameed, B. H., Tan, I. A. W., & Ahmad, A. L. (2008). Adsorption isotherm, kinetic modeling and mechanism of 2,4,6-trichlorophenol on coconut husk-based activated carbon. *Chemical Engineering Journal*, 144(2), 235–244.
- Hu, Z., & Vansant, E. F. (1995). A New Composite Adsorbent Produced by Chemical Activation of Elutrilithe with Zinc Chloride. *Journal of Colloid and Interface Science*, 176(2), 422–431.
- Ho, Y.S., & McKay, G. (1998). Process Saf. Environ. Prot: *Trans. Inst. Chem. Eng. Part B*, 76, 332–340.
- Hesas, R. H., Arami-Niya, A., Daud, W. M. A. W., & Sahu, J. N. (2013). Comparison of oil palm shell-based activated carbons produced by microwave and conventional heating methods using zinc chloride activation. *Journal of Analytical and Applied Pyrolysis*, 104, 176-184.
- Kwaghger, A. & Adejoh, E., (2012). Optimization of condition for the preparations of activated carbon from mango nuts using ZnCl₂. *International Journal of Engineering Research and Development*, 1(8), 1-7.
- Mahamad, M. N., Zaini, M. A. A., & Zakaria, Z. A. (2015). Preparation and characterization of activated carbon from pineapple waste biomass for dye removal. *International Biodeterioration and Biodegradation*, 102, 274–280.
- Métivier-Pignon, H., Faur-Brasquet, C., & Le Cloirec, P. (2003). Adsorption of dyes onto activated carbon cloths: Approach of adsorption mechanisms and coupling of ACC with ultrafiltration to treat coloured wastewaters. *Separation and Purification Technology*, 31(1), 3–11.
- Ofori-Boateng, C., & Lee, K. T. (2013). The potential of using cocoa pod husks as green solid base catalysts for the transesterification of soybean oil into biodiesel: Effects of biodiesel on engine performance. *Chemical Engineering Journal*, 220, 395–401.
- Ozdemir, I., Şahin, M., Orhan, R., & Erdem, M. (2014). Preparation and characterization of activated carbon from grape stalk by zinc chloride activation. *Fuel Processing Technology*, 125, 200–206.
- Soleimani, M. & Kaghazchi, T. (2007), Agricultural Waste Conversion to Activated Carbon by Chemical Activation with Phosphoric Acid. *Chemical Engineering Technology*, 30, 649–654.

- Salleh, M. A. M., Mahmoud, D. K., Karim, W. A. W. A., & Idris, A. (2011). Cationic and anionic dye adsorption by agricultural solid wastes: A comprehensive review. *Desalination*, 280(1-3), 1–13.
- Shukla, A., Zhang, Y. H., Dubey, P., Margrave, J. L., & Shukla, S. S. (2002). The role of sawdust in the removal of unwanted materials from water. *Journal of Hazardous Materials*, 95(1-2), 137–152.
- Tan, I. A. W., Hameed, B. H., & Ahmad, A. L. (2007). Equilibrium and kinetic studies on basic dye adsorption by oil palm fibre activated carbon. *Chemical Engineering Journal*, 127(1-3), 111–119.
- Tan, I. A. W., Ahmad, A. L., & Hameed, B. H. (2008). Adsorption of basic dye using activated carbon prepared from oil palm shell: batch and fixed bed studies. *Desalination*, 225(1-3), 13–28.
- Tuah, Y. (2013). Commodities: Malaysia's natural treasures. Retrieved November 14, 2014, from <http://www.theborneopost.com/2013/08/25/commodities-malaysias-natural-treasures/>
- Wang, L., Zhang, J., Zhao, R., Li, C., Li, Y., & Zhang, C. (2010). Adsorption of basic dyes on activated carbon prepared from *Polygonum orientale* Linn: Equilibrium, kinetic and thermodynamic studies. *Desalination*, 254(1-3), 68–74.
- Yagub, M. T., Sen, T. K., Afroze, S., & Ang, H. M. (2014). Dye and its removal from aqueous solution by adsorption: A review. *Advances in Colloid and Interface Science*, 209, 172–184.
- Yang, T., & Lua, A. C. (2003). Characteristics of activated carbons prepared from pistachio-nut shells by potassium hydroxide activation. *Microporous and Mesoporous Materials*, 63(1-3), 113–124.

New Method of Curve Number Derivation with Inferential Statistics

Lloyd Ling^{1,2*}, Zulkifli Yusop² and Yuk Feng Huang¹

¹Centre for Disaster Risk Reduction, Department of Civil Engineering, Lee Kong Chian Faculty of Engineering and Science, Universiti Tunku Abdul Rahman (UTAR), Jalan Sungai Long, Bandar Sungai Long, 43000 Cheras, Selangor, Malaysia

²Centre for Environmental Sustainability and Water Security, Research Institute for Sustainable Environment, Faculty of Civil Engineering Department, Universiti Teknologi Malaysia (UTM), 81310 Skudai, Johor, Malaysia

ABSTRACT

The selection of curve number to represent watersheds with similar land use and land cover is often subjective and ambiguous. Watershed with several soil groups further complicates curve number selection process while wrong curve number selection often produces unrealistic runoff estimates. The 1954 simplified Soil Conservation Services (SCS) runoff model over-predicted runoff with significant amount and further magnified runoff prediction error toward higher rainfall depths in this study. The model was statistically insignificant with the rejection of two null hypotheses and paved the way for regional model calibration study. This paper proposes a new direct curve number derivation technique from the given rainfall-runoff conditions under the guide of inferential statistics. The technique offers a swift and economical solution to improve the runoff prediction ability of the SCS runoff model with statistically significant results. A new rainfall-runoff model was developed with calibration according to the regional hydrological conditions. It out-performed the runoff prediction of the simplified SCS runoff model and the asymptotic runoff model. The derived curve number = 89 at alpha = 0.01 level. The technique can be adopted to predict flash flood and forecast urban runoff.

Keywords: Bootstrapping, CN, non-parametric inferential statistics, runoff prediction, SCS

ARTICLE INFO

Article history:

Received: 28 September 2016

Accepted: 03 February 2017

E-mail addresses:

linglloyd@utar.edu.my (Lloyd Ling),

zulyusop@utm.my (Zulkifli Yusop),

huangyf@utar.edu.my (Yuk Feng Huang)

*Corresponding Author

INTRODUCTION

In Malaysia, surface runoff contributed about 97% of total water demand (Department of Irrigation and Drainage (DID), 2000). As a result of rapid urban development and growing anthropogenic activities, frequency of flooding in downstream urban watersheds have increased significantly (Adams & Papa,

2000). Therefore, a thorough understanding of the rainfall-runoff processes is crucial for the planning and management of water resources (Chan, 2005).

In 1954, the United States Department of Agriculture (USDA) Soil Conservation Services (SCS) proposed a rainfall-runoff prediction model. It even led to the derivation and development of curve number (CN) methodology. Since its inception, the model was incorporated into many official hydro design manuals worldwide and was also adopted by Malaysian agencies. Nevertheless, the major limitation of the model is its inability to predict runoff results accurately where researchers reported inconsistent runoff prediction results throughout the world and casted doubt on the validity of the model (Sharpley & Williams, 1990; Hawkins & Khojeini, 2000; Hawkins et al., 2002; Baltas et al., 2007; Elhakeem & Papanicolaou, 2009; Shi et al., 2009; Shumei & Tingwu, 2011; D'Asaro & Grillone, 2012; Ling & Yusop, 2013; D'Asaro et al., 2014; Yuan et al., 2014). According to the National Engineering Handbook (NEH-4) Soil Conservation Services, Curve Number (SCS-CN) is one of the most popular methods to compute the volume of direct surface runoff amount from a rainfall event (USDA-SCS, 1964, 1972). It is also most frequently used to estimate direct runoff from un-gaged areas. The SCS defined CN as a function of maximum potential retention (S) of a watershed which can also be implied as the water storage ability of different land cover conditions. Tabulated SCS-CN value ranged from 0 to 100 to represent a watershed with infinite infiltration to fully impermeable respectively. In general, observed CN values range from 40 to 98 but forested watersheds may have lower CN values (Van Mullem et al., 2002). The SCS Technical Release 55 (TR-55) tabulated discrete site conditions classification to demarcate CN selection. Forested watersheds faced the utmost challenge in terms of appropriate CN classification and faced huge risk of potential misclassification (Hawkins, 1984) while wrong CN selection often produces unrealistic runoff estimates (Cazier & Hawkins, 1984; Hawkins, 1993).

A common approach for SCS practitioners was to perform "trial and error" CN tweaking with observed data in order to improve the runoff prediction results. However, such practice lacks statistical justification. The practice might produce CN value for a watershed but the "calibrated" CN value might not be able to even represent the same land use and land cover condition again in other watersheds. The CN variation affects direct runoff estimates more than rainfall variability. Several researches concluded CN as a random variable between storm events and varied based on the antecedent runoff condition (ARC) of storm events (Hjelmfelt, 1991; Van Mullem et al., 2002). In situ measurement of site CN becomes difficult while watershed with several soil groups further complicates CN selection process. SCS-CN method almost offers no guidance to account for runoff generation under dry and wet conditions. The SCS practitioners often adopt the model for the sake of its simplicity and rarely explore site specific calibration possibility leading to inconsistent or poor runoff estimate results (Ponce & Hawkins, 1996).

The selection of CN to represent a watershed often becomes subjective, ambiguous and even inconsistent to represent similar land cover area (Hawkins, 1984). As such, there is an imminent need for hydrologists and modellers to improve the modelling approach. The CN values should be determined from rainfall-runoff ($P-Q$) dataset in order to reflect the realistic local situations (Hjelmfelt, 1980; Hawkins, 1993; Hawkins & Ward, 1998; Soulis et al.,

2009; Soulis & Valiantzas, 2013). In literature, various methods for CN determination from observed P - Q data have been reported. The most common and widely used are least-squares method (LSM) (Hawkins et al., 2002) and asymptotic fitting method (AFM) (Hawkins, 1993; Hawkins et al., 2009). This article presents the new approach to derive regional specific CN directly from P - Q dataset with the guide from inferential statistics. The base SCS model was proposed in 1954 as below:

$$Q = \frac{(P - I_a)^2}{P - I_a + S} \quad [1]$$

Q = Runoff amount (mm)

P = Rainfall depth (mm)

I_a = the initial abstraction (mm)

S = maximum potential water retention of a watershed (mm)

The initial abstraction is also known as the initial rainfall retention prior to the initiation of runoff process. The SCS also hypothesised that $I_a = \lambda S = 0.20S$. The value of 0.20 was proposed as a constant and referred to as the initial abstraction coefficient ratio (λ) which is a correlation parameter between I_a and S . The substitution of $I_a = 0.20S$ simplifies Eq. [1] into a common and widely adopted simplified SCS runoff prediction model listed below:

$$Q = \frac{(P - 0.2S)^2}{P + 0.8S} \quad [2]$$

Eq. [2] is subjected to a constraint that $P > 0.2S$, else $Q = 0$. However, the increasing evidential study results are leaning against the prediction accuracy of Eq. [2] and the hypothesis that $I_a = 0.20S$. This study performed regional hydrological conditions calibration according to the given P - Q dataset instead of blindly adopting Eq. [2]. The proposed CN derivation methodology utilised supervised numerical optimisation algorithm guided by inferential statistics to derive λ and S value for the formulation of a new rainfall-runoff model based on Eq. [1].

METHOD

The present authors are unaware of any previous attempts to perform regional hydrological characteristics calibration with inferential statistics on the SCS base runoff prediction model (Eq. 1) and apply it in urban runoff study in Malaysia until now. This study adopted the rainfall-runoff dataset from a research which was carried out in Melana watershed. It is located in Johor between 1° 30' N to 1° 35' N and 103° 35' E to 103° 39' E (Figure 1). Drained by Melana River which starts in the hilly area of Gunung Pulai in the north, the watershed covers an area of 21.12 km². Melana watershed underwent rapid urbanisation whereby in 1993, about 20% of the area in Melana watershed was covered by urbanised area; by 2010, more than 60% of the area was developed as residential area (Majlis Perbandaran Johor Bahru Tengah (MPJBT), 2001). This study derived CN value and formulated a calibrated SCS runoff predictive model for Melana watershed through rainfall-runoff dataset directly.

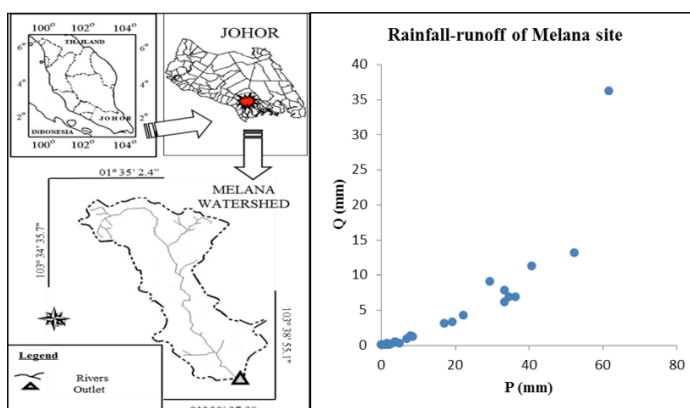


Figure 1. Melana watershed in Johor (Chan, 2005) and its rainfall-runoff graph

A total of 27 rainfall-runoff data pairs were recorded between July and October of 2004 at this site. This study used rainfall-runoff dataset which was collected within a short period in order to minimise the impact of further land use and land cover change. Inferential statistics was conducted by using IBM PASW version 18. Non-parametric Bootstrapping technique, Bias corrected and accelerated (BCa) procedure with 2,000 sampling (Efron & Tibshirani, 1994; Efron, 2010) was conducted at 99% confident interval (CI) for the derivation of key parameters (λ and S) in order to calibrate Eq. [1] (Wright, 1997; Howell, 2007; Rochoicz, 2011). Bootstrapping BCa statistics was selected for its robustness and the inferential ability through its confident interval (Davison & Hinkley, 1997; Young, 2005; Cox, 2006).

Eq. [1] can be re-arranged to solve for $S = f(P, Q, \lambda)$. Substitute $I_a = \lambda S$ into Eq. [1] and isolate S through completing the square technique will yield the S general formula. Different λ will yield different S value, denotes by S_λ . New derived λ value will have a corresponding S_λ value which is different from $S_{0.2}$ (where $\lambda = 0.2$). Given P - Q data pairs of any storm event, when λ value is known, the general S_λ formula can be used to derive its corresponding S values. When $\lambda = 0.2$, the corresponding $S_{0.2}$ value leads to the derivation of the conventional CN ($CN_{0.2}$) value(s) which has been in use since 1954. Any other λ value will result in S_λ leading to the derivation of CN_λ known as the “Conjugate CN” (Jiang, 2001; Hawkins et al., 2009; Hawkins, 2014). In the event that the calibrated optimum λ value is different from the conventional value where $\lambda = 0.2$, a correlation between S_λ and $S_{0.2}$ must be identified in order to convert the CN_λ back to an equivalent $CN_{0.2}$ with the CN formula ($CN = \frac{25,400}{S+254}$) which was proposed by SCS for CN comparison. The general S_λ formula which we solved is listed below:

$$S_\lambda = \frac{\left[P - \frac{(\lambda-1)Q}{2\lambda} \right] - \sqrt{PQ - P^2 + \left[P - \frac{(\lambda-1)Q}{2\lambda} \right]^2}}{\lambda} \quad [3]$$

Non-parametric inferential statistics were employed for two claim assessments set forth by the 1954 SCS proposal with two null hypotheses (Young, 2005; Cox, 2006). Both hypotheses will assess Eq. [2] on its validity according to the site dataset.

Null Hypothesis 1 (H_{01}): Eq. [2] is applicable globally with the assumption of: $I_a = 0.20S$.

Null Hypothesis 2 (H_{02}): The value of 0.20 is a constant in Eq. [2].

Rejection of H_{01} implies that Eq. [2] is invalid and not applicable to model runoff conditions of Melana watershed, while H_{02} rejection indicates that λ is not a constant as initially proposed by SCS in 1954 but a variable. Rejection of both hypotheses will pave way to derive new regional specific λ value. The P - Q data pairs from Melana watershed were used to derive S and λ values. The difference of rainfall depth (P) and initial abstraction (I_a) is the effective rainfall depth (P_e) to initiate runoff (Q) thus $P - I_a = P_e$ (Schneider & McCuen, 2005; Hawkins et al., 2009; Hawkins, 2014). If this relationship is expressed as Eq. [1], the model can be re-arranged in order to calculate corresponding S and λ value for each P - Q data pair. Bootstrapping, Bias corrected and accelerated (BCa) procedure was then used to aid numerical optimisation technique in the selection of the optimum λ and S value to represent the entire dataset within the BCa confident intervals (Hansen, 1992; Fattorini, 1999). The selection of the optimum λ and S value will then formulate a new calibrated SCS runoff prediction model of Melana watershed. Past researchers used AFM to determine the representative CN for the watershed of interest through its P - Q dataset (Hawkins, 1973; Hjelmfelt, 1980; Zevenbergen, 1985; Sneller, 1985; Hjelmfelt et al., 2001; Van Mullem et al., 2002; Hawkins et al., 2009) and therefore, the asymptotic CN will also be derived for the formulation of another rainfall-runoff model for Melana watershed. This study will assess and benchmark the runoff prediction accuracy of the new calibrated SCS runoff prediction model against Eq. [2] and the Asymptotic CN runoff model.

Runoff Models Assessment

Model's prediction efficiency index (E also known as Nash-Sutcliffe index), residual sum of squares (RSS) and predictive model $BIAS$ are calculated in order to draw further comparison between different runoff model with following formulas:

$$RSS = \sum_{i=1}^n (Q_{predicted} - Q_{observed})^2 \quad [4]$$

$$E = 1 - \frac{RSS}{\sum_{i=1}^n (Q_{predicted} - Q_{mean})^2} \quad [5]$$

$$BIAS = \frac{\sum_{i=1}^n (Q_{predicted} - Q_{observed})}{n} \quad [6]$$

Q = Runoff amount (mm)

n = Total number of data pairs

RSS value indicates the residual spread from a model. Lower RSS indicates a better runoff predictive model. Model efficiency index (E) ranges from minus to 1.0 where index value = 1.0 indicates a perfect predictive model. When $E < 0$, the predictive model performs worse than using the average to predict the dataset. Predictive model $BIAS$ shows the overall model

prediction error calculated by the summation of predictive model's residual to indicate the overall model prediction pattern. Zero *BIAS* value indicates a perfect overall runoff model prediction with no error, the negative value indicates the overall model tendency of under-prediction in runoff and vice versa.

RESULTS AND DISCUSSION

Statistics and Null Hypotheses Assessment

Twenty-seven λ values were derived from Melana dataset with the proposed methodology. λ optimization study was conducted via numerical analyses approach based on Eq. [1]. The supervised numerical optimisation algorithm was set to identify an optimum λ value by minimizing the *RSS* between final runoff model's predicted Q and its observed values. λ value was optimised within the BCa CI at alpha = 0.01 level. The descriptive statistics of the data distribution of twenty-seven derived λ values was tabulated in Table 1.

Table 1
Bootstrapping BCa 99% CI results of derived λ values at Melana watershed

Melana dataset	Descriptive Statistics λ	(λ) 99% Lower	BCa Upper	Descriptive Statistics S	(S) 99% Lower	BCa Upper
Mean	0.059	0.009	0.154	58.083	37.191	81.958
Median	0.009	0.004	0.015	42.120	23.600	90.600
Skewness	4.677			0.771		
Kurtosis	22.778			-0.593		
Std. Deviation	0.188	0.013	0.306			

The supervised optimisation study was based on λ variation within the median confident interval [0.004, 0.015] due to the skewed λ dataset (Table 1). The optimised λ value was identified as 0.015. The skewness of S dataset is near to zero which can be considered as normal hence the S optimisation was conducted within [37.191, 81.958]. The best collective representation S value was identified as 81.804 mm for Melana watershed. Since $I_a = \lambda S$ the substitution of λ and S value yields $I_a = 1.248$ mm. With the substitution of I_a and S back to Eq. [1], the calibrated SCS rainfall-runoff prediction model was formulated as:

$$Q_{0.015} = \frac{(P - 1.248)^2}{P + 80.555} \quad [7]$$

The formulation of the calibrated SCS runoff prediction model Eq. [7] using the optimum λ and S value will have the same inherent significant level (at alpha = 0.01). BCa results provided CI span for λ at Melana watershed (Table 1) which can also be used to assess Null hypotheses. The span of λ BCa CI was used to assess H_{01} while H_{02} assessment was based on the standard deviation of the derived λ dataset (Ling & Yusop, 2014, 2014b). The standard deviation of λ

dataset is not equal to zero but with high variation percentages to imply the fluctuation nature of λ . Neither the mean nor the median's BCa CI span includes λ value of 0.2 (Table 1) and therefore, $\lambda \neq 0.2$ for this dataset. H_{01} and H_{02} were both rejected at alpha = 0.01 level. As such, Eq. [2] is statistically insignificant and invalid to model runoff.

The Correlation between $S_{0.015}$ and $S_{0.2}$ for Melana Watershed

$S_{0.015}$ and $S_{0.2}$ can be calculated for the P - Q dataset using Eq. [3] through the substitution of respective $\lambda = 0.015$ and 0.20 corresponding to the same P - Q dataset for Melana watershed. A statistical significant correlation between $S_{0.051}$ and $S_{0.2}$ is expressed as:

$$S_{0.2} = 0.366S_{0.015}^{1.013} \tag{8}$$

$S_{0.051}$ = Total abstraction amount (mm) of $\lambda = 0.051$

$S_{0.2}$ = Total abstraction amount (mm) of $\lambda = 0.2$

Eq. [8] has an adjusted $R^2 = 0.962$, standard error = 0.325 and $p < 0.001$. Since the best collective representation $S_{0.051}$ value was calculated as 81.804 mm for Melana watershed, its equivalent value of $S_{0.2}$ can be determined from Eq. (8). Through the substitution of the $S_{0.2}$ parameter in SCS-CN formula ($CN = \frac{25.400}{S_{0.2} + 254}$) and derive the CN value of 89 to represent the given runoff condition of Melana watershed. On the other hand, when $\lambda = 0.2$, the best collective $S_{0.2} = 23.35$ mm for SCS model which led to the CN value of 92. The substitution of $S_{0.2}$ value into Eq. [2] formulated the SCS runoff model to predict runoff conditions at Melana watershed.

The Asymptotic CN of Melana Watershed

Using the Asymptotic CN fitting method, CN_∞ was derived as 81.72 as shown in Figure 2. Rounding to the nearest positive integer, $CN_\infty = CN_{0.2} = 82$ for Melana watershed.

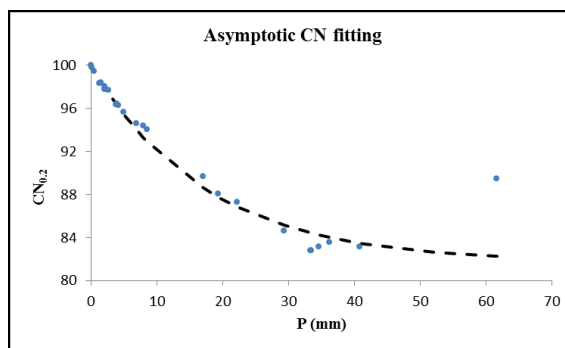


Figure 2. For AFM, standard behaviour pattern, $CN_\infty = 82$

Through SCS-CN formula ($CN = \frac{25,400}{S_{0.2} + 254} = 82$), the $S_{0.2}$ value of the asymptotic CN can be calculated as 56.8 mm and $I_a = 0.20 \times 56.8 \text{ mm} = 11.36 \text{ mm}$. These values are used to formulate an Asymptotic runoff model using Eq. [1] and benchmark its runoff prediction accuracy against Eq. [2] and [7]. The assessment and comparison of runoff models' prediction results are shown in Table 2.

Table 2
Descriptive statistics and 99% BCa results of three runoff predictive models

Predictive model	Asymptotic model	Eq. [7]	Eq. [2]
<i>E</i>	0.82	0.87	0.37
<i>RSS</i>	264.70	193.20	910.37
<i>BIAS</i>	-4.63	0.07	3.11
$CN_{0.2}$	82	89	92
Residual Skewness	-2.39	-1.74	1.71
Residual Kurtosis	8.39	9.63	2.55
Median Residual	0.62	-0.10	0.89
Median Residual: 99% BCa CI	[-1.04, 1.66]	[-0.31, -0.01]	[0.00, 3.64]
Model error Standard Deviation	3.19	2.73	4.99
Residual Variance	10.16	7.43	24.98

Eq. [7] has lowest *RSS* with highest *E* index compared with the other two runoff models. Every model's residual skewness and Kurtosis are greater than 1.0 and hence, the median residual value can be used as the indicator for predictive model's accuracy. Eq. [7] has the median residual value and 99% BCa confident interval range nearest to zero which indicates that the model is capable of achieving near to zero (residual) runoff prediction error ($p < 0.01$). On the contrary, Eq. [2] tends to over predict runoff amount as its median residual confident interval range spans within positive figures only. Eq. [7] also has the lowest standard deviation and variance in its model's residual with smaller confident interval ranges than the other two models and therefore, is the most stable and reliable runoff predictive model for the dataset in this study.

CONCLUSION

This study affirmed that the SCS runoff prediction model had to be calibrated according to regional specific characteristics. Inferential statistics assessment rejected both H_{01} and H_{02} at $\alpha = 0.01$ level. Therefore, Equation [2] became obsolete and not applicable to model runoff conditions in this study. Blind adoption of Eq. [2] will commit a type II error.

A new CN derivation approach was presented with supervised numerical optimisation technique under the guide of inferential statistics. The new calibrated runoff predictive model out-performed its counterpart models. It has high model efficiency (*E*), low *BIAS* with 99% BCa confident level and *RSS* to produce the smallest runoff prediction error. As such, the derived CN value of 89 to represent the given runoff conditions of Melana watershed also has the inherent

statistical significance at $\alpha = 0.01$ level. This study proved that SCS base runoff predictive model can be calibrated to predict urban runoff conditions accurately.

On average, Eq. [2] over-predicted nearly 150,000 m³ at rainfall depth scenarios larger than 16 mm in comparison to the Eq. [7] in this study. The over-prediction risk (error) was significant and further magnified by increased rainfall. Rapid urbanisation and landscape change post a challenge to correctly identify CN according to tabulated handbook value. Extreme weather conditions due to global climate change will compound the challenge to induce frequent unexpected flash flood at unseen magnitude. Direct CN derivation from the given rainfall-runoff conditions offers a swift and economical solution to restore the runoff prediction ability of the SCS runoff model and it can be calibrated for a specific region to reflect the latest rainfall-runoff condition.

It is noteworthy to mention that the extrapolation of Eq. [7] to higher rainfall depths will involve unknown uncertainties as the dataset of this study has an upper constraint of 62 mm. However, the authors already calibrated the SCS model to achieve high runoff prediction accuracy with bigger dataset up to 427 mm rainfall depth with this method in Peninsula Malaysia in another study. Design engineers and SCS practitioners are encouraged to conduct regional specific calibration for SCS rainfall-runoff model.

ACKNOWLEDGEMENTS

The authors would like to thank Universiti Tunku Abdul Rahman, Centre for Disaster Risk Reduction and Universiti Teknologi Malaysia, Centre for Environmental Sustainability and Water Security, Research Institute for Sustainable Environment of UTM, vote no. Q. J130000.2509.07H23 and R. J130000.7809.4L175 for its financial support to undertake this study. This study was also supported by the Asian Core Program of the Japanese Society for the Promotion of Science (JSPS) and the Ministry of Higher Education (MOHE) Malaysia. The authors would also like to acknowledge the guidance provided by Professor Richard H. Hawkins (University of Arizona, USA).

REFERENCES

- Adams, B. J., & Papa, F. (2000). *Urban Stormwater Management Planning with Analytical Probabilistic Models*. New York: John Wiley & Son.
- Baltas, E. A., Dervos, N. A., & Mimikou, M. A. (2007). Determination of the SCS initial abstraction ratio in an experimental watershed in Greece. *Hydrol. Earth Syst. Sci.*, 11, 1825–1829.
- Cazier, D. J., & Hawkins, R. H. (1984). Regional application of the curve number method. In *Water Today and Tomorrow, Proceedings, ASCE Irrigation and Drainage Division Special Conference*, Replogle JA (ed.). ASCE: New York, NY.
- Chan, C. H. (2005). *Modelling Watershed Cumulative Effects on Runoff Based on Major Land Uses* (Master's thesis).
- Cox, D. R. (2006). *Principles of Statistical Inference*, Cambridge University Press. ISBN 0-521-68567-2.
- D'Asaro, F., & Grillone, G. (2012). Empirical investigation of curve number method parameters in the Mediterranean area. *Journal of Hydrologic Engineering*, 17, 1141–1152.

- D'Asaro, F., Grillone, G., Hawkins, R. H., (2014). Curve number: empirical evaluation and comparison with curve number handbook tables in Sicily. *Journal of Hydrologic Engineering*, 19(12), 04014035 (1–13).
- Davison, A. C., & Hinkley, D. V. (1997). *Bootstrap methods and their application*. Cambridge Series in Statistical and Probabilistic Mathematics. Cambridge University Press. ISBN 0-521-57391-2.
- Department of Irrigation and Drainage (DID). (2000). *Urban Stormwater Management Manual for Malaysia*. Kuala Lumpur, Malaysia.
- Efron, B. (2010). *Large-Scale Inference: Empirical Bayes Methods for Estimation, Testing, and Prediction*. Institute of Mathematical Statistics Monographs/Cambridge University Press. ISBN 9780521192491.
- Efron, B., & Tibshirani, R. (1994). *An Introduction to the Bootstrap*. Chapman & Hall/CRC. ISBN 978-0-412-04231-7.
- Elhakeem, M., & Papanicolaou, A. N., (2009). Estimation of the runoff curve number via direct rainfall simulator measurements in the state of Iowa, USA. *Water Resources Management*, 23(12), 2455–2473.
- Fattorini, H. O. (1999). *Infinite Dimensional Optimization and Control Theory*, Cambridge Univ. Press, 1999.
- Hansen, E. R. (1992), *Global Optimization using Interval Analysis*, Marcel Dekker, NY.
- Hawkins, R. H. (1984). *A comparison of predicted and observed runoff curve numbers*, In ASCE, Special Conference of Irrigation and Drainage Division, pp. 702–709.
- Hawkins, R. H. (1973). Improved prediction of storm runoff in mountain watersheds. *J. Irrig. Drain. Div.*, 99(4), 519–523.
- Hawkins, R. H. (1993). Asymptotic determination of runoff curve numbers from data. *J. Irrig. Drain. Eng.*, 119(2), 334–345.
- Hawkins, R. H. (2014 e-mail communication).
- Hawkins, R. H., & Khojeini, A. (2000). Initial Abstraction and Loss in the Curve Number Method, in Arizona Hydrological Society Proceedings.
- Hawkins, R. H., & Ward, T. J. (1998). Site and cover effects on event runoff, Jornada Experimental Range, New Mexico. In Proceedings: American Water Resource Association Conference on Rangeland Management and Water Resources (pp. 361-370). Reno, NV.
- Hawkins, R. H., Jiang, R., Woodward, D. E., Hjelmfelt, A. T., van Mullem, J. A., & Quan, Q. D. (2002). Runoff curve number method: examination of the initial abstraction ratio. Proceedings of the Second Federal Interagency Hydrologic Modeling Conference. ASCE Publications, Las Vegas.
- Hawkins, R. H., Ward, T., Woodward, D. E., & Van Mullem, J. (2009): *Curve Number Hydrology: State of the Practice*. Reston, Virginia, ASCE.
- Hjelmfelt, A. T. (1980). Empirical investigation of curve-number technique. *Journal of Hydraulic Division*, 106(9), 1471–1476.
- Hjelmfelt, A. T. (1991). Investigation of Curve Number Procedure. *Journal of Hydraulic Engineering*, 117(6):725-737.

- Hjelmfelt, A. T., Woodward, D. A., Conaway, G., Quan, Q. D., Van Mullem, J., & Hawkins, R. H. (2001, September). Curve numbers, recent developments. *In XXIX IAHR Congress Proceedings, Beijing, China*.
- Howell, D. C. (2007). *Statistical methods for psychology (6th Ed.)*. CA: Thomson Wadsworth, Belmont.
- Jiang, R. (2001). Investigation of Runoff Curve Number, Initial Abstraction Ratio, University of Arizona.
- Ling, L., & Yusop, Z. (2013). A micro focus with macro impact: Exploration of initial abstraction coefficient ratio (λ) in Soil Conservation Curve Number (CN) methodology. *IOP Conf. Ser.: Earth Environ. Sci.* issue 1.
- Ling, L., & Yusop, Z. (2014). Inferential Statistics of Claim assessment. *AIP Conference Proceedings*: ISBN: 978-0-7354-1274-3.
- Ling, L., & Yusop, Z. (2014b). Inferential Statistics Modelling and Claim re-assessment. *ICCEMS Conference Proceedings*: ISBN: 978-967-11414-7-2.
- Majlis Perbandaran Johor Bahru Tengah (MPJBT). (2001). *Rancangan Tempatan Skudai (1993-2010)*. Johor Bahru, Malaysia: Pihak Berkuasa Perancangan Tempatan Daerah Jahor Bahru.
- Ponce, V. M., & Hawkins, R. H. (1996). Runoff Curve Number: Has It Reached Maturity?. *Journal of Hydrologic Engr.* 1(1), 11–19.
- Rochoxicz Jr, J. A. (2011). Bootstrapping Analysis, Inferential Statistics and EXCEL. *Spreadsheets in Education (eJSiE)*. 4(3).
- Schneider, L. E., & McCuen, R. H. (2005). Statistical guidelines for curve number generation. *Journal of Irrigation and Drainage Engineering*, 131(3), 282-290.
- Sharpley, A. N., & Williams, J. R. (1990). EPIC-erosion/productivity impact calculator: 1. Model determination. *Technical Bulletin*, No. 1768US Department of Agriculture.
- Shi, Z. H., Chen, L. D., Fang, N. F., Qin, D. F., & Cai, C. F. (2009). *Research on the SCS-CN initial abstraction ratio using rainfall-runoff event analysis in the Three Gorges Area, China*. *Catena*, 77, 1–7.
- Shumei, Z., & Tingwu, L. (2011). Calibration of SCS-CN Initial Abstraction Ratio of a typical small watershed in the Loess Hilly-Gully region. *China Agriculture Science*.
- Sneller, J. A. (1985). "Computation of runoff curve number from landsat data." Technical rep. HL86-2, United States Department of Agriculture- Agricultural Research Service Hydrology Laboratory, Beltsville, MD, 52.
- Soulis K. X., & Valiantzas J. D. (2013), Identification of the SCS-CN parameter spatial distribution using rainfall-runoff data in heterogeneous watersheds, *Water Resour. Manage*, in press, DOI: 10.1007/s11269-012-0082-5
- Soulis, K. X., Valiantzas, J. D., Dercas, N., & Londra, P. A. (2009). Investigation of the direct runoff generation mechanism for the analysis of the SCS-CN method applicability to a partial area experimental watershed. *Hydrol. Earth Syst. Sci.*, 13(5), 605–615.
- USDA-SCS. (1964). *National engineering handbook, Sect. 4 Hydrology*, Washington, DC.
- USDA-SCS. (1972). *National engineering handbook, Sect. 4 Hydrology*, Washington, DC.

- Van Mullem, J. A., Woodward, D. E., Hawkins, R. H., Hjelmfelt, A. T., & Quan, Q. D. (2002, July). Runoff curve number method: Beyond the handbook. In *Proceedings of Second Federal Interagency Hydrologic Modeling Conference, Las Vegas, Nevada*.
- Wright, D. B. (1997). *Understanding statistics: an introduction for the social sciences*. London, Sage.
- Young, G. A., & Smith, R. L. (2005). *Essentials of Statistical Inference*, CUP. ISBN 0-521-83971-8.
- Yuan, Y., Nie, J., McCutcheon, S. C., & Taguas, E. V. (2014). Initial abstraction and curve numbers for semiarid watersheds in south eastern Arizona. *Hydrol. Process.* 28, 774–783.
- Zevenbergen, A. D. (1985). "Runoff curve numbers for rangeland landsat data." Technical Rep. HL85-1, United States Dept. of Agriculture-Agricultural Research Service Hydrology Laboratory, Beltsville, MD, 72.



Discrepancy in the Accuracy of Vision Screening Program Performed by Allied Health Personnel in a Preschool

Nurul Farhana Abu Bakar¹ and Ai-Hong Chen^{2*}

¹*Pejabat Komuniti Penyelidikan (CoRe), Institut Pengurusan Penyelidikan dan Inovasi (IRMI), Aras 3, Bangunan Wawasan, Universiti Teknologi MARA (UiTM), 40450 Shah Alam, Selangor, Malaysia*

²*Optometry, Faculty of Health Sciences, Universiti Teknologi MARA (UiTM) Selangor, 42300 Bandar Puncak Alam, Selangor, Malaysia*

ABSTRACT

The purpose of this study is to assess the performance of allied health personnel, after attending a training programme, in conducting vision screening for preschool children. A total of 43 allied health personnel (20 assistant medical officers (AMOs) and 23 nurses) attended a two-day training program prior to conducting vision screening for preschool children. Vision screening was conducted among 136 preschool children using four similar HOTV visual acuity chart at 6 m. The cut-off referral criterion for visual acuity (VA) testing was 6/9 or worse in either eye. All children were referred to two qualified optometrists for a comprehensive eye examination. The accuracy was based on the sensitivity and specificity of screening by each group of personnel. The overall prevalence of reduced VA in the studied population was about 10%. The sensitivity and specificity of vision screening performed by AMOs were 100% and 98% respectively while that performed by nurses were 56% and 94% respectively. Thus, there were discrepancies in the sensitivity of visual acuity testing despite them being conducted by healthcare providers with similar background and training. This suggests that their performance might be influenced by factors other than their professional training.

Keywords: Accuracy, nurses, preschool, vision screening

ARTICLE INFO

Article history:

Received: 28 September 2016

Accepted: 03 February 2017

E-mail addresses:

farhana_sb@yahoo.com (Nurul Farhana Abu Bakar),

aihong0707@yahoo.com (Ai-Hong Chen)

*Corresponding Author

INTRODUCTION

Visual acuity testing is the most common method used in preschool vision screening worldwide (Adhikari & Shrestha, 2011; Khandekar et al., 2004; Sabri et al., 2016; Teerawattananon et al., 2014; The Vision in Preschoolers Study Group, 2005). Precision and accuracy of visual acuity testing is important as it may affect the efficacy of the

programme. The accuracy of vision testing, especially among young children, is determined by several factors such as tool selection, competency of vision screener and appropriate response by children. Findings of Vision in Preschooler (VIP) pointed to the discrepancy in visual acuity testing which depended on the format of the test, the screening environment and the vision screener (The Vision in Preschoolers Study Group, 2005).

Age-appropriate vision screening tool selection and modification of visual acuity testing techniques and procedures among young children have led to marked improvement in the testability and sensitivity of these tests regardless of the personnel assigned as vision screener (Anstice & Thompson, 2014; Fern & Manny, 1986). These findings imply that a child's physical and cognitive ability as well as its psychology might also influence the outcome of visual acuity testing.

Visual acuity testing was reported to be one of the most effective methods when performed by professional eyecare practitioners but showed much less effectiveness when performed by non-eyecare practitioners (The Vision in Preschoolers Study Group, 2005). However, screenings conducted by professionals in the national vision screening programme might not be ideal and practical considering their limited numbers as well as the issue of cost-effectiveness. The engagement of non-eyecare practitioners as vision screeners might be more suitable despite the competency issue as it could be managed through proper training (Adhikari & Shrestha, 2011; Khandekar et al., 2004; Sabri et al., 2016; The Vision in Preschoolers Study Group, 2005).

This study was aimed at assessing the performance of allied health personnel (nurses and AMOs) in conducting vision screening for preschool children after attending a two-day training program. The AMOs are classified as "medical assistant practitioners" in the International Standard Classification of Occupations, 2008 revision (World Health Organization (WHO), 2008). Both groups of allied health personnel completed a diploma programme under the Ministry of Health, Malaysia and have work experience of more than three years. The two groups of vision screeners were chosen because they were currently involved in the National School Health Service and in the Maternal and Child Health clinics.

METHOD

This cross-sectional study examined data collected in a preschool vision screening programme conducted in Sri Aman, Sarawak in October 2013. This project adhered to ethical considerations that were put forth in the Declaration of Helsinki, 1975. The approval to conduct vision examination was obtained from Sri Aman Department of Health and parental consent of all children who underwent the visual screening.

A total of 43 allied health personnel (20 assistant medical officers (AMOs) and 23 nurses) attended a two-day training programme prior to conducting vision screening for preschool children. In the training programme, the vision screeners were exposed to the objective of vision screening, brief description of the anatomy, physiology and pathology of the eye of young children as well as vision screening guidelines. The vision screening guidelines include

the planning and preparation for screening, vision screening methods and procedures, referral procedures and tips on effective communication with young children. All vision screeners were evaluated before and after training programme based on a theory examination which consisted of 20 multiple-choice questions.

All preschools in Sri Aman Division were invited to participate in a one-day vision screening programme. Five preschools responded and vision screening was conducted among 136 children aged between 4 and 6 years from participating preschools. All children underwent visual acuity (VA) testing using four similar HOTV visual acuity chart at 6 meters performed randomly either by AMOs or nurses. Visual acuity testing was performed under normal room illumination by using letter-matching technique. The cut-off referral criterion for VA testing was 6/9 or worse in either eye. The children were randomly selected for screening. However, their call number was given according to their age during registration and they were screened in groups according to age to reduce the possibility of screening more children in a certain age group. Based on the total number of registered children, the screening assessment was designed to ensure that each screener screened at least two children instead of three because there were screeners who were also involved in the registration procedures.

All children were referred to and examined by two qualified optometrists for refractive assessment as well as ocular function and ocular health examination after the screening procedure. Two similar VA chart were used by optometrists. Children were considered as having reduced vision if their habitual VA is 6/9 or worse in either eye caused by any refractive errors or ocular health conditions. Both vision screening and optometrist's examination results were double blinded by using different recording forms and conducted in separate rooms. The age and ethnicity of the children were determined based on information contained in their birth certificates.

Data entry and analysis were performed using SPSS version 15.0 (SPSS Inc., Chicago, IL, US). A non-parametric Wilcoxon Sign Rank test was used in the analysis of pre-and post-training evaluation score because data was not normally distributed. The evaluation on the performance of the vision screeners was based on the sensitivity and specificity of visual acuity testing confirmed by optometric examination.

RESULTS

A majority of children were 6-year olds (57%), were females (55%) and were Malay (94%). About 6% of the children were Iban. The distribution of the children according to their age is shown in Figure 1. Almost all children completed the screening test. Only one child was uncooperative during the vision screening and was considered as failed the screening test. The overall prevalence of reduced VA among the population was about 10%. All children (13 children) with reduced VA had refractive error. Two of the children were found to have refractive error and amblyopia while one child had strabismic amblyopia.

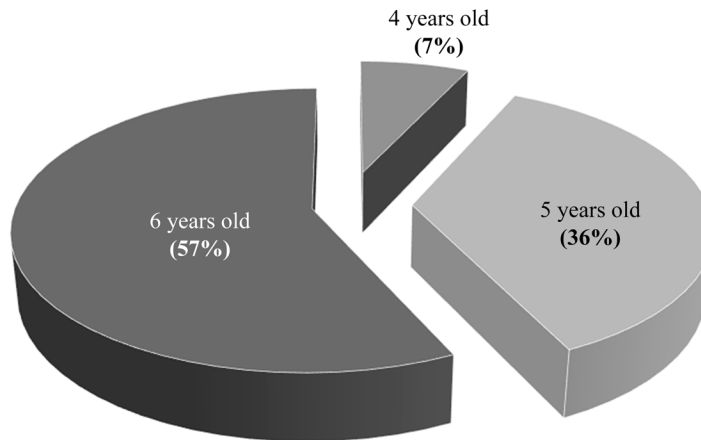


Figure 1. The age distribution of preschool children (n = 136)

The outcome of vision screening is shown in Table 1. A relatively higher number of false positive and false negative among nurses group in comparison to AMOs group might indicate lower accuracy of vision screening performed by nurses group. The total sensitivity and specificity of the vision screening was 69% and 95% respectively. The sensitivity and specificity of vision screening performed by AMOs were 100% and 98% respectively while that done by nurses were 56% and 94% respectively.

An analysis on the pre- and post-training evaluation test score showed that the mean score for the pre-test and post-test evaluation were 5.05 ± 2.10 and 8.54 ± 1.47 respectively. The Wilcoxon Sign Rank test showed a significant improvement between pre-and post-test evaluation score ($p < 0.001$).

Table 1
The outcome of vision screening

Vision screener	True positive (n)	False positive (n)	False negative (n)	True negative (n)
Nurses	5	5	4	72
Assistant medical officers (AMOs)	4	1	0	45

DISCUSSION

About 99% of the children successfully completed the vision screening test in this study. It has to be noted that age-appropriate tool selection and vision testing techniques may improve outcome. This finding suggests the use of distance visual acuity chart with letter-matching technique in visual acuity testing among pre-school children was an appropriate method as supported by previous research (Anstice & Thompson, 2014; Fern & Manny, 1986; The Vision in Preschoolers Study Group, 2005). Young children in this study have limited communicative

ability that affected reliability of their verbal responses. The lower accuracy of vision screening using Snellen notation chart by verbal response among younger children compared with older children in the government primary school was also previously reported (Abu Bakar et al., 2012).

This study showed that there was a discrepancy in the sensitivity of the visual acuity testing despite it being conducted by healthcare providers with similar educational and professional background as well as training programme. The nurses group exhibited a higher number of under referral cases, in fact, the AMO group detected all cases of reduced vision accurately in this study. High accuracy of visual acuity screening performed by AMOs was supported by previous study (Adhikari & Shrestha, 2011). However, inconsistent findings were found among nurses (Khandekar et al., 2004; The Vision in Preschoolers Study Group, 2005; Tong et al., 2004). Certain studies reported lower accuracy of vision screening by nurses which resulted in high over referral, such as in USA (sensitivity: 49%) and Malaysia (Accurate referrals: 51%) (Abu Bakar et al., 2012; The Vision in Preschoolers Study, 2005). While studies in Oman (Sensitivity: 72%) and Singapore (Sensitivity: 86%) have reported high accuracy after training programme (Khandekar et al., 2004; Tong et al., 2004).

The accuracy of vision screening among children could be influenced by the types of vision test and age of children besides the selection of the screener as described in Table 2 (Adhikari & Shrestha, 2011; Khandekar et al., 2004; OstadiMoghaddam et al., 2012; Sabri et al., 2016; Teerawattananon et al., 2014; The Vision in Preschoolers Study Group, 2005; Tong et al., 2004). The accuracy of vision screening was reported higher among older children of target population and simplified visual acuity testing (Khandekar et al., 2004; Teerawattananon et al., 2014; The Vision in Preschoolers Study Group, 2005; Tong et al., 2004). Vision screening done by nurses in Oman showed a lower accuracy among younger children (sensitivity: 55%) compared to older children (Sensitivity: 72%) despite similar training provided (Khandekar et al., 2004). These findings suggest that the differences in the performance of vision screeners might be influenced by other factors, such as the reliability of the child's response and interpersonal attitudes of the screener rather than their professional background.

Visual acuity testing is a psychophysical procedure that requires a subject to relate the perception of the physical characteristics of a stimulus and the outcome responses (Bailey & Lovie-Kitchin, 2013). Therefore, the physical ability, cognitive aptitude and psychological factors may influence the performance of visual acuity testing among young children (Abu Bakar & Chen, 2014; Anstice & Thompson, 2014). The variability in the sensitivity of the VA testing between the two groups of personnel may be associated with those aspects. Young children may present certain kinds of behavioural problem which is a normal part of their developmental progress. Professions dealing with young children should be properly trained and competent to handle them. Vision screeners for young children should be provided a good understanding of children's conditions and should be encouraged to sustain their attentiveness during the screening (Sharma et al., 2008).

Table 2
Sensitivity and specificity of vision acuity screening performed by non-eyecare professional

Country (Study)	Screeener	Target population	Visual acuity test	Sensitivity	Specificity
Nepal (Adhikari & Shrestha, 2011)	Medical assistant	3-7 years old	HOTV Chart	80%	98%
USA (The Vision in Preschoolers Study Group, 2005)	Lay screener	3-5 years old	Linear Lea Symbol (10ft)	37%	90%
			Single Lea Symbol (5ft)	61%	91%
	Nurse	Linear Lea Symbol (10ft)	49%	90%	
Oman (Khandekar et al., 2004)	Nurse	6-10 years old	Snellen E	55%	99%
		12-17 years old	Snellen E	72%	99%
Iran (OstadiMoghaddam et al., 2012)	Teacher	School-aged	E Chart	38%	92%
Canada (Sabri et al., 2016)	Trained technician	6-14 years old	Snellen Chart	96%	71%
China (Sharma et al., 2008)	Teacher	School-aged	Tumbling E Chart	93%	91%
Thailand (Teerawattananon et al., 2014)	Teacher	4-6 years old	Lea Symbol	35%	98%
		7-12 years old	E chart (7 years old) & Snellen Chart (8-12 years old)	65%	97%
Singapore (Tong et al., 2004)	Nurse	8-11 years	Simplified visual acuity screening	86%	92%
Malaysia (Current study)	Nurse	4-6 years old	HOTV chart	56%	94%
	Assistant Medical Officer	4-6 years old	HOTV chart	100%	98%

The improvement in post training evaluation score but lower accuracy of vision testing outcome among the nurses in this study suggests that the significant increment of post training evaluation score should not be the only indicator for the effectiveness of the training program as it only portrayed the general theoretical competency. Therefore, the evaluation of the effectiveness of a training program should include theoretical and practical assessments. The improvement on the current training module was recommended to enhance the performance of vision screening outcomes.

Although the screening assessment was designed to reduce age biases and number of children screened by each group of vision screeners, the nurse group screened relatively more children compared with the AMO group which suggest that the nurses group might perform vision screening faster than the AMOs. Shorter duration in conducting vision screening also could influence the quality and accuracy of screening because young children usually

need more time to understand the instruction and accurately respond to the vision screening procedure. However, no further discussion was made with the screeners post screening in order to determine the factors causing under or over referral to limit the claims.

CONCLUSION

The discrepancy in the sensitivity of visual acuity testing conducted by health providers with similar professional background who also attended a similar training programmes suggests that their performance might be influenced by factors other than their professional background. To achieve an effective and sustainable programme, preschool vision screening should be continuously evaluated, structured, and have quality control mechanisms. However, evaluation of the efficacy of the tool-based vision screening should be made collectively and should consider every aspect, including tools selection, target population and competency of vision screener. Evaluating each aspect discretely may affect the operational judgment of the screening program.

ACKNOWLEDGEMENTS

The authors would like to thank the Director General of Health Malaysia for granting the authors permission to publish this paper and all staff from the Department of Health of Sri Aman Division for their contribution to this study. Most sincere appreciation to Universiti Teknologi MARA for the RMI Research Entity Initiative Grant (600-RMI/DANA5/3/REI (12/2014)) for the financial support.

REFERENCES

- Abu Bakar, N. F., Chen, A. H., Abdul Rahim, M. N., & Goh, P.-P. (2012). Pilot study: A review of personnel involved in school vision screening and the training module in Betong, Malaysia. *International Medical Journal Malaysia*, *11*(2), 23–27.
- Abu Bakar, N. F., & Chen, A.-H. (2014). Comparison on testability of visual acuity, stereo acuity and colour vision tests between children with learning disabilities and children without learning disabilities in government primary schools. *Indian J Ophthalmol*, *62*(2), 141–144. <http://doi.org/10.4103/0301-4738.116481>
- Adhikari, S., & Shrestha, U. (2011). Validation of performance of certified medical assistants in preschool vision screening examination. *Nepalese Journal of Ophthalmology: A Biannual Peer-Reviewed Academic Journal of the Nepal Ophthalmic Society: NEPJOPH*, *3*(6), 128–133.
- Anstice, N. S., & Thompson, B. (2014). The measurement of visual acuity in children: An evidence-based update. *Clinical and Experimental Optometry*, *97*(1), 3–11. <http://doi.org/10.1111/cxo.12086>
- Bailey, I. L., & Lovie-Kitchin, J. E. (2013). Visual acuity testing. From the laboratory to the clinic. *Vision Research*, *90*, 2–9. <http://doi.org/10.1016/j.visres.2013.05.004>
- Fern, K. D., & Manny, R. E. (1986). Visual acuity of the preschool child: a review. *American Journal of Optometry and Physiological Optics*, *63*(5), 319–345.

- Khandekar, R., Harby, S. Al, Abdulmajeed, T., Helmi, S. A., & Shuaili, I. S. (2004). Validity of vision screening by school nurses in seven regions of Oman, *10*, 528–536.
- OstadiMoghaddam, H., Fotouhi, A., Hashemi, H., Yekta, A., Heravian, J., Ghalandarabadi, M., ... Khabazkhoob, M. (2012). Validity of Vision Screening Tests by Teachers Among School Children in Mashhad, Iran. *Ophthalmic Epidemiology*, *19*(3), 166–171. <http://doi.org/10.3109/09286586.2011.602503>
- Sabri, K., Thornley, P., Waltho, D., Warren, T., Laverty, L., Husain, S., ... Higgins, D. (2016). Assessing accuracy of non-eye care professionals as trainee vision screeners for children. *Canadian Journal of Ophthalmology / Journal Canadien d'Ophthalmologie*, *51*(1), 25–29. <http://doi.org/http://dx.doi.org/10.1016/j.jcjo.2015.10.008>
- Sharma, A., Li, L., Song, Y., Choi, K., Lam, D. S. C., Zhang, M., ... Congdon, N. (2008). Strategies to improve the accuracy of vision measurement by teachers in rural Chinese secondary schoolchildren: Xichang Pediatric Refractive Error Study (X-PRES) report no. 6. *Archives of Ophthalmology*, *126*(10), 1434–1440. <http://doi.org/10.1001/archoph.126.10.1434>
- Teerawattananon, K., Myint, C.-Y., Wongkittirux, K., Teerawattananon, Y., Chinkulkitnivat, B., Orprayoon, S., ... Jenchitr, W. (2014). Assessing the accuracy and feasibility of a refractive error screening program conducted by school teachers in pre-primary and primary schools in Thailand. *PloS One*, *9*(6), e96684. <http://doi.org/10.1371/journal.pone.0096684>
- The Vision in Preschoolers Study Group. (2005). Preschool vision screening tests administered by nurse screeners compared with lay screeners in the vision in preschoolers study. *Investigative Ophthalmology and Visual Science*, *46*(8), 2639–2648. <http://doi.org/10.1167/iovs.05-0141>
- Tong, L., Saw, S.-M., Chan, E. S.-Y., Yap, M., Lee, H.-Y., Kwang, Y.-P., & Tan, D. (2004). Screening for myopia and refractive errors using LogMAR visual acuity by optometrists and a simplified visual acuity chart by nurses. *Optometry and Vision Science: Official Publication of the American Academy of Optometry*, *81*(9), 684–91. <http://doi.org/http://dx.doi.org/10.1097/01.opx.0000144747.88341.b2>
- World Health Organization (WHO). (2008). Classifying health workers: Mapping occupations to the international standard classification. *World Health Organization*, 1–14. Retrieved from http://www.who.int/hrh/statistics/workforce_statistics/en/.



Effect of Blood Cockle Shell and Palm Kernel Shell Weight Ratio on the Acid Neutralizing Capacity of Calcined Products

Noor Mohamad Amin Salleh, Dayangku Kamilah Pengiran Ismail and Yong Soon Kong*

Faculty of Applied Sciences, Universiti Teknologi MARA (UiTM), 40450 Shah Alam, Selangor, Malaysia

ABSTRACT

Heavy metals from mining sites can contribute to adverse health and environmental issues. Conventional liming practice depletes natural limestone deposits. Blood cockle shell (BCS) and palm kernel shell (PKS) calcination produced alkaline ash to immobilize heavy metals in soil. This study investigates the acid neutralizing capacity (ANC) of calcined BCS and PKS composites. BCS and PKS composites were prepared at various weight ratios (i.e. 1:0, 1:1, 1:5, 1:10, and 0:1) and were combusted for 1 hour at 400°C and 900°C, respectively. BCS and PKS composites were determined by its yield, pH, and ANC. The combustion characteristics for composites was conducted using thermogravimetric analysis (TGA). Elemental analysis was conducted using X-ray fluorescence (XRF) spectroscopy. Fourier transform infra-red (FTIR) was conducted for functional groups analysis. Ash content of composites increased when the portion of PKS feedstock is decreased. Increasing combustion temperature from 400°C to 900°C reduced the ash contents. The pH of raw and combusted composite (at 400°C) decreased as the portion of PKS feedstock is increased. Calcined composites at 900°C have slightly different pH value except for 0:1 sample. ANC value increased as PKS portion in composites reduced. Higher content of calcium oxide (CaO) in the composites increased the ANC value.

Keywords: Bioaccumulation, bivalve waste, heavy metals, pyrolysis, soil remediation

ARTICLE INFO

Article history:

Received: 28 September 2016

Accepted: 03 February 2017

E-mail addresses:

noormohdamin84@gmail.com (Noor Mohamad Amin Salleh),
deekay1705@yahoo.com (Dayangku Kamilah Pengiran Ismail),
yongsk@salam.uitm.edu.my (Yong Soon Kong)

*Corresponding Author

INTRODUCTION

Widespread heavy metal contamination of soil is a global issue. Leachate from mine soil can contain hazardous levels of heavy metals (Ali et al., 2004). Prolonged exposure to heavy metals may contribute to anaemia and severe damage to the nervous system. The conventional remediation method for mine soil is liming with alkaline minerals such as

ground magnesium limestone (GML) or dolomite. Liming neutralizes the pH of acidic soil, and immobilizes toxic metals in the soil (Trakal et al., 2011). Consequently, large amounts of limestone are required for in-situ remediation of contaminated soil. Excessive quarrying may lead to depletion of natural limestone reserves.

Blood cockle shell (BCS) has a high calcium carbonate (CaCO_3) content, and can be a potential liming agent for soil remediation. Combustion increases the alkalinity of BCS as CaCO_3 is converted to calcium oxide (CaO). The increased alkalinity in the calcined BCS is essential for effective heavy metal immobilization in the mine soil. Palm oil milling industry generates an abundance of biomass, such as palm kernel shell (PKS) and empty fruit bunches (EFB). Palm oil milling production in Malaysia contributed around 4506 kilotonnes of PKS as waste produced. Burnt PKS may improve soil fertility by providing nutrients such as magnesium and potassium.

Calcination on BCS and PKS composite with various weight ratios generates a different percentage of CaO. The addition of PKS may aid in the combustion of BCS. Acid neutralizing capacity (ANC) determines the capability of materials to neutralize acidity and is significantly influenced by the CaO contents in the combustion of BCS and PKS composite. The aim of this study is to evaluate the effect of BCS and PKS calcination at various weight ratios on the chemical and physical characteristics of ash (i.e. yields, pH, elemental composition and ANC). The study hopes to determine the optimum BCS and PKS feedstock composition for producing ash with high ANC value for immobilizing heavy metals in soil.

METHOD

Preparation for BCS and PKS

Blood cockle shell was collected from Sabak Bernam, Selangor. The as-received BCS was boiled with deionized water for 2 hours and oven-dried for 72 hours. Dried BCS were crushed and pulverized to 75 μm in diameter. Palm kernel shell from Jengka, Pahang was sun-dried and oven-dried for 48 hours and 24 hours, respectively. Then, PKS was crushed and pulverized to 75 μm in diameter. Both BCS and PKS were kept in polyethylene zip lock bags.

Pyrolysis of BCS and PKS

Blood cockle shell and PKS were homogenized at various weight ratios (i.e. 1:0, 1:1, 1:5, 1:10, and 0:1). 10 g from each composite were placed in an uncovered crucible and combusted for 1 hour using muffled furnace under air condition at 400°C and 900°C, respectively. The ash samples from pyrolysis process was cooled in a desiccator.

TGA/DSC 1 Star System (Mettler Toledo, USA) instrument was used for TGA analysis. Composites sample (20 mg) was combusted to 900°C at 10°C/min of heating rate. Air flow rate was set at 50 mL/min for combustion process.

Ash samples from combustion and commercial liming products (i.e. ground magnesium limestone (GML) and dolomite) were homogenized prior to chemical characterization. Elemental compositions for ash samples were determined using X-ray fluorescence (XRF) spectroscopy (Epsilon3-XL PANalytical, Netherlands). FTIR spectra were recorded from KBr

disc containing 10% w/w of ash samples, using an FTIR spectrometer (Perkin Elmer Spectrum One, USA). 2 g of ash samples were mixed with 20 mL of 10 mM CaCl_2 , and the pH values were determined using a calibrated pH meter. The ANC values were determined based on the method described by Venegas et al. (2015). All analyses were conducted in duplicate and the average values were determined using MS Excel spreadsheet.

RESULTS AND DISCUSSION

Figure 1 shows the pH and weight percentage of ash for BCS and PKS composites. Increasing portion of PKS reduced the composites ash content weight percentage. In addition, composites that were combusted at 900°C produced lower ash content compared to those at 400°C. Composites with more PKS portion (i.e. 1:10) and combusted at 900°C produced only about 13% of ash. Compared to others weight ratio, the 1:10 composite contains more lignocellulosic component, and was mostly combusted. For comparison, 1:0 composites have higher ash content due to the high content of CaCO_3 in BCS feedstock.

Reduction in pH value can be traced once the PKS ratio is increased for raw and 400°C composites samples. Composites samples calcined at 900°C have slightly similar pH value except for 0:1 composite. This may due to the presence of calcium oxide (CaO), produced by the decomposition of CaCO_3 in the BCS-added composites. Combustion of PKS in the 0:1 composite has negligible amount of CaO (i.e., 0.8 and 1.8% at 400°C and 900°C, respectively).

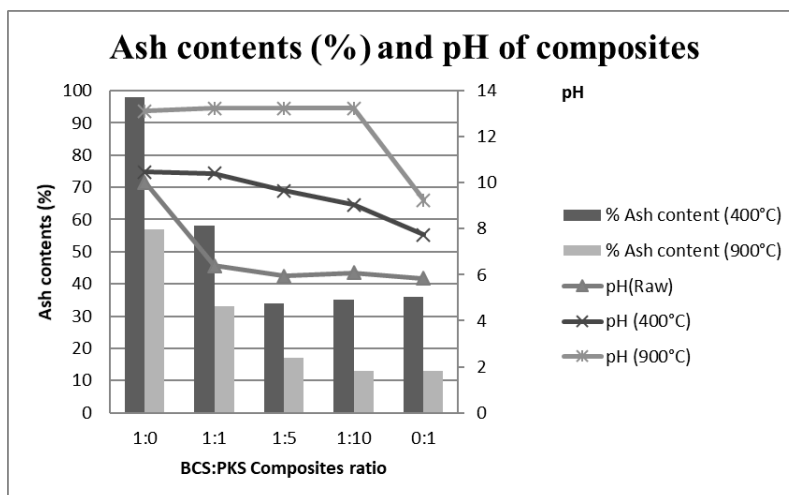


Figure 1. Ash content (%) and pH values of BCS: PKS composites (BCS:PKS feedstock ratio: 1:0, 1:1, 1:5, 1:10, and 0:1)

Figure 2 illustrates thermogram for BCS and PKS composites (1:0, 1:1, 1:5, 1:10 and 0:1). BCS samples (1:0) that contain primarily aragonite decomposed at 830.47°C (Mustakimah et al., 2012). High temperature was required for thermal decomposition of aragonite to calcite (Mustakimah et al., 2012). Decomposition of PKS (0:1) involved four stages: (1) the removal

of moisture (at temperature between 30.38°C to 114.79°C); (2) decomposition of hemicellulose (at temperature between 114.79°C to 192.94°C); (3) decomposition of cellulose (at 192.94°C up to 343.26°C); and lignin decomposition (at 346.34°C up to 531.46°C). Composite samples that contain a greater portion of PKS (i.e., 1:10) decomposed faster than those with the lower portion of PKS (i.e., 1:1 composite). Moisture removal from 1:10 composites samples occurred between 35.44°C and 113.37°C. Decomposition of hemicellulose and cellulose started rapidly at 113.37°C to 158.16°C, and 158.16°C to 543.78°C, respectively. The addition of PKS into BCS increased lignocellulosic material in the composite, and may have accelerated the decomposition process.

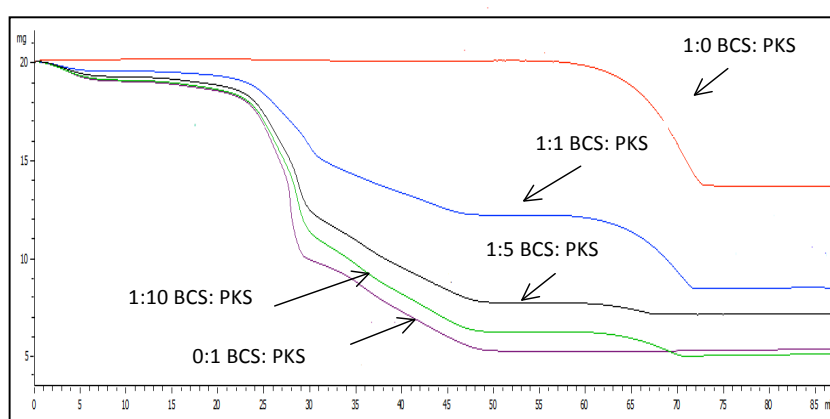


Figure 2. Thermograms for BCS and PKS composites (BCS:PKS feedstock ratio: 1:0, 1:1, 1:5, 1:10, and 0:1)

Table 1 shows FTIR wavenumber for 900°C BCS: PKS composites. FTIR wavenumber obtained is essential to distinguish present of calcium oxide from several ratios of 900°C BCS: PKS composite samples. Presence of medium bands at 3644 cm^{-1} and 3645 cm^{-1} for three composite samples (i.e., 1:0, 1:1 and 1:5) indicates that CaO is present (Zaki et al., 2006). 1:0 composites ratio has slightly more content of CaO as compared to 1:1 and 1:5 ratios. 1:10 composites have SiO- band due to presence of PKS that contain more silicate components.

Table 1
FTIR wavenumber for BCS: PKS composites (BCS:PKS feedstock ratio: 1:0, 1:1, 1:5, 1:10, and 0:1) produced at 900°C

Composites Ratio	Wavenumber (cm^{-1})			
	CaO ⁺ (medium band)	CaO ⁺ (medium broad band)	COO ⁻	SiO ⁻
1:0	3645	1458	-	-
1:1	3645	1412	876	-
1:5	3644	1416	876	-
1:10	-	1416	-	1036

Table 2
 Chemical composition of BCS and PKS composites (BCS:PKS feedstock ratio: 1:0, 1:1, 1:5, 1:10, and 0:1) produced at 400°C and 900°C

Elemental Composition [%]	1:0 BCS:PKS		1:1 BCS:PKS		1:5 BCS:PKS		1:10 BCS:PKS		0:1 BCS:PKS						
	Raw	400°C	900°C	Raw	400°C	900°C	Raw	400°C	900°C	Raw	400°C	900°C			
CaO	55.68	49.53	61.42	37.73	48.70	56.74	16.2	20.49	41.76	11.0	16.63	30.90	0.52	0.82	1.80
K ₂ O	0.14	0.09	0.17	0.68	0.85	0.60	1.23	1.63	1.85	1.41	2.89	2.76	1.54	3.04	5.42
MgO	4.08	3.80	3.52	4.37	3.05	5.56	3.59	3.44	3.24	3.36	3.53	4.24	3.85	3.78	4.35
Al ₂ O ₃	6.45	6.64	7.84	7.62	9.87	8.65	6.18	7.39	16.29	4.35	11.60	22.98	3.76	10.57	29.98
Fe ₂ O ₃	0.07	0.08	0.06	1.21	1.45	1.23	3.71	3.41	5.17	4.89	7.49	7.95	6.70	10.98	20.07
SiO ₂	0.95	0.88	0.78	4.52	8.47	6.20	7.30	12.86	25.45	8.19	22.65	35.56	7.26	22.43	55.23

Table 3 shows ANC values for BCS and PKS composites prepared at 400°C and 900°C. Raw samples for BCS and PKS composites have lower ANC value than BCS (1:0). As the samples undergo thermal degradation, high temperature altered the condition and chemical composition of feedstock materials. The calcined 1:0 composite (900°C) has the highest ANC value (746 meq kg⁻¹), followed by calcined 1:1 composite (900°C) (698 meq kg⁻¹). ANC value increased as the combustion temperature was increased to 900°C. In contrast, the value of ANC was reduced when the composition of PKS feedstock were increased in the composite samples. The pH values for both calcined composites of 1:0 (13.12) and 0:1 (9.24) were slightly lower than the 1:1 composite (13.23). Major chemical compounds that have contributed to the increase of the ANC value are CaO, MgO and SiO₂. As illustrated in Table 2, calcined BCS has about 61.42% of CaO, slightly higher than the 1:1 composite (56.74%). Surprisingly, the calcined 1:1 composite has about 0.60 % K₂O, 5.56% MgO and 6.20% SiO₂ compare to the 1:0 composites (900°C) (0.17% K₂O, 3.52% MgO and 0.78% SiO₂). Higher content of K₂O, MgO and SiO₂ in the calcined 1:1 composite (900°C) contributed to the shifting of the ANC value of samples (Paul et al., 2005).

Table 3
Acid neutralizing capacity value of various materials

Samples	Acid Neutralizing Capacity value (meq kg ⁻¹)		
	Raw	400°C	900°C
CaO (Bendosen, 99.0%)	845	-	-
CaCO ₃ (John Kollin, 99.80%)	399	-	-
CaCO ₃ (Merck, 98.50%)	358	-	-
Dolomite	348	-	-
GML	369	-	-
1:0 BCS: PKS	369	434	746
1:1 BCS: PKS	112	437	698
1:5 BCS: PKS	46	191	474
1:10 BCS: PKS	42	136	296
0:1 BCS: PKS	11	10	25

CONCLUSION

The calcined 1:0 composite has an outstanding ANC value of 746 meq kg⁻¹. Data obtained from this study revealed that chemical compositions of BCS and PKS composites were changed when different weight ratio of BCS and PKS feedstock were selected. High yield of ash from the combustion process, and increasing CaO content in the combusted composite samples) increased the ANC value. High ANC values for the combusted composite indicates that it is a suitable material for liming contaminated soil.

ACKNOWLEDGEMENTS

The authors would like to thank Ministry of Higher Education for funding this study under Research Acculturation Collaborative Effort (RACE) (Phase 3, 2014). The authors are also grateful to the management of FELDA Palm Industries Sdn. Bhd., Kilang Sawit Felda Jengka 21, Bandar Pusat Jengka, Pahang Darul Makmur and Perlis Dolomite Industries Sdn. Bhd., Pusat Perniagaan Adenium Seksyen BB5, 48300 Bukit Beruntung, Selangor Darul Ehsan for providing raw materials.

REFERENCES

- Ali, M.F., Heng, L.Y., Ratnam, W., Nais, J., & Ripin, R. (2004). Metal Distribution and contamination of the Mamut river, Malaysia caused by copper mine discharge. *Bulletin of Environmental Toxicology*, 73, 535-542.
- Mustakimah, M., Nor Adilla, R., Suzana, Y., Umer, K. T. R., & Razol, M. A. (2012). Effects of experimental variables on conversion of cockle shell to calcium oxide using thermal gravimetric analysis *Journal of Cleaner Production*, 37, 394-397.
- Paul, A. W., Joan, E. T., William, M. S., & Roger, S. T. S. (2005). A methodology to determine the acid-neutralization capacity of rock samples *Journal of The Canadian Mineralogist*, 43, pp 1183-1192.
- Trakal, I., Neuberger, M., Tlustos, P., Szakova, J., Tejnecky, V., & Drabek, O. (2011). Dolomite limestone application as a chemical immobilization of metal-contaminated soil. *Plant Soil Environment*, 57(4), 173-179.
- Venegas, A., Rigol, A., & Vidal, M. (2015). Viability of organic wastes and biochars as amendments for the remediation of heavy metal-contaminated soils. *Chemosphere*, 119.
- Zaki, M. I., Knözinger, H., Tesche, B., & Mekhemer, G. A. H. (2006). Influence of Phosphonation and Phosphation on Surface Acid-Base and Morphological Properties of CaO as Investigated by in-situ FTIR Spectroscopy and Electron Microscopy, *Journal of Colloid and Interface Science*, 303, 9-17.



Optimization of Headspace Solid Phase Microextraction (HS-SPME) for the Extraction of Volatile Organic Compounds (VOCs) in Mangoes (*Harumanis* cv.) Using 2 Stages Multivariate Analysis

Siti Raihan Zakaria^{1*}, Ruziyati Tajuddin², Rozita Osman², Norashikin Saim² and Mardiana Saaid²

¹Faculty of Applied Sciences, Universiti Teknologi MARA (UiTM) Pahang, 26400, Jengka, Pahang, Malaysia

²Faculty of Applied Sciences, Universiti Teknologi MARA (UiTM), 40450 Shah Alam, Selangor, Malaysia

ABSTRACT

Headspace solid phase microextraction (HS-SPME) was used to isolate volatile compounds (VOCs) from mangoes (*Harumanis* cv.). Among the four SPME fibres investigated, the mixed phase coating, 65 µm polydimethyl siloxane–divinylbenzene (DVB/PDMS) showed the highest efficiency in extracting VOCs as 26 compounds were detected with the total area of 9.6 x 10⁹. The optimization of SPME factors was conducted in 2 stages using multivariate design. The first stage involved screening of the significant factors using the Plackett–Burman (P–B) design, followed by the optimization of the significant factors utilizing Central Composite Design (CCD). The experimental design for both P-B and CCD design was generated using Design-Expert version 6.0.4 (Stat Ease Software). Extraction time and temperature appeared to be the most significant factors in extracting VOCs in mangoes, with the optimum conditions prevailing at 55°C and 34 minutes respectively.

Keywords: CCD, *Harumanis*, HS-SPME, VOCs

ARTICLE INFO

Article history:

Received: 28 September 2016

Accepted: 03 February 2017

E-mail addresses:

sitiraihan@pahang.uitm.edu.my (Siti Raihan Zakaria),

ruziy039@salam.uitm.edu.my (Ruziyati Tajuddin),

rozit471@salam.uitm.edu.my (Rozita Osman),

noras691@salam.uitm.edu.my (Norashikin Saim),

mardiana6951@salam.uitm.edu.my (Mardiana Saaid)

*Corresponding Author

INTRODUCTION

Mango (*Mangifera indica* L.) is a popular fruit that is rich in nutrients and a desirable taste, belonging to the Anacardiaceae family it is also known as the King of Fruits due to its aroma and sweetness. The pleasant aroma and flavour of the fruit is derived from various volatile compounds such as esters, lactones, monoterpenes and sesquiterpenes as identified in previous studies (Ansari et al., 2004; Kulkarni et al., 2012).

The volatile organic compounds (VOCs) refers to the molecules that have appreciable vapour pressure at room temperature with molecular weight lesser than 300 Dalton (El Hadi et al., 2013). The VOCs can be used to develop a volatile profile of mangoes and used for authentication and quality control studies (Shyam et al., 2013). The isolation of VOCs in fruit is crucial as the VOCs are generally present in trace amounts and the complexity of the fruit as the matrix. Additionally, VOCs are also thermolabile requiring rapid and effective isolation technique that can extract, concentrate and clean them in a single step (Cheng et al., 2011).

Solid-phase microextraction (SPME) has proven to be a useful extraction method that is rapid, versatile and simple (Pawliszyn, 1999). Previous studies (Laohaprasit et al., 2011; Liang et al., 2012; Chidley et al., 2013) reported that use of SPME to extract VOCs in fruit matrix, however there is no clear conclusion on the choice of fibre especially in non-targeted analysis. Thus, it is important to find the most efficient fibre prior to optimization study. Apart from using the most efficient fibre, there are many other factors such as extraction time, extraction temperature, stirring effect, desorption temperature and time, sample amount, and salt addition may affect the efficiency of HS-SPME (Ouyang & Pawliszyn, 2008). Optimizing these factors is crucial in order high SPME efficiency in extracting VOCs from mangoes is achieved.

Optimisation is a process of balancing several aspects of a system to attain the best result for a set of criteria. Traditionally, the optimization of SPME was done using univariate optimization method; each factor being optimized and studied in isolation (Massart et al., 1997). The drawback of this technique is it leaves interaction between factors unexamined. Multivariate design is able to overcome this shortcoming by using experimental software to identify the significant factors of the SPME parameters and thereby maximize the response of an experiment. Thus, in addition to saving time as the number of experiments done can be cut down, the chromatographic response of the analytes can be improved as interference can be eliminated (Miller & Miller, 2010). One of the widely used multivariate designs to optimize extraction of VOCs in food is the Response Surface Methodology (RSM) (Stalikas et al., 2009). To directly optimize all the factors that may affect the efficiency of SPME screening using Plackett-Burman (PB) should be done, thus reducing number of experiments to estimate the significant factors (Scheppers, 1999).

The aim of this study is to initially screen the significant factors affecting HS-SPME extraction of VOCs in *Harumanis* mangoes using PB design and optimize the significant factors through RSM.

METHOD

Chemical reagents

All chemicals used in this study were of analytical quality and all solvents were HPLC grade. Deionized water was obtained from a Mili-Q water purification system (Milipore, Bedford, PA, USA). Sodium chloride used in screening experiments was supplied by Merck (Darmstadt, Germany). All the SPME fibres used together with clear glass screw cap vials (PTFE/silica septa) were purchased from Supelco.

Sample preparation

Ripe *Harumanis* mangoes were obtained from local orchards in Perlis, Malaysia. For the volatile analysis of homogenized mango pulp, fresh mango will be sliced and homogenized using a blender. The homogenized mango pulp was stored in a freezer with temperature less than 0°C and analysed in triplicate.

Fibre selection

4 commercially available SPME fibres differing in the thickness and solvent phase coating were tested and compared. The tested fibres were non-polar 100 µm polydimethyl (PDMS), semi polar fibres, 65 µm polydimethyl siloxane-divinylbenzene (PDMS-DVB) and 75 µm CAR-PDMS and also polar fibre, polyacrylate (PA) to study the efficiency of different fibre in extracting the aroma volatiles. Prior to extraction, each of the chosen fibre was conditioned at the GC injection port according to the guidelines given by the manufacturer. The criteria used to select the best fibre is the fibre with the highest total area and the highest number of compounds detected.

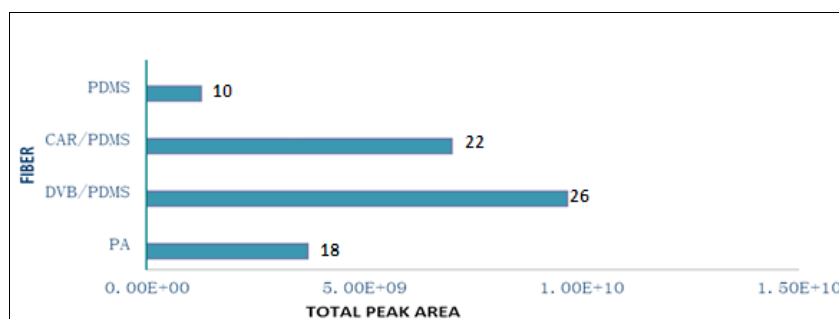


Figure 1. Efficiency of each fibre on the VOCs extraction by HS-SPME

SPME optimization

The optimization of SPME was done in 2 stages; screening stage and optimization stage using multivariate analysis.

Screening of significant factors

The screening of SPME significant factors was carried out using Plackett–Burman (P–B) design matrix with a 2^{7-4} . Seven factors were selected for the screening stage using 2^{7-4} Plackett–Burman design matrix include: extraction temperature (30°C and 60°C), time (10 min and 40 min) salt addition (0 g and 1 g), stirring rate (0 and 500 rpm), desorption time (1 min and 5 min) and desorption temperature (100°C and 240°C). The significant factors given by P-B design were further optimized using RSM.

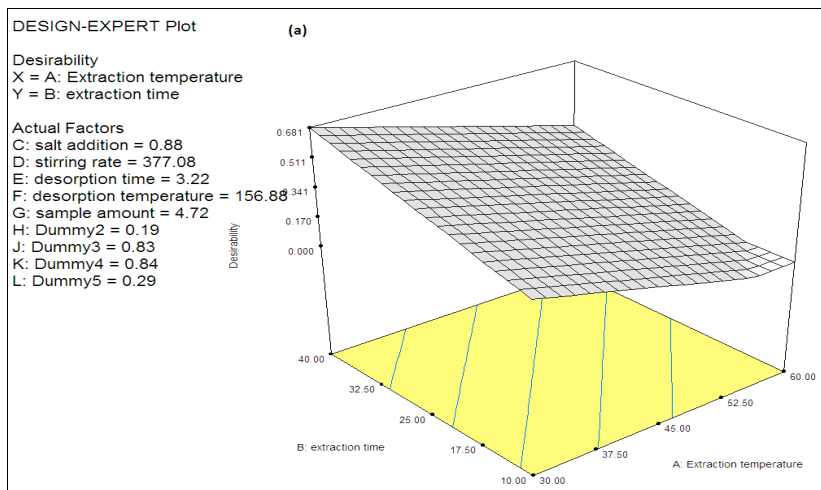


Figure 2. 3D surface plot from Plackett-Burman design

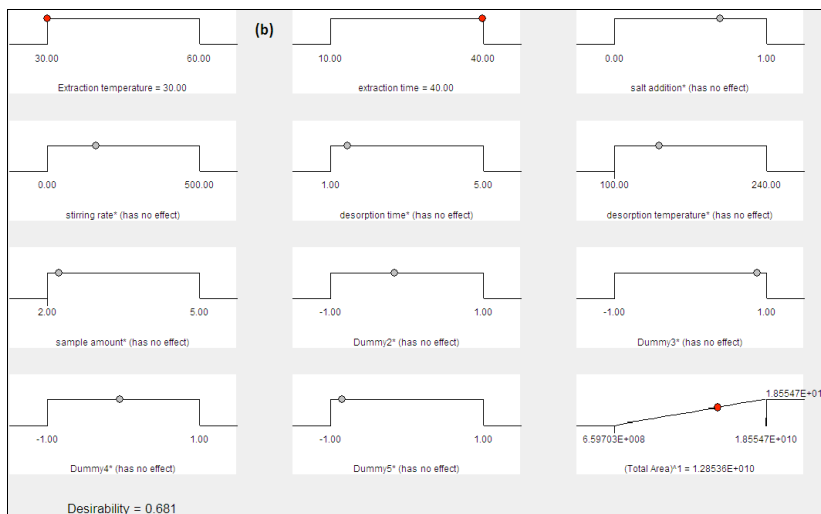


Figure 3. The ramps from Plackett-Burman design

Optimization of significant factors

The extraction temperature and time found to be significant in the screening stage was further optimized using RSM (Central Composite Design). Three responses will be evaluated, that is, total area, trans-beta ocimene and 2, 4, 6-octatriene. Trans-beta-ocimene and 2,4,6-octatriene was selected as the response for the CCD design in view of their having recorded the highest frequency of occurrences in early preliminary studies.

GC-MS conditions

The volatile compounds were analysed using a GC-MS system (Agilent Technologies 5977 Inert Mass Selective Detector and Agilent 7890B) under the following operating conditions: HP-5MS capillary column (Agilent 19091S-433, 0.25 mm 30 m 0.25 μ m) was used. GC/MS detection was done using ionization energy of 70 eV in the 50–550 a.m.u. mass range. Column temperature was increased from 40°C to 250°C with temperature program: starting at 40°C with hold time 2 mins, to be subsequently increased 150°C (5°C min⁻¹) with hold time of 1 min. Finally, the temperature was increased to 250°C (10°C min⁻¹) with hold time of 5 mins and total run time of 40 minutes. The injector temperature and mode was 280°C with split ratio of 1:00. The ion source temperature was 230°C and the interface temperature was 280°C. At a flow rate of 1.2 mL/min, Helium was used as the carrier gas. The VOCs in *Harumanis* mangoes were identified by comparing their spectra with those available in the NIST14 digital library.

Experimental design approach

The experimental designs for both screening and optimization stages were generated using Design-Expert version 6.0.4 (Stat Ease Software).

RESULTS AND DISCUSSIONS

Fibre selection

Different kinds of analytes may require different type of SPME fibres as each fibre provides different absorption/adsorption properties. To use the correct fibre is very important for the SPME method to ensure highest efficiency can be achieved. Therefore, to obtain the highest efficiency for the extraction of VOCs from mangoes using the HS-SPME-GCMS, 4 commercially available SPME fibre differing in the thickness and solvent phase coatings were tested (PDMS, PDMS/DVB, CAR/PDMS and PA). The overall efficiency of the selected SPME fibre was assessed by examining the total area of GC-MS peaks, in addition to examining the total area, the number of VOCs detected from each of the fibre was assessed.

As shown in Figure 1, DVB/PDMS fibre recorded the highest total peak area of 9.6×10^9 besides also showing that the most number of VOCs recorded i.e. 26 peaks was chosen as the most efficient fibre in this study, and used for the optimization study using PB and RSM. A study of VOCs extraction from tomato plant using SPME (Sousa et al., 2006) also showed the same trend. This may due to the fact that DVB part of DVB/PDMS fibre consist of wide pores (meso and macro) that may contribute to fast equilibrium and lead to the efficient extraction. The results show both mixed phase coatings (DVB/PDMS and CAR/PDMS) recorded higher total area when compared with single coating fibres (PA and PDMS). Mixed phase coatings expressed complementary properties in contrast with single phase films because they managed to adsorb a broad range of analytes with different chemical properties.

Screening of significant factors

The screening of SPME significant factors were carried out using Plackett–Burman (P–B) design matrix with a 2^{7-4} . Seven SPME factors (extraction temperature, extraction time, salt addition, stirring rate, desorption time, desorption temperature and sample amount) were tested with two runs of high and low level for each factor.

According to the results shown in Figure 2 and Figure 3, the significant factors for this study were extraction temperature and extraction time. As presented in the 3D surface plot of Figure 2, as the extraction temperature and extraction time increased from low value to high value extraction efficiency also increased (Abdulra'uf et al., 2015). Other factors such as the addition of salt, sample size, stirring rate, desorption time and desorption temperature showed no significant effect, allowing it to be fixed at any value, since their adjustment will have equal effect on extraction efficiency. Clicia et al. (2014) obtained a similar result when using fractional factorial design (2^{4+1}) to find the most HS-SPME significant factors in extracting VOCs from varieties of mangoes in Brazil. Hence, only these two factors were further evaluated in the optimization process by means of the Response Surface Methodology (CCD).

Optimization of Extraction Temperature and Time

In the first stage of the optimization method, PB design indicated that only extraction temperature and extraction time were the significant factors that needed to be further optimized using Central Composite Design in RSM. 14 experiments were run in 3 blocks of points and the CCD experiments were run in a random manner to reduce the effect of uncontrolled variables. Three responses were used to optimize the extraction time and temperature for the total area of all detected compounds, area of trans-beta ocimene and also the area of 2,4,6- octatriene. Trans-beta ocimene and 2,4,6- octatriene was chosen as the response due to the fact that these two compounds recorded the highest frequency of occurrences in preliminary experiments (data not shown here) including the fibre selection experiment. The results obtained from CCD experiments are summarized in Table 1.

Table 1
Summary of Central Composite Design for HS-SPME of VOCs in mangoes

Response	Transform	Model	Lack Of Fit	R ²	Equation	Significant
Total area	Square root	Quadratic significant	Not significant	0.8305	Sqrt(TotalArea) = +71264.06+16957.4A+30761.33 B-12686.95A2-28439.83B2- 4612.69AB	A ² , A
Trans-beta ocimene	None	Quadratic significant	Not significant	0.8826	Trans-beta ocimene = +5.429E+008+1.858E+008A+ 4.354E+008B-5.723E+007A2-3.873E+ 008B2-4.381E+007AB	A, B ²
2,4,6-octatriene	Square root	Linear significant	Not significant	0.5317	Sqrt(2,4,6,octatriene) = +13568.79+2383.14A-1222.11B	A

The value of coefficient of determination (R^2) for the total area of the compounds, trans-beta-ocimene and 2,4,6-octatriene was 0.8305, 0.8826, and 0.5317 respectively. The ANOVA showed that the statistical analysis of the data was significant ($p < 0.05$). In addition, there was a non-significant ($p > 0.05$) lack of fit in all the 3 responses which validate the models. In optimizing the extraction conditions, the goals were set at the maximum level of total area of the compounds, trans-beta-ocimene and 2,4,6-octatriene. Extraction time of 34 minutes and extraction temperature of 55°C are found to be the optimum conditions with desirability of 0.992. The value of desirability higher than 0.80 and approaching unity is good. The total area of the compounds obtained from this study also increased with temperature but it started to decrease after extraction temperature reached 55°C as shown in Figure 4. Trans-beta ocimene also recorded the same trend.

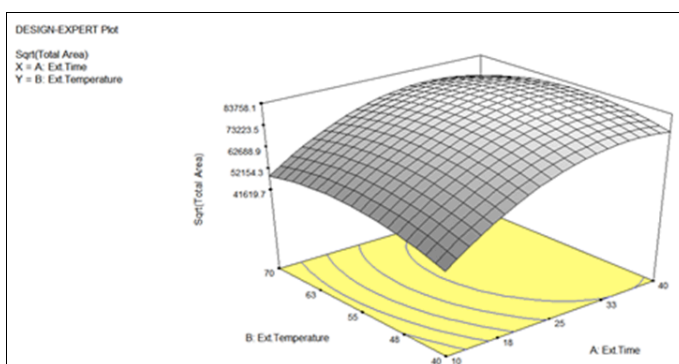


Figure 4. 3D surface plot for total area from Central Composite Design

CONCLUSION

Mixed coating phase, DVB/PDMS has demonstrated to be an efficient fibre in isolating VOCs from mangoes. Results from this study also indicated the successful utilization of the two-stage multivariate analysis to screen and optimize the significant factors for HS-SPME extraction. Total area of compounds found from the optimization results along with trans-beta ocimene and 2,4,6-octatriene were significantly influenced by extraction temperature and time with optimum conditions of 55°C for 34 minutes respectively with 0.992 desirability.

ACKNOWLEDGEMENTS

Authors are grateful to the Ministry of Higher Education, Malaysia for funding this study (Project number: 600-IRMI/FRGS 5/3 (70/2016)).

REFERENCES

- Abdulrafuf, L. B., & Tan, G. H. (2015). Chemometric approach to the optimization of HS-SPME/GC-MS for the determination of multiclass pesticide residues in fruits and vegetables. *Food Chemistry*, 177, 267-273.

- Ansari, S. H., Ali, M., Velasco-Neguerela, A., & Pe'rez-Alonso, M. J. (2004). Volatile of the fruits of three mango cultivars, *Mangifera Indica* L. *Journal of Essential Oil Research*, 11, 65-68.
- Cheng, C., Seal, A., MacRae, E., & Wang, M. (2011). Identifying Volatile Compounds Associated with Sensory and Fruit Attributes in Diploid *Actinidia chinensis* (Kiwi fruit) Using Multivariate Analysis. *Euphytica*, 181(2), 179-195.
- Chidley, H. G., Kulkarni, R. S., Pujari, K. H., Giri, A. P., & Gupta, V. S. (2013). Spatial and Temporal Changes in the Volatile Profile of Alphonso mango upon Exogenous Ethylene Treatment. *Food Chemistry*, 136(2), 585-594.
- El Hadi, M. A. M., Zhang, F-J., Wu, F-F., Zhou, C-H., & Tao, J. (2013). Advances in Fruit Aroma Volatile Research. *Molecules*, 18(7), 8200-8229.
- Kulkarni, R. S., Chidley, H. G., Keshav, H., Pujari, K. H., Giri, A. P., & Gupta, V. S. (2012). Geographic Variation in the Flavour Volatiles of Alphonso mango. *Food Chemistry*, 130(1), 58-66.
- Laohaprasit, N., Ambadipudi, D. S., & Szrednicki, G. (2011). Optimisation of Extraction Conditions of Volatile Compounds in 'Nam Dok Mai' Mangoes. *International Food Research Journal*, 18(3), 1043-1049.
- Liang, Y. Z., Guang, M. S., Yu, G. L., Ling, L. L., Wen, X. Y., Wei, F. Z., & Chang, B. W. (2012). Aroma volatile compounds from two fresh pineapple varieties in China. *International Journal of Sciences*, 13, 7383-7392.
- Massart, D. L., Vandeginste, B. G. M., Buydens, L. M. C., De Jong, S., Lewi, P. J., & Smeyers-Verbeke, J. (1997). Handbook of chemometrics and qualimetrics: Part A. Amsterdam, The Netherlands: Elsevier.
- Miller, J. N., & Miller, J. C. (2010). Statistics and chemometrics for analytical chemistry (6th ed.). Essex, England: Pearson.
- Ouyang, G., & Pawliszyn, J. (2008). A critical review in calibration methods for solid- phase microextraction. *Analytica Chimica Acta*, 627(2), 184-197.
- Pawliszyn, J. (1999). Applications of Solid Phase Microextraction. *The Royal Society of Chemistry*. Hertfordshire, UK.
- Scheppers W. S. A. (1999). Solid Phase Microextraction. A Practical Guide. Marcel Dekker, Inc., New York.
- Shyam, N. J., Jaiswal, P., Narsaiah, K., Kumar, R., Sharma, R., Gupta, M., Bhardwaj, R., & Singh, A. K. (2013). Authentication of Mango Varieties using Near-Infrared Spectroscopy. *Agricultural Research*, 2(3), 229-235
- Sousa, E. T., Rodrigues, F. M., Martins, C. C., Oliveira, F. S., Pereira, P. A. P., & Andrade, J. B. (2006). Multivariate Optimization and HS-SPME/GC-MS Analysis of VOCs in Red, Yellow and Purple Varieties of *Capsicum chinensis* sp. Peppers. *Microchemical Journal*, 82(2), 142-149.
- Stalikas, C., Fiamegos, Y., Sakkas, V., & Albanis, T. (2009). Developments on chemometric approaches to optimize and evaluate microextraction. *Journal of Chromatography A*, 1216(2), 175-189.



Optimisation of Pressurised Liquid Extraction of Bioactive Compounds from *Ananas comosus* (Pineapple) Fruit

Almie Amira Munaras Khan*, Norashikin Saim and Rossuriati Dol Hamid

Faculty of Applied Sciences, Universiti Teknologi MARA (UiTM), 40450 Shah Alam, Selangor, Malaysia

ABSTRACT

In this study, pressurized liquid extraction (PLE) was used with methanol as extraction solvent to extract bioactive compounds from *Ananas comosus* (pineapple) flesh. Response surface methodology (RSM) was used to evaluate the correlative effects of temperature (60 – 150°C) and extraction time (10 – 30 min) on the yield of selected bioactive compounds. In this model, the R² obtained was 0.8788 for selected bioactive compounds for *Ananas comosus* suggesting a satisfactory agreement between the predicted and experimental values. Two-dimensional high-performance liquid chromatography (2D-HPLC) with a diode array detector (DAD) was used for the separation and detection of the bioactive compounds. Extraction temperature was found to significantly increase the yield of three selected bioactive compounds following which the optimum operating extraction conditions for PLE for *Ananas comosus* was determined to be 105°C and a static time of 20 min.

Keywords: *Ananas comosus*, bioactive compounds, extraction optimization, HPLC, pineapple, pressurized liquid extraction, RSM

INTRODUCTION

Tropical fruits have an important role in promoting health particularly its antioxidant properties. *Ananas comosus* (pineapple) is rich in bioactive compounds such as anthocyanins, polyphenols and health inducing enzyme bromelain. *Ananas comosus* belongs to Bromeliaceae family that produced edible fruits (Kudom & Kwapong, 2010), and ranked as the third most important tropical fruit produced in the world (Bartholomew et al., 2003). In Malaysia, out of the eleven reported varieties of pineapple available in the market, only Josephine, Morris, MD2 and Sarawak are popularly cultivated (Yuris & Siow, 2014).

ARTICLE INFO

Article history:

Received: 28 September 2016

Accepted: 03 February 2017

E-mail addresses:

almie.amiramk@yahoo.com (Almie Amira Munaras Khan),

noras691@salam.uitm.edu.my (Norashikin Saim),

rossuriati2996@salam.uitm.edu.my (Rossuriati Dol Hamid)

*Corresponding Author

While popular with its nicknames, 'healthy fruit' that rich with antioxidant, pineapple reported to consist chlorogenic acid, catechin, kaempferol, myricetin, gallic acid, gentisic acid, vanillin, ferulic acid, sinapic acid, isoferulic acid, o-coumaric acid, protocatechuic acid, tyrosine, p-coumaroylquinic acid and arbutin, tons of bioactive compounds as claimed (Yapo et al., 2011; Wen, 2001; Taussig & Batkin, 1988).

Fast extraction and low solvent consumption are the main advantages of automated pressurized liquid extraction (PLE). PLE has been successfully applied for the extraction of thermal-sensitive bioactive compounds from plants and fruits (Pettersson et al., 2010). It involves extraction using solvents in liquid state at elevated temperature and pressure to enhance the extraction process. The properties possess by solvent to remain liquefied above their boiling point helps high-temperature extraction activity that happened due to enhanced solubility and mass transfer properties (Richter et al., 1997). Solvents such as ethanol, methanol and water which are reported to be inefficient for extracting anthocyanins and other bioactive compounds at low temperatures, may be much more efficient at the elevated temperatures used in PLE (Ju & Howard, 2003) and thereby obtain an anthocyanin rich extract (Gizir et al., 2008). The present study was undertaken to evaluate the extraction temperature and extraction time on the recovery of bioactive compounds from *Ananas comosus* and to determine the optimal conditions for obtaining maximum yield of bioactive compounds using response surface methodology (RSM). The bioactive compounds selected in this study are catechin, myricetin and bromelain.

METHOD

Catechin, bromelain and myricetin reference standards was purchased from Sigma. Methanol (MeOH) and acetonitrile (ACN) of HPLC grade were purchased from Merck (Germany). Fruits of *Ananas comosus* with different varieties (Morris, MD2 and Josaphine) were obtained locally in Malaysia.

Preparation of Extract

Fresh ripened fruits of *Ananas comosus* were purchased from the market in Selangor, Malaysia. Following which the fruits were peeled, cut into thin pieces and dried for 48 hours at 45°C in an oven (Memmert UN110). The dried flesh was stored in dark-covered container prior to extraction.

Pressurized Liquid Extraction (PLE)

Pressurized Liquid Extraction (PLE) was performed on a Dionex ASE 350 accelerated solvent extractor (Thermo Scientific Ltd. Surrey, UK). Dried *Ananas comosus* was weighed 30.0 grams and were thoroughly put in 100 mL stainless steel extraction cell (PLE) with an adequate amount of diatomaceous earth. The cell containing the sample was heated before filled with methanol and undergone pressurization process. Methanol was selected as extraction solvent based on the polarity of targeted bioactive compounds. To ensure the sample of *Ananas comosus* reaches the desired temperature (60 - 150°C), the cell was placed in heating system for 5 minutes. The sample with pressurized solvent at 1500 psi for 10-30 minutes. All extracts

were covered in aluminium foil to prevent exposure to light and stored at -4°C . A total of 14 experiments were performed to determine the effects of temperature and extraction time on extraction yield. See Table 1.

Experimental Design and Data Analysis

The design of experiments, analysis of the results and prediction of the response were carried out using Design-Expert software (Version 6.0.4). Total of 14 experiments were carried out in randomised run order and central composite design (CCD) was used consisting 5 coded level; $-\alpha$, -1 , 0 , 1 , α . The response variable (catechin, bromelain and myricetin) was evaluated using response surface methodology (RSM) and comparison of means was performed by one-way ANOVA (analysis of variance).

Model Verification

The optimum extraction conditions were based on the maximum yield of bioactive compounds in sample and analysed based on the regression analysis and 3D surface plots of the independent variables. The response was determined under the recommended conditions of extraction and the predicted value was compared with the experimental value to prove the validity of the model.

Analysis using Two-Dimensional Liquid Chromatography (2D-LC)

2D-LC analysis was performed on a Dionex Ultimate 3000 Liquid Chromatography system equipped with diode array detector. 2D-LC chromatographic separation was done on C_{18} column ($5\ \mu\text{m}$, $4.6 \times 250\ \text{mm}$). The mobile phase comprised of 0.01% acidified pure water (A), methanol (B) and acetonitrile (C) using gradient elution (0-2.5 minutes; 50:20:30, 2.5-10.00 minutes; 40:30:30 and 10.00-25.00min ;20:50:30) with flow rate kept at 1 mL/min.in HPLC system, column temperature was maintained at 37°C and injection volume was $100\ \mu\text{L}$. Data acquisition was performed by Chromeleon software version 6.8 Dionex, U.S.A. Eluted compounds were monitored over a wavelength range of 200 – 400 nm.

RESULTS AND DISCUSSION

Optimization of PLE Parameters

For the optimization of extraction of *Ananas comosus* using pressurized liquid extraction static time and temperature ranging from 10 min to 30 minutes and 60°C to 150°C respectively was assigned. Multilinear regression was applied to the results of the central composite design. The results were based on the amount of bioactive compounds obtained from the extract as shown in Table 1. Repetition of same combination of temperature and extraction time which can be seen in Table 1 was designated experiment that determined by central composite design (CCD) method. The effect of independent variables; (a) extraction temperature (T); and (b) extraction time (t), on the amount of bioactive compounds was evaluated by second order (quadratic) model.

Fitting the Model

The adequacy of the model was determined using model analysis, lack of fit test and coefficient of determination (R^2), and its fitness assessed with lack of fit test ($p > 0.05$). ANOVA result showed that the model was significant, $p < 0.05$ ($p = 0.042$) with not significant lack of fit, $p > 0.05$ ($p = 0.1793$). The significance of the equation parameters for each response variable was also assessed by F-ratio at a probability (p) of 0.05. The closer the value of R^2 to unity, the better the empirical model fits the actual data. The quality criteria for a good fit of a model, the coefficient of determination (R^2) should be at least 0.80. In this model, the R^2 was 0.8788 for selected bioactive compounds for *Ananas comosus*. The high value of R^2 (> 0.80) indicates the adequacy of the applied quadratic model. In Table 2, the summary for optimization using Central Composite Design were tabulated and be concluded.

Table 1
Results of the CCD for the analysis of *Ananas comosus*

No.	Factor		Compounds			
	Temperature T (°C)	Extraction Time t(min)	Catechin (mAu*min)	Myricetin (mAu*min)	Bromalein (mAu*min)	Total Area (mAu*min)
1	169	34	295.7	13.57	40.16	322.5
2	41	06	88.23	0.360	10.54	397.9
3	169	06	213.6	73.58	35.49	99.13
4	105	20	271.1	12.32	39.17	104.2
5	105	20	333.7	20.02	44.88	349.4
6	41	34	92.26	0.140	11.73	322.6
7	105	20	348.1	39.43	42.27	429.8
8	169	20	308.9	74.09	38.07	421.0
9	105	34	325.1	41.49	44.15	103.5
10	105	20	344.4	27.57	42.87	206.2
11	41	20	92.29	0.250	11.01	450.6
12	105	06	163.7	12.24	30.24	410.7
13	105	20	375.1	27.17	48.39	414.8
14	105	20	311.6	26.81	42.57	381.0

Table 2
Summary of Central Composite Design for selected bioactive compound in *Ananas comosus*

Response	Transform	Model	Lack of Fit	R^2	Equation
Total Area	Square root	Quadratic Significant	Not Significant	0.8788	Sqrt (Total Area) = +394.03+131.05* A+39.38*B-114.98*A ² -68.78*B ² +5.44*A *B

Effect of Extraction Conditions on Total Bioactive Compounds Content

Parameters such as time and temperature used in extraction plays a vital role in determining the quantity of extractable bioactive compounds from a sample. Temperature is a critical factor that affects extraction processes, as it increases solubility of the substances and recovery of bioactive compounds (Karacabey & Mazza, 2010). Variation in extraction temperature (T) for selected bioactive compounds revealed that increases in temperature also increases the amount of each compounds extracted. When the temperature is increased from 41°C to 73°C the yield of total selected bioactive compounds increased simultaneously, to reach stability when it reaches 105°C before declining. This may be due to thermal degradation occurring in bioactive compounds in extreme temperature thus affecting yields of extraction. It was observed that temperature significantly affects the yield of selected major bioactive compounds in *Ananas comosus* during the extraction process. In general, more components are extracted, when the temperature is elevated through the increased of solubility and mass transfer properties which improved the penetration of solvent into sample matrix.

Long extraction time resulted in high yield of compounds extracted as shown in Figure 1 with maximum yield at 20 minutes. However, prolonged extraction time may increase degradation of bioactive compounds which will affect the yield of response as noted in this study.

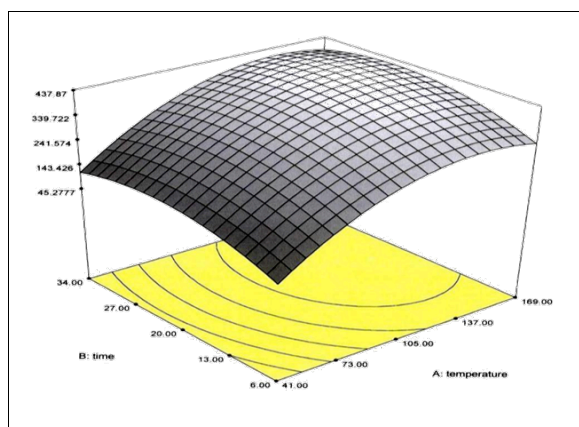
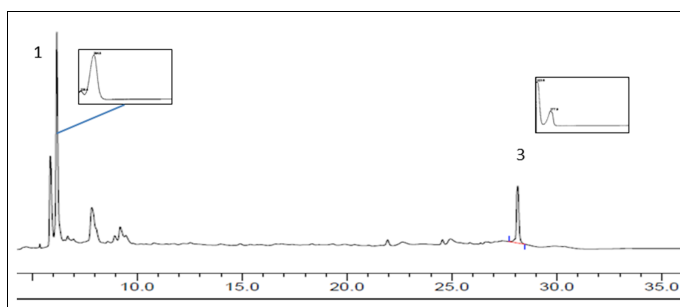


Figure 1. Contour and 3D-response surface plot of static time against temperature for selected major compounds in *Ananas comosus* obtained using Central Composite Design

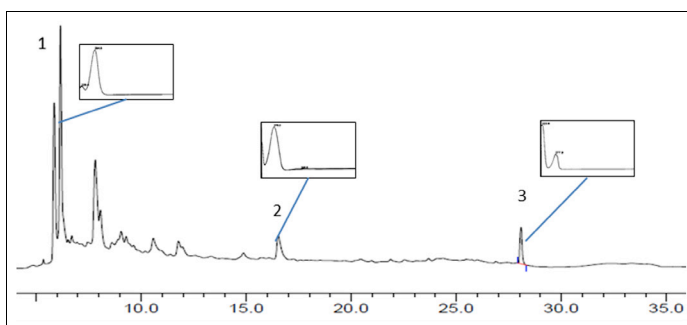
Experimental Validation of the Predictive Model

Establishing the optimal extraction parameters was done using Design-Expert statistical software. The goal was to obtain the highest yield of bioactive compounds extraction from the fruit flesh. The optimal PLE conditions for the extraction of catechin, myricetin and bromelain were pressure of 1500 Psi, and optimal temperature of 105°C overall extraction time of 20 min. Under these optimal conditions and parameters a large amount of extract with a high content of bioactive compounds from *Ananas comosus* flesh was obtained. The adequacy of

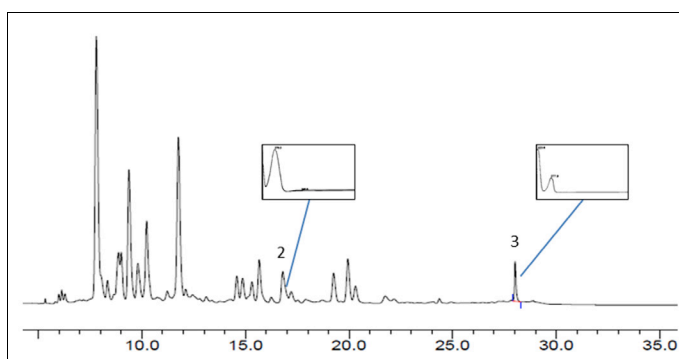
the model was verified as the experimental values were in close agreement with the predicted value, and the deviation too was found to be insignificant. By minimizing the possible strong effect such as origin, time of production and pre-processing storage, the performance of extraction technique can fairly be compared and optimized (Al-Farsi et al., 2005; Dourtoglou et al., 2006; Gizir et al., 2008).



(a)



(b)



(c)

Figure 2. Chromatogram of extract from three varieties of *Ananas comosus*; (a) MD2; (b) Morris; and (c) Josaphine using PLE optimum condition with static time of 20 minutes and temperature of 105°C with their respective UV spectra

HPLC Analysis of *Ananas comosus* Extract

Chromatographic analysis of bioactive compounds in the extract at optimized conditions was conducted using high performance liquid chromatography (HPLC). Several samples of *Ananas comosus* from Morris, MD2 and Josaphine varieties were extracted using the PLE optimum parameters at 105°C, pressure of 1500 psi and a static time of 20 min. Figure 2 shows the chromatograms of *Ananas comosus* extract from respective varieties of pineapple revealed the bioactive compounds mainly present are catechin, myricetin and bromelain. The concentration of the compounds in particular varieties can help to distinguish them apart. Such as in Morris, each of these bioactive compounds were reported present compared to the absence of myricetin in MD2 varieties. In Josaphine, the absence of catechin that appeared in other types of pineapple acts as a distinguishing marker. The identities of the compounds were confirmed by standard reference of the compounds and UV comparison that detected at selected wavelength, 280 nm.

Peak 1 representing catechin with retention time of 6.32 min followed by peak 2, myricetin with retention time of 11.82 min and peak 3; bromelain retention with time 28.08 min.

CONCLUSION

Optimization of extraction procedure for selected bioactive compounds of *Ananas comosus* fruit extract was examined using response surface methodology. This is the first report on optimization of bioactive compound from *Ananas comosus* using this particular extraction technique i.e. pressurized liquid extraction (PLE). The optimized condition was validated and found to be in close agreement with experimental values. The results showed that extraction temperature and extraction time play significant roles in measured responses. Under the optimal conditions of 105°C extraction temperature and 20 min of extraction time, pressurized liquid extraction yield maximum responses of selected bioactive compounds. These conditions can be used to produce extraction yields with higher concentration. The PLE method can contribute to the further isolation of bioactive compound from varieties of *Ananas comosus*.

ACKNOWLEDGEMENTS

Authors are thankful for the financial support from Ministry of Higher Education, Malaysia for this project (Project number: 600-IRMI/DANA 5/3/REI (0005/2016)).

REFERENCES

- Al-Farsi, M., Alasalvar, C., Morris, A., Baron, M., & Shahidi, F. (2005). Comparison of antioxidant activity, anthocyanins, carotenoids, and phenolics of three native fresh and sun-dried date (*Phoenix dactylifera* L.) varieties grown in Oman. *Journal of Agricultural and Food Chemistry* 53(19), 7592–7599.
- Bartholomew, D. P., Paull, R. E., & Rohrbach, K. G. (2003). *The pineapple: botany, production and uses*. CABI Publishing, Wallingford, UK.

- Camel V, (2001). Recent extraction techniques for solid matrices-supercritical fluid extraction, pressurized fluid extraction and microwave-assisted extraction: their potential and pitfalls, *Analyst* 126(7), 1182–1193.
- Chaisakdanugull, C., Theerakulkait, C., & Wrolstad, R. E. (2007) Pineapple juice and its fractions in enzymatic browning inhibition of banana [Musa (AAA Group) Gros Michel]. *Journal of Agriculture and Food Chemistry*, 55, 4252-4257.
- Dourtoglou, V. G., Mamalos, A., & Makris, D. P. (2006). Storage of olives (*Olea europaea*) under CO₂ atmosphere: effect on anthocyanins, phenolics, sensory attributes and in vitro antioxidant properties. *Food Chemistry* 99(2), 342–349.
- Gizir, A. M., Turker, N., & Artuvan, E. (2008). Pressurized acidified water extraction of black carrot [*Daucus carota* ssp. *sativus* var. *atrorubens* Alef.] anthocyanins. *European Food Research and Technology* 226, 363–370.
- Hale, L. P., Greer, P. K., Trinh, C. T., & Gottfried, M. R. (2005) Treatment with oral bromelain decreases colonic inflammation in the IL- 10-deficient murine model of inflammatory bowel disease. *Clinic Immunology*, 116, 135-142.
- Ju, Z. Y., & Howard, L. R. (2003). Effects of solvent and temperature on pressurized liquid extraction of anthocyanins and total phenolics from dried red grape skin. *Journal of Agricultural and Food Chemistry* 51, 5207–5213.
- Karacabey, E., & Mazza, G. (2010). Optimisation of antioxidant activity of grape cane extracts using response surface methodology. *Food Chemistry*, 119, 343-348.
- Kudom, A. A., & Kwabong, P. K. (2010). Floral visitors of *Ananas comosus* in Ghana: A preliminary assessment. *Journal of Pollination Ecology*, 2, 27–32.
- Larrauri, J. A., Ruperez, P., & Saura-Calixto, F. (1997). Pineapple shell as a source of dietary fiber with associated polyphenols. *Journal of Agricultural and Food Chemistry*, 45, 4028-4031.
- Mustafa A., & Turner C. (2011). Pressurized liquid extraction as a green approach in food and herbal plants extraction: A review, *Analytica Chimica Acta*, 703, 8– 18.
- Richter, B. E., Jones, B. A., Ezzell, J. L., Porter, N. L., Avdalovic, N., & Pohl, C. (1996). Accelerated solvent extraction: a technique for sample preparation, *Analytical Chemistry*, 68(6), 1033.
- Taussig, S. J., & Batkin, S. (1988). Bromelain, the enzyme complex of pineapple (*Ananas comosus*) and its clinical application. An update. *J Ethnopharmacol.* 1988 Feb-Mar; 22(2):191-203.
- Wen, L. (2001). Pineapple juice: Phenolic composition and enzymatic browning inhibition. Ph.D. thesis, Oregon State University.
- Yapo, E. S., Kouakou, H. T., Kouakou, L. ., Kouadio, J. ., Kouame, P., & Mérillon, J. (2011). Phenolic profiles of pineapple fruits (*Ananas comosus* L. Merrill) Influence of the origin of suckers. *Australian Journal of Basic and Applied Sciences*, 5, 1372-1378.
- Yuris, A. & Siow, L. (2014). A comparative study of the antioxidant properties of three pineapple (*Ananas comosus* L.) varieties. *Journal of Food Studies*, 3, 40-56.



Physical and Conductivity Studies of Plasticised Methyl Cellulose-Lithium Triflate based Polymer Electrolyte

Nursyahida Sahli^{1*}, Nordiana Nabilla Ramly¹, Muhd Zu Azhan Yahya²
and Ab Malik Marwan Ali^{1,3}

¹Faculty of Applied Sciences, Universiti Teknologi MARA (UiTM), 40450 Shah Alam, Selangor, Malaysia

²Faculty of Defence Science and Technology, Universiti Pertahanan Nasional Malaysia (UPNM),
Kem Sungai Besi, 57000, Kuala Lumpur, Malaysia

³Institute of Science, Universiti Teknologi MARA (UiTM), 40450 Shah Alam, Selangor, Malaysia

ABSTRACT

Solid polymer electrolyte based on methyl cellulose (MC)-lithium triflate (LiCF_3SO_3) plasticised with ethylene carbonate (EC) was prepared using solution cast technique. The X-ray diffraction (XRD) studies proved that the amorphous nature of the electrolyte systems was increases due to the addition of salt and plasticiser. The improved surface morphology of plasticised polymer system ensures it has good electrode-electrolyte contact during performance testing. The polymer electrolyte was found to have high thermal stability indicating that the electrolyte can be used at higher temperature. The ionic conductivity increased up to $1.24 \times 10^{-4} \text{ S cm}^{-1}$ at optimum amount of EC plasticiser associated to the effect of plasticiser that initially leads to the formation of Li^+ -EC complex. Consequently, it reduces the fraction of polymer- Li^+ complex which contributes to the increase of the segmental chain flexibility in the plasticized system. Temperature dependent studies indicate ionic conductivity increase due to the temperature increase and is in line with Arrhenius behaviour pattern. An activation energy of 0.26 eV at highest conductivity sample was obtained. The addition of plasticiser lowers the activation energy thus increasing the ion mobility of the system and contributing to ionic conductivity increment. The plasticization method is a promising means to dealing with the solid polymer electrolyte problem and producing electrolytes that meet the needs of electrochemical devices.

Keywords: Lithium triflate, ethylene carbonate, impedance spectroscopy, X-ray diffraction

ARTICLE INFO

Article history:

Received: 28 September 2016

Accepted: 03 February 2017

E-mail addresses:

syahidasahli@gmail.com (Nursyahida Sahli),

dianaramly@gmail.com (Nordiana Nabilla Ramly),

mzay@upnm.edu.my (Muhd Zu Azhan Yahya),

ammali@salam.uitm.edu.my (Ab Malik Marwan Ali)

*Corresponding Author

INTRODUCTION

Solid polymer electrolytes (SPEs) has great potential in electrical energy storage systems such as batteries, super capacitors, fuel cell and solar cell as the alternative sources

(Dissanayake et al., 2002; Malathi et al., 2010; Shukur et al., 2013). This electrolyte also is known for its ability to overcome the leakage problem of toxic liquid electrolyte, high energy density, good thermal stability and high conductivity (Gopalan et al., 2008; Johan et al., 2013). However, the conductivity achievement and electrode-electrolyte contact still needs to be improved for commercial purposes.

The plasticization method is a promising method to modify the SPE beside formation of cross-linked network (Wetjen et al., 2013), copolymerization (Li et al., 2013), and insertion of ceramic filler (Tan et al., 2007). It involves the introduction of plasticiser into SPEs system which also known as gel polymer electrolytes (GPEs). Several plasticiser such as propylene carbonate (PC) and ethylene carbonate (EC) are widely used in polymer electrolyte (Ali et al., 2011; Mahmud et al., 2012).

Pradhan et al. (2010) in their work reported that the conductivity of SPE increases with the addition of plasticiser due to the lowering of glass transition temperature and increasing the amorphous phase of the polymer. In the present study, EC is selected as the plasticiser due to its low molecular weight and higher dielectric constant ($\epsilon = 89.6$) compare to the polymer host (Ramesh et al., 2011). The high dielectric constant of the plasticiser helps the ions to have better dissociations. The study investigates the physical and electrical performance in producing better polymer electrolyte with plasticiser content.

METHOD

Polymer electrolytes consisting of methylcellulose (MC) as polymer host, lithium triflate (LiCF_3SO_3 or LiTf) as a doping salt and EC as plasticiser was prepared using solution cast technique. Dimethyl formamide (DMF) was used as a solvent to dissolve all the materials. Prior to the preparation of polymer-salt solution the LiCF_3SO_3 salt was dried at 100°C in order to eliminate the excessive water. 1 g of MC and lithium salt were dissolved separately in DMF and then were mixed together in a Scott bottle. The mixture was stirred for about 24 hours before casting on Teflon petri dish to let the solvent evaporate slowly until the polymer-salt film form. The procedure repeated with different stoichiometric ratios of lithium salt. For GPEs systems, the sample with the highest ionic conductivity was mixed with different weight percent of EC using the similar procedures. The free-standing film forms were obtained through slowly drying process inside a vacuum oven at temperature of 60°C . All the samples were prepared at room temperature and stored in desiccators for further use. The thicknesses of the films were between 0.1 mm and 0.2 mm.

For structural analysis, X-ray diffraction pattern of the films were recorded by PAN Analytical X-ray diffractometer with $\text{CuK}\alpha$ radiation wavelength (1.54056 \AA) in the 2θ angle range between 10° to 40° with scanning rate 5° min^{-1} . Environmental scanning electron microscopy (ESEM) was used to determine the morphology of the samples with $5000\times$ scanning magnification. The thermal studies were performed using thermogravimetric analysis (TGA) at heating temperature from 25°C to 500°C , and conductivity measured by AC impedance spectroscopy studies using HIOKI 3531 Z Bridge at frequency range between 100 Hz and 1

MHz at amplitude 10mV. The polymer electrolytes were sandwiched between two stainless steel blocking electrodes with humidity controlled. The conductivity-temperature dependence study was conducted in the temperature range 303 K to 363 K.

RESULTS AND DISCUSSION

Figure 1 shows the X-ray diffractograms of pure MC film, pure LiCF_3SO_3 , MC with 30wt.% LiCF_3SO_3 and MC- LiCF_3SO_3 with 40wt.% EC content. The broad peaks of pure MC appeared between $2\theta = 10^\circ$ and 30° correlated to the crystalline nature of methylcellulose known as amorphous hump. The pattern shows that the amorphous character of the samples increased as the crystalline peaks decreased gradually and their width began to broaden following the addition of lithium salt (Caruso et al., 2002). The crystalline peak of pure lithium which exhibited at $2\theta = 16.27^\circ, 19.5^\circ, 22.24^\circ, 31.98^\circ, 39.65^\circ$ (Figure 1(d)) appeared to disappear in the polymer-salt system (Figure 1b) indicating the complete dissolution of lithium salt in the polymer system (Ahmad et al., 2011). Figure 1c shows the X-ray diffractogram of plasticized film is similar with the X-ray diffractogram of polymer salted film. The crystalline nature of this film was decreased compared to the pristine polymer sample indicates that the addition of EC increase the amorphous domain of MC- LiCF_3SO_3 polymer matrix. The reduction in crystallinity could explain increases in conductivity, suggesting crystallinity and conductivity are related in the sample (Johan et al., 2011).

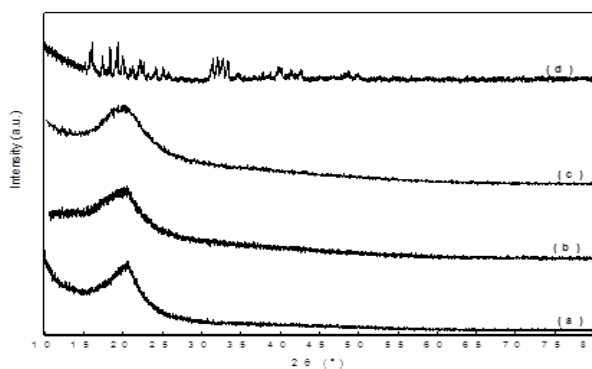


Figure 1. XRD pattern of (a) Pure MC; (b) MC-30wt% LiCF_3SO_3 ; (c) MC- LiCF_3SO_3 -40wt% EC; and (d) Pure LiCF_3SO_3

Figure 2 shows the surface morphology (ESEM) of pure MC film, polymer salt system and polymer salt-plasticiser system. The results show pure MC image has rough wrinkles surface with micro-pores. The addition of lithium salt onto the MC polymer in Figure 2(b) shows a reduction of the roughness of the surface structure while the XRD analysis shows the amorphous hump became less sharp and broadened in polymer salt system implying that the amorphousness phase in the electrolyte has increased. Due to this observation, it is suggested that the increase of the amorphousness phase in MC polymer is associated with the smooth surface morphology of the polymer electrolyte as a result of the interaction of ether oxygen of

MC and Li^+ ions (Johan et al., 2011). In Figure 2(c) it can be noticed that the surface morphology of the plasticised polymer-salt appears very smooth, dense and absent of pores. Predictably, larger plasticisers were entrapped within the polymer matrix thus increase the flexibility of the segmental motion of where influenced in the transporting of charge carriers and successfully improved the surface layer of the electrolyte. This result ensures good electrode-electrolyte contact and impedance spectroscopy characterization and device applications (Shukur et al., 2014).

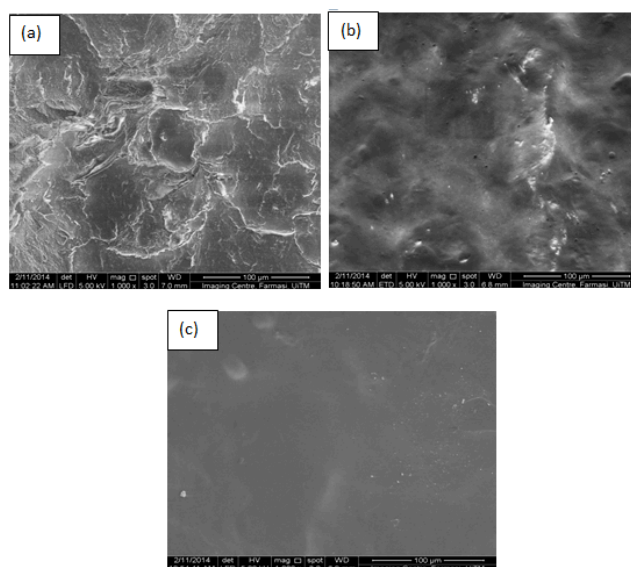


Figure 2. FESEM image (a) Pure MC; (b) MC-30wt% LiCF_3SO_3 ; and (c) MC- LiCF_3SO_3 -40wt% EC complexes

The thermogravimetric curve at different polymer electrolyte systems shows in Figure 3. The initial degradation of the % weight loss at temperature below $100\text{ m}^\circ\text{C}$ is due to the removal of moisture, transition of the sample or volatilization of small molecules and/or monomers (Guirguis & Moselhey, 2012; Ramesh & Yi, 2009). For pure MC (Figure 3(a)) no further weight loss is observed until decomposition commenced at approximately 302.2°C before drastically decline. This indicates that the film preparation method was stable at up to 300°C . The total weight loss for pure MC film is 83.18%. In MC-30wt.% LiCF_3SO_3 system (Figure 3(b)) show steps of temperature degradation. The film constantly stable from 130°C to 250°C until second degradation occurs at 256.7°C . The degradation begins from 256.7°C to 302.1°C might be cause by decomposition of MC. This remark that the thermal stability for sample containing MC-30wt.% LiCF_3SO_3 stable up to 250°C before decomposition. Finally, degradation from 302.1°C to 499°C indicates the main thermal degradation of MC and LiCF_3SO_3 complexes. Thermal stability with the presence of LiCF_3SO_3 reduces the thermal stability of MC from 300°C to 256.7°C . This may be attributable to the weak interaction between MC and LiCF_3SO_3 caused the disruption in the complexes proved by FTIR results from previous studies (Sahli

& Ali, 2012). The addition of EC plasticiser on polymer-salt system (Figure 3(c)) shows the thermal stability increased where the major decomposition temperature for the second stage occurs at 269.9°C. The final degradation at 421°C to 500°C with the mass loss of 19.25% indicates the degradation of plasticizer EC. It is relevant to use MC based polymer electrolyte in electrochemical devices since the thermal stability is higher than 100°C.

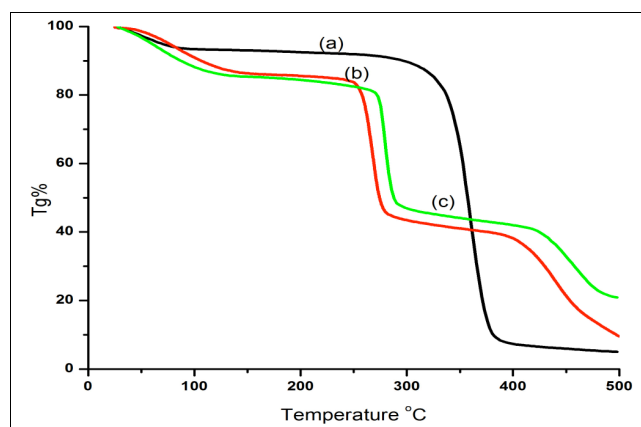


Figure 3. Thermograms for (a) Pure MC; (b) MC-30wt% LiCF₃SO₃ and (c) MC-LiCF₃SO₃-40wt% EC complexes

Figure 4 shows the ionic conductivity at variation wt.% of EC plasticiser in polymer electrolyte system. It can be observed that the highest ionic conductivity is $1.24 \times 10^{-4} \text{ S cm}^{-1}$ for 40 wt.% EC at room temperature. This phenomenon can be explained by the relatively low viscosity of the plasticiser which decreases the local viscosity around the charge transporting ion thereby increasing ionic mobility. The high dielectric constant of the plasticiser interrupts the coulombic force between the anions and cations of the salt contributed to the salt dissociation in the system therefore more free Li⁺ ions are produced (Saikia et al., 2008). The addition of plasticiser initially leads to the formation of Li⁺-EC complex which will reduce the fraction of polymer-Li⁺ complex. The flexibility of polymer chains will increase and contribute to improvement in conductivity.

Figure 5 represents the temperature dependence measurement for unplasticised polymer-salt and plasticized polymer-salt system at highest conductivity. The $\log \sigma$ versus $1000/T$ plot shows that the conductivity for both systems increases with increases in temperature, when a small amount of space surrounding its own volume is created through which ionic motion can take place and thereby increase conductivity. A similar tendency can be observed with ionic crystal where the ions jump into neighbouring vacant sites and increases conductivity when the temperature is raised. The regression values are near to unity indicating ion transport in the temperature dependence system follows the Arrhenius rules shown below Equation (1).

$$\sigma(T) = \sigma_0 \exp(-E_a/kT) \quad [1]$$

Where σ_0 is the exponential factor, E_a is the activation energy, K is the Boltzmann constant and T is the absolute temperature. The activation energy, E_a is the energy required for an ion to begin movement which calculated from the slope of the $\log \sigma$ versus $1000/T$ plot. The activation energies at the highest conducting samples for unplasticised and plasticized of the MC-based systems are presented in Table 1. It shows that the electrolytes with high conductivity exhibit the E_a (Yap et al., 2012). This can explained that in plasticized system the sufficient energy of ion is lower for the ion to transfer from the donor site to another thus leading increase the ion mobility (Johan et al., 2011).

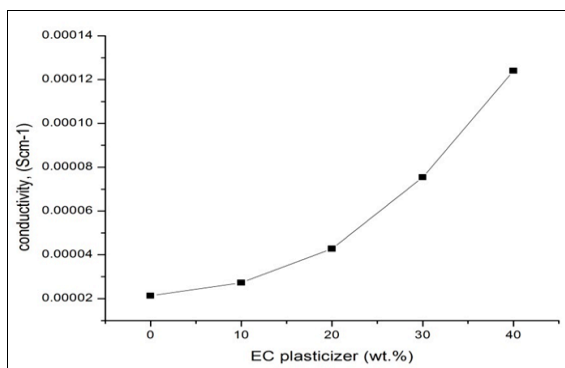


Figure 4. The conductivity plot of GPE system at different concentration of plasticiser at 303 K

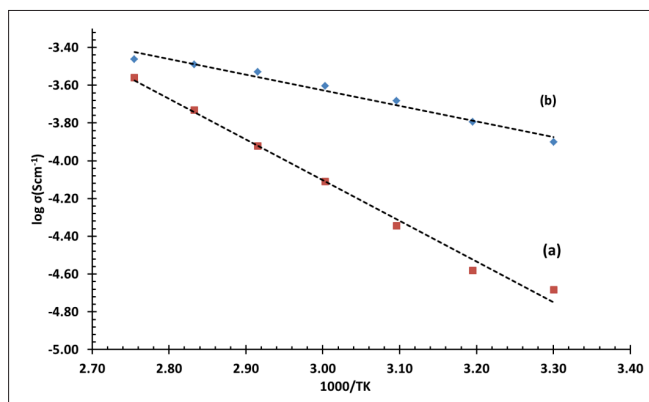


Figure 5. Temperature dependence of ionic conductivity for (a) MC-30wt% LiCF₃SO₃; and (b) MC-LiCF₃SO₃-40wt% EC at 303-363 K

Table 1

The activation energy, E_a values for the highest conductivities of MC-30wt.% LiCF₃SO₃ and MC-LiCF₃SO₃-40wt.% EC

Electrolyte	Conductivity, σ (S cm ⁻¹)	Activation energy, E_a (eV)
MC- LiCF ₃ SO ₃	2.13×10^{-5}	0.68
MC- LiCF ₃ SO ₃ -EC	1.24×10^{-4}	0.26

CONCLUSION

Polymer electrolytes consisting of MC-LiCF₃SO₃-EC have successfully prepared and investigated showed good thermal stability at high temperature. The XRD proved that by reducing crystallinity ionic conductivity can be enhanced as it has been noted to increase with rises in temperature increases.

ACKNOWLEDGEMENTS

The authors are grateful for financial assistance from the Ministry of Higher Education (MOHE) under the RAGS grant 600-RMI/RAGS 5/3 (12/2012) and to the Faculty of Applied Sciences and Institute of Science, Universiti Teknologi MARA for providing facilities.

REFERENCES

- Ahmad, A., Isa, K. B. M., & Osman, Z. (2011). Conductivity and Structural Studies of Plasticized Polyacrylonitrile (PAN) – Lithium Triflate Polymer Electrolyte Films. *Sains Malaysiana*, 40(7), 691–694.
- Ali, R. M., Harun, N. I., Ali, A. M. M., & Yahya, M. Z. A. (2011). Conductivity studies on plasticised cellulose acetate–ammonium iodide based polymer electrolytes. *Materials Research Innovations*, 15(2), 39–42.
- Caruso, T., Capoleoni, S., Cazzanelli, E., Agostino, R. G., Villano, P., & Passerini, S. (2002). Characterization of PEO-Lithium Triflate Polymer Electrolytes: Conductivity, DSC and Raman Investigations. *Ionic*, 8, 36–43.
- Dissanayake, M. A. K. ., Bandara, L. R. . K., Bokalawala, R. S., Jayathilaka, P. A. R. ., Ileperuma, O. ., & Somasundaram, S. (2002). A novel gel polymer electrolyte based on polyacrylonitrile (PAN) and its application in a solar cell. *Material Research Buletin*, 37, 867–874.
- Gopalan, A., Santhosh, P., Manesh, K., Nho, J., Kim, S., Hwang, C., & Lee, K. (2008). Development of electrospun PVdF–PAN membrane-based polymer electrolytes for lithium batteries. *Journal of Membrane Science*, 325(2), 683–690.
- Guirguis, O. W., & Moselhey, M. T. H. (2012). Thermal and structural studies of poly(vinyl alcohol) and hydroxypropyl cellulose blends. *Natural Science*, 4(1), 57–67.
- Johan, M. R., Shy, O. H., Ibrahim, S., Mohd Yassin, S. M., & Hui, T. Y. (2011). Effects of Al₂O₃ nanofiller and EC plasticizer on the ionic conductivity enhancement of solid PEO–LiCF₃SO₃ solid polymer electrolyte. *Solid State Ionics*, 196(1), 41–47.
- Kumar Kiran, K., Ravi, M., Pavani, Y., Bhavani, S., Sharma, A., & Narasimha Rao, V. V. . (2012). Electrical conduction mechanism in NaCl complexed PEO/PVP polymer blend electrolytes. *Journal of Non-Crystalline Solids*, 358(23), 3205–3211.
- Li, L., Wang, J., Yang, P., Guo, S., Wang, H., Yang, X., ... Wu, B. (2013). Preparation and characterization of gel polymer electrolytes containing N-butyl-N-methylpyrrolidinium bis(trifluoromethanesulfonyl) imide ionic liquid for lithium ion batteries. *Electrochimica Acta*, 88, 147–156.

- Mahmud, Z. S., Adam, N. I., Zaki, N. H. M., Ali, A. M. M., & Yahya, M. Z. A. (2012). Conductivity and optical studies of plasticized polymer electrolytes based on 49% PMMA-grafted natural rubber. *2012 IEEE Symposium on Business, Engineering and Industrial Applications*, 504–508.
- Malathi, J., Kumaravadivel, M., Brahmanandhan, G. M., Hema, M., Baskaran, R., & Selvasekarapandian, S. (2010). Structural, thermal and electrical properties of PVA–LiCF₃SO₃ polymer electrolyte. *Journal of Non-Crystalline Solids*, 356, 3377–2281.
- Pradhan, D. K., Samantaray, B. K., Choudhary, R. N. P., Karan, N. K., Thomas, R., & Katiyar, R. S. (2010). Effect of plasticizer on structural and electrical properties of nanocomposite solid polymer electrolytes. *Ionics*, 17(2), 127–134.
- Ramesh, S., Shanti, R., & Durairaj, R. (2011). Effect of ethylene carbonate in poly (methyl methacrylate)-lithium tetraborate based polymer electrolytes. *Journal of Non-Crystalline Solids*, 357(5), 1357–1363.
- Ramesh, S., & Yi, L. J. (2009). Structural, thermal, and conductivity studies of high molecular weight poly(vinylchloride)-lithium triflate polymer electrolyte plasticized by dibutyl phthalate. *Ionics*, 15(6), 725–730.
- Sahli, N., & Ali, A. M. M. (2012). Effect of lithium triflate salt concentration in methyl cellulose-based solid polymer electrolytes. *Humanities, Science and Engineering (CHUSER), 2012 IEEE Colloquium on*, 739 – 742.
- Saikia, D., Chen-Yang, Y. W., Chen, Y. T., Li, Y. K., & Lin, S. I. (2008). Investigation of ionic conductivity of composite gel polymer electrolyte membranes based on P(VDF-HFP), LiClO₄ and silica aerogel for lithium ion battery. *Desalination*, 234(1-3), 24–32.
- Shukur, M. F., Ithnin, R., Illias, H. a., & Kadir, M. F. Z. (2013). Proton conducting polymer electrolyte based on plasticized chitosan–PEO blend and application in electrochemical devices. *Optical Materials*, 35(10), 1834–1841.
- Shukur, M. F., Ithnin, R., & Kadir, M. F. Z. (2014). Electrical characterization of corn starch-LiOAc electrolytes and application in electrochemical double layer capacitor. *Electrochimica Acta*, 136, 204–216.
- Tan, C. G., Siew, W. O., Pang, W. L., Osman, Z., & Chew, K. W. (2007). The effects of ceramic fillers on the PMMA-based polymer electrolyte systems. *Ionics*, 13(5), 361–364.
- Wetjen, M., Kim, G.-T., Joost, M., Winter, M., & Passerini, S. (2013). Temperature dependence of electrochemical properties of cross-linked poly(ethylene oxide)–lithium bis(trifluoromethanesulfonyl) imide–N-butyl-N-methylpyrrolidinium bis(trifluoromethanesulfonyl)imide solid polymer electrolytes for lithium batteries. *Electrochimica Acta*, 87, 779–787.
- Yap, K. S., Teo, L. P., Sim, L. N., Majid, S. R., & Arof, A. K. (2012). Investigation on dielectric relaxation of PMMA-grafted natural rubber incorporated with LiCF₃SO₃. *Physica B: Condensed Matter*, 407(13), 2421–2428.



The Effect of Saccharin Concentration on the Electrochemical Behaviour of Electrodeposited Nanocrystalline Cobalt-Iron Coating

Nik Rozlin Nik Masdek^{1*}, Wan Muhammad Aniq Aiman¹, Mardziah Che Murad¹, Zuraidah Salleh¹ and Koay Mei Hyie²

¹Faculty of Mechanical Engineering, University Teknologi MARA (UiTM), 40450 Shah Alam, Selangor, Malaysia

²Faculty of Mechanical Engineering, University Teknologi MARA (UiTM), 13200 Pulau Pinang, Malaysia

ABSTRACT

In the electrodeposition system, adding saccharin alters the properties of the metal deposits by changing the electrode kinetics of the deposited surface. In this study, nanocrystalline cobalt-iron (CoFe) coating was synthesised using the electrodeposition technique with different saccharin concentrations. The results obtained showed that the coating thickness increased while the grain size decreased from 51 nm to 40 nm when the saccharin concentration increased from 0 to 2 g/L. The nanocrystalline CoFe coating produced with 2 g/L of saccharin concentration resulted in the smallest particle size of 71.22 nm and the highest microhardness of 251.86 HV. From the salt spray test (24 and 48 hours) it was found that the use of saccharin at higher concentration of 2 g/L improves the corrosion resistance of the nanocrystalline CoFe coating significantly due to the change of surface morphology as well as the decrease in grain size.

Keywords: CoFe, corrosion, electrodeposition, nanocrystalline, saccharin

ARTICLE INFO

Article history:

Received: 28 September 2016

Accepted: 03 February 2017

E-mail addresses:

nikrozlin@yahoo.com (Nik Rozlin Nik Masdek),
aniqqaiman@gmail.com (Wan Muhammad Aniq Aiman),
mardziahcm@yahoo.com (Mardziah Che Murad),
a_kzue@yahoo.com (Zuraidah Salleh),
hyie1105@yahoo.com (Koay Mei Hyie)

*Corresponding Author

INTRODUCTION

Since its discovery by Gleiter (1981), nanocrystalline materials have had a huge impact on many material properties. These materials are defined as having grain sizes in the nanometre range, typically less than 100 nm. Grain refinement of materials into the nanometre range has been shown to result in unique and improved properties compared with their conventional polycrystalline counterparts.

Since the first production of nanocrystalline materials through inert gas condensation method, several processing techniques have been developed and available for producing these materials. However, electrodeposition has been reported to be the oldest and most economical and viable technique to produce these very fine grain materials. Uniform depositions on complex shaped substrates, low cost, high production rates, good reproducibility, and the reduction of waste attributed to synthesising nanocrystalline material are among the many advantages to employ this method in producing nanostructured metal and alloys (Schwarzacher et al., 2006).

Saccharin is often added to electrolyte as a grain refiner and brightener during the electroplating process. Saccharin adsorbs on the deposited surface forming a condensed phase where the density and coverage of adsorbed saccharin depends on the potential of electrode surface and the concentration inside the solution (Buessherman, 1994; Kwon & Gewirth, 2007). In this study, nanocrystalline cobalt-iron (CoFe) coating was synthesised with various saccharin concentrations through the electrodeposition method at a current density of 1.1 A/cm^2 in an acidic solution of pH 2.9. The effect of saccharin concentration on the surface morphology, particle and grain size, hardness, and corrosion behaviour was investigated.

METHOD

Mild steel was used as the substrate with the dimension of 15 mm x 45 mm. Prior to the deposition process, the substrates were mechanically polished with silicon carbide papers of 120, 320, 600, 800 and 1200 grits. The substrates were cleaned using distilled water to remove any unwanted particles and then immersed in sulphuric acid to remove any contaminants. The substrates were then dried to prevent trapped moisture inside the coating before the electrodeposition process starts.

Nanocrystalline CoFe alloy deposits were synthesised from a sulphate solution. The plating bath consisted of a mixture of cobalt sulfate, iron sulfate, boric acid, sodium chloride and different concentrations of saccharin. The chemical composition of the solution is listed in Table 1. All chemicals were dissolved in 500 ml of distilled water using a magnetic stirrer to ensure the chemicals were evenly mixed. The operating temperature and pH value were maintained at 40°C and 2.9. Sulphuric acid (H_2SO_4) was added in small drops to the electrolyte bath in order to adjust the pH of the bath solution. The electrodeposition process which took about 30 minutes was synthesised using a direct current of 1.1 A/cm^2 . The mild steel plate (cathode) and graphite (anode) were placed parallel to each other at a distance of 5 cm. The saccharin concentrations ranged between 0 g/L and 2 g/L while other parameters remained constant. The specimen was later rinsed with distilled water and dried at room temperature.

Table 1
Electrodeposition bath composition

Chemicals	Concentration (g/L)
Cobalt Sulphate (CoSO ₄ , 7H ₂ O)	14.2
Iron Sulphate (FeSO ₄ , 7H ₂ O)	5.6
Boric Acid (H ₃ BO ₃)	16.6
Sodium Chloride (NaCl)	4.2
Saccharin	0 - 2

The Field Emission Scanning Electron Microscope (FESEM) was used to characterise the surface morphology and microstructure of the nanocrystalline CoFe coatings. The chemical composition was measured using an energy dispersive X-ray spectroscopy (EDX) system. The XRD investigation was carried out using a RIGAKU ULTIMA IV instrument operated at 40 kV and 20 mA with Cu K α radiation ($\lambda=0.1542$ nm) at a scan speed of 3° min⁻¹ in the range of 30-100°. The XRD was used to identify the preferred crystallographic orientation as well as calculate grain sizes of the electrodeposits. Furthermore, the microhardness of the CoFe coating was measured using a Vickers microhardness tester (MITUTOYO MVK-H1). The microhardness test used a 1kg load and an indentation time of 15 s. The test was carried out by taking five measurements at different locations on each of the CoFe coatings to ensure accuracy and the average value was taken as the final hardness value. Corrosion behavior was studied using a salt spray test according to ASTM B117 respectively.

RESULTS AND DISCUSSION

Figure 1 (a), (b) and (c) show the FESEM images of deposited nanocrystalline CoFe coatings with different saccharin concentration. Different surface morphology was obtained for CoFe coatings produced with different saccharin concentration. The morphology of the CoFe coating produced with 0 g/L saccharin resulted in a dendritic morphology as shown in Figure 1(a). The dendritic morphology contained secondary and tertiary arms and branches originated from the main trunk, which is similar to the results reported by Zhu et al. (2008). Meanwhile, a spherical morphology was obtained for CoFe coatings with saccharin concentration of 1 g/L as shown in Figure 1(b). The spherical morphology showed smaller grain sizes compared with the dendritic morphology. This decrease in grain size could be attributed to electrocrystallisation process where new crystals were shaped on the existing crystal (Bockris et al., 1967). It was also found that as the saccharin concentration increased, agglomerations were produced as shown in Figure 1(c) for CoFe coatings electrodeposited with 2 g/L of saccharin. Furthermore, the increase of saccharin concentration significantly improved the surface morphology of the electrodeposited nanocrystalline CoFe coating where a smoother, more compact and brighter deposits were obtained. In addition, the increase in saccharin concentration has also decreased the grain sizes of the CoFe coatings (Masdek & Alfantazi, 2012, 2014; Jin-Ku et al., 2009).

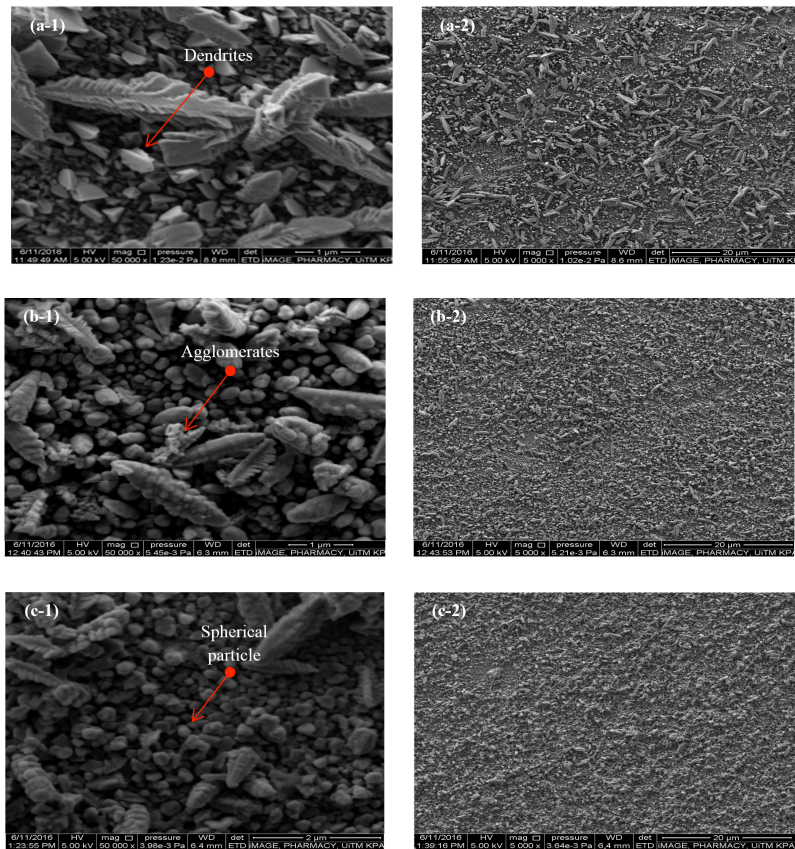


Figure 1. FESEM images under: (1) = 1 μm ; and (2) = 20 μm microscopy of electrodeposited CoFe with different saccharin concentration at: (a) = 0 g/L; and (b) = 1 g/L (c) 2 g/L

The electrodeposited nanocrystalline CoFe coating with 0, 1 and 2 g/L of saccharin concentrations produced different particle sizes, which are 86.27 nm, 84.31 nm and 71.22 nm respectively. The particle size was measured from five different regions of each sample by using Image J software and the average value was taken as the final particle size. The smallest particle size was obtained from the CoFe coating deposited with 2 g/L of saccharin. It has been reported that the decrease in particle size is related to the cathode efficiency as well as the deposition rates (Masdek & Alfantazi, 2014; Prado et al., 2009). In addition, the reduction of particle size and the presence of enormous quantities of grain boundaries in the microstructures are also reported to produce good mechanical and physical properties (Hye et al., 2014). The thickness of the coating was also measured using the FESEM as shown in Figure 2. It was found that the coating thickness corresponded with an increase in saccharin concentration. The thickness of the CoFe coating was in the range of 25.47 μm to 40.68 μm .

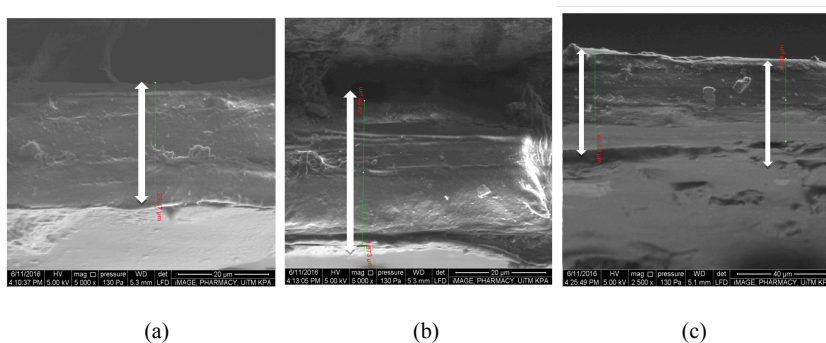


Figure 2. The thickness of CoFe coating with: (a) 0g/L (25.55 μm); (b) 1 g/L (29.47 μm); and (c) 2 g/L (40.68 μm)

The EDX analysis was used to study elemental composition of the electrodeposited nanocrystalline CoFe coatings. Table 2 shows the elemental composition of the electrodeposited nanocrystalline CoFe coatings with different saccharin concentrations (0, 1 and 2 g/L). The EDX confirmed the presence of cobalt (Co), oxygen (O), carbon (C) and a small amount of sulphur (S) in all the samples. The element of Co showed the increase amount of weight (%) when saccharin concentration was increased from 0 to 1 g/L. However, a slight decrease of weight (%) was noted when saccharin concentration was increased from 1 to 2 g/L. The element of O showed a decrease of weight (%) as the saccharin concentration increased from 0 to 1 g/L. However, the weight (%) corresponded with an increase of saccharin from 1 to 2 g/L. The carbon was found to slightly decreased in weight (%) when the saccharin concentration was increased from 0 to 1 g/L. interestingly, no carbon content was found from CoFe coatings deposited with saccharin concentration of 2 g/L. This may be due to the carbon tape that was used during sample preparation (Hyie et al., 2012).

Table 2
The elemental composition of CoFe coatings at different saccharin concentrations

Sample	Saccharin concentration (g/L)		
	0	1	2
Element	Weight (%)	Weight (%)	Weight (%)
C	0.21	0.20	-
O	21.77	21.71	21.76
Co	40.21	47.94	46.41
Fe	37.73	30.09	31.78
S	0.01	0.05	0.03

The application of XRD can be used to determine the characteristics of a compound based on diffraction pattern. The electrodeposited nanocrystalline CoFe coatings for all samples were characterised using XRD. Figure 3 shows the XRD patterns for deposited nanocrystalline CoFe alloy deposits with different saccharin concentrations. The CoFe alloys existed at three distinct phases, namely the ϵ (HCP), γ (FCC) and α (BCC) phases at room temperature.

The XRD patterns of nanocrystalline CoFe coating obtained with different saccharin concentrations resulted in different Co and CoFe peaks. The Co-Fe phase exposed its characteristic peak at approximately 2θ angle, 45°, 65°, and 83°. These conditions were also reported in a previous study by Hyie et al. (2012). The CoFe phase was identified as the body-centred cubic (BCC) crystal structure with JCPDS No. 010717170 (Masdek & Alfantazi, 2014; Hyie et al., 2012; Abdullah et al., 2013). The Co phase was also observed in the sample and its peaks were observed approximately at 2θ angle of 99°. The Co phase was identified as the hexagonal close-packed (HCP) structure. Similar results were also reported by previous studies (Jin-Ku et al., 2009; Hyie et al., 2012; Hyie et al., 2014). The crystallite size of these deposited CoFe coatings with 0, 1 and 2 g/L saccharin concentrations were obtained from the XRD results by using Debye Scherrer's formula as followed:

$$D = \frac{k\lambda}{\beta \cos\theta} \quad [1]$$

Where D is the grain size, k is the constant of proportionality which is 0.9, λ is referred to the wavelength of X-ray (Cu Kα=0.152 nm), β is the full-width half maximum (FWHM) in radian, and θ is the Bragg angle. The average grain size of crystallites calculated for each sample with different saccharin concentrations is shown in Table 3. The crystallite size of CoFe coatings ranges from 51 nm to 40 nm. The increment of saccharin concentration resulted in the decrease of grain size. This may be due to the ability of saccharin to refine the grain size and reduce internal stress of electrodeposited coatings (Masdek & Alfantazi, 2014; Jin-Ku et al., 2009; Hassani et al., 2008; Rashidi et al., 2009). It has been reported that the ability of saccharin to adsorb onto the coating surface slows down the surface distribution of ions to the active spots of growth resulting in a smaller grain size (Wu, 2002).

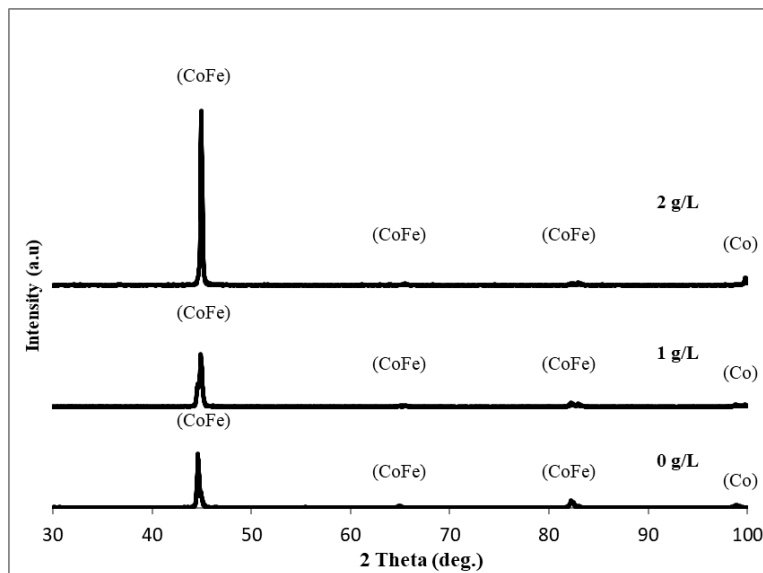


Figure 3. The X-ray diffraction pattern for three electrodeposited nanocrystalline CoFe coatings obtained in 0 g/L, 1 g/L and 2 g/L saccharin concentration

Table 3

The grain size of electrodeposited nanocrystalline CoFe coatings with different saccharin concentrations

Saccharin concentration (g/L)	Grain size (nm)
0	51
1	45
2	40

The relation between microhardness of the deposited nanocrystalline CoFe coatings and grain size is shown in Figure 4. The measurements resulted in a decrease of hardness as the grain size increases. From the figure, it can be seen that the hardness decreased linearly from about 252 HV for CoFe coatings with the smallest grain size of 40 nm to 185 HV for the coatings with the largest grain size of 51 nm. Similar results were also reported where the decrement of grain size of nanocrystalline materials resulted in an increase of hardness (Hassani et al., 2008; Rashidi et al., 2009; Suryanarayana, 2002). The increase in hardness of the nanocrystalline CoFe coating deposited with 2 g/L of saccharin is also due to the compact surface structure produced compared with the other samples obtained with lower saccharin concentration. This compact structure is believed to reduce the formation of void and thus improved the hardness of these electrodeposited nanocrystalline CoFe coatings.

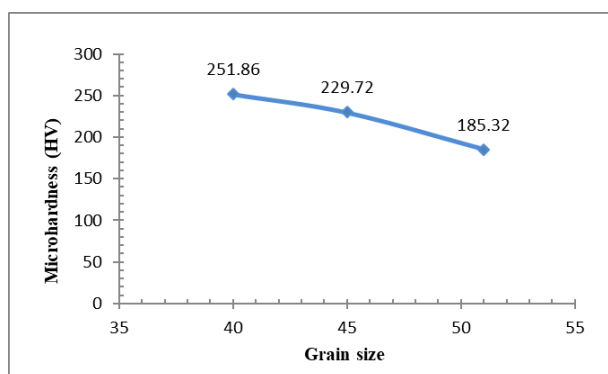


Figure 4. The variation of microhardness of nanocrystalline CoFe coatings as a function of grain size

The corrosion behaviour of the electrodeposited nanocrystalline CoFe coatings with different saccharin concentrations was evaluated using the salt spray test. The corrosion test done followed the ASTM B117 standard. Salt fog test had been conducted for 24 hours and 48 hours to observe the effect of the corrosion on the surface coatings. Table 4 shows the conditions of all CoFe coating samples deposited with different saccharin concentrations before and after (24 and 48 hours) the tests were done. The results obtained clearly showed that the nanocrystalline CoFe coating produced with 0 g/L saccharin concentration has the lowest corrosion resistance where it was easily corroded for both 24 and 48 hours. The corrosion resistance significantly improved where it shows only a slight corroded area from

the nanocrystalline CoFe coating obtained using 2 g/L saccharin that was tested for 24 hours. However, the deposit showed white rust due to the fog of droplets that had accumulated on the surface coating after 48 hours. This was also reported by Nayana and Venkatesha (2010). On the other hand, it was found that the coating was still intact on the mild steel even though there was some yellowish-brown colour corrosion that was developed on the nanocrystalline CoFe coating. After 48 hours salt spray test, the entire surface coating from the deposit that was produced with 1 g/L saccharin concentration showed a brown colour of rust. The CoFe coating obtained with 0 g/L saccharin that was tested for 24 and 48 hours clearly showed a large area of reddish brown colour indicating a severe corrosion had occurred. Based on the three-different saccharin concentration used to deposit the nanocrystalline CoFe coating, the sample with 2 g/L saccharin concentration showed highest corrosion resistance from with 24 and 48 hours salt spray test compared with two coatings produced with lower saccharin concentration.

Table 4
The conditions of nanocrystalline CoFe coatings with different saccharin concentrations before and after 24 hours and 48 hours salt spray test

Saccharin concentration	Before	After	
		24 hours	48 hours
0 g/L			
1 g/L			
2 g/L			

CONCLUSION

This study had studied the effect of saccharin concentrations on the electrodeposited nanocrystalline CoFe coatings which were found to have had a remarkable effect on the microstructure, grain size, microhardness and corrosion behaviour. The increase in saccharin concentration significantly improved the surface morphology of the electrodeposited nanocrystalline CoFe coating where a smoother, thicker, more compact and brighter deposits were obtained. The increase in saccharin concentration had also decreased the grain sizes of the

CoFe coatings from 51 nm to 40 nm. Furthermore, the microhardness of the electrodeposited nanocrystalline CoFe coatings also increased from 185 HV to 252 HV with higher saccharin concentrations in the electrolyte solution due to the smaller grain size. The corrosion resistance also improved significantly with higher saccharin concentration. Thus, it can be concluded that the presence of saccharin in higher concentration in the electrolyte changed the surface morphology, increased the coating thickness and microhardness as well as improve the corrosion resistance of the electrodeposited nanostructured CoFe coatings.

ACKNOWLEDGEMENTS

The authors gratefully acknowledge the assistance of the Research Management Centre (RMC) and Ministry of Higher Education (MOHE) Malaysia in providing the Fundamental Research Grant Scheme (Project Number: 600-RMI/FRGS 5/3 (80/2015) and 600-RMI/DANA 5/3/LESTARI (67/2015) research grants, and Universiti Teknologi MARA for its support.

REFERENCES

- Abdullah, W. N. R., Resali, N. A., Hyie, K. M., Roselina, N. R. N., Mardziah, M., & Salleh, Z., (2013). Co-Fe Nanoparticles Coated on Copper Substrate: Effect of Different Deposition Times. *Applied Mechanics and Materials*, 393, 222-227.
- Bockris, J. O. M., & Razumney, G. A. (1967). *Fundamental Aspects of Electrocrystallization*. Plenum Press, New York 27.
- Buess-Herman, C. (1994). Self-assembled monolayers at electrode metal surfaces. *Prog. Surf. Sci*, 46, 335–375.
- Gleiter, H. (1981). Materials With Ultra-Fine Grain Sizes, *Proceedings of the 2nd Riso International Symposium on Metallurgy and Materials Science* (edited by Hansen N. et al), Roskilde, 15.
- Hassani, S., Raeissi, K., & Golozar, M. A. (2008). Effects of Saccharin on the Electrodeposition of Ni-Co Nanocrystalline Coatings. *Journal of Applied Electrochemistry*, 38, 689-694.
- Hyie, K. M., Abdullah, W. N. R., Resali, N. A., Chong, W. T., Salleh, Z., & Ghani, M. A. A. (2012). The Physical and Magnetic Properties of Electrodeposited Co-Fe Nanocoating with Different Deposition Times. *Journal of Nanomaterials*, 2013, 1-6.
- Hyie, K. M., Ahmad, A., Resali, N. A., Munir, M. F., Li, C. S., & Saidin, S. (2014). Corrosion study of electrodeposited Co-Ni-Fe Protective Coating on Electroless Nickel Immersion Gold (ENIG) Flexible Printed Circuit. *Procedia Technology*, 15, 792-797).
- Hyie, K. M., Resali, N. A., Abdullah, W. N. R., & Chong, W. T. (2012). Synthesis and Characterization of Nanocrystalline Pure Cobalt Coating: Effect of pH. *Procedia Engineering*, 41, 1627-1633).
- Jin-ku, Y., Ming-zhi, W., Qun, L., Jun, Y. & Lian, L. (2009). Effects of Saccharin on Microstructure and Property of Electrodeposited Ni-Fe Alloys. *Transactions of Nonferrous Metals Society of China*, 19, 805-809.
- Karami, H., & Mohammadzadeh, E. (2010). Synthesis of Cobalt Nanorods by the Pulsed Current Electrochemical Method. *Int. J. Electrochem. Sci.*, 5, 1032-1045.

- Kwon, H., & Gewirth, A. A. (2007). SERS Examination of Saccharin Adsorption on Ni Electrodes. *J Electrochem Soc*, 154(11), D577-D583.
- Masdek, N. R. N., & Alfantazi, A. M. (2012). Nanocrystalline Cobalt-Iron Alloy: Synthesis and Characterization. *Material Science and Engineering A*, 550, 388-394.
- Masdek, N. R. N. (2014). *Electrodeposition and Corrosion Study of Nanocrystalline Cobalt and Cobalt-Iron Alloy Coatings* (PhD Dissertation). University of British Columbia.
- Masdek, N. R. N., & Alfantazi, A. M. (2014). An EQCM study on the influence of saccharin on the corrosion properties of nanostructured cobalt and cobalt-iron alloy coatings. *Journal of Solid State Electrochemistry*, 18, 1701-1717.
- Nayana, K. O. & Venkatesha, T. V. (2010). Influence of Condensation Product on Bright Nanocrystalline Zinc Electrodeposition and its Properties. *Synthesis and Reactivity in Inorganic, Metal-Organic, and Nano-Metal Chemistry*, 40, 170-178.
- Prado, R. A., Facchini, D., Mahalanobis, Gonzalez, N. F., & Palumbo, G. (2009). Electrodeposition of Nanocrystalline Cobalt Alloy Coatings as a Hard Chrome Alternative. *NAVAIR Public Release*, 9, 776.
- Rashidi, A. M., & Amadeh, A. (2009). The Effect of Saccharin Addition and Bath Temperature on the Grain Size of Nanocrystalline Nickel Coatings. *Surface and Coatings Technology*, 204, 353-358.
- Resali, N. A., Hyie, K. M., Abdullah, W. N. R., & Saad, N. H. (2014). Morphological Studies of Electrodeposited Cobalt Based Coatings: Effect of Alloying Elements. *Adv. Mater.Res.*, 938, 52-57.
- Schwarzacher, W., Deligianni, H., & Schwartz, D. (2006). Electrodeposition: A Technology for the Future. *The Electrochemical Society Interface*, 32-35.
- Suryanarayana, C. (2002). The Structure and Properties of Nanocrystalline Materials: Issues and Concerns," *JOM*, 54, 24-27.
- Wu, B. Y. C. (2002). Synthesis and characterization of nanocrystalline alloys in the binary Ni-Co system (MSc. Dissertation). University of Toronto.
- Zhu, L. P., Xiao, H. M., Zhang, W. D., Yang, Y., & Fu, S. Y. (2008). Synthesis and Characterization of Novel Three-Dimensional Metallic Co Dendritic Superstructures by a Simple Hydrothermal Reduction Route. *Crystal Growth and Design*, 8, 1113-1118.



Wear Properties of Carbon Nanotubes Filled Epoxy Polymers and Woven Glass Fiber Reinforced Polymer Composites

Anis Adilah Abu Talib, Aidah Jumahat*, Napisah Sapiai and Ahmad Shahrul Mohd Roslan

Faculty of Mechanical Engineering, Universiti Teknologi MARA (UiTM), 40450 Shah Alam, Selangor, Malaysia

ABSTRACT

This research investigated the wear properties of Carbon Nanotube (CNT) filled epoxy polymer and fiber reinforced composites. The CNT/epoxy composites with 0.5 wt% and 1.0 wt% CNT contents were mixed at 50°C for 1 hour at a speed of 400 rpm using mechanical mixer, while woven glass fiber reinforced polymer (GFRP) nanocomposites were fabricated using vacuum bagging technique. The effect of CNT on wear properties was evaluated using dry sliding abrasion wear test that used vitrified bonded silicon carbide as abrasive wheels. The mass loss and specific wear rate curves show that wear properties of epoxy polymer and GFRP composite systems were enhanced when CNT was added. Epoxy polymer and GFRP nanocomposites showed the highest wear resistance when CNT content was 1.0 wt% and 0.5 wt% respectively. The CNT-filled composite showed improvement till up to 78.9 % from its pure system. This suggested that the load transferability between CNT and epoxy was more effective in nanomodified systems than in its pure systems. Therefore, adding CNT improves the wear properties of epoxy polymer and woven GFRP composite.

Keywords: CNT, dry abrasion, epoxy, glass fiber, specific wear rate

ARTICLE INFO

Article history:

Received: 28 September 2016

Accepted: 03 February 2017

E-mail addresses:

anisadilah86@gmail.com (Anis Adilah Abu Talib),
aidahjumahat@salam.uitm.edu.my (Aidah Jumahat),
napisahsapiai@gmail.com (Napisah Sapiai),
syahrulroslan92@gmail.com (Ahmad Shahrul Mohd Roslan)

*Corresponding Author

INTRODUCTION

In recent years, the demand for advanced composite materials has increased due to their availability and their utility in many applications. Wear performance of a material is based on the material properties in terms of its wear rate and friction coefficient. It can be defined as the loss of material when subjected to relative motion, and it further includes any form of surface damage caused by rubbing processes. Thus, composite materials embed

reinforcement into the matrix to improve the properties of the material. Epoxy resin matrix, a thermoset type polymer, has been used extensively in engineering applications, due to its flexible processing characteristics, good affinity to heterogeneous materials, considerable creep and solvent resistance as well as its high operating temperatures (Guo et al., 2010). However, there are still limitations to using epoxy matrix, such as brittleness, rigidity, and poor resistance to crack propagation (Mirmohseni & Zavareh, 2010). Therefore, fillers and fibers have been reinforced to formulate high mechanical and wear resistant composite materials. The fillers have been developed from micro-size to nano-size today to give a better impact on the matrix. Nano-size fillers are added for better stiffness, strength, toughness, dimensional stability, and thermal properties (Jumahat et al., 2013). Fillers such as carbon nanotubes (CNTs) have high aspect ratio (Meng et al., 2009) and outstanding mechanical, electrical, thermal, and other characteristics, making them a multi-functional reinforcement material for polymer matrices (Sapiai et al., 2015; Kim et al., 2012).

Fiber reinforced polymer composites hold extra credit because of their lightweight, excellent specific stiffness and strength, and liberty in design due to tailored anisotropy behaviour (Chen et al., 2014). Glass fibers on the other hand, is a remarkable material due to their high strength to weight ratio and high corrosion and chemical resistance (Kanny & Mohan, 2014), besides their wide availability as well as being inexpensive (Zhao et al., 2013). However, the properties of FRP composite depend on several factors such as fiber orientation, fiber content, fiber length, fiber/matrix compatibility and its interface strength (Guignier et al., 2015; Sapiai et al., 2015).

Many studies have been conducted in the past decade on CNT (nanofillers) reinforced polymer composites and glass fiber reinforced polymer focusing on their mechanical and tribological properties. While for advanced type composite structure where fiber serves as primary reinforcement and nanofiller as secondary reinforcement, studies on tribological properties have are new (the past 5 to 7 years). A study by Suresha et al. (2010) looked at carbon and glass fabric reinforced vinyl ester composites, where a test was conducted using block on ring dry wear test to find out wear behaviour of the composites. The result showed that carbon fiber showed better wear resistance than glass fiber, due to the abrasiveness of the latter that ruptured transfer film and adhesive bonds at the interface of the composite.

Larsen et al. (2008) examined glass and carbon/aramid weave epoxy composite using pin on disc to determine wear performance at 9 different p-v conditions. It was found that glass/epoxy is beneficial if fibers in the weave are oriented parallel and anti-parallel with respect to sliding direction instead of normal and parallel. The findings are also affected by fiber properties, as reported by (Suresha et al., 2010). Dong et al. (2005) studied the tribological properties of nanocomposites where 0-4.0 wt% MWCNT content was incorporated into epoxy matrix and tested under dry sliding contact condition. It was found that MWCNTs/EP composites have higher wear resistance and also smaller friction coefficient compared with pure epoxy system. Nanocomposites with 1.5wt% MWCTNs content showed smallest wear rate and friction coefficient. Yan et al. (2013) on the other hand had studied the performance of aligned CNT (ACNTs) epoxy composite when undergoing water-lubricated sliding contact.

They concluded that first, ACNTs improved wear resistance of ACNTs/EP composites by 219 times than pure epoxy, and second, water lubricant improved wear mechanism from fatigue wear to slightly abrasive wear.

Although enhanced mechanical properties of CNT filled polymer composite have been extensively investigated, the wear properties of advanced nano-filled fiber reinforced composite have not yet been fully studied. In the present work, wear behaviour (mass loss and specific wear rate) of CNT-filled epoxy and CNT-filled Glass Fiber Reinforced Polymer (GFRP) composites under abrasive condition was studied. Sample characterisations such as TEM, density, heat distribution and optical micrograph were conducted.

METHOD

In this work, the epoxy resin (Miracast 1517 A) and hardener (Miracast 1517 B) used in this research were supplied by Miracon (M) Sdn. Bhd; the mixing ratio was 100:30. A FloTube 9000 Series Multi-wall Carbon Nanotube (CNT) was used as nanofiller, supplied by CNano Technology (Beijing) Ltd, China. The CNT was produced by a catalytic vapour deposition process with average diameter and length of 11 nm and 10 μm respectively. The glass fiber used was CWR200 plain weave C-glass fiber supplied by Vistec Technology Service (M) Sdn. Bhd.

The desired amount of CNT (0.5 wt%, and 1.0 wt%) was measured and mixed in epoxy resin using mechanical stirrer at 50°C temperature and speed of 400 rpm for 1 hour. The mixture was then degassed under high vacuum oven for 1 hour to remove oxygen and air bubbles. Finally, the mixture was blended with hardener for 15 minutes before used.

For CNT-filled epoxy system, the samples were prepared using silicon mould. The silicon mould was prepared following dimension shown in Figure 1. The surface of silicon mould was coated with release agent to ease sample removal once it cures. Curing process was done at room temperature for 24 hours. For CNT-filled GFRP composite system, vacuum bagging method was used to laminate glass fiber and CNT-filled epoxy resin. The CNT-filled epoxy resin of 0.5 wt% and 1.0 wt% was prepared by following the exact procedure mentioned above. 24 sheets of glass fiber was layered with mixture of CNT-filled epoxy resin to ensure the 6mm sample thickness, as required by machine specification. Vacuum process was done for 1 hour to remove trapped air. Finally, the laminates were cured at room temperature for 24 hours. The cured laminates were cut based on the dimension shown in Figure 1, in accordance with machine specification.

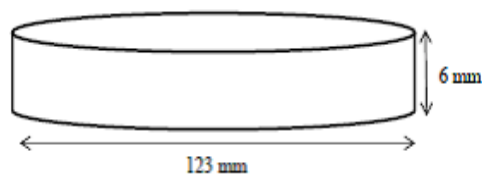


Figure 1. Dimensions for dry sliding abrasion test

The degree of CNT dispersion in epoxy matrix was observed using Transmission Electron Microscopy (TEM). The sample was cut into a thickness of 85nm using Leica UC2 Ultra-microtome machine at room temperature. The TEM machine used was FEI Tecnai TEM at accelerating voltage of 80 kV. Gatan MS6000CW high-resolution digital camera was used to capture the image, while Gatan digital micrograph software was used to collect the image with magnifications of 43000x and 300000x.

The density of sample was determined by Archimedes' principle using density balance. The size of the composite sample was 15 mm x 15 mm x 3.0 mm and calculated in accordance to ASTM D792. The density was obtained following Eq. [1]. Measurement was repeated 5 times for each sample system.

$$\rho_{sample} = \frac{A}{A - B} \times [(\rho_{water} - d) + d] \quad [1]$$

Where ρ_{sample} is density of sample, ρ_{water} is density of water at room temperature (20°C) = 0.9982 g/cm³, A is mass of dry sample and B is mass of sample in water.

Abrasion Resistance Tester (TR-600) was used to conduct dry sliding abrasion wear test. The schematic diagram of the tester is shown in Figure 2. The test was conducted based on ASTM D3389 standard. The disc of 123 mm diameter and 6 mm thickness was the sample, located in contact with two vitrified bonded silicon carbide as the abrasive wheels. In each test run, the wheels were cleaned using metal brush to eliminate any dust, particle and contaminant. The weight of sample at initial stage and after each run was taken using high precision balance. The sample was set at 267 rpm speed and 20 N load for 10,000 m distance travel with interval of 2000 m. A total of five readings of mass was taken for 10,000 m distance travel. Based on the mass loss recorded, the specific wear rate was calculated using Archard's wear model (Archard, 1953), stated in Eq. [2]. The summary of operational conditions is given in Table 1.

$$W_s = \frac{\Delta m}{L \times \rho \times F} \quad [2]$$

Where W_s in (mm³/Nm), Δm is mass loss (g), L is sliding distance (m), ρ is density (g/mm³) and F is applied load (N).

The thermal distribution at the contact surface was captured using Infrared camera (PTI 160) to obtain the amount of heat generated during testing. To further investigate the worn surface, optical microscopy was done using Stereo-zoom Microscope. This was facilitated using IMAP software, where the software is able to enlarge the image of sample in order to investigate the scratch and wear mechanisms on the surface.

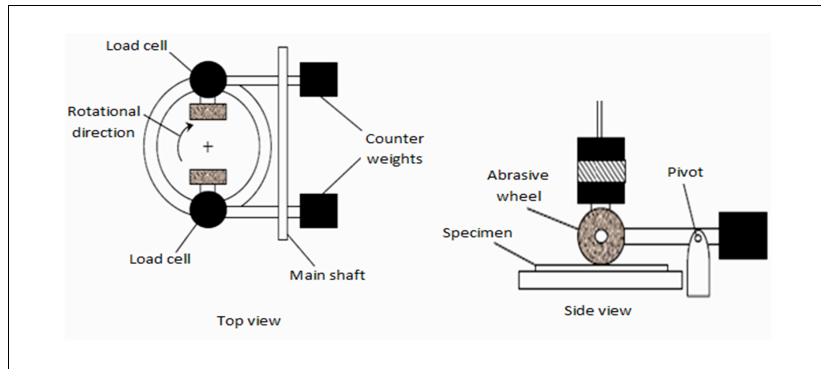


Figure 2. Schematic diagrams of Abrasion Resistance Tester (TR-600) (Jumahat et al., 2015)

Table 1
Operating parameters of Dry Sliding Abrasion Test

Parameters	Experimental Conditions
Contact geometry	Cylinder on flat
Type of motion	Unidirectional sliding
Applied load	20 N
Sliding speed	267 rpm
Sliding distance	10,000 m at interval 2000 m

RESULTS AND DISCUSSION

Based on Eq. (1), the density of CNT-filled epoxy and CNT-filled GFRP composite was obtained, shown in Table 2. The density of epoxy filled with CNT was increased as CNT content increased while CNT-filled GFRP composite showed different trend as CNT content increased. Although fiber reinforcement did increase the density of composite, the latter decreased as CNT content increased. This may be due to the presence of voids in the composite and uneven dispersion of CNT inside the matrix. The density further affects the result of specific wear rate of samples, as shown in Eq. (2).

Table 2
Density of sample

Epoxy content (wt%)	CNT content (wt%)	Glass Fiber content (vol%)	Density of composite (g/cm ³)
100.0	-	-	1.14850
99.5	0.5	-	1.14981
99.0	1.0	-	1.14998
100.0	-	10.0	1.65552
99.5	0.5	10.0	1.48892
99.0	1.0	10.0	1.41586

The dispersion of 0.5 wt% and 1.0 wt% CNT in epoxy resin is shown in Figure 3 and Figure 4 respectively. At high magnification, TEM images showed the presence of clusters of entangled CNT in epoxy. The CNT has an average diameter of 10 nm as shown in high magnification TEM images.

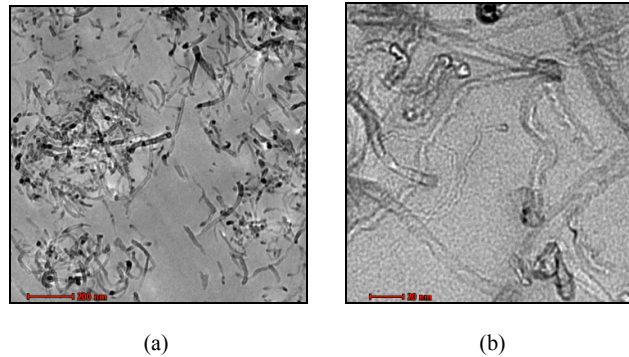


Figure 3. TEM images for dispersion of 0.5 wt% CNT-filled epoxy at magnification of: (a) 43000x; and (b) 300000x

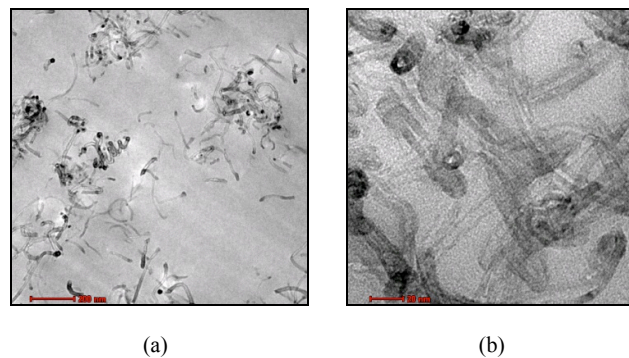


Figure 4. TEM images for dispersion of 1.0 wt% CNT-filled epoxy at magnification of: (a) 43000x; and (b) 300000x

The results for accumulated mass loss of CNT-filled epoxy and CNT-filled GFRP composite are shown in Figure 5(a) and Figure 5(b) respectively. The results were compared with pure epoxy and pure GFRP composite system. The mass loss over 10,000 m distance follows a similar increasing trend for all samples of pure epoxy, pure GFRP composite, CNT-filled epoxy and CNT-filled GFRP composite. In Figure 5(a), the accumulated mass loss for pure epoxy, 0.5 wt% CNT and 1.0 wt% CNT-filled epoxy composites are 0.725 g, 0.325 g and 0.300 g respectively. The 1.0 wt% CNT-filled epoxy showed lowest mass loss, improving by 58.2 % from epoxy without nanofillers. It can be observed that the CNT incorporation in epoxy has reduced the amount of accumulated mass loss of the samples, although the improvement was not that significant.

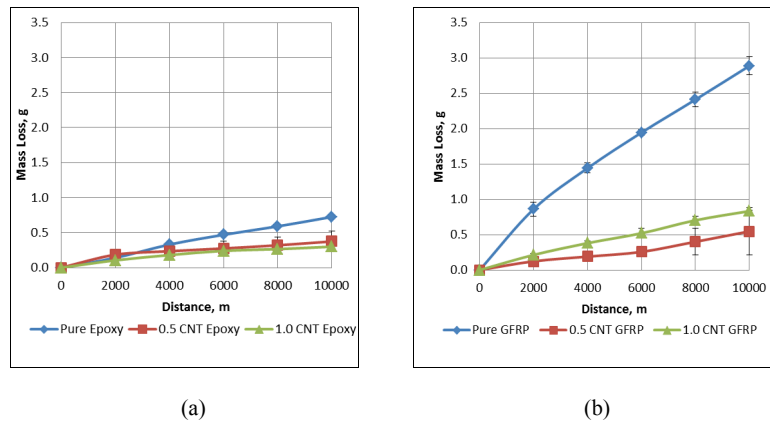


Figure 5. Curves of accumulated mass loss versus distance for: (a) CNT-filled epoxy; and (b) CNT-filled GFRP composite when compared to pure system using dry sliding abrasive test

In Figure 5(b), the profile trend for 0.5 wt% and 1.0 wt% CNT-filled GFRP composite have shown great improvement compared with that of pure GFRP composite. The lowest mass loss is 0.547 g from sample with 0.5 wt% CNT content. Both samples of 0.5 wt% and 1.0 wt% CNT-filled GFRP composite have shown wear improvement up to 81.1% and 71.1% respectively. However, pure GFRP composite has highest accumulative mass loss up to 2.887 g, very high compared with pure epoxy in Figure 5(a). This is due to the presence of glass fiber in the composite. Glass fibers are abrasive and brittle in nature (Suresha et al., 2010). Its debris may form third-body abrasive wear, leading to higher mass loss (Larsen et al., 2008). Moreover, 1.0 wt% CNT-filled GFRP composite performance was not at par as 1.0 wt% CNT-filled epoxy performance, might be due to agglomeration of CNT in the matrix. However, by observing both figures, the results actually proved that resins incorporated with nanofillers do improve its wear resistant compared with their pure system.

From accumulated mass loss values, corresponding specific wear rate profiles after 10,000 m distance travel were plotted in Figure 6 using Eq. (2) and the density results obtained before. In Figure 6(a), the specific wear rate after 10000 m is highest for pure epoxy compared with 0.5 wt% and 1.0 wt% CNT-filled epoxy composites with a value of 0.003156 mm³/Nm. The lowest specific wear rate is using 1.0 wt% CNT-filled epoxy composite with a value of 0.0013044 mm³/Nm, indicating its high wear resistance. The percentage improvement was about 56.67 % from pure epoxy. Furthermore, by observing the three profiles, the presence of CNT showed improvement on the composite, although the improvement only occurred after 4000 m distance travel. This is due to the run-in wear stage or initial wear stage that begins from 0 m to 4000 m distance, and above 4000 m, the composite has achieved its steady-state stage (Lee et al., 2014).

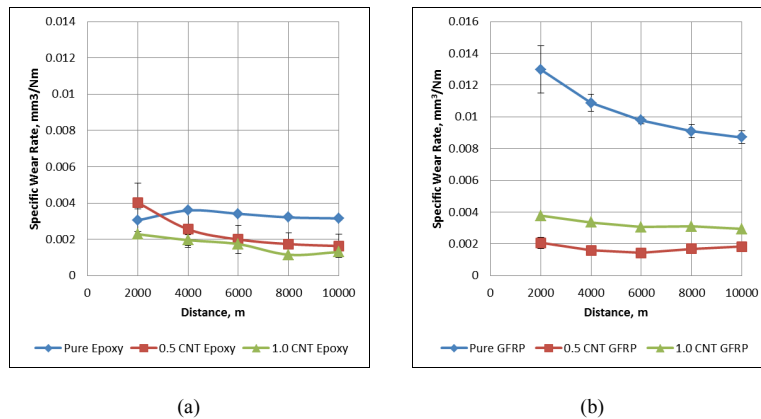


Figure 6. Curves of specific wear rate versus distance for: (a) CNT-filled epoxy; and (b) CNT-filled GFRP composite compared with pure system using dry sliding abrasive test

For the case of CNT-filled GFRP composite, shown in Figure 6(b), the specific wear rate profiles for pure, 0.5 wt% and 1.0 wt% CNT content showed a more consistent improvement. As described in Figure 5(b), 0.5 wt% CNT-filled GFRP composite has the highest wear performance, thus the lowest specific wear rate with a value of 0.0018358 mm³/Nm, improving by 78.9% compared with pure GFRP composite. The sample with 1.0 wt% CNT content has shown less wear improvement that may be due to nanofiller agglomeration (Dong et al., 2005).

Figure 7 and Figure 8 show thermal distribution of the contact at the wheel for both systems after 6000 m distance travel, for CNT-filled epoxy system and CNT-filled GFRP composite system respectively. The maximum temperature recorded for CNT-filled epoxy system was 37.3°C and 34.6°C for 0.5 wt% and 1.0 wt% CNT content respectively. The thermal distribution showed that the frictional heat for 1.0 wt% CNT-filled epoxy is lower, which resulted in lower wear rate. On the other hand, higher maximum temperature was recorded for CNT-filled GFRP composite systems. 0.5 wt% CNT content recorded temperature of 40.2°C while 1.0 wt% CNT content recorded even higher temperature up to 42°C. The frictional heat created on the surface of the latter sample was very high, resulting in a higher mass loss, complying with the low specific wear rate discussed before. Besides that, the presence of glass fiber contributed to the frictional heat due to the abrasive nature of glass fiber (Suresha et al., 2010).

The worn surface of pure GFRP composite and CNT-filled GFRP composite for dry sliding abrasion test after 10,000 m distance travel was selected to evaluate the effect of CNT content on the worn surface, as shown in Figure 9.

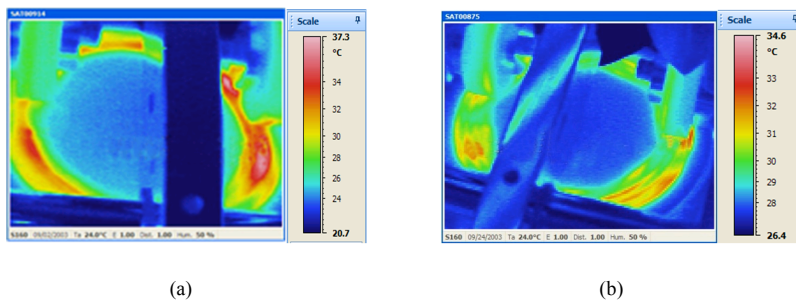


Figure 7. Thermal distribution of: (a) 0.5 wt%; and (b) 1.0 wt% CNT-filled epoxy composite

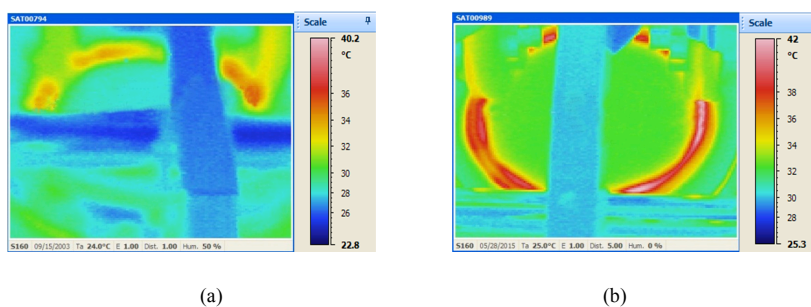


Figure 8. Thermal distribution of: (a) 0.5 wt%; and (b) 1.0 wt% CNT-filled GRFP composite

The worn surface of samples exhibited different morphologies due to different interfacial strengths. The worn surface of pure GFRP composite shows signs of adhesion and abrasive wear (Figure 9(a)). The surface displayed plucked and ploughing marks indicating adhesive wear and ploughing. The damage starts with microcracks leading to resin removal. Once the fiber is not protected by resin, they become exposed to fracture due to their brittle and fragile behaviour (Larsen et al., 2008). The boundary of wear track and unworn surface (Figure 9(b)) was not easily distinguished due to the high resin removal. The matrix/fiber interface strength was not strong, corresponding with the result obtained in Figure 5(b).

Incorporating CNT in GFRP composite showed improvement in worn surfaces as displayed in Figure 9(c and d) and Figure 9(e and f). No fiber pull out or ploughing was found in either samples. The surface was also smoother, uniform and compact, without any microcracks of resin. The adhesive wear was clearly reduced, as proven by results in Figure 5(b). The boundaries can also be distinguished easily due to the strong interface strength between fiber and matrix. Therefore, incorporating CNT into epoxy matrix reduces wear of GFRP composites.

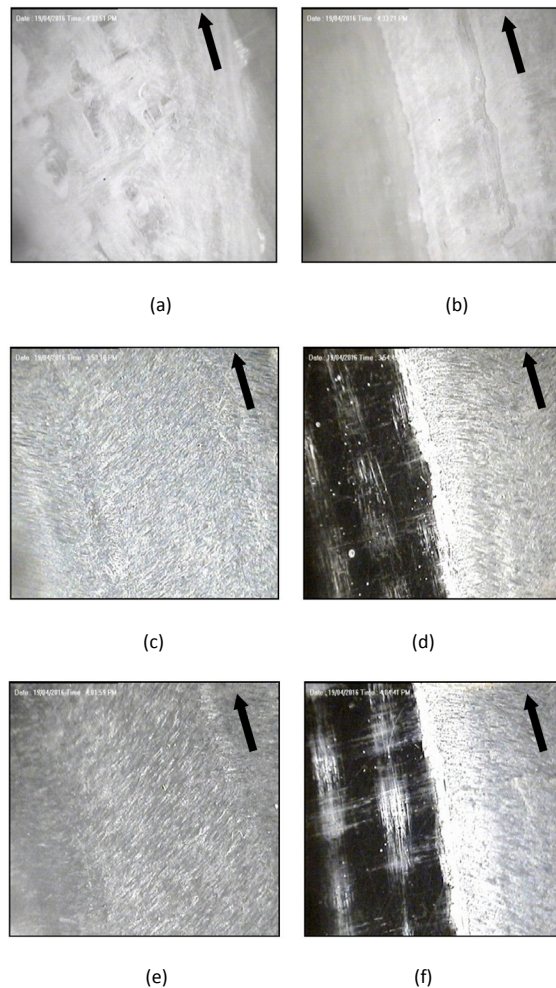


Figure 9. Worn surface and track boundary of dry sliding abrasion test for: (a and b) Pure; (c and d) 0.5 wt% CNT-filled; and (e and f) 1.0 wt% CNT-filled GFRP composite

CONCLUSION

This study had examined the wear properties (mass loss and specific wear rate) for CNT-filled epoxy and CNT-filled GFRP composite under dry sliding abrasive test. It was found that the wear properties of pure epoxy and pure glass fiber reinforced composite were improved when CNT is used as a filler. For nano-filled epoxy, CNT content of 1.0 wt% have the lowest specific wear rate with 56.67% improvement from pure epoxy system, while for nano-filled glass fiber reinforced composite, composite with 0.5 wt% of CNT have the lowest specific wear rate, with improvement of 78.9% from pure glass fiber reinforced composite. The presence of CNT improved the interface strength between fiber and matrix for fiber reinforced composite system. In order to further investigate the wear resistance of these systems, it is recommended future studies focus on the effect of operating parameter during testing.

ACKNOWLEDGEMENTS

The authors thank Institute of Research Management and Innovation (IRMI), Ministry of Education Malaysia and Institute of Graduate Studies (IPSIS) UiTM for their financial support under Geran Inisiatif Penyelidikan 600-IRMI/GIP 5/3 (0018/2016). This experiment was performed at the Faculty of Mechanical Engineering, UiTM Malaysia.

REFERENCES

- Archard, J. F. (1953). Contact and rubbing of flat surfaces. *Journal of Applied Physics*, 24, 981–988.
- Chen, J., Trevarthen, J. A., Deng, T., Bradley, M. S. A., Rahatekar, S. S., & Koziol, K. K. K. (2014). Aligned carbon nanotube reinforced high performance polymer composites with low erosive wear. *Composites Part A: Applied Science and Manufacturing*, 67, 86–95.
- Dong, B., Yang, Z., Huang, Y., & Li, H.-L. (2005). Study on Tribological Properties of Multi-walled Carbon Nanotubes/Epoxy Resin Nanocomposites. *Tribology Letters*, 20, 251–254.
- Guignier, C., Bueno, M.-A., Camillieri, B., Tournalias, M., & Durand, B. (2015). Tribological behaviour and wear of carbon nanotubes grafted on carbon fibers. *Composites Part A: Applied Science and Manufacturing*, 71, 168–175.
- Guo, Q. B., Lau, K. T., Rong, M. Z., & Zhang, M. Q. (2010). Optimization of tribological and mechanical properties of epoxy through hybrid filling. *Wear*, 269, 13–20.
- Jumahat, A., Kasolang, S., & Bahari, M. T. (2015). Wear properties of nanosilica filled epoxy polymers and FRP composites. *Jurnal Tribologi*, 6, 24–36.
- Jumahat, A., Soutis, C., Abdullah, S. A., & Bahsan, R. (2013). Dimensional and Thermal Stabilities of Nanomodified-Epoxy Systems. *Applied Mechanics and Materials*, 393, 161–166.
- Kanny, K., & Mohan, T. P. (2014). Resin infusion analysis of nanoclay filled glass fiber laminates. *COMPOSITES PART B*, 58, 328–334.
- Kim, M. T., Rhee, K. Y., Park, S. J., & Hui, D. (2012). Effects of silane-modified carbon nanotubes on flexural and fracture behaviors of carbon nanotube-modified epoxy / basalt composites. *Composites Part B*, 43, 2298–2302.
- Larsen, T. Ø., Andersen, T. L., Thorning, B., & Vigild, M. E. (2008). The effect of particle addition and fibrous reinforcement on epoxy-matrix composites for severe sliding conditions. *Wear*, 264, 857–868.
- Lee, S. M., Shin, M. W., & Jang, H. (2014). Effect of carbon-nanotube length on friction and wear of polyamide 6, 6 nanocomposites. *Wear*, 320, 103–110.
- Meng, H., Sui, G. X., Xie, G. Y., & Yang, R. (2009). Friction and wear behavior of carbon nanotubes reinforced polyamide 6 composites under dry sliding and water lubricated condition. *Composites Science and Technology*, 69, 606–611.
- Mirmohseni, A., & Zavareh, S. (2010). Preparation and characterization of an epoxy nanocomposite toughened by a combination of thermoplastic, layered and particulate nano-fillers. *Materials and Design*, 31, 2699–2706.
- Sapiai, N., Jumahat, A., & Mahmud, J. (2015). Flexural and tensile properties of kenaf/glass fibers hybrid composites filled with carbon nanotubes. *Jurnal Teknologi*, 76, 115–120.

- Suresha, B., Kumar, K. S., Seetharamu, S., & Kumaran, P. S. (2010). Friction and dry sliding wear behavior of carbon and glass fabric reinforced vinyl ester composites. *Tribology International*, *43*, 602–609.
- Yan, L., Wang, H., Wang, C., Sun, L., Liu, D., & Zhu, Y. (2013). Friction and wear properties of aligned carbon nanotubes reinforced epoxy composites under water lubricated condition. *Wear*, *308*, 105–112.
- Zhao, G., Hussainova, I., Antonov, M., Wang, Q., & Wang, T. (2013). Friction and wear of fiber reinforced polyimide composites. *Wear*, *301*, 122–129.

Effect of Acid and Silane Treated Carbon Nanotubes on Wear Properties of Epoxy Polymer Composite

Aidah Jumahat*, Napisah Sapiai and Eliya Farah Hana Mohd Kamal

Faculty of Mechanical Engineering, Universiti Teknologi MARA (UiTM), 40450 Shah Alam, Selangor, Malaysia

ABSTRACT

This paper investigates the effect of acid and silane treatment of Carbon Nanotubes (CNT) on wear properties of epoxy polymer composite. The wear test done was based on ASTM D3389 standard using the Abrasive Wear Tester (TR 600). Characterisation analysis was also done using Transmission Electron Microscopy (TEM) in order to study the dispersion of the CNT inside the epoxy matrix. When untreated CNT was added to the epoxy with amounts of 0.5, 0.75 and 1.0 wt%, the wear rates did not improve except for 0.5 wt% CNT filled epoxy. This was due to the lack of dispersion which causes larger chunks of material being dug out, thus contributing to a higher mass loss and wear rate. When treated with acid and silane, 0.75 wt% and 1.0 wt% CNT filled epoxy composites showed improvement. The TEM images of 0.5 wt%, 0.75 wt% and 1.0 wt% PCNT filled epoxy supported the claim of the lack of dispersion of PCNT inside the epoxy.

Keywords: Abrasive wear, dry sliding, nanoparticles, polymer composite

INTRODUCTION

Wear is the progressive loss of substance from the surface of a solid body caused by mechanical action when in contact and in relative motion with solid, liquid and gaseous counter body. Many factors affect wear resistance of materials, apart from the type of material used. For instance, test

parameters and environment may affect wear behaviour of the material. When using higher sliding speed and applied load, increased pressure will be exerted onto the surface of the material. This will induce friction, and the heat generated from the friction may cause the matrix to soften leading to the peeling off resin process of wear (Agrawal et al., 2016). There are a lot of mechanisms that contribute to wearing of a material, such as

ARTICLE INFO

Article history:

Received: 28 September 2016

Accepted: 03 February 2017

E-mail addresses:

aidahjumahat@gmail.com (Aidah Jumahat),

napisahsapiai@gmail.com (Napisah Sapiai),

eliya.kamal@gmail.com (Eliya Farah Hana Mohd Kamal)

*Corresponding Author

the reinforcement and matrix debonding, the breakage of matrix, the peeling off resin and also the essential micro-ploughing, micro-cutting, micro-fatigue and micro-cracking processes of abrasive wear which could be observed on the surface of the material when abraded with a counter face (Agrawal et al., 2016; Morioka et al., 2015). Micro-cutting is a process where a particle is detached by an abrasive particle. Micro-ploughing could be observed when there is presence of ridges and grooves as a result of materials being removed sideways. Micro-cracking is usually observed in brittle materials due to a high-stress concentration exerted on the surface of the material by the abrasive counter face. Micro-fatigue could be seen as the rough surface topography of the worn material after being repeatedly scratched by the counter face (Morioka et al., 2015). These micro-mechanisms of wear are depicted in Figure 1.

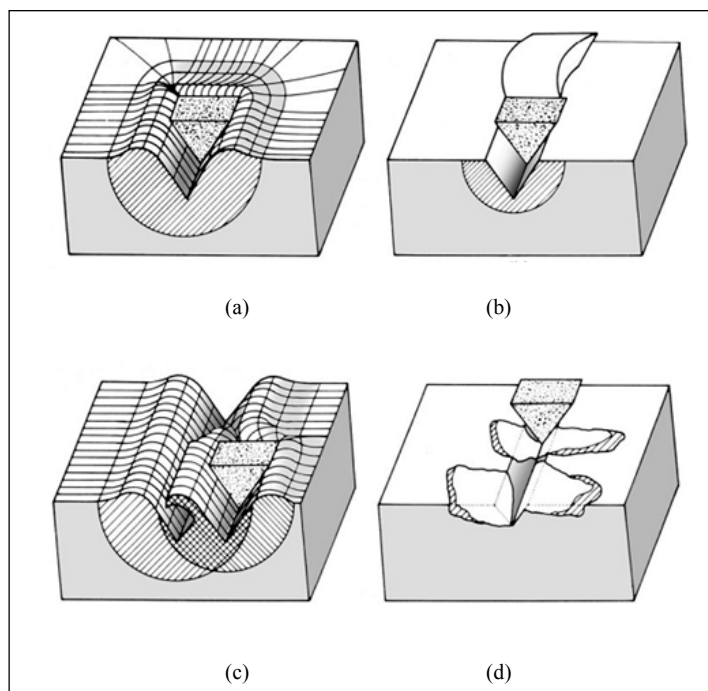


Figure 1. Schematic diagram of abrasive wear mechanisms: (a) micro-ploughing; (b) micro-cutting; (c) micro-fatigue; and (d) micro-cracking

In order to improve wear resistance of polymer, particulate fillers are incorporated into the polymer matrix (Basavarajappa & Ellangovan, 2012; Chauhan & Thakur, 2013; Friedrich et al., 2005; Zhang et al., 2013; Hrabě & Müller, 2016; Jumahat et al., 2015; Österle et al., 2016; Guo et al., 2010; Yan et al., 2010). Fillers were found to have a cushioning effect on asperities and shocks (Basavarajappa & Ellangovan, 2012; Chauhan & Thakur, 2013) Since the bond strength relates closely to wear, it was deduced by Basavarajappa et al. (2012) and Jumahat et al. (2015) that nano-sized particle would be more beneficial in improving wear resistance

since it has a higher surface area compared with micro sized fillers. The higher surface area will result in a higher intensity of bond strength (Friedrich et al., 2005). When using nano-sized fillers, the debris produced would also be smoother and smaller. This debris will then form the tribo-protective layer which will act as a barrier between the surface of the material and the counter face. The smoother debris also will help in preventing any three-body abrasive wear effect (Zhang et al., 2013). Three-body abrasive wear effect occurs when large size debris produced during wearing becomes a foreign body that will wear out the material's surface (Hrabě & Müller, 2016). Previous studies had reported a promising effect of the incorporation of nano-sized fillers in improving the wear properties of polymer matrix composites (Jumahat et al., 2015; Jumahat et al., 2016; Österle et al., 2016; Guo et al., 2010; Yan et al., 2010).

Yan et al. (2013) reported the enhancement of wear resistance of Carbon Nanotubes (CNT) filled epoxy. However, the CNT has the tendency to agglomerate inside the epoxy resin and this lack of dispersion will affect the wear resistance as bigger chunks of CNT could be dug out easily leading to a higher mass loss i.e. higher wear rate. Therefore, some treatments have been introduced to the CNT in order to improve impregnation of the CNT in the polymer matrix and the dispersion ability of the CNT (Lee et al., 2011; Noh et al., 2013; Bose et al., 2010; Wan et al., 2014). Acid treatment removes any impurities that may cause the inability of CNT to bond well with the epoxy matrix. Although the acid treatment may have improved the dispersion of CNT and also the mechanical properties of the composites, it was highlighted that the acid treatment may also have some implications. The acid might reduce the crosslinking network density of the CNT, lowering the glass transition temperature of the composites, and may interfere with the functionalised group of the CNT which serves as the active bonding sites with the matrix (Lee et al., 2011; Noh et al., 2013; Bose et al., 2010; Wan et al., 2014). On the other hand, silane modification was reported to help in improving dispersion, glass transition temperature, flexural modulus and strength of the composites (Lee et al., 2011; Bose et al., 2010; Wan et al., 2014). However, the silane modification of CNT may lead to reduction of electrical conductivity of the latter due to the wrapping of the CNT. Therefore, this paper aims to investigate the effect of incorporating acid and silane treated CNT on the wear resistance of epoxy polymer composites.

METHOD

Materials

This study used commercial epoxy (Miracast 1517 A/B) supplied by Miracon (M) Sdn Bhd. The yarn kenaf fibres was supplied by Innovative Pultrusion Sdn Bhd. The Multi-wall CNT (Flo Tub 9000 Series) was synthesised by the catalytic vapour deposition process, having an average diameter of 11 nm and 10 µm in length. The CNT was supplied by CNano Technology (Beijing) Ltd. The reagents used in the acid treatment are nitric acid (62-65%, R&M Chemicals), acetone (99.5%, R&M Chemicals), ethanol (99.5%, R&M Chemicals), and sulphuric acid (95%, R&M Chemicals).

Acid Treatment on CNT

An acid solution was prepared with a ratio of 3:1 (nitric acid: sulphuric acid) and 3.0 g of as received CNT was weighed and dispersed in a flask containing 300 ml of the solution. This mixture was then mixed and refluxed at 80°C for four hours using a hot-plate and magnetic stirrer. The mixture was then placed in a 2000 ml beaker. Distilled water was added and stirred continuously for another six hours in order to ensure a uniform dispersion of CNT. The mixture was then filtered and washed using distilled water together with acetone until 6 to 7 pH value was achieved in order to get rid of excess acid. The oxidised CNT was then dried in the oven at a temperature 80°C for 24 hours. Finally, the dried acid-treated CNT was ground using agate mortar and planetary ball milling for 30 minutes.

Silane Modification of Pre-treated CNT

1.8 g of the previously acid treated CNT was dispersed in a 300-ml ethanol-water-silane solution. The solution was then diluted with 2 wt% of three-amino propyltriethoxysilane to an aqueous solution of 300 ml ethanol water (95:5, v/v) solution. The solution was stirred at 70°C for four hours before being filtered and washed several times using acetone and distilled water. The washed CNT was dried for 12 hours at 80°C. Lastly, the CNT was ground and milled in order to obtain fine powder.

Fabrication of Composites

First, a series of pristine CNT (PCNT) with the weight fractions of 0.5%, 0.75% and 1.0% were mixed with epoxy using the mechanical stirrer at 400 rpm for one hour. The mixture was then degassed under high vacuum machine for one hour and simultaneously adding a hardening agent with the ratio of 100:30 (epoxy: hardener). The composite mixture was left at room temperature for 24 hours before being post cured at 60°C for two hours, and further two hours at 80°C, and 100°C respectively and finally at 120°C for two hours. The composite plates were then cut into test specimens. The whole process was repeated using the acid-treated CNT (ACNT) and silane-treated CNT (SCNT).

Abrasive Wear Test

The specimens were subjected to abrasive wear tester (TR 600) in accordance with the ASTM D3389 test standard. The diameter of the disc specimens was 123 mm and the thickness ranged between 5 to 6 mm. The load used was 10 N, the speed was 2.5 m/s and the sliding distance of 20,000 m was set with 2000 m interval (Agrawal et al., 2016). The experimental set up is shown in Figure 2.



Figure 2. The experimental set up for the Abrasion Wear Test

For every 2000 mm interval, the machine was stopped and the specimen was weighed. In between each interval, the rollers were scrubbed and dusted in order to ensure a fine surface of the abrasive roller. Using the mass loss recorded, the specific wear rate of the composite was calculated using the formula [1]:

$$W_s = \frac{\Delta m (g)}{L (m) \times \rho \left(\frac{g}{mm^3}\right) \times F (N)} \quad [1]$$

Where the specific wear rate (W_s) is described as the function of mass loss (Δm) over the multiplication of the sliding distance (L), density (ρ), and applied load (F). The specific wear rate is expressed in mm^3/Nm unit (Nordin et al., 2013).

Transmission Electron Microscopy (TEM)

Transmission electron microscopy (TEM-Tecnai 120KV BioTwin) was used to evaluate the structure of PCNT, ACNT, and SCNT inside the epoxy. The images were captured at magnifications of 43000x. The characterisation analysis was carried out at Microscopy Laboratory, Hospital Universiti Kebangsaan Malaysia.

RESULTS AND DISCUSSION

Based on Figure 3, the specific wear rate of PCNT filled epoxy composites can be observed. The wear rates for 0.5 wt% PCNT filled epoxy improved slightly compared with pure epoxy. However, the wear rates show increment of 0.75 wt% PCNT and 1.0 wt% PCNT filled epoxy composites. This may be due to the lack of dispersion of CNT that may enable larger chunks of composites being removed at once, since CNT, as reported by Yan et al. (2010), tends to agglomerate. Higher weight fraction of CNT increases the probability for the CNT to agglomerate. Although 0.5 wt% of PCNT filled epoxy showed improvement in wear rates, the improvement could not be deemed as significant. This is because 0.5 wt% of CNT was too little to inflict any major changes to wear resistance of the composites.

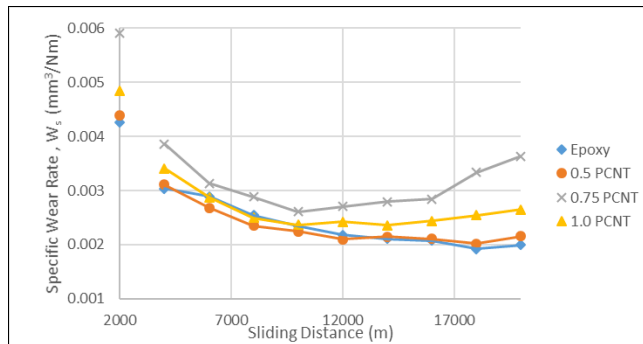


Figure 3. Specific Wear Rate against Sliding distance for PCNT filled epoxy composites

When treated with acid and silane, 0.5 wt% of CNT filled composites showed different effect as observed in Figure 4. When treated with acid, the wear rates showed increment rather than decrement. However, when silane was used to modify the CNT, the wear rate showed slight decrement i.e. improvement on the wear rates compared with epoxy and 0.5 wt% PCNT filled epoxy. The slight increment seen in wear rates for the 0.5 wt% ACNT filled epoxy may be due to the interruption made by the acid which might have caused the reduction of crosslinking network density (Bose et al., 2010). However, when 0.5 wt% SCNT was added into the epoxy, the wear rates improved and may be caused by the silane producing covalent bond; thus, increasing the bond strength between the SCNT and epoxy, and eventually leading to the improvement on wear rates (Friedrich et al., 2005; Bose et al., 2010).

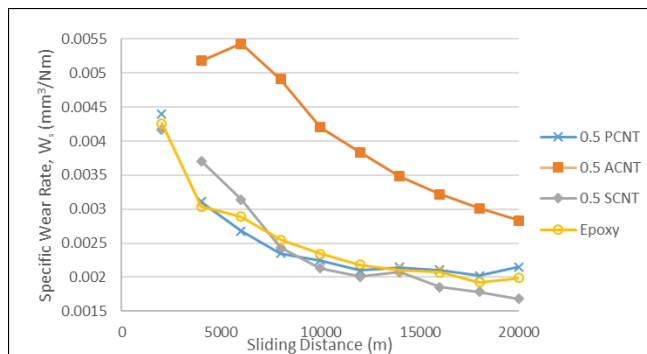


Figure 4. Specific Wear Rate for different treatment used for 0.5 wt% PCNT filled epoxy composite

From Figure 5, it could be observed that both the acid and silane treatment had improved the wear rates of the CNT filled epoxy composites compared with 0.75 wt% PCNT filled epoxy and pure epoxy. An improvement was seen on the wear rates of 0.75 wt% ACNT filled epoxy which was then further improved for the 0.75 wt% SCNT filled epoxy. This proves that the dispersion of the CNT was improved by the acid treatment and the covalent bonds are produced

through the silane modification process. The enhanced dispersion ensures that smaller and smoother debris are produced during wearing, thus, avoiding the three-body abrasive wear effect as reported by Zhang et al. (2013) and Bose et al. (2010). The covalent bonds produced help in improving the adhesion between the CNT and epoxy. As highlighted previously, increasing bond strength helps in improving wear resistance (Friedrich et al., 2005; Bose et al., 2010).

For 1.0 wt% CNT filled epoxy, the effect of treatments show outcome with the 0.75 wt% CNT filled epoxy as shown in Figure 6. When treated with acid, the wear rates improved slightly compared with the 1.0 wt% PCNT filled epoxy and pure epoxy. The wear rates continued to improve when modified using silane. However, for the 1.0 wt% ACNT filled epoxy, after travelling for 10,000 m of distance, the wear rates started to worsen. This may be due to presence of voids which provide a good surface topography which allows better digging out process of wearing as explained by Rückdaschel et al. (2013).

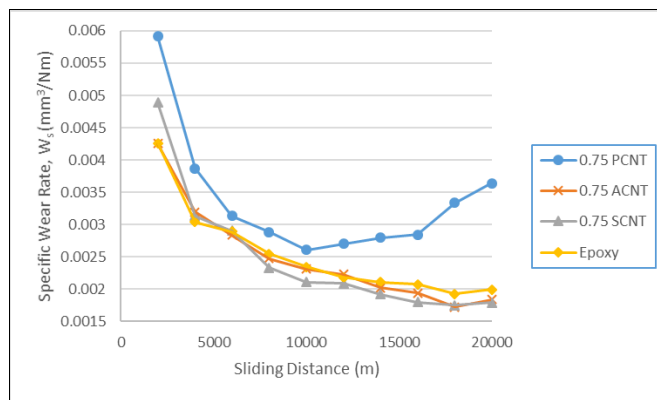


Figure 5. Specific Wear Rate for different treatment used for 0.75 wt% PCNT filled epoxy composite

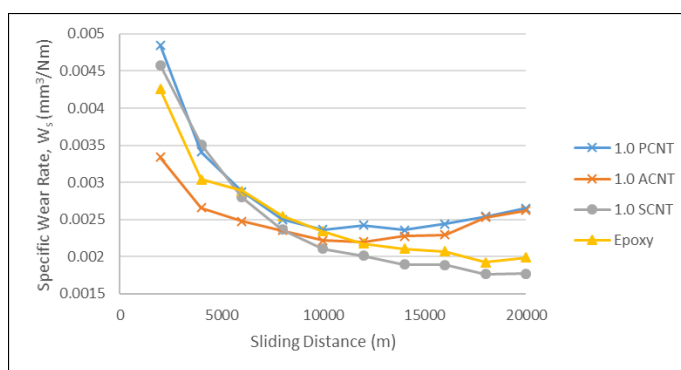


Figure 6. Specific Wear Rate for different treatment used for 1.0 wt% PCNT filled epoxy composite

From Figure 7, it could be observed that the CNT was not well dispersed for all three systems of 0.5, 0.75 and 1.0 wt% PCNT filled epoxy composites. This explains why the wear rates did not improve for 0.75 wt% and 1.0 wt% PCNT filled epoxy. For 0.5 wt%, it was not well-dispersed, though improvement on wear rates had been observed. The lack of dispersion may inhibit the improvement of wear rates, thus, slight improvement was seen for this composite.

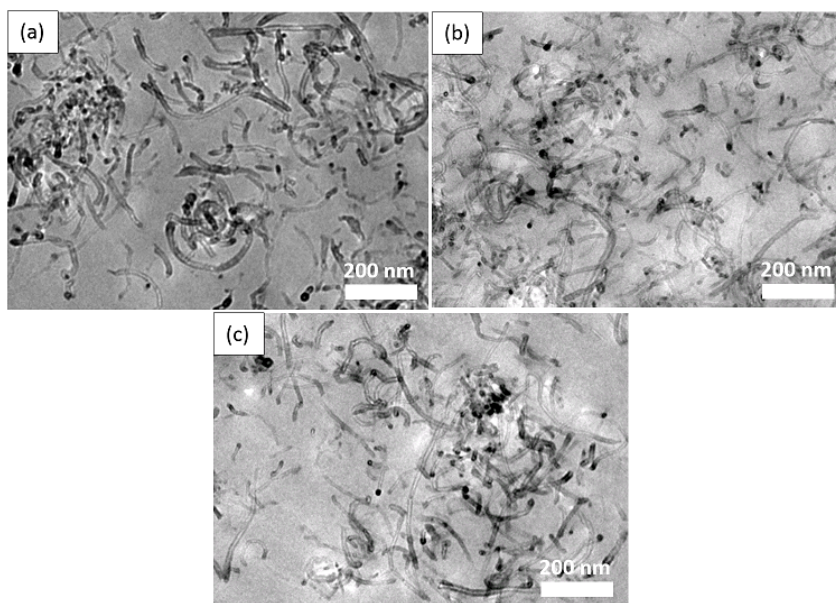


Figure 7. TEM images for: (a) 0.5 PCNT; (b) 0.75 PCNT; and (c) 1.0 PCNT filled epoxy composites

The TEM images for the 0.5 wt% of PCNT, ACNT and SCNT filled epoxy are shown in Figure 8. Regardless of the increment on the wear rate seen for the 0.5 wt% ACNT filled epoxy, the dispersion of ACNT showed improvement in terms of the dispersity compared with the PCNT filled epoxy. The acid might have interfered with the functionalised group and this eventually lead to the reduction of the crosslink network density of the CNT. Due to this, the bond strength between CNT and epoxy may have been reduced. Therefore, despite having a good dispersion of ACNT, the wear rates did not improve because the micro-cutting and micro-ploughing processes may have occurred due to the weak bond strength of the composites as noted by previous studies (Morioka et al., 2015; Friedrich et al., 2005; Bose et al., 2010). When further treated with silane, the SCNT was seen to agglomerate. SCNT filled epoxy showed better wear resistance compared with PCNT filled epoxy. This may be due to the silane aiding the covalent bonding which helped to improve the bond strength between the SCNT and epoxy. The wear rates would eventually improve since a tougher bond requires more energy in order to break it (Friedrich et al., 2005; Bose et al., 2010).

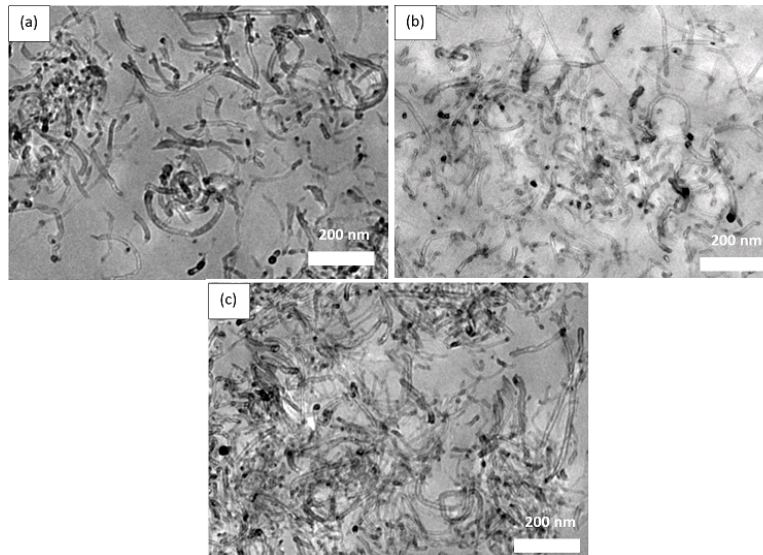


Figure 8. TEM images for: (a) 0.5 PCNT; (b) 0.5 ACNT; and (c) 0.5 SCNT filled epoxy composites

CONCLUSION

The effect of acid and silane treated CNT on the wear properties of the epoxy polymer composites was thoroughly discussed in this study. Incorporating PCNT did not improve the wear rates of the epoxy due to the lack of dispersion of the CNT inside the epoxy. Though 0.5 wt% PCNT filled showed slight improvement, the amount of PCNT added was too little to inflict any major improvement on the wear rates. By treating the CNT with acid, the dispersion and bond strength between the CNT and epoxy was improved and therefore, improvement on wear rates could be seen. In conclusion, CNT has a great potential to be used as fillers to improve wear resistance of polymer composites.

ACKNOWLEDGEMENTS

The authors would like to thank Institute of Research Management and Innovation (IRMI), Ministry of Education Malaysia and Institute of Graduate Studies (IPSIS) UiTM for their support. This research experiment was performed at the Faculty of Mechanical Engineering, UiTM Malaysia under the grant titled Geran Inisiatif Penyelidikan 600-IRMI/MYRA 5/3/GIP (053/2017).

REFERENCES

- Agrawal, S., Singh, K. K., & Sarkar, P. K. (2016). A comparative study of wear and friction characteristics of glass fibre reinforced epoxy resin, sliding under dry, oil-lubricated and inert gas environments. *Tribology International*, 96, 217-224.
- Basavarajappa, S. & Ellangovan, S. (2012). Dry sliding wear characteristics of glass-epoxy composite filled with silicon carbide and graphite particles. *Wear*, 296, 491-496.

- Bose, S., Khare, R. A., & Moldenaers, P. (2010). Assessing the strengths and weaknesses of various types of pre-treatments of carbon nanotubes on the properties of polymer/carbon nanotubes composites: A critical review. *Polymer*, *51*, 975-993.
- Chauhan, S. R., & Thakur, S. (2013). Effects of particle size, particle loading and sliding distance on the friction and wear properties of cenosphere particulate filled vinylester composites. *Materials and Design*, *51*, 398-408.
- Friedrich, K., Zhang, Z., & Schlarb, A. K. (2005). Effects of various fillers on the sliding wear of polymer composites. *Composites Science and Technology*, *65*, 2329-2343.
- Guo, Q. B., Lau, K. T., Rong, M. Z., & Zhang, M. Q. (2010). Optimization of tribological and mechanical properties of epoxy through hybrid filling. *Wear*, *269*, 13-20.
- Hrabě, P., & Müller, M. (2016). Three-body abrasive wear of polymer matrix composites filled with *Jatropha Curcas* L. *Procedia Engineering* (Vol. 136, pp. 169-174).
- Jumahat, A., Kasolang, S., & Bahari, M. T. (2015). Wear properties of nanosilica filled epoxy polymers and FRP composites. *Jurnal Tribologi*, *6*, 24-36.
- Jumahat, A., Talib, A. A. A., & Abdullah, A. (2016). Wear Properties of Nanoclay Filled Epoxy Polymers and Fiber Reinforced Hybrid Composites. *Nanoclay Reinforced Polymer Composites: Nanocomposites and Bionanocomposites* Singapore: Springer, 247-260.
- Lee, J. H., Rhee, K. Y., & Park, S. J. (2011). Silane modification of carbon nanotubes and its effects on the material properties of carbon/CNT/epoxy three-phase composites. *Composites: Part A*, *42*, 478-483.
- Morioka, Y., Tsuchiya, Y., & Shioya, M. (2015). Correlations between the abrasive wear, fatigue, and tensile properties of filler-dispersed polyamide 6. *Wear*, *338-339*, 297-306.
- Noh, Y. J., Pak, S. Y., Hwang, S. H., Hwang, J. Y., Kim, S. Y., & Youn, J. R. (2013). Enhanced dispersion for electrical percolation behavior of multi-walled carbon nanotubes in polymer nanocomposites using simple powder mixing and in situ polymerization with surface treatment of the fillers. *Composites Science and Technology*, *89*, 29-37.
- Nordin, N. A., Yussof, F. M., Kasolang, S., Salleh, Z., & Ahmad, M. A. (2013). Wear Rate of Natural Fibre: Long Kenaf Composite. *Procedia Engineering* (Vol. 68, pp. 145-151).
- Österle, W., Dmitriev, A. L., Wetzels, B., Zhang, G., Hausler, I., & Jim, B. C. (2016). The role of carbon fibers and silica nanoparticles on friction and wear reduction of an advanced polymer matrix composite. *Materials and Design*, *93*, 474-484.
- Ruckdäschel, H., Sandler, J. K. W., & Altstädt, V. (2013). On the friction and wear of carbon nano fiber reinforced PEEK-based polymer composites, 272-281.
- Wan, Y. J., Gong, L. X., Tang, L. C., Wu, L. B., & Jiang, J. X. (2014). Mechanical properties of epoxy composites filled with silane-functionalized graphene oxide. *Composites: Part A*, *64*, 79-89.
- Yan, L., Wang, H., Wang, C., Sun, L., Liu, D., & Zhu, Y. (2013). Friction and wear properties of aligned carbon nanotubes reinforced epoxy composites under water lubricated condition. *Wear*, *308*, 105-112.
- Zhang, J., Chang, L., Deng, S., Ye, L., & Zhang, L. (2013). Some insights into effects of nanoparticles on sliding wear performance of epoxy nanocomposites. *Wear*, *304*, 138-143.



Mechanical Behaviour and Microstructure Aluminium Foam Tube Produce (AFTP) Using Infiltration Method with Vacuum-Gas

Ismail Lias^{1*}, Muhammad Hussain Ismail², Iskandar Dzulkernain Md Raffee² and Mohd Aman Ihsan Mamat²

¹*Department of Polytechnic Education, Gelaria PjH, Presint 4, 62100 Wilayah Persekutuan Putrajaya, Malaysia*

²*Centre for Advanced Materials Research (CAMAR), Faculty of Mechanical Engineering, Universiti Teknologi MARA (UiTM), 40450 Shah Alam, Selangor, Malaysia*

ABSTRACT

Aluminium foam tube is a metal that consists of porous medium with special characteristics such as good energy absorption, good heat transfer and high thermal conductivity. These make it suitable to be used in a wide range of applications such as in heat exchangers. The aim of this project is to identify and analyse mechanical behaviour and microstructure aluminium foam tube produced and fabricated with infiltration method with vacuum-gas. The density of aluminium foam tube was also determined and an average aluminium foam tube with porosity 50% - 80% with the average NaCl particle size 2mm, 3mm and 4mm was produced. Foams with porosity 60%-75% NaCl has higher energy absorption. These was based on foam structure, density and maximum compressive load test result.

Keywords: AFTP, infiltration method, mechanical behaviour, microstructure, vacuum gas)

ARTICLE INFO

Article history:

Received: 28 September 2016

Accepted: 03 February 2017

E-mail addresses:

ismailjmsk@gmail.com (Ismail Lias),
hussain305@salam.uitm.edu.my (Muhammad Hussain Ismail),
eastacis@yahoo.com (Iskandar Dzulkernain Md Raffee),
amanihsan@salam.uitm.edu.my (Mohd Aman Ihsan Mamat)

*Corresponding Author

INTRODUCTION

Aluminium foam, especially open and close cell, is a new class of structural material and has good potential to be used in aerospace and automotive industry, railway, building construction and also chemical applications, where weight reduction, chemical pollutant minimisation and improvement in comfort and safety are key issues (Duarte & Oliveira, 2012; Guarino et al., 2015; Zhu et al., 2014; Z. Hussain & Suffin, 2011). Aluminium

foam is a kind of cellular material and highly porous with enclosed voids. These physical and mechanical features are potentially suitable for a number applications in engineering fields (Zaragoza, 2014; Mujeebu et al., 2009; M. Shiomia, Osakada, & Matsumoto, 2010; Ashby et al., 2000; Quadrini Fabrizio, 2011). Open cell metal foam structures are random but mostly homogeneous in size and shape. Most of the commercially available metal foam are produced in aluminium, copper, nickel and metal alloys. Metal foams have interesting applications in heat exchangers, cryogenics, combustion chambers, cladding on buildings, strain isolation, geothermal operations, petroleum reservoirs, catalytic beds, compact heat exchangers for airborne equipment, air-cooled condensers for air conditioning and refrigeration systems, and compact heat sinks for power electronics (Babcsan et al., 2014; Guarino et al., 2015; Zhu et al., 2014).

There are many methods of producing aluminium foam, namely melt-foaming, melt-gas injection, investment casting, powder metallurgy, and melt infiltration (Ashby et al., 2000). In this study, to produce open-cell aluminium foam tube, the researcher used infiltration casting process that utilised Sodium Chloride particle as a space holder (Lucai et al., 2008; Hussain & Suffin, 2011). This process uses aluminium as the main material because aluminium melting temperature is 660°C while melting temperature of Sodium Chloride is 801°C. Therefore, the aluminium will melt first and infiltrate through the sodium chloride particle.

A compression test determines the mechanical behaviour of materials under crushing loads. The testing specimen will be compressed and at certain loads and point, the specimen will experience deformation. Compressive strength diagram (see Figure 1) of stress and strain is plotted and used in order to determine the value of modulus of elasticity of the specimen. Subsequently, the elastic limit is obtained together with yield strength and compressive strength (Ruan et al., 2002; Ashby et al., 2000; Fiedler et al., 2014).

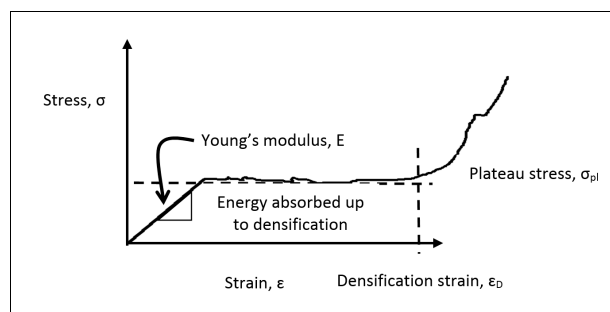


Figure 1. Compression curve for a metal foam (Ashby et al., 2000)

The aim of this study was to identify first, value energy absorption and compressive properties based on porosity and density difference and second to find the correlation between microstructure aluminium foam tube before by using infiltration method with vacuum-gas.

METHOD

Preparation of Aluminium Foam Tube

In the fabrication of aluminium foam tube, mould was designed according to the specified dimension. The schematic diagram of the mould is shown in Figure 2(a) and Figure 2(b). It consists of a base plate, main cylinder, core, and mould cap. All parts are made of stainless steel. The core was placed at the centre of main cylinder to produce hollow on the foam sample. The assembly was tightened using screw and nut.

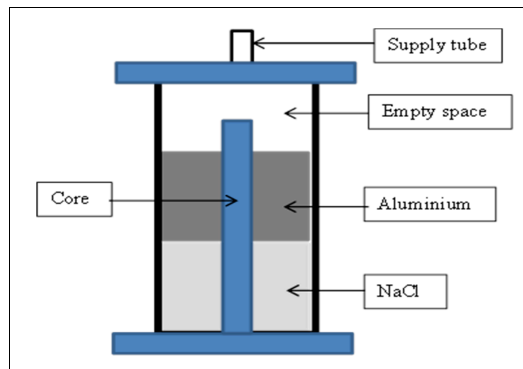


Figure 2(a). Schematic diagram of mould



Figure 2(b). Picture of schematic diagram of mould

Experimental Procedure

The Infiltration method with vacuum-gas used aluminium as main material and NaCl particle as space holder with the help of gas. This method was used by Barari et al. (2013) to manufacture metal foam. The schematic diagram of apparatus for infiltration method is shown in Figure 3(a) and Figure 3(b). The mould was coated with boron nitride. The NaCl particle was poured

into the mould cavity followed by aluminium ingot on top of the NaCl. The mould was tightly closed by using a nut and placed in the furnace for heating. After a few hours of heating, the vacuum pump valve was opened to remove the air from the mould. The argon gas valve was immediately opened after vacuum pump valve was closed to purge gas into the mould cavity. The gas then pushed the aluminium molten to flow through the NaCl particle.

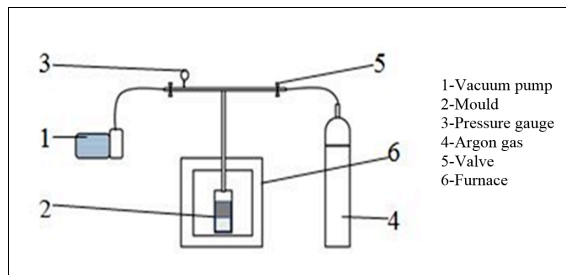


Figure 3(a). Schematic diagram of apparatus



Figure 3(b). Picture of schematic diagram of apparatus

After solidification and cooling, the sample was removed from the mould and then cut into required dimension by using lathe machine. Finally, the sample was cleaned by using ultrasonic cleaner. The water was set at 90°C and the process was repeated a few times to ensure the NaCl particle was completely removed. The microstructure of aluminium foam tube fabricated was observed using stereomicroscope and CT-scan to get the correlation between the spaces holders used.

Compression Test

Compression test was conducted under a monotonic condition by using the universal compression testing machine available in the laboratory which is the INSTRON 3382 machine. The machine did the compression test as well as data acquisition controlled by the computer unit. The compression test was conducted up to the fracture point of each sample of the aluminium foam and the compression stress and load at the particular time is recorded. Each

stroke of the compression for all tests was done by first placing the sample on the testing mat. Then the upper die was set to be exactly at the same height with the sample. Then, all data, compression load and load extension were both set to zero. Finally, the compression test was carried out on each of the samples which had the same dimension of (40 mm × 20 mm × 20 mm) and the compression test was conducted 12 times for all 12 random samples. The energy absorption formula of the aluminium foam tube was calculated from the stress-strain curves using equation 1, where W is the energy absorption capability and σ and ϵ are the compression stress and strain, respectively (Yuan et al., 2015; Ashby et al., 2000; Z. Hussain & Suffin, 2011). Figure 4(a) (i & ii) shows the experimental setup of foam making and Figures 4b, 4c and 4d) represent aluminium foam tube sample and cutting sample using EDM wire cut (Rajak et al., 2016; G. Castro, Nutt, & Wenchen, 2013; Duarte, Krstulović-Opara, & Vesenjak, 2015).

$$W = \int_0^{\epsilon_m} \sigma d\epsilon \quad [1]$$

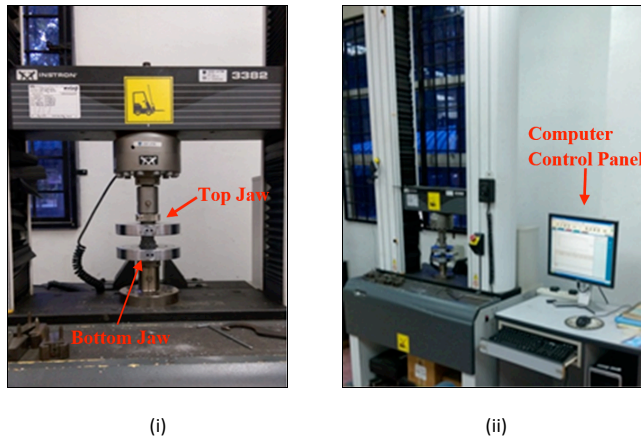


Figure 4(a). The experimental and foam making setup (i and ii)

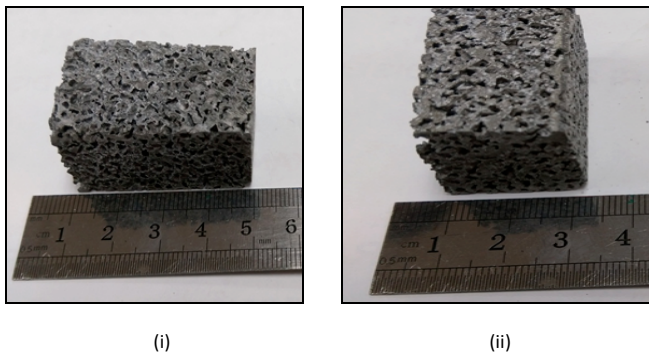


Figure 4(b). Aluminium foam tube samples 2 cm × 2 cm × 4 cm (i and ii) after process EDM wire cut from sample as shown in Figure 5

RESULTS AND DISCUSSION

Infiltration Process

In the infiltration vacuum-gas method, the main parameters are the design of mould, the vacuum and gas pressure. The design of mould is important to ensure that there is no leak during the fabrication process. A leaking mould may prevent the gas from being compressed. During the infiltration process, gas is necessary to push the molten metal to flow through the NaCl particle. Therefore, the gas pressure must be carefully controlled. The time taken to purge gas depends on the height and size of the sample. Figure 5 shows samples produced in this process and Figure 6 shows the graph containing the percentage of porosity and density of aluminium foam tube.



Figure 5. Example of aluminium foam tube fabricated combined pore size (2 mm + 3 mm and 4 mm)

Table 1
Porosity % and density of aluminium foam tube

No	1	2	3	4	5	6	7	8	9	10	11	12
Sample	12	5	9	6	19	1	7	2	11	3	8	4
Porosity (%)	58.38	60.39	63.07	63.87	64.10	64.15	66.78	67.27	70.96	71.83	74.81	76.48
Density (kg/m ³)	1.12	1.07	1.00	0.98	0.97	0.97	0.90	0.88	0.78	0.76	0.68	0.64

Compressive Properties

Figure 6 shows stress-strain curves plotted based on 12 samples randomly with porosity between 50% and 80% (Lias et al., 2016). The curves are plotted during compression testing for different aluminium foams prepared using NaCl particle contents at 2 mm 3 mm and 4 mm. The graph shows sample 6 has a higher value for energy at maximum compressive load 23.950 J and the maximum compressive load value 6.084 kN. Sample 3 has the lowest value for maximum compressive load 0.328 J with the maximum compressive load 0.206 kN. Figure 7 shows compression test during experimental testing.

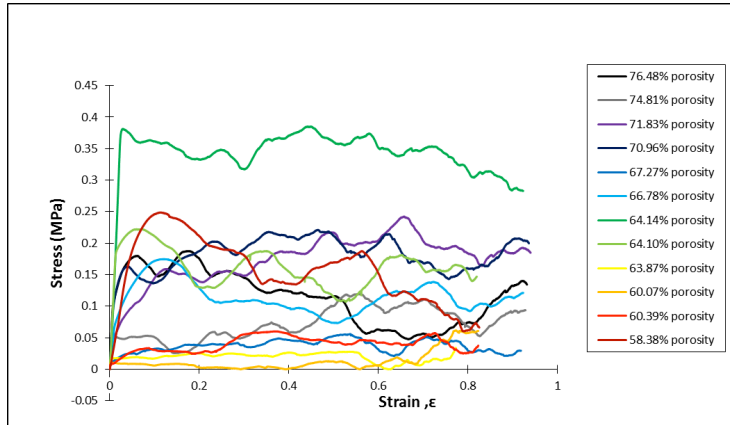


Figure 6. Compressive stress-strain curve aluminium foam tube with different porosity or density

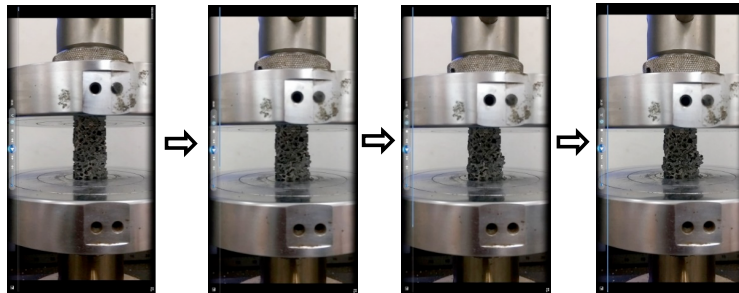


Figure 7. Compression test view visual observation of the specimens during experimental testing

Energy Absorption

The energy absorption and efficiency of aluminium foam tube can be calculated as per Equation 1 and the results are shown in Figure 8 and Figure 9. It can be seen that its energy absorption capability based on different porosity and density grows with increasing strain based on 12 samples. Sample 8 and 4 show a higher energy absorption, 38.50 kJ and 45.47 kJ respectively. This trend is based on porosity and density of the structure of the aluminium foam tube.

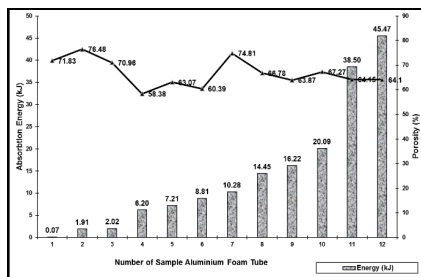


Figure 8. Graph energy absorption and porosity versus number of sample

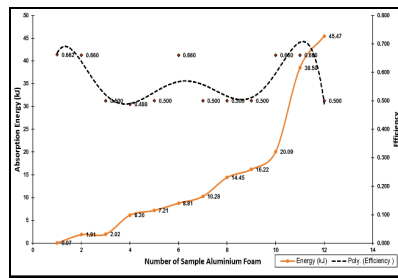


Figure 9. Graph energy absorption and efficiency versus number of sample

Foam Morphology

Figure 10 shows SEM micrograph of aluminium tube with selected sample while figure 11 shows X-ray diffraction patterns to identify the main content material. Based on figure 10, for sample aluminium foam tube (a) until (f) show the SEM micrograph of aluminium foam tube and the size of the particle which can be viewed clearly. There are a number of similarities between sample 1, sample 5, sample 7, sample 8, sample 11 and sample 12 because of their pore structure. Meanwhile, Figure 11 show the X-ray diffractions trace aluminium in aluminium foam tube produced based on Sample 1, sample 5. Sample 7, sample 8, sample 11 and sample 12. This is illustrated by the graph below which shows the same patent and the peak of location of main material of aluminium.

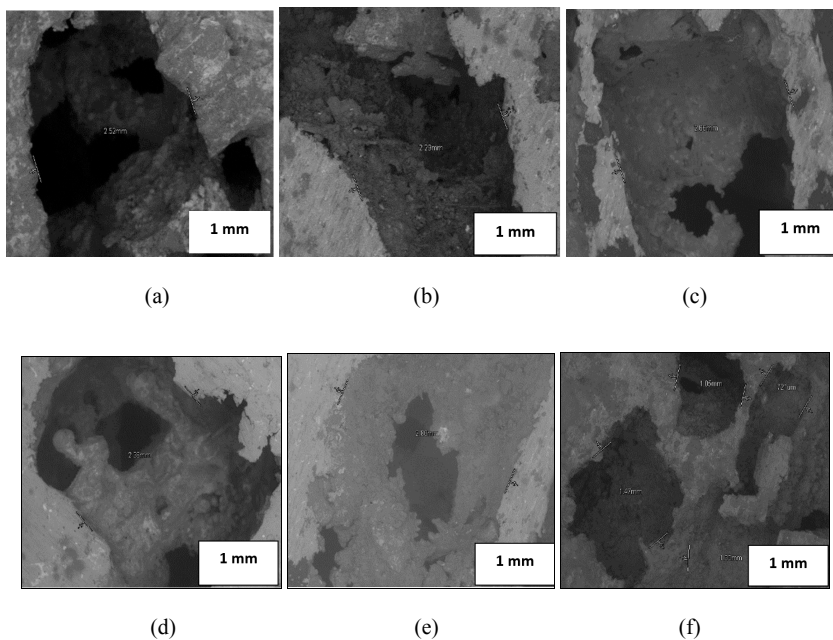


Figure 10. SEM micrograph of aluminium foam tube: (a) sample 1; (b) sample 5; (c) sample 7; (d) sample 8; (e) sample 11; and (f) sample 12 used in the current study

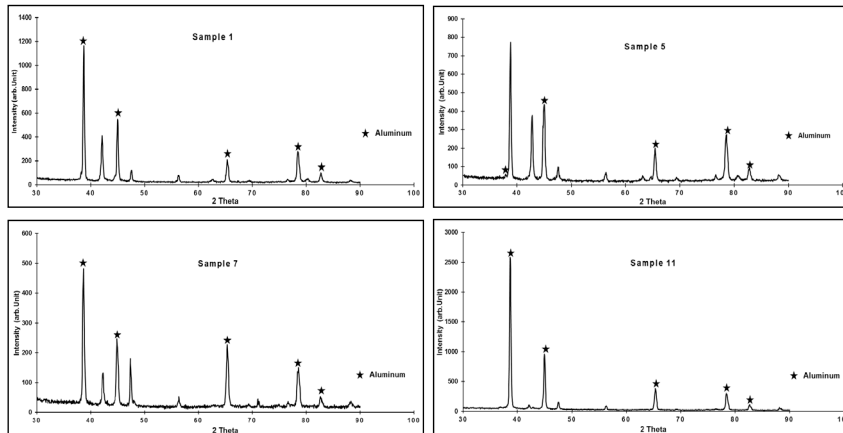


Figure 11. X-ray diffractions trace aluminium in aluminium foam tube

CONCLUSION

The method for producing aluminium foam tube was identified in which using infiltration with vacuum-gas with NaCl space holder was found to be suitable to manufacture the aluminium foam tube for difference sizes or diameters. Compression test analysis was able to identify maximum compressive load, modulus young, energy absorption as well as efficient energy absorption.

ACKNOWLEDGEMENT

The authors express their gratitude to RMI UiTM Shah Alam for RACE grant 600-RMI/RACE 16/6/2(6/2013) and Faculty of Mechanical Engineering UiTM Shah Alam, Department of Polytechnic Education, and Ministry of Education, Malaysia and their technicians for their contribution to this research.

REFERENCES

- Ashby, M. F., Evans, T., Fleck, N. A., Hutchinson, J. W., Wadley, H. N. G., & Gibson, L. J. (2000). *Metal foams: a design guide*. Elsevier.
- Babcsan, N., Beke, S., Makk, P., Szamel, G., & Kadar, C. (2014). Pilot production and properties of ALUHAB aluminium foams. *Procedia Materials Science*, 4, 127-132.
- Barari, F., Luna, E. M. E., Goodall, R., & Woolley, R. (2013). Metal foam regenerators; heat transfer and storage in porous metals. *Journal of Materials Research*, 28(17), 2474-2482.
- Castro, G., Nutt, S. R., & Wenchen, X. (2013). Compression and low-velocity impact behavior of aluminum syntactic foam. *Materials Science and Engineering: A*, 578, 222-229.
- Duarte, I., & Oliveira, M. (2012). Aluminium alloy foams: production and properties. In *Powder metallurgy*. InTech.

- Duarte, I., Krstulović-Opara, L., & Vesenjak, M. (2015). Characterisation of aluminium alloy tubes filled with aluminium alloy integral-skin foam under axial compressive loads. *Composite Structures*, *121*, 154-162.
- Fiedler, T., Sulong, M. A., Mathier, V., Belova, I. V., Younger, C., & Murch, G. E. (2014). Mechanical properties of aluminium foam derived from infiltration casting of salt dough. *Computational Materials Science*, *81*, 246-248.
- Guarino, S., Rubino, G., Tagliaferri, V., & Ucciardello, N. (2015). Thermal behavior of open cell aluminum foams in forced air: experimental analysis. *Measurement*, *60*, 97-103.
- Hussain, Z., & Suffin, N. S. A. (2011). Microstructure and mechanical behaviour of aluminium foam produced by sintering dissolution process using NaCl space holder. *J. Eng. Sci*, *7*, 37-49.
- Lias, I., Nasir, M. I., Ismail, M. H., & Mamat, A. M. I. (2006). Design and fabrication of aluminium foam tube for heat exchanger application.
- Lucai, W., Yuyong, C., Fang, W., Jianguo, W., & Xiaohong, Y. (2008). Preparation of big size open-cell aluminum foam board using infiltration casting. *Matrix*, *1*, 5.
- Mujeebu, M. A., Abdullah, M. Z., Bakar, M. A., Mohamad, A. A., & Abdullah, M. K. (2009). Applications of porous media combustion technology—a review. *Applied Energy*, *86*(9), 1365-1375.
- Rajak, D. K., Kumaraswamidhas, L. A., Das, S., & Kumaran, S. S. (2016). Characterization and analysis of compression load behaviour of aluminium alloy foam under the diverse strain rate. *Journal of Alloys and Compounds*, *656*, 218-225.
- Ruan, D., Lu, G., Chen, F. L., & Siores, E. (2002). Compressive behaviour of aluminium foams at low and medium strain rates. *Composite Structures*, *57*(1), 331-336.
- Shiomi, M., Imagama, S., Osakada, K., & Matsumoto, R. (2010). Fabrication of aluminium foams from powder by hot extrusion and foaming. *Journal of Materials Processing Technology*, *210*(9), 1203-1208.
- Yuan, J., Chen, X., Zhou, W., & Li, Y. (2015). Study on quasi-static compressive properties of aluminum foam-epoxy resin composite structures. *Composites Part B: Engineering*, *79*, 301-310.
- Zaragoza, G., & Goodall, R. (2014). Development of a device for the measurement of thermal and fluid flow properties of heat exchanger materials. *Measurement*, *56*, 37-49.
- Zhu, X., Ai, S., Lu, X., Ling, X., Zhu, L., & Liu, B. (2014). Thermal conductivity of closed-cell aluminum foam based on the 3D geometrical reconstruction. *International Journal of Heat and Mass Transfer*, *72*, 242-249.



Analysis of Fill Time and Injection Pressure of Multiple 20 gram Parisons during Injection Moulding Process

Najiy Rizal Suriani Rizal¹, Azuddin Mamat² and Aidah Jumahat^{1*}

¹Faculty of Mechanical Engineering, Universiti Teknologi MARA (UiTM), 40450, Shah Alam, Selangor, Malaysia

²Department of Mechanical Engineering, Faculty of Engineering, Universiti Malaya (UM), 50603 Kuala Lumpur, Malaysia

ABSTRACT

In recent years, injection moulding process is one of the most advanced and efficient manufacturing processes for mass production of plastic bottles. However, a good quality of parison is difficult to achieve due to uncontrollable humidity, pressure inlet and water inlet velocity. This paper investigates the effect of using multiple mould cavities to improve the process fill time and injection pressure in the production of PET plastic bottles using MoldFlow software. The modelling of parison was developed using CATIA with the consideration of every part of the parison. MoldFlow software was used to analyse the flow of 20 g parison with different cavity numbers (1, 8, 16, 24 cavity), as well as its corresponding runner size towards its fill time and injection pressure. Other important parameters that affect the production of parison, such as melting temperature, mould temperature, atmospheric temperature and cooling time, were remained constant. The fill time required to produce 24 moulds was improved by 60% compared to using 8 mould cavity only, and this enable the production of more plastic bottles in a day. Therefore, fill time and injection pressure are two important parameters to be considered in the injection moulding process, especially to reduce parison defect and increase its production rate.

Keywords: Injection moulding, MoldFlow, mould design, parison, thermoplastic

ARTICLE INFO

Article history:

Received: 28 September 2016

Accepted: 03 February 2017

E-mail addresses:

najiyrizal@gmail.com (Najiy Rizal Suriani Rizal),
aidahjumahat@salam.uitm.edu.my (Aidah Jumahat),
azuddin@um.edu.my (Azuddin Mamat)

*Corresponding Author

INTRODUCTION

The plastic industry is one of the most vibrant sectors in Malaysia. The growth of domestic downstream plastic processing activities is attributed to the tremendous development in the petrochemical sector in the country. However, higher production costs and environmental concerns are plaguing the

industry. The conventional injection moulding machine that is exported to Malaysia is small in size and limited in shape, both critical factors that affect the production process of parison, also called preform (Rizal et al., 2015).

Daver and Demirel (2012) examined the effects of preform deformation behaviour and the optimum cooling time on the quality of bottle preform. These effects were determined by conducting structural analysis on the actual bottles. Hedia, Aldousari and Zager (2010) studied the optimal design for PET bottle in order to maximise its reliability by using numerical simulation to analyse the effect of the design (Hedia, Aldousari, & Zager, 2010). De Miranda et al. (2011) studied the design optimisation and weight reduction of 500 mL CSD PET bottle through FEM simulations. These studies examined the simulation of the process and the mechanical demands related to the PET bottle application with the aim of assessing the efficiency of packaging design and enabling efficient and correct sizing. Chen (2011) used a genetic algorithm method to simulate and analyse optimisation process parameters for Multi-cavity injection moulding parts warpage. It was found that multi-cavity mould runner arrangements could seriously affect the warpage changes of the parts.

Li and Jia (2011) studied the structural characteristics of mould for precise injection moulding. The current paper examined the influence of mould structure on the quality of injection-moulded parts. Taghizadeh et al. (2013) focused on warpage prediction in plastic injection moulded part using artificial neural network. Similarly, Nian et al. (2015) studied warpage control of thin-walled injection moulding using local mould temperatures. Wang et al. (2013) investigated the reduction of sink mark and warpage of the moulded part in rapid heat cycle moulding process.

The amount of materials injected into the parison mould is difficult to control, contributing to low quality products. This leads to an increase in the number of rejected products, which translates into high production cost and wastage. There has been no comprehensive study on the effect of number of cavity on fill time and injection pressure.

The present work used MoldFlow with Polyethylene Terephthalate (PET) mechanical properties and parameters to stimulate and investigate the effect of 20 g parison on fill time and injection pressure. A robust design of parison mould with greener injection moulding system was modelled using CATIA V5R20.

METHOD

The Geometrical Acquisition and general parameter of actual mould 20 g parison was done and analysed. The mould is taken from Bakal Sejati to undergo Coordinate Measuring Machine (CMM) BEYOND707 Mitutoyo to get the geometrical measurement of the actual size of the parison. The general parameter for the injection moulding process was also acquired from the same company as shown in Table 1.

Table 1
General acquired parameters for 20 g parison

Factor	Parameter of 20 g Parison
Mould Temperature	100°C
Melt Temperature	280°C
Packing time	10 Sec
Packing Pressure	140 MPa
Cooling time	17 Sec
Cooling temperature	30°C
Ambient temperature	35°C

After the measurement was collected from CMM, the geometrical measurement is modelled using CATIA V5R20 Dassault System to produce a CAD model of 20 g parison as shown in Figure 1. The measurement is based on the actual model with dimensions drawn in mm.

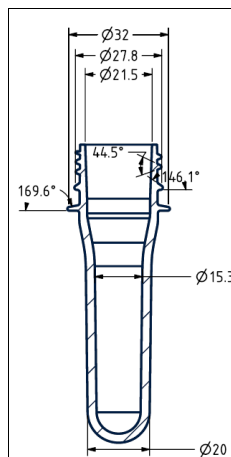


Figure 1. The geometry of the 20 g parison

The modelled geometry was then transferred to Autodesk MoldFlow Insight 2011 Educational Edition software to analyse the parison model by following the actual injection moulding process. The parameter and material properties are input into this software. Simulation of the injection moulding process was conducted using a variation of number cavities consisting of 1 cavity, 8 cavities, 16 cavities and 24 cavities respectively, with the process parameter in Table 1. Figure 2 below is the parison modelled using MoldFlow simulation. The input parameters for simulation are shown in Table 2.

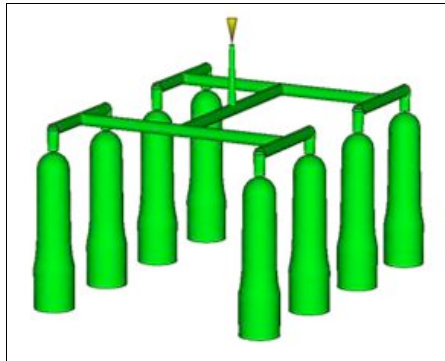


Figure 2. The parison of multi-cavity using MoldFlow software

Table 2
The parameter input for MoldFlow software

Factor	Parameter of 20 g Parison
Mould temperature	100°C
Melt Temperature	280°C
Atmospheric temperature	35°C
Cooling time	17 s
Runner Size	8 mm

The properties of materials correlate with the process parameters of injection moulding and mould modelling. The Polyethylene Terephthalate (PET) used in this research is Eastar Copolyester EN067 that was supplied by Eastman Chemical Products. PET is a thermoplastic polymer that has good ductility, strength, hardness and stiffness while the amorphous PET has better ductility.

20 g parison on the viscous plastic flow and the rate of filling time is analysed. The effect of number of cavities and on fill time and on injection pressure is examined.

RESULTS AND DISCUSSION

Four different numbers of cavities (1 cavity, 8 cavities, 16 cavities and 24 cavities) were analysed using MoldFlow to determine the fill time and injection pressure. The number of cavities affect the fill time and injection pressure of the parison. The runner size also varies as the number of cavities increases. Figure 3 shows the time taken to fill 1, 8, 16 and 24 cavities are 0.5236 s, 0.7745 s, 0.8737 s and 1.145 s respectively. The result shows the increase in number of cavities actually increases production. The difference in time between these four cavities was an increase of about 60%.

Table 3 shows the percentage of volume filling at specific flow time for 1 cavity, 8 cavities, 16 cavities and 24 cavities. Data shows that it takes a longer time to fill 24 cavities. However, in terms of production, the 24 cavity produced much higher parison compared with 8 cavities. The efficiency of the 24 cavity parisons in terms of production is better than a 16 cavity and 8 cavity parisons but in terms of overhead cost, it is more expensive to produce a 24 cavity parison.

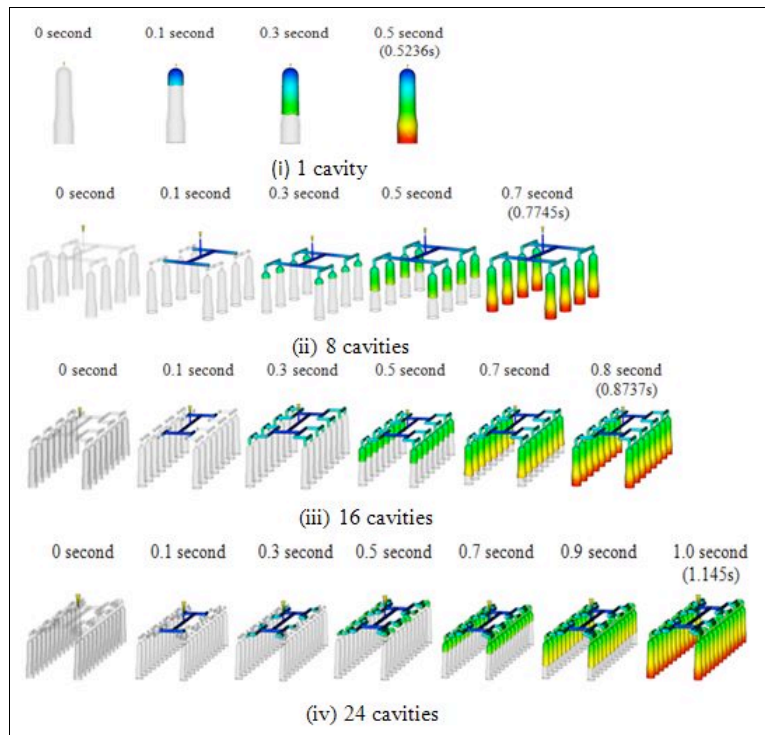


Figure 3. Viscous plastic flow analysis of PET material for four different models; (i) 1 cavity; (ii) 8 cavities; (iii) 16 cavities; and (iv) 24 cavities

Table 4 shows the result for the fill time and injection pressure for the four cavities (1 cavity, 8 cavities, 16 cavities and 24 cavities). From the tabulation below, the fill time for 24 cavity parison is within 1.145s which is higher compared with a single cavity. However, if the comparison is made in terms of fill time per parison, a 24-mould cavity parison filled much faster compared with single cavity, which is 0.0475 s per parison and 0.5236 s per parison respectively.

Table 3
Percentage of volume filling at specific flow time of parison by number of cavity

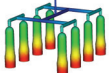
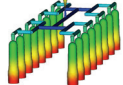
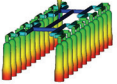
Cavity & percentage		1		8		16		24	
Fill Time (s)		(%)		(%)		(%)		(%)	
0		0%	at 0s		0%	at 0s		0%	at 0s
0.1		20.84%	at 0.1091s		16.67%	at 0.1291s		12.46%	at 0.1089s
0.3		58.35%	at 0.3055s		41.67%	at 0.3227s		37.50%	at 0.3276s
0.5		100%	at 0.5236s		66.66%	at 0.5163s		58.33%	at 0.5097s
0.7					100%	at 0.7745s		83.34%	at 0.7281s
0.8								100%	at 0.8737s
1.0								100%	at 1.1450s

Table 4
Parameter analysis for number of cavity

Number of Cavity	1	8	16	24
Fill time (s)	0.5236	0.7745	0.8737	1.145
Fill time / parison	0.5236	0.0968	0.0546	0.0475
Injection pressure (MPa)	20.1371	36.8453	32.6802	30.6973

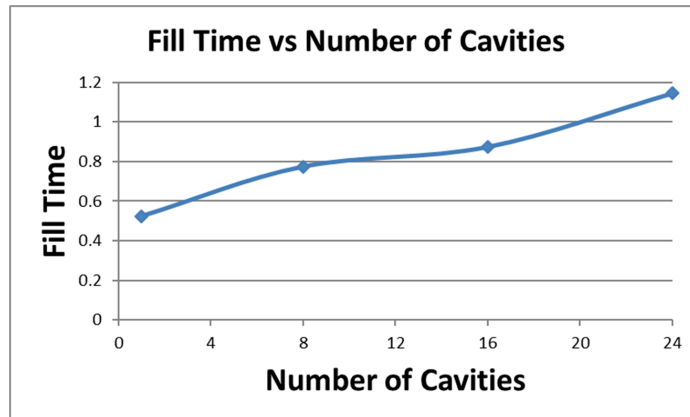


Figure 4. Fill time against number of cavities

Figure 4 shows that when the number of cavity increases the fill time also increases. The number of cavities affects the fill time in mass production. Increasing the number of cavities will produce more parison in terms of mass production. In order to produce 24 parison, the process will take 1.145 s when using 24 cavities mould, whereas it takes 12.5664 s for single cavity and 2.3235 s for 8 cavities to produce 24 parison respectively.

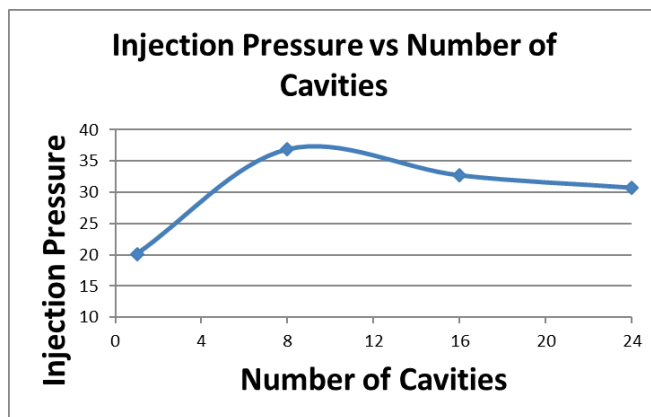


Figure 5. Injection pressure against number of cavities

Figure 5 shows the injection pressure affects the number of cavities from 8 to 24 cavities. There was a decrease in injection pressure from 8 to 24 cavities mould. This was due to the increase of sprue, runner and gate as they automatically change with the increase of mould cavity to reduce part malfunction from excessive pressure.

CONCLUSION

The main objective of this study was to investigate the effect of number of cavity on fill time and injection pressure. The simulation using MoldFlow was carried out to study the effect of cavity numbers on fill time and injection pressure. The process parameters considered during the analysis are melting temperature, mould temperature, atmospheric temperature and cooling time. The change in fill time and injection pressure differs based on Figure 4 and Figure 5. Future studies can look at how to overcome the change in mould temperature.

ACKNOWLEDGEMENTS

The authors thank Institute of Research Management and Innovation (IRMI), Ministry of Education Malaysia and Institute of Graduate Studies (IPSIS) UiTM for their financial support. This research was performed at the Faculty of Mechanical Engineering, UiTM Malaysia under Grant BESTARI 600-IRMI/DANA 5/3/BESTARI (0006/2016).

REFERENCES

- Chen, W. J. (2011). Simulation and Analysis of Optimization Process Parameters for Multi Cavity Injection Molding Parts Warpage by Genetic Algorithm Method. *Applied Mechanics and Materials*, 142, 54–57.
- Daver, F., & Demirel, B. (2012). A simulation study of the effect of preform cooling time in injection stretch blow molding. *Journal of Materials Processing Technology*, 212(11), 2400–2405. <https://doi.org/10.1016/j.jmatprotec.2012.06.004>
- De Miranda, C. A. S., Camara, J. J. D., Monken, O. P., & Dos Santos, C. G. (2011). Design Optimization and Weight Reduction of 500 mL CSD PET Bottle through FEM Simulations. *Journal of Materials Science and Engineering B*, 1(7), 947–959.
- Hedia, H. S., Aldousari, S., & Zager, F. B. (2010). Optimal Design for PET Bottle to Maximize Reliability: Finite Element Analysis and Experimental Work. *Materials Testing*, 52(6), 383–393.
- Li, H. L., & Jia, Z. X. (2011). Study of the Structural Characteristics of Mold for Precise Injection Molding. *Advanced Materials Research*, 291–294, 610–613. <https://doi.org/10.4028/www.scientific.net/AMR.291-294.610>
- Nian, S.-C., Wu, C.-Y., & Huang, M.-S. (2015). Warpage control of thin-walled injection molding using local mold temperatures. *International Communications in Heat and Mass Transfer*, 61, 102–110. <https://doi.org/10.1016/j.icheatmasstransfer.2014.12.008>
- Suriani Rizal, N. R., Jumahat, A., Hashim, U. R., & Omar, M. S. (2015). Effect of Pet Parison Size on Injection Moulding Mould Design. *Jurnal Teknologi*, 76(6), 115–119. <https://doi.org/10.11113/jt.v76.5702>
- Taghizadeh, S., Ozdemir, A., & Uluer, O. (2013). Warpage Prediction in Plastic Injection Molded Part using Artificial Neural Network, 37, 149–160.
- Wang, X., Zhao, G., & Wang, G. (2013). Research on the reduction of sink mark and warpage of the molded part in rapid heat cycle molding process. *Materials and Design*, 47, 779–792. <https://doi.org/10.1016/j.matdes.2012.12.047>



Fuzzy Lambda-Max Criteria Weight Determination for Feature Selection in Clustering

Nurul Adzlyana Mohd Saadon*, Rosma Mohd Dom and Nurazzah Abd Rahman

Faculty of Computer & Mathematical Sciences, Universiti Teknologi MARA (UiTM), 40450 Shah Alam, Selangor, Malaysia

ABSTRACT

Clustering refers to reducing selected features involved in determining the clusters. Raw data might come with a lot of features, including unimportant ones. A hybrid similarity measure (discovered in 2014) used in selecting features can be improvised as it might select all the attributes, including insignificant ones. This paper suggests Fuzzy Lambda-Max to be used as a feature selection method since Lambda-Max is normally used in ranking of alternatives. A set of AIDS data is used to measure the performance. Results show that Fuzzy Lambda-Max has the ability to determine criteria weights and ranking the criteria. Hence, feature selection can be done by choosing only the important criteria.

Keywords: Clustering, criteria weight determination, feature selection, Fuzzy Lambda-Max

INTRODUCTION

Clustering is actively studied in statistics, pattern recognition, machine learning and many other fields. Mining a big dataset is complicated as it involves many different attributes. Cluster analysis divides data into meaningful and useful clusters. It groups data based on information found in the data that describes the objects and their relationships. The goal of cluster analysis is to have similar object within a group (Rokach & Maimon, 2008).

One popular clustering technique is similarity measure. Cluster analysis aims to group a collection of patterns into clusters based on similarity. Clustering aims at grouping a set of objects into clusters so that objects in the same clusters should be similar as possible, whereas objects in one cluster should be as dissimilar as possible from objects in other clusters. Similarity measures in data mining is usually described as a

ARTICLE INFO

Article history:

Received: 28 September 2016

Accepted: 03 February 2017

E-mail addresses:

nuruladzlyana@gmail.com (Nurul Adzlyana Mohd Saadon),

rosma@tmsk.uitm.edu.my (Rosma Mohd Dom),

nurazzah@tmsk.uitm.edu.my (Nurazzah Abdul Rahman)

*Corresponding Author

distance with dimensions representing features of the objects. A small distance means a high degree of similarity and vice versa. Similarity is very subjective and is highly dependent on the domain and application (Yong, 2010). Similarity between two objects plays an important role in data mining jobs such as clustering and classification which involve distance computations. The distance or similarity for integer-type data and ratio-scaled data are well defined and understood (Alamuri et al., 2014).

Alamuri et al. (2014) has suggested a hybrid similarity measure that combines learning algorithm for context selection and distance computation based on the learned context. Nonetheless, the existing context selection algorithm has the tendency to select all the given attributes, making it more complicated. Therefore, a suitable threshold is needed.

This study uses Fuzzy Analytic Hierarchy Process (AHP) (Saaty, 1980; Ernest, 1999) in order to limit the features as AHP is commonly used in Multi Criteria Decision Making. It is an effective way of determining the criteria weight as it is based on the pair wise comparison method and thus no criterion is ignored. It is also a good method for dealing with human knowledge because AHP does not use artificial intelligence in the process to convert human thinking to fuzzy rule base. In AHP, the input is obtained from experts themselves and it is not randomly given by the system. This means information from professional people is still appreciated in the computer intelligence system. For each pair of criteria, the decision maker is required to do a pair wise comparison evaluation on the relative importance of the two. It is based on a well-defined mathematical structure of consistent matrices and eigenvectors to generate true or approximate weights (Saaty, 1980).

Ernest (1999) agreed that AHP is a good method to be used in determining criteria weight based on three primary steps involved in AHP. First, the structuring technique in AHP works similar to the way humans deal with complexity. Second, the measurement on a ratio scale which ranges from the lowest to the highest in terms of properties makes AHP necessary to represent proportion and fundamental to physical measurement and finally the synthesis technique in AHP places together parts into a complete system.

The AHP has been used in many criteria weight decision making problem. It can be used in determining criteria weights and also ranking of alternatives. It is also often used for criteria weight determination only or combined with other method for multi criteria decision making problem. The AHP can be the substitute of finding the weights in Artificial Neuro Fuzzy Inference System (ANFIS). Dom et al. (2013) used Lambda-Max AHP to find criteria weight for determining criteria weights of factors impacting the melt flow index of degradable plastics. The weights are then applied in back-propagation method in ANFIS for forecasting purposes (Saadon, 2013). Besides that, AHP is used to find the criteria weights for Extract, Transform and Load (ETL) software solution. It is used to determine the criteria weights for six characteristics given by ISO/IEC 9126-1 (2001): functionality, reliability, usability, efficiency and maintainability. After criteria weights is found, another method called TOPSIS is used to rank the alternative and to select the best ETL software for running the Business Intelligence systems (Hanine et al., 2016).

In AHP, there are three common criteria weight determination methods. The first method is the Fuzzy Logarithmic Least Square method (LLSM), proposed by Van Laarhoven and Pedrycz,

in 1983. In LLSM method, the criteria weight is obtained in the form of triangular fuzzy weights from a fuzzy comparison matrix. The second method in criteria weight determination in fuzzy AHP is the Extent Analysis method which was proposed by Chang, in 1996. It derives crisp weights from fuzzy comparison matrices. The third method is Lambda-Max method, which is the direct fuzzification method by Csutora and Buckley in 2001. In this study, only Lambda-Max is used as it is found to be the most suitable method in determining the weight as well as the ranking process (Saadon et al., 2010).

The objectives of this paper are apply the Fuzzy Lambda-Max AHP method to find the criteria weights and to rank the criteria according to their importance so that the appropriate criteria can be used in clustering purposes.

Fuzzy Lambda-Max AHP for feature selection in clustering is described in this paper. The methodology is described in detail and its implementation in clustering HIV patients is illustrated to demonstrate the feasibility using Fuzzy Lambda-Max AHP for feature selection. Criteria weights found can be used to rank the importance of features to be used for clustering purposes.

LITERATURE REVIEW

Feature Selection

In many data analysis problems, one is often confronted with very high dimensional data. Feature selection techniques are invented to find the relevant feature subset of the original features, which can help clustering, classification and retrieval.

Feature selection has been widely used in the field of pattern recognition, machine learning, statistics and data mining tasks. The objective of feature selection is to choose a subset of input variables by eliminating features, which are irrelevant and have no predictive information. Feature selection has proven to be helpful in enhancing learning efficiency, increasing predictive accuracy and reducing complexity of learned results (Koller & Sahami, 1996). The supervised feature selection has the main goal of finding a feature subset that produces higher classification accuracy.

As the element of a domain increases, the number of features increases. Finding an optimal feature subset is difficult and it is even hard to find problems related to feature selection are d (Kohavi & John, 1997). At this stage, it is essential to describe conventional feature selection process, which consists of four basic steps: subset generation, subset evaluation, stopping criterion, and validation (Dash & Liu, 1997).

Fuzzy Lambda-Max Criteria Weight Determination

Fuzzy Lambda-Max is one of the methods in Analytics Hierarchy Process (AHP), often used for Multi Criteria Decision Making. Csutora and Buckley (2001) propose Lambda-Max which involves the direct fuzzification of the well-known Lambda-Max method which is used in Saaty's Analytical Hierarchy Process method. This method is easy to apply as it only uses basic computations (Csutora & Buckley, 2001).

This method works better than LLSM as its calculations take more time and hence, delay in solving the problem (Csutora & Buckley, 2001). Lambda-Max also is found to be the most appropriate method to use for finding criteria weights among all the Fuzzy AHP methods (Saadon et al., 2010), not only because the calculation is less complex, but also because it gives good results.

METHOD

The methodology for Fuzzy Lambda-Max AHP for criteria weight determination consists of four steps. Csutora and Buckley (2001) developed Lambda Max method to calculate the fuzzy weights as follows:

Step 1: Apply α -cut. Let $\alpha = 1$ to obtain the positive matrix of decision maker k . $\widetilde{TM}_m^k = [\widetilde{r}_{ij}]_m^k$, and let $\alpha = 0$ to obtain the lower bound and upper bound positive matrices of decision maker k , $\widetilde{TL}_l^k = [\widetilde{r}_{ij}]_l^k$ and $\widetilde{TU}_u^k = [\widetilde{r}_{ij}]_u^k$. Calculate weight vector proposed in $AHWM_m^k = (w_i)_m^k$, $W_l^k = (w_i)_l^k$, and $W_u^k = (w_i)_u^k$, $i = 1, 2, \dots, n$.

Step 2: Choose two constants QL_l^k and QU_u^k to minimise the fuzziness of the weight.

$$QL_l^k = \min \left\{ \frac{w_{im}^k}{w_{iu}^k} \right\}, 1 \leq i \leq n$$

$$QU_u^k = \max \left\{ \frac{w_{im}^k}{w_{iu}^k} \right\}, 1 \leq i \leq n$$

The upper bound and lower bound of the weight are defined as:

$$w_{i_l}^{*k} = QL_l^k w_{i_l}^k$$

$$w_{i_u}^{*k} = QU_u^k w_{i_u}^k$$

So, the lower and upper bound of the weight vectors are $(w_i)_l^k$ and $(w_i)_u^k$.

Step 3: Combine the lower bound, the middle, and the upper bound weight vectors. The fuzzy weight matrix for decision maker k can be obtained and is defined as

$$\widetilde{W}_l^{k*} = (w_{i_l}^{*k}, w_{i_m}^{*k}, w_{i_u}^{*k}), i = 1, 2, \dots, n.$$

Step 4: Repeat step 1, 2, and 3 to calculate the local fuzzy weights and global fuzzy weights.

Application of Lambda-Max in Finding the Criteria Weights

To investigate the feasibility, Fuzzy Lambda-Max is applied to find the criteria weight for the given example:

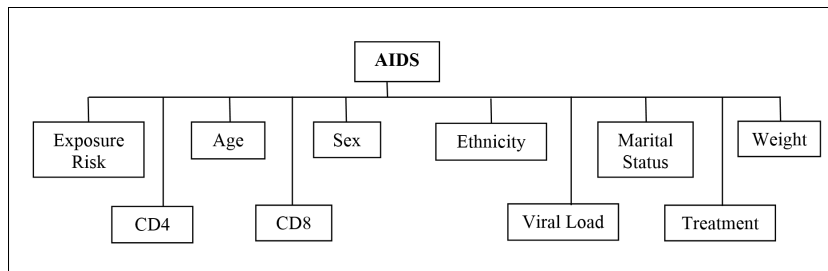


Figure 1. The criteria involved in determining AIDS survival

The Acquired Immune Deficiency Syndrome (AIDS) is a set of infections caused by the damage done to the human immune system affected by Human Immunodeficiency Virus (HIV). According to the San Francisco AIDS Foundation, HIV is transmitted through direct contact of the blood stream or the mucous membrane with a human fluid containing HIV (Dom et al., 2009).

Ten criteria are known factors that affect the potential of someone having AIDS. As shown in Figure 1, the 10 criteria are exposure risk, age, gender, ethnicity, marital status, weight, and level of CD4, level of CD8, HIV viral load and treatment.

The exposure risk means whether the patient is homosexual, heterosexual, bisexual, or getting HIV from their mother. It includes all ages. Gender is either female or male. Ethnicity is either the patient is a Malay, Chinese, Indian or other. Marital status includes single, married, divorced and widowed. There is no limit on weight in the data. The CD4 cells are a type of white blood cell which is important to the immune system while CD8 cells are the killer of abnormal body cells in human immune system. The last two factors are the HIV viral load in patient's body and the treatment received by the patients such as Didanoside (ddI) 100 mg -2, Didanosine (videx)-3, Kaletra (lopinavir/rit)-7 and many more.

Three experts have given their opinion on the level of effects of one criteria on the other criteria based on the rates of equal, moderate, strong and very strong (see Figure 2) towards the possibility of one having AIDS.

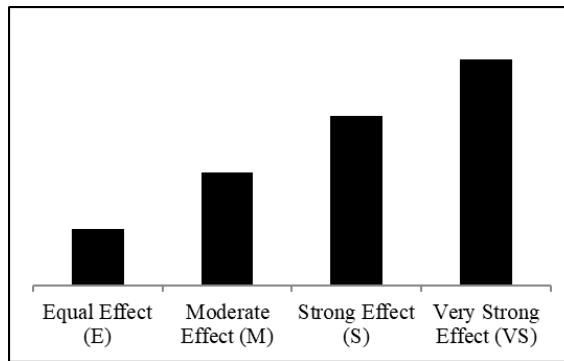


Figure 2. Rates of opinion

The inputs are in terms of pairwise comparison and are presented in matrix form. The comparison matrix of the three experts are shown in the following tables:

Table 1
Comparison matrix of 10 factors with respect to AIDS survival (Expert 1)

	E Risk	Age	Gender	Ethnic	Marital Stat	Weight	CD4	CD8	Viral Load	Treatment
E Risk	E	M	M	E	VS	E	M	M	M	E
Age		E	E	E	M					
Gender			E	M	E	E				
Ethnic				E	E					
Marital Stat		M		VS	E	E	E	E	E	E
Weight		M		VS		E	E	E	E	E
CD4		VS	M	M			E			
CD8		VS	M	VS			M	E	E	E
Viral Load		VS	M	M			M		E	E
Treatment		VS	VS	M			M			E

Table 2
Comparison matrix of 10 factors with respect to AIDS survival (Expert 2)

	E Risk	Age	Gender	Ethnic	Marital Stat	Weight	CD4	CD8	Viral Load	Treatment
E Risk	E	VS	VS	VS	VS	VS	VS	VS	VS	VS
Age		E	E	E	E	E	E	E	E	E
Gender			E	E	E	E	E	E	E	E
Ethnic				E	E	E	E	E	E	E
Marital Stat					E	S	M	M	M	E
Weight						E	E	E	E	E
CD4							E	E	E	M
CD8								E	E	E
Viral Load									E	S
Treatment										E

Table 3
Comparison matrix of 10 factors with respect to AIDS survival (Expert 3)

	E Risk	Age	Gender	Ethnic	Marital Stat	Weight	CD4	CD8	Viral Load	Treatment
E Risk	E	M	E	S	S	S	E	E	E	S
Age		E	M	E	E	E	E	E	E	
Gender			E	E	E	E	E	E		
Ethnic				E	E	E	E	E	E	E
Marital Stat			S		E	E	E	E	E	E
Weight						E	E	E	E	E
CD4							E	E	S	S
CD8								E	S	S
Viral Load			S						E	S
Treatment		S	S							E

Then, the rates of opinion are converted into triangular fuzzy numbers as given in Table 4.

Table 4
Fuzzy numbers for degree of importance (Wang, 2007)

Linguistic variable	Triangular Fuzzy Number
Equal	(1,1,1)
Moderate	(1,3,5)
Strong	(3,5,7)
Very Strong	(5,7,9)

Tables of pairwise comparison in triangular fuzzy number of the 10 factors that determine AIDS survival are as shown as follows:

Table 5
Fuzzy comparison matrix of 10 factors with respect to AIDS survival (Expert 1)

	E Risk	Age	Gender	Ethnic	Marital Stat	Weight	CD4	CD8	Viral Load	Treatment
E Risk	(1,1,1)	(1,3,5)	(1,3,5)	(1,1,1)	(5,7,9)	(1,1,1)	(1,3,5)	(1,3,5)	(1,3,5)	(1,1,1)
Age	(1/5,1/3,1)	(1,1,1)	(1,1,1)	(1,1,1)	(1,3,5)	(1/5,1/3,1)	(1/5,1/3,1)	(1/9,1/7,1/5)	(1/9,1/7,1/5)	(1/9,1/7,1/5)
Gender	(1/5,1/3,1)	(1,1,1)	(1,1,1)	(1,3,5)	(1,1,1)	(1,1,1)	(1/5,1/3,1)	(1/5,1/3,1)	(1/5,1/3,1)	(1/9,1/7,1/5)
Ethnic	(1,1,1)	(1/5,1/3,1)	(1/5,1/3,1)	(1,1,1)	(1,1,1)	(1/9,1/7,1/5)	(1/5,1/3,1)	(1/9,1/7,1/5)	(1/5,1/3,1)	(1/5,1/3,1)
Marital Stat	(1/9,1/7,1/5)	(1,3,5)	(1,1,1)	(5,7,9)	(1,1,1)	(1,1,1)	(1,1,1)	(1,1,1)	(1,1,1)	(1,1,1)
Weight	(1,1,1)	(1,3,5)	(1,1,1)	(5,7,9)	(1,1,1)	(1,1,1)	(1,1,1)	(1,1,1)	(1,1,1)	(1,1,1)
CD4	(1/5,1/3,1)	(5,7,9)	(1,3,5)	(1,3,5)	(1,1,1)	(1,1,1)	(1,1,1)	(1/5,1/3,1)	(1/5,1/3,1)	(1/5,1/3,1)
CD8	(1/5,1/3,1)	(5,7,9)	(1,3,5)	(5,7,9)	(1,1,1)	(1,1,1)	(1,3,5)	(1,1,1)	(1,1,1)	(1,1,1)
Viral Load	(1/5,1/3,1)	(5,7,9)	(1,3,5)	(1,3,5)	(1,1,1)	(1,1,1)	(1,3,5)	(1,1,1)	(1,1,1)	(1,1,1)
Treatment	(1,1,1)	(5,7,9)	(5,7,9)	(1,3,5)	(1,1,1)	(1,1,1)	(1,3,5)	(1,1,1)	(1,1,1)	(1,1,1)

Table 6
Fuzzy comparison matrix of 10 factors with respect to AIDS survival (Expert 2)

	E Risk	Age	Gender	Ethnic	Marital Stat	Weight	CD4	CD8	Viral Load	Treatment
E Risk	(1,1,1)	(5,7,9)	(5,7,9)	(5,7,9)	(5,7,9)	(5,7,9)	(5,7,9)	(5,7,9)	(5,7,9)	(5,7,9)
Age	(1/9,1/7,1/5)	(1,1,1)	(1,1,1)	(1,1,1)	(1,1,1)	(1,1,1)	(1,1,1)	(1,1,1)	(1,1,1)	(1,1,1)
Gender	(1/9,1/7,1/5)	(1,1,1)	(1,1,1)	(1,1,1)	(1,1,1)	(1,1,1)	(1,1,1)	(1,1,1)	(1,1,1)	(1,1,1)
Ethnic	(1/9,1/7,1/5)	(1,1,1)	(1,1,1)	(1,1,1)	(1,1,1)	(1,1,1)	(1,1,1)	(1,1,1)	(1,1,1)	(1,1,1)
Marital Stat	(1/9,1/7,1/5)	(1,1,1)	(1,1,1)	(1,1,1)	(1,1,1)	(3,5,7)	(1,3,5)	(1,3,5)	(1,3,5)	(1,1,1)
Weight	(1/9,1/7,1/5)	(1,1,1)	(1,1,1)	(1,1,1)	(1/7,1/5,1/3)	(1,1,1)	(1,1,1)	(1,1,1)	(1,1,1)	(1,1,1)
CD4	(1/9,1/7,1/5)	(1,1,1)	(1,1,1)	(1,1,1)	(1/5,1/3,1)	(1,1,1)	(1,1,1)	(1,1,1)	(1,1,1)	(1,3,5)
CD8	(1/9,1/7,1/5)	(1,1,1)	(1,1,1)	(1,1,1)	(1/5,1/3,1)	(1,1,1)	(1,1,1)	(1,1,1)	(1,1,1)	(1,1,1)
Viral Load	(1/9,1/7,1/5)	(1,1,1)	(1,1,1)	(1,1,1)	(1/5,1/3,1)	(1,1,1)	(1,1,1)	(1,1,1)	(1,1,1)	(3,5,7)
Treatment	(1/9,1/7,1/5)	(1,1,1)	(1,1,1)	(1,1,1)	(1,1,1)	(1,1,1)	(1/5,1/3,1)	(1,1,1)	(1/7,1/5,1/3)	(1,1,1)

Table 7
Fuzzy comparison matrix of 10 factors with respect to AIDS survival (Expert 3)

	E Risk	Age	Gender	Ethnic	Marital Stat	Weight	CD4	CD8	Viral Load	Treatment
E Risk	(1,1,1)	(1,3,5)	(1,1,1)	(3,5,7)	(3,5,7)	(3,5,7)	(1,1,1)	(1,1,1)	(1,1,1)	(3,5,7)
Age	(1/5,1/3,1)	(1,1,1)	(1,3,5)	(1,1,1)	(1,1,1)	(1,1,1)	(1,1,1)	(1,1,1)	(1,1,1)	(1/7,1/5,1/3)
Gender	(1,1,1)	(1/5,1/3,1)	(1,1,1)	(1,1,1)	(1/7,1/5,1/3)	(1,1,1)	(1,1,1)	(1,1,1)	(1/7,1/5,1/3)	(1/7,1/5,1/3)
Ethnic	(1/7,1/5,1/3)	(1,1,1)	(1,1,1)	(1,1,1)	(1,1,1)	(1,1,1)	(1,1,1)	(1,1,1)	(1,1,1)	(1,1,1)
Marital Stat	(1/7,1/5,1/3)	(1,1,1)	(3,5,7)	(1,1,1)	(1,1,1)	(1,1,1)	(1,1,1)	(1,1,1)	(1,1,1)	(1,1,1)
Weight	(1/7,1/5,1/3)	(1,1,1)	(1,1,1)	(1,1,1)	(1,1,1)	(1,1,1)	(1,1,1)	(1,1,1)	(1,1,1)	(1,1,1)
CD4	(1,1,1)	(1,1,1)	(1,1,1)	(1,1,1)	(1,1,1)	(1,1,1)	(1,1,1)	(1,1,1)	(3,5,7)	(3,5,7)
CD8	(1,1,1)	(1,1,1)	(1,1,1)	(1,1,1)	(1,1,1)	(1,1,1)	(1,1,1)	(1,1,1)	(3,5,7)	(3,5,7)
Viral Load	(1,1,1)	(1,1,1)	(3,5,7)	(1,1,1)	(1,1,1)	(1,1,1)	(1/7,1/5,1/3)	(1/7,1/5,1/3)	(1,1,1)	(3,5,7)
Treatment	(1/7,1/5,1/3)	(3,5,7)	(3,5,7)	(1,1,1)	(1,1,1)	(1,1,1)	(1/7,1/5,1/3)	(1/7,1/5,1/3)	(1/7,1/5,1/3)	(1,1,1)

Finally, from the fuzzy numbers, the criteria weights are calculated using Fuzzy Lambda-Max method as described in the previous section, to rank the criteria from the most important to the least important. The results will be presented in the next section.

RESULTS AND DISCUSSION

Based on the expert opinion, the criteria weights are calculated using the computations given in the previous section. The following table shows the final criteria weights obtained using Fuzzy Lambda-Max method.

Table 8
Final criteria weights

Criteria	Criteria weights
E Risk	(0.221, 0.318, 0.440)
Age	(0.063, 0.075, 0.102)
Gender	(0.061, 0.067, 0.100)
Ethnic	(0.064, 0.075, 0.097)
Marital Stat	(0.103, 0.128, 0.155)
Weight	(0.096, 0.108, 0.118)
CD4	(0.090, 0.129, 0.161)
CD8	(0.112, 0.154, 0.164)
Viral Load	(0.096, 0.127, 0.106)
Treatment	(0.085, 0.110, 0.137)

Then, the criteria are ranked. The criteria with the most weight is placed on top. The following table shows the ranking of criteria.

Table 9
Ranking of criteria

Rank	Criteria	Criteria weights
1	E Risk	(0.221, 0.318, 0.440)
2	CD8	(0.112, 0.154, 0.164)
3	CD4	(0.090, 0.129, 0.161)
4	Marital Stat	(0.103, 0.128, 0.155)
5	Viral Load	(0.096, 0.127, 0.106)
6	Treatment	(0.085, 0.110, 0.137)
7	Weight	(0.096, 0.108, 0.118)
8	Ethnic	(0.064, 0.075, 0.097)
9	Age	(0.063, 0.075, 0.102)
10	Gender	(0.061, 0.067, 0.100)

Ranking of criteria shows the importance of factors that indicate AIDS survival. The criteria that ranked first is the most important factor affecting the potential of the patient having AIDS. In this study, based on expert opinion and criteria weight obtained, it has been shown that the exposure risk, level of CD8 and CD4 cells are three most important factors towards the AIDS survival. Ethnicity, age and gender are found to be the least important factors. The ability of Fuzzy Lambda-Max AHP method in determining criteria weights and ranking the criteria is beneficial so that we know the important criteria to be used in clustering the patients whether they are likely to have AIDS or not. From the ranking of criteria, feature selection can be done by choosing only the important criteria.

CONCLUSION

The study has shown that Fuzzy Lambda-Max can be used for determining criteria weights. Hence, the criteria could be ranked according to importance. This is very useful for feature selection in clustering process. For future work, the accuracy of clustering result will be measured based on percentage accuracy by comparing actual and experimental clustering results. To further validate the method, comparison with existing methods of determining the criteria weights and their ranking can be carried out.

ACKNOWLEDGEMENTS

The authors would like to thank the Faculty of Computer and Mathematical Sciences, Universiti Teknologi MARA for its financial assistance to carry out this research.

REFERENCES

- Alamuri, L., Surampudi, B. R. & Negi, A. (2014). A survey of distance/similarity measure for categorical data. *International Joint Conference on Neural Network (IJCNN)*. 1907-1914.
- Chang, D. Y. (1996). Application of Extent Analysis Method on Fuzzy AHP. *European Journal of Operation Research*, 95, 649-655.
- Csutora, R., & Buckley, J. J. (2001). Fuzzy Hierarchical Analysis: The Lamda-Max Method. *Fuzzy Sets and Systems*, 120, 181-195.
- Dash, M. & Liu, H. (1997). *Intelligent Data Analysis*. 1,131–156.
- Dom, R. M., Kareem, S. A., Abidin, B., Kamaruzaman, A., & Kajindran, A. (2009). Prediction of AIDS Survival: A Data Mining Approach. *2nd WSEAS International Conference on Multivariate Analysis and its Application in Science and Engineering*. 48-53.
- Dom, R. M., Saadon, N. A., & Mohamad, D. (2013). The criteria weight determination of factors impacting the melt flow index using Lambda-Max method. *International Conference on Mathematical Sciences and Statistics, ICMSS2013*. 1557. 78-81.
- Ernest, H. F. (2001). The Analytic Hierarchy Process - An Exposition. *Operation Research 2001 INFORMS*, 469-486.

- Hanine, M., Boutkhom, O., Tikniouine, A., & Agouti, T. (2016). Application of an integrated multi-criteria decision making AHP-TOPSIS methodology for ETL software selection. *SpringerPlus*, 5(1), 263.
- ISO/IEC 9126-1. (2001). *Software Engineering – Product Quality - Part 1: Quality Model, International Organization for Standardization*.
- Kohavi, R. & John, G. H. (1997). *Artificial intelligence*.
- Koller, D. & Sahami, M. (1996). Toward Optimal Feature Selection. *Proceedings of the Thirteenth International Conference on Machine Learning (ICML)*. 284-292
- Rokach L. & Maimon O. (2008). “CLUSTERING METHOD (CHAPTER 15)”. *Data Mining and Knowledge Discovery Handbook*.
- Saadon, N. A. M., Mohamed, D. & Dom, R. M. (2010). Comparative Analysis of Criteria Weight Determination in AHP Models. *International Conference on Science and Social Research*. 965-969.
- Saadon, N. A. M. (2013). *Lambda-Max Neuro Fuzzy System*.
- Saaty, T. L. (1980). *The Analytic Hierarchy Process*. McGraw-Hill Book Co., New York.
- San Francisco AIDS Foundation. (2006). *How HIV is Spread*.
- Van Laarhoven, P. J. M. & Pedrycz, W. (1983). A Fuzzy Extension of Saaty's Priority Theory. *Fuzzy Sets and Systems*, 11, 229-241.
- Wang, Y. M., Ying, L., & Hua, Z. (2007). On the Extent Analysis Method for Fuzzy AHP and Its Applications. *European Journal of Operation Research*, 186, 735-747.
- Yong, J. B. (2010). Data Mining Portfolio: Similarity Measure. Retrieved from: humanoriented.com/classes/2010/fall/csci568/portfolio_exports/bhoenes/similarity.htm.





Green Lean TQM Islamic Management Practices in Malaysian Food Companies

Nur Asiah Kuzaiman*, Argustina Zainuddin, Nor Azlina Mohd Salleh and Salmiah Kasolang

Faculty of Mechanical Engineering, Universiti Teknologi MARA (UiTM), 40450 Shah Alam, Selangor, Malaysia

ABSTRACT

Islam is the fastest growing religion in the world. The number of the Muslim worldwide has been increasing through birth and conversion rate. As the number of Muslim population grow so does that the demand for halal product worldwide. While quality is seen as an integral part of related companies 'strategic business plan. Leadership is difficult to characterise and it implies different things to various individuals. However, it is considered as a noteworthy driver for the TQM practices. This paper examines Lean Manufacturing (LM), Total Quality Management (TQM), Environmental Management System (EMS) and Islamic Manufacturing practices (IMP) and explores the possibility to integrate this management system into a new Islamic model for in the Malaysian food industry as the country moves forward to becoming a Halal Hub Country. This is a conceptual study, and provides a foundation for future research on this topic.

Keywords: Environmental Management System, food industry, Islamic Manufacturing Practices, Lean Manufacturing, Total Quality Management

ARTICLE INFO

Article history:

Received: 28 September 2016

Accepted: 03 February 2017

E-mail addresses:

Asiah.kuzaiman@gmail.com (Nur Asiah Kuzaiman),
argustina@gmail.com (Argustina Zainuddin),
noorazlinamohdsalleh@gmail.com (Nor Azlina Mohd Salleh),
salmiahk@salam.uitm.edu.my (Salmiah Kasolang)

*Corresponding Author

INTRODUCTION

The halal food sector, currently worth USD700 billion, is growing rapidly (Spire, 2015), with Asia accounting for 65% of its market, driven by demand primarily from Malaysia, Pakistan, India, Indonesia and China.

The global halal food sector is expected to grow by six per cent by 2020, according to findings from the State of the Global Islamic Economy Report 2015/2016 (the report is commissioned and supported by the

Dubai Islamic Economy Development Centre in partnership with Thomson Reuters, and in collaboration with Dinar Standard).

Malaysia remained a net importer of food in 2013 (RM15.6 billion). Major food imports were sugar & sugar confectionery (RM3.4 billion), dairy products (RM3.2 billion), cereal and cereal preparations (RM1.5 billion), vegetable and fruits (RM1.2 billion) and cocoa and cocoa products (RM1.0 billion). A total of RM24.6 billion has been set aside as a target investment for the food processing industry under the Industrial Malaysia Plan 2006-2020 (IMP3) (Ministry of International Trade and Industry, 2012). Halal food was listed as current industry's key growth together with functional food, health food, convenience food and food ingredient. According to Malaysian Investment Development Authority (MIDA) the processing food industry is predominantly Malaysian-owned, and that Malaysia is the third largest producer of poultry meat in the Asia Pacific region. The country is self-sufficient in poultry, pork and eggs, but imports about 80% of its beef requirements. The potential value of the global halal food market was estimated US\$560 billion per year. Not to mention the world Muslim consumer expenditure in 2018 is expected to grow to US\$2.4 trillion and the value could rise to US\$3.7 trillion by 2019 (MIDA, 2017; Global Halal Data Pool, 2016).

METHOD

Journal articles, reports, books and theses related to TQM and LM were reviewed to develop an integrated model for the food industry in Malaysia.

RESULTS AND DISCUSSION

Lean Manufacturing (LM)

Lean Manufacturing is an extended version of the Toyota Production System (TPS) with the objective to eliminate waste (Gwen, Michael, & Hendrickson, 2014). According to Dombrowski and Mielke (2014), and Salleh et al. (2015), many versions of the lean implementation fall short of expectation though some organisations accomplish noteworthy results in the first years of lean implementation by performing Kanban 5S, SMED, FIFO. Many suffer from stagnation at some point or another. The explanation behind the stagnation could be the sole focus on waste reduction and related strategies. Without a doubt, waste elimination is a vital component of lean implementation but it doesn't lead to genuine lean thinking and therefore, no continuous improvement process (CIP) (Dombrowski & Mielke, 2014).

Total Quality Management (TQM)

Total Quality Management (TQM) is both a methodology and a technique to diminish the impact of a product, service or process in order by enhancing its quality and productivity and satisfying customer demands. This calls for better financial execution, and thus TQM can offer a competitive advantage. The quest for product and service enhancement is driven by survival needs. Hence, this study aims to show that TQM can bolster and complement production

performance and meet customer demand. In addition, Agus and Hassan (2011) confirm that TQM improves value added production.

Environmental Management System (EMS)

Environmental Management System (EMS) is a fundamental component to help firms in assessing, managing and organising their environmental activities. The system keeps track of the organisation's effect on the environment by keeping up with environmental regulations, reducing ecological costs, diminish dangers, train employees, create indicators of effect, as well as enhance ecological performance. An EMS usually comprises policies, goals, details frameworks, task lists, data collection and companies, emergency plans, reviews, administrative necessities, and annual reports (Gwen, Michael, & Hendrickson, 2014).

Islamic Manufacturing Practices (IMP)

Islamic Manufacturing Practices (IMP) is a set or practices or guidelines to ensure the manufacturer meets the requirements of Shariah Compliance in term of quality, efficacy and purity of the product in order to meet the 'halalan toyyiban' concept. Sidratul Enterprise, established in 1995, is a company wholly owned by Bumiputera. An initiative of its founder, Mr. Arshad bin Haji Ahmad Tajuddin, the company was a product of the high demand of biotechnology-based industry in the market.

Good Manufacturing Practices (GMP)

In Malaysia, MS1514 is a complementary document to MS1500, MS1480 and Manual Procedure of Halal Certification. The process of halal food certification begins when the manufacturers or food industries submit their application to JAKIM. The applicants need to provide details of ingredients, name/s and address of manufacturer/s or supplier/s of ingredients, original halal status of ingredients such as halal certificates from recognised Islamic bodies or product specification, manufacturing processes and procedures, such as HACCP and GMP (Mohd Amri, 2008; Sazly, 2008). In order to get the halal certification, applicants must comply with all the guidelines underlined in halal food standard, GMP standard, HACCP standards as well as the manual.

Historical Timeline of TQM, LM, EMS, GMP and IMP

Figure 1 shows the historical background and evolution of LM, TQM, EMS and IMP. It can be surmised that the concept of LM was first introduced in the 1980s, while GMP was during 1900s followed by the publishing of TQM and EMS in 1920s and 1992. The MS1900, the first of its kind in Islamic Quality Management System in the world, was introduced in 2006 by JAKIM while IMP was established a year before in 2005 by Sidratul Enterprise.

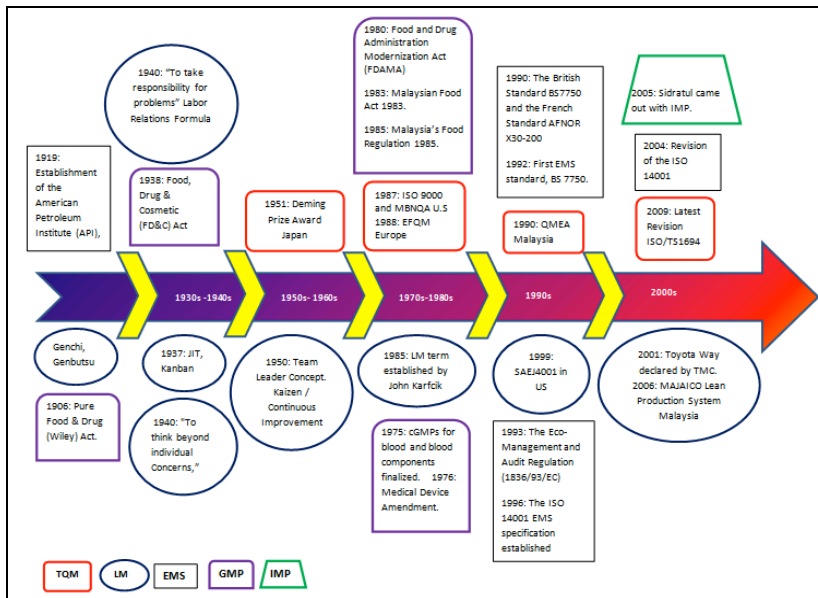


Figure 1. Historical timeline of TQM, LM, EMS, GMP and IMP

Pre-Status of TQM, LM, EMS and IMP in Malaysian Food Industry

The number of studies on TQM, LM, EMS and IMP in Malaysian food industry is recorded in Table 1. The data gained for the pre-status implementation of the systems are based on the search on the Malaysian Thesis Online (MyTO) website. As seen in Table 1, the number of studies of TQM recorded the highest with 249 studies followed by LM and EMS with 95 and 18 studies. However, none of the studies have been done in Malaysian food industry. It is more saddening with the fact of number of IMP studies in Malaysia which is none.

Table 1
TQM, LM, EMS and IMP studies in Malaysian based on Malaysian Thesis Online (MyTO)

Initiatives	TQM	LM	EMS	IMP
Implementation year	1923	2000	2003	2005
Availability in Malaysian Food Industry	None	None	None	None
Availability in Malaysian other Industry	Yes (249)	Yes (95)	Yes (18)	None
Total Studies	249	95	18	None

The driving factors to implement LM and EMS frameworks can be internal (requirement for such systems by the directors) or external (associations need to conform with client requirements and external partners) as shown in Table 1. Among the internal reasons, the most important are cost and defect lessening, productivity improvement, and environmental/quality enhancement (Puvanasvaran, 2012). The LM and EMS in particular have a distinctive impact on business goals. However, it needs to be emphasised lean manufacturing alone would not enhance environmental performance due to the potential clashes between environmental performance objectives and lean manufacturing principles.

Lean manufacturing focuses on internal and waste reduction process by enhancing environmental management practices to ultimately boost company effectiveness. Besides, environmental management practices do require extra assets. Yang, Hong and Sachin (2011) believe it is imperative for manufacturing firms to implement lean manufacturing and environmental management practices for environmental protection. A study shows that EMS practices are more common compared with LM and TQM. However, Salleh, Kasalong and Jaafar (2012a, 2012b) found that the EMS practices though actively implemented internally in the organisation, it is weakly practised by their supplier.

Consumers are beginning to show interest in the integrity status of Halal products. All parties in the supply chain, downstream and upstream, must take individual and joint responsibilities to protect the Halal food products from being cross contaminated. Factors such as Halal certification, Halal standard, Halal traceability, Halal dedicated assets, trust and commitments between supply chain members that are important to enhance the integrity of Halal products are considered when IMP is implemented as part of quality control (Zulfakar, Anuar, & Talib, 2014). If halal is taken as the most critical standard for products, then the idea to synergise halal concept with worldwide established quality management system such as LM, TQM, and EMS is one of the ways to maximise quality of management system. A comprehensive system that covers all of these can be set up in order to reduce time and cost of compliance.

The prerequisite for TQM and its planning differ between industries. Thus, there is necessity for a model for the Malaysian food industry based on the TQM approach. Therefore, TQM is not “one-size-fits-all” in terms of implementation TQM. A framework or the TQM model in food industry requires integration of all parties involved in the food chain (Talib, H. 2013).

The conceptual framework proposed in this paper is developed based on the previous models developed by others (Salleh, Kasalong, & Jaafar, 2012b). Moreover, components of the global and national quality awards from Japan (Deming Prize), America (Malcolm Baldrige National Quality Award), Europe Countries (European Quality Foundation Award) and Malaysia (Malaysian Prime Minister Award Model) while ISO/TS 16949 or ISO 9000 for TQM and three system from LM (America - SAEJ4001, Japan - Toyota Production System and Malaysia - MAJAICO Lean Production System) were considered in the proposed framework for evaluating quality management practices among SMEs in Malaysian food industry.

CONCLUSION

Integrating quality, environment, and health and safety management has been extensively discussed in literature. Integrated Total Quality Management (TQM) with Lean Manufacturing (LM) for example were proposed in order to focus on accomplishing consumer satisfaction by eliminating wastes in an organisation association. This also led to the establishment of The Green Lean TQM model by integrating Total Quality Management, Lean Manufacturing and Environmental Management System.

Organisations need to use distinctive instruments and frameworks, especially Integrated Management Systems, to ensure specific quality standard. There is a dearth of studies on financial and non-financial performance gains using these quality systems.

ACKNOWLEDGEMENTS

This study was funded by Ministry of Education Malaysia and Universiti Teknologi MARA Malaysia under the FRGS (600-RMI/ST/FRGS 5/3 (143/2014)).

REFERENCES

- Agus, A., & Hassan. Z. (2011). Enhancing Production Performance and Customer Performance Through Total Quality Management (TQM): Strategies For Competitive Advantage. *Procedia Social and Behavioral Sciences*, 24, 1650–1662).
- Dombrowski, U., & Mielke. T. (2014). Lean Leadership – 15 Rules for a sustainable Lean Implementation. *Procedia CIRP*, 17, 565 – 570.
- Global Halal Data Pool (GHDP). (2016). Global Halal Food Market to Reach US\$3.7tr by 2019. Retrieved from <http://globalhalaldatapool.com/index.php/details/item/107-global-halal-food-market-to-reach-3-7tr-by-2019>
- Gwen, C., Michael, F., & Hendrickson, C. (2014). Environmental Management Systems and ISO14001 Certification for Construction Firms. *Journal of Construction Engineering and Management* © Asce / May/June.
- Malaysian Investment Development Authority (MIDA). (2017). Food Technology and Sustainable Resources. Retrieved from <http://www.mida.gov.my/home/food-technology-and-sustainable-resources/posts/>
- Malihe, M., Ab-Rahman, M. N., Che Mohd Zain, C. R., & Jamsari, E. A. (2014). Increasing Production and Eliminating Waste through Lean Tools and Techniques for Halal Food Companies. *Sustainability*, 6, 9179-9204.
- Mohd Ali, K. A., & Abdul Talib, H. H. (2013). Total Quality Management Approach for Malaysian Food Industry: Conceptual Framework. *Journal of Advanced Management Science*, 1(4).
- Puvanasvaran, P., Tian, R. K. S., Suresh, V., & Muhamad, M. R. (2012). Lean principles adoption in environmental management system (EMS): A survey on ISO 14001 certified companies in Malaysia. *Journal of Industrial Engineering and Management*, 5(2), 406-430.
- Salleh, N. A. M., Kasolang, S., Jaffar A., & Halim. N. H. A., (2015). Lean Tqm Leadership, Management Practices In Malaysian Automotive Companies. *Jurnal Teknologi*, 76, 1–6.

- Salleh, N. A. M., Kasolang, S., & Jaffar. A., (2012b). Review study of developing an integrated TQM with LM framework model in Malaysian automotive industry. *The TQM Journal*, 24(5), 399 – 417.
- Salleh, N. A. M., Kasolang S., & Jaffar. A., (2011). Lean TQM Automotive Factory Model System. *World Academy of Science, Engineering and Technology*, 79, 627-633.
- Salleh, N. A. M., Kasolang S., & Jaffar. A., (2012a). Green Lean TQM Practices in Malaysian Automotive Companies. *International Journal of Mechanical, Aerospace, Industrial and Mechatronics Engineering*, 6(10).
- Sumiani, Y, Haslinda, Y., & Glen, L. (2007). Environmental reporting in a developing country: a case study on status and implementation in Malaysia. *Journal of Cleaner Production*, 15(10), 895-901.
- Talib, H. H. A., Ali, K. A. M. & Idris, F. (2013). Quality management framework for the SME's food processing industry in Malaysia. *International Food Research Journal*, 20(1), 147-164.
- Ulle, R. S., & Kumar, A. S. (2014). A Review on Total Quality Leadership in TQM Practices-Industrial Management and Organizations. *International Journal of Emerging Research in Management and Technology*, 3(5), 152-155.
- Yang, M. G., Hong, P., & Sachin, B. M. (2011). Impact of lean manufacturing and environmental management on business performance: An empirical study of manufacturing firms. *Int. J. Production Economics*, 129, 251–261.
- Zulfakar, M. H., Anuar, M. M., & Ab Talib, M. S. (2014). Conceptual Framework on Halal Food Supply Chain Integrity Enhancement. *Procedia - Social and Behavioral Sciences*, 121, 58 – 67.





GPU Implementation of Sub-Iris Technique in Iris Recognition System

Shahrizan Jamaludin^{1,2*}, Nasharuddin Zainal² and W. Mimi Diyana W. Zaki²

¹Centre for Computer Engineering Studies, Faculty of Electrical Engineering, Universiti Teknologi MARA (UiTM), 40450 Shah Alam, Selangor, Malaysia

²Department of Electrical, Electronic and Systems Engineering, Faculty of Engineering and Built Environment, Universiti Kebangsaan Malaysia (UKM), 43600 Bangi, Selangor, Malaysia

ABSTRACT

Iris recognition has become a widely popular biometric system. The stable textures and features of the human iris have made such biometric systems efficient and accurate for purposes of verification and identification. The term non-ideal iris refers to a situation in which the iris is occluded by noise, including reflections, eyelashes, eyelids and so on. Most current iris recognition algorithms assume that the iris is not occluded, which is less accurate. A method using only some parts of the iris may be suitable to deal with a non-ideal iris. The current application of iris recognition systems are plagued by weaknesses such as slow processing times, especially when dealing with many irises. In this study, a sub-iris recognition technique is proposed to deal with the non-ideal iris, while reducing execution time via an embedded system using a graphical processing unit (GPU). The experiment revealed that the proposed method was accurate and fast.

Keywords: Execution time, graphical processing unit, iris recognition system, non-ideal iris, sub-iris technique

INTRODUCTION

Many studies have examined the performance of iris recognition systems which have significant advantages such as high identification rate and high feasibility. Each iris is unique, with the possibility of locating two identical irises being only 1 in 10^{72} (Flom & Safir, 1987). Its pattern might be stable for a lifetime (Daugman & Downing, 2001). The iris also has rich features such as arching ligaments, rings, freckles, coronas, collarettes and crypts (Muron & Pospisil, 2000). Unfortunately, existing iris recognition

ARTICLE INFO

Article history:

Received: 28 September 2016

Accepted: 03 February 2017

E-mail addresses:

mile_mal@yahoo.com (Shahrizan Jamaludin),
nasharuddin.zainal@ukm.edu.my (Nasharuddin Zainal),
wmdiyana@ukm.edu.my (W. Mimi Diyana W. Zaki)

*Corresponding Author

systems are disappointing in terms of execution time and/or processing speed (Tozer, 2012). Additionally, shape of the iris is not always circular and may be occluded by eyelids, eyelashes, reflections and noises, becoming a non-ideal iris. Thus, a new method must be introduced in order to improve accuracy and speed of an iris recognition system.

Conventional iris recognition systems are based on three algorithms: the integro-differential operator, the Hough transform, and the active contour. The integro-differential operator (IDO) was introduced by Daugman (1993), and it is used in order to detect two circles that represent the pupil and iris regions respectively. Meanwhile, a method to locate two circles of pupil and iris regions based on Hough transform (HT) was introduced by Wildes (1997). This method also uses the edge detection method to detect the edges that represent the pupil and iris boundaries. The active contour method was introduced by Daugman (2007) in order to detect the irregular boundary of the iris.

Most current methods are partly based on these pioneer works and implemented in a CPU. Unfortunately, existing algorithms suffer from slow operations time (Yu & Zhou, 2012). Because of that, an iris recognition system must be developed on another platform with better performance than the CPU. Not all regions of the iris are rich with features. According to Krichen (2007), the region near the pupil boundary is rich with patterns and is also less occluded by eyelids, eyelashes, and noise. Hence, a method that uses only the important parts in of the iris must be developed in order to reduce the complexity of the system and to make it more efficient by excluding the unimportant parts. This method may reduce resources, thus reducing the processing time of the iris recognition system.

Therefore, in this paper, a method using only the important part of the iris region (sub-iris technique) is proposed to reduce the complexity of the iris recognition system. The proposed method will be implemented on the graphical processing unit (GPU) to reduce execution time.

Previous Works

Recently, the conventional iris recognition methods have been modified to improve their performance. Radman et al. (2013) modified the existing IDO method which made it more adaptable to locate the irregular boundary of iris. Meanwhile, Hilal et al. (2012) modified the active contour method to be more accurate in locating the irregular boundary of pupil. This method also used HT to detect the iris boundary. Additionally, Abdullah et al. (2014) used a morphological operator to estimate the location of pupil and iris boundaries. After that, the active contour was used to detect the exact pupil and iris boundaries. The HT was improved by Qin et al. (2013), where the edge gradient direction information was used along with HT to locate the exact boundary.

All of the methods described above use the entire or full-iris region for iris recognition systems. The full-iris region contains more iris textures and features which are more accurate to allow recognition of identity. Unfortunately, acquisition of full-iris region is not always possible. Some people may have small eyes that are occluded by eyelids. The iris region can also be occluded by eyelashes, reflections, and other objects. There are few methods that use

only some parts of iris region in the iris recognition system. The lower part of iris is used in the phase-based algorithm (Miyazawa et al., 2006; Ito & Aoki, 2013) for iris recognition system instead of the full-iris region. Unfortunately, some iris images may consist of the lower eyelid, leading to less accurate performance. Thus, the eyelid masking has been used to eliminate the eyelid region. Unfortunately, eyelid detection requires a longer execution time. Du et al. (2005) introduced the partial iris for iris recognition system. This method generated four options for partial iris. The partial iris was defined as the combination of upper and lower parts of iris region with a reduced radius. Unfortunately, the heavy occlusion of eyelid on the upper iris may reduce accuracy. Zhao and Kumar (2015) have used some parts of the iris region based on the total variation model to suppress noises and to obtain an accurate localisation. In the present study, the above methods are analysed, and the disadvantages addressed in order to create a better sub-iris or partial iris technique. Generally, the full-iris technique has higher recognition accuracy compared with the sub-iris technique if the iris features themselves are not occluded. Unfortunately, this is impossible due to the nature of human eyes, especially in non-cooperative environments (Zhao & Kumar, 2015). Hence, the sub-iris technique is proposed to obtain almost similar recognition accuracy with the full-iris technique, but with reduced execution time.

Most iris recognition systems are implemented on the CPU but the latter is not fast enough to handle many processes (Sakr et al., 2012). The processes of iris localisation and feature extraction have the most extensive computation in the system (Sakr et al., 2012). Thus, GPU is proposed to reduce the execution time of the iris recognition system. It was used by Sakr et al. (2012) to implement the Daugman (1993) algorithm to compute localisation and feature extraction processes, achieving 9.6 and 14.8 times speedup compared with CPU. Meanwhile, Nazneen et al. (2016) used the GPU for iris template matching and achieved good performance. Based on these findings, the proposed sub-iris technique will be implemented on the GPU in order to further improve the time performance of the iris recognition system.

METHOD

The iris recognition system consists of iris acquisition, iris segmentation, normalisation, feature extraction, and matching as shown in Figure 1. In iris acquisition, the iris image is captured by using a camera under the near infrared or visible wavelength environment. The near infrared image consists of grey level values. Meanwhile, the visible wavelength image consists of colour values (red, green and blue). The near infrared image is suitable for security and verification systems, while the visible wavelength image is suitable for surveillance and forensic systems. In this work, the near infrared iris image is used for iris acquisition because the rich iris features can be captured under the near infrared environment. The near infrared iris images are taken from the CASIA v4 database (Chinese Academy of Sciences' Institute of Automation (CASIA), 2002).

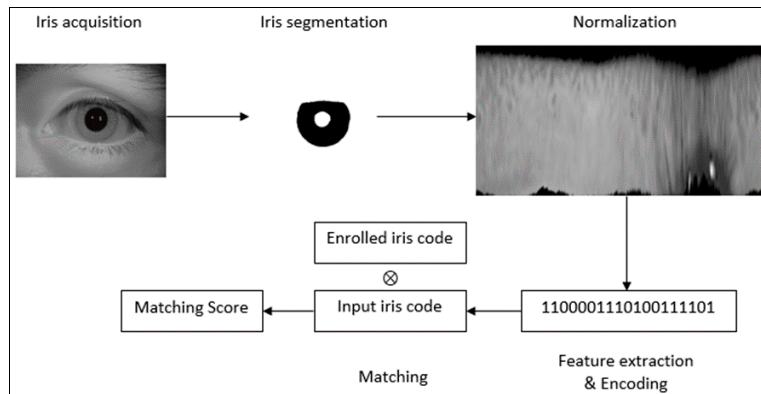


Figure 1. The iris recognition system

In iris segmentation, the iris region is segmented from the rest of iris image. The iris image may consist of eyelids, eyelashes, eyebrows, reflections, noise, and so on. The iris region can be occluded because of those elements, thus, reducing the iris features in the iris region. A non-ideal iris is common in real-time compared with the ideal iris that has circular shape without any occlusion. In this work, iris segmentation is developed based on the active contour of Chan and Vese (2001). This active contour is less dependent on the gradient information, which is suitable to segment the irregular boundary of iris region.

First, pupil boundary is located by investigating pixel property in the iris image based on calculated threshold; the latter is obtained from the average value of pupil region in the iris image. The threshold value is calculated from the 100 iris images of CASIA v4 database. Based on these calculations, the threshold value is set at 35. After that, the iris image is analysed according to the threshold. Based on the threshold, all black connected components in the pupil region can be located. The pupil region is presumed to be the largest connected component in the iris image based on the threshold value. Finally, the pupil boundary can be located from the detected pupil region.

The iris boundary is later located using the active contour method. The active contour method introduced by Chan and Vese (2001) is the segmentation method without edges. It uses an energy function instead of gradient information to segment the desired object boundary. The active contour is defined as in (1) where $\mu_0(x, y)$ is input image, c_1 is average input image when $\phi \geq 0$ and c_2 when $\phi < 0$, λ_1 is fit weight inside curve C , and λ_2 is outside of curve C . This function is minimised by adding the functions of length in curve, C and area inside of curve, C .

$$\begin{aligned}
 F(c_1, c_2, C) &= \mu \cdot Length(C) + v \cdot Area(inside(C)) \\
 &+ \lambda_1 \int_{inside(C)} |\mu_0(x, y) - c_1|^2 dx dy \\
 &+ \lambda_2 \int_{outside(C)} |\mu_0(x, y) - c_2|^2 dx dy
 \end{aligned}
 \tag{1}$$

The initial contour is an evolution contour used in the active contour as the starting place for the latter to start converging towards the desired object boundary. The accurate initialisation of initial contour is important in order to avoid segmenting the separate boundary (Getreuer, 2012). The initial contour in this work is based on a circular shape, so a circle function (Hilal et al., 2012) as in (2) is used, where r is circle radius, and (x, y) is circle centre point.

$$circle = r - \sqrt{(x - a)^2 + (y - b)^2} \quad [2]$$

In order to create the initial contour, the parameters of centre point and radius as in (2) need to be defined. Since the position of initial contour on the desired object boundary is crucial, few conditions need to be met. First, the initial contour must be located within the desired object boundary. Due to this, the proposed initial contour must be located at the top of the iris boundary. Second, the initial contour must not regularly intercept the desired object boundary in order to avoid segmenting the wrong boundary. Because of this, the boundary of the proposed initial contour must not regularly intercept the iris boundary. Finally, the oversized initial contour may include the unwanted boundary. Thus, the proposed initial contour must not be too big in order to avoid the unwanted elements such as eyelids, eyelashes, and reflections to be included into the correct iris boundary.

Based on above considerations, the proposed initial contour is designed with the following properties: its centre point must be at the centre of the iris region; the radius must not be too long in order to avoid oversized initial contour; and the initial contour must not regularly intercept the iris boundary. Since the iris centre is not necessarily similar to the pupil centre, an initial contour centre is proposed which is not always at the centre of pupil. Hilal et al. (2012) used a HT to detect the pupil centre. Unfortunately, this method is less accurate if the pupil region is occluded. Because of that, the pixel property in the occluded pupil is analysed to calculate the centroid which represents the initial contour centre. After that, the initial contour is shifted towards the negative y-axis to reduce error of detecting complex upper eyelid boundary. Meanwhile, for initial contour radius, a radius value must be assigned for which the initial contour must not be oversized. The iris and pupil radius of 100 iris images are observed to obtain the initial contour radius value. An iris radius is then assigned which does not exceed three times of the pupil radius. The example of the proposed initial contour can be observed in Figure 2.

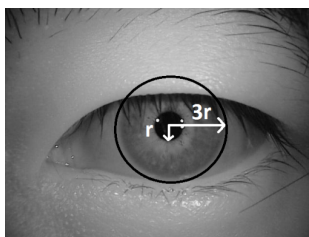


Figure 2. The example of the proposed initial contour

After creating the initial contour, the parameters of iteration number, contraction bias (ν), and smooth factor (μ) must be assigned. The pre-test of the proposed Chan-Vese active contour is conducted on 100 iris images. From the pre-test, the average values of parameters are obtained as follows: iteration number = 35, contraction bias (ν) = 0.7 and smooth factor (μ) = 1.5. Finally, the active contour can be deployed on the iris image to segment the irregular iris boundary.

In order to reduce complexity and improve the performance of the iris recognition system, the sub-iris technique is proposed, in which only the important parts of iris region are used in the system. Based on our observation of the previous methods (Miyazawa et al., 2006; Ito & Aoki, 2013; Du et al., 2005; Zhao & Kumar, 2015) and work by Krichen (2007), three sub-iris regions are proposed for the sub-iris technique. The iris region is divided into two regions: the upper iris ($\theta=0^\circ - 180^\circ$) and the lower iris ($\theta=180^\circ - 360^\circ$). The upper iris can be occluded by the upper eyelid and eyelashes. Meanwhile, the lower iris can be occluded by the lower eyelid only. The occlusion of the lower eyelid on the lower iris can simply be eliminated by reducing the radius value, r of the iris boundary. Because of that, the lower iris is selected for the proposed sub-iris region. The three proposed sub-iris regions can be observed in Figure 3. Each sub-iris region has similar value of θ but with a different value of r . The value of r represents the following: when $r=0.4$ means that 40% of iris radius, $r=0.6$ means that 60% of iris radius and $r=0.9$ means that 90% of iris radius. Each sub-iris region will be analysed in order to determine which region has the best performance.

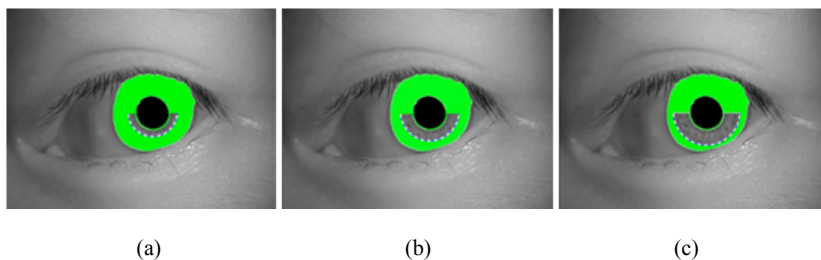


Figure 3. The proposed sub-iris regions of: (a) $\theta=180^\circ - 360^\circ$, $r=0.4$; (b) $\theta=180^\circ - 360^\circ$, $r=0.6$; and (c) $\theta=180^\circ - 360^\circ$, $r=0.9$

After implementation of sub-iris technique, the roundness of sub-iris region is converted into a fixed rectangular polar coordinate in a process known as normalisation. In this work, the normalisation method of Daugman (1993) is used, which is known as the rubber sheet model. The codes of rubber sheet model from Masek (2003) and Aydi et al. (2014) are modified in order to reduce their complexity and execution time. After normalisation, the iris features in the iris image are extracted by using the 1D log-Gabor filter (Daugman, 2003). Next, the extracted features are encoded into a binary code to create the iris template (Daugman, 2003). Finally, the iris template is matched with the database template in order to calculate the matching score using the Hamming distance method (Daugman, 2003).

The CPU implementation of iris recognition system is not fast enough in terms of execution time and operation (Yu & Zhou, 2012). The CPU used the sequential computation while the embedded system such as graphical processing unit (GPU) and field-programmable gate array (FPGA) used the parallel computation. According to Pauwels et al. (2012), a GPU has major advantages over a FPGA in terms of absolute performance, external and random memory access, and development time. Because of these advantages, GPU is selected as a platform for the proposed method. First, the code of the proposed iris recognition system is modified in order to accommodate the parallel processing of the GPU. The iris segmentation code is modified to locate the pupil region in parallel. After that, the normalisation and feature extraction codes of Masek (2003) and Aydi et al. (2014) are modified so that these processes can be calculated in parallel. Finally, the matching score of the iris template and the database template is calculated in parallel. In this work, NVIDIA GTX 960 GPU with 4 GB RAM and 1127 MHz base clock was used. The CPU specifications are Intel Core i5 (2.3 GHz) and 4 GB RAM. The iris recognition algorithm is implemented on MATLAB with parallel computing toolbox.

RESULTS AND DISCUSSION

Figure 4 shows the comparison between full-iris and the sub-iris technique. Figure 4(a) shows the proposed iris segmentation method based on the pixel property in the iris image and the active contour method. The results show the proposed method is able to segment the irregular boundary of iris and pupil regions. This method can locate an iris boundary which is occluded by the upper and lower eyelids. Meanwhile, the eyelashes region can be eliminated by using a simple thresholding technique. Figure 4(b) shows the sub-iris region of $r=0.9$. Based on this observation, the sub-iris region does not need to locate the upper iris (occluded by eyelash) and the lower eyelid (no eyelid detection) but at the same time it can capture the rich iris features near the pupil region. The sub-iris region excludes the iris features at the upper iris (50% of iris features near the pupil region), but the captured iris features in the lower iris can be used to match the full-iris features in the database. The sub-iris technique may reduce the possibility of capturing the unwanted eyelashes and eyelids into the iris template. This technique can also save time and resources needed to locate eyelids and eyelashes in the iris image.

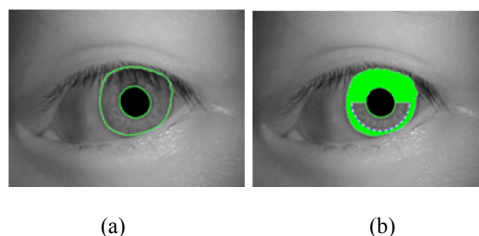


Figure 4. The segmentation example of: (a) full-iris; and (b) sub-iris ($r=0.9$)

Figure 5 shows the location of the proposed sub-iris region in the full-iris template in the database. The red box is the iris features captured by the proposed sub-iris technique. Meanwhile, the blue box is the iris region occluded by the upper and lower eyelids. The green box is the possible location of the eyelashes. Based on this figure, the proposed sub-iris technique has managed to avoid capturing the iris region that is occluded by the eyelids and eyelashes. The presence of both eyelids and eyelashes are quite common in the non-ideal iris. The occluded regions have no iris features which leads to waste of time and resource if added into the system.

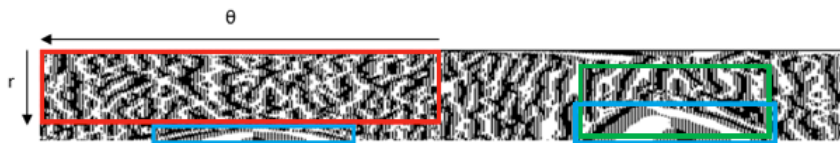


Figure 5. The sub-iris region ($r=0.9$) in the database template

Table 1 shows a comparison of all three sub-iris regions in terms of equal error rate (EER) and area under curve (AUC). The sub-iris region of $r=0.9$ achieved the lowest EER and the highest AUC compared with other sub-iris regions. This is because the sub-iris region of $r=0.9$ managed to capture the most iris features without the inclusion of noise and occlusion. The captured iris features are similar with the database template. The low value of EER means that this method has high recognition accuracy. The EER is obtained on the receiver operating characteristic (ROC) curve when the proportion of acceptance and rejection error is equal. The ROC curve is plotted from the matching score to show the genuine acceptance rate (GAR) against the false acceptance rate (FAR). Meanwhile, AUC is another indicator for the accuracy of the proposed method. The AUC refers to the probability of the algorithm classifier to indicate the acceptance rate is higher than the rejection rate. The AUC is obtained from the ROC curve by calculating the area under the respective graph. Based on the result, the sub-iris region of $r=0.9$ achieves the highest value of AUC which indicates that this method has the highest recognition accuracy.

Table 1
Analysis of three sub-iris regions

Method	Equal Error Rate (%)	Area Under Curve
$r=0.4$	6.21	0.9710
$r=0.6$	4.55	0.9755
$r=0.9$	3.77	0.9821

Table 2 shows the performance comparison between the CPU implementation and the GPU implementation of the proposed iris recognition system. The full-iris technique used the entire iris features and implemented on the CPU. Meanwhile, the sub-iris region of $r=0.9$ is used because it has the optimal performance compared with $r=0.4$ and $r=0.6$. The sub-iris technique was implemented on both CPU and GPU. In terms of recognition accuracy, the full-iris technique achieved the lowest EER and the highest AUC compared with the sub-iris technique. This is understandable because the full-iris technique has more iris features to be matched with the database template compared with the sub-iris technique, resulting in less error. But the differences between full-iris and sub-iris in terms of EER and AUC were quite small (differences of $EER=3\%$ and $AUC=0.1\%$). This shows that even though the sub-iris technique used fewer than 50% of full-iris features, it still managed to achieve a relatively small difference of EER and AUC compared with the full-iris technique. Meanwhile, the EER and AUC values of the sub-iris CPU and the sub-iris GPU were similar because only the programming and platform were changed, which did not affect the accuracy. The IDO-based method of Radman et al. (2013) achieved the lowest recognition accuracy because it was not able to capture the iris features that were occluded by the reflections.

Table 2
Performance comparison between CPU and GPU

Method/Technique	Equal Error Rate (%)	Area Under Curve	Execution Time (s)
Radman et al. (2013) (full-iris with CPU)	7.23	0.9576	2.420
Proposed full-iris with CPU	3.66	0.9831	1.017
Proposed sub-iris ($r=0.9$) with CPU	3.77	0.9821	0.954
Proposed sub-iris ($r=0.9$) with GPU	3.77	0.9821	0.573

In terms of execution time, the sub-iris GPU was the fastest compared with the sub-iris CPU and the full-iris CPU. The sub-iris GPU achieved speedups of 43.66% and 39.94% over the full-iris CPU and the sub-iris CPU respectively. This shows that the parallel processing of GPU is faster than the sequential processing of CPU. The GPU implementation is also more efficient than the CPU implementation for the iris recognition system. Meanwhile, Radman et al. (2013) achieved the slowest execution time because their method used two IDOs to locate the pupil and iris boundaries. The IDO is a complex algorithm with extensive computation. This method also uses a separate eyelid detection based on the live-wire method to locate the eyelid boundary, which results in longer execution time for the iris recognition system. This method is also implemented on the CPU, in which all processes are executed sequentially.

Based on the discussions, the GPU implementation of the sub-iris technique was the fastest compared with the CPU implementation of the sub-iris technique. On the other hand, the recognition accuracy of the sub-iris and the full-iris techniques was not too different. This

shows that the proposed GPU implementation of sub-iris technique can be used in the iris recognition system. The proposed method is suitable for real-time implementation because of its speed and high recognition accuracy.

CONCLUSION

This study had looked at the GPU implementation of the sub-iris technique in the iris recognition system. The iris segmentation algorithm is based on the pixel property and active contour methods. The proposed segmentation was combined with the sub-iris technique and implemented on a GPU platform. Based on the results, the proposed method managed to achieve a fast execution time and acceptable recognition accuracy compared with the iris recognition system using the full-iris technique. The proposed method is suitable for screening identification, which is the first line of identification in the airport and immigration. It is also suitable for the non-ideal iris, in which the iris region is occluded by unwanted elements. Future research should look at how GPU performance may be increased by overclocking it to the higher clock speed by increasing the core voltage, core clock and memory clock. Other than that, the scalable link interface (SLI) can be used by linking two or more GPUs to carry out parallel processing in order to increase processing speed. The GPU is the future since most computers nowadays have a dedicated GPU, reducing upfront costs. The GPU offers great potential due to its advanced technology in terms of speed and memory.

ACKNOWLEDGEMENTS

The authors gratefully acknowledge Universiti Kebangsaan Malaysia (UKM) for funding this projec (Project Number: DPP-2015-009). The authors acknowledge the Ministry of Higher Education Malaysia (MOHE) and Universiti Teknologi MARA (UiTM) for making available their University Academic Training Scheme (SLAI) and Young Lecturers Scheme (TPM). In addition, the authors acknowledge CASIA for allowing the use of its iris database.

REFERENCES

- Abdullah, M. A., Dlay, S. S., & Woo, W. L. (2014). Fast and accurate method for complete iris segmentation with active contour and morphology. In *IEEE International Conference on Imaging Systems and Techniques*. (p. 123-128). Santorini, Greece: IEEE.
- Aydi, W., Masmoudi, N., & Kamoun, L. (2014). A fast and accurate circular segmentation method for iris recognition systems. *International Review on Computers and Software*, 9(3), 468-477.
- Chan, T. F., & Vese, L. A. (2001). Active contours without edges. *IEEE Transactions on Image Processing*, 10(2), 266-277.
- Chinese Academy of Sciences' Institute of Automation (CASIA). (2002). CASIA iris image database. Retrieved from <http://biometrics.idealtest.org/>

- Daugman, J. (1993). High confidence visual recognition of persons by a test of statistical independence. *IEEE Transactions on Pattern Analysis and Machine Intelligence*, 15(11), 1148-1161.
- Daugman, J. (2007). New methods in iris recognition. *IEEE Transactions on Systems, Man, and Cybernetics, Part B*, 37(5), 1167-1175.
- Daugman, J., & Downing, C. (2001). Epigenetic randomness, complexity and singularity of human iris patterns. *Proceedings of the Royal Society of London B: Biological Sciences*, 268(1477), 1737-1740.
- Du, Y., Ives, R., Bonney, B., & Etter, D. M. (2005). Analysis of partial iris recognition. In *Proc. SPIE 5779*. (p. 31-40). Orlando, Florida, USA: SPIE.
- Flom, L., & Safir, A. (1987). *U.S. Patent No. 4,641,349*. Washington, DC: U.S. Patent and Trademark Office.
- Getreuer, P. (2012). Chan-Vese segmentation. *Image Processing On Line*, 2, 214-224.
- Hilal, A., Daya, B., & Beausery, P. (2012). Hough transform and active contour for enhanced iris segmentation. *International Journal of Computer Science Issues*, 9(2), 1-10.
- Ito, K., & Aoki, T. (2013). Phase-based image matching and its application to biometric recognition. In *Signal and Information Processing Association Annual Summit and Conference*. (p. 1-7). Kaohsiung, Taiwan: IEEE.
- Krichen, E. (2007). *Recognition of people by iris in degraded mode* (Doctoral thesis). Evry-Val Essonne University, France.
- Masek, L. (2003). *Recognition of human iris patterns for biometric identification* (Master thesis). University of Western Australia, Australia.
- Miyazawa, K., Ito, K., Aoki, T., Kobayashi, K., & Nakajima, H. (2006). A phase-based iris recognition algorithm. In *International Conference on Biometrics*. (p. 356-365). Hong Kong, China: Springer.
- Muron, A., & Pospisil, M. L. (2000). The human iris structure and its usages. *Acta. Univ. Palacki Phisica*, 39, 87-95.
- Nazneen, N., Shafiq, M., & Hameed, A. (2016). Template matching of aerial images using GPU. In *International Bhurban Conference on Applied Sciences and Technology*. (p. 206-212). Islamabad, Pakistan: IEEE.
- Pauwels, K., Tomasi, M., Alonso, J. D., Ros, E., & Van Hulle, M. M. (2012). A comparison of FPGA and GPU for real-time phase-based optical flow, stereo, and local image features. *IEEE Transactions on Computers*, 61(7), 999-1012.
- Qin, H., Wang, X., Liang, M., & Yan, W. (2013). A novel pupil detection algorithm for infrared eye image. In *International Conference on Signal Processing, Communication and Computing*. (p. 1-5). Kunming, Yunnan, China: IEEE.
- Radman, A., Jumari, K., & Zainal, N. (2013). Fast and reliable iris segmentation algorithm. *IET Image Processing*, 7(1), 42-49.

- Sakr, F. Z., Taher, M., Ei-Bialy, A. M., & Wahba, A. M. (2012). Accelerating iris recognition algorithms on GPUs. *Cairo International Biomedical Engineering Conference*. (p. 73-76). Giza, Egypt: IEEE.
- Tozer, J. (2012). £9million down the drain as airports scrap iris passport scanners which were meant to speed up queues... because they are slower than manual checks. Retrieved from <http://www.dailymail.co.uk/news/article-2102076/Millions-drain-airports-SCRAP-iris-passport-scanners.html>
- Wildes, R. P. (1997). Iris recognition: An emerging biometric technology. *Proceedings of the IEEE*, 85(9), 1348-1363.
- Yu, L., & Zhou, X. (2012). Fast iris location based on window mapping method. *Instrumentation, Measurement, Circuits and Systems*, 519-526.
- Zhao, Z., & Ajay, K. (2015). An accurate iris segmentation framework under relaxed imaging constraints using total variation model. *Proceedings of the IEEE International Conference on Computer Vision*. (p. 3828-3836). Santiago, Chile: IEEE.



Adaptive Particle Swarm Optimisation for Solving Non-Convex Economic Dispatch Problems

Nurhafizah Jamain¹, Ismail Musirin¹, Mohd Helmi Mansor^{2*},
Muhammad Murtadha Othman¹ and Siti Aliyah Mohd Salleh²

¹Faculty of Electrical Engineering, Universiti Teknologi MARA (UiTM), Shah Alam, Selangor, Malaysia

²Department of Electrical Power Engineering, College of Engineering, UNITEN, Kajang, Selangor, Malaysia

³Faculty of Electrical Engineering, Universiti Teknologi MARA (UiTM), Pasir Gudang, Johor, Malaysia

ABSTRACT

This paper presents adaptive particle swarm optimization for solving non-convex economic dispatch problems. In this study, a new technique was developed known as adaptive particle swarm optimization (APSO), to alleviate the problems experienced in the traditional particle swarm optimisation (PSO). The traditional PSO was reported that this technique always stuck at local minima. In APSO, economic dispatch problem are considered with valve point effects. The search efficiency was improved when a new parameter was inserted into the velocity term. This has achieved local minima. In order to show the effectiveness of the proposed technique, this study examined two case studies, with and without contingency.

Keywords: Adaptive Particle Swarm Optimization (APSO), economic dispatch, valve-point effects

INTRODUCTION

The aim to achieve secure power delivery with minimal cost is important. Thus, economic dispatch has become an important issue in power system operation and planning. Optimal

results within the generators in a system need to be achieved at the lowest possible cost, operational constraints and subject to transmission (Momoh, 2001; Wood & Wollenberg, 1996). The US Energy Policy Act of 2005 defines economic dispatch as “the operation of generating facilities to produce energy at the lowest cost to reliably serve consumers, recognizing any operational limits of generation and transmission facilities”

ARTICLE INFO

Article history:

Received: 28 September 2016

Accepted: 03 February 2017

E-mail addresses:

norhafizahjamain@yahoo.com (Norhafizah Jamain),

ismailbm@salam.uitm.edu.my (Ismail Musirin),

mhelmi@uniten.edu.my (Mohd Helmi Mansor),

mamat505my@yahoo.com (Muhammad Murtadha Othman),

aliyah385@johor.uitm.edu.my (Siti Aliyah Mohd Salleh)

*Corresponding Author

(109th Congress, 2005). Economic dispatch is the short-term determination of the optimal output of a number of electricity generation facilities, to meet the system load, at the lowest possible cost, subject to transmission and operational constraints and has non-convex characteristics (Lee & EI-Sharkawi, 2002). Characteristics of the input-output of generating units are not smooth due to valve-point loadings, prohibited operating zones and multi-fuel effects. Solving this problem using mathematical methods requires presentation as a non-convex optimisation problem with constraints (Park, Jeong, Shin, & Lee, 2010). Yare et al. introduced Heuristic Algorithms for solving convex and non-convex economic dispatch. Three heuristic algorithms, namely genetic algorithm, differential evolution and modified particle swarm optimisation, have been introduced to solve economic dispatch problem. The modified particle swarm optimisation offer a better solution to solve economic dispatch problem in terms of locating optimal solution compared with genetic algorithm and differential evolution (Yare, Venayagamoorthy, & Saber, 2009). Lin, Cheng and Tsay (2001) have applied integrated artificial intelligence which is evolutionary programming, tabu search and quadratic programming methods for solving non-convex economic dispatch problem. Based on the results, the proposed methods are effective compared with the previous evolutionary computation algorithm (Lin, Cheng, & Tsay, 2001). In the past few decades, many different methods have been developed to solve economic dispatch problems, such as gradient method, Newton method, lambda iteration, linear programming and quadratic programming method. However, most of these methods cannot solve non-convex economic dispatch problem and highly nonlinear solution space due to the curse of dimensionality or local optimality (Abdullah, Bakar, Rahim, Jamian, & Aman, 2012). Modern heuristic algorithm such as evolutionary programming (Yang, Yang, & Huang, 1996), genetic algorithm (Chen & Chang, 1995), simulated annealing, Hopfield neural network, evolutionary strategy optimisation, differential evolution, bacterial foraging algorithm, ant colony optimisation, tabu search (Lin et al., 2001), artificial immune system and particle swarm optimisation show potential to solve complex economic dispatch problems. Though these methods cannot guarantee to find global optima, they often achieve a near global optimal solution (Abdullah et al., 2012). Particle swarm optimisation (PSO) is a modern heuristic algorithm that is widely implemented in the economic dispatch problem because of the less storage requirement, simple implementation and able to find a global optimum solution. The PSO was introduced by Kennedy and Eberhart in 1995, inspired by the group behaviour of animals such as bird flocks or fish schools (Harman, 1995). It is also suitable to solve large scale of non-convex optimisation problems due to its simplicity (Basu, 2015). However, PSO still has disadvantages such as insufficient capability to find nearby extreme points, lack of efficient mechanism to treat constraints and local optimal trapping due to premature convergence (Park et al., 2010).

This paper presents adaptive particle swarm optimization (APSO) to solve non-convex economic dispatch problem. In this study, a new parameter on velocity has been added to enhance search efficiency. In addition, local minimum has been achieved without exacerbating the speed of convergence and the quality of the structure of the particle swarm optimisation. To show effectiveness of the proposed algorithm, two case studies, namely with and without contingency, are examined in this study. Classical particle swarm optimization methods were also compared.

METHOD

Problem Formulation

This section describes the objective function for the optimisation process and relevant mathematical equation of economic dispatch.

Objective Function

Cost minimisation of thermal generator is the main objective in economic dispatch. Various constraints need to be satisfied for this reason. Determination of optimal combination of power output to meet the demand at minimum cost while satisfying the constraints are also considered. The fuel cost production is given in (2):

$$\text{Minimize } F_t = \sum_{i=1}^N F_i(P_i) \quad i = 1, 2, \dots, N \quad [1]$$

$$\text{Min } \sum_{i=1}^N F_i(P_i) = \sum_{i=1}^N a_i + b_i P_i + c_i P_i^2 \quad [2]$$

where:

- F_t : total generation cost; N : number of committed generators;
 F_i : fuel cost for generator i ; P_i : power output of i th generating unit.
 a_j, b_j, c_j : cost coefficients of i th generating unit;

The APSO is proposed to address economic dispatch problems considering valve point effects. Ripple in the heat rate function due to valve-point effects can result in the fuel cost function have multiple local optima, discontinuous and highly non-linear. Therefore, the cost function (2) considering valve-point effects can be described as follows:

$$\text{Min } \sum_{i=1}^N F_i(P_i) = \sum_{i=1}^N a_i + b_i P_i + c_i P_i^2 + |e_i \times \sin(f_i \times (P_i, \text{min} - P_i))| \quad [3]$$

where d_i and e_i are the fuel cost coefficients of generator i with valve-point effects.

Equality and Inequality Constraints

Power balance equation. Power balance equation represents the relationship between the total generated power, load power and total transmission loss. The total generated power must be equal to total load demand and total transmission loss.

$$\sum_{i=1}^N P_i = P_{\text{load}} + P_{\text{loss}} \quad [4]$$

Where Pload is the total load demand and Ploss is total transmission loss. The transmission loss can be represented using B coefficients as follows:

$$P_{loss} = \sum_{i=1}^N \sum_{j=1}^N P_i B_{ij} P_j + \sum_{i=1}^N B_{oi} P_i + B_{oo} \quad [5]$$

where Bij, Boj and Boi are B coefficients.

Minimum and maximum power limits. Corresponding inequality constraint for each generator power output should be within its minimum and maximum limits such as

$$P_{i,min} \leq P_i \leq P_{i,max} \quad [6]$$

where Pi,min and Pi,max are minimum and maximum limit output of generator i.

Optimisation Techniques

In this section, algorithms for optimisation techniques, namely the particle swarm optimization (PSO) and the proposed adaptive particle swarm optimization (APSO), are explained.

Particle Swarm Optimization (PSO). Particle Swarm Optimization (PSO) is an optimisation technique based on swarm algorithm. It emulates the behaviour of animals such as bird flocks or fish schools (Harman, 1995). Additionally, it is an optimisation tool that provides a population-based search algorithm. It also searches in parallel style using a group of particles and each particle represents a solution to the problem. Particles change their states or positions with time and fly in multidimensional search space. Each particle approaches the optimum point through present velocity, previous experience and experience of its neighbours. The position and velocity of particle i in n-dimensional search space are represented as vectors $X_i = (x_{i1}, \dots, x_{in})$ and $V_i = (v_{i1}, \dots, v_{in})$ respectively. The updated velocity and position of each particle are calculated as follows:

$$V_i^{(k+1)} = w \cdot V_i^k + c_1 \cdot r_{n1} \cdot (Pbest_i^k - X_i^k) + c_2 \cdot r_{n2} \cdot (Gbest^k - X_i^k) \quad [7]$$

$$X_i^{(k+1)} = X_i^k + V_i^{(k+1)} \quad [8]$$

where:

- V_i^k : velocity of particle i at iteration k; r_{n1}, r_{n2} : random numbers between 0 and 1
- w : inertia weight factor; X_i^k : position of particle i at iteration k
- c_1, c_2 : acceleration coefficients;

Rate of convergence for PSO algorithm depends on the inertia weight factor, w . This parameter is used based on descending linear function. The mathematical relationship for w is expressed by the following equation: -

$$w = w_{max} - \frac{w_{max} - w_{min}}{iter_{max}} \times iter \tag{9}$$

Where $iter$ is the current iteration, $iter_{max}$ is the maximum iteration number and w_{max} and w_{min} are maximum and minimum value of weighting factor respectively.

Proposed Adaptive Particle Swarm Optimization (APSO). The PSO performance is affected by variation of its parameters, in particular the inertia weight and two acceleration coefficients. Modification of equation (7) is done by incorporating momentum for particles to search for broader space. The proposed updated velocity of APSO is given by the following relationship: -

$$V_i^{(k+1)} = w \cdot V_i^k + rand(1) \cdot r_{n_1} \cdot (P_{best_i}^k - X_i^k) + rand(1) \cdot r_{n_2} \cdot (G_{best}^k - X_i^k) \tag{10}$$

Acceleration coefficients of c_1 and c_2 are random in nature ranging from 0 to 1.

$$0 \leq c_1 \leq 1 \quad i.e: c_1 = rand(1) \tag{11}$$

$$0 \leq c_2 \leq 1 \quad i.e: c_2 = rand(1) \tag{12}$$

Algorithm of APSO for Economic Dispatch Problem with Valve-Point Effects

Figure 1 is, the flowchart of the proposed APSO algorithm and the mechanics describe how to solve economic dispatch problem with valve-point effects.

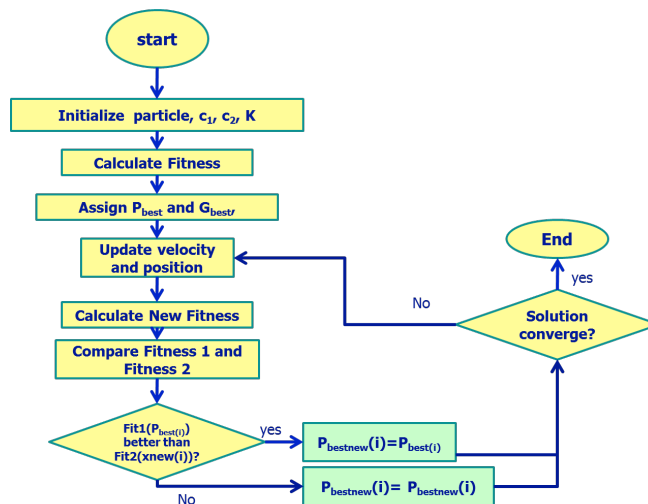


Figure 1. Flowchart of Adaptive Particle Swarm Optimization (APSO)

The steps are as follows: -

Step 1: Initialise the particle's parameters randomly, such as position, velocity, iteration number and counter. The number of generating units in economic dispatch problem is the dimension in APSO. The initial velocity is set to zero. The i th particle for n -dimension is represented as:

$$P_i = (P_{i1}, P_{i2}, \dots, P_{in}) \quad [13]$$

The particles of each dimension are generated randomly within the minimum and maximum bound as given in equation (14): -

$$P_i = r \times (P_{max} - P_{min}) + P_{min} \quad [14]$$

Step 2: Objective function evaluation: In this step, computation of fitness for each particle is performed in order to determine whether the fitness needs to be minimised or vice versa. Minimisation of the fitness value is the objective function of the study which correlates with cost minimisation. In short, the objective function is minimisation of the fitness values in the problem formulations. The fitness equation is expressed below:-

$$f(P_i) = \sum_{i=1}^N F_i(P_i) + k \left| \sum_{i=1}^N P_i - P_D - P_L \right| \quad [15]$$

Where k is penalty parameter, P_i is input power of generator at bus i , P_D is load demand at bus i and P_L is loss at bus i .

Step 3: Assign p_{best} and g_{best} are identified. From the whole population, p_{best} will be identified which is in matrix form. P_{best} is identified after the population undergoes selection.

Step 4: Update the velocity and position of each particle by using equation (10).

Step 5: Fitness evaluation (Fitness 2). Second fitness calculation is performed in order to evaluate their values once they have undergone updating process.

Step 6: Compare Fitness 1 and Fitness 2 values. In this phase, new values for p_{best} and g_{best} will be deduced.

Step 7: Stopping criterion test. After number of iteration is reached, APSO algorithm will be terminated. If otherwise, otherwise goes to step 4.

RESULTS AND DISCUSSION

Two case studies with contingency and without contingency were examined to show effectiveness of the proposed APSO technique. For each test system, 10 runs were conducted to minimise total fuel cost subjected to various constraints in a power system. The generator's real power limits are:

Table 1
Generator real power limits

Gen.	Min. MW	Max. MW
1	100	500
2	50	200
3	80	300
4	50	150
5	50	200
26	50	120

Case Study 1: Normal condition

In this case, 26 generator bus with valve-point effects was examined. The values for c_1 and c_2 were set to 2 for PSO technique, while in APSO c_1 and c_2 were set to random value from 0 to 1. The idea is to use the best value of acceleration coefficients which is 2. It is used to avoid premature convergence using the full range of the search space with low social coefficient. The iteration was set to 300 in both methods. 10 runs have been done to get the best cost and to calculate the average cost of the system. Table 2 and Table 3 tabulate the results of the PSO and APSO for 10 runs respectively.

Table 2
Results of the PSO for 10 runs in normal condition

No. of runs	e	f	P1 (MW)	P2 (MW)	P3 (MW)	P4 (MW)	P5 (MW)	P26 (MW)	Gbest (\$)
1	0.9364	0.6326	441.74	169.95	278.05	134.47	177.47	74.21	15447
2	0.5976	0.7745	440.82	165.48	261.41	127.66	200.00	80.49	15453
3	0.8866	0.4188	428.72	165.06	300.00	134.57	161.94	85.76	15447
4	0.4342	0.3691	488.91	127.17	256.37	116.29	167.54	120.00	15461
5	0.6244	0.547	423.89	179.28	256.75	126.88	169.31	120.00	15461
6	0.211	0.7667	449.70	200.00	257.93	129.41	168.19	70.72	15456
7	0.6323	0.0517	463.92	169.52	237.66	134.69	200.00	69.95	15453
8	0.3667	0.6112	432.82	165.73	257.93	150.00	187.92	81.17	15449
9	0.9565	0.0426	441.77	176.38	257.08	150.00	169.94	80.46	15449
10	0.8408	0.3715	445.03	143.86	252.92	150.00	164.02	120.00	15467

It consists of the coefficient of c_1 , c_2 , e and f , output generator which is P1, P2, P3, P4, P5 and P26 and the value of Gbest. The coefficients of c_1 , c_2 , e and f are in the ranges.

All of the output generators are in the generator real power limits. Table 4 shows a comparison of performance for PSO and APSO after 10 runs. From the results, PSO and APSO have the same value of best cost which is \$15447. However, APSO shows lower average cost compared with PSO, which is \$15447.3. It means APSO have achieved the global optimum solution as compared to PSO. The new acceleration coefficients in the APSO method can enhance search ability and minimise the fuel cost subjected to the various constraints of a power system.

Table 3
The result of the APSO for 10 runs in normal condition

No. of runs	$c1$	$c2$	e	f	P1 (MW)	P2 (MW)	P3 (MW)	P4 (MW)	P5 (MW)	P26 (MW)	Gbest (\$)
1	0.7725	0.411	0.9871	0.8752	445.48	170.57	262.05	133.65	175.73	88.36	15447
2	0.8322	0.1784	0.2839	0.0093	445.85	171.19	263.65	132.15	177.19	85.82	15447
3	0.6701	0.3788	0.0233	0.9787	446.11	170.94	263.57	134.13	175.59	85.49	15447
4	0.8935	0.8668	0.7143	0.3494	448.76	167.69	258.36	139.37	176.91	84.65	15447
5	0.1992	0.6033	0.8737	0.6297	481.11	166.94	253.02	150.00	174.73	50.00	15449
6	0.2472	0.6309	0.3465	0.5762	445.11	174.40	264.28	132.66	173.31	86.11	15447
7	0.6135	0.7282	0.8803	0.9149	448.09	169.83	264.40	131.56	176.75	85.22	15447
8	0.9994	0.9554	0.7175	0.9087	447.69	170.43	260.02	134.29	179.14	84.23	15447
9	0.7408	0.7437	0.0905	0.9543	446.87	171.09	261.97	135.61	176.97	83.29	15447
10	0.9189	0.5654	0.9147	0.5171	443.42	172.10	257.85	143.16	176.10	83.07	15448

Table 4
Comparison of performance for PSO and APSO in normal condition

Method	Worst cost (\$)	Best cost (\$)	Average cost (\$)
PSO	15467	15447	15454.3
APSO	15449	15447	15447.3

Table 5
The results of the PSO for 10 runs with contingency

No. of runs	e	f	P1 (MW)	P2 (MW)	P3 (MW)	P4 (MW)	P5 (MW)	P26 (MW)	Gbest (\$)
1	0.7142	0.7477	449.45	171.73	259.57	138.17	175.97	81.24	15452
2	0.7411	0.2215	453.29	200.00	243.12	131.72	169.67	78.51	15461
3	0.2309	0.6416	444.95	167.58	256.40	150.00	172.64	84.39	15454
4	0.7507	0.0538	447.13	170.89	263.28	134.53	175.21	85.14	15452
5	0.1714	0.5278	421.56	184.21	260.10	150.00	171.03	89.08	15454
6	0.2324	0.5619	446.16	171.25	258.88	137.33	177.02	85.47	15452
7	0.5014	0.6109	437.31	200.00	242.44	116.63	160.37	####	15481
8	0.1589	0.7631	440.72	142.41	300.00	124.40	200.00	68.93	15479
9	0.4725	0.8258	451.07	176.84	267.56	150.00	180.68	50.00	15465
10	0.5417	0.3579	476.67	145.33	257.58	133.05	176.68	86.96	15452

Case Study 2: Contingency condition

In this case, 26 generator bus with valve-point effects was examined. For PSO method, c_1 and c_2 values were set to 2 while in APSO c_1 and c_2 were set to random value which is from 0 to 1. The idea is to use the best value of acceleration coefficients which is 2. It is used to avoid premature convergence using the full range of the search space with low social coefficient. The iteration was set to 300 in both methods. Ten runs were done to get the best cost and to calculate the average cost of the system. Table 5 and Table 6 show the results of PSO and APSO for 10 runs respectively. It consists of the coefficient of c_1 , c_2 , e and f , output generator which is P1, P2, P3, P4, P5 and P26 and the value of Gbest. The coefficients of c_1 , c_2 , e and f are between the ranges. All of the output generators are in the range of the generator real power limits.

Table 6
The results of the PSO for 10 runs with contingency

No. of runs	$c1$	$c2$	e	f	P1 (MW)	P2 (MW)	P3 (MW)	P4 (MW)	P5 (MW)	P26 (MW)	Gbest (\$)
1	0.7873	0.1716	0.4236	0.784	446.53	174.59	260.30	135.67	177.89	81.17	15452
2	0.1153	0.5452	0.4553	0.118	444.56	169.53	266.22	134.77	186.11	74.98	15452
3	0.5141	0.9474	0.0921	0.732	447.97	172.30	262.27	136.10	174.42	83.10	15451
4	0.6126	0.582	0.1081	0.793	446.23	170.58	263.11	139.19	176.38	80.63	15452
5	0.9747	0.6514	0.9751	0.981	447.00	171.18	260.41	136.93	175.66	84.96	15451
6	0.2291	0.7643	0.4568	0.132	431.61	164.91	265.19	137.46	200.00	76.93	15458
7	0.0619	0.9838	0.98	0.624	444.51	152.32	246.22	145.99	200.00	86.98	15459
8	0.0245	0.9388	0.8024	0.329	446.92	176.69	248.26	150.00	173.59	80.57	15455
9	0.3766	0.5573	0.3791	0.258	439.52	167.62	261.43	129.62	200.00	78.00	15458
10	0.9042	0.6085	0.8656	0.785	438.49	166.31	259.13	135.52	200.00	76.66	15458

Table 7 compares performance for PSO and APSO after 10 runs with contingency. From the results, APSO methods displayed minimal cost compared with PSO which is \$15451. This means APSO achieved global optimum solution compared to PSO. The new acceleration coefficients in the APSO method can enhance search ability and minimise fuel cost subjected to various constraints of a power system.

Table 7
Comparison of performance for PSO and APSO with contingency

Method	Worst cost (\$)	Best cost (\$)	Average cost (\$)
PSO	15481	15452	15460.2
APSO	15459	15451	15454.6

CONCLUSION

This paper had discussed adaptive particle swarm optimization (APSO) method for solving non-convex economic dispatch problem considering valve-point effects. A random value of acceleration coefficients or social parameter is assigned to enhance search ability and escape from a local minimum for two case studies which is in normal condition and contingency condition. Both cases show that APSO have lower average cost in the system. This means that APSO achieved global optimum solution compared with particle swarm optimization (PSO). The entire coefficients are in the range. The new acceleration coefficients in the APSO method can enhance search ability and minimise fuel cost subjected to the various constraints of a power system. Output of the generator shows that it is in the limit which means the power output meets the demand at minimum cost. Thus, it can be concluded that the objectives of this system are achievable which is able to minimise the fuel cost subjected to the various constraints of a power system and determine an optimal combination of power output to meet the demand at minimum cost. When classical particle swarm optimisation methods were compared, the proposed adaptive particle swarm optimization was able to provide better solution. Thus, APSO can be applied for solution of complex power system optimisation problems.

ACKNOWLEDGEMENTS

The authors acknowledge cooperation rendered by Institute of Research Management and Innovation (IRMI) UiTM, Shah Alam, Selangor, Malaysia and Ministry of Higher Education (MOHE) to undertake this research. This research was supported by MOHE under the Research Acculturation Grant Scheme (RAGS) with project code: 600-RMI/RAGS 5/3 (187/2014).

REFERENCES

- 109th Congress. Energy Policy Act of 2005, 8 Public Law 109-58 594–1143 (2005).
- Abdullah, M. N., Bakar, A. H. A., Rahim, N. A., Jamian, J. J., & Aman, M. M. (2012). Economic dispatch with valve point effect using iteration particle swarm optimization. In *2012 47th International Universities Power Engineering Conference (UPEC)* (pp. 1–6). IEEE. <http://doi.org/10.1109/UPEC.2012.6398693>
- Basu, M. (2015). Modified particle swarm optimization for nonconvex economic dispatch problems. *International Journal of Electrical Power & Energy Systems*, *69*, 304–312. <http://doi.org/10.1016/j.ijepes.2015.01.015>
- Chen, P. -H., & Chang, H. -C. (1995). Large-scale economic dispatch by genetic algorithm. *IEEE Transactions on Power Systems*, *10*(4), 1919–1926. <http://doi.org/10.1109/59.476058>
- Harman, R. (1995). A very brief introduction to particle swarm optimization.
- Lee, K. Y., & El-Sharkawi, M. A. (2002). Tutorial on Modern Heuristic Optimization Techniques with Applications to Power Systems. *IEEE Power Engineering Society (02TP160)*. Retrieved from http://sites.ieee.org/pes-resource-center/files/2013/10/TP160_Full_Content.pdf
- Lin, W. M., Cheng, F. S., & Tsay, M. T. (2001). Nonconvex economic dispatch by integrated artificial intelligence. *IEEE Transactions on Power Systems*, *16*(2), 307–311.
- Momoh, J. A. (2001). *Electric power system applications of optimization*. Marcel Dekker, Inc., New York.
- Park, J. B., Jeong, Y. W., Shin, J. R., & Lee, K. Y. (2010). An improved particle swarm optimization for nonconvex economic dispatch problems. *IEEE Transactions on Power Systems*, *25*(1), 156–166.
- Wood, A. J., & Wollenberg, B. F. (1996). *Power generation, operation and control. 2nd edition*. Wiley and Sons, New York.
- Yang, H. T., Yang, P. C., & Huang, C. L. (1996). Evolutionary programming based economic dispatch for units with non-smooth fuel cost functions. *IEEE transactions on Power Systems*, *11*(1), 112–118.
- Yare, Y., Venayagamoorthy, G. K., & Saber, A. Y. (2009). Heuristic Algorithms for Solving Convex and Nonconvex Economic Dispatch. In *2009 15th International Conference on Intelligent System Applications to Power Systems* (pp. 1–8). IEEE. <http://doi.org/10.1109/ISAP.2009.5352852>



SURF Based 3D Object Recognition for Robot Hand Grasping

Nurul Hanani Remeli*, Ruhizan Liza Ahmad Shauri, Faieza Hanum Yahaya, Norshariza Mohd Salleh, Khairunnisa Nasir and Ahmad Ihsan Mohd Yassin

Faculty of Electrical Engineering, Universiti Teknologi Mara (UiTM), 40450 Shah Alam, Selangor, Malaysia

ABSTRACT

This paper proposes a 3D object recognition method based on 3D SURF and the derivation of the robot space transformations. In a previous work, a three fingered robot hand had been developed for grasping task. The reference position of the robot hand was programmed based on predetermined values for grasping two different shapes of object. The work showed successful grasping but it could not generate the reference position on its own since no external sensor was used, hence it is not fully automated. Later, a 2D Speed-Up Robust Features (SURF) and 3D point cloud algorithm were applied to calculate the object's 3D position where the result showed that the method was capable of recognising but unable to calculate the 3D position. Thus, the present study developed 3D SURF by combining recognised images based on 2D SURF and triangulation method. The identified object grasping points then are converted to robot space using the robot's transformation equation which is derived based on dimensions between robot and camera in the workplace. The result supported the capability of the SURF algorithm for recognising the target without fail for nine random images but produced errors in the 3D position. Meanwhile, the transformation has been successful where the calculated object positions are inclined towards the directions of actual measured positions accordingly related to robot coordinates. However, maximum error of 3.90 cm was observed due to the inaccuracy of SURF detection and human error during manual measurement which can be solved by improving the SURF algorithm in future.

Keywords: 3D SURF, object recognition, robot coordinates, robot hand, transformation, triangulation

ARTICLE INFO

Article history:

Received: 28 September 2016

Accepted: 03 February 2017

E-mail addresses:

hananiremeli@gmail.com (Nurul Hanani Remeli),
ruhizan @salam.uitm.edu.my (Ruhizan Liza Ahmad Shauri),
faieza55@gmail.com (Faieza Hanum Yahaya),
shahrizasalleh@gmail.com (Norshahriza Mohd Salleh),
khairunnisanasir@yahoo.com (Khairunnisa Nasir),
ihsan.yassin@gmail.com (Ahmad Ihsan Mohd Yassin)

*Corresponding Author

INTRODUCTION

Image processing method has been used in many robot manipulator applications for object recognition and determination of grasping position by the end effector. Robots that can grasp object without damaging the object and themselves, must have the capability of recognising an object using

external sensors. Camera is one of the sensors that can provide visual information for object recognition purposes.

A suitable technique of image processing is needed for a fully autonomous robot to execute an assigned task without human intervention. Collet et al. (2009) built 3D models of objects from a set of images captured from different angles. Key point features of each image were extracted and matched with those from the 3D models. The pose estimation results were used by a Barret Hand to grasp the pre-identified objects. However, the work required a huge amount of image data during the training of the 3D models. Saxena et al. (2008) proposed a method for grasping several household objects based on training of predicted optimal grasping points of objects for a Barret arm robot manipulation. Their method did not require 3D model of object but instead identified grasping points were triangulated to obtain the 3D location. Sushkov et al. (2011) proposed a robot that could autonomously acquire object images and applied a recognition method to extract features from the multiple image frames captured. However, their robot faced problem in rotating the object to obtain multiple image views to be learned and therefore resulted in less efficient feature detection.

Object recognition using image processing can be implemented by finding object's interest point correspondences between a target image which consists of only the target object and a scene image which consists of the target object in a cluttered background. Scale Invariant Feature Transform (SIFT) which has been introduced by Lowe (1999) is one of the most robust and stable object recognition methods that detect objects despite a scale change or in-plane rotation in cluttered background. This method works best for objects that exhibit non-repeating texture patterns, which give rise to unique feature matches. The SIFT detects distinctive local keypoints using Laplacian of Gaussian approximated by Difference of Gaussians (DOG). Lee et al. (2006) combined SIFT and line geometric features in sequence of image frame captured by the camera to produce the 3D object recognition and pose estimation. Kuş et al. (2008) implemented SIFT technique with new features related to colour classification of local region to recognise traffic signs. The above studies showed the application of SIFT without implementation for robot task while the previous studies have applied SIFT for robot manipulation and (Collet et al., 2009; Sushkov et al., 2011).

However, Wu et al. (2013) used SIFT to produce low extraction time and slow matching step compared with PCA-SIFT, GSIFT, CSIFT, SURF and A-SIFT due to the application of high 128-dimensional vector to describe each keypoint. For example, in order to improve the dimensionality vector of keypoint, Ke et al. (2004) introduced PCA-SIFT where Principal Component Analysis (PCA) has been used to replace gradient histogram to produce more accurate and quick results. Meanwhile, Bay et al. (2008) proposed SURF with improvement key point detector and feature vector algorithms. Its computation time is faster than SIFT and shows similar performance (Kim et al., 2012). For example, Desai et al. (2015) applied SURF algorithm combined with frame difference method to detect the objects in real-time condition. While Anitha et al. (2014) used SURF descriptor and Harris corner detection for continuous recognition and tracking through video images. Desai et al. (2015) and Anitha et al. (2014) reported better detection rate as well as more accurate. Anh et al. (2012) proposed a high-speed

object tracking method based on a window approach and SURF descriptor. Using the window approach, the object region can be iteratively tracked to reduce the time for object recognition.

This paper focuses on improving grasping capability of a 7-DOF three-fingered robot hand using an image processing method discussed in a previous work by Shauri et al. (2014). Based on this, Kasim et al. (2016) who had successfully used PID control for grasping based on predetermined values of motor angles. However, the motor position was manually programmed by user since no external sensor was used. A 2D SURF and 3D point cloud algorithm were applied to recognise the object's 3D position where it has been observed that the method was capable of recognising but unable to calculate the 3D position. Therefore, this study proposed an object recognition using 3D SURF method based on static images captured by a stereo camera and a robot space transformation to calculate the 3D object position related to robot coordinates.

METHOD

Object Recognition and 3D Position

There are two stages involved in this study: object recognition and robot space transformation. Object recognition is initially used to detect and locate the object position based on image coordinates. Then, it is transformed in relation to camera and robot coordinates to be used as reference for grasping in a later study.

Image Processing Using SURF

The SURF process can be divided into three main steps. In the first step, Hessian matrix based blob detector is used to find the interest points or object features at the distinctive locations in the image. The computation time is reduced significantly due to the application of integral image in finding the interest points. Next, Haar wavelet patterns are distributed to the neighbourhood of every interest point to produce the feature vector typically known as feature descriptor. Finally, the descriptor vector of the target and scene images are matched using Euclidean distance.

Calculation of 3D Object Position

Initially, SURF produces object information in pixel values. It is necessary to transform the image data to provide reliable information for the robot's operation. The 2D object's centre point provided by SURF needs to be converted to 3D position in the robot plane. The conversion process involves mathematical calculation which will be discussed later.

After the location of the object is recognised in the scene image, the next step is to find the centre point of object related to image coordinates. The object position from SURF which is represented as polygon matrix is used to obtain the centre point by averaging its four corners. The conversion of (u, v) in image plane to (X_C, Y_C) in camera plane which is from pixel to unit in centimetre is performed by using equation (1). *Width* and *height* represent the width and

height of the image respectively. Note that only left side camera is considered to perform the conversion of X_C and Y_C as shown in Figure 1 (a).

$$\begin{bmatrix} X_C \\ Y_C \end{bmatrix} = \begin{bmatrix} \frac{u - \left(\frac{\text{width}}{2}\right)}{q} \\ \left(\frac{\text{height}}{2}\right) - v \\ q \end{bmatrix} \quad [1]$$

The centre points of object from two cameras are used to calculate the 3D position (X_C, Y_C, Z_C). Z_C is determined using triangulation formula in equation (2) and as illustrated in Figure 1 (b). f is the focal length of image, T is the physical distance between the two lenses, X_{left} and X_{right} are the projected x position on the left and right image planes, O_{left} and O_{right} are the centre projection of both camera planes and Q is the distance of camera to object.

$$Z_C = \frac{fT}{X_{left} - X_{right}} \quad [2]$$

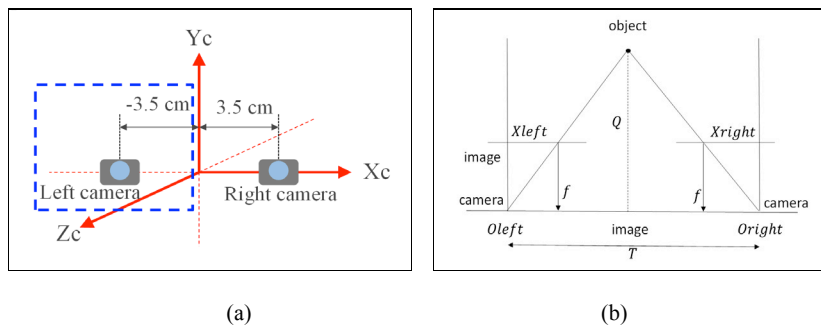


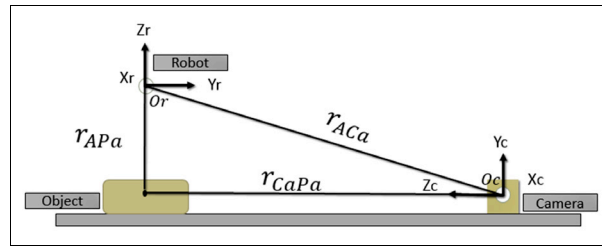
Figure 1. 3D calculation of object position: (a) stereo camera setup; and (b) triangulation (top view)

Robot Space Transformation

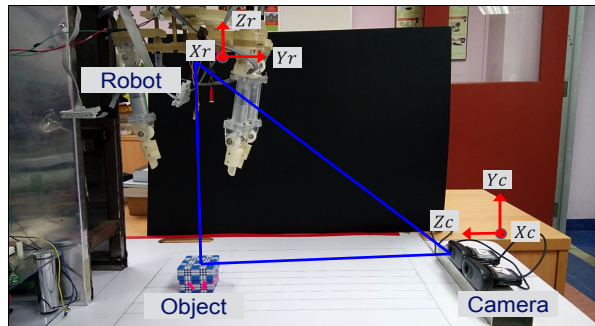
Robot space transformation refers to data conversion from (X_C, Y_C, Z_C) in camera coordinates to (X_r, Y_r, Z_r) in robot coordinates. The relationship between both coordinates is depicted in Figure 2. r_{APa} which is the position vector for moving the end effectors towards the object based on (X_C, Y_C, Z_C) can be calculated using equation (3). In this equation, r_{ACa} represents the position of camera in the robot coordinates, while r_{CaPa} represents the position of object in the camera coordinates. $Rot_X(\theta_c)$ and $Rot_Y(\theta_c)$ are the rotation matrices for camera in z and y axes respectively as written in equation (4).

$$r_{APa} = r_{ACa} + (Rot_X(\theta_c) * Rot_Y(\theta_c))^{-1} * r_{CaPa} \quad [3]$$

$$Rot_X(\theta_c) \begin{bmatrix} 1 & 0 & 0 \\ 0 & \cos \theta_c & -\sin \theta_c \\ 0 & \sin \theta_c & \cos \theta_c \end{bmatrix}, Rot_Y(\theta_c) \begin{bmatrix} \cos \theta_c & 0 & \sin \theta_c \\ 0 & 1 & 0 \\ -\sin \theta_c & 0 & \cos \theta_c \end{bmatrix} \quad [4]$$



(a)



(b)

Figure 2. Camera and robot coordinates: (a) illustration of coordinates; and (b) coordinates in real setup

Experimental Setup

A box which can fit the size of the robot hand and has unrepeated pattern is selected as the target for the SURF experiment. Ten images which consist of the target object were placed at different positions in x , y and z axes of the robot coordinates. Two main objectives in this experiment were to detect the target object using SURF in a cluttered background and to verify its 3D position where the centre point of object in image were calculated related to camera and robot planes using the above transformation equations.

RESULTS AND DISCUSSION

Object Recognition

In early process of object recognition, interest points were extracted from the target image and the scene image. Figure 3 shows the set of extracted interest points from both images represented by circles. About 100 and 300 interest points have been extracted from the target image and the scene image respectively. After that, the descriptor of interest point from the target object is stored in the database as are reference for similarity test.

In the similarity test, as the target object is placed at ten different positions, both the feature vectors of the target image in the database and the scene image were compared. Based on the different positions of object, about 30-60 verified interest points have passed the similarity test using nearest neighbourhood algorithm before a target is found. Figure 4(a) shows the result of matching process where about 14 inlier points represented by the yellow lines were

found. Finally, the result of SURF detecting the target object in the scene image is indicated by a transformed polygon line as shown in Figure 4(b).

3D Object Position and Robot Transformation

The conversion for the centre point of object from image plane to camera plane is tabulated in Table 1. L01 until L09 represent the scene images that consist of the target object captured by the stereo camera. L01 is where the target object is placed at the centre of robot origin while L02 until L05 is where the target object is displaced in the negative and positive directions along Y_r axis. L06 and L07 is where the target object is displaced in the positive direction of X_r axis. Meanwhile, L08 and L09 are the locations of the displaced object in the negative direction of Z_r axis. r_{CaPa} is the 3D centre point of object in camera plane in pixel values.

Next, r_{CaPa} in centimetre unit is compared with the manually measured distance from camera to object, r_{CaO} . The difference between r_{CaPa} and r_{CaO} is presented as Error 1 in Table 1. As the position of target object is varied from the robot origin O_r , r_{CaPa} varied accordingly in x, y and z directions. However, when the object is placed far to the left of camera, the object detected by SURF produced bigger error as shown in Figure 5 for L03, L06 and L07 which can be shown by comparing the polygon lines.

Finally, the result of calculated object position from the robot r_{APa} is compared with manually measured distance from object to robot r_{AO} in Table 2. The difference between r_{APa} and r_{AO} is presented as Error 2. The 3D illustration of the data is shown in Figure 6.

When the object is placed at L01 the position error is almost zero. When it is displaced in the direction of Y_r from 2.5 cm to 5 cm in L04 and L05, r_{APa} showed positive increments in y from 2.67 cm to 4.56 cm. When the object is displaced in the positive direction of X_r from 2.5 cm to 5 cm in L06 and L07, L07 showed the highest error of 3.90 cm in x direction while L06 showed error of only -2.16 cm. This is due to the error in Z_C calculated from SURF which is as much as 2.27 cm. As the object position in Z_r is displaced towards negative direction from -26.5 cm to -24.5 cm in L08 and L09, r_{APa} also showed negative increments in z direction from -28.47 cm to -26.38 cm which contributed by error from 1.88 cm to 1.97 cm.

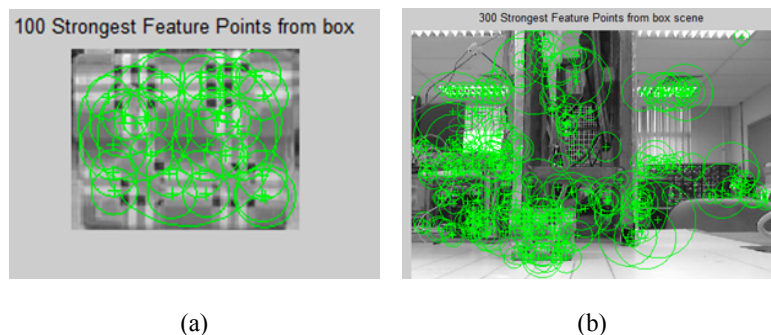


Figure 3. Detected feature points from box and scene: (a) interest point from a box; and (b) interest point from the scene

SURF based 3D Object Recognition for Robot Hand Grasping

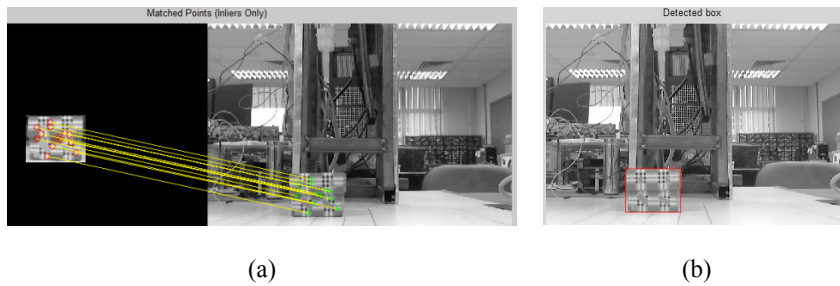


Figure 4. Features matching and detected object in scene image: (a) matching features; and (b) detected object in scene image

Table 1
Comparison of measured and calculated camera to object distance

Image	Axis	Camera to object		Error_1
		r_{CaO} Measured (cm)	r_{CaPa} Calculated (cm)	
L01	Xc	-3.50	-3.50	0.00
	Yc	0.00	0.00	0.00
	Zc	37.90	36.15	1.75
L02	Xc	-6.00	-5.84	-0.16
	Yc	0.00	-0.01	0.01
	Zc	37.90	36.75	1.15
L03	Xc	-8.50	-8.16	-0.34
	Yc	0.00	-0.07	0.07
	Zc	37.90	36.78	1.12
L04	Xc	-1.00	-1.20	0.20
	Yc	0.00	-0.06	0.06
	Zc	37.90	37.21	0.69
L05	Xc	1.50	1.17	0.33
	Yc	0.00	-0.04	0.04
	Zc	37.90	37.24	0.66
L06	Xc	-3.50	-3.55	0.05
	Yc	0.00	0.20	-0.20
	Zc	35.40	36.53	-1.13
L07	Xc	-3.50	-5.71	2.21
	Yc	0.00	0.50	-0.50
	Zc	32.90	35.17	-2.27
L08	Xc	-3.50	-3.63	0.13
	Yc	6.00	4.21	1.79
	Zc	37.90	37.47	0.43
L09	Xc	-3.50	-3.63	0.13
	Yc	8.00	6.46	1.54
	Zc	37.90	37.84	0.06

Table 2
Comparison of measured and calculated robot to object distances

Image	Axis	Robot to object		Error_2
		r_{AO} Measured (cm)	r_{APa} Calculated (cm)	$r_{AO} - r_{APa}$ (cm)
L01	X	0.0	0.09	-0.09
	Y	0.0	0.38	-0.38
	Z	-32.5	-32.44	-0.06
L02	X	0.0	1.60	-1.60
	Y	-2.5	-1.27	-1.23
	Z	-32.5	-33.29	0.79
L03	X	0.0	2.84	-2.84
	Y	-5.0	-3.01	-1.99
	Z	-32.5	-34.18	1.68
L04	X	0.0	0.00	0.00
	Y	2.5	2.67	-0.17
	Z	-32.5	-31.36	-1.14
L05	X	0.0	-1.05	1.05
	Y	5.0	4.56	0.44
	Z	-32.5	-30.39	-2.11
L06	X	2.5	0.34	2.16
	Y	0.0	0.36	-0.36
	Z	-32.5	-32.23	-0.27
L07	X	5.0	1.10	3.90
	Y	0.0	-1.68	1.68
	Z	-32.5	-33.03	0.53
L08	X	0.0	1.31	-1.31
	Y	0.0	-1.08	1.08
	Z	-26.5	-28.47	1.97
L09	X	0.0	1.66	-1.66
	Y	0.0	-1.94	1.94
	Z	-24.5	-26.38	1.88

Overall, the transformation was successful where the object positions inclined to the directions of the actual measured positions according to robot coordinates. However, the errors attributed to inaccuracy of SURF detection and human error during manual measurement.

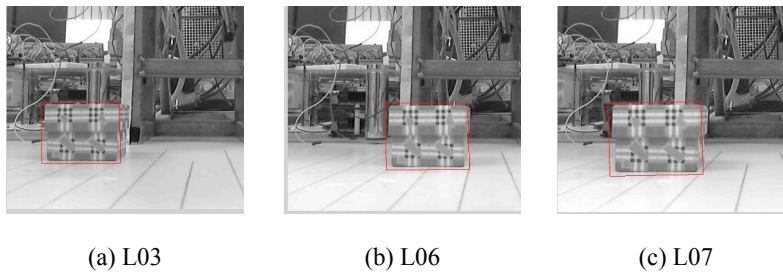


Figure 5. Position errors from SURF: (a) L03; (b) L06; and (c) L07

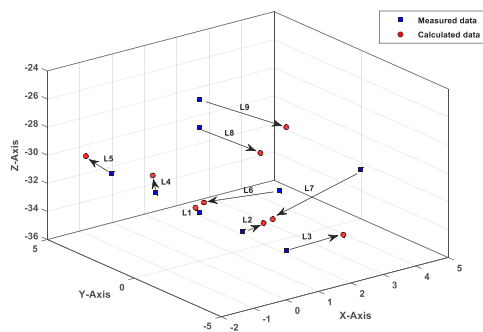


Figure 6. The comparison of measured and calculated data

CONCLUSION

This study used vision algorithm technique called SURF feature to detect a target object in cluttered backgrounds. In order to obtain the object position in robot coordinates, transformation was applied according to the translations and rotations of camera related to robot coordinates. The result showed that SURF algorithm can recognise the target object without fail for nine random images. Furthermore, the transformation was successfully implemented where the calculated 3D positions were observed to incline towards the direction of actual measured positions. However, the errors occurred in the 3D positions were due to the limitation in SURF as well as human error during manual measurements with the highest error observed at 3.90cm. The SURF technique had displayed weaknesses when the object is rotated and when the camera's viewpoint is changed. The result showed that the more the object is rotated, the bigger the error. Therefore, a combination of SURF with geometric algorithm or machine learning methods could be considered in future work to overcome these limitations.

ACKNOWLEDGEMENTS

This research was made possible by the financial support from Ministry of Higher Education fund (600-RMI/FRGS 5/3 (86/2013)). The authors would like to thank Research Management Institute (RMI) and Faculty of Electrical Engineering, UiTM for their financial and technical assistance to conduct this research.

REFERENCES

- Anh, T., & Song, J.-B. (2012). Robotic grasping based on efficient tracking and visual servoing using local feature descriptors. *International Journal of Precision Engineering and Manufacturing*, 13(3), 387–393. /10.1007/s12541-012-0049-8
- Anitha, J. J., & Deepa, S. M. (2014). Tracking and Recognition of Objects using SURF Descriptor and Harris Corner Detection. *International Journal of Current Engineering and Technology*, 4(2), 775–778.
- Bay, H., & Ess, A. (2008). Speeded-Up Robust Features (SURF), 110, 346–359. /10.1016/j.cviu.2007.09.014
- Collet, A., Berenson, D., Srinivasa, S. S., & Ferguson, D. (2009). Object recognition and full pose registration from a single image for robotic manipulation. *2009 IEEE International Conference on Robotics and Automation*, 48–55. /10.1109/ROBOT.2009.5152739
- Desai, H. M., Gandhi, V., & Desai, M. (2015). Real-time Moving Object Detection using SURF. *IOSR Journal of Computer Engineering Ver. VII*, 17(3), 2278–661. /10.9790/0661-17377578
- Kasim, M. K. M., Shauri, R. L. A., & Nasir, K. (2016). PID position control of three-fingered hand for different grasping styles. *Proceedings - 2015 6th IEEE Control and System Graduate Research Colloquium, ICSGRC 2015*, 7–10. /10.1109/ICSGRC.2015.7412455
- Ke, Y. K. Y., & Sukthankar, R. (2004). PCA-SIFT: a more distinctive representation for local image descriptors. *Proceedings of the 2004 IEEE Computer Society Conference on Computer Vision and Pattern Recognition, 2004. CVPR 2004.*, 2, 2–9. /10.1109/CVPR.2004.1315206
- Kim, H.-J., Lee, J. Y., Kim, J. H., Kim, J. B., & Han, W. Y. (2012). Object recognition and pose estimation using KLT. *Control, Automation and Systems (ICCAS), 2012 12th International Conference on*. CONF .
- Kuş, M. C., Gökmen, M., & Etaner, Ş. (2008). Traffic Sign Recognition using Scale Invariant Feature Transform and Color Classification. *Computer and Information Sciences*, 1–6. /10.1109/ISCIS.2008.4717875
- Lee, S., Kim, E., & Park, Y. (2006). 3D object recognition using multiple features for robotic manipulation. *Proceedings 2006 IEEE International Conference on Robotics and Automation, 2006. ICRA 2006.*, (May), 3768–3774. /10.1109/ROBOT.2006.1642278
- Lowe, D. G. (1999). Object recognition from local scale-invariant features. *Proceedings of the Seventh IEEE International Conference on Computer Vision*, 1150–1157 vol.2. /10.1109/ICCV.1999.790410
- Saxena, A., Driemeyer, J., & Ng, A. Y. (2008). Robotic grasping of novel objects using vision. *The International Journal of Robotics Research*, 27(2), 157-173.
- Shauri, R. L. A., Salleh, N. M., & Hadi, A. K. A. (2014). PID position control of 7-DOF three-fingered robotic hand for grasping task. *Proceedings - 4th IEEE International Conference on Control System, Computing and Engineering, ICCSCE 2014*, (November), 70–74. /10.1109/ICCSCE.2014.7072691
- Sushkov, O., & Sammut, C. (2011). Feature segmentation for object recognition using robot manipulation. *Australian Conf. on Robotics and Automation*, 7–9.
- Wu, J., Cui, Z., Sheng, V. S., Zhao, P., Su, D., & Gong, S. (2013). A Comparative Study of SIFT and its Variants. *Measurement Science Review*, 13(3), 122–131. /10.2478/msr-2013-0021



EIS and DFT Investigations on Corrosion Inhibition of Imines containing Mono- and Diisatin Moieties

Aliyin Abdul Ghani^{1*}, Hadariah Bahron¹, Mohamad Kamal Harun¹,
Karimah Kassim³ and El Hassane Anouar²

¹Faculty of Applied Sciences, Universiti Teknologi MARA (UiTM), 40450 Shah Alam, Selangor, Malaysia

²Department of Chemistry, College of Science and Humanities Studies, Prince Sattam bin Abdulaziz University, P.O.Box 83, Al-Kharj 11942, Saudi Arabia

³Institute of Science, Universiti Teknologi MARA (UiTM), 40450 Shah Alam, Selangor, Malaysia

ABSTRACT

Two imines of different molecular sizes namely 3-(phenylimino) indolin-2-one (PII) and 3,3-(1,4-phenylenebis (azan-1-yl-1-ylidene) diindolin-2-one (PDI) were investigated for their corrosion inhibition on mild steel in 1 M HCl solution using electrochemical impedance spectroscopy (EIS). The bigger molecule PDI containing double the amount of isatin moiety exhibited higher inhibition efficiency of 87.3% while PII that contained monoisatin moiety showed a lower inhibition efficiency of 74.8%. Both compounds had an increase in inhibition efficiencies percentage as concentrations increased. Density functional theory (DFT) was used to determine the correlation between the corrosion inhibition efficiency and electronic parameters. The DFT calculations indicated that the corrosion inhibition efficiency was mainly dependant on the frontier orbital energy gap and the chemical softness/hardness of the imines.

Keywords: Corrosion inhibition, DFT, Isatin, mild steel, Schiff base

ARTICLE INFO

Article history:

Received: 28 September 2016

Accepted: 03 February 2017

E-mail addresses:

aliyinabdulghani@gmail.com (Aliyin Abdul Ghani),

hadariah@salam.uitm.edu.my (Hadariah Bahron),

mkharun@gmail.com (Mohamad Kamal Harun),

karimah@salam.uitm.edu.my (Karimah Kassim),

anouarelhassane@yahoo.fr (El Hassane Anouar)

*Corresponding Author

INTRODUCTION

Imines or Schiff bases are organic compounds synthesised from the condensation of amines and aldehydes/ketones, with characteristic C=N functional group (Shakir et al., 2009). They are prevalent due to ease of synthesis, facile fine tuning of electronic structure; the presence of lone pair of electrons on the imine nitrogen that make them ideal chelating agents with metal centres, producing compounds that have interesting properties

and activities (Bahron et al., 1994). Imines are known for their various fields of application, including biological, physical and analytical chemistry (Vicini et al., 2003; Anouar et al., 2013). Furthermore, they are widely used as effective organic corrosion inhibitors, especially in acidic environments, for various types of metal (Ghani et al., 2012; Daoud et al., 2014). Hydrochloric acid solutions are commonly used for the removal of rust and undesired scales on mild steel in many industrial purposes. To resolve the issue of the corrosion of mild steel in hydrochloric acid solutions many fundamental scientific studies and industrial studies have been conducted (Hegazy et al., 2009).

Density functional theory (DFT) calculations have been extensively used to show the interaction between the corrosion inhibitor and mild steel surface (Ju et al., 2008; Ghailane et al., 2013). The corrosion inhibition efficiency mainly depends on the physicochemical, electronic properties of inhibitors, as well as the binding interaction between the inhibitor and the metal surface. For instance, frontier molecular orbitals (HOMO and LUMO) and the Mulliken atomic charge distributions are used in locating the active sites in the organic inhibitors (Daoud et al., 2014; Ghailane et al., 2013).

The present study is aims to show the relationships between the inhibition efficiencies of two Schiff bases, 3-(phenylimino) indolin-2-one (PII) and 3,3-(1,4-phenylenebis(azan-1-yl-1-ylidene) diindolin-2-one (PDI) on mild steel in 1 M HCl with physicochemical and electronic properties of the studied compounds. The DFT calculations were carried out using the hybrid functional B3LYP combined with 6-311+G (d,p) basis set.

METHOD

The synthesis, characterisation, preparation of working electrode and test solution of PII (4) and PDI (5) were based on Ghani et al. (2014).

Electrochemical Measurement

A conventional three-electrode system was employed for the electrochemical studies consisting of a mild steel working electrode, a platinum rod and Ag/AgCl electrode with a Luggin capillary as both counter and reference electrode. The mild steel working electrode was immersed for 15 minutes in test solutions to achieve a steady state open circuit potential or OCP. Electrochemical impedance spectroscopy (EIS) measurements were done at open circuit potential over frequency ranging from 0.05 Hz to 100 kHz and sinusoidal potential perturbation was 10 mV in amplitude with data density of 10 points per decade.

Theoretical Details

The optimisation and frequency calculations of the ground states of the two Schiff bases and its precursor compounds as in Figure 1 were carried out using the DFT hybrid functional B3LYP combined with a triple-Pople-type basis set 6-311+G (d,p) as implemented in Gaussian software (Frisch et al., 2009).

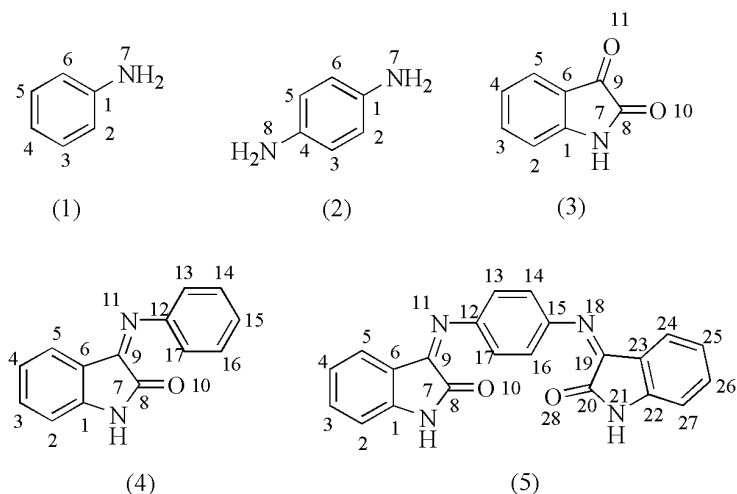


Figure 1. Molecular structures of the precursor compounds: (1) Aniline; (2) p-phenyldiamine; (3) Isatin; and its Schiff bases; (4) PII; (5) PDI

To correlate the corrosion inhibition efficiencies of the compounds on mild steel, a set of electronic properties such as HOMO and LUMO energies, ionisation potential (IP), electronic affinity (EA), energy gap between the HOMO and LUMO, electronegativity (χ), chemical hardness/softness (η), electrophilicity (ω) and dipole moment (μ) were calculated. Mulliken atomic charges were calculated to determine the active sites for the titled inhibitors binding to the mild steel surface. The polarisable continuum model (PCM) were used to take the solvent effects into account when the compound is embedded into a cavity surrounded by solvent described by its dielectric constant ϵ (e.g., for water $\epsilon = 78.3553$) (Tomasi et al., 2005). The frontier molecular orbitals were visualised with Molden software.

RESULTS AND DISCUSSION

Electrochemical Impedance Spectroscopy (EIS)

The corrosion behaviour of mild steel in 1 M HCl in absence of PII and PDI (blank solution) and in the presence of the PII and PDI at different concentrations are shown in Nyquists plots in Figure 2. The capacitive loops have the appearance of slightly depressed semicircles due to a phenomenon called “dispersing effect” where there is heterogeneity, roughness and porosity on the mild steel surface (Tang et al., 2013). The impedance values were significantly enhanced after the addition of both the inhibitors in the acidic solution. The diameter of the semicircles increased with the concentrations of both compounds, but more so in PDI, resulting from the effective surface coverage of the Schiff base inhibitors on mild steel substrate.

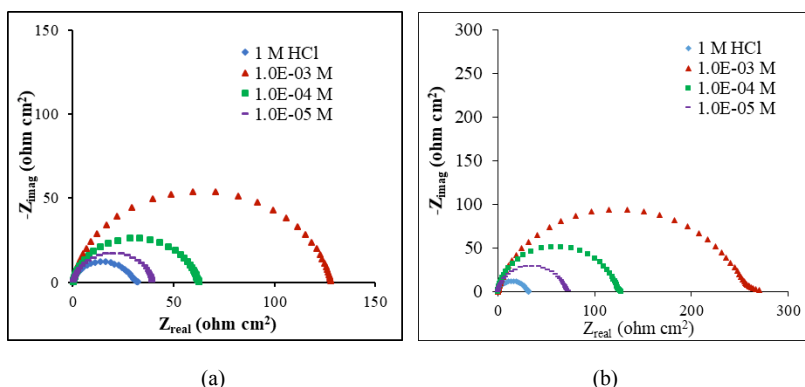


Figure 2. Nyquist plots for mild steel in 1 M HCl with and without the presence of: (a) PII; and (b) PDI in different concentrations

Table 1 shows the parameters obtained from EIS fitting of both inhibitors using the equivalent circuit in Figure 3. R_s and R_p represent the solution resistance and the polarisation resistance respectively. Meanwhile, Constant phase element (CPE) is used in the equivalent circuit to replace a double layer capacitance (C_{dl}) for an accurate impedance spectra fit.

Table 1
Impedance parameters for mild steel electrode in 1 M HCl in the presence of different concentrations of PII and PDI.

	C (M)	R_s (Ω cm ²)	R_p (Ω cm ²)	Y_o (S.sec ⁿ /cm ²)	n	IE (%)
Blank	1 M HCl	0.13	31.9	197.2×10^{-6}	0.89	-
PII	1×10^{-5} M	0.16	38.9	153.0×10^{-6}	0.90	17.9
	1×10^{-4} M	0.15	61.9	124.1×10^{-6}	0.89	48.4
	1×10^{-3} M	0.18	126.9	78.1×10^{-6}	0.91	74.8
PDI	1×10^{-5} M	0.19	72.6	97.3×10^{-6}	0.88	56.1
	1×10^{-4} M	0.17	125.7	78.3×10^{-6}	0.91	74.6
	1×10^{-3} M	0.24	250.9	36.9×10^{-6}	0.86	87.3

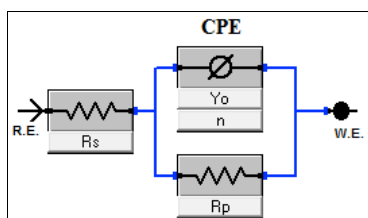


Figure 3. Equivalent circuit used to fit the Nyquist plots

The impedance of constant phase element consists of Y_0 (proportional factor) and n (exponential parameter). n represents the degree of surface roughness where small deviations from 1 indicate a homogenous surface. R_p values represent the degree of difficulty for corrosion reaction to occur, where increasing R_p values indicate decreasing corrosion rate. It can be observed from Table 1 that the R_p values increased with inhibitor's concentrations upon which corrosion reactions were retarded, thus showing improved inhibition efficiency. This effect was more pronounced with PDI, which exhibited higher inhibition efficiency than PII.

The Bode plots for mild steel in the presence and absence of PII and PDI are presented in Figure 4. The Bode phase plots for both inhibitors show a onetime constant feature with only one peak detected per plot as shown in Figure 4(b) and 4(d). This can be correlated with the single semicircle acquired from the Nyquist plot. This one-time constant feature indicates that the inhibitors form intact homogenous layer of protection on the mild steel surface. These plots can also determine the capacitive and resistive behaviour of the system. Both inhibitors show a capacitive behaviour based on Bode phase plot with the phase angle in the range of 69-78° which is approaching 90°, denoting an ideal capacitive response.

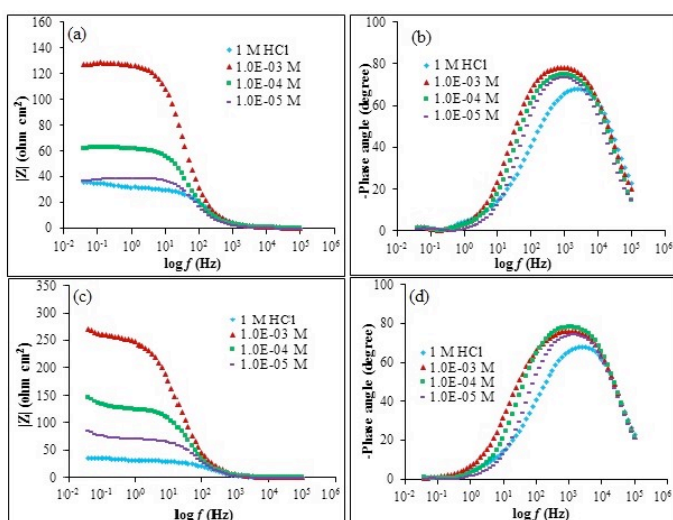


Figure 4. Bode plots of mild steel in 1 M HCl: (a) bode modulus of PII; (b) bode phase of PII; (c) bode modulus of PDI; and (d) bode phase of PDI

Bode modulus plots 4(a) and 4(c) indicate the real impedance (Z_{real}) values from high to low frequency region. Z_{real} at low frequency increases with the increase in concentration of the Schiff base inhibitors. This demonstrates that at higher concentrations, the adsorption of inhibitors increases, hence improving the corrosion resistance.

Theoretical Calculations

The corrosion inhibition efficiencies IE (%) and the calculated electronic properties of the compounds 1-5 are shown in Table 2. Simple and multiple linear regression curves between the inhibition efficiencies (IE) and the electronic parameters of the compounds 1-5 are displayed in Figure 5.

Table 2
Electronic properties (eV) of the 1-5 compounds calculated at the B3LYP/6-311+G (d, p) level of theory.

	ϵ_{HOMO}	ϵ_{LUMO}	IP	EA	ϵ_{Gap}	c	h	S	ΔN	μ (D)	IE %
1	-5.69	-0.47	5.69	0.47	5.22	3.08	2.61	0.19	0.75	2.46	20.8
2	-4.81	-0.43	4.81	0.43	4.38	2.62	2.19	0.23	1.00	0.00	35.3
3	-6.84	-3.18	6.84	3.18	3.66	5.01	1.83	0.27	0.54	8.99	46.3
4	-6.37	-2.96	6.37	2.96	3.41	4.66	1.70	0.29	0.69	3.04	74.8
5	-5.92	-3.06	5.92	3.06	2.86	4.49	1.43	0.35	0.88	2.79	87.3

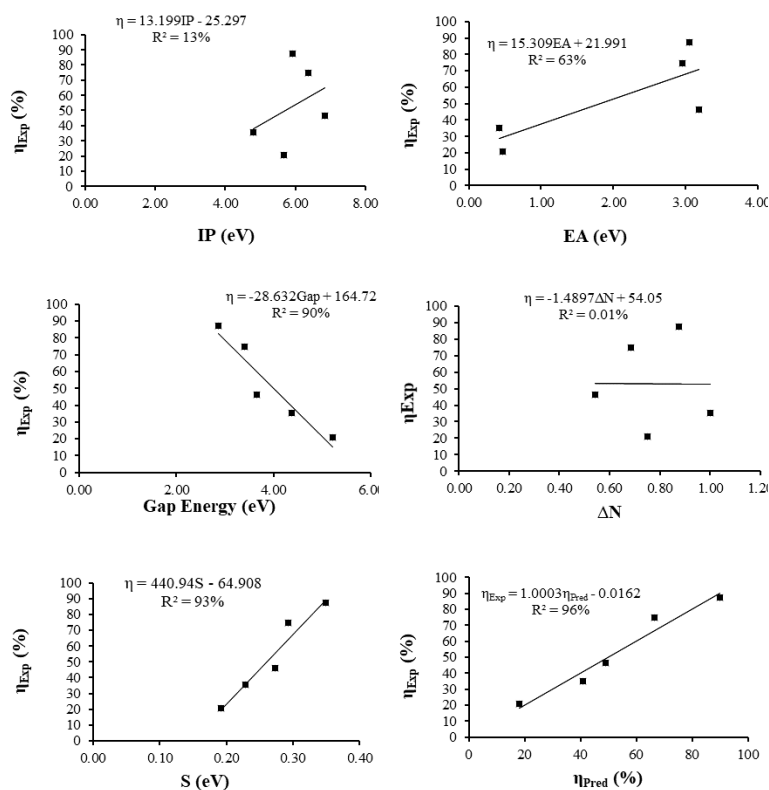


Figure 5. Regression curves between the corrosion inhibition efficiency and electronic properties of the compounds 1-5

There were strong correlations between energy gap, hardness and softness parameters with correlation coefficients (R^2) of 90, 90 and 93%, respectively. Moderate correlations were obtained with the electronic affinity and electrophilicity with R^2 of 63 and 66% respectively. Surprisingly, weak correlations were obtained with the number of transferred electron, dipole moment and ionisation potential with R^2 of 0.01, 0.03 and 13% respectively.

In order to improve the correlation, different parameters were combined using multiple linear regressions. The combination of the gap energy, softness and hardness parameters give the best correlation with R^2 of 96%. The band gap energy plays an important role in determining the inhibitors capability to donate/accept electrons to/from the mild steel surface. The energy gap of PDI and PII are 2.86 and 3.41 eV respectively. The low gap energy value for PDI is an indication that it is easier for the electrons to be transferred due to the low energy barrier between the HOMO and LUMO. Thus, explaining the higher inhibition efficiency value of PDI compared with PII.

The HOMO and LUMO molecular orbitals of compounds 1-5 are shown in Figure 6. The HOMO orbitals are well delocalised over the whole compounds, except for the PDI where the delocalisation is mainly in the central part. Similar observation has been obtained with the LUMO orbitals. HOMO and LUMO orbitals are useful to predict the adsorption centres of interaction between the inhibitor and metal surface (Fang et al., 2002; Bereket et al., 2002).

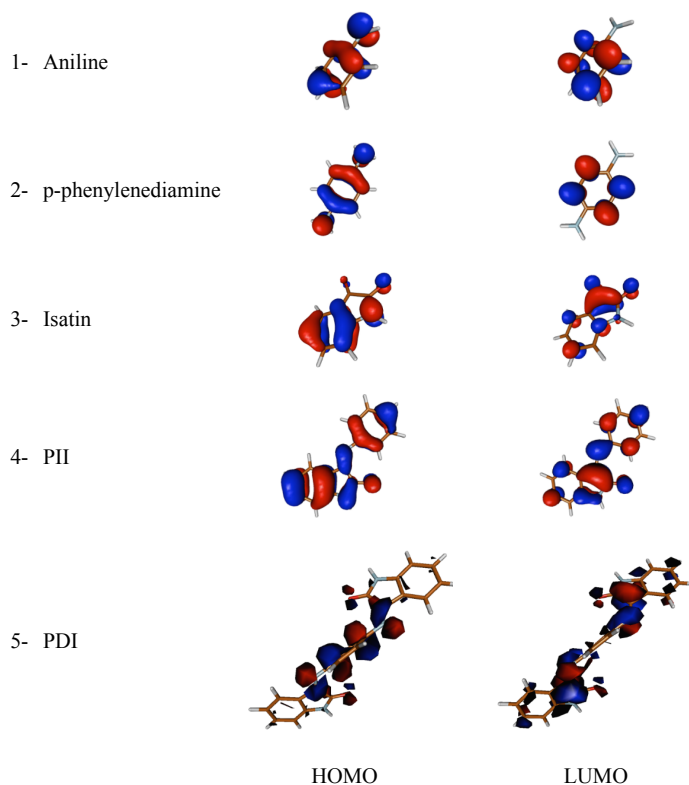


Figure 6. Frontier molecular orbitals of the Schiff base inhibitors (Isovalue 0.03)

The efficient inhibitors are those donating electrons to *d*-orbital of the metal, and accepting electrons from the metal surface (Ju et al., 2008). The electronic density delocalisation of HOMO and LUMO orbitals clearly showed that the compounds have donor/acceptor electron to/from the metal surface.

The number of transferred electrons from the inhibitor to the metal (ΔN) was calculated. The higher inhibition efficiency of PDI compared with PII is in good agreement with the increased ΔN values (0.69 and 0.88 for PII and PDI respectively). This is consistent with previous studies, which reported that the inhibition efficiency increased with electron-donating ability of the metal surface (ΔN) (Torres et al., 2013).

In order to determine the main active sites for the compounds, Mulliken atomic charges were calculated at the B3LYP level of theory as in Table 3 where some of the atomic centres possess negative charges, while others positive ones. As for aniline and PPD there are excess of negative charge on nitrogen heteroatoms (N7 and N8 with atomic charges of -0.49 and -0.53 Cb in aniline and PPD respectively). These heteroatoms play the role of electron donors to the vacant d-orbitals of metal surface atoms. Meanwhile, the carbon atoms C1, C2, C4, C5, C22, C24 and C27 in aromatic rings of isatin, PII and PDI are the most active sites compared with nitrogen heteroatoms. Therefore, the adsorption/interaction between isatin, PII and PDI with the metal surface atoms are mainly related to the electrostatic interactions between aromatic rings in the compounds with the metal substrate. The N atoms are weaker adsorption centres due to the steric hindrance of benzyl rings.

Table 3
Mulliken atomic charges for the 1-5 compounds calculated at the B3LYP/6-311+G (d, p) level of theory

Inhibitor	1	2	3	4	5
C1	-0.024	-0.023	-0.988	-0.705	-0.57991
C2	-0.075	-0.127	-0.923	-0.564	-0.57067
C3	-0.195	-0.126	-0.233	-0.234	-0.25756
C4	-0.189	-0.023	-0.064	-0.430	-0.24313
C5	-0.195	-0.127	-0.405	-0.509	-0.67136
C6	-0.075	-0.126	2.545	1.350	1.253635
N7	-0.490	-0.530	-0.170	-0.256	-0.21951
N8	-	-0.530	-	-	-
C8	-	-	0.382	0.398	0.102577
C9	-	-	-0.388	0.213	0.308284
O10	-	-	-0.407	-0.395	-0.35462
O11	-	-	-0.343	-	-
N11	-	-	-	0.034	0.193489
C12	-	-	-	0.274	-0.42945
C13	-	-	-	0.027	0.229582
C14	-	-	-	-0.426	0.229758
C15	-	-	-	-0.093	-0.42937
C16	-	-	-	-0.577	-0.0293

Table 3 (continue)

C17	-	-	-	0.112	-0.02919
N18	-	-	-	-	0.193549
C19	-	-	-	-	0.308038
C20	-	-	-	-	0.102552
N21	-	-	-	-	-0.2195
C22	-	-	-	-	-0.57975
C23	-	-	-	-	1.253771
C24	-	-	-	-	-0.67141
C25	-	-	-	-	-0.24314
C26	-	-	-	-	-0.25753
C27	-	-	-	-	-0.57079
O28	-	-	-	-	-0.35461

CONCLUSION

The corrosion inhibition investigation through EIS showed that both Schiff base compounds displayed inhibitor properties where the inhibition efficiencies increased with concentration of inhibitors. The higher inhibition efficiency of PDI compared with PII was confirmed by DFT calculations. Simple and multiple linear regressions showed that the corrosion inhibition efficiency mainly depends on energy gap, chemical hardness and softness of the studied compounds. Frontier orbital delocalisation and Mulliken atomic charge clearly showed that the PDI compound have different active sites as donor or acceptor of electrons to/from mild steel, which promotes the protection of mild steel against corrosion in acidic solution.

ACKNOWLEDGEMENTS

The authors express their gratitude to the Research Management Institute for its Research Acculturation Grant Scheme (600-RMI/RAGS 5/3 (139/2014)), the Faculty of Applied Sciences and Institute of Science of Universiti Teknologi MARA for providing research facilities. Authors would also like to thank Mr. Mohamad Safwan bin Jusof from Universiti Malaya for his help to access the supercomputer (PTMLXSMP).

REFERENCES

- Anouar, E., Raweh, S., Bayach, I., Taha, M., Baharudin, M. S., Di Meo, F., Hasan, M. H., Adam, A., Ismail, N. H., Weber, J. -F. F., & Trouillas, P. (2013). Antioxidant properties of phenolic Schiff bases: structure–activity relationship and mechanism of action. *Journal of Computer Aided Molecular Design*, 27, 951-964.
- Bahron, H., Larkworthy, L. F., Marecaux, A., Povey, D. C., & Smith, G. W. (1994). Structures of bis (Nn-butylsalicylideneiminato) cobalt (II) and bis (N-tert-butylsalicylideneiminato) cobalt(II) complexes and reactivity towards oxygen and nitric oxide. *Journal of Chemical Crystallography*, 24(2), 145-150.

- Behpour, M., Ghoreishi, S., Mohammadi, N., Soltani, N., & Salavati-Niasari, M. (2010). Investigation of some Schiff base compounds containing disulfide bond as HCl corrosion inhibitors for mild steel. *Corrosion Science*, *52*, 4046-4057.
- Bereket, G., Hür, E., & Öğretir, C. (2002). Quantum chemical studies on some imidazole derivatives as corrosion inhibitors for iron in acidic medium. *Journal of Molecular Structure – THEOCHEM*, *578*, 79-88.
- Daoud, D., Douadi, T., Issaadi, S., & Chafaa, S. (2014). Adsorption and corrosion inhibition of new synthesized thiophene Schiff base on mild steel X52 in HCl and H₂SO₄ solutions. *Corrosion Science*, *79*, 50-58.
- Emregül, K. C., Düzgün, E., & Atakol, O. (2006). The application of some polydentate Schiff base compounds containing aminic nitrogens as corrosion inhibitors for mild steel in acidic media. *Corrosion Science*, *48*, 3243-3260.
- Fang, J., & Li, J. (2002). Quantum chemistry study on the relationship between molecular structure and corrosion inhibition efficiency of amides. *Journal of Molecular Structures-THEOCHEM*, *593*, 179-185.
- Frisch, M. J. (2009). *Gaussian 09*, Revision A.02.
- Ghailane, T., Balkhmima, R., Ghailane, R., Souizi, A., Touir, R., Ebn Touhami, M., Marakchi, K., & Komiha, N. (2013). Experimental and theoretical studies for mild steel corrosion inhibition in 1M HCl by two new benzothiazine derivatives. *Corrosion Science*, *76*, 317-324.
- Ghani, A. A., Bahron, H., Harun, M. K., & Kassim, K. (2012). Corrosion inhibition study of a heterocyclic Schiff base derived from isatin. *Advanced Materials Research*, *554-556*, 425-429.
- Ghani, A. A., Bahron, H., Harun, M. K., & Kassim, K. (2014). Schiff bases derived from isatin as mild steel corrosion inhibitors in 1 M HCl. *The Malaysian Journal of Analytical Sciences*, *18*, 507-513.
- Hegazy, M. (2009). A novel Schiff base-based cationic gemini surfactants: Synthesis and effect on corrosion inhibition of carbon steel in hydrochloric acid solution. *Corrosion Science*, *51*, 2610-2618.
- Ju, H., Kai, Z.P., & Li, Y. (2008). Aminic nitrogen-bearing polydentate Schiff base compounds as corrosion inhibitors for iron in acidic media: a quantum chemical calculation. *Corrosion Science*, *50*, 865-871.
- Keleş, H. (2011). Electrochemical and thermodynamic studies to evaluate inhibition effect of 2-[(4-phenoxy-phenylimino) methyl]-phenol in 1M HCl on mild steel. *Materials Chemistry and Physics*, *130*, 1317-1324.
- Li, J., & Zhang, M. (2014). Atomic insights into adsorption of thiophenol derivatives as corrosion inhibitors for mild steel in hydrochloric acid solution. *Materials Research Innovations*, *18*, 38-42.
- Pearson, R. G. (1988). Absolute electronegativity and hardness: application to inorganic chemistry. *Inorganic Chemistry*, *27*, 734-740.
- Shakir, M., Azam, M., Parveen, S., Khan, A. U., & Firdaus, F. (2009). Synthesis and spectroscopic studies on complexes of N, N'-bis-(2-pyridinecarboxaldehyde)-1, 8-diaminonaphthalene (L); DNA binding studies on Cu (II) complex. *Spectrochimica Acta Part A: Molecular and Biomolecular Spectroscopy*, *71*, 1851-1856.

- Tomasi, J., Mennucci, B., & Cammi, R. (2005). Quantum Mechanical Continuum Solvation Models. *Chemical Reviews*, *105*, 2999-3093.
- Touir, R., Dkhireche, N., Ebn Touhami, M., Lakhrici, M., Lakhrici, B., & Sfaira, M. (2009). Corrosion and scale processes and their inhibition in simulated cooling water systems by monosaccharides derivatives: Part I: EIS study. *Desalination*, *249*, 922-928.
- Torres, V., Rayol, V., Magalhães, M., Viana, G., Aguiar, L., Machado, S., Orofino, H., & D'Elia, E. (2013). Study of thioureas derivatives synthesized from a green route as corrosion inhibitors for mild steel in HCl solution. *Corrosion Science*.
- Vicini, P., Geronikaki, A., Incerti, M., Busonera, B., Poni, G., Cabras, C. A., & La Colla, P. (2003). Synthesis and biological evaluation of benzo [d] isothiazole, benzothiazole and thiazole Schiff bases. *Bioorganic and Medicinal Chemistry*, *11*, 4785-4789.





Synthesis and characterisation of Mononuclear and Tetranuclear Zinc(II) Complexes of Schiff Bases Derived from Phenylenediamine

Hadariah Bahron*, Siti Solihah Khaidir, Amalina Mohd Tajuddin and Syed Abdul Illah Alyahya Syed Abd Kadir

Faculty of Applied Sciences, Universiti Teknologi MARA (UiTM), 40450 Shah Alam, Selangor, Malaysia

ABSTRACT

A mononuclear and new tetranuclear metal complexes of Zn(II) with Schiff base ligands L1 and L2 respectively, were synthesised. L1 was obtained through the condensation of salicylaldehyde with *ortho*-phenylenediamine while L2 was the product of reaction between of *ortho*-vanillin with 2,4,6-trimethyl-*m*-phenylenediamine. The ligands and complexes were characterised via elemental analysis, melting point, IR and NMR spectroscopy. The shifting of $\nu(\text{C}=\text{N})$, $\nu(\text{C}-\text{OH})$ and $\nu(\text{O}-\text{CH}_3)$ infrared peaks upon coordination with Zn(II) indicated that these three moieties play a significant role in the complexation. It was found that L1 acted as tetradentate ligand, coordinating with Zn(II) centres through phenolic oxygen and imine nitrogen. The ligand L2 acted as a hexadentate ligand, bonded to metal via phenolic oxygen, imine nitrogen and methoxy oxygen, where four Zn(II) centres formed bridges to connect two ligands.

Keywords: Schiff base, metal complexes, mononuclear, tetranuclear

INTRODUCTION

The condensation reaction of primary amines with active carbonyl compounds results in the formation of Schiff base compounds and this was reported by Hugo Schiff in 1864 (Qin et al., 2013). Schiff bases have the general formula of $\text{RR}'\text{C}=\text{NR}''$ containing C=N functional group. Structurally, a Schiff base is a nitrogen analogue of an aldehyde or ketone in which the carbonyl group (C=O) is replaced by an imine or azomethine group (Abu-Dief et al., 2015). The formation of a Schiff base involves two steps: a nucleophilic addition of primary

ARTICLE INFO

Article history:

Received: 28 September 2016

Accepted: 03 February 2017

E-mail addresses:

hadariah@salam.uitm.edu.my (Hadariah Bahron),

s.solihah92@gmail.com (Siti Solihah Khaidir),

amalina9487@salam.uitm.edu.my (Amalina Mohd Tajuddin),

illah.alyahya@salam.uitm.edu.my

(Syed Abdul Illah Alyahya Syed Abd Kadir)

*Corresponding Author

amine followed by formation of a carbinolamine intermediate (Cordes & Jencks, 1963) before elimination of a water molecule.

Schiff bases can be effective chelating agents acting as mono-, di- or polydentate ligands depending on the number of donor atoms present in the molecule and can form generally five or six-membered chelate rings upon reaction with a metal ion (Alim et al., 2015). Schiff bases with sulphur and nitrogen donor atoms in their structures act as good chelating agents for transition and non-transition metal ions. Coordination compounds to metal ions, such as copper, nickel, zinc, cadmium and cobalt, have been reported to enhance their biological activities (El-Sonbati et al., 2016).

METHOD

Materials

All the chemicals and solvents used were of analytical grade. Salicylaldehyde (Sal), ortho-vanillin (Ovan), 2,4,6-trimethyl-m-phenylenediamine (3CH₃-MPD), ortho-phenylenediamine (OPD), zinc(II) acetate dihydrate, methanol, ethanol, chloroform, deuterated chloroform and dimethylsulfoxide (DMSO) were purchased from Sigma Aldrich and used without further purification.

Synthesis of Ligands and Metal Complexes

Synthesis of L1. Sal was mixed with OPD in 2:1 ratio in absolute ethanol. The mixture was refluxed and stirred under N₂ for an hour. The orange precipitate formed was filtered off, rinsed with cold methanol and dried in-vacuo over blue silica gel, yielding 93.0%. The reaction scheme is shown in Figure 1.

Synthesis of L2. 3CH₃-MPD and Ovan were mixed in absolute ethanol in 2:1 ratio. The mixture was refluxed and stirred under N₂ for an hour. The orange precipitate formed was filtered off, rinsed with cold methanol and dried under vacuum over blue silica gel, yielding 88.6%. The reaction scheme is shown in Figure 2.

Synthesis of ZnL1. L1 and zinc(II) acetate dihydrate were mixed in 1:1 ratio in ethanol and refluxed with stirring for an hour. The yellowish precipitate formed was filtered off, rinsed with cold ethanol and dried in desiccator over blue silica gel, yielding 97.0%.

Synthesis of Zn₄L2. Synthesis of Zn₄L2 was carried out via a microwave method where L2, zinc(II) acetate dihydrate, triethylamine and absolute EtOH were mixed in a microwave reaction capsule, heated at 160°C for 15 minutes in a microwave at 1000 rpm. A yellow precipitate was observed and the reaction mixture was chilled overnight. The solid was filtered off, rinsed with cold ethanol and dried in a desiccator over blue silica gel, yielding 50.4%.

Physical measurement

The elemental analyses of the synthesised compounds were carried out using Flash EA 110 Elemental Analyzer. IR spectra were recorded as KBr discs using Perkin Elmer FT-IR 1600 Spectrometer from 450 cm^{-1} to 4000 cm^{-1} . The ^1H and ^{13}C NMR spectra were recorded in CDCl_3 and deuterated DMSO using Bruker Avance 300 MHz spectrometer. The melting points of the compounds were recorded using Stuart Melting Point SMP10.

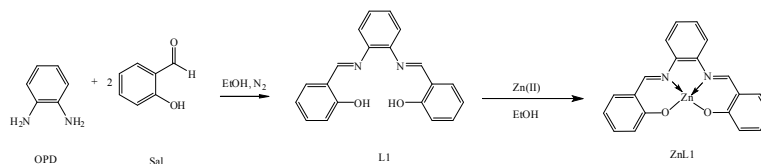


Figure 1. Reaction scheme for synthesis of L1 and ZnL1

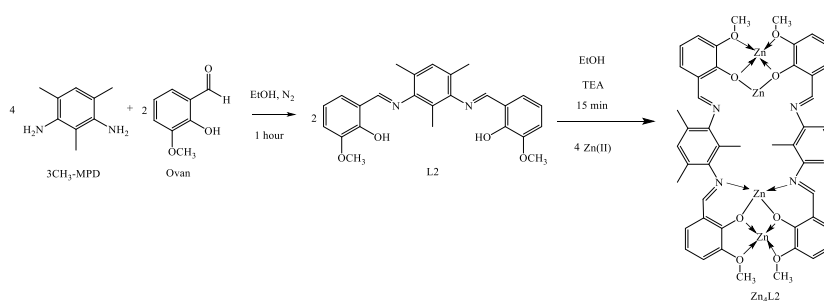


Figure 2. Reaction scheme for synthesis of L2 and Zn₄L₂

RESULTS AND DISCUSSION

Table 1 displays the physical properties and results of elemental analysis of the compounds. The melting points of the organic ligands were much lower than those of the metal complexes, as expected, mostly due to the larger molecular sizes of the complexes and presence of stronger dative covalent bond and ionic bond. The experimental and calculated C, H and N percentages were in close accord, indicating that the expected compounds have been obtained.

Table 1
Physico-chemical data of L1, L2, Zn(L1) and Zn₄(L2)₂

Compound	Molecular Formula (RMM)	Melting Point (°C)	Elemental Percentages Found (Calculated)		
			C (%)	H (%)	N (%)
L1	C ₂₀ H ₁₆ N ₂ O ₂	170	75.07	5.10	8.32
Zn(L1)	(316.36)		(75.93)	(5.00)	(8.86)
	C ₂₀ H ₁₄ N ₂ O ₂ Zn(CH ₃ CO ₂)	> 300	59.29	4.03	8.11
(CH ₃ CO ₂)	(438.72)		(60.22)	(3.91)	(6.38)
L2	C ₂₅ H ₂₆ N ₂ O ₄	151	71.74	6.38	6.57
	(418.49)		(71.75)	(6.26)	(6.69)
Zn ₄ (L2) ₂	C ₅₀ H ₄₈ N ₄ O ₈ Zn ₄	> 300	53.60	4.44	4.35
	(1094.47)		(54.87)	(4.42)	(5.12)

Infrared Spectroscopy

The relevant infrared data are tabulated in Table 2. The spectra of L1 (Figure 3) and L2 (Figure 4) exhibit a peak around 3200 cm⁻¹ due to the O-H stretching vibrations in concordance with the report by Fugu et al. (2013) and this peaks are absent in the ZnL1 and Zn₄L2 spectra, indicating deprotonation of phenolic oxygen upon coordination with zinc(II). This was corroborated by the shifting to lower frequencies of the ν(C-O) (phenolic) in both ZnL1 and Zn₄L2 when compared with the parent ligands L1 and L2 respectively, indicating direct involvement of phenolic O in complexation.

The strong sharp peaks at 1612 and 1617 cm⁻¹ in L1 and L2 respectively, are attributed to the ν(C=N) as reported by Bahron et al. (2012) and Abdel-Kader et al. (2016). These peaks shifted in ZnL1 and Zn₄L2 spectra indicating that the imine nitrogen is involved in the coordination with Zn(II), where the lone pair of electrons on N is shared with the Zn centre in a dative manner.

Arshad et al. (2016) reported that the ν(M-N) and ν(M-O) peaks would appear in the region below 600 cm⁻¹. New weak bands at 550 cm⁻¹ and 560 cm⁻¹ in the spectra of ZnL1 and Zn₄L2 respectively, are attributable to ν(M-N). The peaks for ν(M-O) were not detected, and expected to be below 500 cm⁻¹. The ν(C-O) of the methoxy group in Zn₄L2 is observed in a lower frequency than in the parent ligand L2, signifying the involvement of methoxy oxygen in bonding with Zn to form the tetranuclear complex. This data supports the suggested structure of Zn₄L2 in Figure 2.

L1 is indicated to act as a tetradentate chelating agent as it bonds to metal ion via two phenolic oxygens and two azomethine nitrogen. On the other hand, L2 acts as a hexadentate ligand, coordination to zinc(II) centres via two methoxy O, two phenoxo O and two imino N donor atoms.

Table 2
Infrared data of L1, L2, Zn(L1) and Zn₄L2

Compound	$\nu(\text{C}=\text{N})$	$\nu(\text{C}-\text{O})$ Phenolic	$\nu(\text{C}-\text{O})$ Methoxy	$\nu(\text{M}-\text{N})$
L1	1612	1276	-	-
ZnL1(CH ₃ CO ₂)	1615	1179	-	550
L2	1617	1255	1088	-
Zn ₄ L2	1607	1219	1076	560

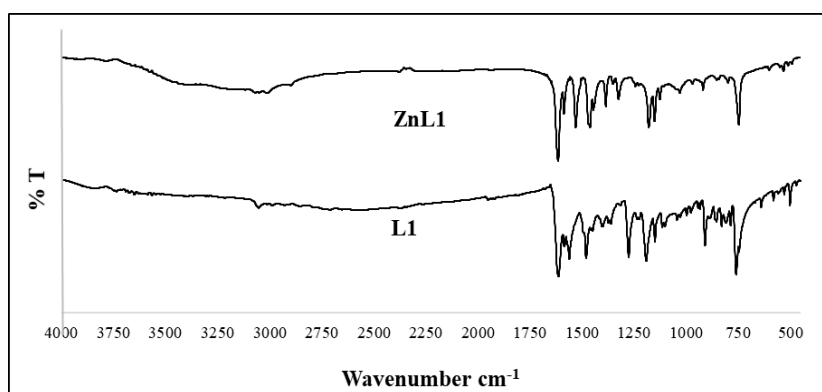


Figure 3. The IR spectra of L1 and ZnL1

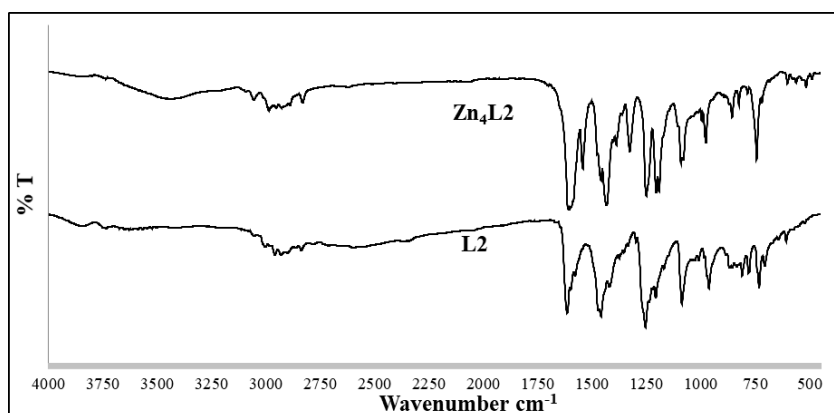


Figure 4. The IR spectra of L2 and Zn₄L2

¹H NMR Spectroscopy

¹H NMR data provided additional support and significant evidence regarding the formation of complexes. The spectrum of L1 (Figure 5) shows signals at 13.12, 9.92 and 6.87-7.53 ppm corresponding to phenolic, azomethine and aromatic protons respectively. The O-H signal in

L1 appears around 13.0 ppm, heavily shielded due to the presence of O and possible inter- or intramolecular hydrogen bonding. The absence of O-H peak in ZnL1 spectrum indicated the deprotonation of OH upon coordination with zinc(II) through the phenolic oxygen.

The imine proton signal shifted slightly upfield in ZnL1 complex indicating that the imine nitrogen is involved in coordination with the metal ion. Similar observation was made in ¹H NMR spectra of L2 and Zn₄L2 (Figure 6). The OH signal at 9.95 ppm disappeared in Zn₄L2 indicating deprotonation upon complexation. The singlet at 8.30-8.37 attributed the signal of azomethine proton of L1. This peak shows an upfield shift in Zn₄L2 complex. The methoxy and methyl chemical shifts of both L2 and Zn₄L2 appear at regions 3.95-3.89 ppm and 1.60-2.30 ppm respectively.

The chemical shift at 0.85 ppm of ZnL1 assignable to acetate corroborated with elemental analysis data that shows the presence of acetate Najjihah et al.(2010), either as part of the compound or as an impurity.

Table 3
¹H NMR data of L1, L2, Zn(L1) and Zn₄(L2)₂

Compound	N=C-H	O-H	Ar-H	OCH ₃	CH ₃	CH ₃ CO ₂
L1	9.92 (s)	13.12 (s)	6.87-7.53 (m)	-	-	-
ZnL1(CH ₃ CO ₂)	8.98 (s)	-	6.47-7.85 (m)	-	-	-
L2	8.30-8.37 (s)	9.95 (s)	6.92-7.29 (m)	3.95-4.10 (s)	2.07-2.30 (s)	-
Zn ₄ L2	7.88-8.37 (s)	-	6.56-7.21 (m)	3.89-3.98 (s)	1.60-2.35 (s)	0.85 (s)

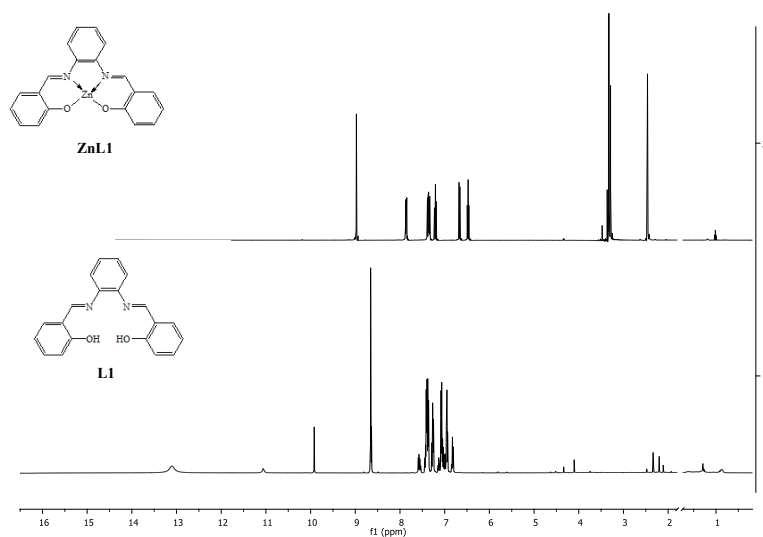


Figure 5. ¹H NMR spectra of L1 and ZnL1

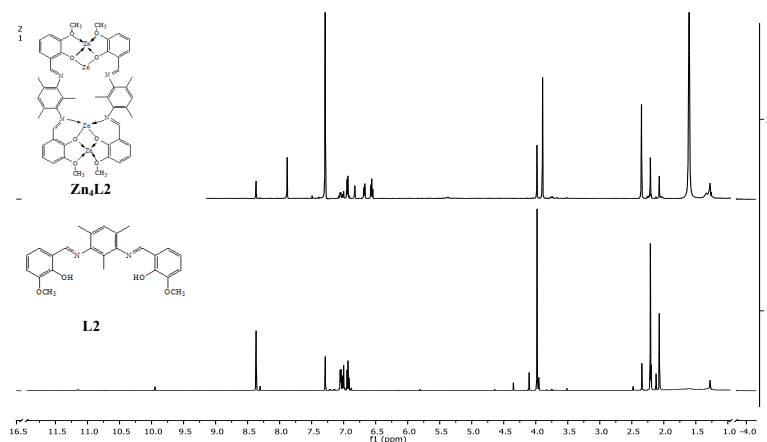


Figure 6. ^1H NMR spectra of L2 and Zn_4L_2

CONCLUSION

A mononuclear and new tetranuclear zinc complexes were synthesised by complexation of phenylenediamine Schiff base ligands L1 and L2 with zinc(II). All compounds were successfully characterised using elemental analysis, melting point, ^1H NMR and IR spectroscopy.

ACKNOWLEDGEMENT

The authors would like to thank the Ministry of Higher Education for the Research Acculturation Grant Scheme 600-RMI/RAGS 5/3 (139/2014) and Universiti Teknologi MARA for their assistance in carrying out this research.

REFERENCES

- Abdel-Kader, N. S., El-Ansary, A. L., El-Tayeb, T. A., & Elnagdi, M. M. F. (2016). *Synthesis and characterization of Schiff base complexes derived from cephradine: Fluorescence, photostability and photobiological applications. Journal of Photochemistry and Photobiology A: Chemistry* (Vol. 321). Elsevier B.V. <https://doi.org/10.1016/j.jphotochem.2016.01.021>
- Abu-Dief, A. M., & Mohamed, I. M. A. (2015). A review on versatile applications of transition metal complexes incorporating Schiff bases. *Beni-Suef University Journal of Basic and Applied Sciences*, 4(2), 119–133. <https://doi.org/10.1016/j.bjbas.2015.05.004>
- Alim, A., Zahan, K. E., Haque, M., & Tarafder, M. (2015). Synthesis and Characterization of Some Metal Complexes of Cu(II), Ni(II), Zn(II), Cd(II), Sn(II), Co(II), Sb(III) AND Fe(III) Containing Bidentate Schiff Base of Smdtc. *Science Journal of Chemistry*, 3(3), 35–39. <https://doi.org/10.11648/j.sjc.20150303.11>

- Arshad, R., Bukhari, I. H., Anum, F., & Aftab, Z. (2016). Spectral and Biological studies of transition metal complexes of schiff base derived from Ofloxacin. *International Journal of Advanced Research in Biological Sciences Synthesis*, 3(4), 99–108.
- Bahron, H., Bakar, N. A., Yamin, B. M., & Yusof, M. S. M. (2012). 6,6'-Dimethoxy-2,2'-[(E, E')-(2,4,6-trimethyl-1,3-phenylene)bis(nitrilomethanylylidene)]diphenol chloroform monosolvate. *Acta Crystallographica Section E Structure Reports Online*, 68(4), o1176–o1176. <https://doi.org/10.1107/S1600536812011531>
- Cordes, E. H., & Jencks, W. P. (1963). The Mechanism of Hydrolysis of Schiff Bases Derived from Aliphatic Amines. *Journal of the American Chemical Society*, 85(18), 2843–2848. <https://doi.org/10.1021/ja00901a037>
- El-Sonbati, A. Z., Diab, M. A., El-Bindary, A. A., Mohamed, G. G., Morgan, S. M., Abou-Dobara, M. I., & Nozha, S. G. (2016). Geometrical structures, thermal stability and antimicrobial activity of Schiff base supramolecular and its metal complexes. *Journal of Molecular Liquids*, 215, 423–442. <https://doi.org/10.1016/j.molliq.2015.12.006>
- Fugu, M. B., Ndahi, N. P., Paul, B. B., & Mustapha, A. N. (2013). Synthesis, characterization, and antimicrobial studies of some vanillin schiff base metal (II) complexes. *Journal of Chemical and Pharmaceutical Research*, 5(4), 22–28.
- Najihah, S., Bakar, A., Bahron, H., & Kassim, K. (2010). Synthesis and Characterization of a Novel Schiff Base Derived from 2, 4, 6-trimethyl- m - phenylenediamine with o -vanillin and Its Metal Complexes. *CSSR 2010 - 2010 International Conference on Science and Social Research*, (Ccsr), 463–466. <https://doi.org/10.1109/CSSR.2010.5773821>
- Qin, W., Long, S., Panunzio, M., & Biondi, S. (2013). Schiff bases: A short survey on an evergreen chemistry tool. *Molecules*, 18(10), 12264–12289. <https://doi.org/10.3390/molecules181012264>



Corrosion Inhibition of Azomethines Containing Hydroxyl Group at *Ortho* and *Para* Positions on Mild Steel

Syaidah Athirah Dzolin^{1*}, Yusairie Mohd¹, Hadariah Bahron¹ and Nurul Huda Abdul Halim²

¹Faculty of Applied Sciences, Universiti Teknologi MARA (UiTM), 40450 Shah Alam, Selangor, Malaysia

²Faculty of Applied Sciences, Universiti Teknologi MARA (UiTM), 72000, Kuala Pilah, Negeri Sembilan, Malaysia

ABSTRACT

The syntheses of salicylideneaniline (L1a) and 4-hydroxybenzalaniline (L1b) was carried out via condensation reaction giving yields of 80.74% and 81.65% respectively. The compounds were characterised by physical and spectroscopic techniques, namely melting point, micro elemental analysis (C, H and N), ¹H Nuclear Magnetic Resonance (NMR) and Infrared (IR) spectroscopy. The characteristic $\nu(\text{C}=\text{N})$ peaks were observed at 1615 cm^{-1} and 1575 cm^{-1} respectively. Chronoamperometry (CA) was employed to electrodeposit both compounds on mild steel at 0.1 M inhibitor concentration in 0.3 M NaOH at three different potentials, +0.8 V, +1.05 V and +1.7 V. Formation of yellow imine films was observed on the mild steel. The corrosion behaviour of coated and uncoated mild steel was studied using Linear Polarization Resistance (LPR) in 0.5 M NaCl. Coated mild steel showed better corrosion resistance and with the highest inhibition efficiency of 90.34%, L1a provides a better protection against corrosion for mild steel than L1b.

Keywords: Azomethine, chronoamperometry, corrosion inhibition, electrodeposition, LPR

ARTICLE INFO

Article history:

Received: 28 September 2016

Accepted: 03 February 2017

E-mail addresses:

syaidahzolin@yahoo.com (Syaidah Athirah Dzolin),

hadariah@salam.uitm.edu.my (Hadariah Bahron),

yusairie@salam.uitm.edu.my (Yusairie Mohd),

nurulhuda1596@ns.uitm.edu.my (Nurul Huda Abdul Halim)

*Corresponding Author

INTRODUCTION

The use of mild steel is ubiquitous in everyday life in most constructions, vehicles, pipelines and even in household items. However, mild steel has its own disadvantages in which it has poor corrosion resistance. When iron or steel is exposed to atmospheric oxygen in the presence of water, the process of rusting takes place. Iron is degraded to ferric rust, a red-brown compound, which signals the electrochemical oxidation of the metal.

Inhibitors are chemicals when added in small amount into a system can protect it from corrosion. The inhibitors retard corrosion by either increasing the anodic or cathodic polarisation resistance of the cell or preventing the diffusion of ions onto the metallic surface (Harun, 2010). Many organic compounds have been studied for their corrosion inhibition potential, for example, the effect of organic nitrogenous compounds on the corrosion behaviour of iron and steel in acidic medium (Abdul Ghani et al., 2014) and these organic compounds are usually employed because of their rapid action (Myint et al., 1996; Behpour et al., 2009).

Azomethines or Schiff bases are commonly synthesised through condensation of primary amines with active carbonyl compounds and they were first reported in 1864 by Hugo Schiff (Cimerman et al., 2000). Schiff bases with their characteristic C=N functional group are known as nitrogen bearer inhibitors, commonly chosen due to the presence of lone pairs of electrons in their molecular structures. Their planarity increases the absorptivity on the active sites of metal surface as reported by several investigators (Hashim et al., 2014; Mallaiya et al., 2011; Ju et al., 2008). Electronic tuning of the molecular structures to study their adsorption behaviour, hence corrosion inhibition, may include addition of electron rich aromatic rings as well as electron donating and withdrawing moieties as reported by Sauri et al. (2009).

The purpose of this study was to synthesise and characterise two Schiff bases, salicylideneaniline (L1a) and 4-hydroxybenzaldehyde (L1b) which have very similar chemical structures except for the position of -OH (Figure 1). The corrosion behaviour of mild steel coated with L1a and L1b was studied in 0.5 M NaCl using linear polarisation resistance (LPR) and compared with that of the uncoated mild steel. The differences of inhibition efficiency of the compounds are explained based on their chemical structures.

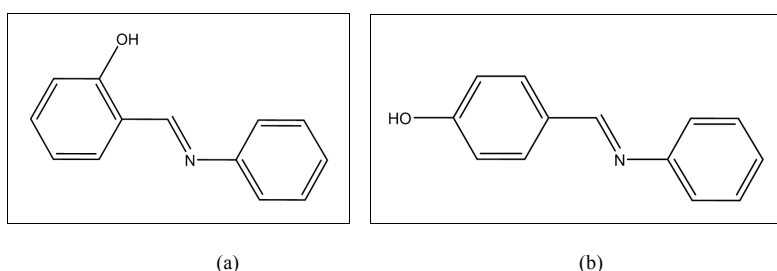


Figure 1. Molecular structures of (a) salicylideneaniline (L1a) and (b) 4-hydroxybenzaldehyde (L1b)

METHOD

Materials

All the chemicals and solvents used were of analytical grade. Salicylaldehyde, 4-hydroxybenzaldehyde, aniline, absolute ethanol, chloroform, deuterated chloroform (CDCl_3) and deuterated dimethylsulfoxide (DMSO), and potassium bromide (KBr) were purchased from commercial suppliers and used without further purification. The micro-analytical data (C, H and N) of L1a and L1b were obtained from Thermo Scientific Flash 2000 Elemental Analyzer. Melting points were determined using Stuart SMP10. Perkin-Elmer model 1750X

FTIR spectrophotometer using KBr pellets was employed to record Infrared (IR) spectra of synthesised compounds in range of 4000-450 cm^{-1} . ^1H NMR spectra were analysed on a Bruker Varian-500 and 600 MHz spectrometer using deuterated chloroform (CDCl_3) and deuterated dimethylsulfoxide (DMSO) and expressed in a unit of parts per million (d, ppm).

Synthesis and Characterisation Of Salicylideneaniline (L1a)

A mixture of 20 mmol of salicylaldehyde and 20 mmol of aniline in absolute ethanol (15 mL) was refluxed for three hours. The yellow precipitate formed was filtered off and washed thoroughly with cold ethanol, dried and weighed (3.185 g, 80.74%). Melting point 53°C , (Found: C, 78.16; H, 5.57; N, 6.95. $\text{C}_{13}\text{H}_{11}\text{NO}$ requires C, 79.16; H, 5.62; N, 7.10 %); n_{max} (KBr): C=N, 1615; Ar-OH, 1274; C=C, 1400 cm^{-1} ; ^1H NMR (CDCl_3) δ/ppm : 7.24-7.31 (4 H, m, aromatic), 7.35-7.45 (4H, m, aromatic), 8.63 (1 H, s, CH), 13.27 (1H, s, OH).

Synthesis and Characterization of 4-hydroxybenzaldehyde (L1b)

A mixture of 20 mmol of 4-hydroxybenzaldehyde and 20 mmol of aniline in absolute ethanol (15 mL) was refluxed for 3 hours. The light yellow precipitate formed was filtered off and washed thoroughly with cold ethanol. It was air dried and weighed (3.2208 g, 81.65%). Melting point 198°C , (Found: C, 78.15; H, 5.58; N, 6.90. $\text{C}_{13}\text{H}_{11}\text{NO}$ requires C, 79.16; H, 5.62; N, 7.10 %); n_{max} (KBr): C=N, 1575; Ar-OH, 1285; C=C, 1400 cm^{-1} ; ^1H NMR (DMSO) δ/ppm : 7.17-7.24 (3H, m, aromatic), 8.46 (1 H, s, CH), 10.15 (1 H, s, OH).

Electrodeposition of Mild Steel and Corrosion Test

A conventional three-electrode cell was used consisting of mild steel as working electrode, an Ag/AgCl electrode as reference electrode and platinum rod as counter electrode. The working electrode of mild steel was prepared by embedding the mild steel in epoxy resin and exposing a flat surface area of 1 cm^2 . The working electrode was abraded with a series of silica carbide paper from 320 grit up to 4000 grit, and then polished to mirror finish using diamond paste. Finally, it was washed with distilled water, degreased with acetone and left to dry in a desiccator.

The electrodeposition was carried out via chronoamperometry (CA) technique in alkaline bath solution containing L1a or L1b at 0.1 M concentration. All electrolytes were freshly prepared for each experiment. The corrosion behaviour of coated mild steel in 0.5 M NaCl was studied using Linear Polarization Resistance (LPR). Before the measurement, the working electrode was immersed in electrolyte for 15 minutes to obtain a steady state open circuit potential (OCP).

RESULTS AND DISCUSSION

The successful synthesis of L1a and L1b was indicated by the close agreement between the calculated and the experimental percentages of C, H and N. The signature IR peaks $n(\text{C}=\text{N})$ of azomethine were detected as strong bands at 1615 and 1575 cm^{-1} for L1a and L1b respectively.

Comparing these two compounds, it is interesting to note that the closer proximity of –OH to C=N in L1a, where the two functional groups are located *ortho* to one another, resulted in a stronger C=N bond indicated by the significantly higher IR absorption frequency than in L1b.

In the ¹H NMR spectroscopy, the presence of –OH in L1a and L1b is indicated by the chemical shift at 13.3 and 10.15 ppm respectively. The phenolic proton in L1a is highly deshielded by the C=N which is close to –OH, making hydrogen bonding possible. This causes the chemical shift to appear at the downfield region of 13.3 ppm, compared with the less deshielded –OH of L1b. Both the IR and NMR results showed intramolecular interaction between the hydroxyl and imine groups, especially for L1a.

Electrodeposition of L1a and L1b on Mild Steel

Chronoamperometry (CA) method was used to electrodeposit both compounds on mild steel. Figure 2 shows the chronoamperometric curves at three different potentials of 0.8 V, +1.05 V and +1.7 V based on the potential obtained from a cyclic voltammogram curves. CA was carried out in 0.3 M NaOH containing either 0.1 M L1a or 0.1 M L1b and recorded for 15 minutes of deposition. Current reduction was observed during the 15 minutes of deposition, particularly in the first minute.

For L1a, stationary current was achieved after about 5 minutes (300 seconds) for all deposition potentials used until deposition is completed. But for L1b, the stationary current was achieved after 10 minutes (600 seconds) for potentials at +0.8 V and +1.05 V, and 5 minutes (300 seconds) for +1.7 V. This shows that inhibitive layer of L1a forms faster than L1b. The suppression suggests that insulating properties of the film caused the disturbance of current flow causing current reduction (Genbour et al., 2000).

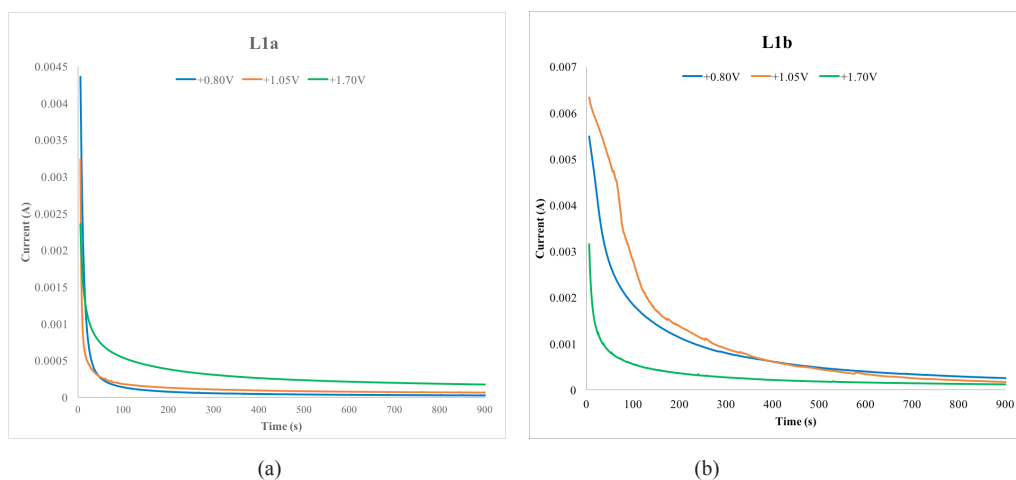
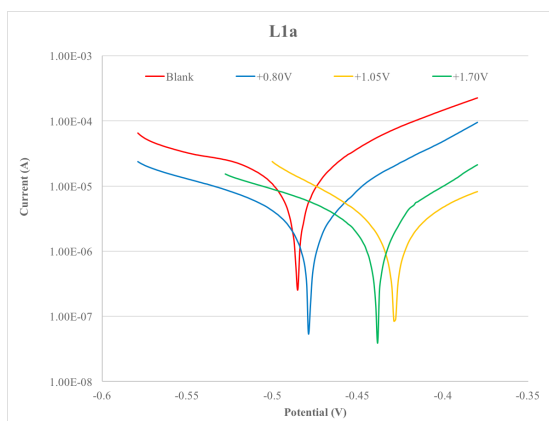


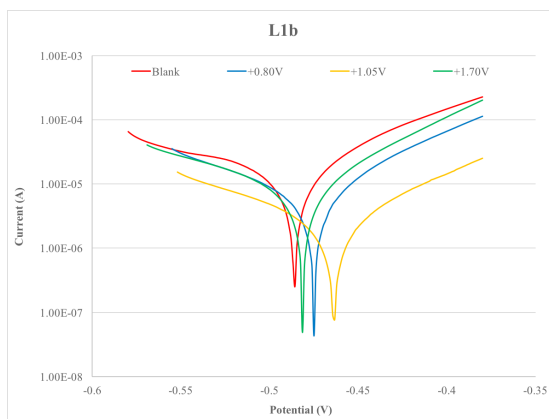
Figure 2. Chronoamperometric curves of deposition of: (a) L1a; and (b) L1b coatings on mild steel at three different deposition potentials

Potentiodynamic Polarization Measurements

The mild steel samples coated with L1a and L1b Schiff bases using chronoamperometry at three different deposition potentials were investigated for their corrosion inhibition efficiency. Figure 3 shows the Tafel polarisation curves of uncoated mild steel and mild steel coated with L1a (Figure 3(a)) and coated mild steel with L1b (Figure 3(b)) in 0.5M NaCl.



(a)



(b)

Figure 3. Tafel polarisation curves of uncoated and coated mild steel with: (a) L1a; and (b) L1b prepared at different deposition potential in 0.5M NaCl

Table 1 shows electrochemical parameters i.e. anodic Tafel slope (β_a), cathodic Tafel slope (β_c), corrosion potential (E_{corr}), corrosion current density (i_{corr}), corrosion rate (mm/yr), polarisation resistance ($k\Omega$) and inhibition efficiency (IE%). The inhibition efficiency of L1a and L1b Schiff bases was calculated using the following equation (Bagavathy & Ganesan, 2015):

$$IE\% = \frac{i_{corr}^o - i_{corr}}{i_{corr}^o} \times 100 \quad [1]$$

Where, i_{corr}^o and i_{corr} are uncoated and coated current densities, respectively.

Table 1
Corrosion inhibition of L1a and L1b on mild steel in 0.5 M NaCl

Compound	Potential (V)	β_a (mV/dec)	β_c (mV/dec)	E_{corr} (mV)	i_{corr} (mA/cm ²)	Corrosion rate (mm/year)	Polarisation resistance (k Ω)	Inhibition efficiency (%)
Blank	-	543.270	124.880	-485.120	35.3800	0.41111	1.24640	-
L1a	+0.8V	118.840	63.3960	-462.600	3.83920	0.044611	4.67660	90.34
	+1.05V	111.260	145.870	-412.950	4.62430	0.053734	5.92790	86.93
	+1.7V	672.330	121.150	-420.890	8.35880	0.097129	5.33360	76.37
L1b	+0.8V	187.510	90.0850	-443.780	10.7200	0.12457	2.46520	69.70
	+1.05V	196.520	117.580	-431.530	4.66170	0.054169	6.85370	86.82
	+1.7V	237.700	92.6370	-455.440	14.3040	0.16621	2.01170	59.57

From Figure 3(a), it is observed that current densities of the polarisation curves have decreased for all mild steel coated with L1a compared with the blank uncoated mild steel. For L1a, the inhibition efficiencies of all deposition potentials have defeated those of L1b. The highest inhibition efficiency was recorded by mild steel coated at +0.8 V with 90.34% efficiency corresponding to 0.044611 mm/yr corrosion rate. Meanwhile, data extracted from Figure 4(b) indicates that the inhibition efficiency of L1b is lower than that of L1a. The highest inhibition efficiency by L1b was recorded to be 86.82% which was mild steel coated at +1.05 V.

Thus, it can be concluded that the inhibitive film formed using the azomethine with hydroxyl group at *ortho* position (L1a) is more protective than the corresponding compound with hydroxyl group at *para* position (L1b). This shows that the L1a inhibitive film formed on the mild steel using low deposition potential deposited from bath solution provided more efficient corrosion protection than L1b.

Generally, both Schiff bases (L1a and L1b) have good corrosion protection efficiency for mild steel in 0.5 M NaCl. It may be associated with the presence of: (a) aromatic π electrons with conjugated double bonds; (b) π electrons of azomethine group; and (c) the electronegative heteroatom (N) bearing lone pairs of electrons present in both compounds. In addition, high inhibition efficiencies of both compounds are also due to the presence of hydroxyl substituent group on the aromatic ring.

Electron donating hydroxyl group has the inductive effect which enriches electron density and activates the aromatic ring and C=N, giving good absorptivity for the inhibitors. It was also found that the position of -OH in azomethine compound is shown to affect the corrosion inhibition efficiency. L1a has -OH at the *ortho* position while L1b has -OH at the *para* position of the aromatic ring. The closer proximity of -OH to C=N in L1a can activate the lone pair of electrons on N for adsorption on mild steel better than L1b. The mechanism of this effect is illustrated in Figure 4.

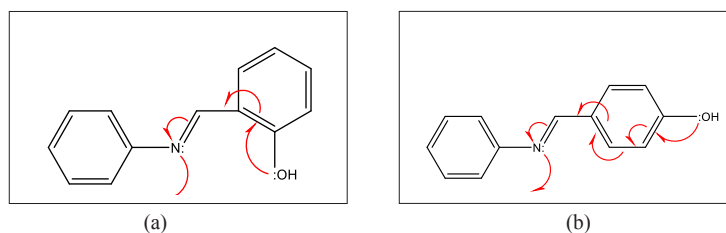


Figure 4. Mechanisms of inductive effect of: (a) L1a; and (b) L1b

This mechanism is strongly supported by the spectral evidence discussed above. The relatively strong C=N bond in L1a apparent in the higher IR frequency of 1615 cm^{-1} is in concordance with its more active role in adsorption to mild steel, resulting in stronger film coverage and better corrosion inhibition.

The lesser activated C=N in L1b due to the relative distance of -OH group showed a less efficient corrosion protection of mild steel. It is clear that intramolecular interaction between the -OH and C=N moieties in both compounds affect their corrosion inhibition properties.

CONCLUSION

Both Schiff bases, L1a and L1b, were successfully synthesised and characterised. Electrodeposition using chronoamperometry technique shows good formation of both films on mild steel surface. Corrosion inhibition studies using linear polarisation resistance show that both compounds have inhibition properties. The highest inhibition efficiency was mild steel coated with L1a at +0.8 V with 90.34% efficiency corresponding to 0.044611 mm/yr corrosion rate, while the inhibition efficiency of L1b Schiff base was lower than mild steel coated with L1a in 0.5 M NaCl. The highest inhibition efficiency by L1b was 86.82% with mild steel coated at +1.05 V. The position of hydroxyl group nearer the imine (*ortho* position) group in L1a activated the lone pair of N more effectively than L1b.

ACKNOWLEDGEMENTS

The authors express their gratitude to the Ministry of Higher Education, Malaysia, for its Research Acculturation Grant Scheme 600-RMI/RAGS 5/3 (20/2014) and Universiti Teknologi MARA (UiTM) for enabling them to avail its research facilities.

REFERENCE

- Abdul Ghani, A., Bahron, H., Harun, M. K., & Kassim, K. (2014). Schiff bases derived from isatin as mild steel corrosion inhibitors in 1 M HCl. *The Malaysian Journal of Analytical Science*, 18(3), 507-513.
- Bagavathy, S. M. S., & Ganesan, P. K. (2015). Corrosion inhibition studies on Schiff bases derived from 2-amino-6-methoxy-benzothiazole. *Journal of Chemical and Pharmaceutical Research*, 7(2), 830-839.

- Bao, L., Xiong, R., & Wei, G. (2010). Electrochemical polymerization of phenol on 304 stainless steel anodes and subsequent coating structure analysis. *Electrochimica Acta* 55(12), 4030-4038.
- Behpour, M., Ghoreishi, S. M., Gandomi-Niasar, A., Soltani, N., & Salavati-Niasari, M. (2009). The inhibition of mild steel corrosion in hydrochloric acid media by two Schiff base compounds. *Journal of Material Science*, 44, 2444–2453.
- Cimerman, Z., M., & Galic, S. N. (2000). The geometry and electronic structure of substituted Schiff's bases. *Croatia Chemica Acta*, 73(1), 81- 95.
- Guenbour, A., Kacemi, A., Benbachir, A., & Aries, L. (2000). Electropolymerization of 2-aminophenol: Electrochemical and spectroscopic studies. *Progress in Organic Coating*, 38(2), 121-126.
- Harun, M. K. (2010). Corrosion Protection by Paints and Organic Inhibitors: The Inside Story. *University Publication Centre (UPENA)*, ISBN 978-967-363-007-3.
- Hashim, N. Z. N., & Kassim, K. (2014). The Effect of Temperature on Mild Steel Corrosion in 1M HCl by Schiff Bases. *The Malaysian Journal of Analytical Sciences*, 18(1), 28-36.
- Ju, H., Kai, Z.P., & Li, Y. (2008). Aminic nitrogen-bearing polydentate Schiff base compounds as corrosion inhibitors for iron in acidic media: A quantum chemical calculation. *Corrosion Science*, 50, 865-871.
- Mallaiya, K., Subramaniam, R., Srikandan, S.S., Gowri, S., Rajasekaran, N., & Selvaraj A. (2011). Electrochemical characterization of the protective film formed by the unsymmetrical Schiff's base on the mild steel surface in acid media. *Electrochimica Acta*, 56(11), 3857-3863.
- Myint, S., Daud, W. R. W., Mohamad, A. B., & Kadhum, A. A. H. (1996). Gas chromatographic determination of eugenol in ethanol extract of cloves. *Journal Chromatography*, 679(1-2), 193–195.
- Sauri, A. S. M., Kassim, K., Bahron, H., & Yahya, M. Z. A. (2009). Investigation on effects of substituents in N,N'-dibenzylidene ethane-1,2- diamine towards corrosion inhibition on steel in 1 M HCl. *Materials Research Innovations*, 13(3), 305-308.
- Tahar, N. B., & Savall, A. (2009). Electropolymerization of phenol on a vitreous carbon electrode in alkaline aqueous solution at different temperatures. *Electrochimica Acta.*, 55(2), 465-469.



Assessment of the Genetic Variability and Fibre Composition of Gamma Ray induced Mutant Lines of Ginger (*Zingiber officinale* Roscoe)

Nor Yusliza Kamaruddin^{1*} and Shamsiah Abdullah^{1,2}

¹Faculty of Plantation and Agrotechnology, Universiti Teknologi MARA (UiTM), 40450 Shah Alam, Selangor, Malaysia

²Agricultural Biotechnology Research Group, Faculty of Plantation and Agrotechnology, Universiti Teknologi MARA (UiTM), 40450 Shah Alam, Selangor, Malaysia

ABSTRACT

This study looked at mutagenic effectiveness of gamma rays on two varieties of *Zingiber officinale* Roscoe: Bentong and Tanjung Sepat. The rhizomes were exposed to different doses (0, 5, 7, 9, 11, 13 and 15 Gy) using Caesium-137 as source of the gamma rays. The effect of different gamma doses on the crude fibre composition of irradiated ginger was studied and genetic variability was assessed using molecular marker technique, RAPD. Findings showed different doses of gamma rays could induce variability in these two ginger varieties and the effect was found to be variety-dependent. Bentong variety irradiated with 9 Gy recorded 8.53% of crude fibre composition while Tanjung Sepat irradiated ginger with 5 Gy recorded 8.70% of crude fibre which gave the lowest composition compared with other irradiated ginger. A total of nine different arbitrary decamers were used as primers to amplify DNA from mutant plant material to assess their polymorphism level of ginger mutant lines. Polymorphism of all mutant lines was 97.62% indicating that there were significant changes in genetic sequences in irradiated ginger genotypes.

Keywords: Gamma rays, mutation, RAPD, *Zingiber officinale* Roscoe

ARTICLE INFO

Article history:

Received: 28 September 2016

Accepted: 03 February 2017

E-mail addresses:

noryusliza91@gmail.com (Nor Yusliza Kamaruddin),

shamsiah3938@salam.uitm.edu.my (Shamsiah Abdullah)

*Corresponding Author

INTRODUCTION

Ginger (*Zingiber officinale* Roscoe) from the family Zingiberaceae, is a rhizomatous and monocotyledonous perennial herb. Much valued as a spice, medicine, it has pungent taste and a spicy aroma. In Malaysia, ginger has been cultivated commercially in Pahang, Selangor, and Sabah and Sarawak regions. The main ginger varieties that have been

cultivated in Malaysia are Bentong, Tanjung Sepat, Bara and China (Suhaimi et al., 2012). Ginger cultivation is seriously handicapped by its low variability, absence of natural seed set, and asexual reproduction with exclusive vegetative propagation (Jatoi & Watanabe, 2013; Palai & Rout, 2007). Moreover, local farmers prefer ginger varieties with which have low crude fibre content suitable for local market and also for industrial processing at commercial scale. It is widely believed that the Tanjung Sepat ginger is highly fibrous and hence not suitable for local markets. Thus, broadening the genetic base of ginger through mutagenesis is an alternative way for variability modification of plant with desirable traits. Induced mutation using gamma rays is one of the most effective techniques for morphological and genetically variability in plants mainly among those with limited genetic background. Many crop improvement programmes apply this technique (Aziliana et al., 2015; Varsha, Gowda, & Ramesh, 2009; Mohammadzai et al., 2010), so it is a proven practical approach of creating or altering physiological characters within crop varieties to induce desired quality traits which either cannot be expressed in nature or lost during evolution (Iwo et al., 2012).

Molecular markers are gaining attention to determine the direct comparison of the effects of gamma rays at DNA level. Random Amplified Polymorphisms DNA (RAPD) provides a quick and efficient screen for DNA sequence based polymorphism due to the sum of a very large number of loci (Kumari & Thakur, 2014). The mutation detection, PCR based RAPD technique, is reliable and reproducible and used in various mutant as shown by Varsha, Gowda and Ramesh (2009) on groundnut, Mullainathan et al., (2014) on chili, and Afrasiab and Iqbal (2012) on potato. The PCR based RAPD method provides excellent DNA profiling for phylogenetic analysis, population studies and molecular selection (Williams et al., 1990). Considering the effect of radiation on plants, the objective of this study is to determine the effect of gamma rays on crude fibre composition and assessment on the genetic variability in ginger mutant lines.

METHOD

Plant Materials and Gamma Irradiation

Rhizomes samples of Bentong and Tanjung Sepat varieties were obtained from Agricultural Department of Putrajaya, Malaysia. The rhizomes were cut into smaller pieces of about 4-5 cm long and contained 2 or 3-point buds. The rhizomes moisture content was equilibrated prior to irradiation. The irradiation treatments were 0 (control), 5, 7, 9, 11, 13 and 15 Gray at dose rate of 4.31 Gy per minute with eight replications. Gamma rays used in this study was emitted from the Caesium-137 source using Biobeam GM 8000 Germany machine at Agensi Nuklear Malaysia (AMN), Bangi, Selangor. The irradiated rhizomes bits were planted in a polyethylene bags containing a mixture of garden loam soil, sand and cocoa peat sowing media at the ratio of 3:2:1. The irradiated plants were placed in a rain shelter located at Universiti Teknologi MARA (UiTM), Kampus Puncak Alam, Selangor, Malaysia. The duration of the experiment was between March and December 2015.

Determination of Crude Fibre Composition

Based on previous research by Kamaruddin et al., (2016), the optimum lethal dose for ginger was around 9 Gy thus only samples obtained from four treatments (0, 5, 7 and 9 Gy) were factored in the crude fibre and moisture content analysis. Fresh rhizomes were broken up so that all adhering soil could be removed during washing under the running tap water. The washed pieces were cut into 0.3 cm thick slices and stained using food colouring solution to observe the effect of gamma rays on crude fibre composition. Crude fibre composition was determined using Fibertec™ 2010 machines and was carried out at Malaysian Agricultural Research and Development Institute (MARDI) Serdang, Selangor, Malaysia. About 1.0 g of Celite 545 powder and ground rhizomes sample (W1) were added into a crucible. The function of Celite 545 was to simplify the filtration process. Later, 150.0 ml of pre-heated 1.25% H₂SO₄ was poured followed by 150.0 ml of pre-heated of 1.25% NaOH solution into each column of crucible. The treatments were carried out to dissolve all the soluble and insoluble fibres in ginger. All crucibles were transferred to the Fibertec Cold Extraction Unit. The crucibles were dried for at least five hours at 105 ± 2°C and were weighed (W2). Later, samples were exposed to 525 ± 15°C for three hours to obtain ash. The crucible containing white and grey ash (free of carbonaceous material) was cooled in a desiccator and weighed (W3). The crude fibre content in ginger rhizome was estimated using the following formula:

$$\frac{(W2-W3)}{(W1)} \times 100 \quad [1]$$

Where, W1 = Fresh ground rhizomes, W2= Empty crucible, W3= Crucible + ash weight

Plant DNA Extraction and RAPD-PCR Condition

All irradiated ginger (except 15 Gy treatment dose) were assessed for genetic variability. Approximately 10 mg of young and partially opened ginger leaves were ground to powder in liquid nitrogen using a mortar and pestle. The DNA extraction was done using Qiagen Plant Mini Kit to achieve good quality, faster and high purity intact DNA. The nine primers in series OPA, OPD, OPN, OPP, OPU, RN and S designed primarily by Operon Technologies (Alameda, California, USA) (Table 1) were used for genetic variability study. The component of PCR reaction with single primer was performed in a final volume of 25 µl containing 30 ng template DNA, 5 µl 1XTaq Buffer, 1µl 100 µM deoxyribonucleotide triphosphate (dNTP), 3 µl 1.5 mM MgCl₂, 2 µl primer, 0.25 µl 0.5 U Taq DNA polymerase. PCR amplifications were performed with initial denaturation at 94°C for 4 min, followed by 35 cycles of amplification with denaturation at 94°C for 45 seconds, annealing at 37°C for 1 min and extension at 72°C for 2 min and finally at 72°C for 8 min. The amplified products were electrophoresed on 1.5 % agarose gel using 1X TAE buffer and pre-stained by adding 0.20 µL GelStar™ Nucleic Acid Gel stain into the buffer. The size of amplified DNA fragments was examined under UV light.

Table 1
The nucleotide sequences (5' to 3') of the primers from OPERON Tech., USA, RAPD-PCR (Gosh et al., 2014; Harisaranraj et al., 2009)

Primer's name	Primer sequences	(G + C) %
OPA-12	5' T C G G C G A T A G 3'	60
OPA-27	5' G A A A C G G G T G 3'	60
OPA-28	5' G T G A C G T A G G 3'	60
OPN-10	5' C A G C G A C T G T 3'	60
OPN-15	5' A C A A C T G G G G 3'	60
OPP-16	5' C C A A G C T G C C 3'	70
OPU-03	5' C T A T G C C G A C 3'	60
RN-08	5' A C C T C A G C T C 3'	60
S-11	5' G T A G A C C C G T 3'	60

PCR-RAPD Data Analysis

Data analysis was done using a gel documentation system (Gel Doc 1000 System, Sastec) to record the banding patterns on the agarose gel. Amplified products were scored using PYELPH (Version 1.4) software which showed sensitivity in detecting the presence (1) or absence (0) of homologous bands separately for each primer. This was used for estimating polymorphic loci and average linkage or Unweighted Pair Group Mean Averaging (UPGMA) dendrogram of the populations based on Nei's (1972) genetic distance using the POPGENE (Version 1.32) (Yeh et al., 1999) software package. In order to determine pair wise similarity, a similarity index "S" was calculated from band-sharing data of each fingerprint following the formula (Nei & Lei, 1979):

$$\frac{2N_{xy}}{(N_x + N_y)} \quad [2]$$

Where, N_x = the total number of fragments detected in individual 'x', N_y = The total number of fragments shown by individual 'y' and N_{xy} = The number of fragments shared by individuals 'x' and 'y'.

RESULTS AND DISCUSSION

Crude Fibre Composition

The average crude fibre composition of all mutant lines is presented in Table 2. Percentage of crude fibre Bentong mutant lines was between 8.53% and 13.6%. The control ginger had 10.02% crude fibre composition, while mutant lines from ginger irradiated with 5 Gy had the highest composition (13.6%) in accordance with it cross section that showed it was highly fibrous (Figure 1) while the least 8.53 % was found in mutant lines irradiated with 9 Gy in

accordance with its cross section that showed it was less fibrous. For Tanjung Sepat mutant lines irradiated with various doses fibre composition was between 8.7% and 10.19%. The control ginger has 10.10% crude fibre content, while mutant lines irradiated with 9 Gy had the highest composition (10.19%). The lowest composition (8.70 %) was found in mutant lines irradiated with 5 Gy in accordance with its cross section that showed less fibrous content (Figure 2). Crude fibre content in Nigeria ginger varieties were between 8.30% and 21.90 as reported by (Ajayi et al., 2013) another study showed different ginger varieties had crude fibre content in average between 4.8% and 9.0% (Natarajan et al., 1972). Crude fibre analysis of both gingers varied significantly among the mutant lines and a slight decreased fibre composition was observed after irradiation. The decreasing pattern of crude fibre was in conformity with a study by Mohammadzai et al. (2010) and Abdelwhab et al. (2009) on crude fibre content of dry irradiated beans and palm date respectively. Additionally, Bhat et al. (2009), and Bamidele and Akanbi (2013) also reported a decrease in crude fibre content of irradiated lotus seed flour and pigeon pea flour respectively.

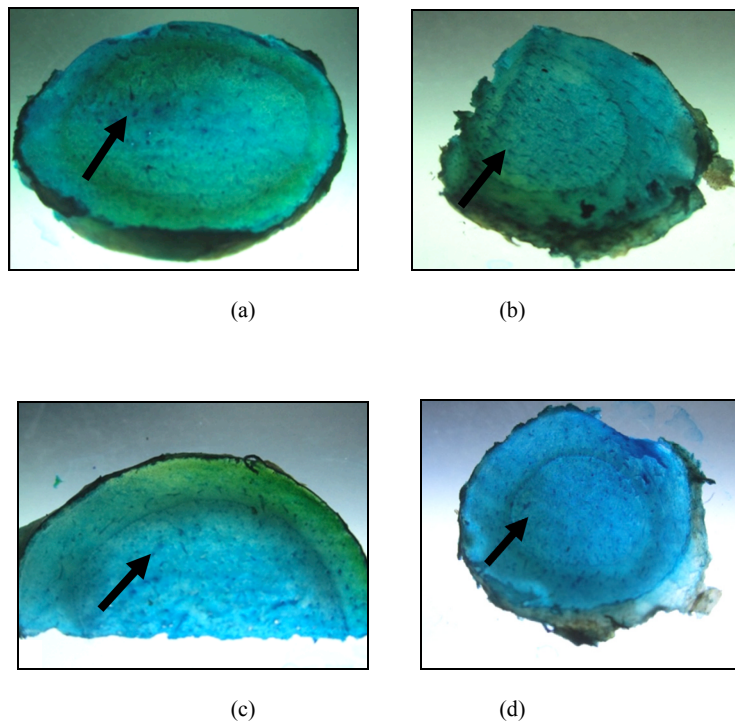


Figure 1. The cross section of irradiated and non-irradiated rhizomes of Bentong variety. Arrow shows the fibre structure: (a) Control ginger; (b) Irradiated ginger at 5 Gy; (c) Irradiated ginger at 7 Gy; and (d) Irradiated ginger at 9 Gy

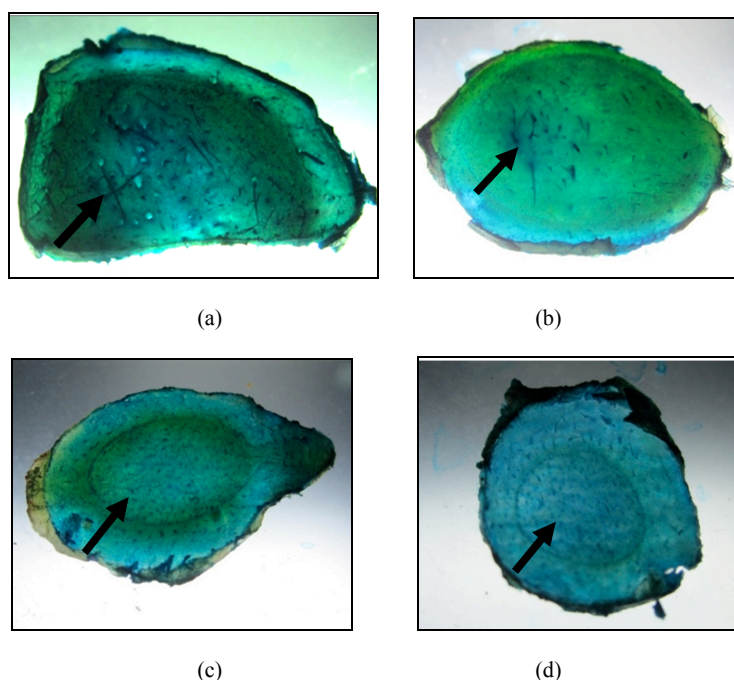


Figure 2. The cross section of irradiated and non-irradiated rhizomes of Tanjung Sepat variety. Arrow shows the fibre structure: (a) Control ginger; (b) Irradiated ginger at 5 Gy; (c) Irradiated ginger at 7 Gy; and (d) Irradiated ginger at 9 Gy

Table 2
Crude fibre of Bentong and Tanjung Sepat ginger

Gamma rays dosage (Gray)	Crude fibre (%)	
	Bentong	Tanjung Sepat
0	10.02±0.20	10.1±0.42
5	13.6±0.22	8.7±1.01
7	11.0±0.84	9.08±0.89
9	8.53±0.33	10.19±1.14

*Data are expressed as mean ± standard error

Genetic variation analysis

In this study, 125 reproducible RAPD bands were scored across two varieties of ginger for all primers and used to evaluate genetic diversity relationships among mutant lines (Figure 3). Scores indicate three were monomorphic and 125 were polymorphic. The overall polymorphism was 97.6% and the rest monomorphic bands. The number of bands (DNA fragments) per primer ranged from six (OPA-12) (OPA-27) to 23 (RN-08), the average number of bands per primer being 13.89 per primer and 13.56 polymorphic bands per primers (Table 3).

Table 3
Analysis of RAPD banding pattern for Bentong and Tanjung Sepat ginger

Primer's name	No. amplified products	No. of polymorphic products	Polymorphic loci (%)
OPA-12	6	6	
OPA-27	6	6	
OPA-28	14	13	
OPN-10	20	20	
OPN-15	14	14	97.62
OPP-16	10	8	
OPU-03	11	11	
RN-08	23	23	
S-11	21	21	
Total	125	122	
Average	13.89	13.56	

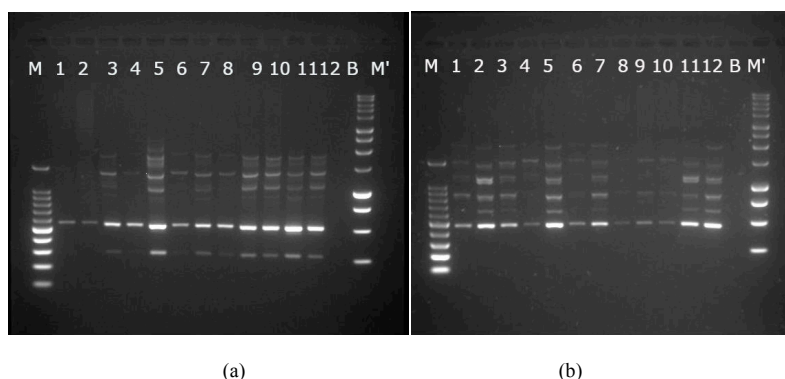


Figure 3. RAPD pattern obtained in gamma ray induced mutant in ginger plant amplified using different primers: (a) OPA-28; and (b) S-11

Based on the Nei's (1972) coefficient, the genetic distances of different irradiated ginger genotype were obtained (see Table 4). The maximum genetic distance of Bentong ginger (0.69) was found between irradiated ginger at 5 and 11 Gy. Minimum genetic distance (0.32) was found between control and irradiated ginger at 7 Gy. Two main clusters were delineated from the dendrogram (Figure 3). However, irradiated Bentong ginger at 5 Gy were found to be quite divergent and did not fall in any of the major clusters. Cluster 1 comprised irradiated ginger at 9, 11 and 13 Gy. Cluster 2 comprised control and irradiated ginger at 7. The proximity matrix based on RAPD analysis of Bentong mutants showed control ginger was more closely genetically related to irradiate ginger at 7 Gy. Other irradiated ginger showed highly genetic variation between them which revealed significant differences in the genotypic diversity among themselves. For Tanjung Sepat ginger, the maximum genetic distance (0.64) was found between control and irradiated ginger at 13 Gy while minimum genetic distance (0.32) was

found between irradiated ginger at 5 and 9 Gy (Table 5). Two main clusters were grouped from the dendrogram (Figure 4). Cluster 1 comprised control, irradiated ginger at 7 and 11 Gy while Cluster 2 comprised irradiated ginger at 5, 9 and 13 Gy.

Overall, both varieties showed genetic variability was not exactly proportional to the doses of gamma rays when genetic distances were examined. This is because the trend of genetic variability sometimes was proportional to the doses of gamma rays within a certain range (Teng et al. 2008). However, the findings of this research provide insights for the RAPD analysis which had been found to be useful for detecting the mutation changes in plant DNA induced by gamma rays. The mutants showed differences in morphological traits from the DNA polymorphism analysis in PCR profile amplified by RAPD marker. Thus, it can be concluded that DNA polymorphism detected by RAPD analysis offers a useful molecular marker for the identification of mutants in gamma radiation treated plants. This finding was also supported by Musa et al., (2004) and Ashraf et al. (2014) who detected the genetic variation among three ginger varieties in Malaysia and subcontinent of India using RAPD markers.

Table 4
Genetic distance of five mutant lines of Bentong (BT) ginger

	BT 0	BT 5	BT 7	BT 9	BT 11	BT 13
BT 0	***					
BT 5	0.51	***				
BT 7	0.32	0.57	***			
BT 9	0.36	0.48	0.48	***		
BT 11	0.54	0.69	0.59	0.41	***	
BT 13	0.39	0.41	0.51	0.34	0.46	***

Table 5
Genetic distance of five mutant lines of Tanjung Sepat (TS) ginger

	TS 0	TS 5	TS 7	TS 9	TS 11	TS13
TS 0	***					
TS 5	0.50	***				
TS 7	0.45	0.43	***			
TS 9	0.50	0.32	0.51	***		
TS 11	0.51	0.61	0.50	0.55	***	
TS 13	0.64	0.48	0.51	0.41	0.58	***

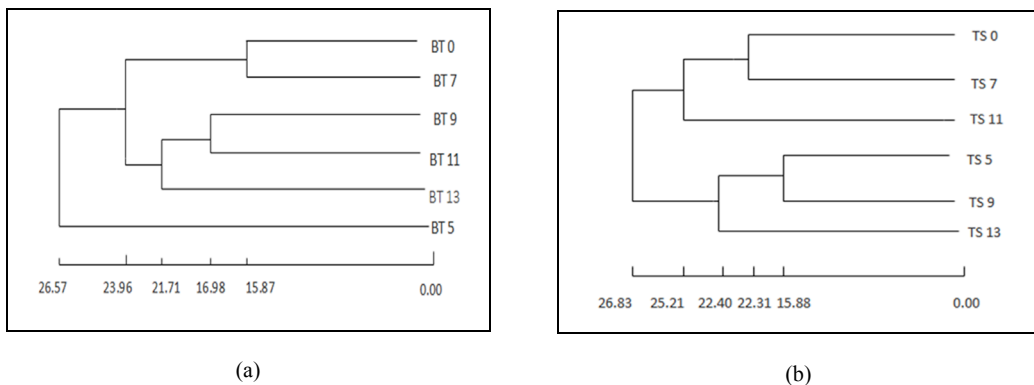


Figure 4. Dendrogram showing genetic distance, summarizing the data on differentiation between ginger genotypes according to RAPD genetic diversity analysis in: (a) Bentong (BT); and (b) Tanjung Sepat (TS) varieties

CONCLUSION

The present study had examined the fibre content of the two locally consumed ginger varieties, Bentong and Tanjung Sepat, after gamma irradiation treatment. Results showed the difference in fibre content after gamma ray treatment. The genetic variation analysis through molecular markers provides a strong evidence for the existence of high level of variability among mutant lines of ginger.

ACKNOWLEDGMENT

The authors gratefully acknowledge the support by Faculty of Plantation and Agrotechnology, Universiti Teknologi MARA (UiTM), Shah Alam, Selangor, Malaysia.

REFERENCES

- Abdelwhab, N. M., Nour, A. M., & Fageer, A. S. M. (2009). The nutritive and functional properties of dry bean (*Phaseolus vulgaris*) as affected by gamma irradiation. *Pakistan Journal Nutritional*, 8(11), 1739-1742.
- Afrasiab, H., & Iqbal, J. (2012). Genetic analysis of somaclonal variants and induced mutants of potato (*Solanum Tuberosum* L.) cv. Diamant using RAPD markers. *Pakistan Journal of Botany*, 44(1), 215-220.
- Ajayi, O., Akomolafe, S., & Akinyemi, F. (2013). Food Value of Two Varieties of Ginger (*Zingiber officinale*) Commonly Consumed in Nigeria. *ISRN Nutrition*, 1-5.
- Ashraf, K., Ahmad, A., Chaudhary, A., Mujeeb, M., Ahmad, S., Amir, M., & Mallick, N. (2014). Genetic diversity analysis of *Zingiber Officinale* Roscoe by RAPD collected from subcontinent of India. *Saudi Journal of Biological Sciences*, 21, 159-169.
- Aziliana, N., Abdullah, S., Faiz, A. R., Rusli, K., & Noorzuraini, S. (2015). The effect of chronic irradiation on Malaysia Upland Rice (*Oryza sativa*) Kuku Belang. *Aust. J. Basic & Appl. Sci.*, 9(31): 1-6, 2015. *Australian Journal of Basic and Applied Sciences*, 9(31), 1-6.

- Bamidele, O. P., & Akanbi, C. T. (2013). Effect of gamma irradiation on physicochemical properties of stored pigeon pea (*Cajanus cajan*) flour. *Food Science and Nutrition*, 1(5), 377-383.
- Bhat, R., Sridhar, K. R., Karim, A. A., Young, C. C., & Arun, A. B. (2009). Influence of γ -radiation on the nutritional and functional qualities of lotus seed flour. *Journal of Agricultural and Food Chemistry*, 57(20), 9524-9531.
- Harisaranraj, R., Suresh, K., & Saravanababu, S. (2009). DNA finger printing analysis among eight varieties of *Zingiber officinale* Rosc. by using RAPD markers. *Global Journal of Molecular Sciences*, 4(2), 103-107.
- Jatoi, S., & Watanabe, K. (2013). Diversity analysis and relationship among ginger landraces. *Pakistan Journal of Botany*, 45(4), 1203-1214.
- Kamaruddin, N. Y., Abdullah, S., & Harun, A. R. (2016). The Effect of Gamma rays on the Radiosensitivity and Cytological Analysis of *Zingiber officinale* Roscoe Varieties Bentong and Tanjung Sepat. *International Journal of Advances in Agricultural and Environmental Engineering*, 3(1), 143-145.
- Kumari, N., & Thakur, S. K. (2014). Randomly amplified polymorphic DNA-a brief review. *American Journal of Animal and Veterinary Sciences*, 9(1), 6-13.
- Mohammadzai, I. U., Shah, Z., Ihsanullah, I., Khan, H., Khan, H., & Rashid, H. (2010). Effect of gamma irradiation, packaging and storage on the nutrients and shelf life of palm dates. *Journal of Food Processing and Preservation*, 34(s2), 622-638.
- Mullainathan, L., Sridevi, A., Umavathi, S., & Gandhi, S. (2014). Genetic variation in mutants of chilli (*Capsicum annum*) revealed by RAPD marker. *International Letters of Natural Sciences*, 6.
- Natarajan, C. P., Bai, R. P., Krishnamurthy, M. N., Raghavan, B., Shankaracharya, N. B., Kuppuswamy, S., ... & Lewis, Y. S. (1972). Chemical composition of ginger varieties and dehydration studies on ginger. *Journal of Food Science and Technology*, 9(3), 120-124.
- Nei, M., & Lei, W.-H. (1979). Mathematical model for studying genetic variation in terms of restriction endonucleases. *Proceedings of the National Academy of Sciences*, 76(10), 5269-5273.
- Palai, S. K., & Rout, G. R. (2007). Identification and genetic variation among eight varieties of ginger by using Random Amplified Polymorphic DNA markers. *Plant Biotechnology*, 24, 417-420.
- Suhaimi, M. Y., Mohamad, A. M., Mahamud, S., & Khadzir, D. (2012). Effects of substrates on growth and yield of ginger cultivated using soilless culture. *J. Trop. Agric. and Fd. Sc.*, 40(2), 159-168.
- Teng, N., Chen, F., Jiang, Z., Fang, W., & Chen, T. (2008). Detection of genetic variation by RAPD among chrysanthemum plantlets regenerated from irradiated calli. *Acta Horticulturae*, 766, 413-420.
- Varsha, K., Gowda, M. V. C., & Ramesh, B. (2009). Molecular characterization of induced mutants in groundnut using random amplified polymorphic DNA markers. *Karnataka Journal of Agricultural Sciences*, 22(2), 276-279.
- Williams, J. G., Kubelik, A. R., Livak, K. J., Rafalski, J. A., & Tingey, S. V. (1990). DNA polymorphisms amplified by arbitrary primers are useful as genetic markers. *Nucleic Acids Research*, 18(22), 6531-6535.
- Yeh, F., Yang, R.-c., & Boyle, T. (1999). POPGENE, the user-friendly shareware for population genetic analysis University of Alberta, Canada: Molecular and Biotechnology Centre.



Development of Palm Oil Extraction Performance Index (EPI) Based on Oil Extraction Rate (OER) and Oil Loss (OL)

Julia Andrew¹, Alawi Sulaiman^{1*}, Mohd Noriznan Mokhtar²,
Azhari Samsu Baharuddin² and Norzaidi Mohd Daud³

¹Faculty of Plantation and Technology, Universiti Teknologi MARA (UiTM), 40450 Shah Alam, Selangor, Malaysia

²Department of Process and Food Engineering, Faculty of Engineering, Universiti Putra Malaysia (UPM), 43400 Serdang, Selangor, Malaysia

³Faculty of Business Management, Universiti Teknologi MARA (UiTM), 40450 Shah Alam, Selangor, Malaysia

ABSTRACT

This study proposes a new method to evaluate the performance of palm oil extraction based on Predictive Scoring Index methodology. The variables, Oil Extraction Rate (OER) and Oil Loss (OL), were identified as important to develop a new extraction index based on three different steriliser systems. There were six performance categories: Excellent, Very Good, Good, Average, Poor and Very Poor. Based on 75 selected palm oil mills data from 2009-2013, Continuous Sterilizer (CS) system and Conventional Sterilizer (CV) system recorded 2.7% and 1.3% respectively under the Excellent category. The Compact Modular Concept (CMC) system only recorded 'Very Good' (20%) and 'Good' (13.3%). This study showed that EPI could be used to monitor palm oil extraction performance to ensure maximum oil extraction and minimum losses.

Keywords: Extraction performance index, oil extraction rate, oil loss, palm oil mill

ARTICLE INFO

Article history:

Received: 28 September 2016

Accepted: 03 February 2017

E-mail addresses:

jue.andrew90@gmail.com (Julia Andrew),

dr_alawi@salam.uitm.edu.my (Alawi Sulaiman),

noriznan@upm.edu.my (Mohd Noriznan Mokhtar),

azharis@upm.edu.my (Azhari Samsu Baharuddin),

zaidiuitm2000@yahoo.com (Norzaidi Mohd Daud)

*Corresponding Author

INTRODUCTION

Currently, oil extraction rate (OER) is the only method used to assess the palm oil mill performance (Oberthur, 2014). At the management level, it is used to indicate the profitability of the plantation in order to measure the amount of oil extracted per hectare (Chang et al., 2003). The OER is defined as the percentage of oil recovered from the oil palm fresh fruit bunches (FFB) processed in the mill. Previous studies showed

that there were several factors affecting OER such as rainfall, crop variety, ergonomic practices and cage weight (Salmiyati et al., 2014; Vincent et al., 2014; Sambanthamurthi et al., 2009). At present, there is no study conducted to understand the effects of using different steriliser systems on OER and oil loss (OL). The standard types of sterilisation system widely employed in Malaysia are continuous steriliser (CS), conventional steriliser (CV) and compact modular concept (CMC) (Hadi et al., 2014; Sivasothy et al., 2006; Sivasothy et al., 2005). Nowadays, sustainability in the palm oil industry, especially in the aspect of environmental management, is a major concern for better biomass waste management (Choong & McKay, 2013; Umar et al., 2013). The largest palm biomass material produced at the mill are oil palm empty fruit bunches (EFB) (Baharuddin et al., 2013), palm oil mill effluent (POME) (Sulaiman et al., 2010; Rupani et al., 2010), oil palm mesocarp fibre (MF) (Nordin et al., 2013) and oil palm decanter cake (OPDC) (Adam et al., 2014; Sahad et al., 2014). Abdullah and Sulaiman (2013) reported the presence of oil in palm biomass means it had a good potential to be recovered for various utilisation. The percentage of Oil Loss (OL) contained in palm biomass are between 0.25% and 1.38% dry EFB (Md. Yunus et al., 2015), 5% - 11% MF (Subramaniam et al., 2013; Nik Norulaini et al., 2008), 0.6% - 0.7% POME (Wan Sharifudin et al., 2015), and 12% OPDC (Sahad, 2015). Oil loss refers to the amount of crude palm oil absorbed in the palm biomass produced in the palm oil mill. An efficient palm oil milling process produces high OER whilst maintaining low OL. The OL is produced due to equipment inefficiency in extracting the maximum crude palm oil during the milling process and therefore the oil is absorbed in the palm biomass generated. Thus, high OL will reduce the palm oil extraction performance of the mill.

Nevertheless, the current extraction performance tool should be updated with the addition of a new factor in the consideration of sustainability issues in palm oil production (Cock et al., 2014). The objective of this study is to develop a new extraction performance index (EPI) with OER and OL as main variables due to their dependent relationship affecting the oil extraction performance (Juliano et al., 2013; Lin, 2011). This empirical study is unique as it analyses OL and the variables of existing palm oil mill production. The straightforward of OER and OL approach in EPI assist the performance assessment. Hence, the relationship between the variables and new EPI were studied for better understanding of their role in oil extraction performance.

METHOD

The approach in correlating the variables and new index through Predictive Scoring Index methodology was done in three steps; in the first step, the OER was calculated to represent the effectiveness of mill production. In the second step, the components involved in OL were identified and calculated to represent their effectiveness in palm oil production. The last step was to examine the composition of OER and OL in the EPI. The identification and equation development were essential steps to provide guidance and basic information on the index.

Project Framework and Data Collection

Predictive Scoring Index methodology was adapted for the analysis of variables and index formation (Inami et al., 2013; Bernabeu-Wittel et al., 2011; Chen & Yang, 2004). The method

adaptability enabled the identification of each variable related to the index. Index is the combination of score measurement between two or more types of variable. The OER and OL were identified as the main variables used in the index and equation measurement. OER, OL, fresh fruit bunches (FFB) were obtained from selected palm oil mills using different steriliser systems. Due to confidential purposes, the identity of mills remains unclosed and 25 data were selected from each type of sterilizer systems. The study period was between 2009 and 2013.

Equation Development

The equation developments were formed for the identified variables. Each variable was expressed in a single equation. Eq. (1) shows the calculation of OER.

$$\text{OER} = \frac{\text{CPOr}}{\text{FFB}_p} \times 100\% \quad [1]$$

Where;

- OER = Oil extraction rate
- CPOr = Crude palm oil recovered
- FFB_p = Fresh fruit bunches processed

For the OL, three main sources of palm biomass - Empty Fruit Bunches (EFB), Mesocarp Fibres (MF) and Palm Oil Mill Effluent (POME) - were selected for the equation. The selection process of the palm biomass was based on uniform availability across different steriliser systems in the mills. Eq. (2) represents the calculation for the OL.

$$\text{OL} = \text{EFB}_{R1} + \text{MF}_{R2} + \text{POME}_{R3} \quad [2]$$

Where;

- OL = Oil loss
- EFB_{R1} = Rate of OL from empty fruit bunches
- MF_{R2} = Rate of OL from mesocarp fibres
- POME_{R3} = Rate of OL from palm oil mill effluent

However, there is a certain level of OL imposed on the milling process. The standardised OL released into the palm biomass must not exceed 5% (MPOB, 2004). Hence, loss effectiveness (OLE) is defined by the total subtraction between the standard limit and OL

$$\text{OLE} = 5.00 - \text{OL} \quad [3]$$

Where;

- OLE = Oil loss effectiveness
- 5.00 = Standard limit permitted for OL
- OL = Total oil loss calculation (Eq.2)

OER, OL and OLE Range Scale

Table 1
Oil Extraction Rate (OER) scale

Indicator	OER Ranges		
	CS	CV	CMC
Very High	≥23.00	≥23.00	≥22.00
High	21.30-22.99	21.70-22.99	21.00-21.99
Average	19.60-21.29	20.40-21.69	20.00-20.99
Low	18.00-19.59	19.00-20.39	19.00-19.99
Very Low	<18.00	<19.00	<19.00

Table 2
Oil Loss (OL) scale

Indicator	OL Ranges		
	CS	CV	CMC
Very Low	<1.10	<1.10	<1.30
Low	1.10-1.39	1.10-1.39	1.30-1.69
Average	1.40-1.69	1.40-1.69	1.70-2.09
High	1.70-1.99	1.70-1.99	2.10-2.49
Very High	>2.00	>2.00	>2.50

Table 1 and 2 show the OER and OL ranges respectively, according to different steriliser systems. The range scale was statistically set according to data collected from palm oil mills. Each of the range has indicator remarks whereby positive OER performance increases along with the ranges, while the positive OL performance decreases along the ranges. The purpose of the range table is to categorise the OER and OL data trend series and compare them with the EPI application.

Table 3
Oil Loss Effectiveness (OLE) scale

Indicator	OLE Ranges
<4.01	Very High
4.00 – 3.01	High
3.00 – 2.01	Average
2.00 – 1.01	Low
>1.00	Very Low

The oil loss effectiveness scale is shown in Table 3. Ranges of the OLE is determined based on Equation 3 indicate the palm oil mill effectiveness in maintaining the OL limits set by the MPOB. The increases in OLE ranges indicate positive performance of palm oil mill maintaining its OL level.

Extraction Performance Index (EPI) Equation Formulation

Index equation was defined using the function of geometric average. It is a function of the combination of each factor scores to aggregate the measurement into the equation and the derivation of the EPI equation (Pejman et al., 2015; Brigham & Houston, 2003).

$$EPI = \sqrt{(OER \times OLE)} \quad [4]$$

Where;

EPI = Extraction performance index

OER = Oil extraction rate (Eq.1)

OLE = Oil loss effectiveness (Eq.3)

Table 4
EPI Indicator

Index	Range Indicator	Remarks
<6.00	Very Poor	Unsatisfied mill performance with very low OER and OLR
6.00 – 6.79	Poor	Poor mill performance with low OER and OLR.
6.80 – 7.49	Average	Average mill performance with average OER and OLR.
7.50 – 8.29	Good	Good mill performance with high OER and OLR.
8.30 – 8.99	Very Good	Very satisfied mill performance with very high OER and OLR.
≥9.00	Excellent	Excellent mill performance with both excellent in OER and OLR standards.

Equation 4 relates to OER and OLE index measurement. It shows the EPI of the composite between variables. Interpretation of EPI range is shown in Table 4 whereby the increase of EPI ranges shows positive result of the palm oil mill extraction performance.

Statistical Analysis

Actual data of the selected palm oil mills (OER and OL) were analysed statistically using SPSS statistical software (Ver.19.0). Data ranges were presented with mean ± SD and interquartile range. The Likert - type scale was used as indicator for each range. The correlation between OER and OL were analysed using Pearson rank correlation coefficient.

RESULTS AND DISCUSSION

Validation of Extraction Performance Index

The final stage in new index development is the validation process. The purpose is to evaluate and measure the index effectiveness and describes the outcome of the variables in the sample selected. Midi et al. (2010) suggests index validation is needed to ensure the index measurement is compatible with field data and able to predict accurately the related measures. The OER and OL data series are shown in Table 1 and Table 2 respectively. For the EPI measurement, OER and OL are expressed in Equation 4 and its interpretation shown in Table 4.

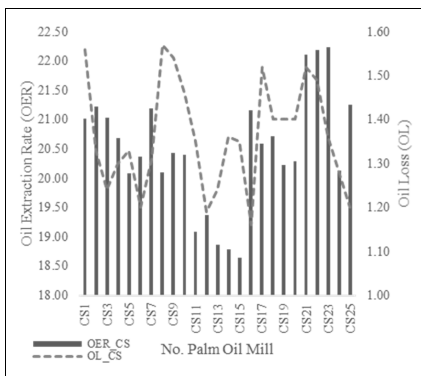


Figure 1. OER vs OL in CS system

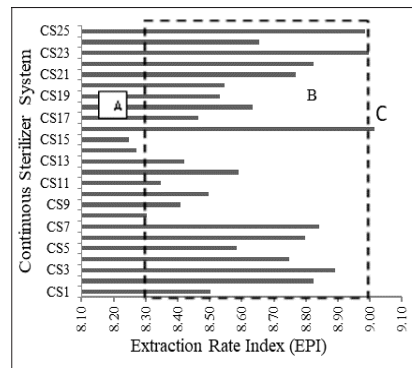


Figure 2. EPI result of CS system

Figure 1 shows data trend of OER and OL in CS system. From the figure, the highest and lowest OER are 22.24 and 18.64 respectively. Table 1 shows overall OER trend recorded 12% higher oil extraction, 68% average oil extraction and 20% low oil extraction. The highest and lowest OL (Table 2) are 1.57 and 1.16 respectively with an overall trend recorded showed 60% low OL and 40% average OL.

EPI result (Figure 2) referred to Table 3 were compared with trends in Figure 1. Highest EPI category is excellent (9.01) and the lowest category is good (8.25). According to Figure 2, the CS16 is identified as “Excellent” EPI with the OER and OL recorded at 21.16 and 1.16 respectively. Based on Table 1, CS16 recorded “Average” category of OER. However, the EPI showed the mill performed at the “Excellent” category. This supported by its oil loss effectiveness (OLE) which recorded high performance (see Table 3) and thus, it has lifted the CS16 level to excellent EPI.

Meanwhile, CS15 recorded lowest EPI in good category. Though its OER recorded low category, 1.35 (Table 1), the OLE result showed high performance; 3.65 in OL management. The OLE result complies with the EPI indicator on good performance as the CS15 achieved high OER and OLE.

The overall EPI for CS system showed two mills (2.7%); Excellent, 21 mills (28%); Very Good and 2 mills (2.7%); Good.

EPI Application of CV System

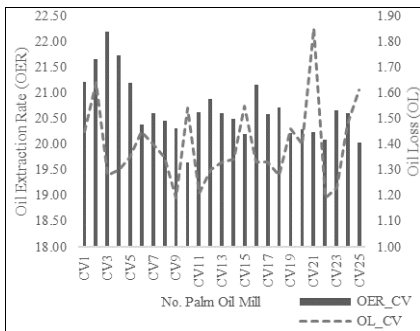


Figure 3. OER vs OL in CV system

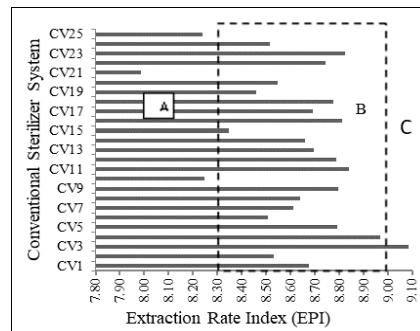


Figure 4. EPI result of CV system

Data trend of OER (Figure 3) showed highest and lowest records at 22.20 and 19.65 respectively. The CV system showed only 8% high oil extraction, 56% average oil extraction and 9% low oil extraction (Table 1). It is also reported 4% high OL, 40% average OL and 56% low OL (Table 2). The highest and lowest OL are 1.85 and 1.19 respectively. Figure 4 shows the EPI of CV system with the highest category 9.09 and lowest category 7.98.

CV3 has the highest EPI category with OER 22.20 and OL 1.28. According to Figure 3 and 4 CV3 recorded excellent performance for its highest OER while maintaining low OL. The OLE (Table 3) also recorded high performance.

Meanwhile CV21 showed lowest EPI in good performance. Despite recording low OER 20.24 (Table 1) and high OL 1.85 (Table 2); CV21 showed good EPI performance. This can be explained by OLE result showing high performance; 3.15 (Table 3). CV21 complied with the EPI in terms of high OLE.

Similar to CS system, the CV system recorded one as “Excellent” (1.3%), while remaining 21 mills (28%) as “Very Good” and 3 mills (4%) as “Good” EPI.

EPI Application of CMC System

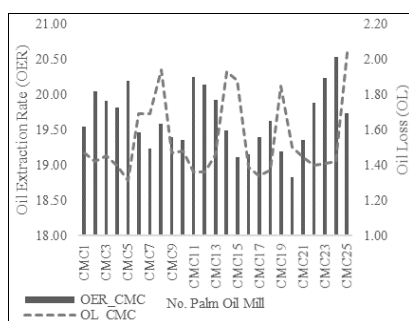


Figure 5. OER vs OL in CMC system

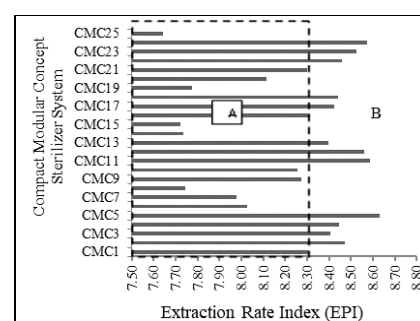


Figure 6. EPI result of CMC system

Unlike the previous steriliser system, data trend of OER for CMC system (Figure 5) recorded 24% average oil extraction, 72% low oil extraction and 4% very low oil extraction with highest OER 20.53 and lowest OER 18.82. As for the OL, 20% average OL and 80% low OL were recorded.

Figure 6 shows the highest EPI is 8.63 and lowest is 7.64. CMC5 showed highest EPI with OER is 20.19 indicating “Very Good” performance. Though its OER is at the average performance, this is supported by OLE (Table 3) at high performance. Hence, the OLE had placed the CMC5 at “Very Good” category in EPI.

Meanwhile, the CMC25 showed lowest EPI, placing it in the good category. Similar to previous CMC5 performance, the CMC25 OER which is at the lowest category is also supported by the high OLE.

In the CMC system, the EPI recorded only two categories of 15 mills namely “Very Good” (20%) and 10 mills (13.3%) as “Good”.

CONCLUSION

In this study, a new method to evaluate palm oil extraction performance was developed based on Predictive Scoring Index methodology. It looked at 75 selected palm oil mills: the EPI showed 4% ‘Excellent’, 76% ‘Very good’ and 20% ‘Good’. For each EPI related to steriliser systems, CS system recorded 2.7% ‘Excellent’, 28% ‘Very good’ and 2.7% ‘Good’ meanwhile CV system recorded 1.3% ‘Excellent’, 28% ‘Very good’ and 4% ‘Good’ performances. The CMC system only recorded ‘Very good’ (20%) and ‘Good’ (13.3%) performances. Among the steriliser systems, only CS and CV achieved the ‘Excellent’ EPI, which indicate excellent efficiency in OER extraction whilst sustaining OL level. Though the CMC system simply achieved ‘Very good’ EPI, the EPI result benefits from upgrading the system to achieve a higher category of EPI.

ACKNOWLEDGEMENTS

The authors are grateful for the financial support of Ministry of Higher Education (MOHE) Malaysia through Long-term Research Grant Scheme (600-RMI/LRGS 5/3 1/2012) awarded to the Universiti Putra Malaysia and Universiti Teknologi MARA, Shah Alam. Thanks also to FELDA Palm Industries Sdn. Bhd for its technical support to complete this study.

REFERENCES

- Abdullah, N., & Sulaiman, F. (2013). The Oil Palm Wastes in Malaysia. Chapter 3. In *Biomass Now Sustainable Growth and Use*. Matovic M.D. (ed.), InTech Publishing, Rijeka, Croatia, 75-10.
- Adam, M., Sulaiman, A., Said, C., Som, A., Bahruddin, A. S., & Mokhtar, M. N. (2014). Preliminary Study of Oil Palm Decanter Cake Natural Polymer Composite (OPDC-NPC). *Advanced Materials Research, 911*, 40-44.
- Baharuddin, A. S., Sulaiman, A., Kim, D. H., Mokhtar, M. N., Hassan, M. A., Wakisaka, M. (2013). Selective component degradation of oil palm empty fruit bunches (OPEFB) using high-pressure steam. *Biomass Bioenergy, 55*, 268-275.

- Bernabeu-Wittel, M., Olloro-Baturone, M., Moreno-Gavino, L., Baron-Franco, B., Fuertes, A., Murcia-Zaragoza, J. (2011). Development of a new predictive model for polypathological patients: The PROFUND index. *European Journal of Internal Medicine*, 22, 311-317.
- Brigham, E. F., & Houston, J. F. (2003). *Fundamental of financial management: Concise 4th Edition*. Fort Worth, Texas: Harcourt College Publication.
- Chang, L., Abdul, R. A., & Basran, Z. (2003). An Economic Perspective of Oil Extraction Rate in the Oil Palm Industry of Malaysia. *Oil Palm Industry Economic Journal*, 3(1), 25-31.
- Chen, J. R., & Yang, Y. T. (2004). A predictive risk index for safety performance in process industries. *Journal of Loss Prevention in the Process Industries*, 17, 233-242.
- Choong, C., & McKay, A. (2013). Sustainability in the Malaysian palm oil industry. *Journal of Cleaner Production*, 1-7.
- Cock, J., Donough, C. R., Oberthur, T., Indrasura, K., Rahmadsyah, Gatot, A. R. (2014). Increasing Palm Oil Yields by Measuring Oil Recovery Efficiency from the Fields to the Mills. *IPNI: Southeast Asia Program*. Indonesia.
- Gasperz, V. (2003). Sistem Manajemen Kinerja Terintegrasi: Balanced scorecard dengan six sigma untuk organisasi bisnis dan pemerintah. *Jakarta: PT Gramedia Pustaka Utama*.
- Hadi, H., Tamrin, S. B., & Karrupiah, K. (2014). Hazard and Risk Analysis of Different Sterilizer Technology in Palm Oil Mills. *Advances in Environmental Biology*, 8(15), 85-90.
- Inami, T., Kataoka, M., Shimura, N., Ishiguro, H., Yanagisawa, R., & Taguchi, H. (2013). Pulmonary Edema Predictive Scoring Index (PEPSI), a New Index to Predict Risk of Reperfusion Pulmonary Edema and Improvement of Hemodynamics in Percutaneous Transluminal Pulmonary Angioplasty. *JACC Cardiovascular Interventions*, 6(7), 725-736.
- Juliano, P., Swiergon, P., Mawson, R., Knoerzer, K., & Augustin, M. A. (2013). Application of Ultrasound for Oil Separation and Recovery of Palm Oil. *Journal of the American Oil Chemists' Society*, 90, 579-588.
- Lin, S. W. (2011). *Palm Oil: Edible Oil Processing*. Retrieved from AOCS Lipid Library website: <http://lipidlibrary.aocs.org/oilsFats/content.cfm?Itemnumber=40334>.
- Md. Yunos, N. S., Baharuddin, A. S., Md. Yunos, K. F., Hafid, H. S., Busu, Z., & Mokhtar, M. N. (2015). The physicochemical characteristics of residual oil and fibers from oil palm empty fruit bunches. *Bioresources*, 14-29.
- Midi, H., Rana, S., & Sarkar, S. (2010). Binary response modeling and validation of its predictive ability. *Wseas Transactions on Mathematics*, 9(6), 438-447.
- MPOB Test Methods. (2004) A compendium of test on palm oil products, palm kernel products, fatty acids, food related products and others Malaysian Palm Oil Board. Kuala Lumpur, Malaysia: Malaysian Palm Oil Board.
- Nik Norulaini, N. A., Ahmad, A., Omar, F. M., Banana, A. A., Zaidul, I., & Kadir, M. O. (2008). Sterilization and extraction of palm oil from screw pressed palm fruit fiber using supercritical carbon dioxide. *Separation and Purification Technology*, 272-277.
- Nordin, N. I., Ariffin, H., Andou, Y., Hassan, M. A., Shirai, Y., & Nishida, H. (2013). Modification of oil palm mesocarp fiber characteristics using superheated steam treatment. *Molecules*, 8, 9132-9146.

- Oberthur, T. (2014). *To increase oil yield from palms, you have to measure it*. Retrieved from The International Plant Nutrition Institute (IPNI) website: <http://seap.ipni.net/article/SEAP-3117>
- Pejman, A., Bidhendi, G. N., Ardenstani, M., Saeedi, M., & Baghvand, A. (2015). A new index for assessing heavy metals contamination in sediments: A case study. *Ecological Indicators*, 58, 365-373.
- Rupani, P. F., Singh, R. P., Ibrahim, M. H., & Esa, N. (2010). Review of Current Palm Oil Mill Effluent (POME) Treatment Methods: Vermicomposting as a Sustainable Practice. *World Applied Sciences Journal*, 10(10), 1190-1201.
- Sahad, N., Som, A. M., Baharuddin, A. S., Mokhtar, N., Busu, Z., & Sulaiman, A. (2014). Physicochemical characterization of oil palm decanter (OPDC) for residual oil recovery. *Bioresources*, 6361-6372.
- Sahad, N. (2015). Characterization of oil palm decanter cake (OPDC) and comparison of residual crude palm oil recovery from OPDC using d-limonene and n-hexane. Unpublished MSc thesis. Universiti Teknologi MARA.
- Sambanthamurthi, R., Singh, R., Kadir, A. P., Abdullah, M., & Kushairi, A. (2009). Opportunities for the Oil Palm via Breeding and Biotechnology. In *Breeding Plantation Tree Crops: Tropical Species* (pp. 377-421). New York, USA: Springer Science + Business Publishing.
- Sivasothy, K., Basiron, Y., Suki, A., Taha, R. M., Tan, Y. H., & Sulong, M. (2006). Continuous sterilization: The New Paradigm for Modernizing Palm Oil milling. *Journal of Oil Palm Research*, 144-152.
- Sivasothy, K., Halim, R. M., & Basiron, Y. (2005). A new system for continuous sterilization of oil palm fresh fruit bunches. *Journal of Oil Palm Research*, 17, 145-151.
- Subramaniam, V., Menon, N. R., Sin, H., & Choo, Y. M. (2013). The development of a residual oil recovery system to increase the revenue of a palm oil mill. *Journal of Oil Palm Research*, 25, 116-122.
- Salmiyati, Arien, H., Ida, I., & Eko, S. (2014). Oil palm plantations management effects on productivity fresh fruit bunch (FFB). *APCBEE Procedia*, 8, 282-286.
- Sulaiman, A., Tabatabaei, M., Yusoff, M. Z., Ibrahim, M. F., Hassan, M. A., & Shirai, Y. (2010). Accelerated start-up of a semi-commercial digester tank treating palm oil mill effluent with sludge seeding for methane production. *World Applied Sciences Journal*, 8(2), 247-258.
- Umar, M. S., Jennings, P., & Urmee, T. (2013). Strengthening the palm oil biomass renewable energy industry in Malaysia. *Renewable Energy*, 60, 107-115.
- Vincent, C. J., Shamsudin, R., & Baharuddin, A. S. (2014). Pre-treatment of oil palm fruits: A review. *Journal of Food Engineering*, 123-131.
- Wan Sharifudin, W., Sulaiman, A., Mokhtar, N., Baharuddin, A. S., Meisam, T., & Busu, Z. (2015). Presence of Residual Oil in Relation to Solid Particle Distribution in Palm Oil Mill Effluent. *Bioresources*, 7591-7603.

Chromatographic Fingerprint and Chemometric Approach for Quality Control of Tongkat Ali (*Eurycoma longifolia*)

Nor Nasriah Zaini¹, Mardiana Saaid¹, Hafizan Juahir² and Rozita Osman^{1*}

¹Faculty of Applied Sciences, Universiti Teknologi MARA (UiTM), 40450 Shah Alam, Selangor, Malaysia

²East Coast Environmental Research Institute, Universiti Sultan Zainal Abidin (UNISZA), 21300 Kuala Terengganu, Malaysia

ABSTRACT

Tongkat Ali (*Eurycoma longifolia*) is one of the most popular tropical herbal plants as it is believed to enhance virility and sexual prowess. This study looked examined chromatographic fingerprint of Tongkat Ali roots and its products generated using online solid phase-extraction liquid chromatography (SPE-LC) combined with chemometric approaches. The aim was to determine its quality. Pressurised liquid extraction (PLE) technique was used prior to online SPE-LC using polystyrene divinyl benzene (PSDVB) and C18 columns. Seventeen Tongkat Ali roots and 10 products (capsules) were analysed. Chromatographic dataset was subjected to chemometric techniques, namely cluster analysis (CA), discriminant analysis (DA) and principal component analysis (PCA) using 37 selected peaks. The samples were grouped into three clusters based on their quality. The PCA resulted in 11 latent factors describing 90.8% of the whole variance. Pattern matching analysis showed no significant difference ($p > 0.05$) between the roots and products within the same CA grouping. The findings showed the combination of chromatographic fingerprint and chemometric techniques provided comprehensive evaluation for efficient quality control of Tongkat Ali formulation.

Keywords: Chemometric, chromatographic fingerprint, cluster analysis, discriminant analysis, eurycomanone, online SPE-LC, principal component analysis

ARTICLE INFO

Article history:

Received: 28 September 2016

Accepted: 03 February 2017

E-mail addresses:

nasriah_zaini@yahoo.com (Nor Nasriah Zaini),

mardiana6951@salam.uitm.edu.my (Mardiana Saaid),

hafizanjuahir@unisza.edu.my (Hafizan Juahir),

rozit471@salam.uitm.edu.my (Rozita Osman)

*Corresponding Author

INTRODUCTION

Recently, quality control of herbal medicines has become a major concern in consumer protection (Bhat & Karim, 2010). Tongkat Ali is one of the most well-known traditional herbs and it is attracting researchers' interest due to its medicinal values (Mohamad et al., 2013). Tongkat Ali has active chemical

components such as quassinoids which contribute to its bitter taste. The five quassinoids markers are eurycomanone, eurycomanol, eurycomanol-2-O- β -D-glucopyranoside, 13,21-dihydroeurycomanone, and 13 α (21)-epoxyeurycomanone (Teh et al., 2011).

Currently, marker compounds are used in quality control and authentication of herbal products (Wang et al., 2015; Li et al., 2010). However, the use of a single compound may not be able to evaluate the quality consistency of herbal products (Li et al., 2010). Thus, it is important to provide a more comprehensive chemical profile of a sample for quality control purposes. Chromatographic fingerprint technology has been accepted by leading organisations such as the Federal Drug Administration (FDA), World Health Organization (WHO) and the British Herbal Medicine Association (Zaini et al., 2016).

In this study, online SPE-LC method was used in obtaining fast and comprehensive chromatographic fingerprint of Tongkat Ali. The chromatographic dataset was subjected to chemometric techniques by means of multivariate statistical analysis. Unsupervised pattern recognition techniques, principal component analysis (PCA) and cluster analysis (CA) were utilised for data visualisation by observing the relationship between samples and variables with no predetermined class. Supervised pattern recognition, discriminant analysis (DA) and pattern matching analysis were employed in supporting the clusters obtained by CA.

METHOD

Online Solid Phase Extraction-Liquid Chromatography (SPE-LC)

A Dionex Ultimate 3000 Liquid Chromatography system equipped with diode array detector (DAD) was used for online SPE-LC analysis, performed utilising polystyrene divinyl benzene (PSDVB) and C18 column by two pumps (right and left) operated simultaneously. Solvents carried by right pump were acetonitrile, methanol and ultrapure water, while left pump were 5% ultrapure water and 95% Methanesulfonic acid (MSA). The identification of eurycomanone and eurycomanol were performed using Q Exactive Plus Liquid Chromatography-Mass Spectrometer (Thermo Fisher Scientific). For root samples, extraction was done using pressurised liquid extraction (Osman et al., 2016) prior to online SPE-LC.

Chemometric Analysis

The chemometric analysis was done using XLSTAT Software (XLSTAT, 2015, Addinsoft, New York, NY, USA) for statistical analysis. A total 37 peaks were chosen and their areas were used as variables.

Cluster Analysis (CA). CA is used for classification of variables into clusters with high similarities within the class and high dissimilarity between different classes.

Discriminant Analysis (DA). Subsequently, DA was applied to confirm the results of the CA analysis. DA specifies the variables that discriminate between two or more clusters obtained from CA (Goncalves et al., 2006). DA was performed to the raw data in standard, stepwise forward and stepwise backward modes.

Principal Component Analysis (PCA). PCA provides information on the most significant factors that explain the total dataset by excluding the less meaningful factors with a minimum loss of original information (Goncalves et al., 2006). The PCA helps to determine in what respect one sample is different from another and which variables contribute most to this difference. It also helps to find out which variables contribute most to this difference, and whether those variables contribute in the same way (positively correlated) or are inversely correlated (Saim et al., 2009).

Pattern Matching. Pattern matching was conducted by plotting 2D-chromatograms. T-statistics was used to evaluate whether two groups differ from one another for a tested variable.

RESULTS AND DISCUSSION

Chromatographic Fingerprint

Chromatographic fingerprints of four representative Tongkat Ali root samples from different sources in Malaysia and four of its products (Figure 1) were obtained using SPE-LC (Zaini et al., 2016). The main quassinoids of Tongkat Ali are eurycomanone and eurycomanol (Hajjoui et al., 2014), eluted at retention times of 5.6 and 5.7 minutes respectively. The chromatographic fingerprint clearly showed similarities and dissimilarities among the samples.

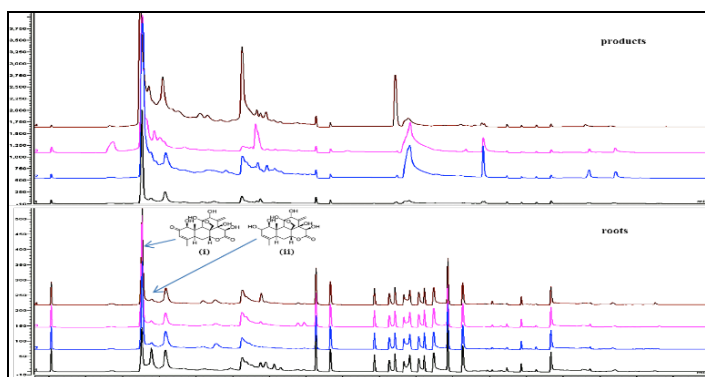


Figure 1. Chromatographic fingerprint selected Tongkat Ali roots and products: (i) eurycomanone; and (ii) eurycomanol

Chemometric Analysis

In this study, 17 Tongkat Ali root samples (R1 to R17) from four states in Malaysia - R1 (Sarawak), R2 to R8 (Pahang), R9 to R13 (Kedah) and R14-R17 (Perak) - and 10 products (capsules) from various manufacturers were analysed. In order to perform chemometric analysis, 37 variables based of reproducible peak areas were selected.

Cluster Analysis (CA). The dendrogram (Figure 2) clearly showed that all samples were formed into three clusters. All root samples from Kedah were clustered in cluster II. In addition, five

root samples from Pahang and three from Perak were clustered in cluster III. However, two samples from Pahang were separated and clustered into cluster I, suggesting their dissimilarity in chemical constituents. The composition of Tongkat Ali may vary depending on cultivation conditions, maturity, soil properties, harvesting age, storage, and processing temperature (Li et al., 2010).

The clustering of products in the same group with the roots of Tongkat Ali may suggest that they were from the same source. As the products are formulated using Tongkat Ali extract, the extraction solvent used may affect the fingerprint composition (Locatelli et al., 2012). The CA provides initial evaluation based on dissimilarity between samples but it does not show details of these differences. Thus, CA should be confirmed by DA and PCA.

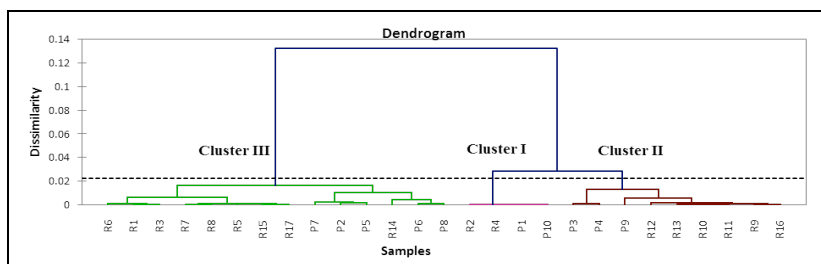


Figure 2. Dendrogram showing the cluster of Tongkat Ali roots and products

Discriminant Analysis (DA). In DA, the three clusters (CI, CII and CIII) obtained from CA in addition to sources or locations of Tongkat Ali were used as dependent variables. Peak areas of chromatographic fingerprints were the independent variables. The DA showed that each group differed from the others in terms of different compositions (Al-Odaini et al., 2012). The results from standard, stepwise forward and stepwise backward modes gave 100% correct classification based on the confusion matrix of the estimation sample (Figure 3).

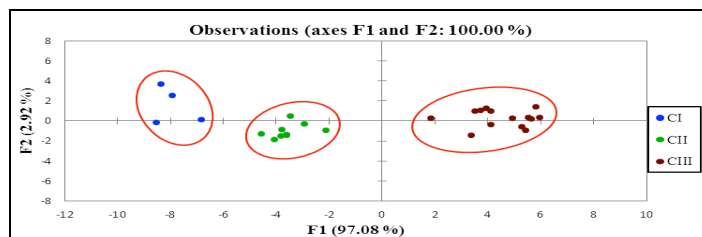


Figure 3. Plot of discriminant functions showing three clusters of Tongkat Ali roots

Stepwise backward mode yielded 100% correctly assigned with 19 discriminant peaks or variables whereas stepwise forward mode contributed 100% with only one discriminant peak. Stepwise forward mode yielded little difference in matching for each sample compared

with the stepwise backward mode. The discriminant variable was determined by the value of p-value. Variable with p-value of <0.05 was considered as discriminant variable. Although some compounds have p-values of >0.05 , they are still able to discriminate Tongkat Ali. Therefore, result obtained by stepwise backward mode was chosen, suggesting all 19 discriminant variables (Table 1) as significant in discriminating the quality of Tongkat Ali whereas the remaining 18 peaks did not correlate significantly in discriminating the Tongkat Ali. As shown in Table 1, A10 has the highest discriminant capacity (F) followed by A27 probably because the compounds have high variations of peak areas between clusters (Al-Odaini et al., 2011).

The Wilks' Lambda value test gives Lambda value of 0.054 and $p < 0.0001$. The null hypothesis stated that the mean vectors of the three clusters (roots and products) are equal. The alternative hypothesis, alongside, stated that at least one of the mean vectors is different from another. Since the computed p-value is lower than the significance level of $\alpha = 0.05$ (at 95% confidence level), one should reject the null hypothesis and accept the alternative hypothesis. The risk to reject the null hypothesis while it is true is lower than 0.01%. Thus, the three clusters are indeed different from one another.

Table 1
Wilks' lambda and F test of group means

Variable	Lambda	F	p-value
A3	0.832	2.116	0.146
A6	0.958	0.459	0.638
A7	0.864	1.656	0.215
A8	0.781	2.951	0.074
A10	0.457	12.461	0.000
A12	0.691	4.691	0.021
A14	0.893	1.255	0.306
A15	0.855	1.784	0.193
A16	0.805	2.541	0.103
A21	0.886	1.358	0.279
A25	0.960	0.440	0.650
A26	0.838	2.033	0.156
A27	0.590	7.308	0.004
A28	0.770	3.138	0.064
A31	0.788	2.821	0.082
A32	0.722	4.041	0.033
A33	0.952	0.531	0.596
A34	0.755	3.408	0.052
A35	0.829	2.166	0.140

Principal Component Analysis. In this study, the peak areas of 37 selected peaks were treated as variables. The principal components (PCs) generated by PCA are sometimes not readily

interpreted (Al-Odaini et al., 2011). Varimax rotations applied on the PCs with eigenvalues more than 1 are considered significant (Baharudin et al., 2014) in order to obtain new groups of variables called varimax factors (VFs).

The first two PCs (PC1 and PC2) were selected to provide the highest variation of data objects (31.15% and 9.30% of the variation). Figure 4 showed that the Tongkat Ali roots and products were distinctively separated. The result suggested that roots and products have their own unique chemical compositions.

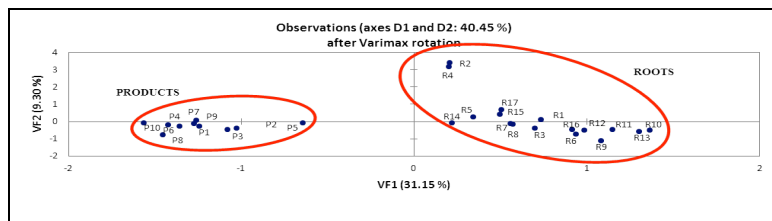


Figure 4. PCA plot of Tongkat Ali

Based on PCA analysis results, only the first 11 PCs with eigenvalue > 1 were considered to perform varimax rotations. The parameter loading for the 11 components from PCA of the data set after varimax rotation is given in Table 2. The results explain approximately 90.8% of the total variances, where a correlation greater than 0.75 is considered “strong”; 0.50-0.75, “moderate”; and 0.30-0.50 as “weak” significant factor loading. The higher the loading of the variable (either positive or negative), the more that variable contributes to the variatio accounted for the particular varifactors (Baharuddin et al., 2014). Table 2 shows factor loadings of PCA, the first VF explained total variances of 31.15 % with 9 strong and 9 moderate factor loadings. The VF2 contributed 9.30% of data variability. The third factor described 6.17% of the variance in the dataset. VF4, VF5 and VF6 accounted for 7.46%, 5.25% and 4.38% of the total variances respectively. VF7 and VF8 exhibited moderate loadings for eurycomanol and eurycomanone, the major quassinoids in Tongkat Ali by 8.08% and 4.74% of the total variance respectively. VF9, VF10, VF11 demonstrated 4.78%, 5.29% and 4.16% respectively.

Table 2
Factor loadings of PCA

Peaks	VF1	VF2	VF3	VF4	VF5	VF6	VF7	VF8	VF9	VF10	VF11
A1	-0.0559	0.1851	0.1629	0.2429	0.4189	0.0921	-0.3546	-0.6374	-0.1140	-0.1312	-0.0943
A2	0.2518	0.1959	0.0133	0.0547	0.1717	0.0409	0.7990	-0.1161	-0.3104	0.0055	-0.0721
A3	0.5736	0.1312	-0.1392	0.2513	-0.0202	0.2125	0.4088	-0.0823	0.1400	-0.1737	0.2979
A4	-0.1058	-0.0367	-0.0105	-0.8932	0.0471	0.0791	-0.0564	-0.2897	-0.0395	-0.0973	0.0039
A5	0.6013	-0.1841	0.1464	0.1921	0.0747	0.1205	-0.1873	-0.0697	0.1360	-0.0654	-0.6005
A6	-0.5939	0.2451	-0.0799	0.2395	0.1549	0.2340	0.1012	-0.0019	0.1124	0.1231	0.5856
A7	-0.2401	-0.0387	-0.0691	0.1644	0.0180	0.2493	0.6995	-0.1903	0.2995	-0.0490	0.2014
A8	0.1841	-0.2554	-0.1705	0.0358	-0.7123	0.1223	-0.2068	0.0433	0.1344	0.3249	-0.1478
A9	0.0280	0.0311	0.9656	0.0414	0.0136	-0.0739	-0.0444	-0.0176	0.0564	0.0035	-0.1361
A10	0.5466	-0.4900	-0.1548	0.0966	0.1185	0.2093	-0.1330	-0.0130	0.1353	-0.2266	0.5009
A11	0.1166	0.9340	-0.1059	0.0133	0.0474	-0.0264	0.2387	0.0028	0.0740	0.0026	0.1410
A12	0.8124	0.1527	0.2146	0.2751	0.1561	0.2761	0.0683	-0.0685	0.0391	-0.0476	0.1007
A13	-0.2030	0.1369	0.1633	0.1124	-0.8834	0.0019	-0.1251	-0.0990	0.0193	-0.1055	0.0251
A14	-0.3219	-0.0534	0.0923	0.0554	0.0786	-0.8262	-0.0026	-0.1723	0.0479	0.0230	-0.0443
A15	0.5058	0.0025	-0.1935	0.1254	0.2499	0.0850	0.2868	0.0621	0.3986	-0.4032	0.0585
A16	0.1153	0.1725	-0.0395	0.0193	0.0873	-0.0781	0.9359	0.0387	0.0602	-0.0526	0.0283
A17	0.0812	0.6544	0.6733	0.0605	-0.1119	0.0568	0.0031	-0.1149	0.1628	-0.0773	-0.0295
A18	0.1533	0.9330	0.1560	0.0642	-0.0391	0.0749	-0.0236	-0.0721	-0.0515	-0.0079	0.0098
A19	0.4409	0.0706	-0.1070	0.2915	-0.0118	-0.5805	-0.1034	0.4437	-0.0252	0.0082	-0.0217
A20	0.9648	0.1444	-0.0239	0.0521	0.0032	0.1162	0.0202	0.0448	-0.0245	-0.0063	-0.0422
A21	-0.8519	-0.1984	-0.0734	0.2112	0.0098	0.2791	-0.0363	0.2074	0.0326	0.1044	0.1208
A22	0.9137	0.0131	-0.0218	0.1873	-0.1555	-0.0836	0.0688	0.1385	0.0171	0.1863	-0.0707

Table 2 (continue)

A23	0.9478	0.0469	-0.0020	0.1705	-0.0254	-0.0076	-0.0009	0.0741	-0.1365	-0.0057	-0.0618
A24	0.9723	0.1068	0.0421	0.1154	0.0556	0.0610	0.0373	0.0639	-0.0468	0.0022	-0.0136
A25	0.0739	-0.0811	-0.0243	0.0722	0.2282	0.1506	-0.2751	0.8164	-0.0514	0.0732	-0.0025
A26	0.7330	0.1786	-0.0378	0.0099	0.0128	-0.0749	0.3685	0.1274	0.0665	-0.1054	0.4184
A27	0.9033	-0.0521	-0.0049	0.1106	0.0700	0.1042	-0.0716	0.1107	-0.0795	0.1467	-0.1358
A28	0.8903	-0.0763	0.1320	0.0631	0.0628	0.0330	0.1711	0.0739	-0.2336	0.2426	-0.0321
A29	0.2920	0.6308	-0.2165	0.1089	0.2163	-0.0548	0.2923	-0.0554	0.2921	-0.3485	-0.0970
A30	0.3632	-0.1568	0.6715	0.0888	-0.0708	0.0514	-0.0844	-0.0632	-0.4689	-0.2315	0.1795
A31	0.5832	0.0452	-0.1874	-0.0672	-0.0035	0.0267	-0.0907	0.1265	0.0016	0.7205	-0.0706
A32	-0.8568	-0.2240	-0.1044	-0.2800	-0.1767	-0.0864	-0.0933	0.2013	0.0669	0.0832	-0.0372
A33	0.2207	-0.1127	-0.0652	0.0847	0.1229	0.0270	0.0158	0.0102	-0.8921	-0.0516	-0.0409
A34	0.6654	-0.1733	-0.0846	-0.0963	0.0441	-0.0078	0.0605	0.1024	0.2142	0.6131	0.0531
A35	-0.5441	0.0636	-0.0656	-0.7288	0.1119	0.0150	-0.0104	0.1701	0.1468	-0.0450	-0.0480
A36	-0.2757	-0.1398	-0.0934	-0.8302	0.0096	0.0217	-0.1010	0.2316	0.0629	0.2537	-0.0209
A37	-0.2447	-0.1875	-0.0636	0.1242	-0.2906	-0.2963	-0.1827	0.0600	0.0794	0.4980	0.2972
Eigenvalue	12.2650	4.7826	3.3002	2.4682	2.3612	1.7287	1.6942	1.4975	1.2784	1.1337	1.0706
Variability %	31.1496	9.2995	6.1749	7.4550	5.2509	4.3818	8.0785	4.7386	4.7754	5.2906	4.1622
Cumulative %	31.1496	40.4491	46.6240	54.0790	59.3299	63.7118	71.7902	76.5288	81.3042	86.5949	90.7571

Note: Strong loadings (> 0.75) are shown in bold; moderate loading (0.5-0.75) in italic bold; weak loading (< 0.50)

Pattern Matching. Pattern matching is used in comparing the percentage similarities among the roots of Tongkat Ali and its products. Peak areas of 58 peaks were used as variables. Figure 5 (a) shows 2D chromatogram of Tongkat Ali root and product within the same cluster (R6 and P8 of cluster III) while Figure 5 (b) shows the 2D chromatogram of Tongkat Ali root and product of different clusters (R6 of cluster III, P1 of cluster I). At 95% confidence level, the computed p-value is greater than the significance level $\alpha = 0.05$ for both groups (within same cluster and of different clusters). However, within the same cluster, a high percentage similarity (92.6 %) was obtained compared with that of different clusters (88.0 %).

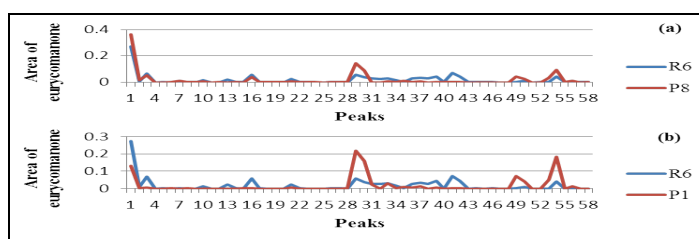


Figure 5. 2D chromatograms of representative Tongkat Ali roots and products: (a) within same cluster; and (b) of different clusters

CONCLUSIONS

A fast, reliable and comprehensive chromatographic fingerprint of Tongkat Ali root was obtained using an online SPE-LC method. Chemometric techniques were applied on Tongkat Ali datasets to show the relationship between variables. The CA was useful in showing similarities among the roots and products forming three clusters. DA confirmed the results of CA and yielded 100% correct assignment with 19 discriminant compounds while PCA is able to differentiate between roots and products, resulted in 11 varifactors with a total variance of 90.8 %. For pattern matching, the root and product within the same cluster have high percentage of similarity, 92.6 %. The results showed that chromatographic fingerprint of Tongkat Ali obtained using online SPE-LC combined with chemometrics could be a promising approach for quality control of herbal formulation.

ACKNOWLEDGEMENTS

The authors would like to acknowledge the financial support of Ministry of Higher Education (MOHE), Malaysia (Project number: 600-RMI/FRGS /5/3 (48/2014) and Universiti Teknologi, MARA. The technical support provided by Thermo Fisher Scientific, Shah Alam is greatly appreciated.

REFERENCES

- Al-Odaini, N. A., Zakaria, M. P., Zali, M. A., Juahir, H., Yaziz, M. I., & Surif, S. (2012). Application of chemometrics in understanding the spatial distribution of human pharmaceuticals in surface water. *Environmental Monitoring and Assessment*, 184, 6735-6748.

- Baharuddin, N., Saim, N., Zain, S. M., Juahir, H., Osman, R., & Aziz, A. (2014). Characterization of spatial patterns in river water quality using chemometric techniques. *Sains Malaysian*, 43(9), 1355-1362.
- Bhat, R., & Karim, A. A. (2010). Tongkat Ali (*Eurycoma longifolia* Jack): A review on its ethnobotany and pharmacological importance. *Fitoterapia*, 81, 669-679.
- Goncalves, C., Joaquim, C. G., Silva, E., & Alpendurada, M. F. (2006). Chemometric interpretation of pesticide occurrence in soil samples from an intensive horticulture area in north Portugal. *Analytica Chimica Acta*, 560, 164-171.
- Hajjouli, S., Chateauvieux, S., Teiten, M. H., Orlikova, B., Schumacher, M., Dicato, M., Choo, C.Y., & Diederich, M. (2014). Eurycomanone and eurycomanol from *Eurycoma longifolia* Jack as regulators of signaling pathways involved in proliferation, cell death and inflammation. *Molecules*, 19, 14649-14666.
- Li, Y., Wu, T., Zhu, J., Wan, L., Yu, Q., Li, X., Cheng, Z., & Guo, C. (2010). Combinative method using HPLC fingerprint and quantitative analyses for quality consistency evaluation of an herbal medicinal preparation produced by different manufacturers. *Journal of Pharmaceutical and Biomedical Analysis*, 52, 597-602.
- Locatelli, M., Genovese, S., Carlucci, G., Kremer, D., & Randic, M. (2012). Development and application of high performance-liquid chromatography for the study of two new oxyprenylated anthraquinones produced by *Rhamnus* species. *J. Chromatography A*, 1225, 113-120.
- Mohamad, M., Ali, M. W., Ripin, A., & Ahmad, A. (2013). Effect of Extraction Process Parameters on the Yield of Bioactive Compounds from the Roots of *Eurycoma longifolia*. *Journal Technology (Sciences & Engineering)*, 60, 51-57.
- Osman, R., Saim, N., Saaid, M., & Zaini, N. N. (2016). An experimental design approach for the extraction of eurycomanone from Tongkat Ali (*Eurycoma longifolia*) roots using pressurised liquid extraction (PLE). *Malaysian Journal of Analytical Science*, 20, 342-350.
- Saim, N., Osman, R., Spian, D. R. S. A., Jaafar, M. Z., Juahir, H., Abdullah, M. P., & Ghani, F. A. (2009). Chemometric approach to validating faecal sterols as source tracer for faecal contamination in water. *Water Research*, 43, 5023-5030.
- Teh, C. H., Murugaiyah, V., & Chan, K. L. (2011). Developing a validated liquid chromatography-mass spectrometric method for the simultaneous analysis of five bioactive quassinoid markers for the standardization of manufactured batches of *Eurycoma longifolia* Jack extract as antimalarial medicaments. *Journal of Chromatography A*, 1218(14), 1861-1877.
- Wang, P. & Yu, Z. (2015). Species authentication and geographical origin discrimination of herbal medicines by near infrared spectroscopy: A review. *Journal of Pharmaceutical Analysis*, 5, 277-284.
- Zaini, N. N., Osman, R., Juahir, H., & Saim, N. (2016). Development of chromatographic fingerprints of *Eurycoma longifolia* (Tongkat Ali) roots using online solid phase extraction-liquid chromatography (SPE-LC). *Molecules*, 21, 583.

Optimisation of Distributed Generation Unit Using Particle Swarm Optimisation Method and Voltage Stability Indicator

Aimi Iznina Ahameed Tarmizi, Roslina Mohamad, Saiful Izwan Suliman* and Murizah Kassim

Faculty of Electrical Engineering, Universiti Teknologi MARA (UiTM), 40450 Shah Alam, Selangor, Malaysia

ABSTRACT

Distributed generator is one of the most common sources of electric power as it has many advantages. However, it might cause negative effects to the distribution system if appropriate conditions are undermined. Thus, this paper describes ways to optimise the use of distributed generator in a distribution system in order to reduce total power losses and to improve system performance by increasing stability of the voltage profile. This study focuses on the installation of distributed generator that is installed on 69-bus radial distribution system. Optimisation are done through Particle Swarm Optimization and Voltage Stability Indicator. The findings show that total power loss was reduced by 44.6%, and there was improvement in voltage profile stability.

Keywords: Distributed generator, Particle Swarm Optimization, Voltage Stability Indicator

INTRODUCTION

Distributed generator (DG) is an alternative source of energy to increase efficiency of a distribution system. Installation of DG is aimed at reducing overall power loss and the capability of DG to improve the voltage profile (Gallano & Nerves, 2014). The integration

of DG units has contributed to system upgrade. However, emission is a real concern aggravated by climate change. Thus, there is a need for low emission generating unit. As the machine requires a large amount of space (Davis, 2002a, 2002b), DGs can replace the generation station. Hence, the DG unit can serve as a good alternative as it only requires minimal space in the distribution system.

A DG unit is a type of generator that supplies small-scale electricity to consumers.

ARTICLE INFO

Article history:

Received: 28 September 2016

Accepted: 03 February 2017

E-mail addresses:

saifulizwan@salam.uitm.edu.my (Saiful Izwan Suliman),

aimiiznina@gmail.com (Aimi Iznina Ahameed Tarmizi),

roslina780@salam.uitm.edu.my (Roslina Mohamad),

murizah@salam.uitm.edu.my (Murizah Kassim)

*Corresponding Author

It is different from central generation station (Nara, Ishizu, & Mishima, 2005) in terms size, effect on the environment and community, emission level, voltage stability and location. The DG is located at a site nearer to the customers compared with the generating station that has to be located at a certain distance from the consumers for safety reason and comfort issues.

A previous research used `fmincon` function in Matlab by considering the power demand and availability of the system generating units and equality restrictions. This was tested on three conditions: (i) the DG source connected to the system; (ii) the DG source not connected to the system; and (iii) steady state condition. It uses four generators and one load (Dulau & Bica, 2015). Other research used conventional optimisation techniques such as Genetic Algorithm (GA) to find the size and location of the capacitors, while another used a new method in determining a suitable location in placing the embedded generator. The latter was proposed based on new sensitivity indices that has been derived from the voltage stability improvement with respect to the changes in injected power towards the bus (Rahman, Rahim, & Musirin, 2004).

Installing a DG unit can present several challenges which include causing adverse effects if installed randomly, causing bigger total power loss towards the distribution system. This paper therefore explains how strategically installed DG compares favourably in terms of performance compared with randomly installed DG. Moreover, since the big central generation station needs a long transmission line, the DGs is a better solution. The objectives of this paper are to understand the characteristics of the DG in order to reduce total power losses in 69-bus distribution system and to improve the stability of the voltage profile and for this purpose, the study utilizes Voltage Stability Indicator (VSI) and Particle Swarm Optimization (PSO) algorithm. Both methods were implemented using Matlab (Dulau & Bica, 2015).

This study therefore aims to ensure installed DGs do not contribute to any negative issues, have the appropriate size, and reduce power losses during transmission from the generation part to the distribution part. By reducing the length of transmission lines, the chances of having lower total power losses is higher.

METHOD

The study used two methods to optimise the usage of DG units: which are Voltage Stability Indicator (VSI) and Particle Swarm Optimization (PSO).

Voltage Stability Indicator

The voltage stability indicator (VSI) was proposed by Kayal and Chanda (2013). In this paper, VSI is used to find the optimal location to place the DG units in the distribution network. By using VSI, the stability of the voltage profile will increase. In this way, electricity can be delivered efficiently. The conventional power flow equations of the receiving bus is as follows (Kayal & Chanda, 2013):

$$I^2 = (P_{i+1}^2/Q_{i+1}^2)/V_{i+1}^2 \quad [1]$$

$$I^2 = \frac{P_{L,i}^2 + Q_{L,i}^2}{(V_i - V_{i+1})^2} \quad [2]$$

$P_{L,i}$ and $Q_{L,i}$ are the active and reactive power losses of the line connected between two nodes respectively. Equation (3) is the power balance equation that needs to be balanced at all time to ensure steady operation.

$$\frac{(P_{i+1}^2 + Q_{i+1}^2)}{V_{i+1}^2} = \frac{P_{L,i}^2 + Q_{L,i}^2}{(V_i - V_{i+1})^2} \quad [3]$$

P_{i+1} and Q_{i+1} can be found by using these two equations

$$P_{i+1} = P_i - P_{L,i} \quad [4]$$

$$Q_{i+1} = Q_i - Q_{L,i} \quad [5]$$

After computing the previous calculation, the VSI is expressed as

$$L_{i+1} = \frac{4 \sqrt{((P_{i+1}^2 + Q_{i+1}^2) \cdot (r_i^2 + x_i^2))}}{V_i^2} \leq 1 \quad [6]$$

Where V_i is the voltage magnitude while r_i and x_i is the resistance and impedance of each bus.

Particle Swarm Optimization

Particle Swarm Optimization (PSO) is a technique proposed by Kennedy and Eberhart in 1995. This algorithm is an intelligent-based optimisation that simulates the migration of bird flock when seeking for foods. The PSO actually finds the optimal solution by applying the movement trends of particle population and their interaction. It also finds the particle swarm and parallel global search. Figure 1(a) is the flowchart of PSO algorithm (Kai, Agalgaonkar, Muttaqi, & Perera, 2008; Rugthaicharoencheep, Lantharthong, & Auchariyamet, 2011).

The methods used in this paper are VSI and PSO; the former was used to determine the most suitable bus to install the DGs while the latter was used to obtain the value to be injected to the chosen bus. The ways to implement both methods are shown in Figure 1(b). First, the 69-bus was loaded in the Matlab software. In this simulation, 69-bus was used with the details of the simulation parameters provided in Table 1. Next, load flow analysis was done using the Newton-Raphson method to determine the total power loss of the system. The losses on each bus were recorded. After that, the choice of either to apply the VSI or not was done. If the choice is yes, then data for VSI calculations are recorded. Data was taken from the workspace in the Matlab software and the data were real and reactive power, real and reactive power losses, voltage magnitude, resistance and impedance for each bus. Then, the priority list was made by sorting the VSI value in descending order. The installation of DGs was made according to the priority list. The top four buses will be installed with DGs. The DGs can also be added at any location without applying the VSI calculation.

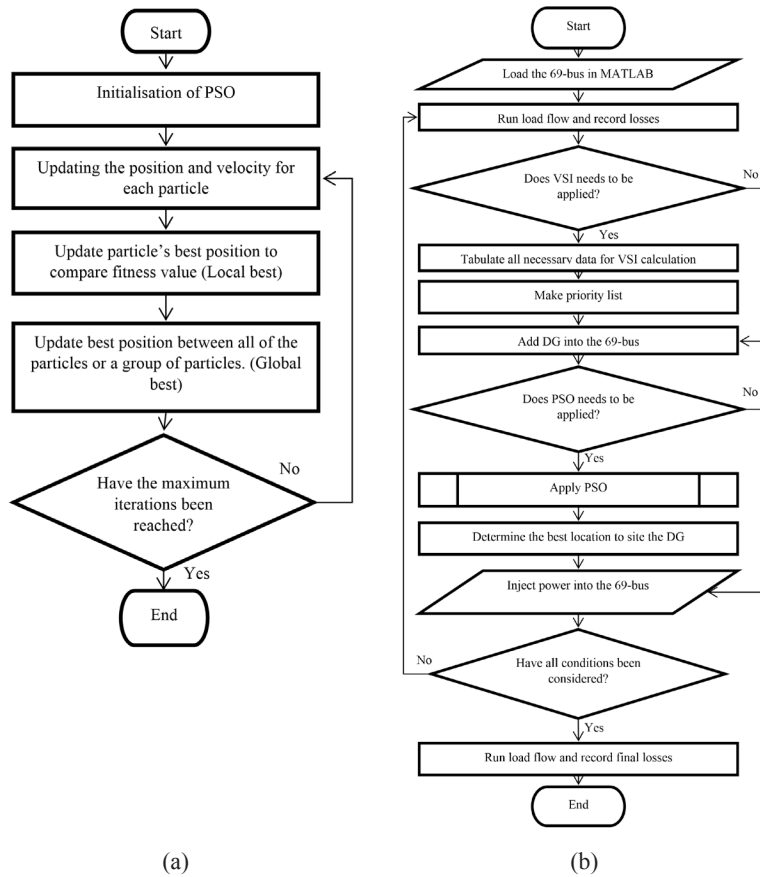


Figure 1. (a) PSO algorithm; and (b) Flowchart of DG Optimisation

Table 1
Simulation parameters of 69-Bus

Bus	Voltage magnitude (V)	Load		Power loss		Resistance (Ω)	Impedance (Ω)
		(MW)	(Mvar)	(MW)	(Mvar)		
1-23	1.0000 to 0.9674	0.0000 to 0.0000	0.0000 to 0.0000	0.0000 to 0.0000	0.0000 to 0.0000	0.0003 to 0.3153	0.0007 to 0.1043
24-34	0.966 to 1.768	0.0280 to 0.0195	0.0200 to 0.0140	0.0010 to 0.0510	0.0000 to 0.0510	0.6832 to 1.9853	0.2259 to 0.6563
35-46	1.736 to 0.972	0.0060 to 0.0392	0.0040 to 0.02630	0.0480 to 0.0010	0.0480 to 0.0000	0.9197 to 0.6245	0.3040 to 0.3127
47-64	0.9997 to 0.9593	0.0000 to 0.2270	0.0000 to 0.1620	0.0030 to 0.0000	0.0070 to 0.0000	0.0552 to 1.0928	0.1352 to 0.5566
65-69	0.9612 to 0.9719	0.0590 to 0.0280	0.1620 to 0.0200	0.0000 to 0.0000	0.0000 to 0.0000	1.2734 to 0.0029	0.6428 to 0.0010

A decision needs to be made whether to apply or not to apply the PSO algorithm. If yes, then the PSO program is run using Matlab and results analysed. From the result, the appropriate sizes of DGs are determined. Next, the DGs are added into the 69-bus. If the previous decision is no, the DGs can be added in random sizes. Finally, the last decision is made where, either all the conditions have been considered or not. If yes, the last step is to run the load flow and the

final losses recorded. However, if decision is no conditions were considered, then the next step is to run the load flow analysis and record the losses but after that, again, the consideration of VSI calculation needs to be made. Four cases were used in this paper. Those cases are as follows:

- a) Apply both VSI and PSO
- b) Apply only VSI
- c) Apply only PSO
- d) Without applying both PSO and VSI

Referring to Figure 2, the DGs are located at four chosen buses. The program then calculates the suitable size for each chosen bus. Each bus might have similar or different values which is determined by the program. Next, the total power loss in this system was calculated and displayed. The latest values were assumed as better than the values from the previous iteration(s). The current iteration number was checked in order to know whether the maximum iteration has been reached or not. If the maximum iteration has not been reached, it will repeat Step 2, if it has been reached, it will end the program.

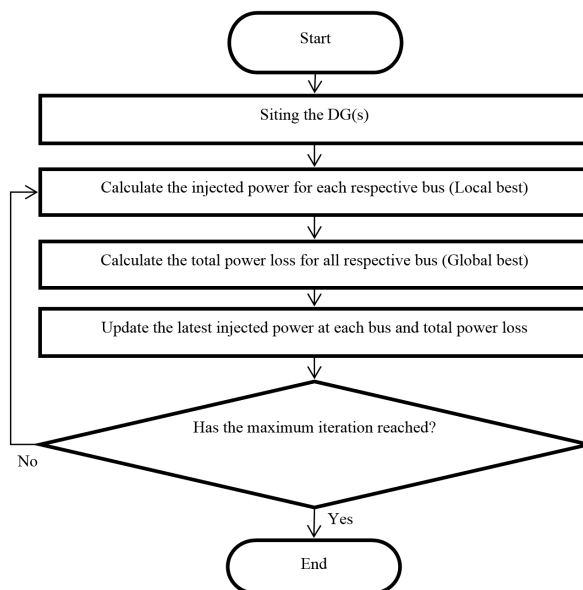


Figure 2. Flowchart of PSO implementation

RESULTS AND DISCUSSION

Table 2 presents the result of the total loss of 69-bus distribution system before and after the installation of DG units. The results showed that the total loss before installation of DG units is 0.166 MW. The total loss after DG units installation by using both PSO and VSI methods are the least compared with the other three conditions where it conserves the power by 74 kW. The least power conservation, which is 10 kW, was demonstrated by the system with

installed DG units that inly applied PSO method. The other two conditions that applied VSI only or neither algorithm in the installation of DG units both decreased the power loss by 69 kW and 52 kW respectively. This proved that the system that installed DGs by applying both PSO and VSI successfully reduced 74 kW compared. This gives the system 44.6% reduction of total power loss.

Table 2
Result of the total power loss before and after installation of DGs

Conditions of Distribution System	Total Power Loss	
	Real Power (MW)	Reactive Power (Mvar)
Without DGs	0.166	0.132
With DGs (Considering VSI and PSO)	0.092	0.081
With DGs (Considering PSO)	0.156	0.119
With DGs (Considering VSI)	0.097	0.085
With DGs (Without considering VSI and PSO)	0.114	0.092

The first bar chart (see Figure 3) shows the system voltage profile without DGs installation and after DGs were installed using both VSI and PSO techniques. Bus 1 to 4 and 28 to 30 do not show any difference while Bus 4 displays a slight difference. This condition is due to the selection of location of installed DG. It can affect only the buses. The other buses display quite clear differences between these two states. The highest difference was shown at bus 27 which is 0.024 pu.

Figure 4 shows the difference between part of the system without DG installed and with the DG installed after only using PSO method to determine the amount of power that needs to be injected into the system while the location of the DGs was selected randomly. The pattern of this bar chart is quite similar to Figure 3. Bus 1 to 4 and 28 to 30 once again does not show any differences. The same goes to Bus 5 that only shows a slight difference. However, in this case, the voltage profiles are quite wavy and show higher differences between both conditions compared with the previous figure. Moreover, the largest difference of voltage magnitude is shown by Bus 16 which is 0.033 pu.

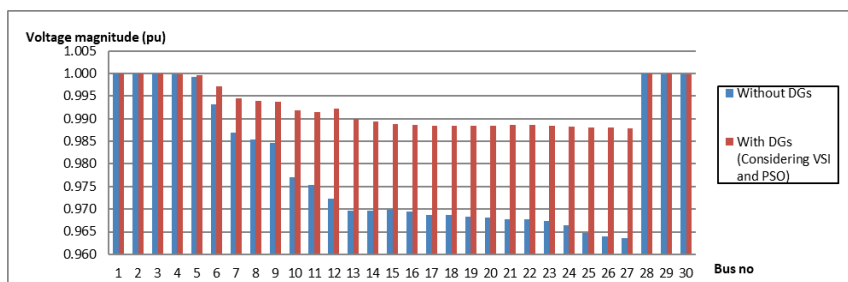


Figure 3. Voltage profile for the first thirty buses before and after installing the DG using VSI and PSO

As seen in Figure 5, the voltage profile after adding the DG units are also better, as shown in Figure 3 and Figure 4. The voltage profile shown in Figure 5 is pre-and post DG units installation but by only using the VSI method. Figure 5 shows quite similar patterns to Figure 3. However, there is a slight difference between these figures where the highest difference between both states was shown with Bus 12 by 0.023 pu.

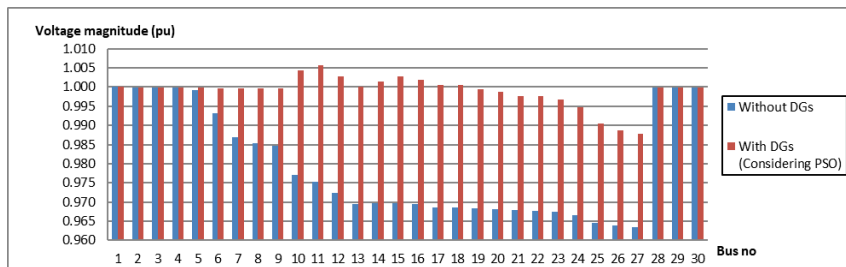


Figure 4. Voltage profile for the first 30 buses before and after installing the DG using PSO

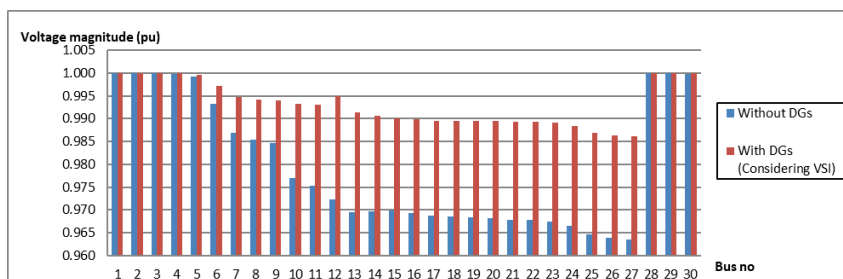


Figure 5. Voltage profile for the first 30 buses before and after installing the DG using VSI

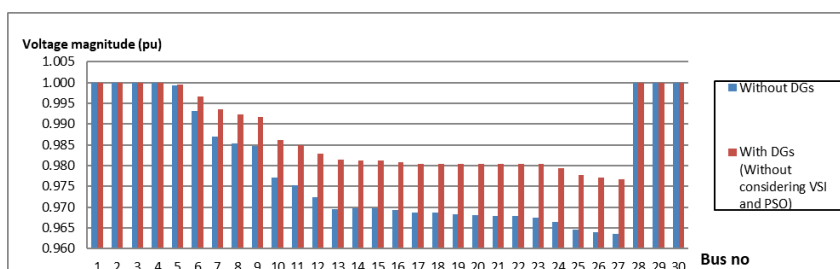


Figure 6. Voltage profile for the first 30 buses before and after installing the DG randomly

As for Figure 6, the DGs were added but at random locations and sizes. This figure shows the least difference of voltage magnitude for the two conditions between all four figures explained previously. Although the same bus as Figure 3 shows the highest difference of voltage magnitude, the value of the difference differs. For Figure 6, the difference is only 0.132 pu. This is the lowest difference shown by all four conditions.

CONCLUSION

This paper has presented two ways to optimise the installation of DGs in the 69-bus distribution system which is by using PSO and VSI. It can be concluded that the implementation of both methods improves the performance of the system with installed DGs. The total power loss was successfully reduced by 44.6%. At the same time, the voltage profile of the system has also improved in the aspect of stability as the system installed with DGs by applying both PSO and VSI showed more consistency. This paper proves that the use of both methods provides the most stable distribution system and the least total power loss. For future research, it is recommended to include a few systems for comparison. Moreover, comparing these methods to others is also good for the development of a better distribution system.

REFERENCES

- Davis, M. W. (2002a). Distributed resource electric power systems offer significant advantages over central station generation and T & D power systems. I. *IEEE Power Engineering Society Summer Meeting*, 25-25 July 2002, Atlanta, USA.
- Davis, M. W. (2002b). Distributed resource electric power systems offer significant advantages over central station generation and T & D power systems. II. *IEEE Power Engineering Society Summer Meeting*, 25-25 July 2002, Atlanta, USA.
- Dulau, L. I., & Bica, D. (2015). Optimization of a power system with distributed generation sources. *13th International Conference on Engineering of Modern Electric Systems (EMES)*, 11-12 June 2015. Bucharest, Romania.
- Gallano, R. J. C., & Nerves, A. C. (2014). Multi-objective optimization of distribution network reconfiguration with capacitor and distributed generator placement. *IEEE Region 10 TENCON 2014 Conference*, 22-25 Oct. 2014. Bangkok, Thailand.
- Kai, Z., Agalgaonkar, A. P., Muttaqi, K. M., & Perera, S. (2008). Optimisation of distributed generation units and shunt capacitors for economic operation of distribution systems. *Australasian Universities Power Engineering Conference*. 14-17 Dec. 2008, Sydney, Australia.
- Kayal, P., & Chanda, C. K. (2013). A simple and fast approach for allocation and size evaluation of distributed generation. *International Journal of Energy and Environmental Engineering*, 4(1), 1-9.
- Nara, K., Ishizu, S., & Mishima, Y. (2005). Voltage control availability of distributed generators in power distribution system. *2005 IEEE Russia Power Tech*. 27-30 June 2005, St. Petersburg, Russia.
- Rahman, T. K. A., Rahim, S. R. A., & Musirin, I. (2004). Optimal allocation and sizing of embedded generators. *National Power and Energy Conference*. 29-30 Nov. 2004, Kuala Lumpur, Malaysia.
- Rugthaicharoencheep, N., Lantharthong, T., & Auchariyamet, S. (2011). Optimal operation for active management of distribution system with distributed generation. *International Conference on Clean Electrical Power*. 14-16 June 2011, Ischia, Italy.

Electrical Properties of Plasticised Proton Conducting MG49 Polymer Electrolyte

Zaidatul Salwa Mahmud^{1*}, Siti Nor Hafiza Mohd Yusoff²,
Nur Hamizah Mohd Zaki³, Mohamad Fariz Mohamad Taib³,
Mohamad Kamil Yaakob³, Oskar Hasdinor Hassan⁴ and Ab Malik Marwan Ali^{2,5}

¹Faculty of Applied Sciences, Universiti Teknologi MARA (UiTM) Perak, 35400 Tapah, Perak, Malaysia

²Faculty of Applied Sciences, Universiti Teknologi MARA (UiTM) Johor, Pasir Gudang, 81750 Masai, Johor, Malaysia

³Faculty of Applied Sciences, Universiti Teknologi MARA (UiTM), 40450 Shah Alam, Selangor, Malaysia

⁴Department of Industrial Ceramic, Faculty of Art and Design, Universiti Teknologi MARA (UiTM), 40450 Shah Alam, Selangor, Malaysia

⁵Ionics Materials and Devices Research Laboratory (iMADE), Institute of Sciences, Universiti Teknologi MARA (UiTM), 40450 Shah Alam, Selangor, Malaysia

ABSTRACT

A free-standing film consisting of 49% PMMA grafted-natural rubber electrolytes was prepared. Potassium hydroxide (KOH) and propylene carbonate (PC) was added to the preparation and the properties of the electrolytes measured using complex impedance analysis at various temperatures. The addition of plasticiser in alkaline polymer electrolyte gives rise to the ionic conductivity up to $2.647 \times 10^{-6} \text{ S cm}^{-1}$ at composition consisting of 50wt.% of PC. The dielectric properties of the GPEs were studied and the relaxations at higher frequencies appear in both imaginary and real part of the permittivity. These relaxations are related with the interface ion polarisations at the polymer-electrode interface and segmental motion of the polymer electrolyte molecular chains. The influence of the impedance spectra on temperature was studied. Results showed rising temperature increased conductivity, top frequency (f^*), relative dielectric constant (ϵ_r) and geometrical capacitance (C_g) due to the mobility of free ion carriers

Keywords: Dielectric analysis, ionic conductivity, MG49, plasticised polymer electrolyte

ARTICLE INFO

Article history:

Received: 28 September 2016

Accepted: 03 February 2017

E-mail addresses:

zaidatulsalwa@perak.uitm.edu.my (Zaidatul Salwa Mahmud),

sitiorhafiza@johor.uitm.edu.my (Siti Nor Hafiza Mohd Yusoff),

hamizah.zaki@gmail.com (Nur Hamizah Mohd Zaki),

mfariz@salam.uitm.edu.my (Mohamad Fariz Mohamad Taib),

muskamil20@yahoo.com (Mohamad Kamil Yaakob),

oskar@alam.uitm.edu.my (Oskar Hasdinor Hassan),

ammali@salam.uitm.edu.my (Ab Malik Marwan Ali)

*Corresponding Author

INTRODUCTION

Proton-conducting electrolytes have been identified as promising separator in batteries, supercapacitors and fuel cells (Qiao et al., 2010, Zukowska et al., 2000). Alkali-based

electrolytes exhibit high proton conductivity even at temperatures below 370 K (Zukowska et al., 2000; Nikulin et al., 2014). Metal hydroxides containing hydrogen have been attracting attention as promising proton conducting materials with unique characteristic of occupying an intermediate position between electronic and ionic conductors (Qiao et al., 2010). Potassium hydroxide (KOH), the subject of investigation in this paper, is an alkali metal that provides hydrogen or proton charge carriers in the electrolytes (Nikulin et al., 2014). However, safety issues concerning the commercial batteries using alkaline liquid based electrolytes make them unsuitable for practical use. Thus, an alternative is solid polymer electrolytes as the problems resulting from usage of liquid electrolytes can be avoided to a great extent. Polymer electrolytes are known for their good mechanical properties and ease of fabrication (Mohamad et al., 2008; Chandra et al., 2002). Unfortunately, these solid polymer electrolytes suffer low conductivity at room temperature. Hence, to improve conductivity, several techniques are useful, such as grafting, plasticisation (Woo et al., 2013; Zaki et al., 2012), polymer blending (Alias et al., 2012) and fillers (Adam et al., 2012). Plasticisation involves adding a substantial amount of plasticiser into the polymer matrix which produces gel polymer electrolytes (GPEs) (Kato et al., 2002). Plasticisers have been proven to soften the rigid polymer chain, allow greater mobility of charge carriers, and lower the glass transition temperature (Chandra et al., 2002; Alias et al., 2005; Kamisan et al., 2010). Plasticisers of low molecular weight and high dielectric constant are frequently selected, such as propylene carbonate (PC), ethylene carbonate (EC), dimethylformamide (DMF), etc (Latham et al., 2002). These plasticisers were reported to be compatible with poly (methyl methacrylate) (PMMA) and accommodate the enhancement of conductivity (Alias et al., 2005). The MG49 is a polymer consisting of natural rubber grafted with 49% PMMA and the former is suitable to be applied as polymer host of electrolytes. The MG49 contains functional groups of carbonyl (C=O) and carboxyl (C-O-O-H), which will covalently bond with the hydroxide ions (OH⁻) of KOH. The high permittivity and high dielectric constant of MG49 assist in ionization of salt providing high concentration of charge carriers.

This paper studies the properties of plasticised alkaline based polymer electrolyte using MG49 as the polymer host and KOH as the proton charge contributor. The existence of lone pairs in the molecular structure of the polymer host makes it possible for the complexation of salt-polymer, whereas the cation will be attracted to the lone pairs and enhancing the ion diffusion inside the polymer matrix simultaneously produces free ions (Mahmud et al., 2012). The diffusion and mobility of free ions contribute to ionic conduction while the electrolytes were introduced with propylene carbonate (PC) as the solvent (plasticiser). The electrical properties of MG49-KOH-PC polymer electrolytes are presented and discussed.

METHOD

Sample Preparation and Characterisation

The GPE films comprising MG49-KOH-PC were prepared by solution casting technique. MG49 (Rubber Research Institute of Malaysia, RRIM), potassium hydroxide (KOH) (Aldrich) and propylene carbonate (PC) (purity 98%, Aldrich) were used. The KOH salt was vacuum dried for 12 hours at 383 K prior used. 1.0 g of MG49 was dissolved in 25 ml tetrahydrofuran

(THF) (Aldrich, $\geq 99.9\%$) and was doped with potassium hydroxide (KOH). The solution was then stirred continuously with magnetic stirrer for several hours at room temperature. The homogeneous solution was then cast onto petri dish and allowed to naturally dry in the fume hood at room temperature. The remaining solvent in the cast solution was removed by drying it in vacuum oven for 48 hours at 333 K. Various stoichiometric ratios of KOH and MG49 were then repeated as above procedure. The sample with highest ionic conductivity was selected and added with different weight percent of PC to prepare GPEs in a similar way. The obtained films were stored in desiccator for further use.

The prepared films were studied through impedance data taken from the impedance spectroscopy. The electrolyte films were first sandwiched between two stainless steel blocking electrodes with cross-sectional area of 0.196 cm^2 and connected to HIOKI 3532-50 HiTester Impedance Spectroscopy. The impedance spectroscopy was logged over a frequency range of 1-106 Hz. The samples were placed in a humidity chamber for controlled temperature between 30°C to 100°C .

RESULTS AND DISCUSSION

Nyquist plot studies

Nyquists were plotted to study the ion interaction in the polymer electrolytes. Figure 1(a) and Figure 1(b) shows the Nyquist plot of cells assembled by MG49-KOH-PC electrolyte with stainless steel electrode at 303K. During the impedance test, the polymer electrolytes were placed in between two stainless-steels (SS). The SS acts as a blocking electrode for ion transportation, and an inert electrode for the polymer electrolyte. As a result, a linear line was observed at 10 and 20 wt.% of PC as in Figure 1(a). The plot however was transformed into an inclined arc at higher content of PC. The inclined arc is often observed in Nyquist plane for rough electrodes where a Faradaic reaction takes place in addition to capacitive charging (Bosco et al., 2008).

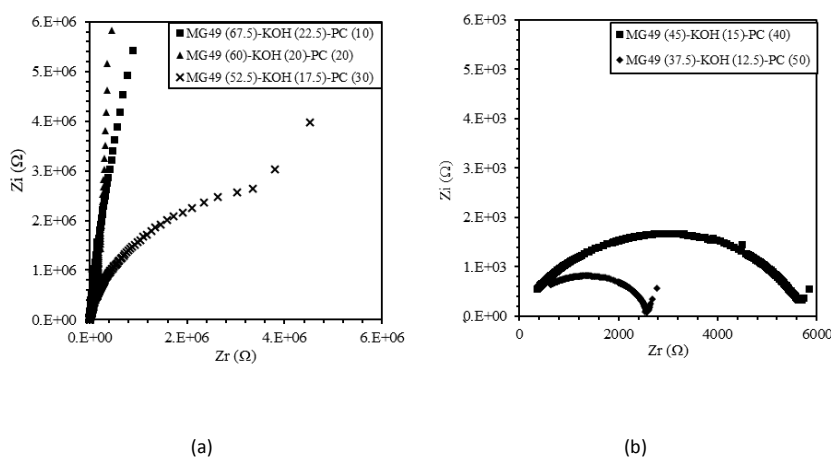


Figure 1. (a), (b) Nyquist plot for MG49-KOH samples of various wt. % PC

The addition of 40 and 50 wt.% of PC results in one semicircle at high frequency range as in Figure 1(b). The intersection of the semicircle and the straight line reflects the bulk resistance R_b of the polymer electrolyte. The straight line in low frequencies is attributed to the ion diffusion in the electrolyte (Xu et al., 1998). The ionic conductivities were calculated based on the following equation:

$$\sigma = \frac{t}{(A.R_b)} \quad [1]$$

Where (R_b) is the bulk resistance, A and t are the electrolyte film surface area and thickness respectively. The ionic conductivities for each sample are shown in Table 1. At higher wt.% of PC, the Nyquist plot is compressed to smaller inclined arc (as in Figure 1(b)), whereas the bulk resistance decreases to smaller values. This indicates that the addition of more plasticiser improves the electrode-electrolyte contact. Plasticiser helps improve the flexibility of the electrolyte, hence increasing its contact with the electrode. The bulk resistances of the samples were also reduced. The good electrode-electrolyte contact contributes to more surface contact area for the ion polarisation to induce and simultaneously increase the conductivity of the polymer electrolyte. The ion polarisation is further investigated through the dielectric relaxation of each sample. The presence of plasticiser also favours the ionic mobility that correlates with the flexibility of the polymer host due to the creation of free volume (Adam et al., 2012; Hashim et al., 2010).

Table 1
Bulk Resistance (R_b) and conductivity values (σ) for MG49-KOH containing different wt. % of PC

PC content (wt. %)	Bulk Resistance, R_b (Ω)	Conductivity, σ (S.cm ⁻¹)
10	5.34x10 ⁷	2.408x10 ⁻¹⁰
20	3.25x10 ⁸	4.210x10 ⁻¹¹
30	9.52x10 ⁶	1.348x10 ⁻⁹
40	8.01x10 ³	1.331x10 ⁻⁶
50	3.23x10 ³	2.647x10 ⁻⁶

Dielectric relaxation studies

Dielectric relaxation is studied to investigate the ion polarisation for samples of different wt.% of PC. The distributions of dielectric constants with frequency are shown in Figure 2. Both real and imaginary parts of dielectric constant rise abruptly at low frequencies (approximately < 3000 Hz) confirming a strong polarisation effect on the blocking electrodes. The ion polarisations are induced by the current flowed through the system. The dipoles within the polymer electrolyte tend to rotate and align according to the electric field applied, resulting in diffusion of ions which accumulate at the electrode-electrolyte interface (Mahmud et al., 2012). The accumulation of ions results in polarisation effect, thus, producing high dielectric values (Sotta et al., 2010; Sheha et al., 2012). These dielectric constant values were observed to be larger at higher content of PC from 10 wt.% to 50 wt.%. The presence of low molecular

weight PC causes the polymer electrolyte to be more flexible, contributes to the increase of ion polarisation occurrence at the electrode-electrolyte interface due to higher surface contact, as proven by the Nyquist plot study. The flexibility is also due to the amorphous nature of the MG49 polymer electrolyte (Mahmud et al., 2012).

At high frequencies though, both real and imaginary dielectric constants were observed to decrease. In this stage, the dipoles are unable to follow the field variation at high frequencies as the periodic reversal is too fast for the dipole to orientate according to the field orientation, causing the dipole to appear ‘frozen’ (Saroj et al., 2013).

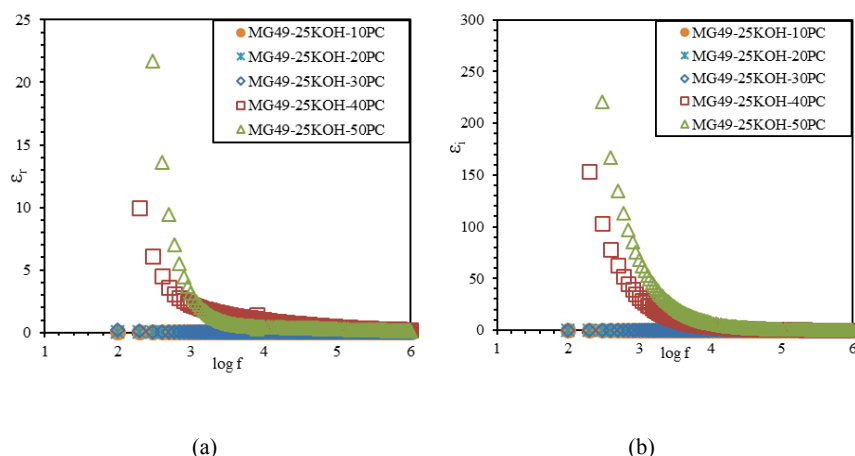


Figure 2. (a) Real; and (b) imaginary part of dielectric constant versus frequencies for MG49 – 25 wt.% KOH with different wt.% of PC

Impedance analysis for varying temperatures

The electrical properties of MG49-KOH-PC samples at different temperatures were studied. The total impedance of the stainless steel (SS) electrode, C_r and Z_w represent the bulk resistance, the real part of the electrolyte capacitance and the Warburg impedance. The real part of the polymer electrolyte capacitance can be expressed as,

$$C_r = A\epsilon_0\epsilon_r/l \quad [2]$$

where ϵ_0 (equal to $8.85 \times 10^{-14} \text{ F cm}^{-1}$) is the dielectric constant of vacuum, ϵ_r is the real part of the dielectric constant of the studied electrolyte film, A is the electrolyte film surface area (cm^2) and l is the electrolyte film thickness (cm). The top frequency, f^* of the impedance spectrum can be expressed as a function of ionic conductivity, σ as below,

$$f^* = \sigma/(2\pi\epsilon_0\epsilon_r) \quad [3]$$

Utilising these equations, the relative dielectric constant (ϵ_r), ionic conductivity (σ), the top frequency (f^*) and the real part capacitance (C_r) of MG49-KOH-PC film can be determined according to the impedance spectrum.

The ionic conductivity, top frequency, relative dielectric constant and geometrical capacitance at various temperatures for MG49-KOH-PC film were plotted as shown in Figure 3(a), (b), (c) and (d). These four parameters appeared to increase with increasing temperature. This is due to the mobility of free ion carriers facilitated by the increment of the segmental motion of the polymer molecular (Woo et al., 2013; Xu et al., 1998; Mahmud et al., 2012). The increase in temperature significantly increases the amorphous nature of the polymer electrolytes, thus providing bigger free volume in the system and increasing the conductivity. Consequently, the increase of temperature will increase the internal energy to the polymer chain allowing it to push against its neighbouring atoms, thus creating more free volume.

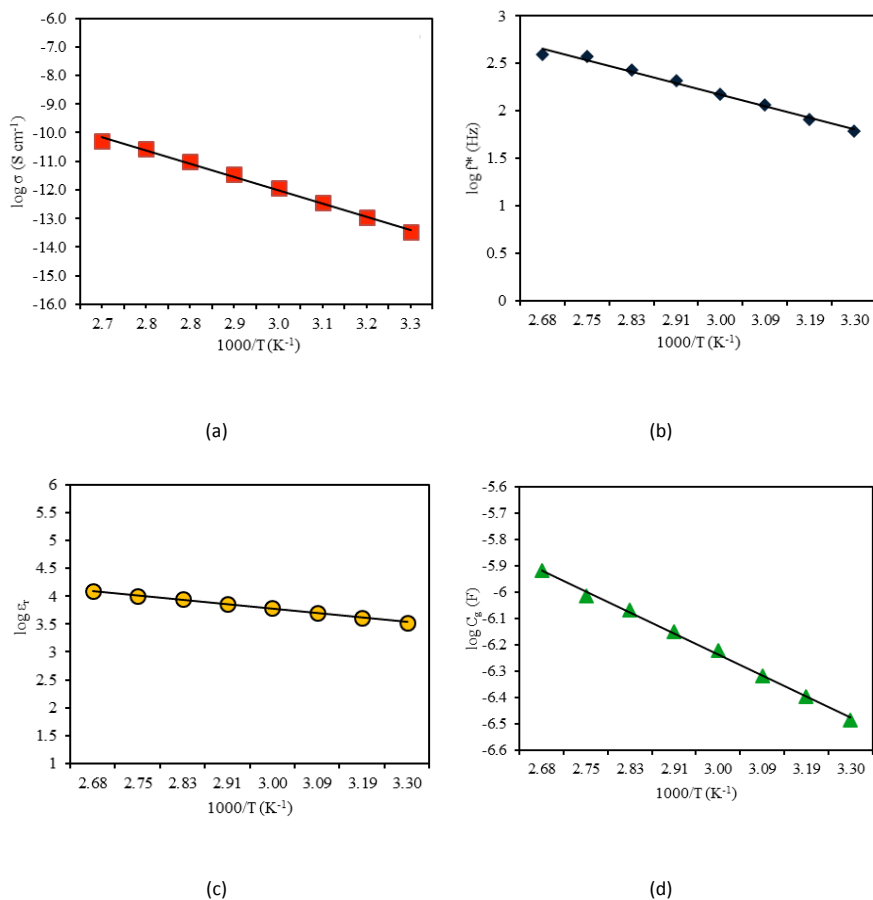


Figure 3. The influence of temperature on the: (a) ionic conductivity (σ); (b) top frequency (f^*); (c) relative dielectric constant (ϵ_r); and (d) geometrical capacitance (C_g) of MG49-25KOH-50PC

CONCLUSION

This study had focused on the role of plasticiser in alkaline based polymer electrolytes in term of its impedance properties. The addition of plasticiser, PC, inside the polymer matrix were observed to increase the ionic conductivity up to $2.65 \times 10^{-6} \text{ S cm}^{-1}$, achieved by MG49-KOH sample containing 50 wt.% PC content. The PC consequently improved the polymer electrolyte flexibility, and provided better electrode-electrolyte contact, whereas its low molecular weight properties provided larger free volume inside the polymer system. The dielectric relaxation indicated improved electrode- electrolyte contact whereas more surface contact area for ions polarisation.

ACKNOWLEDGEMENTS

The authors gratefully acknowledge the financial support from Ministry of Higher Education Malaysia (MOHE) under RAGS grant (600-RMI/RAG 5/3 (23/2014), and University Teknologi MARA (UiTM) for the facilities provided to undertake this study.

REFERENCES

- Adam, N. I., Zaki, N. H. M., Mahmud, Z. S., Yahya, M. Z. A., & Ali, A. M. M. (2012, September). The effect of composition nanofiller Al_2O_3 to the conductivity, morphology and thermal properties of MG30-LiTf polymer electrolyte. In *Business, Engineering and Industrial Applications (ISBEIA), 2012 IEEE Symposium on* (pp. 701-704). IEEE.
- Alias, A. N., Kudin, T. T. I., Zabidi, Z. M., Harun, M. K., & Yahya, M. Z. A. (2012). Optical characterization of luminescence polymer blends using tauc/davis-mott model. In *Advanced Materials Research* (Vol. 488, pp. 628-632). Trans Tech Publications.
- Alias, Y., Ling, I., & Kumutha, K. (2005). Structural and electrochemical characteristics of 49% PMMA grafted polyisoprene-LiCF₃SO₃-PC based polymer electrolytes. *Ionics*, *11*(5), 414-417.
- Bosco, E. (2008). Constant phase elements, depressed arcs and analytic continuation: A critique. *Journal of Electroanalytical Chemistry*, *624*(1-2), 14-20.
- Chandra, S., Sekhon, S. S., Srivastava, R., & Arora, N. (2002). Proton-conducting gel electrolyte. *Solid State Ionics*, *154*, 609-619.
- Hashim, H., Adam, N. I., Zaki, N. H. M., Mahmud, Z. S., Said, C. M. S., Yahya, M. Z. A., & Ali, A. M. M. (2010, December). Natural rubber-grafted with 30% poly (methylmethacrylate) characterization for application in lithium polymer battery. In *Science and Social Research (CSSR), 2010 International Conference on* (pp. 485-488). IEEE.
- Kamisan, A. S., Kudin, T. I. T., Ali, A. M. M., & Yahya, M. Z. A. (2011). Electrical and physical studies on 49% methyl-grafted natural rubber-based composite polymer gel electrolytes. *Electrochimica Acta*, *57*, 207-211.
- Karmakar, A., & Ghosh, A. (2012). Dielectric permittivity and electric modulus of polyethylene oxide (PEO)-LiClO₄ composite electrolytes. *Current Applied Physics*, *12*(2), 539-543.

Zaidatul Salwa Mahmud, Siti Nor Hafiza Mohd Yusoff, Nur Hamizah Mohd Zaki, Mohamad Fariz Mohamad Taib, Mohamad Kamil Yaakob, Oskar Hasdinor Hassan and Ab Malik Marwan Ali

- Kato, Y., Hasumi, K., Yokoyama, S., Yabe, T., Ikuta, H., Uchimoto, Y., & Wakihara, M. (2002). Polymer electrolyte plasticized with PEG-borate ester having high ionic conductivity and thermal stability. *Solid State Ionics*, 150(3), 355-361.
- Latham, R. J., Rowlands, S. E., & Schlindwein, W. S. (2002). Supercapacitors using polymer electrolytes based on poly (urethane). *Solid State Ionics*, 147(3), 243-248.
- Mahmud, Z. S., Adam, N. I., Zaki, N. H. M., & Yahya, M. Z. A. (2012, September). Conductivity and optical studies of plasticized polymer electrolytes based on 49% PMMA-grafted natural rubber. In *Business, Engineering and Industrial Applications (ISBEIA), 2012 IEEE Symposium on* (pp. 504-508). IEEE.
- Mahmud, Z. S., Zaki, N. H. M., Subban, R. H. Y., Ali, A. M. M., & Yahya, M. Z. A. (2012, December). MG49-KOH-PC alkaline gel polymer electrolytes membrane for supercapacitors. In *Humanities, Science and Engineering (CHUSER), 2012 IEEE Colloquium on* (pp. 621-626). IEEE.
- Mohamad, A. A., Haliman, H., Sulaiman, M. A., Yahya, M. Z. A., & Ali, A. M. M. (2008). Conductivity studies of plasticized anhydrous PEO-KOH alkaline solid polymer electrolyte. *Ionics*, 14(1), 59-62.
- Nikulin, E. I., & Baikov, Y. M. (2014). Proton conductivity and phase transition in potassium hydroxide monohydrate. *Physics of the Solid State*, 56(6), 1093-1095.
- Qiao, J., Fu, J., Lin, R., Ma, J., & Liu, J. (2010). Alkaline solid polymer electrolyte membranes based on structurally modified PVA/PVP with improved alkali stability. *Polymer*, 51(21), 4850-4859.
- Saroj, A. L., & Singh, R. K. (2012). Thermal, dielectric and conductivity studies on PVA/ionic liquid [EMIM][EtSO₄] based polymer electrolytes. *Journal of Physics and Chemistry of Solids*, 73(2), 162-168.
- Sheha, E., Khoder, H., Shanap, T. S., El-Shaarawy, M. G., & El Mansy, M. K. (2012). Structure, dielectric and optical properties of p-type (PVA/CuI) nanocomposite polymer electrolyte for photovoltaic cells. *Optik-International Journal for Light and Electron Optics*, 123(13), 1161-1166.
- Sotta, D., Bernard, J., & Sauvart-Moynot, V. (2010). Application of electrochemical impedance spectroscopy to the study of ionic transport in polymer-based electrolytes. *Progress in Organic Coatings*, 69(2), 207-214.
- Woo, H. J., Majid, S. R., & Arof, A. K. (2013). Effect of ethylene carbonate on proton conducting polymer electrolyte based on poly (ϵ -caprolactone)(PCL). *Solid State Ionics*, 252, 102-108.
- Xu, W., Siow, K. S., Gao, Z., & Lee, S. Y. (1998). AC impedance study on the interface of lithium and polymer electrolyte based on lithium-N (4-sulfophenyl) maleimide. *Solid State Ionics*, 112(1), 1-8.
- Zaki, N. H. M., Mahmud, Z. S., Adam, N. I., Ahmad, A. H., Ali, A. M. M., & Yahya, M. Z. A. (2012, September). Characterization of plasticized grafted natural rubber-30% poly (methyl methacrylate) (MG30) based polymer electrolytes. In *Business, Engineering and Industrial Applications (ISBEIA), 2012 IEEE Symposium on* (pp. 705-708). IEEE.
- Żukowska, G., Rogowska, M., Wojda, A., Zygadło-Monikowska, E., Florjańczyk, Z., & Wieczorek, W. (2000). The effect of solvent and proton donor type on the conductivity and physico-chemical properties of poly (vinylidene fluoride)-based proton-conducting gel electrolytes. *Solid State Ionics*, 136, 1205-1209.

**REFEREES FOR THE PERTANIKA
JOURNAL OF SCIENCE AND TECHNOLOGY**

VOL. 25 (S) MAR. 2017
Special Edition

Advances in Science & Technology

The Editorial Board of the Journal of Science and Technology wishes to thank the following:

Affa Rozana Abdul Rashid
(USIM, Malaysia)

Afdalina Tumian
(IIUM, Malaysia)

Ahmad Faris Mohd Adnan
(UM, Malaysia)

Ahmad Nasser Mohd Rose
(UMP, Malaysia)

Aidah Jumahat
(UiTM, Malaysia)

Ainun Rahmahwati Ainuddin
(UTHM, Malaysia)

Amimah Ujir
(UNIMAS, Malaysia)

Anizah Kalam
(UiTM, Malaysia)

Baljit Singh Bhathal Singh
(UiTM, Malaysia)

Dzun Noraini Jimat
(UiTM, Malaysia)

Fatimah Denan
(USM, Malaysia)

Gabriele Anisah Froemming
(University of Waterloo, Canada)

Hairul Azman
(UNIMAS, Malaysia)

Haris Ahmad Israr Ahmad
(UTM, Malaysia)

Harlina Ahmad
(USM, Malaysia)

Hollena Nori
(UNIMAS, Malaysia)

Irfan Hilmy
(IIUM, Malaysia)

Ismail Musirin
(UiTM, Malaysia)

Jeff Hovis
(University of Waterloo, Canada)

Kah Guan Au Eong
(Mount Elizabeth Medical Centre, Singapore)

Kausalyah Venkatasoon
(UiTM, Malaysia)

Mohammad Isa Mohamadin
(UiTM, Malaysia)

Mohd Afian Omar
(SIRIM Berhad, Malaysia)

Mohd Asri Mansor
(UiTM, Malaysia)

Mohd Rozi Ahmad
(UiTM, Malaysia)

Mohd Sukeri Mohd Yusof
(UMT, Malaysia)

Nafisah Mohd Isa @ Osman
(UiTM, Malaysia)

Noor Fitrah Abu Bakar
(UiTM, Malaysia)

Noordini Mohamad Salleh
(UM, Malaysia)

Noorhaniza Wahid
(UTHM, Malaysia)

Nor Fazli Adull Manan
(UiTM, Malaysia)

Noraini Wahab
(UiTM, Malaysia)

Norashikin Yusof
(UiTM, Malaysia)

Noreffendy Tamaldin
(UTeM, Malaysia)

Norizzah Abd Rashid
(UiTM, Malaysia)

Nurin Wahidah Mohd Zulkifli
(UM, Malaysia)

Rohana Hassan
(UiTM, Malaysia)

Sarina Sulaiman
(IIUM, Malaysia)

Shahrani Shahbudin
(UiTM, Malaysia)

Siti Amira Othman
(UTHM, Malaysia)

Soon Kong Yong
(UiTM, Malaysia)

Suhaimi Abdul Latif
(IIUM, Malaysia)

Suraya Hani Adnan
(UTHM, Malaysia)

Sushil Kumar R. Vasudevan
(UiTM, Malaysia)

Syahariza Zainul Abidin
(USM, Malaysia)

Syahidah Akmal Muhammad
(USM, Malaysia)

Tay Chia Chay
(UiTM, Malaysia)

Tengku Ahmad Damitri Al Astani Tengku Di
(USM, Malaysia)

Wan Emri Wan Abdul Rahman
(UiTM, Malaysia)

Zahurin Halim
(IIUM, Malaysia)

IIUM - International Islamic University of Malaysia
SIRIM - Scientific and Industrial Research Institute of Malaysia
UiTM - Universiti Teknologi MARA
UM - Universiti Malaya
UMP - Universiti Malaysia Pahang
UMT - Universiti Malaysia Terengganu

UNIMAS - Universiti Malaysia Sarawak
USIM - Universiti Sains Islam Malaysia
USM - Universiti Sains Malaysia
UTeM - Universiti Teknikal Malaysia Melaka
UTHM - Universiti Tun Hussein Onn Malaysia

While every effort has been made to include a complete list of referees for the period stated above, however if any name(s) have been omitted unintentionally or spelt incorrectly, please notify the Chief Executive Editor, *Pertanika* Journals at nayan@upm.my.

Any inclusion or exclusion of name(s) on this page does not commit the *Pertanika* Editorial Office, nor the UPM Press or the University to provide any liability for whatsoever reason.

Pertanika Journals

Our goal is to bring high quality research to the widest possible audience

INSTRUCTIONS TO AUTHORS (Manuscript Preparation & Submission Guide)

Revised: June 2016

Please read the Pertanika guidelines and follow these instructions carefully. Manuscripts not adhering to the instructions will be returned for revision without review. The Chief Executive Editor reserves the right to return manuscripts that are not prepared in accordance with these guidelines.

MANUSCRIPT PREPARATION

Manuscript Types

Pertanika accepts submission of mainly **four** types of manuscripts for peer-review.

1. REGULAR ARTICLE

Regular articles are full-length original empirical investigations, consisting of introduction, materials and methods, results and discussion, conclusions. Original work must provide references and an explanation on research findings that contain new and significant findings.

Size: Generally, these are expected to be between 6 and 12 journal pages (excluding the abstract, references, tables and/or figures), a maximum of 80 references, and an abstract of 100–200 words.

2. REVIEW ARTICLE

These report critical evaluation of materials about current research that has already been published by organizing, integrating, and evaluating previously published materials. It summarizes the status of knowledge and outline future directions of research within the journal scope. Review articles should aim to provide systemic overviews, evaluations and interpretations of research in a given field. Re-analyses as meta-analysis and systemic reviews are encouraged. The manuscript title must start with "Review Article:".

Size: These articles do not have an expected page limit or maximum number of references, should include appropriate figures and/or tables, and an abstract of 100–200 words. Ideally, a review article should be of 7 to 8 printed pages.

3. SHORT COMMUNICATIONS

They are timely, peer-reviewed and brief. These are suitable for the publication of significant technical advances and may be used to:

- (a) report new developments, significant advances and novel aspects of experimental and theoretical methods and techniques which are relevant for scientific investigations within the journal scope;
- (b) report/discuss on significant matters of policy and perspective related to the science of the journal, including 'personal' commentary;
- (c) disseminate information and data on topical events of significant scientific and/or social interest within the scope of the journal.

The manuscript title must start with "*Brief Communication:*".

Size: These are usually between 2 and 4 journal pages and have a maximum of three figures and/or tables, from 8 to 20 references, and an abstract length not exceeding 100 words. Information must be in short but complete form and it is not intended to publish preliminary results or to be a reduced version of Regular or Rapid Papers.

4. OTHERS

Brief reports, case studies, comments, concept papers, Letters to the Editor, and replies on previously published articles may be considered.

PLEASE NOTE: NO EXCEPTIONS WILL BE MADE FOR PAGE LENGTH.

Language Accuracy

Pertanika **emphasizes** on the linguistic accuracy of every manuscript published. Articles must be in **English** and they must be competently written and argued in clear and concise grammatical English. Contributors are strongly advised to have the manuscript checked by a colleague with ample experience in writing English manuscripts or a competent English language editor.

Author(s) **must provide a certificate** confirming that their manuscripts have been adequately edited. A proof from a recognised editing service should be submitted together with the cover letter at the time of submitting a manuscript to Pertanika. **All editing costs must be borne by the author(s)**. This step, taken by authors before submission, will greatly facilitate reviewing, and thus publication if the content is acceptable.

Linguistically hopeless manuscripts will be rejected straightaway (e.g., when the language is so poor that one cannot be sure of what the authors really mean). This process, taken by authors before submission, will greatly facilitate reviewing, and thus publication if the content is acceptable.

MANUSCRIPT FORMAT

The paper should be submitted in one column format with at least 4cm margins and 1.5 line spacing throughout. Authors are advised to use Times New Roman 12-point font and *MS Word* format.

1. Manuscript Structure

Manuscripts in general should be organised in the following order:

Page 1: Running title

This page should **only** contain the running title of your paper. The running title is an abbreviated title used as the running head on every page of the manuscript. The running title should not exceed 60 characters, counting letters and spaces.

Page 2: Author(s) and Corresponding author information.

This page should contain the **full title** of your paper not exceeding 25 words, with name(s) of all the authors, institutions and corresponding author's name, institution and full address (Street address, telephone number (including extension), hand phone number, and e-mail address) for editorial correspondence. First and corresponding authors must be clearly indicated.

The names of the authors may be abbreviated following the international naming convention. e.g. Salleh, A.B.¹, Tan, S.G^{2*}., and Sapuan, S.M³.

Authors' addresses. Multiple authors with different addresses must indicate their respective addresses separately by superscript numbers:

George Swan¹ and Nayan Kanwal²

¹Department of Biology, Faculty of Science, Duke University, Durham, North Carolina, USA.,

²Office of the Deputy Vice Chancellor (R&I), Universiti Putra Malaysia, Serdang, Malaysia.

A **list** of number of **black and white / colour figures and tables** should also be indicated on this page. Figures submitted in color will be printed in colour. See "5. Figures & Photographs" for details.

Page 3: Abstract

This page should **repeat** the **full title** of your paper with only the **Abstract** (the abstract should be less than 250 words for a Regular Paper and up to 100 words for a Short Communication), and **Keywords**.

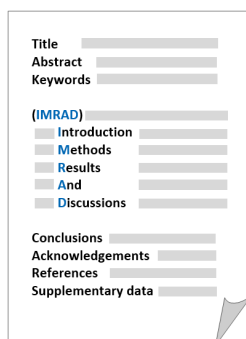
Keywords: Not more than eight keywords in alphabetical order must be provided to describe the contents of the manuscript.

Page 4: Introduction

This page should begin with the **Introduction** of your article and followed by the rest of your paper.

2. Text

Regular Papers should be prepared with the headings *Introduction, Materials and Methods, Results and Discussion, Conclusions, Acknowledgements, References, and Supplementary data* (if available) in this order.



Title _____
 Abstract _____
 Keywords _____
 (IMRAD)
 Introduction _____
 Methods _____
 Results _____
 And _____
 Discussions _____
 Conclusions _____
 Acknowledgements _____
 References _____
 Supplementary data _____

MAKE YOUR ARTICLES AS CONCISE AS POSSIBLE

Most scientific papers are prepared according to a format called IMRAD. The term represents the first letters of the words Introduction, Materials and Methods, Results, And, Discussion. It indicates a pattern or format rather than a complete list of headings or components of research papers; the missing parts of a paper are: Title, Authors, Keywords, Abstract, Conclusions, and References. Additionally, some papers include Acknowledgments and Appendices.

The Introduction explains the scope and objective of the study in the light of current knowledge on the subject; the Materials and Methods describes how the study was conducted; the Results section reports what was found in the study; and the Discussion section explains meaning and significance of the results and provides suggestions for future directions of research. The manuscript must be prepared according to the Journal's instructions to authors.

3. Equations and Formulae

These must be set up clearly and should be typed double spaced. Numbers identifying equations should be in square brackets and placed on the right margin of the text.

4. Tables

All tables should be prepared in a form consistent with recent issues of Pertanika and should be numbered consecutively with Roman numerals. Explanatory material should be given in the table legends and footnotes. Each table should be prepared on a new page, embedded in the manuscript.

When a manuscript is submitted for publication, tables must also be submitted separately as data - .doc, .rtf, Excel or PowerPoint files- because tables submitted as image data cannot be edited for publication and are usually in low-resolution.

5. Figures & Photographs

Submit an **original** figure or photograph. Line drawings must be clear, with high black and white contrast. Each figure or photograph should be prepared on a new page, embedded in the manuscript for reviewing to keep the file of the manuscript under 5 MB. These should be numbered consecutively with Roman numerals.

Figures or photographs must also be submitted separately as TIFF, JPEG, or Excel files- because figures or photographs submitted in low-resolution embedded in the manuscript cannot be accepted for publication. For electronic figures, create your figures using applications that are capable of preparing high resolution TIFF files. In general, we require **300 dpi** or higher resolution for **coloured and half-tone artwork**, and **1200 dpi or higher** for **line drawings** are required.

Failure to comply with these specifications will require new figures and delay in publication.

NOTE: Illustrations may be produced in colour at no extra cost at the discretion of the Publisher; the author could be charged Malaysian Ringgit 50 for each colour page.

6. References

References begin on their own page and are listed in alphabetical order by the first author's last name. Only references cited within the text should be included. All references should be in 12-point font and double-spaced.

NOTE: When formatting your references, please follow the **APA reference style** (6th Edition). Ensure that the references are strictly in the journal's prescribed style, failing which your article will **not be accepted for peer-review**. You may refer to the *Publication Manual of the American Psychological Association* for further details (<http://www.apastyle.org/>).

7. General Guidelines

Abbreviations: Define alphabetically, other than abbreviations that can be used without definition. Words or phrases that are abbreviated in the introduction and following text should be written out in full the first time that they appear in the text, with each abbreviated form in parenthesis. Include the common name or scientific name, or both, of animal and plant materials.

Acknowledgements: Individuals and entities that have provided essential support such as research grants and fellowships and other sources of funding should be acknowledged. Contributions that do not involve researching (clerical assistance or personal acknowledgements) should **not** appear in acknowledgements.

Authors' Affiliation: The primary affiliation for each author should be the institution where the majority of their work was done. If an author has subsequently moved to another institution, the current address may also be stated in the footer.

Co-Authors: The commonly accepted guideline for authorship is that one must have substantially contributed to the development of the paper and share accountability for the results. Researchers should decide who will be an author and what order they will be listed depending upon their order of importance to the study. Other contributions should be cited in the manuscript's Acknowledgements.

Copyright Permissions: Authors should seek necessary permissions for quotations, artwork, boxes or tables taken from other publications or from other freely available sources on the Internet before submission to Pertanika. Acknowledgement must be given to the original source in the illustration legend, in a table footnote, or at the end of the quotation.

Footnotes: Current addresses of authors if different from heading may be inserted here.

Page Numbering: Every page of the manuscript, including the title page, references, tables, etc. should be numbered.

Spelling: The journal uses American or British spelling and authors may follow the latest edition of the Oxford Advanced Learner's Dictionary for British spellings.

SUBMISSION OF MANUSCRIPTS

Owing to the volume of manuscripts we receive, we must insist that all submissions be made electronically using the **online submission system ScholarOne™**, a web-based portal by Thomson Reuters. For more information, go to our web page and [click "Online Submission"](#).

Submission Checklist

1. **MANUSCRIPT:** Ensure your MS has followed the Pertanika style particularly the first four pages as explained earlier. The article should be written in a good academic style and provide an accurate and succinct description of the contents ensuring that grammar and spelling errors have been corrected before submission. It should also not exceed the suggested length.

COVER LETTER: All submissions must be accompanied by a cover letter detailing what you are submitting. Papers are accepted for publication in the journal on the understanding that the article is **original** and the content has **not been published** either **in English** or **any other language(s)** or **submitted for publication elsewhere**. The letter should also briefly describe the research you are reporting, why it is important, and why you think the readers of the journal would be interested in it. The cover letter must also contain an acknowledgement that all authors have contributed significantly, and that all authors have approved the paper for release and are in agreement with its content.

The cover letter of the paper should contain (i) the title; (ii) the full names of the authors; (iii) the addresses of the institutions at which the work was carried out together with (iv) the full postal and email address, plus telephone numbers and emails of all the authors. The current address of any author, if different from that where the work was carried out, should be supplied in a footnote.

The above must be stated in the cover letter. Submission of your manuscript will not be accepted until a cover letter has been received.

2. **COPYRIGHT:** Authors publishing the Journal will be asked to sign a copyright form. In signing the form, it is assumed that authors have obtained permission to use any copyrighted or previously published material. All authors must read and agree to the conditions outlined in the form, and must sign the form or agree that the corresponding author can sign on their behalf. Articles cannot be published until a signed form (*original pen-to-paper signature*) has been received.

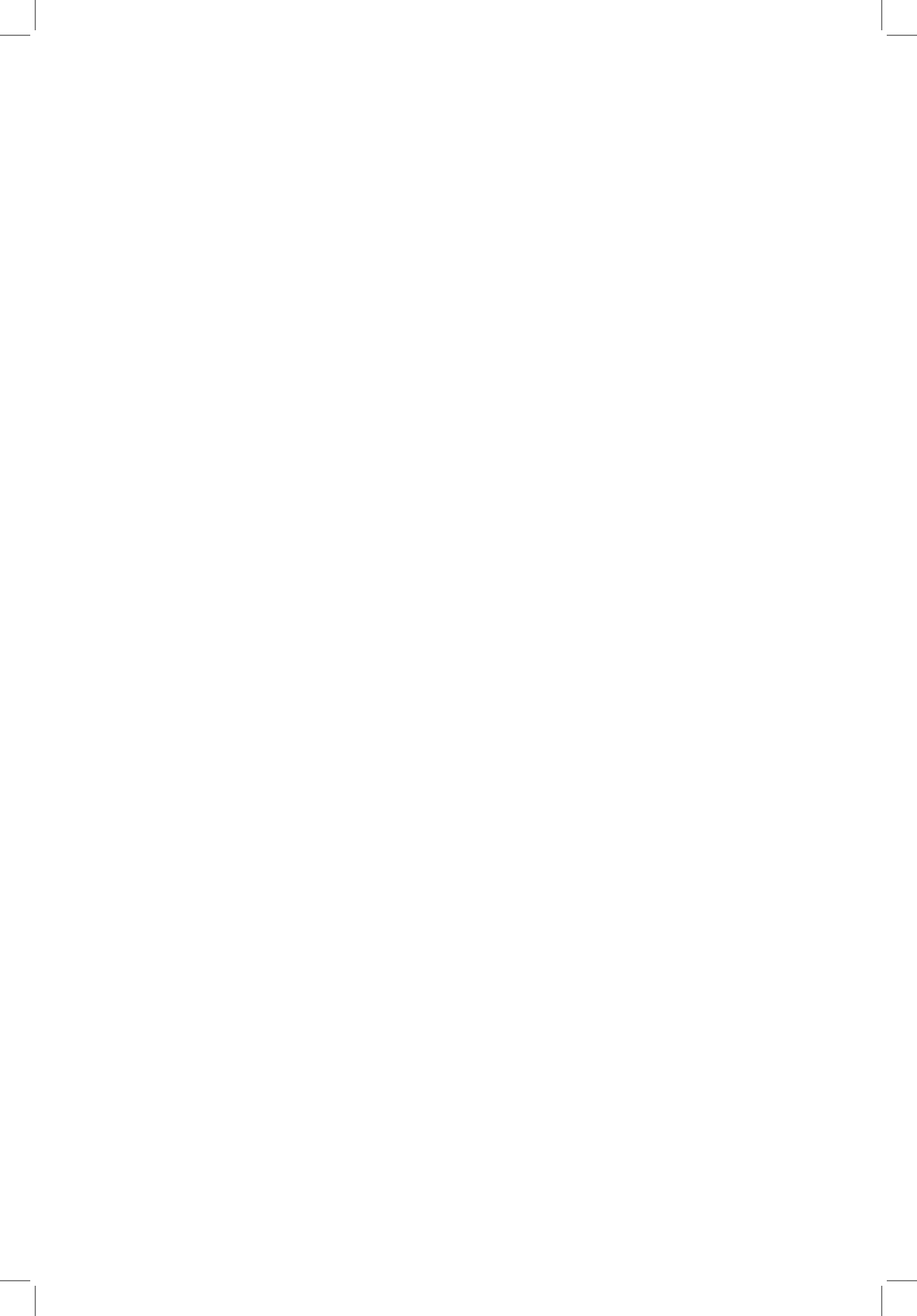
Please do **not** submit manuscripts to the editor-in-chief or to any other office directly. Any queries must be directed to the **Chief Executive Editor's** office via email to nayan@upm.my.

Visit our Journal's website for more details at <http://www.pertanika.upm.edu.my/home.php>.

HARDCOPIES OF THE JOURNALS AND OFF PRINTS

Under the Journal's open access initiative, authors can choose to download free material (via PDF link) from any of the journal issues from Pertanika's website. Under "**Browse Journals**" you will see a link, "*Current Issues*" or "*Archives*". Here you will get access to all current and back-issues from 1978 onwards.

The **corresponding author** for all articles will receive one complimentary hardcopy of the journal in which his/her articles is published. In addition, 20 off prints of the full text of their article will also be provided. Additional copies of the journals may be purchased by writing to the Chief Executive Editor.



Why should you publish in

Pertanika?

BENEFITS TO AUTHORS

PROFILE: Our journals are circulated in large numbers all over Malaysia, and beyond in Southeast Asia. Our circulation covers other overseas countries as well. We ensure that your work reaches the widest possible audience in print and online, through our wide publicity campaigns held frequently, and through our constantly developing electronic initiatives such as Web of Science Author Connect backed by Thomson Reuters.

QUALITY: Our journals' reputation for quality is unsurpassed ensuring that the originality, authority and accuracy of your work are fully recognised. Each manuscript submitted to Pertanika undergoes a rigid originality check. Our double-blind peer refereeing procedures are fair and open, and we aim to help authors develop and improve their scientific work. Pertanika is now over 38 years old; this accumulated knowledge has resulted in our journals being indexed in SCOPUS (Elsevier), Thomson (ISI) Web of Science™ Core Collection, Emerging Sources Citation Index (ESCI), Web of Knowledge [BIOSIS & CAB Abstracts], EBSCO, DOAJ, ERA, AGRICOLA, Google Scholar, ISC, TIB, Journal Guide, Citefactor, Cabell's Directories and MyCite.

AUTHOR SERVICES: We provide a rapid response service to all our authors, with dedicated support staff for each journal, and a point of contact throughout the refereeing and production processes. Our aim is to ensure that the production process is as smooth as possible, is borne out by the high number of authors who prefer to publish with us.

CODE OF ETHICS: Our Journal has adopted a Code of Ethics to ensure that its commitment to integrity is recognized and adhered to by contributors, editors and reviewers. It warns against plagiarism and self-plagiarism, and provides guidelines on authorship, copyright and submission, among others.

PRESS RELEASES: Landmark academic papers that are published in Pertanika journals are converted into press-releases as a unique strategy for increasing visibility of the journal as well as to make major findings accessible to non-specialist readers. These press releases are then featured in the university's UK and Australian based research portal, ResearchSEA, for the perusal of journalists all over the world.

LAG TIME: The elapsed time from submission to publication for the articles averages 3 to 4 months. A decision on acceptance of a manuscript is reached in 3 to 4 months (average 14 weeks).



Address your submissions to:
The Chief Executive Editor
Tel: +603 8947 1622
nayan@upm.my

Journal's Profile: www.pertanika.upm.edu.my/

Call for Papers 2017-18

now accepting submissions...

Pertanika invites you to explore frontiers from all key areas of agriculture, science and technology to social sciences and humanities.

Original research and review articles are invited from scholars, scientists, professors, post-docs, and university students who are seeking publishing opportunities for their research papers through the Journal's three titles; JTAS, JST & JSSH. Preference is given to the work on leading and innovative research approaches.

Pertanika is a fast track peer-reviewed and open-access academic journal published by Universiti Putra Malaysia. To date, Pertanika Journals have been indexed by many important databases. Authors may contribute their scientific work by publishing in UPM's hallmark SCOPUS & ISI indexed journals.

Our journals are open access - international journals. Researchers worldwide will have full access to all the articles published online and be able to download them with zero subscription fee.

Pertanika uses online article submission, review and tracking system for quality and quick review processing backed by Thomson Reuter's ScholarOne™. Journals provide rapid publication of research articles through this system.

For details on the Guide to Online Submissions, please visit http://www.pertanika.upm.edu.my/guide_online_submission.php

About the Journal

Pertanika is an international multidisciplinary peer-reviewed leading journal in Malaysia which began publication in 1978. The journal publishes in three different areas — Journal of Tropical Agricultural Science (JTAS); Journal of Science and Technology (JST); and Journal of Social Sciences and Humanities (JSSH). All journals are published in English.

JTAS is devoted to the publication of original papers that serves as a forum for practical approaches to improving quality in issues pertaining to tropical agricultural research- or related fields of study. It is published four times a year in *February, May, August* and *November*.

JST caters for science and engineering research- or related fields of study. It is published twice a year in *January* and *July*.

JSSH deals in research or theories in social sciences and humanities research. It aims to develop as a flagship journal with a focus on emerging issues pertaining to the social and behavioural sciences as well as the humanities, particularly in the Asia Pacific region. It is published four times a year in *March, June, September* and *December*.



An Award-winning
International-Malaysian Journal
— CREAM AWARD, MoHE
—Sept 2015



SURF Based 3D Object Recognition for Robot Hand Grasping <i>Nurul Hanani Remeli, Ruhizan Liza Ahmad Shauri, Faieza Hanum Yahaya, Norshariza Mohd Salleh, Khairunnisa Nasir and Ahmad Ihsan Mohd Yassin</i>	287
EIS and DFT Investigations on Corrosion Inhibition of Imines containing Mono- and Diisatin Moieties <i>Aliyin Abdul Ghani, Hadariah Bahron, Mohamad Kamal Harun, Karimah Kassim and El Hassane Anouar</i>	297
Synthesis and characterisation of Mononuclear and Tetranuclear Zinc(II) Complexes of Schiff Bases Derived from Phenylenediamine <i>Hadariah Bahron, Siti Solihah Khaidir, Amalina Mohd Tajuddin and Syed Abdul Illah Alyahya Syed Abd Kadir</i>	309
Corrosion Inhibition of Azomethines Containing Hydroxyl Group at <i>Ortho</i> and <i>Para</i> Positions on Mild Steel <i>Syaidah Athirah Dzolin, Yusairie Mohd, Hadariah Bahron and Nurul Huda Abdul Halim</i>	317
Assessment of the Genetic Variability and Fibre Composition of Gamma Ray induced Mutant Lines of Ginger (<i>Zingiber officinale</i> Roscoe) <i>Nor Yuzliza Kamaruddin and Shamsiah Abdullah</i>	325
Development of Palm Oil Extraction Performance Index (EPI) Based on Oil Extraction Rate (OER) and Oil Loss (OL) <i>Julia Andrew, Alawi Sulaiman, Mohd Noriznan Mokhtar, Azhari Samsu Baharuddin and Norzaidi Mohd Daud</i>	335
Chromatographic Fingerprint and Chemometric Approach for Quality Control of Tongkat Ali (<i>Eurycoma longifolia</i>) <i>Nor Nasriah Zaini, Mardiana Saaid, Hafizan Juahir and Rozita Osman</i>	345
Optimisation of Distributed Generation Unit Using Particle Swarm Optimisation Method and Voltage Stability Indicator <i>Aimi Iznina Ahameed Tarmizi, Roslina Mohamad, Saiful Izwan Suliman and Murizah Kassim</i>	355
Electrical Properties of Plasticised Proton Conducting MG49 Polymer Electrolyte <i>Zaidatul Salwa Mahmud, Siti Nor Hafiza Mohd Yusoff, Nur Hamizah Mohd Zaki, Mohamad Fariz Mohamad Taib, Mohamad Kamil Yaakob, Oskar Hasdinor Hassan and Ab Malik Marwan Ali</i>	363

Physical and Conductivity Studies of Plasticised Methyl Cellulose-Lithium Triflate based Polymer Electrolyte <i>Nursyahida Sahli, Nordiana Nabilla Ramly, Muhd Zu Azhan Yahya and Ab Malik Marwan Ali</i>	183
The Effect of Saccharin Concentration on the Electrochemical Behaviour of Electrodeposited Nanocrystalline Cobalt-Iron Coating <i>Nik Rozlin Nik Masdek, Wan Muhammad Aniq Aiman, Mardziah Che Murad, Zuraidah Salleh and Koay Mei Hye</i>	191
Wear Properties of Carbon Nanotubes Filled Epoxy Polymers and Woven Glass Fiber Reinforced Polymer Composites <i>Anis Adilah Abu Talib, Aidah Jumahat, Napisah Sapiai and Ahmad Shahrul Mohd Roslan</i>	201
Effect of Acid and Silane Treated Carbon Nanotubes on Wear Properties of Epoxy Polymer Composite <i>Aidah Jumahat, Napisah Sapiai and Eliya Farah Hana Mohd Kamal</i>	213
Mechanical Behaviour and Microstructure Aluminium Foam Tube Produce (AFTP) Using Infiltration Method with Vacuum- Gas <i>Ismail Lias, Muhammad Hussain Ismail, Iskandar Dzulkernain Md Raffee and Mohd Aman Ihsan Mamat</i>	223
Analysis of Fill Time and Injection Pressure of Multiple 20 gram Parisons during Injection Moulding Process <i>Najiy Rizal Suriani Rizal, Azuddin Mamat and Aidah Jumahat</i>	233
Fuzzy Lambda-Max Criteria Weight Determination for Feature Selection in Clustering <i>Nurul Adzlyana Mohd Saadon, Rosma Mohd Dom and Nurazzah Abd Rahman</i>	241
Green Lean TQM Islamic Management Practices in Malaysian Food Companies <i>Nur Asiah Kuzaiman, Argustina Zainuddin, Nor Azlina Mohd Salleh and Salmiah Kasolang</i>	255
GPU Implementation of Sub-Iris Technique in Iris Recognition System <i>Shahrizan Jamaludin, Nasharuddin Zainal and W. Mimi Diyana W. Zaki</i>	263
Adaptive Particle Swarm Optimisation for Solving Non-Convex Economic Dispatch Problems <i>Nurhafizah Jamain, Ismail Musirin, Mohd Helmi Mansor, Muhammad Murtadha Othman and Siti Aliyah Mohd Salleh</i>	275

Correlation of Case Depth with Mechanical Properties of Low Carbon Steel Using Paste Carburizing Method <i>Bulan Abdullah, Muhammad Hafizuddin Jumadin, Muhammad Hussain Ismail, Siti Khadijah Alias and Samsiah Ahmad</i>	91
Effects of Two Cycle Heat Treatment on the Microstructure and Hardness of Ductile Iron <i>Mohd Faizul Idham, Bulan Abdullah and Khalissah Muhammad Yusof</i>	99
Ferroelectric Stability of Annealed PVDF-TrFE Thin Film Incorporated with MgO Nanofillers <i>Mohamad Hafiz Mohd Wahid, Rozana Mohd Dahan, Adillah Nurashikin Arshad, Habibah Zulkefle, Siti Zaleha Sa'ad, Mohamad Rusop Mahmood, W. C. Gan and Wan Haliza Abd. Majid</i>	107
Occurrence, Source Apportionment and Environmental Risk Assessment of Pharmaceuticals in Klang River, Malaysia <i>Siti Norbayu Mohd. Subari, Rozita Osman and Norashikin Saim</i>	119
Adsorption of Acid Dyes onto Zinc Chloride-Modified Cocoa (<i>Theobroma cacao</i>) Pod Husk-Based Carbon <i>Nur Aqilah Zainal, Shariff Ibrahim and Borhannuddin Arifin</i>	129
New Method of Curve Number Derivation with Inferential Statistics <i>Lloyd Ling, Zulkifli Yusop and Yuk Feng Huang</i>	139
Discrepancy in the Accuracy of Vision Screening Program Performed by Allied Health Personnel in a Preschool <i>Nurul Farhana Abu Bakar and Ai-Hong Chen</i>	151
Effect of Blood Cockle Shell and Palm Kernel Shell Weight Ratio on the Acid Neutralizing Capacity of Calcined Products <i>Noor Mohamad Amin Salleh, Dayangku Kamilah Pengiran Ismail and Yong Soon Kong</i>	159
Optimization of Headspace Solid Phase Microextraction (HS-SPME) for the Extraction of Volatile Organic Compounds (VOCs) in Mangoes (<i>Harumanis</i> cv.) Using 2 Stages Multivariate Analysis <i>Siti Raihan Zakaria, Ruziyati Tajuddin, Rozita Osman, Norashikin Saim and Mardiana Saaid</i>	167
Optimisation of Pressurised Liquid Extraction of Bioactive Compounds from <i>Ananas comosus</i> (Pineapple) Fruit <i>Almie Amira Munaras Khan, Norashikin Saim and Rossuriati Dol Hamid</i>	174

Contents

Advances in Science and Technology Research

- Ganoderma boninense* Efficacy in Delignifying Oil Palm Empty Fruit Bunches 1
Siti Sarah Jumali and Shaleha Ismail
- Numerical Study of Aerodynamic Characteristics on Blended Wing Body Aircraft with Small Canard 9
Zurriati Mohd Ali, Wahyu Kuntjoro, Wirachman Wisnoe, Rizal Effendy Mohd Nasir and Noor Iswadi Ismail
- Investigation on Moisture Susceptibility and Rutting Resistance of Asphalt Mixtures incorporating Nanosilica Modified Binder 19
Ahmad Kamil Arshad, Khairil Azman Masri, Juraidah Ahmad and Mohamad Saifullah Samsudin
- Mechanism of Aloe Emodin-Induced Apoptosis in ER+-Breast Cancer Cells, MCF-7 31
Indah Mohd Amin, Siti Hamimah Sheikh Abdul Kadir, Mohamad Rodi Isa, Nik Mohd Mazuan Nik Mohd Rosdy and Narimah Abdul Hamid Hasani
- Anti- Oral Ulcer Activity of *Ficus deltoidea* Leaves Extract on Animal Model 41
Vivi Noryati Ahmad and Indah Mohd Amin
- Comparison of Energy and Performance from Biodegradation of Freeze Dried and Spray Dried Algae Biomass 53
Muhamad Haikal Zainal, Khairul Baqir Alkhair Khairul Amin, Oskar Hasdinor Hassan, Sharifah Aminah Syed Mohamad, Abd Malik Marwan Ali, Fathiah Abdullah and Muhd Zu Azhan Yahya
- The Effects of Automotive Windscreen Glass Waste Powder (WGWP) On Strength Performance of Cement Mortar 63
Nik Anisah Nik Ngah, Mohamad Awang and Kartini Kamaruddin
- Preliminary Study of Cosmetic Coloured Contact Lenses Chemical Elements Analysis using Energy Dispersive X-Ray Spectroscopy 73
Syazwan Hafiz Mohd, Wan Elhami Wan Omar and Ai-Hong Chen
- Microstructure, Microhardness and Density of Shot Blasting and Paste Boronizing on 316L Stainless Steel 83
Muhamad Hafizuddin Mohamad Basir, Mohd Faizul Idham, Bulan Abdullah and Muhammad Hussain Ismail



Pertanika Editorial Office, Journal Division
Office of the Deputy Vice Chancellor (R&I),
1st Floor, IDEA Tower II,
UPM-MTDC Technology Centre
Universiti Putra Malaysia
43400 UPM Serdang
Selangor Darul Ehsan
Malaysia

<http://www.pertanika.upm.edu.my/>
E-mail: executive_editor.pertanika@upm.my
Tel: +603 8947 1622/1620

PENERBIT
UPM
UNIVERSITI PUTRA MALAYSIA
PRESS

<http://penerbit.upm.edu.my>
E-mail : penerbit@putra.upm.edu.my
Tel : +603 8946 8855/8854
Fax : +603 8941 6172

